Best Available Copy for all Pictures

AD-766 030

MIXING AND COMBUSTION PROCESSES IN
JET ENGINES

A. G. Prudnikov, et al

Foreign Technology Division
Wright-Patterson Air Force Base, Ohio

5 July 1973

FOREIGN TECHNOLOGY DIVISION

MIXING AND COMBUSTION PROCESSES IN JET ENGINES

by

A. G. Prudnikov, M. S. Volynskiy
V. N. Sagalovich

D D C

SEP 11 1973

B

Approved for public release;
distribution unlimited.

551

DOCUMENT CONTROL DATA - R & D

(Security classification of title, body of abstract and indexing annotation must be entered when the overall report is classified)

1. ORIGINATING ACTIVITY *(Corporate author)*	2a. REPORT SECURITY CLASSIFICATION
Foreign Technology Division Air Force Systems Command U. S. Air Force	UNCLASSIFIED
	2b. GROUP

3. REPORT TITLE

MIXING AND COMBUSTION PROCESSES IN JET ENGINES

4. DESCRIPTIVE NOTES *(Type of report and inclusive dates)*

Translation

5. AUTHOR(S) *(First name, middle initial, last name)*

A. G. Prudnikov, M. S. Volynskiy, V. N. Sagalovich

6. REPORT DATE	7a. TOTAL NO. OF PAGES	7b. NO. OF REFS
1971	538	174

8a. CONTRACT OR GRANT NO.	9a. ORIGINATOR'S REPORT NUMBER(S)
b. PROJECT NO. AAHO	FTD-HC-23-1339-72
c.	9b. OTHER REPORT NO(S) *(Any other numbers that may be assigned this report)*
d.	

10. DISTRIBUTION STATEMENT

Approved for public release; distribution unlimited.

11. SUPPLEMENTARY NOTES	12. SPONSORING MILITARY ACTIVITY
	Foreign Technology Division Wright-Patterson AFB, Ohio

13. ABSTRACT

EDITED TRANSLATION

MIXING AND COMBUSTION PROCESSES IN JET ENGINES

By: A. G. Prudnikov, M. S. Volynskiy,
V. N. Sagalovich

English pages: 537

Source: Protsessy Smeseobrazovaniya i goreniya v
Vozdushno-Reaktivnykh 1971, pp. 1-356

Country of Origin: USSR

Translated Under: F33657-72-D-0853

Requester: FTD/PDTA

Approved for public release;
distribution unlimited.

Details of illustrations in
this document may be better
studied on microfiche

ia

Mixing and Combustion Processes in Jet Engines. A. G. Prudnikov, M. S. Volynskiy and V. N. Sagalovich. "Mashinostroyeniye," Moscow, 1971. 356 pp.

The book consists of two parts.

Part One is concerned principally with the physics of the inter-action of droplets or solid particles with a gas stream in the presence of heat and mass exchange and with the influence of these factors on the characteristics of the engine. The problems of liquid injection (the basic parameters of the fuel-supply system and methods of measurement) are considered, dimensionless relationships are cited for spray spectra in a supersonic stream, and ranges and vaporizabilities in fuel sprays are determined.

Part Two describes the process of turbulent mixing for various boundary conditions with or without evolution of heat on the basis of a consistent method of calculation; the relationships obtained can be used to calculate turbulent mixing in the cases of free jet, jet at a wall, a jet in a nozzle, etc.

Generalizing empirical relationships are given for the dispersion of the jet on the initial and the main sections as a function of the initial conditions (ratio of velocities and densities, Mach number, etc.).

Analytical relations that determine the temperature and velocity profiles in a turbulent flame jet and the completeness of physical combustion of the fuel are derived, with a discussion of examples in which model combustion chambers are designed for rocket-ramjet engines with a single fuel jet or grouped delivery of fuel jets in the gaseous state.

The book is intended for scientific workers and engineers in the aviation industry, but may also be found useful by students in senior courses and graduate students at the higher educational institutions who are specializing in the field of turbulent flow with phase transitions and reactions.

With 10 tables, 205 illustrations, and a bibliography of 171 references.

Reviewer: Doctor of Technical Sciences, V. S. Zuyev

FOREWORD

The present volume consists of two parts.

Part One, which was written by M. S. Volynskiy, is concerned with mixing in sprays of liquids and the laws of two-phase flow.

Chapter I is devoted to the theory of one-dimensional two-phase flow with vaporization. The method proposed takes account of the interaction of the gas and the liquid particles in the process of heat and mass transfer, and interaction that affects the elementary processes of mixing and the gasdynamics of the flow. Generalization of the calculated results on a computer yields physically and technically interesting relations, for example, for the vaporization interval and other parameters in subsonic and supersonic flows.

The results of Chapter I are used to construct the theory of the spray jet with phase transitions in supersonic flow. This theory is set forth in Chapter II and is based on dimensionless coefficient relations that have been accumulated in experimental study of injection into a stream for $M > 1$ (shapes of spray jet and shock wave, coarseness of spray).

To the best of our knowledge, this is the first such development of an approximate theory. It defines, among other things, the existence region of subcritical two-phase flow on injection into a supersonic flow. The method and approximate calculations based on this

theory indicate the possible existence of short vaporization intervals in a combustion chamber with flow at M > 1.

The results of the theory are compared with experimental data for the fuel spray and indicate satisfactory agreement.

Part Two of the book was written by A. G. Prudnikov jointly with V. N. Sagalovich, V. L. Zimont, and N. A. Zamyatina, and is devoted to turbulent-mixing processes of gases and the turbulent combustion of gaseous fuel and oxidizer components in jet engines.

Chapter I sets forth the basic physical concepts and definitions, describes models of turbulent mixing, and develops the mathematical formalism that makes it possible to calculate the turbulent mixing of flows with different parameters. The method proposed in this chapter for investigation of turbulent jets, while borrowing certain details from the theory of jets known to the reader from the works of G. N. Abramovich and L. A. Vulis, at the same time makes extensive use of the familiar results of statistical turbulent-diffusion theory.

Chapter II presents results of comparison between theory and experiment. It is shown that a broad range of problems of practical interest can be examined consistently within the framework of the proposed approach: mixing of free jets with different temperatures and densities, wall jets, problems of wake pressure, etc.

Empirical data on the diffusion parameters of turbulent jet flows that have been obtained by processing a large amount of experimental material are collected in Chapter III. Many of these data were obtained by the authors themselves, some for the first time, (mixing-homogeneity characteristics of nonisothermal jets, mixing with large pressure gradients). Knowledge of these parameters forms a sound basis for engineering calculations using the methods developed in Chapter II.

In Chapter IV, the ideas and methods set forth in the previous chapters are applied to problems of homogeneous combustion in turbulent flow.

It is shown that convective turbulent transport, which is determined by the turbulence of the free stream, is the dominant factor in the combustion zone, and that the rate of turbulent combustion at large Reynolds numbers is determined by the local structure of the turbulence.

Chapter V sets forth methods for calculation of single, open diffusion-type sprays and methods for calculating the combustion efficiency and chamber length for various combustion-process designs.

Chapter V contains specific examples of calculations for model rocket-ramjet engine chambers with single central fuel jet and for the case in which fuel is delivered in a group of jets at an angle to the main flow. It is shown that the variation of combustion efficiency as a function of various experimentally observed geometrical and physico-chemical factors can be predicted qualitatively by calculation.

NOMENCLATURE

1. Dimensionless Numbers and Quantities

M — Mach number;

Re — Reynolds number;

Nu — Nusselt number;

Pr — Prandtl number;

We — Weber number;

Fr — Froude number;

Sh — Strouhal number;

k — ratio of specific heats;

ε — intensity of turbulence $(\varepsilon = \frac{u'}{u})$;

z_v — vaporizability;

β — concentration of liquid;

c_x — drag coefficient;

c — concentration;

g — concentration by weight;

p — probability density distribution;

P — probability;

η — combustion efficiency; dynamic viscosity;

m — ratio of longitudinal velocity;

n — density ratio of two gases being mixed;

$N = \dfrac{\sigma_m}{\sigma}$ — degree of mixing homogeneity;

L_T — stoichiometric ratio;

α_T — excess-air ratio.

2. Geometric Characteristics and Time

x, y, z — Cartesian coordinates;

t, τ — time;

a — diameter of droplet or particle;

a_T — average radius of jet;

$\epsilon^2 = (y - \bar{y})^2$ — variance of turbulent transverse deflection of jet volume;

σ_m^2 — variance of microturbulent ("grey") mixing of gas volumes;

d_n — diameter of nozzle orifice;

F — cross-sectional area of flow;

x_v — interval of total vaporization;

λ — scale of dissipation; thermal conductivity coefficient;

δ — characteristic thickness of layer;

α_s — spray angle;

α_M — Mach angle;

l — characteristic length; heat of vaporization of liquid.

3. Working-Fluid Parameters

T — temperature;

ν — density;

γ — specific gravity;

p — pressure;

W — longitudinal velocity of stream in one-dimensional two-phase flow;

u, v, w — stream velocity components;

V — absolute value of average stream velocity;

$\bar{u} \approx V$ — average longitudinal velocity;

V — absolute velocity of drop;

U — relative velocity of drop;

$\sqrt{\overline{u'^2}} = u'$, $\sqrt{\overline{v'^2}} = v'$, $\sqrt{\overline{w'^2}} = w'$ — rms fluctuations of velocity components;

R — gas constant;

m — mass flow rate;

a_{sd} — sound velocity;

G_1 — flow rate of entraining stream in kg/sec (air, oxidizer, etc.);

G_2 — flow rate of jet in kg/sec;

i — enthalpy;

S, s — entropy.

4. Physical Constants

μ — molecular weight;

ν — kinematic viscosity;

σ — surface tension; pressure recovery coefficient;

D — diffusion coefficient;

c_p — heat capacity at constant pressure;

c_v — heat capacity at constant volume;

H_u — efficiency of fuel;

p_v — vapor tension.

5. Subscripts

l — liquid;

v — vapor;

1 — initial cross section of stream; 1 — parameter of entraining stream; 2 — parameter of jet;

mx — mixture of vapor and gas (air);

T — thermal, turbulent, fuel

w — wave;

a — air;

MT — microturbulent;

o — stagnation parameters;

g — gas;

c — combustion.

INTRODUCTION

The combustion chambers of jet engines, and in particular, air-breathing jet engines exist in a wide variety of designs. However, the working processes in the combustion chambers, such as atomization and mixing, turbulent diffusion, and fuel combustion have many physical essentials in common for engines of different types and are often subject to consistent relationships.

The present monograph is devoted to the physics of the working processes in the chambers and nozzles of jet engines and to the development of appropriate calculation techniques. Nevertheless, much of the material is directly or indirectly applicable to other types of reaction engines [Liquid Rocket Engine (LRE), Solid Rocket Engine (SRE), Rocket Ramjet (RRJ), and others]. The results that are submitted may also be useful for industrial boiler and firebox installations running on liquid and gaseous fuel, for anti-pollution systems used on exhaust gases and combustion products, chemical equipment, various types of cooling systems, etc. The present state of development of jet engines (JE) is characterized by more penetrating analysis of the elementary processes (atomization, vaporization, turbulent diffusion, and turbulent combustion) and by the accumulation of extensive theoretical and experimental materials.

1

On the other hand, the data obtained are being synthesized to create whole series of sometimes rather complex methods for calculation of the working process and its specific stages (two-phase flows in the chamber and nozzle, gaseous-jet flows, homogeneous combustion, diffusion combustion, etc.) using electronic computers. The extensive use of computers has made it possible to present a more accurate and complete mathematical description of the working process. It has become possible to include in the computation numerous relationships for individual elementary processes that had previously presented insurmountable computational difficulties.

A whole series of elementary processes makes its appearance when a liquid or gaseous fuel is fed into a subsonic or supersonic stream in a combustion chamber (the latter case is of interest for the chambers of hypersonic engines [1]). It is convenient from the methodological standpoint to examine them one after another. In reality, the individual processes may overlap, and sometimes they unfold simultaneously. For a number of combustion chambers used in existing JE, the initial process is mixing (Part One), whose purpose is to produce a combustible mixture with an appropriate distribution of concentrations in the chamber volume.

After delivery of the fuel by the system of atomizers, a two-phase flow makes its appearance, and vaporization takes place in it under the conditions of a complex interaction between the liquid and gaseous phases. Turbulent diffusion usually becomes the decisive process after vaporization of the bulk of the fuel. In some cases, the stages are divided among different units — atomization and vaporization may be handled in a separate generator, and diffusion of the gaseous components may occur in a mixing chamber. The process in the chamber culminates in turbulent combustion, which must take place with adequate efficiency. A similar sequence of processes is characteristic for delivery of liquid or gas into the exhaust nozzle of a jet engine to control the thrust vector or thrust.

In this respect, the present monograph takes up where a number of other works left off; we refer here in particular to [1], in which some of the authors collaborated. Here we make extensive use of computer results, rational and efficient application of which imposes high requirements on the physical model of the phenomenon that has been "built into" the computer program. For this reason, special attention is given to the construction and legitimacy of the physical models in both parts of the monograph.

Two types of two-phase flows with phase transitions (vaporization) are characteristic for the processes that take place in jet engines. They are of substantial interest from the fundamental and engineering standpoints. The first type is a flow of gas and liquid particles within a channel with various initial conditions and drop sizes. Hence, the importance of establishing relationships for the parameters at the transition through the critical regime $M_1 = 1$ when their nature changes abruptly in accordance with the inversion law of gasdynamics as it applies to phase transitions.

The second type is the more complex flow of a supersonic stream in a spray jet. Some of the difficulty of the problem is associated with finding the initial gasdynamic parameters in the frontal zone of the spray (with its high particle concentration), which usually have a decisive influence on the subsequent development of the process and determine the total-vaporization interval. These parameters (W, T, p) differ substantially from the corresponding quantities in the free stream.

The model construction for the flow in the spray and the method of determining an equivalent one-dimensional two-phase flow are used for the first time in the form in which they appear here. This makes it possible to create a closed theory of the spray jet in a supersonic stream that agrees satisfactorily with experiments.

3

The diffusion model of the mixing and burning of the gaseous turbulent-stream components makes it possible to develop a general calculation method for various problems in the internal gasdynamics of the engine.

On the basis of the relations of statistical turbulent-diffusion theory, the authors' results can be used to determine the empirical constants that appear in the well-known solutions of the semi-empirical theories for various boundary conditions.

Part 1

Mixing Processes and Two-Phase Flows

CHAPTER I

THEORY OF ONE-DIMENSIONAL FLOW OF A TWO-PHASE
MIXTURE WITH PHASE TRANSITIONS

The theory of two-phase gas flows with evaporating droplets has
recently been developed extensively in its one-dimensional idealization
for various engineering calculations. It is a further development of
the theory based on the single-drop model, which is described in
detail in the literature* [1]. It is assumed in this model that the
evaporation of the liquid particles has little influence on the
conditions of the surrounding flow, i.e., only the influence of the
gas on the drops is considered, and not that of the drops on the gas.
As a result, no account is taken of the effects of inverse variation
of the flow parameters (temperature, vapor concentration, etc.) on
the kinematics of the drop or on the rates of the phase transition.

---

*This simple scheme was found most helpful in the development of
the first jet-engine chambers.

5

The theory of two-phase flows set forth in the present chapter takes into account the interaction between the two media, i.e., the effect of heat- and mass-transfer during vaporization of the particles on the gasdynamics of the stream. It describes not only the behavior of the drops, but also the variation of the gas parameters, e.g., cooling due to evaporation, acceleration of the stream as a result of diversion of energy to entrain drops, etc. This, in turn, changes the rate of the vaporization itself.

Problems of this kind arise in the calculation of processes in numerous devices, especially those involving supersonic flows. They include delivery of fuel into a combustion chamber at M > 1 [1] two-phase flow in the exhaust nozzle of a solid-fuel engine [2], liquid injection into the supersonic section of an engine nozzle to control its thrust vector [3], injection of water to cool subsonic and supersonic streams, etc.

In general, high particle concentrations appear in real supersonic-stream spray jets (see Chapter II for greater detail) as a result of the relatively short range of liquid jets. There are segments of the flow in which the phase-interaction effect has a deci ive influence on the nature of the flow farther downstream. Significant changes in the physical constants (molecular weight, heat capacity of the gas, etc.) usually take place in a two-phase flow as a result of vapor influx and changes in the composition of the gaseous phase; they are taken into account in the corresponding equations. The present theory is, in particular, applicable to the flow of a gas with solid non-vaporizing particles (for example, in an engine exhaust nozzle). The calculation procedure then becomes much simpler.

In some of the problems posed by modern engineering, the one-dimensional flow model is found to be too crude. However, it can be used successfully in practice for flows with phase transition where the main parameter is the rate at which the transitions take place or the total-vaporization interval x_v [4].

Let us turn to a discussion of the basic assumptions adopted in construction of the two-phase flow theory.

1.   The flow is assumed to be one-dimensional, and the liquid particles are distributed uniformly throughout the volume of the gas. In each cross section of the stream, an elementary portion of vapor is mixed instantaneously and to full homogeneity with the surrounding medium.

2.   All processes are regarded as quasi-stationary, and the stationary equations of gasdynamics, heat and mass exchange, and drop motion are used. The gas is subject to the Clapeyron equation of state. Generally speaking, the theory also admits of more complex equations of state.

3.   The mixture is assumed to be monodisperse, i.e., to contain drops of equal diameter a. This constraint is not fundamental. A variant of the theory that takes into account the arbitrary particle sizes is possible. It involves increasing the number of initial equations and complication of these equations.

4.   The particles do not interact with one another and do not collide, and no coagulation takes place in the stream. The drops do not influence one another aerodynamically or thermally.* To take coagulation into account would result in unjustified complication of the model, since the role of coagulation during rapid vaporization is quite unclear at the present time (it is known that the flowoff of vapor from drops prevents them from merging).

5.   The decrease in the volume of the gas and in the cross-sectional area of the flow due to the presence of the drops is neglected, as is admissible under the flow conditions considered. This factor can be taken into account by introduction of a special shadowing factor.

---

*This applies for a distance $\delta \geq 10a$ between drops; it must be remembered that δ/a increases rapidly as the drops are vaporized.

7

6. There are no losses of energy through the walls of the channel, and no friction against the walls.

7. Chemical transformations, decomposition of vapor, and dissociation do not occur in the system.

The constraints imposed under the last two points are not mandatory. They need not be used if the law of friction against the channel walls, the heat losses, and the laws governing the chemical transformations are known.

This theory can be extended to the combustion processes of a heterogeneous mixture with consideration of heat release and the corresponding chemical reactions. In it, each fuel particle must be regarded as an isolated seat of combustion and heat source.

This generalization is possible within the framework of the present rough idealization if we have reliable relationships for the combustion of an isolated drop or solid particle in the gas stream (in particular, the laws of flame stabilization on the washed particle).

As a rule, the present chapter will not give consideration to the broad and independent field of liquid-particle combustion.

§1. Equation System of Two-Phase Flow

Let us write the system of initial equations determining the flow of a two-phase mixture in a certain channel (Figure 1.1). We shall consider the motion of gas and drops along the x axis, i.e., neglect the deviation of the streamlines and particle trajectories from the direction of the channel axis (in the case of a cylindrical pipe, these directions coincide exactly). The x coordinate is reckoned from cross section 1-1. The initial flow variables of the gas and drops W_1, p_1, T_1, ρ_1, J_1, a_1, V_1, T_{l1}, and z_1 are given in this cross section, and the shape of the channel is known, being assigned in the form $F/F_1 = f(x)$, where F and F_1 are the present and initial
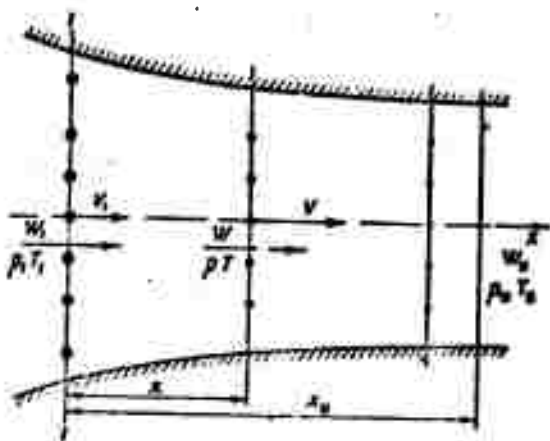
8

Figure 1.1. Diagram of one-dimensional two-phase flow.

cross-sectional areas of the channel. Here z_V is the fraction of vaporized material, put equal to zero for simplicity; in the initial cross section $z_1 = 0$; $x_1 = 0$; $\tau_1 = 0$.

The unknowns are W, T, p, ρ, J, a, V, T_l, z_V, and x as functions of time τ. Two additional (auxiliary) unknowns are attached to the parameters of the problem[*]: the momentum $J(J_1)$ of the two-phase system and the vaporizability z_V. Thus, we obtain a system of ten unknowns. The parameters in the total-vaporization cross section, where $z_V = 1$, are important for many practical problems: W_V, T_V, ..., and especially the length of the vaporization interval and the vaporization time, x_V and τ_V.

The complete system of ten initial equations consists of:

(1) three differential equations describing the motion, vaporization, and heating of the drops and the law of motion, which connects the x coordinate and the time τ;

(2) three equations of conservation of the flow rate, energy, and momentum of the two-phase mixture, the equation of state of the gas, an expression for the momentum of the two-phase mixture, and an expression for the fraction z_V of vaporized material as a function of drop size. The appropriate relationships for the physical constants

---

[*]Since the equations can be solved only numerically, e.g., on electronic computers, an increase in the number of unknowns by two is not of any particular significance. There are a minimum of seven independent variables: W, p, T, a, V, T_l, x.

9

(viscosity of gas, heat capacity, diffusion coefficient, heat of vaporization, and density of liquid, etc.) must be attached to the fundamental equations.

Equation of Motion of the Drop

The drop will be regarded as a nondeformable body of variable mass. If we assume that vapor flows off the liquid surface uniformly at all of its points (in accordance with the spherically-symmetrical mass-flux scheme in the convential theory of vaporization [1]), we may use the usual equation of motion of a rigid sphere* in a medium that offers resistance to it (the weight of the drop, which is usually an order of magnitude smaller than the other forces in operation, can be neglected):

$$\frac{dV}{d\tau} = \frac{3}{4} c_x \frac{\varrho}{\varrho_x} |W - V| \frac{(W - V)}{a}.$$ (1.1)

where ϱ, ϱ_l are the densities of the free-stream gas and the droplet and $|W - V|$ is the absolute difference between the velocities of the gas and the drop.

The drag coefficient c_x is generally expressed as a function of the Reynolds and Mach numbers.

We shall use the results of the analysis in [5] of drop motion after injection into a supersonic stream. In this paper, a numerical method was used to solve the equation of motion of a single drop in the flow field directly behind the shock wave. The shape of the wave was obtained from experiments with spray jets (see Chapter II). For example, calculations for alcohol particles of diameter a = 20 — 30 km at an injection velocity V_1 = 50 -- 100 m/sec (from orifices with d_n = 0.7 — 1 mm) and M_1 = 2.9, $p_\bullet$ = 16 bar, and $T_\bullet \approx$ 300° K indicate

---

*The equation of motion of the center of mass of the drops.

that a drop is swept in its relative motion by a comparatively weak subsonic flow with a velocity below 200 m/sec, even though the absolute velocity of the drop is supersonic.

Consequently, the relative particle velocity $|\vec{V} - \vec{W}|$ is lower than the velocity of sound a_{sd}. Calculations of two-phase flows yield a similar result in many cases.

Calculations indicate that the dependence of c_x on Mach number cannot usually be taken into account for a real spray jet. If necessary, the influence of Mach number can be taken into account with the appropriate formulas from the literature. Among the various relationships encountered in the literature, we might mention the well-known empirical formula of V. A. Olevskiy, which expresses the c_x of a sphere on a rather broad range of Reynolds numbers [6]:

$$c_x = 0.32 + \frac{4.4}{\sqrt{Re}} + \frac{24}{Re},\qquad(1.2)$$

where

$$Re = \frac{|W - V|a\varrho}{\eta},$$
$$0.001 \leqslant Re \leqslant 6 \cdot 10^3.$$

In a more general formulation, corrections for the effect of deformation and evaporation of the drop can be applied to the drag coefficient.

The law of motion of the drop is written in the form

$$\frac{dx}{d\tau} = V,\qquad(1.3)$$

where x is the coordinate of the particle's center of mass.

Equation of the Vaporization of the Drop

This familiar relation expresses the rate of decrease of the surface area of an evaporating drop in a gas stream:

$$\frac{da^2}{d\tau} = -\theta(1 - 0.3\bar{7}\sqrt{Pr}\sqrt{Re}).$$ (1.4)

Reference [1] sets forth the theory of evaporation of drops in a gas stream in detail. Here we present only the basic relations and definitions that will be needed for calculation. The static vaporization coefficient θ characterizes the rate of vaporization of the drop in a still medium at the thermodynamic parameters of the particular cross section; the multiplier

$$\theta_\pi = (1 + 0.3\bar{7}\sqrt{Pr}\sqrt{Re}),$$ (1.5)

the coefficient of dynamic vaporization, takes into account the flow of the stream around the drop

$$\theta = \frac{8\gamma_{c\kappa}D_\pi}{\gamma_\pi} \ln\left(\frac{1 - c_\infty}{1 - c_{\pi\nu}}\right),$$ (1.6)

where D_v is the diffusion coefficient of the vapor:

$$\gamma_{mx} = \gamma_v \frac{\frac{\mu_v}{\mu_a}}{1 - c'_\pi\left(1 - \frac{\mu_a}{\mu_v}\right)}$$ — is the specific gravity of the vapor-air mixture at the point on the boundary layer of the drop with the mean concentration c'_m:

$$c'_\pi = \frac{c_{\pi 0} + c_\infty}{2};$$

$$c_{\pi 0} = \frac{1}{\frac{\mu_a}{\mu_v}\left(\frac{p}{p_v} - 1\right) + 1}$$ — is the vapor concentration at the surface of the drop;

p_v — is the saturation vapor pressure at the liquid surface;

$c_\infty = \dfrac{z_v(\beta-1)}{z_v(\beta-1)+1}$ — is the vapor concentration at infinity (in the free stream);

$\beta = \dfrac{m_a + m_{li}}{m_a}$ — is the ratio of the total flow rate of the air (gas) and liquid in the initial cross section to the air flow rate;

$\varphi = \dfrac{1}{\sqrt{\dfrac{Nu_{st}}{2}\left(\dfrac{1-c_\infty}{1-c_{m0}}\right)^a}}$ — is the influence factor of heat transfer on dynamic vaporization;

$Nu_{st} = \dfrac{2a\ln\left(\dfrac{1-c_\infty}{1-c_{m0}}\right)}{\left[\left(\dfrac{1-c_\infty}{1-c_{m0}}\right)^a - 1\right]}$ — is the Nusselt number in heat transfer with static evaporation of the drop;

Here $\quad a = \dfrac{D_v \gamma_{mx} c_{mx}}{\lambda_{mx}};$

$Pr = \dfrac{\eta_{mx} \gamma_{mx} c_{mx}}{\lambda_{mx}}$ — is the Prandtl number.

In the calculation procedure mentioned above [1], the physical constants of the vapor-air mixture — the specific gravity γ_{mx}, viscosity η_{mx}, thermal conductivity coefficient λ_{mx}, heat capacity c_{mx}, and the specific gravity of the vapor γ_v which appear in the expressions for the vaporization (and heating) of the drop, are calculated from the characteristic temperature and concentration in the conventional boundary layer of the drop. They can be determined approximately from the average values of the concentrations and temperatures at the surface of the drop and in the free stream, c'_m and

$$T'_{cp} = \dfrac{T_\infty + T_1}{2}.$$

13

Relations that can be used to calculate the parameters of gaseous mixtures (for example, λ_{mx} and η_{mx}) will be found in the literature [7], [8].

Equation of the Heating of the Drop

The equation of heating of the drop is obtained from the equations of heat-flux conservation at the boundary of the drop. The change in the total enthalpy of the particle per unit time equals the heat flux into the drop from the outside (first term on the right) less the enthalpy that has been removed with the vapor (convective term):

$$d(m_{\scriptscriptstyle M}i_{\scriptscriptstyle M}) = \alpha_{\scriptscriptstyle T}(T - T_{\scriptscriptstyle M})S\,d\tau - dm_{\scriptscriptstyle M}(i_{\scriptscriptstyle M}+l), \qquad (1.7)$$

where the mass $m_l = \pi a^3/6 \; \rho_l$; $dm_v = dm_l$

$i_l = c'_l(T_l - T_r)$ — is the specific enthalpy of the particle;

α_T — is the coefficient of heat exchange of the drop across the surface $S = \pi a^2$ with the surrounding medium;

l — is the heat of vaporization;

c'_l; T_l — are the average heat capacity and the mass-averaged temperature of the drop.

In accordance with the one-dimensional formulation, the distribution of temperature within the drop is not taken into account here, i.e., it is assumed that the coefficient of thermal conductivity $\lambda_l = \infty$ (instantaneous equalization of temperatures within the liquid).

From Equation (1.7), we obtain (the term $dm_l i_l = -dm_v i_l$ drops out of the equation):

$$m_{\scriptscriptstyle M}\frac{di_{\scriptscriptstyle M}}{d\tau} = \alpha_{\scriptscriptstyle T}(T - T_{\scriptscriptstyle M})\pi a^2 + \frac{dm_{\scriptscriptstyle M}}{d\tau}l. \qquad (1.8)$$

During vaporization, as we know, the temperature of the drop rapidly approaches a certain limiting value T_e known as the temperature of isothermal or equilibrium vaporization:

$$T_{\ell} \rightarrow T_e$$

Unlike that of a solid sphere, therefore, the temperature of a drop in a stream whose parameters vary "fronts" not for the temperature of the gas, but for the corresponding temperature T_e, varying from T_{ℓ_1} to T_e when $T_{\ell} = T_e$. All of the heat absorbed by the particle will be expended on vaporization, and there will be no further change in its temperature; for each liquid, T_e is a function of temperature, pressure, and the concentration c_{∞} in the surrounding medium. It is calculated from the familiar formulas [1].

For $T_{\ell} < T_e (dT_{\ell}/d\tau) > 0$ (heating of the drop);

for $T_{\ell} > T_e (dT_{\ell}/d\tau) < 0$ (cooling of the drop).

The heat-exchange coefficient α_T of the evaporating drop is determined in terms of the Nusselt number of the drop:

$$\alpha_t = \frac{Nu\,\lambda}{a},$$

which is expressed by the formula

$$Nu = Nu_{c_1}\left[1 + 0.3\psi\sqrt{Pr}\sqrt{Re}\right]. \tag{1.9}$$

Vaporizability of the Drop

Vaporizability is the fraction of evaporated matter that has been given off by the drop between the start of the process and the particular (present) cross section of the stream:

$$z_a = \frac{m_{a1} - m_a}{m_{a1}} = 1 - \left(\frac{a}{a_1}\right)^3\Big|\frac{\rho_a}{\ell_{a1}}. \tag{1.10}$$

15

The densities of the liquid are accordingly functions of the drop temperatures T_{l_1} and T_l; $0 \le z_n \le 1$.

Equation of Flow Rate for Two-Phase Mixture

The sum of the flow rates of a mixture of gas (air), vapor, and liquid particles remains constant in each cross section of the stream:

$$W_Q F + m_x = m_a + m_{x1}. \tag{1.11}$$

Equation of Momenta for Two-Phase Mixture

Let us apply the equation of momentum of a stationary stream in its differential form to a two-phase mixture in the absence of frictional forces. In projection onto the x axis, the equation can be expressed in terms of the total momentum J:

$$\frac{dJ}{dx} = p \frac{dF}{dx}. \tag{1.12}$$

Here the formula for J will serve as an additional relation (for the sum of the gas and drop momenta):

$$J = (m_a + m_a) W + m_x V + pF. \tag{1.13}$$

In the particular case of a cylindrical pipe, dF/dx = 0 and Equation (1.12) assumes the form $J = J_1$.

Equation of Conservation of Energy in a Two-Phase Mixture

This equation can be written in enthalpy form. The energy of a two-phase mixture remains constant in each cross section; it is composed of the enthalpy i and kinetic energy for a gas-vapor mixture — the first terms on either side of Equation (1.14) — and the second term for the liquid.

The heat expended to vaporize the drops, including the latent heat of vaporization l, appears on the right side:

$$m_a\left(i_1+\frac{w_1^2}{2}\right)+m_{x1}\left(i_{x1}+\frac{v_1^2}{2}\right)=m\left(i+\frac{w^2}{2}\right)+m_x\left(i_x+\frac{v^2}{2}\right)+m_l l, \qquad (1.14)$$

where $m = m_a + m_v$ is the mass of the air-vapor mixture.

The enthalpy of the gas (or liquid) is written in its usual form (it is assumed that heat capacity does not depend on pressure):

$$i=\int_{T_1}^{T}c_p\,dT+i_1=c_p'(T_{cp})(T-T_1)+i_1;$$

$$c_p'=\frac{1}{T-T_1}\int_{T_1}^{T}c_p\,dT.$$

Here $c'_p(T'_{av})$ is the average specific heat of the gas in the range of integration $T_1 < T'_{av} < T$;

T_1; i_1 are the temperature and enthalpy corresponding to the reference from which the enthalpies are reckoned.

The other enthalpies will be written in similar fashion: i_1; i_{l1}; i_l.

The enthalpy of an air-vapor mixture equals the sum of the enthalpies of its components:

$$i=i_a r_a+i_v r_v=i_a\frac{m_a}{m_a+m_v}+i_v\frac{m_v}{m_a+m_v};$$

$c'_p = r_a c'_a + r_v c'_v$, the average heat capacity of the mixture on the segment $(T_1; T)$, is expressed in terms of the average heat capacity of the components. Here $r_a=\frac{1}{1-r_v(s-1)}$; $r_v=1-r_a$ are the fractions of air and vapor; i_a; i_v are the enthalpies of the air and vapor. For example, if the $c_p(T)$ relation is near-linear (as may be assumed in approximation in many calculations), we have $T_{av}=\frac{T+T_1}{2}$ and the heat capacities are calculated from the arithmetic mean of corresponding temperatures.

17

Equation of State of the Vapor-Gas Mixture

The Clapeyron equation of state for vapor-gas (air) mixture takes the form

$$\frac{P}{\varrho} = R_{cm} T,$$ (1.15)

where $R_{mx} = \dfrac{8314.4}{\mu_{mx}}$ is the gas constant of the mixture,

$$R_{cm} = \frac{1}{\mu_{cm}} = \frac{r_v}{r_s} + \frac{r_a}{\mu_a};$$

μ_{mx}; μ_v; μ_a are the molecular masses of the mixture and its components (vapor and gas).

The 10-equation system written out above includes differential and algebraic relations. For convenience in the later analysis, we must:

(1) reduce the system to dimensionless form (by normalizing the variables with appropriate initial values);

(2) reduce it to differential equations only (by differentiating the appropriate expressions) and solve them for the derivatives of all of the unknowns. This is convenient, for example, in computer solution of the equation.

Thus, we can obtain 10 dimensionless functions of the independent variable

$$\bar{\tau} = \frac{\tau}{\tau^\circ} ; \quad \bar{W} = \frac{W}{W_1} ; \quad \bar{p} = \frac{p}{p_1} ; \quad \bar{T} = \frac{T}{T_1} ; \quad \bar{\varrho} = \frac{\varrho}{\varrho_1} ; \quad \bar{T}_x =$$
$$= \frac{T_s}{T_1} ; \quad \bar{a} = \frac{a}{a_1} ; \quad z_s = 1 - \frac{\varrho_a}{V_{a_1}} \bar{a}^3 ; \quad \bar{V} = \frac{V}{W_1} ; \quad \bar{x} = \frac{x}{x^\circ} ; \quad \bar{J} = \frac{J}{J_1},$$

where $x^* = \tau^* W_1$. These functions appear in 10 initial equations (1.1), (1.3), (1.4), (1.8), (1.10), (1.11), (1.12), (1.13), (1.14), and (1.15). Here the parameters J, θ, z_v and V are auxiliary unknowns that are easily expressed in terms of the others. They could have been eliminated, lowering the order of the system. But for convenience in

18

notation and in the transformations that follow, we shall work with a system of nine equations, eliminating only the unknown J and, accordingly, Equation (1.13) [we substitute the value of J from (1.13) into (1.12)]. Here τ^* is the characteristic vaporization time defined in the single-drop theory, i.e., the time of total static vaporization (with no flow past the drop) when the initial parameters of the medium and the equilibrium vaporization temperature of the liquid remain constant:

$$\tau^* = \frac{d_1^2}{\theta_{\mathrm{ev}}}.$$

were θ_{ev} is the value of the coefficient of vaporization θ at the initial values of the gas parameters and isothermal-vaporization temperature T_{p_1}; x^* is the corresponding characteristic vaporization length.

The universal variable τ is highly convenient for analysis and comparison of various conditions of the process, since it varies in a much narrower range than the absolute time of total vaporization τ_{ev}.

The value of τ^* depends on the properties of the model adopted for static vaporization of a single drop.* Thus the corresponding modifications and improvements of the theory can be taken into account in many cases by applying corrections to the parameter τ^*. The conversion from the universal variable to the variable τ or x is very simple, e.g.:

$$\frac{d}{d\tau} = \tau^* \frac{d}{d\tau} = \tau^* \frac{d}{dx} V, \text{ where } V = \frac{dx}{d\tau}.$$

After simple transformations, we arrive at a system of dimensionless equations.

---

*The theory of dynamic vaporization is based on this model.

Equation of motion of the drop:

$$\frac{d\bar{V}}{d\bar{\tau}} = \frac{3}{4} \frac{\tau^\circ W_1}{a_1} \frac{c_s}{a} \frac{\bar{\varrho}}{\varrho_m} |\bar{W} - \bar{V}|(W - V),\qquad(1.16)$$

where

$$\bar{\varrho}_m = \frac{\varrho_m}{\varrho_1}.$$

Law of motion of the drop:

$$\frac{d\bar{x}}{d\bar{\tau}} = V.\qquad(1.17)$$

Equation of vaporization of the drop:

$$\frac{d\bar{a}}{d\bar{\tau}} = -\frac{1}{2} \frac{1}{a} \frac{\theta}{t_m} (1 + 0.3 \sqrt{\Pr} \sqrt{\overline{\mathrm{Re}}}).\qquad(1.18)$$

Equation of heating of the drop:

$$\frac{d\bar{T}_m}{d\bar{\tau}} = \frac{\dfrac{3}{\bar{a}} \left\{ \dfrac{l}{T_i} - c_{cm}(\bar{T} - \bar{T}_m) \left| \dfrac{d\bar{a}}{d\bar{\tau}} \right. \right\}}{\left(c_m - \dfrac{l}{\varrho_m} \dfrac{d\varrho_m}{dT_m} \right)}.\qquad(1.19)$$

For the liquids of practical importance, the density ϱ_l decreases with rising temperature, so that $\frac{l}{\varrho_l} \frac{d\varrho_l}{dT_l} < 0$ and the denominator of (1.19) cannot vanish.

Vaporizability of the drop

$$\frac{d r_m}{d\bar{\tau}} = -\frac{a^2}{v_m} \left(3 \frac{d\bar{a}}{d\bar{\tau}} \bar{v}_m + \frac{d\bar{v}_m}{d\bar{\tau}} \bar{a} \right).\qquad(1.20)$$

where

$$\bar{v}_{m1} = \frac{v_{m1}}{v_1}; \quad \frac{d\bar{v}_m}{d\bar{\tau}} = \frac{d\bar{v}}{dT_m} \frac{d\bar{T}_m}{d\bar{\tau}} = \frac{T_1}{v} \frac{dv}{dT} \frac{d\bar{T}_m}{d\bar{\tau}}.$$

20

The derivative $\frac{d\bar{a}}{d\tau}$, which appears in Equations (1.19) and (1.20), should be taken from (1.18); $\frac{d\bar{T}_\chi}{d\tau}$ in $\frac{d\bar{T}_\chi}{d\tau}$ is substituted from (1.19).

Equation of momenta for a two-phase mixture:

$$\frac{d\bar{J}}{d\tau} = \frac{\rho_1 F_1}{J_1} \bar{p}\,\frac{d\bar{F}}{d\tau},$$ (1.21)

where J_1 is the initial momentum of the gas and drops;

$$\frac{d\bar{F}}{d\tau} = \bar{V}W'_1\,\Gamma \cdot \frac{d\bar{F}}{dx}; \quad \bar{J} = \frac{J}{J_1} = \frac{J}{\left[1 + (\beta-1)\bar{V}_1 + \frac{\rho_1}{\varrho_1 W_1^2}\right]n_1 W_1};$$

$\frac{d\bar{F}}{dx}$ is the assigned value of $\left[F = \frac{F}{F_1} = f(x)\right]$. Thus, all five equations describing the process as it unfolds with liquid particles are solved directly for the corresponding five derivatives of the unknown parameters:

$$\frac{d\bar{V}}{d\tau}\;;\;\; \frac{d\bar{x}}{d\tau};\;\; \frac{d\bar{a}}{d\tau};\;\; \frac{dT_\chi}{d\tau};\;\; \frac{d\tau_\chi}{d\tau}.$$

The unknown functions themselves and the physical constants remain in the right members of these expressions. The remaining gasdynamic relations can be written after differentiation as linear algebraic equations in the derivatives [the derivative of the right member of the expression for J from (1.13) should be substituted into the left member of the momentum equation (1.12)]:

$$\frac{d\bar{V}}{d\tau};\;\; \frac{d\bar{F}}{d\tau};\;\; \frac{d\bar{p}}{d\tau};\;\; \frac{d\bar{\varrho}}{d\tau}.$$

They take the form:

flow rate equation $a_{11}\dfrac{d\bar{V}}{d\tau} + a_{14}\dfrac{d\bar{\varrho}}{d\tau} = B_1;$ (1.22)

momentum equation $a_{21}\dfrac{d\bar{V}}{d\tau} + a_{23}\dfrac{d\bar{p}}{d\tau} = B_{\nu};$ (1.23)

energy equation
$$a_{31} \frac{d\bar{W}}{d\tau} + a_{33} \frac{d\bar{T}}{d\tau} = B_3;$$
(1.24)

equation of state
$$a_{42} \frac{d\bar{p}}{d\tau} + a_{43} \frac{d\bar{T}}{d\tau} + a_{44} \frac{d\bar{\varrho}}{d\tau} = B_4.$$
(1.25)

We also write the flow rate equation of the gas in nondifferential form:

$$\bar{\varrho} = \frac{[z_n(\beta - 1) + 1]}{\bar{W}\,\bar{F}}$$

the density (flow rate) of the air-vapor mixture increases as a result of vaporization. The coefficients of these equations* are expressed in terms of the aforementioned five derivatives and the various unknown functions.

In writing the energy equation in differential form, use should be made of the expression for the enthalpy of the air-vapor mixture in terms of the quantities r_a, r_v, from which it follows that

$$\frac{di}{d\tau} = \bar{c}_p \frac{d\bar{T}}{d\tau} + \left(\bar{i}_v \frac{dr_v}{dz_n} + i_a \frac{dr_a}{dz_n}\right)\frac{dz_n}{d\tau} = \bar{c}_p \frac{d\bar{T}}{d\tau} + \frac{(\bar{i}_v - \bar{i}_a)(\beta - 1)}{[1 + z_n(\beta - 1)]^2} \frac{dz_n}{d\tau};$$

$$\bar{i} = \frac{i}{c_{p1}T_1}; \quad \bar{i}_v = \frac{i_v}{c_{p1}T_1}; \quad \bar{i}_a = \frac{i_a}{c_{p1}T_1};$$

$$\frac{c_p}{c_{p1}} = \bar{c}_p = r_a \frac{c_a}{c_{p1}} + r_v \frac{c_v}{c_{p1}} = \left[\frac{\bar{c}_a}{c_{p1}} + \frac{\bar{c}_v}{c_{p1}} z_n(\beta - 1)\right] \frac{1}{1 + z_n(\beta - 1)};$$

c_a; c_v; c_p are the absolute heat capacities of the air, the vapor, and the vapor-air mixture and c_{p1} is the heat capacity of the air in the initial cross section.

The linear equations (1.22 — 1.25) can be solved for the derivatives of the unknowns if the system determinant D does not vanish:

---

*See the determinant (1.30) below.

22

$$\frac{d\overline{W}}{d\tau} = \frac{D_W}{D};$$

$$\tag{1.26}$$

$$\frac{d\overline{\rho}}{d\tau} = \frac{D_\rho}{D} = \frac{B_2 - a_{21}\dfrac{D_W}{D}}{a_{22}};$$

$$\tag{1.27}$$

$$\frac{d\overline{Q}}{d\tau} = \frac{D_Q}{D} = \frac{B_1 - a_{11}\dfrac{D_W}{D}}{a_{14}};$$

$$\tag{1.28}$$

$$\frac{d\overline{T}}{d\tau} = \frac{D_T}{D} = \frac{B_4 - a_{42}B_2 - a_{14}B_1 + (a_{21} + a_{11})\dfrac{D_W}{D}}{a_{43}},$$

$$\tag{1.29}$$

where D_W; D_ρ; D_T are the partial determinants corresponding to the unknowns $\frac{d\overline{W}}{d\tau}$; $\frac{d\overline{Q}}{d\tau}$; $\frac{d\overline{T}}{d\tau}$; in these determinants, the appropriate columns are replaced by the right members of Equations (1.22) — (1.25) B_1; B_2; B_3; B_4.

Thus, all unknowns can be found and expressed in terms of D_W/D:

$$D = \begin{vmatrix} a_{11} & 0 & 0 & a_{14} \\ a_{21} & a_{22} & 0 & 0 \\ a_{31} & 0 & a_{30} & 0 \\ 0 & a_{42} & a_{43} & 0 \end{vmatrix};$$

$$\tag{1.30}$$

$$D_T = \begin{vmatrix} B_1 & 0 & 0 & a_{14} \\ B_2 & a_{22} & 0 & 0 \\ B_3 & 0 & a_{30} & 0 \\ B_4 & a_{42} & a_{43} & a_{44} \end{vmatrix}.$$

$$\tag{1.31}$$

Let us denote $\alpha = z_v(\beta - 1) + 1$; the coefficients of the equation system and the elements of the determinants are expressed in the form

$$a_{11} = \alpha \overline{F}; \quad a_{14} = \overline{W}^3\overline{F}^6;$$

23

$$a_{21} = a; \quad a_{22} = \frac{\bar{p}}{k_1 M_1^2};$$

$$a_{31} = 2a\bar{W}; \quad a_{33} = \frac{2\bar{c}a}{M_1^2(k_1-1)};$$

$$a_{42} = a; \quad a_{43} = -\left[\frac{\mu_0}{\mu_0}(\beta-1)z_0+1\right]\bar{Q};$$

$$a_{44} = -\left[\frac{\mu_0}{\mu_0}z_0(\beta-1)+1\right]\bar{T};$$

$$B_1 = (\beta-1)\bar{W}F\frac{dz_0}{d\bar{\tau}} - a\bar{W}\frac{d\bar{p}}{d\bar{\tau}};$$

$$B_2 = -(\beta-1)\left[(\bar{W}-\bar{V})\frac{dz_0}{d\bar{\tau}} + (1-z_0)\frac{d\bar{V}}{d\bar{\tau}}\right] - \frac{\bar{p}}{k_1 M_1^2}\frac{d\bar{T}}{d\bar{\tau}};$$

$$B_3 = -(\beta-1)\left\{\left[\frac{2}{M_1^2(k_1-1)}\left(\bar{T}-\bar{T}_m + \frac{\bar{T}_0-\bar{T}_0}{a}\right) + \bar{W}^2 - \bar{V}^2 + \frac{2l}{\bar{W}_1^2}\right]\frac{dz_0}{d\bar{\tau}} + \right.$$
$$\left. + (1-z_0)\left[2\bar{V}\frac{d\bar{V}}{d\bar{\tau}} + \frac{2}{M_1^2(k_1-1)}\bar{c}_m\frac{d\bar{T}_m}{d\bar{\tau}}\right]\right\};$$

$$B_4 = (\beta-1)\left[\frac{\mu_0}{\mu_0}\bar{T}\bar{Q} - \bar{p}\right]\frac{dz_0}{d\bar{\tau}};$$

$$\bar{l}_n = \frac{l_m}{c_{p1}\bar{T}_1}; \quad \bar{c}_m = \frac{c_m}{c_{p1}\bar{T}_1};$$

$M_1 = \frac{W_1}{\sqrt{k_1 k_a \bar{r}_1}}$ and $k_1 = \frac{c_{p1}}{c_{v1}}$ are the Mach number and adiabatic exponent of the gas in the initial cross section. If we put $z_v = \frac{d z_v}{d\bar{\tau}} = 0$ in the coefficients a_{1j} and B_1, we obtain as a particular case the flow equation of a gas mixture with nonvaporizing solid particles.

Substituting the values from Equations (1.16), (1.19), and (1.20) into the formulas for the coefficients B_1, B_2, B_3, B_4, which contain the derivatives $\frac{d\bar{V}}{d\bar{\tau}}$; $\frac{d\bar{T}_L}{d\bar{\tau}}$; $\frac{dz_V}{d\bar{\tau}}$, we obtain relationships solved for the derivatives of the velocity, pressure, temperature, and density of the gas.

The general system of 9 equations (1.16), (1.17), (1.18), (1.19), (1.20), (1.26), (1.27), (1.28), and (1.29) can be called canonical. It breaks down into two groups. The first group of five equations contains, in its left members, the derivatives of the parameters describing the processes involving the drops, their motion, heating, and vaporization. The second group consists of four equations whose left members contain only the derivatives of the gasdynamic parameters.

The canonical system is convenient for programming computer solutions of the problem.

Let us investigate in greater detail the question as to the conditions under which the solution of the canonical system of equations of two-phase one-dimensional flow is possible. It involves the existence of a singular point for the system of differential equations (1.16), (1.17), (1.18), (1.19), (1.20), (1.22), (1.23), (1.24), and (1.25). The first five equations of this system have no singularities, and the coefficients of the respective derivatives on their left sides do not vanish.

Let us examine the last four equations, which have a singular point. At this point, the (fourth-order) system determinant D, which should appear before the derivatives in the left members of (1.26) — (1.29) vanishes, with the result that uniqueness of solution is violated (it can be shown that two solutions pass through the singular point). The parameters of the gas at this point acquire certain characteristic values. All relations in this chapter can be written in a form that does not contain the Mach number of the gas-drop mixture (and the adiabatic exponent k), since the determination of M presents certain difficulties for a two-phase stream.[*] We introduce the quantity $M = \dfrac{W}{\sqrt{kRT}}$ formally into the expression for the determinants D; here W; $k = \dfrac{c_p}{c_v}$; R; T are the velocity, adiabatic exponents, gas constant, and gas temperature (air-vapor mixture) in the

---

[*]The parameters M_1 and k_1 pertain to the gas in front of cross section 1 — 1.

particular cross section of the two-phase stream. Thus, M is the Mach number of the "frozen" gas in the particular cross section without consideration of particles. Physically, this quantity is the Mach number only of the gaseous phase, and not of the two-phase mixture, since its denominator is not equal to the velocity of sound in a stream containing drops.

We transform the determinant D and find its roots, which will be the roots of the (ninth-order) determinant of the complete canonical system. We substitute the values of the elements α_{ij} into (1.30):

$$D = a \begin{vmatrix} \bar{F} & 0 & 0 & \bar{W}^2 \bar{F}_3 \\ 1 & \dfrac{\bar{F}}{k_1 M_1^2} & 0 & 0 \\ 2\bar{W} & 0 & \dfrac{2\bar{c}_p a}{M_1^2 (k_1 - 1)} & 0 \\ 0 & a & -\left[\dfrac{\mu_0}{\mu_a} z_a (\beta - 1) + 1\right]\bar{Q} & -\left[\dfrac{\mu_0}{\mu_a} z_a (\beta - 1) + 1\right]\bar{F} \end{vmatrix}.$$

and expand the determinant, using the flow rate equation of the gaseous phase:

$$\bar{Q} = \frac{a}{\bar{W}\bar{F}}.$$

The Mach number is easily composed of terms of the form $\bar{W}^2/\bar{T}$ which appear in the course of the transformation:

$$\frac{\bar{W}^2}{\bar{T}} = \frac{M^2}{M_1^2} \frac{kR}{k_1 R_1}.$$

As a result, we obtain an equation for the roots of the determinant:

$$D = \frac{2\bar{F}\bar{f}ka\left[\dfrac{\mu_0}{\mu_a} z_a (\beta - 1) + 1\right]^2}{k_1^2 M_1^4 (k - 1)} (M^2 - 1) = 0. \tag{1.32}$$

The first multiplier in (1.32) is nonvanishing; consequently, the unique solution is M = 1. As we know from the gasdynamics of single-phase streams, a unit Mach number corresponds to a singular point of the equations and to the critical-flow condition. Following the analogy, we shall call a two-phase flow that satisfies Equation (1.32) critical if M = 1, subcritical if M < 1, and supercritical if M > 1.

The parameter M introduced here is not the Mach number of the entire two-phase mixture. For example, processes in it that involve the propagation of sound waves are not determined by the combination M. Solution of the equation system* in the critical cross section M = 1 is possible only if all of the determinants vanish: $D_W = D_p = D_c = D_T = 0$. For a gas flow containing drops that is continuously accelerated $\left(\dfrac{dW}{d\tau} > 0\right)$ from M < 1 to M > 1 the determinant D_W could, according to (1.32), change sign from (-) to (+) at the singular point. Analysis of the determinant D_W (which is more complex than the determinant D) may, generally speaking, establish the mathematical conditions of the transition through the critical cross section in channels with various shapes. Physically, this corresponds to a change in the sign of the resultant gasdynamic disturbance according to the familiar treatment of L. A. Vulis [9]. This reference also examines the vaporization of a liquid in a cylindrical pipe under two extreme assumptions: the absence of dynamic and thermal lagging of the drops with respect to the medium, and conservation of the initial parameters of the drops as they move.**

The right sides of Equations (1.26) and (1.29), i.e., the determinants D_W, include terms (see the elements of the determinant B_1) that correspond to various physical disturbances (terms with the derivatives $dF/d\tau$; $dV/d\tau$, etc.). Numerical calculations indicate, in

*The derivatives of the unknown quantities have finite values.

**The real process under consideration here differs substantially from these extreme cases.

27

agreement with the above, that there is a change in the direction of
an elementary disturbance in a particular process in any small region
containing the point M = 1. For example, utilization of work from
the gas to entrain drops accelerates the gas if M < 1 but decelerates
it if M > 1. In machine calculations, it is helpful to watch the
sign of the determinant D or the quantity $\left(1 - \dfrac{W}{\sqrt{kRT}}\right)$, so as to know
whether the singular point has been passed in the computing process
and the interval in which it occurs. The solution gives the unknown
parameters in all channel cross sections, no matter how close they are
to the section where M = 1 (with any accuracy attainable in machine
calculations). Since the singularity of the equation is an isolated
singular point, the values of the parameters at this point can easily
be found by the corresponding continuity extrapolation.

An inference as to the characteristic value of the parameter M = 1
in a two-phase flow can be arrived at by writing the equation of the
inverted disturbances in the Vulis form.

If we regard the two-phase flow* as a gas in which the particles
act as point forces (or sinks) of heat, mass, and mechanical energy,
the derivation scheme given in [10], for example, yields

$$(M^2 - 1)\frac{dW}{W} = \frac{dF}{F} - \frac{dG}{G} - \frac{1}{a_{sd}^2}\,dL - \frac{k-1}{a_{sd}^2}\,dQ - \frac{dG}{G}\,\frac{k}{a_{sd}^2}\,W^2 - \frac{dR}{R};$$

$$M = \frac{W}{a_{sd}} = \frac{W}{\sqrt{kRT}}. \qquad\qquad (1.33)$$

Here a_{sd} and k are the velocity of sound and the adiabatic exponent
of the gas; $dG = dG_v$ is the elementary flow rate of the vapor given
off by the drops; dQ is the heat given up for heating, vaporization of
the drops, and heating of the vapor to the temperature of the surround-
ing gas (dQ < 0); dL is the work supplied to (or taken from) the drops
during their entrainment or deceleration, with dL > 0 or dL < 0,

---

*With the same starting hypotheses as were used in the present
chapter (neglect of particle volume, absence of friction at the wall,
etc.).

respectively; and dR is the change in the gas constant due to vapori-
zation (with increasing dR < 0).

Each of the terms is expressed with simple relationships in terms
of the gas and liquid parameters. The elementary disturbances expressed
by the terms of (1.33) can be broken down into groups from the stand-
point of their effects on the gas velocity W. For a flow in a cylin-
drical pipe with M < 1, for example, vaporization, i.e., the input of
mass (dG > 0), accelerates the flow, but the utilization of heat for
vaporization (dQ < 0), input of work to the gas from decelerated drops
(dL < 0) (we shall show that the particles characteristically lead
the gas during vaporization in a pipe) and a decrease in the gas
constant of the mixture (dR < 0) — the molecular weight μ_{mx} of the
mixture increases for the fuel considered here — all accelerate the
fl w.

It will be shown later on in a numerical calculation that the
decelerating group of factors prevails in a broad range of flow con-
ditions of practical interest in a cylindrical channel.

Let us also consider the particular case of the flow of non-
vaporizing, e.g., metallic, particles in a nozzle:

$$(M^2 - 1)\frac{dW}{W} = \frac{dF}{F} - \frac{G_{x}}{Ga_{xx}^2}\, dV^2 + c_{x}\frac{G_{x}}{G}\frac{k-1}{a_{xx}^2}\, dT_{x}. \qquad (1.34)$$

Let it be assumed that the velocity and temperature of the particles
and gas are the same in a certain initial cross section of the nozzle.
Then the particles with larger inertia will lag behind the flow
mechanically and thermally: V < W; T_l < T, i.e., the flow must give
up work (to entrain them) and acquire heat (as a result of their
cooling):

$$dV^2 > 0,\; dT_{x} < 0.$$
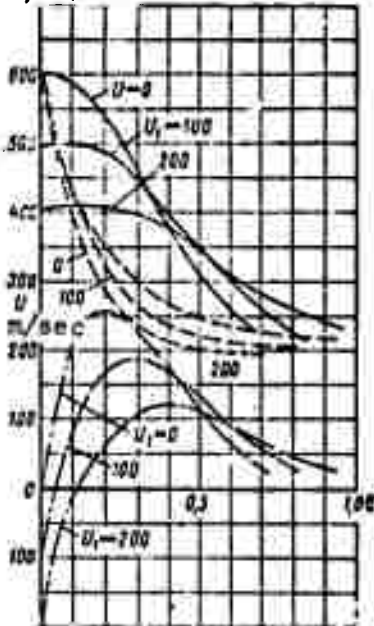
Figure 1.2. Variation of gas and drop velocities in two-phase flow ($M_1 = 0.75$; $a = 16$ μ; $\beta = 1.8$; $T_1 = 1700°$ K).
—— v; --- w; -·-·- U.

In the narrowest cross section, $dF = 0$ and the right side of Equation (1.34) is negative, so that $M < 1$. Consequently, the critical cross section $M = 1$ must be situated far downstream from the cross section with F_{min}.

If the particles lead the flow mechanically and thermally, ($V > W$, $T_l > T$), then the cross section $M = 1$ will be situated at a shorter distance downstream than the cross section with F_{min}.[*]

Thus, we arrive at the well-known fact that, generally speaking, the critical cross section in a two-phase flow does not coincide with the smallest cross section o. the nozzle.

In many practical calculations of two-phase flcws in nozzles, the pressure (or density) distribution along the axis of the nozzle is usually assigned rather than its shape, and the relation $F = f(x)$ is found. This simplifies the calculation by eliminating the afore-mentioned singularity of the equation system. By performing a series of calculations for various initial pressure distributions we can arrive at a nozzle shape quite close to that required.

---

[*]In intermediate cases, when dV and dT_l have different signs, it is necessary to make a special analysis for the sign of the right side of Equation (1.34).
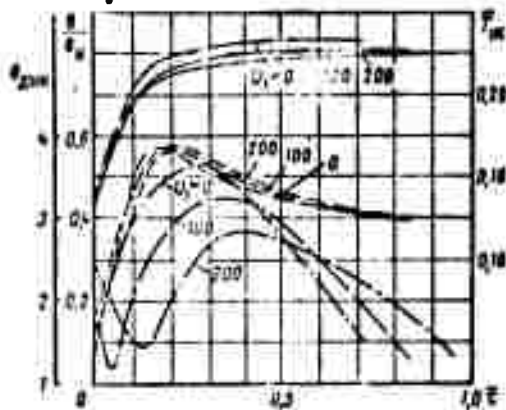
Figure 1.3. Temperature of liquid (gasoline); coefficients of static and dynamic vaporization ($M_1 = 0.75$; $a = 16$ μ; $\beta = 1.8$; $T_1 = 1700°$ K; $W_1 = 600$ m/sec):

$$—\ \frac{T_l}{T_2}; \quad --- \frac{\theta}{\theta_v}; \quad -\cdot-\cdot-\ \theta_{dyn}$$

§2. Results of Solution of the Equation System of Two-Phase Flow

The canonical system of differential equations describing the flow of a gas that contains drops was solved on an M20 electronic computer by the Runge-Kutta method. The accuracy of determining the normalized parameters was $\approx 0.1\%$ (0.01% in certain special cases). For the most part, we studied a flow of air with drops of gasoline in a cylindrical channel (see Figure 1.2 — 1.12 and 1.16 — 1.22); some of the calculations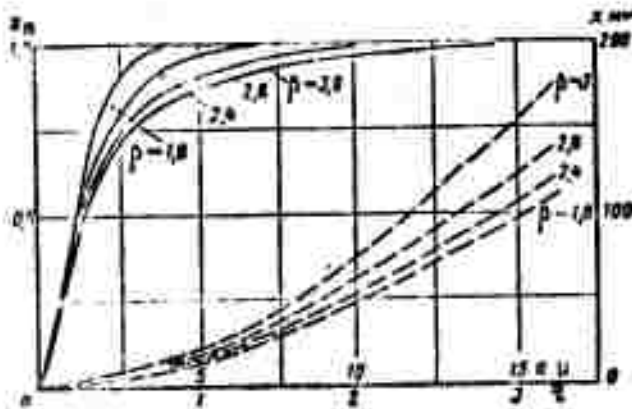 (see Figures 1.6 — 1.15) were made for drops of alcohol. In addition to values for calculations of mixing in cylindrical chambers at M > 1 and M < 1, the flow in a channel of simple shape makes it possible to establish a number of general features of the two-phase flow.

In addition, this regime can be used as a kind of gauge to estimate the parameters of vaporization in a more complex case. Such a case is the spray cone injected into a supersonic stream, to which the next chapter is devoted. It makes clear the importance of analysis of gas flows with drops under local subcritical conditions, such as may arise directly behind the injection zone. In analyzing the phase transitions in a cylindrical pipe, we propose to use the results obtained in Chapter II.

For a broad class of practically important cases, the basic differences between two-phase flows with M < 1 and M > 1 are qualitative differences in the interaction of the two media, the liquid and the gas. Offtake of heat, input of mass, and expenditure of work to entrain drops influence the parameters of sub- and supercritical flows in different ways.

31

Figure 1.4. Vaporizability and vaporization interval of drops at various gasoline concentrations ($M_1 = 0.95$; $a = 10\mu$; $T_1 = 1050°$ K).

—— z_v; --- x_v mm.

However, the laws of the elementary event of flow past a single liquid particle and its heat and mass transfer remain the same, since, as we have noted, the relative velocity of a drop usually remains subcritical. For flows in a cylindrical channel and in many types of nozzles in which the relative particle velocity u can increase rapidly, it still remains s ..,cantially below the local sonic velocity ($5 \leq a \leq 16 \mu$; liquids: gasoline, alcohol, water). The occurrence of flow past an indi·idual drop at sonic velocity ($u = a_{sd}$ and $M_u = u/a_{sd} = 1$) will most probably be preceded by atomization of the drop with a sharp decrease in particle relative velocity. From the relations $M_\bullet = \frac{u}{\sqrt{kRT}}$ and $We = \frac{\rho u^2 a}{\sigma}$ (where We is the Weber number), we obtain

$$M_\bullet = \sqrt{\frac{\sigma We}{ka\rho}}.$$

Under atomization conditions $We \geq 9 — 10.7$, $M_u = M_u^{at}$, the Mach number corresponding to the relative velocity of the gas during atomization of the drop, will be larger the larger the σ of the liquid and the smaller the exponent k, a, and p. Taking, for example, a 10μ drop, $k = 1.4$, and $p = 1$ bar, we obtain accordingly for gasoline (and alcohol) $M_u^{at} \approx 0.37$ (for water, $M_u^{max} \approx 0.7$).

Thus, the necessary conditions for decay of the drop make their appearance before the flow past it is sonic.*

---

*To establish whether atomization actually takes place, it is necessary to perform a special analysis and to compare the time for deformation of the drop with its stay time on a given segment. For simplicity in estimates, it is assumed that $We \approx 10$; $We \approx 17$ may be reached if the parameters are variable.

Turning to our analysis of the computer results, we begin with the kinematics of gasoline drops. The curves of Figure 1.2 illustrate the changes in the absolute and relative drop velocities V and U and the gas velocity W during flow through a cylindrical channel.

In the flow considered here, $V_1 \leq W$ and the drops, which have greater inertia than the gas, will retain their initial velocity at the start of a substantial change in flow velocity. The gas velocity drops off rapidly at first, and the velocity of the drop increases slowly as long as $V < W$; when $dV/d\tau = 0$ the two parameters should, according to the equation of motion ($dV/d\tau \sim u^2$), be equal. Beyond this point, W continues to decrease appreciably, and V slowly (beginning of deceleration of the particles), and the drops "run out ahead," leading the gas by a considerable distance. Then even the drops begin to lose much of their velocity, by the end of the motion, when $a \to 0$, $V \to W$.

The trend of the curves in Figure 1.2 can be explained with the aid of Vulis's generalized-disturbance equation, which we mentioned previously.

In our case, in which $T > T_l$ heat is taken from the gas. It is used to heat the liquid and vaporize it; the heat of vaporization $l dG_v$ is included in the enthalpy of the vapor.* The vapor at the surfaces of the drops has the temperature of the liquid and, on mixing with the gas, is heated to the temperature of the gas mixture. Thus, although the total enthalpy of the gas increases during vaporization, its specific heat decreases as a result of dilution of the mixture with cold vapor: $dQ = c_{mx} dT < 0$.

At the start of the motion from the point $x = \tau = 0$, the phase transitions have, for all practical purposes, not yet started, since the liquid temperature T_{l_1} is low and $dG_v \approx 0$. However, the heat taken from the gas, i.e., the increment $dQ \sim dT_l$ is substantial, since

*It is released again when the liquid condenses.

33

the temperature $\bar{T}_l$ of the drops (Figure 1.3) increases rapidly at the starting point. Owing to the high inertia of the drops, the work increment $dL \sim dV^2$ must be very small (as is indicated by the initial segments of the curves, where $V \approx$ const). Thus, the term dQ will continue to be the prevalent factor on the initial segment of the motion, and the right side of Equation (1.33) will have the sign (+). Thus, with $M < 1$ and $dW < 0$, the gas begins to slow down sharply and it lags behind the drops. On the next segment of the motion, the increased velocity difference $V - W = U$ will result in an increase in the aerodynamic forces acting on the drops, and this will sharply increase the factor dL. Vigorous vaporization of the heated liquid particles will result in an increase in the terms with dG_v and dQ.

Comparison of the computer results and the generalized-disturbance equation leads to the general conclusion that the basic tendencies that lower the velocity of the gas, e.g., input of work from the drops (whose kinetic energy decreases) to the gas $dL < 0$, prevail when $M < 1$. Transfer of heat from the gas to the drops, $dQ < 0$, prevails over the trends that tend to increase velocity, such as input of vapor mass to the gas $dG_v > 0$.

The right side of this equation is always found to be positive, and hence the continuous deceleration of the gas ($dW < 0$) over the entire "lifetime" of the drop.

Thus, a situation similar to the conditions of two-phase flow in a nozzle (where, to the contrary, the gas leads the drops) arises in the cylindrical pipe. The liquid particles are ventilated and, consequently, subjected to a rapid dynamic vaporization. Generally speaking, the maximum relative velocities U'_{max} that the drop encounters on its path can exceed U_1. They are higher (see Figure 1.2) the lower U_1 (the maximum U_{max} is reached at $U_1 = 0$). We observe a kind of "compensation" in which the mean effective relative velocity on the path of the drop remains nearly constant or increases slightly with increasing U.

Figure 1.3 shows curves of the dynamic vaporization coefficient (which depends on the convective heat- and mass transfer between the drop and the surrounding gas) and of the relative static vaporization coefficient θ/θ_v (which is determined by the static heat- and mass transfer of the drop at rest). The vaporization rate of the liquid depends on these parameters. The factor θ_{dyn} which is approximately proportional to $\sqrt{\overline{Re}}$ (where $Re = \frac{U \cdot \delta_0}{\eta}$ is the Reynolds number of the evaporating drop), reaches a maximum at Re_{max} (this point is shifted slightly toward the origin from U_{max}). In accordance with what we said concerning "compensation" of U, the increase of the initial θ_{dyn} is accompanied by a decrease in θ_{dyn}^{max}, which offsets the effect of the initial U_1. If we estimate the average effective value θ_{dyn}^{av} in the vaporization interval from the areas under the curves in Figure 1.3, we obtain closely similar values that increase slowly with decreasing U_1.

For most of the $M < 1$ conditions under investigation here, the vaporization process depends weakly on U_1 (if the gas temperatures are not too low, $T_1 > 800°$ K).

On the other hand, the vaporization rate of the drops in a super-sonic free stream increases only with increasing initial relative velocity. This is explained by the continuous and rapid decrease, $U < U_1$, during the flow with $M > 1$ (a small change in the velocity W compared to subsonic flow). Hence the main effect of the flow past the particles is felt on the initial segment, where U is still near U_1.

The curves of θ/θ_r as a function of the dimensionless time $\bar{\tau}$ (the parameters U_1 and a_1 have no appreciable influence on θ/θ_r) in Figure 1.3 have distinct maxima. The ascending branch of the curve corresponds to a segment in which the drops are heated from a comparatively low initial temperature T_{l1} (in practice, the temperature of the fuel tanks or fuel lines) to a value near the isothermal-vaporization temperature of the drops. The descending branch relates
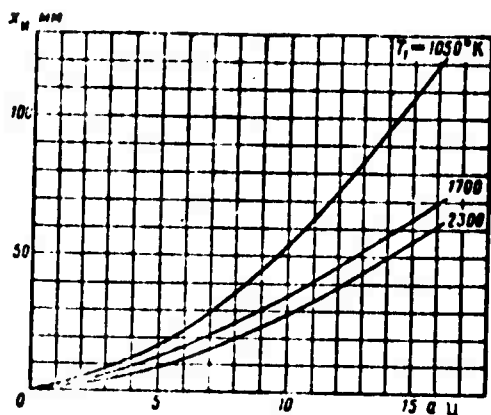
35

Figure 1.5. Influence of gasoline-
drop diameter on vaporization
interval ($M_1 = 0.95$; $\beta = 2.4$).

to the cooling of the gas due
to vaporization of the liquid.
The curves Figure 1.4 indicate
the vaporizabilities of gasoline
drops at various concentrations
β. On a certain initial segment
$\bar{\tau} \leq 0.2 - 0.3$, where ~40% of
the liquid is vaporized, the
curves for the various β practi-
cally coincide.

Vaporization of the rest
of the liquid is strongly
retarded as β increases (especially when $\beta > 2.4$). For $\beta \geq 2.4$, the
parameter $\bar{\tau}$ becomes larger than 1, i.e., $\tau_v > \tau^*$. This means that
the strong flow around the drops with deceleration of the stream
(which intensifies heat transfer) can no longer compensate the
cooling of the gas by liquid drops. The curve for $\beta = 3$, whose main
segment is characterized by asymptotic behavior, corresponds to
vaporization conditions that are approaching but have not yet reached
saturation. The total-vaporization interval x_v of the drops is an
important characteristic of the mixing process. This quantity is
significant for engineering components used in the preparation of
fuel mixtures, e.g., the various types of combustion chambers.

The general theory of two-phase flows tells us that the vaporiza-
tion interval x_v is an extremely complex function of the many variables
that determine the motion and vaporization of the mass of drops in
the gas stream. The results of a series of calculations of the
vaporizability of gasoline are represented in the form of plots
against the basic variables a_1; T_1; β; $M_1(W_1)$; U_1.

In most of the cases of interest to us, the pressure p varies in
a comparatively narrow range, p = 1 — 3 bar, and is not a particularly
essential parameter. To simplify, we shall therefore refer the
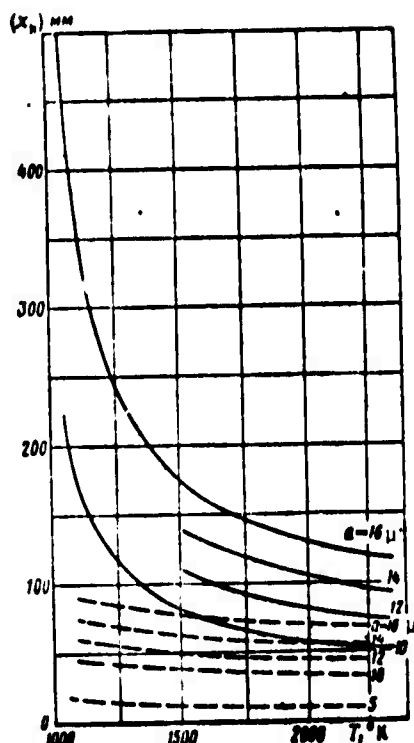results to atmospheric pressure in the initial cross section of the

36

Figure 1.6. Influence of gas temperature on vaporization interval (M_1 = 0.95; β = 2). — alcohol; --- gasoline.
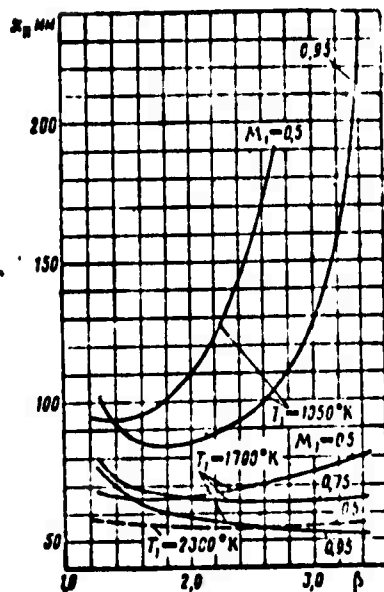

Figure 1.7. Influence of liquid concentration on vaporization interval (a = 14 μ).

stream. The influence of the initial fuel temperature T_l is comparatively weak in the narrow range from 293 to 330° K even when M < 1. Calculations of the vaporization range for M < 1 were made for an initial liquid temperature T_{l_1} = 293° K. The parameters a_1 and T_1 are most important if the concentration of the drop is not too high: $β \leqslant 2 \div 2.4$ $(T_1 \geqslant 1050° K; M_1 \geqslant 0.75)$.

Figure 1.5 illustrates the influence of drop size.

Figure 1.6 shows the influence of gas temperature T_1 on the vaporization range x_v. When T_1 reaches a large enough value $T_1 \approx$ 1500 — 1700° K (at β ≤ 3), further temperature increase has little influence on x_v. The effects of the parameters β and M on the vaporization interval are more complex. Curves showing x_v as a function of β for fixed values of M_1, T_1, a_1, appear in Figure 1.7. They are typically flat over a rather broad range of liquid concentrations and
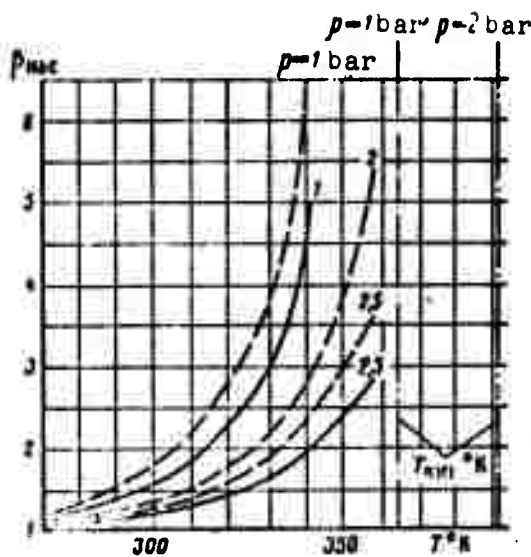
37

Figure 1.8. Saturation concentration during vaporization:

— z_v = 1.0; --- z_v = 0.7; -··-·- T_b.

rise sharply when β reaches large values. This last property results from the existence of a limiting concentration β_s = $f(T, p)$ that corresponds to saturation, at which thermodynamic equilibrium is established between the gas and the liquid and there is no further vaporization. This state is characterized by equal temperatures of the drop and the surrounding gas, T_l = T, and equal vapor concentrations at the surface of the liquid particle and at infinity c_{mo} = c_∞.

As an example, Figure 1.8 shows curves of the saturation concentration β_s as a function of the mixture T and p at vaporized matter ratios z_v = 1.0 and 0.7. If the point (β, T) for a given p and z lies to the right of the corresponding curve, saturation has not been reached. The saturation concentration β_s rises with increasing T (with p = const). This explains the delay in the rise of the curves (large β) as T increases. The aforementioned gently sloping trend of the x_v = $f(\beta)$ curve is explained by the antagonisms among the three basic tendencies of the process.

The following occur as β increases:

1. A decrease in the static-vaporization factor (θ/θ_r) due to cooling of the gas by the drops (an increase in x_v).

2. An increase in the dynamic-vaporization factor θ_{dyn} due to the higher ventilation velocity (a decrease in x_v); see Equations (1.5) and (1.4).

38
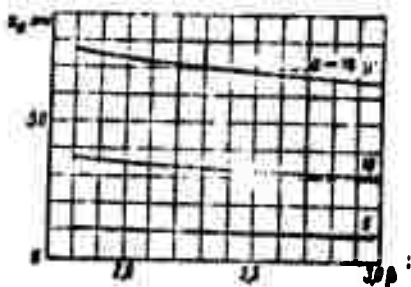
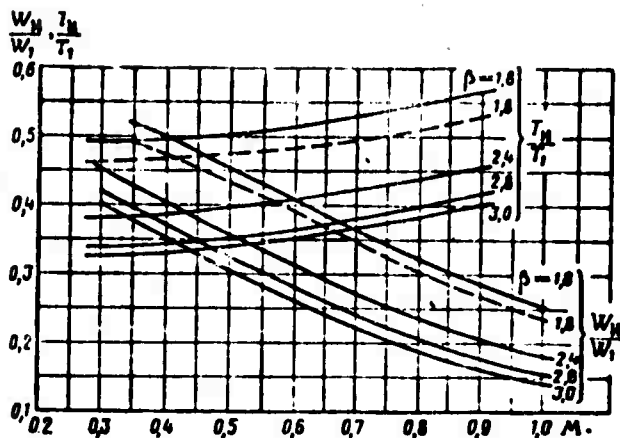Figure 1.9. Influence of liquid concentration on vaporization ($M_1 = 0.95$; $T_1 = 1700°$ K).

Figure 1.10. Temperature and velocity of gas in total-vaporization cross section (a = 16 μ).

— $T_1 = 1050°$ K; --- $T_1 = 1700°$ K.

3. An increase in the flow-stagnation effect and a corresponding decrease in the absolute velocity of the drop (a decrease in x_v). In the range of small β and sufficiently large M_1 ($M_1 \geq 0.75$), tendencies 2 and 3 prevail, and a slowly descending branch with a minimum point appears on the curves of $x_v = f(\beta)$. A transition to larger M_1 strengthens tendency 3. For this reason, the descending branch is protracted and the minimum point is shifted to the right as M_1 increases (see Figure 1.7).

At small values of M_1, $T_1^°$ ($M_1 = 0.5$; $T_1 = 1050°$K), the minimum is filled in and may be absent altogether (monotonically increasing curve). Tendency 1, which results in a longer interval x_v, prevails at large β, but this tendency may be affected by an increase in T_1.

Figure 1.9 shows the influence of β on x_v for various drop sizes a_1. The range of variation of x_v becomes shorter as a_1 decreases, and the curves become progressively straighter.

For given β and T_1, a stronger cooling action of vaporization of the drops on the gas (decrease of T_v in the total-vaporization cross section, see Figure 1.10) should appear at smaller M_1. In these cases,

*For small T_1, the drop in the static vaporization rate has a stronger influence on the range of the drops.

39

the influence of gasdynamic heating on the deceleration of the flow, which retards cooling, becomes weaker. Hence it is precisely at small $M \lesssim 0.5$ and large β that conditions may be created for a sharp decrease in the vaporization rate with a substantial increase in x_v

(see Figure 1.11) all the way to saturation. Such conditions are less probable when $M_1 \approx 1 - 0.7$. Figure 1.11 shows the influence of the parameter M_1 at $T_1 = const,$[*] i.e., in essence the influence of the initial velocity W_1, on the vaporization interval. The $x_v(M_1)$ curves

are characterized by maxima that become more distinct and shifted toward smaller $M_1(W_1)$ the larger $\overset{\circ}{\beta}$ and the smaller T_1. W_1 increases with increasing M_1, but so does the decelerating effect (see Figure 1.10), as is illustrated by the dropping W_v at the end of vaporization.

The increase in W_1 prevails at small M_1, increasing the velocity of the drops and the value of $x_v = f(M_1)$.[**] As M_1 and $W_1 \to 0$ ($T_1 = const$), the interval $x_v \to 0$ (in the limit, the resting drop is vaporized). At large M_1 approaching 1, the decelerating effect of vaporization on the flow "wins out," causing a decrease in $x = f(M_1)$. The maximum corresponding to "equilibrium" of the antagonistic tendencies is shifted toward smaller M as β increases.

At comparatively large $T_1 \geq 1500 - 1700°$ K and $\beta < 2 - 2.2$, this maximum occurs at about $M_1 \approx 0.6 - 0.75$.

In accordance with what was said earlier, the influence of the factor U_1 is negligible ("compensation" effect), see Figure 1.12. Thus all results can be referred to the case $U_1 = 0$ for gasoline and $T_1 \geq 1050°$ K. The transition to lower temperatures $T_1 < 800°$ K brings out a certain effect of U_1. On the whole, the results of the computation indicate that at sufficiently high gas temperatures $T_1 \geq 1700°$ K and not too large $\beta < 2.8 - 3.4$, the vaporization interval x_v varies comparatively weakly with β and M_1 for gasoline drops.

---

[*]The case of $M_1 = var$ with weakly varying T_1 is of interest for what follows (see Chapter II).
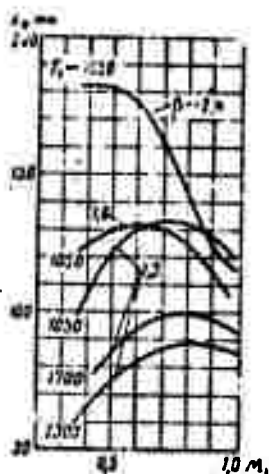
[**]Other conditions the same.

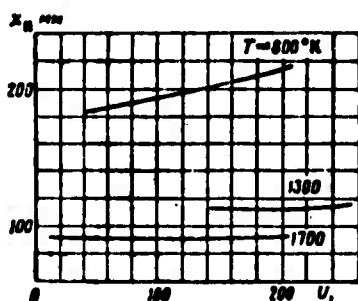Figure 1.11. Influence of M_1 on vaporization interval (a = 16 μ.

Figure 1.12. Influence of relative velocity U_1 on total-vaporization interval (M_1 = 0.75; a = 16 μ; β = 1.5).

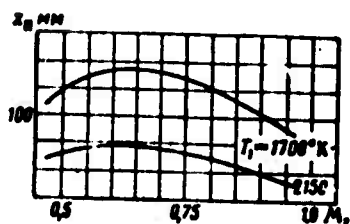Figure 1.13. Influence of M_1 on vaporization of alcohol (a = 12 μ; β = 2).

For gasoline, for example, a = 14 μ, 60 ≤ x ≤ 80 mm at 0.5 ≤ M_1 ≤ 0.95 and 1 ≤ β ≤ 3.4, 0 ≤ U_1 ≤ 200 m/sec. This is a consequence of certain "equilibrium" between the opposing tendencies, which we mentioned earlier, and of the fact that these conditions are still far from saturation. A transition to higher gas temperatures equalizes the effects of M_1 and β (as long as β does not exceed a certain limit).

Figures 1.6, 1.13, 1.14, and 1.15 present the curves for vaporization of ethyl alcohol. The total-vaporization intervals are longer than those for gasoline, especially when T decreases and a increases (Figure 1.6).

In the case of alcohol, the effect of an increase in liquid concentration β on the vaporization interval is even more pronounced. There is no descending branch of the x_v = f(β) curve, and the rise of the characteristic for β ≥ 2.3 — 2.5 is steeper than had previously been observed (Figure 1.14). Figure 1.15 shows the comparatively weak influence of gas pressure (in the range under consideration) on the vaporization of alcohol. The effect observed on comparison of these curves with the corresponding curves for gasoline is explained by the substantial difference between the physical constants of the two liquids, especially their heats of vaporization: $l_{alcohol}$ > $l_{gasoline}$.
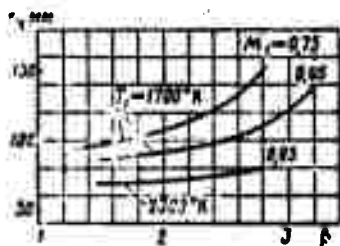
41

Figure 1.14. Influence of concentration on vaporization of alcohol (a = 11.7 μ; U_1 = 38 m/sec)

Figure 1.15. Influence of pressure on vaporization interval of alcohol (M_1 = 0.95; a = 12 μ; β = 2; T_1 = 1700° K).
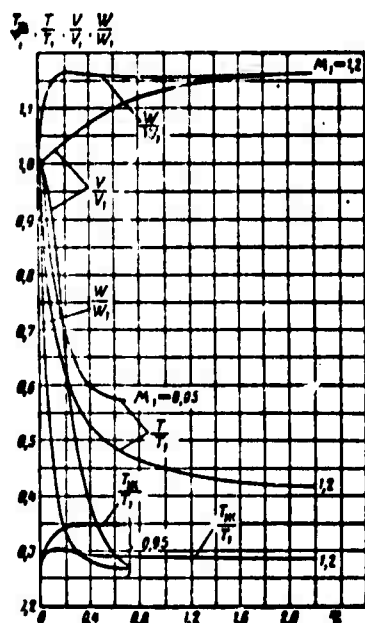

Figure 1.16. Velocity and temperature of gas and drops in subcritical and supercritical conditions (a = 16 μ; β = 1.8; T_1 = 1050° K).

Figure 1.17. Parameter M and gas pressure in subcritical and supercritical conditions (gasoline, a = 16 μ; β = 1.8; T_1 = 1050° K).

—— p/p_1; --- M.

As they evaporate, drops of alcohol remove more heat from the gas. The flow-cooling factor and the decrease in the static vaporization coefficient with increasing β and decreasing T are found to be more significant here.

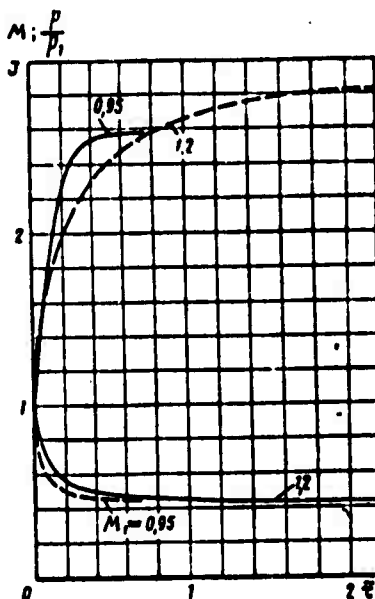To conclude this chapter, let us examine the behavior of the various characteristics of a two-phase mixture as the parameter M_1 of the initial cross section of the pipe passes through the critical value $M_1 = 1$. Numerous calculations in the practically interesting range of variation of the initial data $T_1 = 800 - 2300°$ K, $\beta = 1.3 - 3$, $U_1 = 0 - 200$ m/sec, $5 < a_1 < 16$ µ for gasoline and alcohol have shown that the form of the curves for all parameters of the two-phase flow as functions of $\bar{\tau}$ (or x) and their orders of magnitude change sharply at this transition. Figure 1.16 shows the variations of instantaneous velocity and gas and drop temperatures, and Figure 1.17 — those of M and gas pressure.

Figure 1.18 illustrates the variation of the dynamic and static vaporization coefficients, while Figure 1.19 is a plot of the vaporizability of the drops.

All of these curves pertain to two comparatively similar flow regimes — subcritical, $M_1 = 0.95$, and supercritical $M_1 = 1.2$. Figure 1.20 shows curves of $x_v = f(M_1)$ and the relationships for the gasdynamic parameters W_v/W_1, T_v/T_1, and p_v/p_1 in the total-vaporization cross section.

For computer calculation of these curves, we chose a step $\Delta M_1 = 0.01$; the approach to $M_1 = 1$ was $M_1 = 0.98$ in the subcritical range and $M_1 = 1.02$ in the supercritical range. The aforementioned sharp change in the trend of the curves (which is confirmed by the diagrams) results from the fact that the flow in a cylindrical pipe does not pass through the critical state $M = 1$ in the phase-transformation process (in any event, for a broad range of conditions studied). If, for example, the process began at $M_1 < 1$, it will remain subcritical all the way to the total-vaporization cross section.

For these flows, the reversal of sign of the resultant physical disturbance (which determines the nature of the relationship) will occur only as the initial conditions change from critical to super-critical.
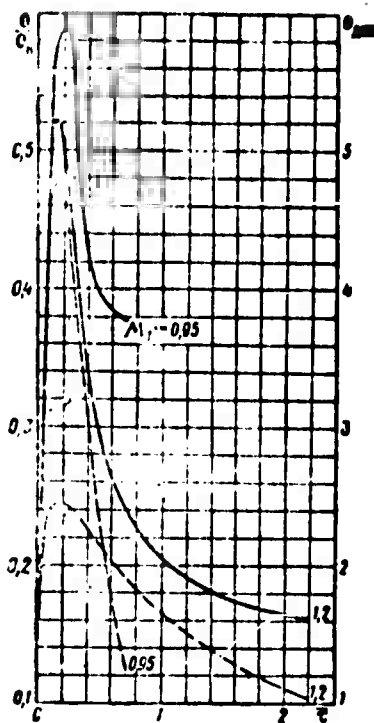
Figure 1.18. Coefficients of static and dynamic vaporization in subcritical and supercritical conditions (gasoline, a = 16 μ; β = 1.8; T_1 = 1050° K).

—— θ/θ_v; --- θ_{dyn}.
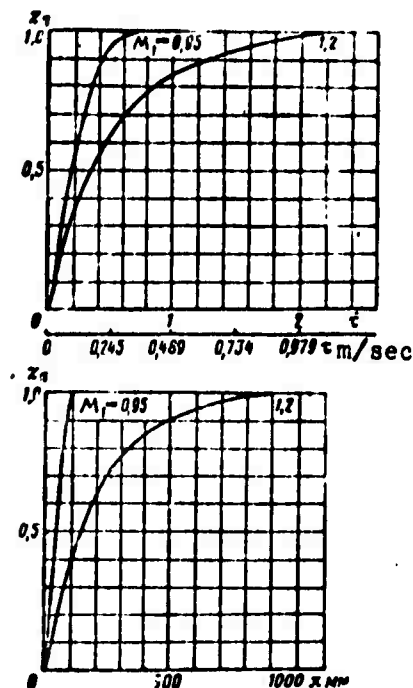

Figure 1.19. Vaporizability in subcritical and supercritical conditions (gasoline, a = 16 μ; β = 1.8; T_1 = 1050° K).

The sharp increase in the length x_v of the vaporization interval with the transition into the supercritical range is highly important in practice. It results primarily from deceleration of the gas in which the drops are being vaporized in subcritical condition and from acceleration of the gas when $M_1 > 1$. In a flow with $M < 1$, as we have noted, the velocity $\bar{V}$ of the drops (which overtake the gas) drops significantly, "following" the decreasing gas velocity $\bar{W}$ (prevalence of the elementary disturbances that decelerate the gas, offtake of heat, etc.). In a supercritical flow, the velocity of the particles (which lag the flow) increases, following the increasing gas velocity. The increase in $\bar{V}$ is associated with an increase in the interval x_v (for a given drop lifetime τ_v). But the time τ_v also changes in the same direction, increasing with the condition from subcritical to supercritical flow. This is due to a substantial decrease in the
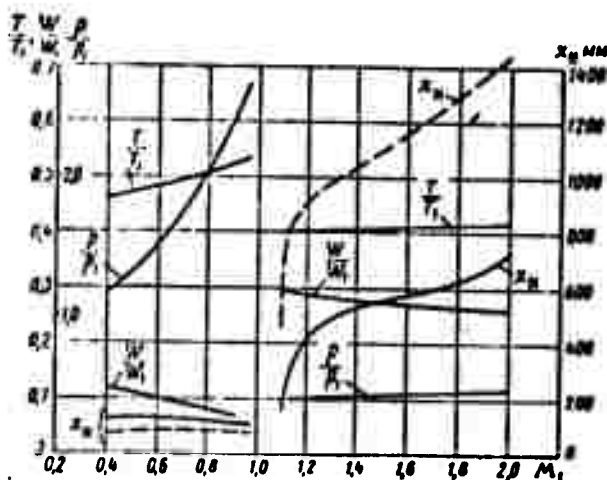
Figure 1.20. Interval x_v and gas-dynamic parameters in total-vaporization cross section in subcritical and supercritical conditions (a = 16 μ; β = 1.8).
—— T_1 = 1700° K; --- T_1 = 1050° K.
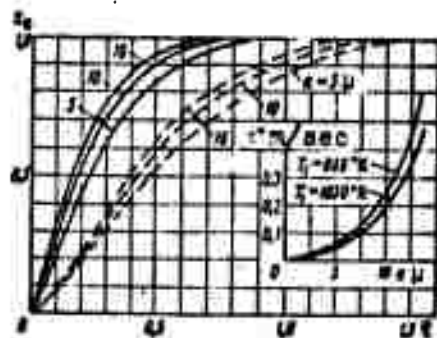
Figure 1.21. Vaporizability in supersonic flow (M_1 = 2.85; β = 1.3; T_1 = 1050° K; W_1 = 1780 m/sec).

—— U_1 = 620 m/sec; --- U_1 = 0.
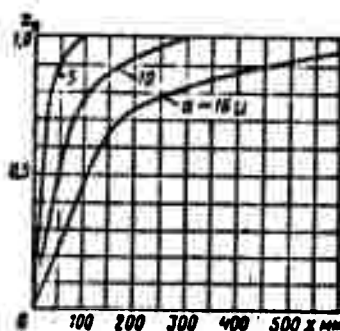
Figure 1.22. Vaporizability in supersonic flow (M_1 = 2.85; β = 1.3; T_1 = 1050° K; U_T = 620 m/sec).

dynamic vaporizability coefficient θ_{dyn} in time in a flow with M > 1 (see Figure 1.18) because of the shorter lag of the drops behind the gas (smaller values of the instantaneous U for a given U_1). The static vaporizability θ/θ_{dyn} (see Figure 1.18) also decreases.

This is a result of the stronger cooling of the flow and the lower temperatures to which the drops are heated (see Figure 1.16) in a supercritical flow. The strong protraction of the vaporization process in time and over length intervenes after vaporization of 40 — 50% of the liquid (see Figure 1.19). Figures 1.21 and 1.22 present an example of vaporizability calculation for a supersonic flow. Figure 1.21 presents curves for determination of the time scale.

This calculation was made under two extreme assumptions concerning the relative velocity: $U_1 = 0$ (no flow around the drops) and $U_1 = 620$ m/sec (flow around the drops at sonic velocity). The true initial relative velocity lies between these limits and is usually closer to the former.

We see from the diagram (Figure 1.17) that vaporization results in a substantial decrease in M at the end of the process for $M_1 < 1 - M < M_1$ and an increase when $M_1 > 1 - M > M_1$. This is why all parameters of the total vaporization cross section differ so sharply from one another as $M_1 = 1$ is approached from the subcritical and supercritical sides.

The following conclusion can be drawn in regards to the rate of the phase transitions: setting up a more rapid vaporization process requires injection into a supersonic flow, which ensures 1) fine atomization and 2) vaporization under the conditions of local sub-critical flow in the injection zone. It is interesting that such conditions, as we shall see in Chapter II, can be obtained in spray cones with a free-stream velocity $M_1 > 1$.

CHAPTER II

THE SPRAY CONE IN A SUPERSONIC FLOW

§1. Formulation of Problem

The present chapter is devoted to construction of a semiempirical
theory of flows with phase transitions in a supersonic-stream spray
cone. It is presently an approximate method for calculation of all
the necessary flow parameters and the characteristics of the total-
vaporization interval, which are of greatest importance for
practice.

In the preceding chapter, we examined the process in a channel
in which gas and liquid particles interact with fully defined initial
conditions. Use of the equations of one-dimensional gasdynamics in
combination with the differential equations of the elementary pro-
cesses for the drops enabled us to solve the problem on comparatively
simple and obvious premises.

The spray cone in a supersonic flow is a more complex object.
The dense swarm of liquid particles formed after injection confronts
the stream as a kind of semipermeable body offering a large hydro-
dynamic resistance. The mass and parameters of the gas that penetrates
into the frontal region of the cone are not known in advance.

47

It is sufficient to inspect any of the accompanying fuel-cone photographs to arrive at the conclusion that the velocity W', temperature T', and pressure p' of the gas in the region of high liquid-particle concentration must differ substantially from the free-stream parameters W_1, T_1, and p_1. Estimation of average flow characteristics in the injection zone presents certain difficulties. In addition to knowledge of the shape of the cone's boundaries, it is necessary to make a special analysis of the flow within them. The shock wave ahead of the cone results in highly nonuniform distributions of all parameters, which are then gradually equalized in the "liquid-grid" zone. At our present level of knowledge, it is highly advantageous to represent the complex two-phase flow that arises on injection into a supersonic stream in the form of an equivalent one-dimensional gas stream that carries the particles. For the time being, this approach is the most rational for investigation of systems with phase transitions.

As we know, solution of the analogous (but simpler) problem of averaging inhomogeneous flows in ordinary gasdynamics has yielded a number of valuable and practically useful results. The present stage is also necessary for the transition (in the future) to solution of the problem of non-one-dimensional flows with phase transitions. Three individual particular problems arise in construction of the theory:

1. determination of the shape of the spray-cone boundaries (and of the shock wave) as a function of the principal dimensionless numbers;

2. establishment of the possibility in principle of equivalent substitution of a one-dimensional two-phase flow for the complex flow within the boundaries of the spray cone;

3. determination of the effective parameters W', T', p', β' of that flow in the frontal region of the spray cone, which contains a dense swarm of particles.

The average parameters found in a certain reference cross section of the spray cone may be taken as initial parameters; they permit use of the results of the one-dimensional idealization (Chapter I) to calculate the characteristics of the next section, in which the bulk of the liquid is vaporized.

The first of the problems formulated is accessible to modern experimental and theoretical methods and has been solved (though perhaps not quite completely) by a number of investigators. In the present chapter, §2 is devoted to the acquisition and generalization of experimental results defining the boundaries in "cold" spray cones with negligible vaporizability.

However, the data can be applied to rather short initial segments of the vaporizing cone in which the shape of the boundaries has not yet undergone substantial changes.

In solving the problems formulated under points 2 and 3 above, it will be necessary to construct a model of the phenomenon under study, and this is done in §3. An analytical discussion of the problem is presented in §4 and 5, to the best of our knowledge for the first time in this form. Essentially, an attempt is made here to calculate the interaction of the supersonic stream and the dense particle swarm for the conditions of the spray cone. We shall formulate the general problem of the present chapter as follows.

All initial free-stream and injection parameters and the corresponding physical constants of the two media are known.

It is required to calculate in approximation: the flow within the spray cone in the supersonic stream with phase transitions, i.e., the average* velocity, temperature, gas pressure, and liquid and vapor concentrations with the object of determining the principal parameter, the length x_v of the total-vaporization interval. Having these data, we can determine the parameters of the fuel-delivery system in a

_____

*In a cross section of the stream.

certain ideal chamber with supersonic flow, i.e., the pressure drop, the number and diameter of the atomizer nozzle orifices, and the vaporization interval, and can determine the total-head loss due to atomization.

At the end of Part 1, the corresponding calculation procedure will be set forth in detail. Naturally, this semiempirical theory requires experimental verification. Measurement of gasdynamic or other quantities in the injection zone is extremely difficult. In the present study (see §6), we present a comparison of theoretical and experimental results for the principal parameter, the total-vaporization interval, in a spray cone in a supersonic stream.

In §7, we examine certain applications — concrete examples of injection-system mathematical design for the mixing section. In our opinion, the following are of independent interest: 1) results on representation of the inhomogeneous flow in the cone behind the shock wave in the form of an equivalent one-dimensional flow; 2) solution of the problem of the existence of a developed subcritical flow region in the initial segment of the spray cone (which is an important factor in the theory to be developed).

§2. Shapes of Spray Cone and Shock Wave

Here we set forth experimental results from determinations of the shapes of the spray cone and shock wave when liquid is injected into a supersonic stream. They pertain to a "cold" cone from a straight-cone atomizer without phase transitions (vaporization). The initial gas-stagnation and liquid-heating temperatures are near room temperature, and the vaporization rate is vanishingly small. The processes within such a cone develop basically as fluid-dynamic processes and are determined by the interaction of the gas with the dense particle swarm. It will become clear from what follows that description of a certain initial (frontal) section of the cone at

distances on the order of $x/d_n = 10 - 30$ and determination of the limiting line that indicates the range of the liquid stream* (the asymptote of the cone) are of greatest interest for the analysis at hand. In subsequent study of fuel cones with phase transitions in a heated stream, it is found possible to use the relationships obtained here as a point of departure.

According to the experiments described below (see §6 of this chapter), vaporization has little effect on the cone-boundary contours on a certain initial interval; the vaporizing cone undergoes a sharp change in shape on a segment farther from the point of injection. In these experiments, the liquid was delivered at an angle to the stream (90°) from a circular orifice on the surface of a streamlined needle-shaped body. This minimized the influence of the flow around the atomizer itself. For example, it was possible practically to eliminate the influence of the complex phenomenon of boundary-layer detachment (confining it to a zone small by comparison with the dimensions of the cone).

Selection of the streamlined atomizer made it easier to analyze the structure of the two-phase flow, to describe its outer boundaries with comparatively simple and general relationships, and to prepare reference material for the theory of flows with phase transitions that is developed in the sections that follow. The basic purpose of the experiments performed was to acquire the most general possible approximate relationships to describe the outer boundaries of the spray cone and shock wave in two coordinate planes in terms of the basic similarity criteria.

It is also known that data on the shapes and ranges of the cones are of direct practical importance. They are needed for rational selection of the number of atomizers and their placement in the volume

---

*The contour of the cone boundary is usually such that relatively arbitrary smooth matching of the initial segment to the asymptote yields a practically correct picture of the entire cone over a considerable part of its length.
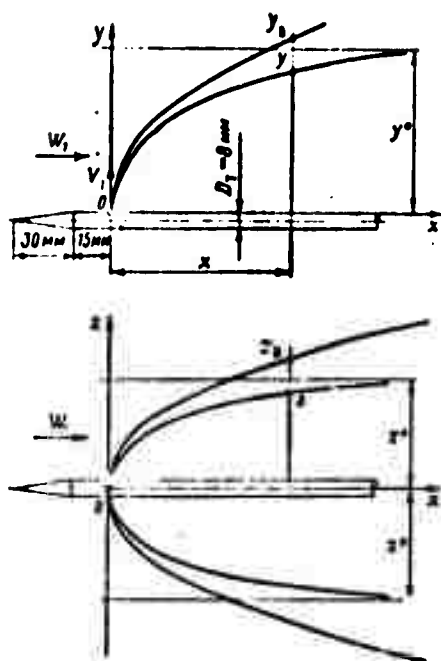
Figure 2.1. Boundary between spray cone and shock wave.

of the combustion chamber.

Turning to the corresponding experiments, we note that similar experiments have been performed by a number of authors, and that most of them have been based on a well-known photographic technique the details of which are set forth in the literature [1].

The experiments performed here also reduced to photographic investigation of a cone in a supersonic stream by the shadow or Töpler method. The photographs were taken in two planes: for the most part in the profile plane xoy (plane of symmetry of the cone), which contains the liquid-outflow and gas velocity vectors V_1 and W_1, respectively, and in the horizontal plane xoz, which passes through the coordinate origin perpendicular to the vector V_1 (Figure 2.1). Special spark photographs were also made of certain segments of the spray (the root of the liquid cone) at known magnification.

A conventional supersonic-flow installation was used for the experiments, with a special (interchangeable) gasdynamic nozzle to produce the desired Mach number in the working section.

Figure 2.2 presents a diagram of this setup. Air from the high-pressure line 1 is delivered into receiver 2, where the stream is sharply decelerated. The total head p_{01} of the gas and, accordingly, the static pressure p_1 in the working chamber can be regulated with a regulator valve installed in the high-pressure line. Thereafter, the stream is accelerated in the gasdynamic nozzle 3, entering a rectangular working chamber with flat 120 × 120 mm optical glasses 5. The object photographed — the atomizer with the spray cone — is situated
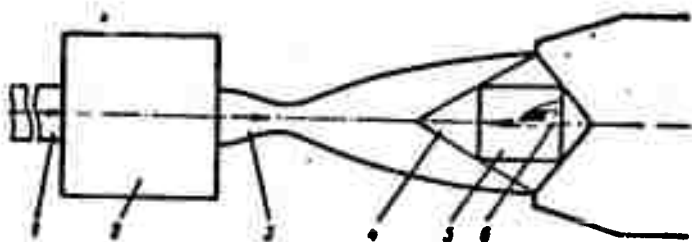
Figure 2.2. Diagram of experimental setup.
1 — high-pressure air line; 2 — receiver; 3 — gasdynamic nozzle; 4 — constant-velocity rhombus; 5 — glass for photography; 6 — object of photography.

in the constant-velocity rhombus 4. The photographs were made with a standard IAB-451 Töpler device (using an RDSh-250 mercury lamp for illumination). To obtain shadow photographs, a knife edge that cuts off part of the light beam is moved aside to a certain position. In spark photography, which permits inferences as to the instantaneous picture of the process, the standard illuminator was replaced with the discharge tube of a special spark apparatus having a flash duration of $\sim 10^{-6}$ sec. The Mach number in the working section was determined from measurements of the total pressure (needle-type manometer with scale conversion factor of ~ 0.2 bar) and of the static pressure at a given point in the stream, using the familiar Rayleigh formula.

The stagnation temperature T_{01} was measured with a thermocouple in the receiver. It was $\sim 253°$ K (cooling due to gas-expansion effect).

The Mach-number field was quite uniform. It was determined with the aid of Pitot and static pressure probes. The measurements were made at 20 points on two mutually perpendicular axes. The uniformity $\Delta M/M_1$ of the field was approximately $\pm 1.5\%$.

Liquid was delivered to the atomizer through a fuel line from a pressurized cylinder, and the delivery pressure Δp was measured with a needle manometer reading to 0.2 bar. The basic parameters of the stream were varied in the following ranges: $M_1 = 2.9 - 2$; $p_0 = 16 - 7$ bar, $5 \leq \Delta p \leq 50$ bar, and the atomizer discharge coefficients

53
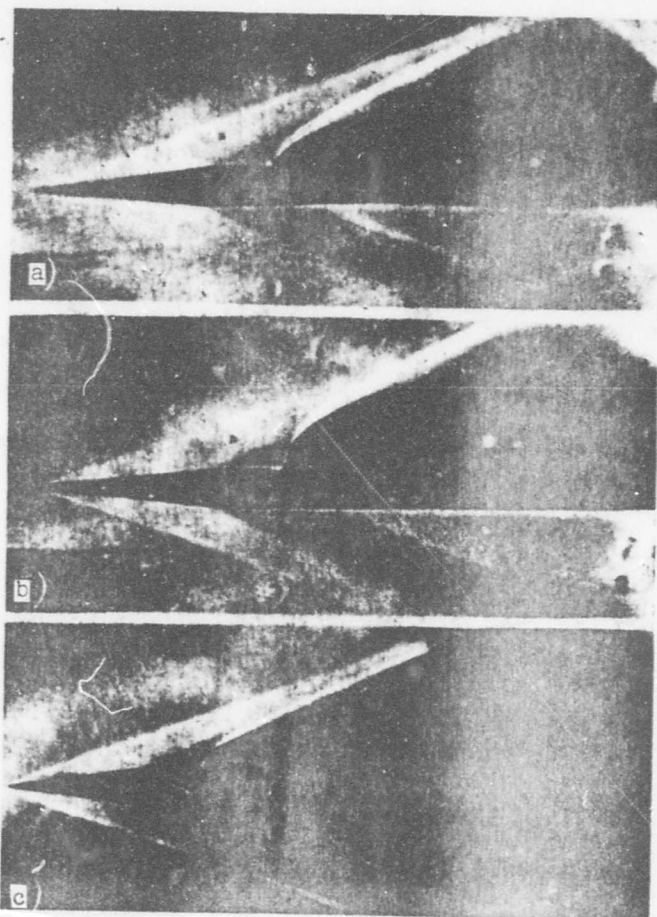
Figure 2.3. Photographs of spray cone ($M_1 = 2.9$; $p_0 = 16$ bar, $d_n = 1$ mm, magnification 0.66 X)

a — $\Delta p = 10$ bar; b — $\Delta p = 40$ bar; c — $\Delta p = 40$ bar; $d_n = 0.4$ mm.

were ≈ 0.7 — 0.75. Some of the experiments were made on a similar setup with an open working section at design cone outflow.

The films were calipered on a special enlarger with a magnifying power of five.

At least two photographs were made in each regime to check the reproducibility of the results; as a rule, it was quite satisfactory.
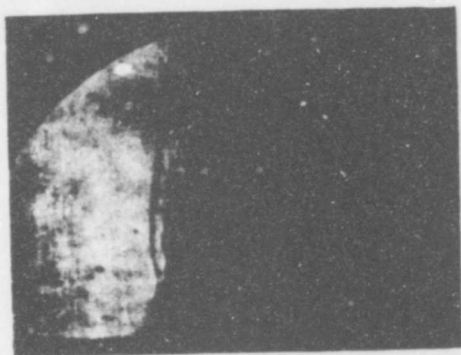
Figure 2.4.   Spark photograph of root section of spray cone ($M_1 = 2.9$; $p_0 = 16$ bar; $d_n = 0.4$ mm; magnification 25 X; $\Delta p = 40$ bar).

Specimen photographs showing the respective images from which the boundaries of the spray cone (alcohol) and shock wave were determined appear in Figures 2.3 and 2.4. Examination of the photographs indicates an increase in the range of the spray with increasing delivery pressure Δp and diameter d_n of the nozzle orifice, as well as asymptotic behavior of the cone.

The scatter of the coordinate points in the measurements averaged $\pm(5 - 8\%)$. An instantaneous image of the cone appears on the spark photograph of Figure 2.4, which is magnified 25 times. In it, we see the root section of the cone in the injection zone. The cone remains intact (under these particular flow conditions) on a length approximately equal to the orifice caliber d_n and then disintegrates rapidly, creating a dense swarm of particles, which are entrained by the stream of gas. Minute filaments and single droplets separate under the influence of the vacuum in the wake zone of the flow past the liquid cone. In the longitudinal plane xoy, the shock wave is closely adjacent to the boundary of the spray. At the base, the wave has an element whose shape approaches that of the normal shock, and it is separated from the wall of the delivery tube by a small subsonic boundary-layer segment.

For segments remote from the injection point, at distances greater than $(8 - 10)d_n$, we need not take account of structural details of the root zone, and may assume that the liquid is delivered from a point source at the center of the nozzle orifice, at which the coordinate origin is placed.

The results of the boundary determinations were found to be practically the same for the Töpler and shadow methods. Nor did they change when the exposure time of the photographs was varied from 0.01 to 0.1 seconds. On the basis of the many photographic images obtained in this and other studies, it is possible to form a quite definite picture of the shape of the spray cone in a supersonic stream.

Dimensionless Numbers in the Problem of the Spray Cone

Let us consider the set of dimensionless numbers in the problem of the spray cone in an unbounded gas stream. They determine the shapes of the cone and the shock wave and other characteristics of the flow, drop size, the gasdynamic variables, etc. The injection process is examined without consideration of phase transitions, i.e., for the initial section of the spray or for a spray in a stream at comparatively moderate temperatures. We shall assume that the phenomenon is quasistationary, neglecting boundary-layer detachment on the solid surfaces in the injection zone and neglecting the influence of the atomizer itself on the flow.

The gas is subject to the Clapeyron equation of state with gas constant R and is regarded as an unbroken continuum.* This last limitation may exclude, for example, streams at very low pressures or streams that contain extremely fine droplets with diameters in the hundredths of a micron (flow conditions that are not studied here). Turbulence in the free stream can be taken into account by the intensity factor $\varepsilon = V'/W_1$ (where V' is the average fluctuation velocity of the gas) and the turbulence scale l_T,** and the hydraulics of the outflow can be allowed for with the atomizer discharge coefficient μ_a. We shall not take account of temperature gradients within the liquid (whose heating is estimated in terms of a certain average temperature T_l), and for this reason the constant λ_l — the thermal conductivity coefficient of the liquid — will also be left out of account.

*The mean free path of the molecules is much shorter than all other characteristic dimensions.

**The characteristic turbulence scale.

For lucidity, our two-phase flow within the boundary surfaces of the spray can be represented as one-dimensional, i.e., it can be characterized by parameters averaged for each cross section x = const: velocity, temperature, gas density and velocity, and drop temperature. For sections of the spray remote from the injection point we shall disregard the deviation of the gas and particle velocity vectors from the direction of the horizontal axis ox (without their projections onto this axis). This limitation is not fundamental.

In the general case, the process is three-dimensional, with the velocities having three projections onto the coordinate axes. In our adopted scheme, we consider the basic hydrodynamic phenomena: the decay of the core into drops, the formation of a dense swarm of particles that create a single "liquid grid," the motion of the system of drops on their subsequent individual trajectories, and the heating of the liquid in the stream.

We write all of the independent dimensional parameters of the problem that characterize the flow of the gas and liquid, taking, for example, the ordinate y of the spray boundary or the ordinate y_w of the shock wave in the xoy plane as the unknown:

$$x;\ W;\ \varrho;\ T;\ c_p;\ v;\ R;\ \iota;\ l_t;\ \lambda;\ a_t;\ V;\ d_c;\ \varrho_\varkappa;\ n_\varkappa;\ \varkappa;\ \mu_b;\ T_\varkappa;\ c_\varkappa;\ b_\varkappa;\ g.$$

Here λ and b_l are the thermal conductivity of the gas and the coefficient of volumetric expansion of the liquid, and g is the acceleration of gravity. Thus, we have a set of 22 parameters defining the boundary of the spray, and of these ε, a_a, μ_a are dimensionless. The fundamental units of measurement will be four in number: the kilogram of force of mass, the meter, the second, and the degree Kelvin, abbreviated kgf or kg, m, sec, and ° K.

The "kcal" unit of thermal energy is derived, and we shall express it in terms of the joule, the universal energy unit (as is done, for example, in the SI* system). Using the Mayer equation for the heat-capacity relation $c_{p_1} - c_{v_1} = R$, we shall take c_{p_1} and R as independent

*Translator's note: This is the International System of Units.

57

parameters from among the three quantities c_{p_1}, c_{v_1}, and R: c_{v_1} = c_{p_1} - R. We shall use the familiar Π-theorem of similarity theory (see, for example, [11] [12]), according to which there are a total of 22 - 4 = 18 dimensionless numbers. Of these, one dimensionless variable y/d_n or y_b/d_n is a function of the other 17 independent criteria.

They may have the following structure:

$$\frac{y}{d_c} \left| \frac{x}{d_c} \right. ; \quad \frac{W_1}{\sqrt{kRT_1}} = M_1; \quad \frac{c_{p1}}{c_{v1}} = \frac{c_{p1}}{c_{p1}-R} = k;$$

$$\frac{W_1 d_c \varrho_1}{\eta} = Re; \quad \frac{V d_c \varrho_x}{\eta_x} = Re_x; \quad \frac{\varrho_1 W_1^2 d_c}{\epsilon} = We;$$

$$\frac{\varrho_1 W_1^2}{\varrho_x V_1^2}; \quad \frac{g d_c}{V_1^2} = Fr; \quad \frac{\varrho_1}{\varrho_x} : \alpha_y; \mu_y;$$

$$\epsilon; \frac{l}{d}; \quad \frac{\eta_1 c_{p1}}{\lambda_1} = Pr; \quad \frac{T_1}{T_x}; \quad \frac{c_{p1}}{c_x} : b_x T_x.$$

We obtain a system of known dimensionless numbers for the dynamic and thermal problem of flow past the spray cone. They have the following physical significance:

M, R, k are the Mach number, the gas constant, and the adiabatic exponent;

Re and Re_l are the Reynolds numbers for the gas and liquid, constructed for the characteristic dimension of the liquid cone;

We is the Weber number (or the drop-atomization number), which expresses the ratio of the hydrodynamic forces and the surface-tension forces of the liquid.

The particle diameter a can be introduced into the expressions for Re, Re_l, and We as a characteristic dimension, using, for example, an experimental non-dimensional relation for the coarseness of atomization or theoretical data [13], [14], [15]:

$\dfrac{\rho_1 w_1^2}{\rho_l v_1^2}$ - is the ratio of the dynamic pressures of the gas stream and the liquid;

Fr is the Froude number for the liquid, which takes its weight into account;

$\dfrac{\rho_1}{\rho_l}$ - is the density ratio of the two media;

a_a, μ_a are the dimensionless spray cone angle and the discharge coefficient of the liquid delivered;

ϵ, $\dfrac{l_\tau}{d_n}$ - are the intensity and dimensionless scale of the turbulence;

$Pr, \dfrac{T_1}{T_l}, \dfrac{c_{p1}}{c_l}$ - are the Prandtl number and the ratios of the temperatures and the heat capacities of the media;

b_l, T_l is a combination that takes account of thermal expansion of the liquid (it can be written in the form of a Grashof number $Gr = \dfrac{b_l g d_n^3 \Delta T_l}{v_l^2}$, if ΔT_l, the temperature difference between characteristic points of the drop or cone, is introduced).

When the shape of the cone depends weakly on thermal processes in the system, e.g., when the drops are only slightly heated on the initial segment or when the free-steam turbulence parameters have little influence (they may make themselves felt at a considerable distance from the point of injection, causing diffusive dispersion of fine droplets), the last six dimensionless parameters may be left out of account. Then the number of dimensionless numbers in the process is reduced to 12. Such conditions are created when unheated liquids are atomized in a stream of gas with a stagnation temperature near room temperature. Workup of experimental results in terms of the dimensionless variables indicates that we may confine ourselves to a much smaller number of dimensionless numbers in describing the shapes of the spray cone and the shock wave (in a certain range of conditions). Study of the photographs and visual observations enables us to describe the process superficially and arrive at certain assumptions concerning it.

A curved shock wave forms in front of the cone and undergoes rapid decreases in curvature and intensity with increasing distance from the root, approaching the straight-line characteristic corresponding to the free-stream Mach number. This is especially conspicuous in the lateral zones of the wave, which can be observed in the vertical projection in the xoz plane. The cone decays near the point of injection, forming a small "liquid foot"; it is deformed under the action of the stream, curving and flattening out into a sheet (similar in shape to the liquid cone in a subsonic stream).

In the zone behind a strong shock wave (a nearly normal shock if the injection angle is 90°), the liquid is atomized to form a dense swarm of drops. At the root of the cone, we observe a small zone of boundary-layer detachment from the surface of the atomizer, in front of which a weak oblique shock can sometimes be seen. To judge from the photographs, the shock wave stands off from the cone at a distance $h \approx 0.25\ d_n$, and its height above the atomizer tube is $h_2 \approx d_n$ (see Figure 2.4). Drops moving behind the wave enter stream filaments with continuously increasing velocity (from subsonic behind the normal shock to supersonic in the free stream), and may be subject to secondary atomization.

Our impression is that the decay to particles of a certain final diameter (determined in the experiments from spray-coarseness measurements) is complete at short distances that do not exceed 0.5 — 3 atomizer-nozzle calibers (this interval may increase substantially for viscous liquids such as glycerine or oil).

Generally speaking, the real atomization process is nonstationary, especially at the root of the cone. Spark photographs with short exposures, ~10^{-6} sec, indicate certain oscillations in the positions of the cone and wave boundaries. However, conventional photographs made with longer exposure times (in hundredths of a second), which average the phenomenon in space and time, yield a fully defined and unchanging picture.

The process will be regarded henceforth as quasistationary. The boundaries of the cone were determined from photographs with exposure times on the order of 0.02 — 0.05 sec, on which the positions of the spray cone and shock wave are averaged, but constant for a given set of conditions.

The outer boundary of the cone is sharply defined in both planes and tends to a horizontal asymptote with which it nearly merges. The spans of the cone boundaries, y^* in the profile plane and $2z^*$ in the vertical plane, are of the same order of magnitude. At greater distances from the point of injection, the boundaries begin to blur under the action of turbulent droplet diffusion. The depth of penetration of the cone into the stream is considerably smaller than in subsonic flows because of the larger velocity heads of the gas (at a given velocity head of the liquid). The bulk of the liquid particles, which are distributed highly nonuniformly on the initial segment of the cone, is apparently to be found in the zone of the cone's profile plane of symmetry xoy.

In addition to the outer boundary of the cone in the xoy plane, we observe a less distinct internal boundary lying near the surface of the atomizer (nearly in the xoz plane). More distinct internal boundaries may be formed when the velocity-head ratio of the gas and the liquid being delivered is sufficiently small (small $p_{\bullet 1}$ and small M_1).

We note that the phenomenon develops basically in the upper half-space, above the xoz plane, where the boundary surfaces of the cone and the main segment of the shock-wave surface are located.

At high liquid flow rates, e.g., $d_n > 2.5$ — 3 mm, a certain amount of liquid may sometimes be carried into the lower half-space (below the xoz plane).

61
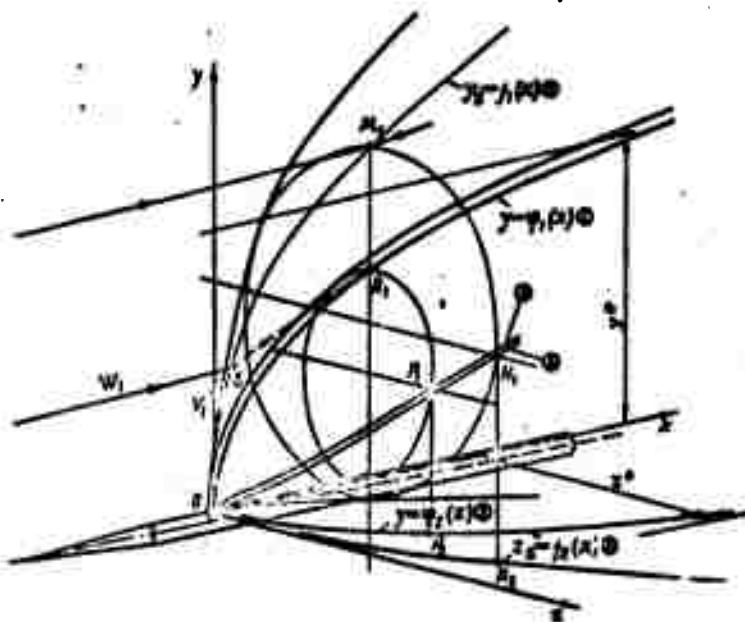
Figure 2.5. Shapes of spray cone and shock wave.

For the analysis to follow, it will be helpful to form a general three-dimensional conception of the shape of the boundary surfaces of the spray cone and shock wave (Figure 2.5).

1.   The boundaries of the cone present a smooth convex surface (the sign of the curvature can evidently change only in the small region in which the cone is in contact with the atomizer pipe or at the very root of the cone).

The boundary of the cone $y = \varphi_1(x)$ in the profile plane xoy and the boundary $z = \varphi_2(x)$ in the horizontal plane xoz have the asymptotes y^* and z^*. The curves approach quite close to their asymptotes, usually at $x \approx y^* - 2y^*$. The boundaries in the horizontal plane, $z = \varphi_2(x)$ and $z_w = f_2(x)$, are the projections of the lines of maximum span (maximum width in the yoz plane) of the cone and the wave.

2. Cutting the cone and shock wave (which follows the general contours of the cone) with planes parallel to yoz produces elliptical curves; their major and minor axes generally differ, but by comparatively small amounts.

3. The surfaces of the cone and the wave have xoy as a plane of symmetry.

4. In the initial segment of the cone, liquid with the highest concentration moves in the zone of the plane of symmetry.

The vertical rise of the particles (for delivery pressures that are not too low; in our experiments $\Delta p \geq 8 - 10$ bar) exceeds the lateral spread of the droplets in the direction of the z axis.

Thus, the segment (strip) of the shock-wave surface corresponds in the zone of its vertical boundary $y_w = f_1(x)$ where the curvature is greatest, to the largest losses of total head p_{01} of the gas that has passed across the wave. The boundary of the shock wave $z_w = f_2(x)$ in the zox plane (perpendicular to the plane of symmetry), passing above the lateral zone of the cone with its low droplet content, has a small curvature. It characterizes the region of smallest total-head losses on passage of the gas through the wave. Let us turn now to determination of the empirical relationships for the boundaries of the cone.

Workup of the results of measurements of the boundaries in the initial segments of the cone in dimensionless variables yields an approximate relation of the form

$$\frac{y}{d_c} = F_1 \left(\frac{x}{d_c}; \frac{\varrho_1 W_1^2}{\varrho_2 V_1^2} \right) \tag{2.1}$$

for the range of variation of the flow parameters indicated below and values of

$$\frac{x}{d_c} \leqslant 20 - 30.$$

The combinations x/d_n and y/d_n take account of the influence of atomizer diameter, and the second criterion, the dynamic-head ratio of the liquid and gas, expresses the action of the stream forces that deform the liquid cone; the larger this quantity, the smaller the span of the cone. Expressing the velocity head $\rho_1 W_1^2$ in accordance with the familiar formula of gasdynamics, we obtain

$$\frac{\rho_1 W_1^2}{\rho_\infty V_L^2} = \frac{M_1^2 k_1 p_1}{2\Delta p} = \frac{M_1^2 k_1 p_{01} \pi(M_1)}{2\Delta p}, \tag{2.2}$$

where p_{01} is the total pressure of the stream; $\pi(M_1) = \left(1 + \frac{k-1}{2} M_1^2\right)^{-\frac{k}{k-1}}$ is the gasdynamic pressure function; Δp is the pressure drop at delivery.

It follows from (2.2) that this ratio takes account of four factors at once in compact form: Δp, p, M_1 and k_1. At a given Mach number and a given k_1, it expresses the influence of the pressure ratio $\Delta p/p_1$. The influence of M_1 itself as the third dimensionless number (which appears explicitly in the general form of the relationship) is found to be not particularly significant, in any event, when $M_1 = 2 - 3$. It begins to make itself felt on downstream segments of the cone boundary. For a broader range of x, it is necessary to use a general relation in the form

$$\frac{y}{d_c} = F_2\left(\frac{x}{d_c} : \frac{\Delta p}{p_1} : M_1 : k_1\right), \tag{2.3}$$

which includes three separate independent variables: $\Delta p/p_1$, M_1, and k_1. The fact that the approximate relations (2.1) and (2.3) do not include the Weber number, which is important for determination of liquid-particle sizes, is evidently explained by the fact that it is not the sizes of the individual drops, but the motion of the particle swarm as a whole, that is important in shaping the frontal segment of the cone.

To a certain degree, the process is also self-similar with respect to the gas Reynolds numbers (which evidently have little effect on the result). For high-viscosity liquids, in which case the decay length of the cone may increase appreciably, Re_l is found to be

64
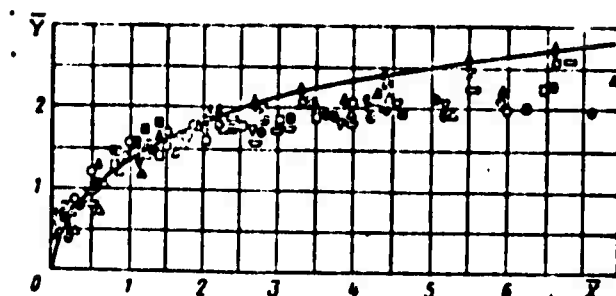
Figure 2.6. Initial section of spray cone boundary.

significant. The small effect of the Froude number of the liquid is natural, since the dynamic forces exceed the weight forces by an order of magnitude (or more). This number may become influential, for example, at low delivery pressures, high liquid specific gravities (molten metals), and large atomizer orifice diameters.

Experience has shown that the following expression can be used as a functional relation in (2.1) (Figure 2.6 and Table 2.1):

$$\bar{Y} = \ln\left[1 + \bar{X} + \sqrt{\bar{X}(\bar{X}+2)}\right], \qquad (2.4)$$

where $\bar{X}$ and $\bar{Y}$ are generalized coordinates containing the dimensionless numbers

$$\left.\begin{array}{l}
\bar{X} = 0.413 \dfrac{x}{d_c}\left(\dfrac{\varrho_1 W_1^2}{\varrho_m V_1^2}\right)^{\frac{1}{3}}; \\[3mm]
\bar{Y} = 0.413 \dfrac{y}{d_c}\left(\dfrac{\varrho_1 W_1^2}{\varrho_m V_1^2}\right)^{\frac{1}{3}}.
\end{array}\right\} \qquad (2.5)$$

The constant in Expression (2.5) is determined experimentally. Expression (2.4) defines a family of affine curves. Any curve is obtained from another by a similarity transformation with the coefficient

$$k_\phi = \frac{0.413}{d_c}\left(\frac{\varrho_1 W_1^2}{\varrho_m V_1^2}\right)^{\frac{1}{3}}.$$

65

TABLE 2.1

Symbol	d_n mm	Δp bar	Symbol	d_n mm	Δp bar
Alcohol $M_1 = 2.9$ $p_\theta = 16$ bar			⊖ △	1.0 1.0	20 10
⌐ ◆ ⊃ ⊙ ◇ ☐ ∪ ■ ▲	1.0 1.0 1.0 0.7 0.7 0.7 0.4 0.4 0.4	40 15–10 5 45 30 15 40 20 10	Gasoline $M_1 = 2.9$ $p_\theta = 7.7$ bar		
			v ⊞ ☐	1.0 1.0 1.0	40 20 10
Alcohol $M_1 = 2.0$ $p_\theta = 12$ bar			Kerosene $M_1 = 2.5$ $p_\theta = 2.0$ bar		
◉	1.0	40	· △	1.0	30

The larger k_c, i.e., the higher the velocity head of the gas compared to that of the liquid, the shorter is the range of the atomized cone.

As an example, Figure 2.7 shows typical cone- and shock-wave boundary shapes in two projections, onto the xoy and xoz planes.

The form of the relationships and the generalized coordinates is suggested by the structure of the analytical solution of the problem of motion of a deformed liquid element when liquid is delivered into a subsonic stream [1].

The motion of the center of mass of the dense swarm of drops should still follow the trajectory of the liquid element on a certain interval.
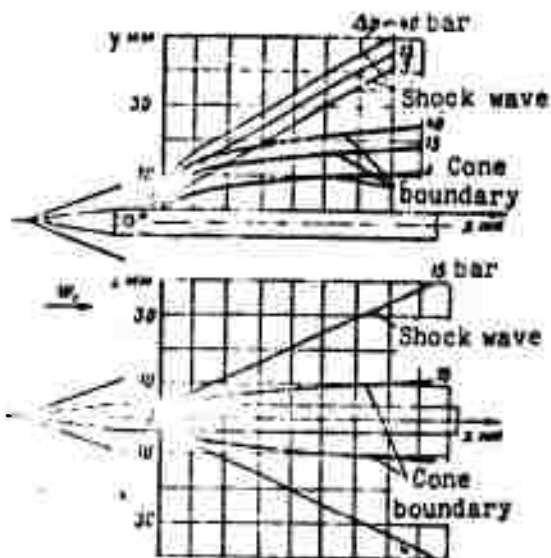
Figure 2.7. Boundary between spray cone and wave at various feed pressures (alcohol, M_1 = 2.9; $p_\bullet$ = 16 bar; d_n = 1 mm; magnification X1).

Let us first consider a rather small zone of the flow at the root of the cone. Here the liquid cone is washed by a stream with parameters approaching those of the gas behind the normal shock. Then, in accordance with the formulas of [1], which sets forth the elementary theory of liquid-cone deformation, we may write an expression for the y coordinate:

$$ky = \ln\left[1 + kx + \sqrt{kx(kx+2)}\right];$$
$$ky = \frac{\varrho W^2}{\varrho_\infty V_1^2}\frac{c_{x0}}{\mathfrak{t}}\, y; \quad kx = \frac{\varrho W^2}{\varrho_\infty V_1^2}\frac{c_{x0}}{\mathfrak{t}}\, x; \qquad (2.6)$$
$$\mathfrak{t} \approx \frac{d_\mathfrak{c}}{3}; \quad c_{x0} \approx 1.2.$$

According to the well-known relation of gasdynamics $\varrho W^2 = \dfrac{\varrho_1 W_1^2}{\lambda_1^3}$

where $\lambda_1 = W_1/a_{cr}$ is the velocity coefficient (a_{cr} is the critical velocity of the gas). The dimensionless coordinates assume the form

$$ky \approx \frac{4}{\lambda_1^3}\frac{\varrho_1}{\varrho_\infty}\left(\frac{W_1}{V_1}\right)^2\frac{y}{d_\mathfrak{c}}; \quad kx \approx \frac{4}{\lambda_1^3}\frac{\varrho_1}{\varrho_\infty}\left(\frac{W_1}{V_1}\right)^2\frac{x}{d_\mathfrak{c}}.$$

Since we are concerned with the range of small $kx(kx \ll 1)$, we may retain only terms of the form $\sqrt{kx}$ in (2.6) and write

$$ky \approx \ln\left[1 + \sqrt{2kx}\right].$$

Expanding the right side of this expression in power series and retaining the first terms of the expansion, we obtain

$$\frac{y}{d_\mathfrak{c}} \approx \sqrt{\frac{\varrho_\infty}{\varrho_1}}\frac{V_1}{W_1}\lambda_1\sqrt{\frac{x}{d_\mathfrak{c}}}. \qquad (2.7)$$
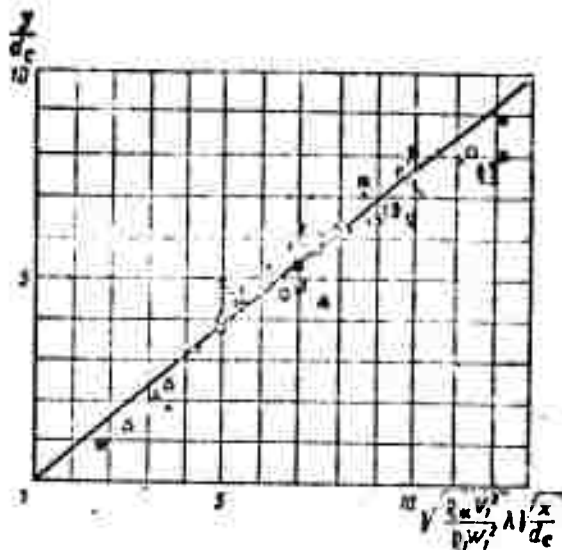
Figure 2.8. Initial segment of spray cone (approximate analytical formula).

Relation (2.7) yields a rough approximate formula for the axis of a curved cone. It is valid only in the range

$$\sqrt{kx} = \frac{2}{\lambda_1} \sqrt{\frac{\varrho_1}{\varrho_m} \frac{w_1}{V_1}} \sqrt{\frac{x}{d_c}} < 1,$$

i.e., at small x/d_n, high delivery pressures, large $M(\lambda)$, and large stream total pressures $p_{\bullet 1}$. Assuming that the forward boundary of the cone is similar in shape to the "liquid line" (geometrically similar), we can use (2.7) for it with an experimentally established proportionality factor. It should be slightly smaller than 1, since the local velocity head of the gas increases with curvature of the shock wave (and y should decrease accordingly).

Figure 2.8 and Table 2.2 compare the curve of (2.7) with experimental data; satisfactory agreement is obtained with a coefficient ≈0.75, and the approximate relation for the boundary at the root of the cone assumes the form

$$\frac{y}{d_c} \approx 0.75 \sqrt{\frac{\varrho_m}{\varrho_1} \frac{V_1}{w_1}} \lambda_1 \sqrt{\frac{x}{d_c}}. \tag{2.8}$$

If we turn now to an initial segment of the cone boundary at a greater distance from the injection point, the stream behind the curved wave will differ substantially from the flow behind the normal shock, and the velocity heads will change sharply.

Use of a formula of the type (2.6) for description of the outer cone boundary behind a certain initial segment of the shock wave requires a change in the degree of the combination $\varrho W^2/\varrho_l V^2$, which appears in the generalized coordinates, from 1 to 1/2. This reasoning

68

<div align="center">TABLE 2.2</div>

Symbol	d_n mm	Δp bar	Symbol	d_n mm	Δp bar
Alcohol ($M_1 = 2.9$; $p_0 = 16$ bar)			**Alcohol** ($M_1 = 2.0$; $p_0 = 12$ bar)		
◊ ⊞ △ ○ □ ◖ ▱	1.0 1.0 0.7 0.7 0.7 0.4 0.4	40 3 45 30 15 40 20	● × △	1.0 1.0 1.0	40 20 10
			Gasoline ($M_1 = 2.9$; $p_0 = 7.7$ bar)		
			▽ ▼ ● □	1.0 1.0 1.0 1.0	40 20 10 5

yields only a certain inductive anology. Formula (2.4) can be taken as an empirical formula.

The plot (see Figure 2.6) indicates that the experimental points follow the logarithmic curve satisfactorily up to $\overline{X}_{1im} \approx 4 - 5$, beyond which the points gradually dip below the curve. The segment on which there is agreement corresponds to the motion of the compact swarm of drops which still has considerable range even though the cone has already decayed. As the swarm thins out and the particle concentration decreases, the particles begin to move in accordance with the single-drop laws. The liquid particles are more easily entrained by the stream and the range of the cone decreases, in accordance with the relative positions of the experimental points and the curve on this figure.

The boundary of the spray cone in the xoz plane is described by a relation having a structure similar to that of (2.1):

$$\frac{z}{d_c} = F_3\left(\frac{x}{d_c}; \; \frac{\varrho_1 W_1^2}{\varrho_m V_1^2}\right) \tag{2.9}$$

and can be approximated by the equation

$$\overline{Z} = \ln\left[1 + \overline{X}_s + \sqrt{\overline{X}_s(\overline{X}_s + 2)}\right]. \tag{2.10}$$

The generalized coordinates

$$\left.\begin{array}{l}
\overline{Z} = 0.65 \, \dfrac{z}{d_c} \left(\dfrac{\varrho_1 W_1^2}{\varrho_{2k} V_1^2}\right)^{\frac{1}{4}}; \\[3mm]
\overline{X}_s = 0.65 \, \dfrac{x}{d_c} \left(\dfrac{\varrho_1 W_1^2}{\varrho_{2k} V_1^2}\right)^{\frac{1}{4}},
\end{array}\right\} \tag{2.11}$$

differ from Expressions (2.5) in the numerical value of the coefficient and the exponent of the factor $\left(\dfrac{\varrho_1 W_1^2}{\varrho_2 V_1^2}\right)$.

The smaller exponent in Formulas (2.11) reflects the lesser significance of the parameters Δp, p_1, M_1, and k_1 in the reshaping of the boundary in xoz as compared to xoy.

The range of validity of Equation (2.10) is approximately the same (but slightly wider) than that of (2.4). The set of experimental curves for y and z permits inferences as to the height and widths of the cone, i.e., its span in the plane of symmetry xoy and the xoz plane perpendicular to it. This determines the orders of the characteristic lengths of the axes in cross sections of the cone parallel to the yoz plane.

Asymptotic Behavior of the Spray Cone

A different approach can be taken to determination of the spray-cone boundary. The largest drops in the spectrum, those with the largest inertia and longest range, should move on the periphery of the cone in the xoy plane.

This is the familiar phenomenon of size separation of drops in a constant-velocity stream. It appears at a certain distance from the point of injection, where the gas variables gradually equalize. Use of the single-drop model has another justification in that the

dense particle swarm thins out here, and the liquid concentration at its periphery drops off sharply (in fuel cones, the concentration-distribution curve is distinguished by a sharp internal maximum and a steep dropoff toward the periphery). If the equation of motion of the drop is solved and the trajectory ordinate is expressed in terms of particle diameter, the entire cone can be represented as a bundle of trajectories corresponding to the particular spray spectrum.

The outer boundary can be regarded as the trajectory of a drop with diameter a_{max}. This approach has been developed in a number of studies, e.g., [15]. From the methodological standpoint, direct determination of the jet boundaries from photographs is evidently simpler than more subtle experiments involving spectrum measurement. Nevertheless, the analytical method is useful and offers additional possibilities for the use of a consistent method of describing the cone boundary when data are available on the coarseness of the spray and it is possible to apply corrections for the properties of the flow in the initial segment of the cone.

Analysis of the equation of motion of the drop indicates that the trajectory of the drop has an asymptote in the real drag-coefficient relations. The trajectory approaches quite close to it in the cone segments that are of practical interest. Thus, the asymptote may be taken as a convenient measure of the range of the spray cone and calculated theoretically if a_{max} is known. The corresponding formulas are given in [15]. In this study, the ordinates y^* of the asymptote are found experimentally as functions of the flow parameters. The cone upper boundary follows, for all practical purposes, a horizontal line at $x \geq 20 - 50$ mm for atomizer diameters $d_n = 0.3 - 0.4$ mm, at $x \geq 60 - 120$ mm for $d_n = 0.8 - 1.2$ mm, and at $x = 80 - 300$ mm for $d_n = 2 - 4$ mm. The average scatter of the measured asymptote ordinates is approximately $\pm 5 - 10\%$.

71
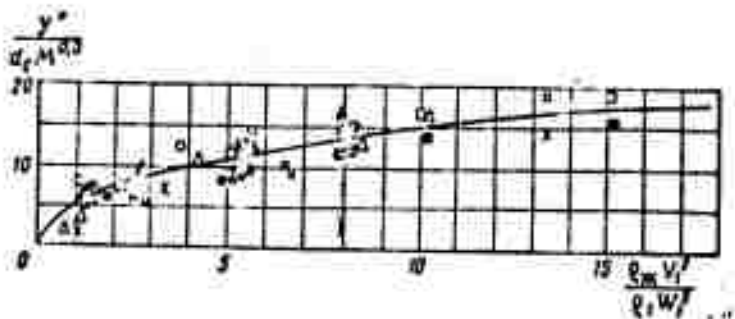
Figure 2.9. Asymptotic behavior of spray cone.

Frocessing of photographs of liquid cones in an air stream yields a general relation (Figure 2.9 and Table 2.3) of the form

$$\frac{y^{\bullet}}{d_c} = 4.3 M_1^{0.3} \left(\frac{\rho_n V_1^2}{\rho_1 W_1^2} \right)^{\frac{1}{3}} .$$

(2.12)

The ranges of variation of the flow parameters corresponding to (2.12) are as follows: $0.4 \leq d_n \leq 4.5$ mm; $1.0 \leq M \leq 2.9$; $5 \leq \Delta p \leq 45$ bar; $2.5 \leq p_0 \leq 16$ bar; $253 \leq T_0 \leq 550°$ K.

The basic factors influencing the height $y^{\bullet}$ of the asymptote are the diameter of the atomizer orifice and the ratio of the velocity heads of the liquid cone and the free stream (a parameter that we have already encountered in our description of the initial cone-boundary segment). The dimensionless ordinate of the asymptote is proportional to the [square] root of this ratio. For a given $\rho_1 W_1^2$, the range $y^{\bullet}$ increases with increasing initial Mach number. As M_1 increases and the shock wave becomes stronger at the root of the cone, the velocity head of the gas, which acts directly on the injected stream behind the wave, decreases, with the resulting increase in range.

The approximate formula (2.12) takes account of the basic factors and will be used in later calculations. It is also possible to use a somewhat more exact formula with a larger number of dimensionless criteria, e.g., in cases in which the surface tension σ of the liquid to be atomized varies over a broad range:

72

TABLE 2.3

Symbol	Fuel	d_n mm	M_1	p_e bar	T °K	Δp bar	$\dfrac{y^*}{d_n}$	$\dfrac{\rho_l V_i^2}{\rho W^2}$
◡	Alcohol	1.0	2.9	16	253	3 10 15 40	11 17 20 26	1.0 3.7 5.6 13.4
⋏.	Alcohol	0.4	2.9	16	253	3 10 20 40	2.3 9.8 13.3 20.0	1.0 3.4 6.7 13.4
⌞	Alcohol	1.0	2.0	12	253	3 5 10 20 40	2.5 4.0 9.0 13.0 16.0	0.1 1.1 2.1 4.2 8.4
▢	Alcohol	0.7	2.9	16	253	15 30 45	15.7 23.6 27.3	5.0 10.0 15.1
⊔	Kerosene	2.5	1.0	2.5 4.5	273	2.7 4.7 9.7 19.7 29.7 8.6 18.6 28.6 3.6 8.6 18.6 28.6	6.0 7.0 8.9 14.0 16.0 6.6 9.8 12.0 5.4 6.4 10.8 12.0	1.7 2.7 5.2 10.2 15.2 2.7 5.4 8.2 1.2 2.7 5.4 8.2
▲	Kerosene	4.0	1.0	2.5 4.5	253	4.7 9.7 19.7 3.6 8.6 18.6 27.6 3.6 18.6 3.3 7.6 3.6 18.6 27.6	9.3 12.5 16.3 5.0 7.7 12.0 15.0 5.3 8.7 5.8 7.3 5.7 12.0 16.3	2.7 5.2 10.2 1.2 2.6 5.4 7.9 1.2 5.4 1.7 2.3 1.2 5.4 7.9
●	Gasoline	0.6	2.5	9.8 13.0 14.7 14.5	300 262	16.3 16.0 19.1 18.9	13.9 10.7 12.2 11.1	6.6 4.9 5.1 5.1

73

$$\frac{y^{\bullet}}{d_{c}} = 0.15 M_{1}^{0.3} \left(\frac{\varrho_{\infty} V_{1}^{2}}{\varrho_{1} W_{1}^{2}} \right)^{\frac{1}{2}} \frac{\left(\frac{W_{1} d_{c}}{\nu_{1}} \right)^{\frac{4}{5}}}{\left(\frac{\varrho_{1} W_{1}^{2} d_{c}}{\sigma} \right)^{\frac{1}{7}}} .$$

(2.13)

Passing to the xoz plane (the vertical projection of the cone), we obtain a relation similar to (2.12) for the lateral-asymptote parameter $z^{\bullet}$, which determines the width of the spray cone:

$$\frac{z^{\bullet}}{d_{c}} = 5 M_{1}^{0.3} \left(\frac{\varrho_{\infty} V_{1}^{2}}{\varrho_{1} W_{1}^{2}} \right)^{\frac{1}{4}} .$$

(2.14)

Comparison of Formulas (2.12) and (2.14) indicates that the effect of the flow parameters on the cone width $2z^{\bullet}$ is weaker than the effect on its height $y^{\bullet}$.

The orders of magnitude of $y^{\bullet}$ and $2z^{\bullet}$ are similar in the range covered by the experiments.

The ordinate $y^{\bullet}$ of the asymptote is used to advantage as a characteristic length scale in the two-phase flow under consideration. It is uniquely related to the atomizer orifice diameter d_{n}, but is more convenient and lucid, since it is comparable to the distances and lengths of various segments of the cone with which we shall eventually have to deal. Thus, we shall measure all lengths in "cone calibers" $y^{\bullet}$.

Using Formulas (2.4), (2.5), (2.10), (2.11), (2.12), and (2.14), we may exclude the dimensional diameter d_{n} from the expressions for the initial segment of the cone boundary, introducing in its place the scales $y^{\bullet}$ and $z^{\bullet}$. This also eliminates a multiplier — the ratio of the gas and liquid velocity heads, since it appears symmetrically in the corresponding expressions:

$$\frac{y}{y^{\bullet}} = F_{1} \left(\frac{x}{y^{\bullet}} : M_{1} \right) = \frac{\ln \left[1 + \bar{X} + \sqrt{\bar{X}(\bar{X} + 2)} \right]}{1.77 M_{1}^{0.3}};$$

(2.15)

$$\overline{X} = 1.77 M_1^{0.3}\, \frac{x}{y^*};$$
(2.16)

$$\frac{z}{z^*} = F_s\left(\frac{x}{z^*};\ M_1\right) = \frac{\ln\left[1 + \overline{X}_s + \sqrt{\overline{X}_s\,(\overline{X}_s + 2)}\right]}{3.24 M_1^{0.3}};$$
(2.17)

$$\overline{X}_s = 3.24 M_1^{0.3}\,\frac{x}{z^*} = 3.24 M_1^{0.3}\,\frac{x}{y^*}\,\frac{y^*}{z^*}.$$
(2.18)

The characteristic scales z^* and y^* are simply related:

$$\frac{z^*}{y^*} = 1.16\left(\frac{\rho_x V_1^2}{\rho_1 W_1^2}\right)^{-\frac{1}{4}}.$$
(2.19)

Excluding z^* with the aid of (2.19), we can express the equation for the cone boundaries in the xoy and xoz planes in terms of the parameters y/y^*, z/y^*, x/y^*, M_1, and $\rho_1 W_1^2/\rho_l V_1^2$, using the single universal length scale y^* and the common dimensionless abscissa x/y^* (in the yox and zox planes). In view of the limits within which the initial formulas agree satisfactorily with experiments, the dimensionless abscissa x/y^* should be limited to

$$0 < \frac{x}{y^*} < \frac{\overline{X}_{np}}{1.77 M_1^{0.3}},$$

for example, we obtain for $M_1 = 3$ and $\overline{X}_{lim} = 5$

$$0 < \frac{x}{y^*} < 2.$$

This range of variation of x/y^* is found to be adequate for analysis of the subject process and for development of the computational technique to be set forth below.

Shape of Spray Cone Shock Wave

The boundary of the spray cone shock wave can be determined from the previously mentioned photographs. Some of the supplementary experiments were performed on other setups similar to that described above. The experiments with water were run in an open stream with slightly heated air: $T_1 \approx 290°$ K.

At the initial point, the wave is tangent to the vertical, and an element taken here nearly coincides with the normal shock. For dimensionless processing, we shall use the scale y^* introduced above, i.e., a certain characteristic dimension of the body past which the flow moves — the spray cone. We may seek relationships that define the shock-wave boundaries in the form

$$\frac{y_0}{y^*} = F_6\left(\frac{x}{y^*} ; M_1\right);$$

(2.20)

$$\frac{z_0}{z^*} = F_7\left(\frac{x}{z^*} ; M_1\right).$$

(2.21)

The influence of M_1, which appears in explicit form in the relation, must be stronger the farther the segment of the wave from the injection point, i.e., the closer it is to the characteristic. The slope angle will approach the Mach angle α_{max} and its tangent will be expressed by the familiar formula

$$\text{tg}\, \alpha_{max} = \frac{1}{\sqrt{M_1^2 - 1}}.$$

(2.22)

In Figure 2.10, we have plotted experimental points processed in the dimensionless coordinates y_w/y^* and x/y^* for shock waves under various injection conditions. Table 2.4 lists the corresponding flow parameters. The experiment indicates that M_1 still has insignificant influence on the trend of the generalized curve for the initial shock-wave segment at $x/y^* \leq 0.1 — 0.5$ and $M_1 = 2 — 2.9$. For rough
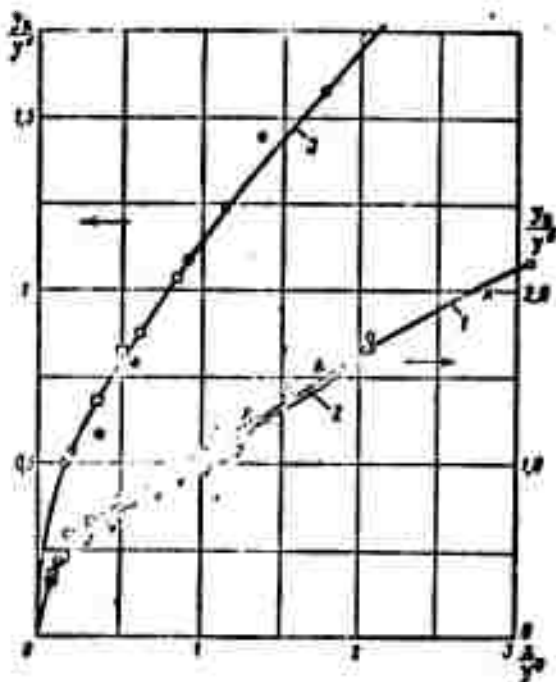
76

Figure 2.10. Spray cone shock wave in dimensionless coordinates.

1 — $M_1 = 2.9 - 2.85$, experimental curve; 2 — exponential approximation ($M_1 = 2.85$); 3 — $M_1 = 2$, experimental curve.

approximation of the shape of the segment, we may use a power-law relation of the form

$$\frac{y_b}{y^\circ} = B_y \left(\frac{x}{y^\circ}\right)^{k_y} \qquad (2.23)$$

$$0 < \frac{x}{y^\circ} < 0.1; \quad B_y = 0.76; \quad k_y = 0.28.$$

The constant B_y and the exponent k_y in (2.23) can be calculated from the coordinates and slope angle α_1 at a certain point N on the experimental curve of the wave for a definite M_1, e.g., $x/y^* = 0.1$. In this case, the constants are found from the two relations

$$\left(\frac{y_b}{y^\circ}\right)_N = B_y \left(\frac{x}{y^\circ}\right)^{k_y}_N;$$

$$\frac{d\left(\frac{y_b}{y^\circ}\right)}{d\left(\frac{x}{y^\circ}\right)} = tg\,\alpha_1 = B_y k_y \left(\frac{x}{y^\circ}\right)^{k_y - 1}_N .$$

Similarly, a power-law approximation (with the constants B_z and k_z) is carried out for the boundary of the wave in the vertical plane:

$$\frac{z_b}{z^\circ} = B_z \left(\frac{x}{z^\circ}\right)^{k_z}; \qquad (2.23')$$

$$B_z = 0.46; \quad k_z = 0.3 \quad \text{for} \quad 0 < \frac{x}{z^\circ} < 0.1.$$

A power-law approximation of the form (2.23) is convenient and accurate only for a rather small range near the coordinate origin with strong curvature of the wave. On longer segments, on which the curvature of the wave decreases appreciably and its angle gradually

77

TABLE 2.4

Symbol	Fuel	M_1	d_n mm	Δp bar	Symbol	Fuel	M_1	d_n mm	Δp bar
●	Alcohol	2,9	1,0	40	▽	Water	2,85	1,0	40
✗	Alcohol	2,9	1,0	15	■	Water	2,85	1,0	65
▲	Gasoline	2,9	2,5	23	□	Alcohol	2,0	1,0	40
○	Gasoline	2,9	0,4	40	○	Alcohol	2,0	1,0	20

approaches the slope of the characteristic, use is made of another function linking the dimensionless numbers and reflecting the asymptotic character of the wave boundary.* It can be sought, for example, in the form of the exponential relation

$$Y = AX - B_y e^{-C_y X} + D_y. \tag{2.24}$$

where $Y = y_w/y^*$ and $X = x/y^*$ are generalized coordinates and A, B_y, C_y and D_y are positive coefficients of the curve.

As follows from the expression given above, the constant A equals the value of the derivative at infinity ($X = \infty$):

$$A = \left(\frac{dY}{dX}\right)_\infty = \left(\frac{dy_n}{dx}\right)_\infty = \operatorname{tg} a_{M_{\text{max}}} = \frac{1}{\sqrt{M_1^2 - 1}}. \tag{2.25}$$

Condition (2.25) expresses the slope of the asymptote of the characteristic into which the shock wave merges at infinity. Generally speaking, the coefficients B_y, C_y, and D_y depend on M_1. They can be found by requiring that the generalized curve pass through three given points on the wave, whose dimensionless coordinates are obtained experimentally.

Let us discuss the method of calculating the coefficients. The condition for passage of the boundary through the three points $M_1(X_1;\ Y_1);\ M_2(X_2;\ Y_2);\ M_3(X_3;\ Y_3)$ yields three starting relationships:

*This formula is used extensively in a number of the later calculations.

$$Y_1 = AX_1 - B_y e^{-C_y X_1} + D_y; \qquad (2.26)$$

$$Y_2 = AX_2 - B_y e^{-C_y X_2} + D_y; \qquad (2.27)$$

$$Y_3 = AX_3 - B_y e^{-C_y X_3} + D_y. \qquad (2.28)$$

Eliminating the unknowns D_y and B_y, we obtain an equation for the constant C_y:

$$F = \frac{Y_2 - Y_1 - A(X_2 - X_1)}{Y_3 - Y_1 - A(X_3 - X_1)} = \frac{1 - e^{-C_y(X_2 - X_1)}}{1 - e^{-C_y(X_3 - X_1)}}. \qquad (2.29)$$

This is a transcendental equation and must be solved numerically (e.g., graphically). It can be shown that the equation system (2.27), (2.28), and (2.29) will always have a solution under the following conditions:

1) $X_3 > X_2 > X_1$; $Y_3 > Y_2 > Y_1$;

2) $\dfrac{Y_2 - Y_1}{X_2 - X_1} > \dfrac{Y_3 - Y_1}{X_3 - X_1}$; 3) $\dfrac{Y_3 - Y_2}{X_3 - X_2} > A.$

In other words, it will always be possible to find constants B, C, and D by drawing a monotonic convex curve through the three selected points. The combinations that appear under items 2 and 3 are the slopes, with respect to the ox axis, of the chords joining the corresponding points, i.e., they are the average slopes of the curve. Clearly, any three points on a curved shock wave satisfy these conditions.

Let us prove rigorously the existence of a solution of transcendental equation (2.29). Let us assume at first that $F \le 1$ for any point coordinates. If this is not the case and $F \ge 1$, we write from Relation (2.29)

$$Y_2 - Y_1 - A(X_2 - X_1) \ge Y_3 - Y_1 - A(X_3 - X_1)$$

and then

$$A \geqslant \frac{Y_1 - Y_2}{X_3 - X_2}.$$

which contradicts condition 3. Let us now show that the right side of (2.29) will be smaller than F with a certain value of C_y, but larger than (or equal to) F at another value. Consider the range of small C_y. As $C_y \to 0$, application of l'Hospital's rule (to evaluate the indeterminate form 0/0) yields

$$\lim_{C_y \to 0} \frac{1 - e^{-C_y(X_0 - X_1)}}{1 - e^{-C_y(X_0 - X_1)}} = \frac{\frac{d\left[1 - e^{-C_y(X_1 - X_1)}\right]}{dC_y}}{\frac{d\left[1 - e^{-C_y(X_0 - X_1)}\right]}{dC_y}} = \frac{X_2 - X_1}{X_3 - X_1},$$

and the ratio is smaller than F; if this were not the case, we should have

$$\frac{Y_2 - Y_1 - A(X_2 - X_1)}{Y_3 - Y_1 - A(X_3 - X_1)} < \frac{X_2 - X_1}{X_3 - X_1},$$

whence, dividing the entire inequality by its right side, we have

$$\frac{Y_2 - Y_1}{X_2 - X_1} < \frac{Y_3 - Y_1}{X_3 - X_1},$$

which contradicts condition 2 and proves the inequality

$$\frac{X_2 - X_1}{X_3 - X_1} < F.$$

Let us now consider the range of large C_y; as $C_y \to \infty$, the right side of (2.29) tends to unity.

In virtue of the continuity of the function

$$\frac{1 - e^{-C_y(X_1 - X_1)}}{1 - e^{-C_y(X_0 - X_1)}},$$

it runs through all values between

$$\frac{X_2 - X_1}{X_3 - X_1}$$

and 1, thus becoming equal to F at a certain value of C_y. It is therefore always possible to find the constant C_y. For approximate estimation of this constant, we chose a sufficiently large interval $X_3 - X_1$ and obtain $e^{-C_y(X_3-X_1)} \approx 0$, which enables us to find the solution of (2.29) in explicit form:

$$C_y \approx \frac{\ln\left(\frac{1}{1-F}\right)}{X_2 - X_1}. \qquad (2.30)$$

Graphical solution is very simple in practice; for quick determination of values of C_y in the region around the point of intersection of the curve

$$\frac{1 - e^{-C_y(X_2-X_1)}}{1 - e^{-C_y(X_3-X_1)}}$$

and the horizontal line $F = \text{const} < 1$, we may use the value obtained from (2.30). Knowing C_y, we find the other two coefficients from relationships obtained by simple transformation of the initial equation:

$$B_y = \frac{Y_2 - Y_1 - A(X_2 - X_1)}{e^{-C_y X_1} - e^{-C_y X_2}}; \qquad (2.31)$$

$$D_y = Y_1 - AX_1 + B_y e^{-C_y X_1}. \qquad (2.32)$$

The expedient of exponential approximation of a sufficiently long segment of the shock wave may also be helpful in other problems, such as those involving the delivery of a gas cone into a supersonic stream. Everything that we said above concerning exponential approximation of the wave boundary in the profile plane xoy can be extended

81

TABLE 2.5

$(x_1=0,1;\ x_2=0,5;\ x=1;\ (x_2)_1=0,1;$
$(x_2)_2=1;\ (x_2)_3=1,8)$

M_1	A	B_y	C_y	D_y	B_z	C_z	G_y
2,0	0,55	0,35	2,06	0,69	0,25	2 99	0,38
2,9	0,37	0,46	2,04	0,74	0,31	1,18	0,46
4,0	0,26	0,55	1,66	0,84	0,51	0,83	0,65

to the boundary curve of the wave in the vertical plane xoz, whose equation takes the form

$$Z = AX_z - B_z e^{-C_z X_z} + D_z;$$
$$Z = \frac{z}{z^*};\quad X_z = \frac{x}{z^*} = X\frac{y^*}{z^*}. \tag{2.33}$$

Like the boundaries of the cone, the boundary of the shock wave (which duplicates its shape) changes less sharply in the xoz plane than in xoy on a changing flow parameter. This is manifested in a weaker dependence of the scale factor z^* on the respective variables compared with the scale y^* (a smaller exponent of the multiplier $\rho_2 V_1^2/\rho_1 W_1^2$).

Thus, using the method set forth above, it is always possible to calculate the coefficients of the approximating functions, which are listed in Table 2.5. In practice, all calculations of the constants B, C, and D will, of course, be included in the computer program of the general method (see below).

Figure 2.10 shows an example in which an approximating curve 2 is compared with an experimental curve 1, which corresponds to points on the boundary of the shock wave in dimensionless coordinates (see Table 2.4). If we consider a comparatively short segment X ≤ 1 — 2, where the influence of M_1 on the shape of the wave is not yet very strong, the existing region of definition of the constants in terms of the Mach numbers can evidently be broadened somewhat to M_1 = 3.5 — 4 by extrapolating the experimental curves for the ordinates Y_1, Y_2, and Y_3 with respect to M_1. For this purpose, we use an approximate relation of the form

$$\frac{y_i'}{y_i''} \approx \left(\frac{M_1''}{M_1'}\right)^{\alpha_i}.$$

where α_i is a constant determined experimentally for the selected x_i (i = 1, 2, 3) points on the boundaries of the wave and two not strongly different Mach numbers M''_1 and M'_1. Below we shall need approximate analytical expressions for the ratios of the areas of certain characteristic cross sections in the initial segment of the

cone (see Figure 2.1) $F^{\#}/F'$, $F^{\#}/F_M$, and F'/F_M. The first two quantities are the ratios of the asymptotic-cross-sectional area $F^{\#}$ of the "cold" cone with semiaxes $y^{\#}/2$ and $z^{\#}$ (in practice, the cross section of the cone is nearly equal to $F^{\#}$ at distances of $\sim 2 - 5$ calibers $y^{\#}$) to the cross-sectional areas F' of the jet and F_M of the shock wave at a fixed x'; the third ratio $F'/F_M = F^{\#}/F_M : F^{\#}/F'$. The exact contours of these ovals are not known. According to general considerations pertaining to the shapes of the cone and wave (which were advanced earlier), the cross section contours can be likened to ellipses with the semiaxes

$$\left(\frac{y^\bullet}{2}; \ z^\bullet\right); \ \left(\frac{y}{2}; z\right)\left(\frac{y_0}{2}; z_0\right)$$

Then

$$F^\bullet \approx \frac{\pi}{2} y^\bullet z^\bullet; \quad F' \approx \frac{\pi}{2} yz; \quad F_u \approx \frac{\pi}{2} y_0 z_0; \tag{2.34}$$

$$\frac{F^\bullet}{F'} = \frac{1}{\dfrac{y}{y^\bullet}\dfrac{z}{z^\bullet}}; \tag{2.35}$$

$$\frac{F^\bullet}{F_M} = \frac{1}{\dfrac{y_0}{y^\bullet}\dfrac{z_0}{z^\bullet}}. \tag{2.36}$$

The dimensionless ratios of the coordinates in the denominator are expressed by the dimensionless formulas given above for the boundaries of the cone and shock wave: (2.15), (2.17), (2.24), and (2.33). In the roughest of estimates, these ovals might be regarded as circles with radii intermediate between the semiaxes of the ellipses or equal to $y^{\#}/2$. Formulas (2.35) and (2.36) express the characteristic-area ratios in terms of three independent dimensionless numbers:

$$\frac{x}{y^\bullet}; \ \frac{z^\bullet}{y^\bullet} = \varphi\left(\frac{v_\infty V^2}{v_1 W_1^2}\right); \ M_1.$$

We also introduce a formula (which will be used later) for the liquid concentration in the spray cone:

$$\beta^* = \frac{m^* + m_\varkappa}{m^*},$$

(2.37)

It equals the concentration at the end of the "cold" cone where its boundaries approach the horizontal asymptote. Thus, this quantity, which corresponds to the highest flow rate of the free stream across the widest cone cross section F^*, is the lowest concentration in the cross sections of the cone:

$$m^* = W_{1\varrho} F^* \approx W_{1\varrho} \frac{\pi y^* z^*}{2};$$

$$m_\varkappa = \mu_p \frac{\pi d_c^2}{4} \varrho_\varkappa V_1 = \mu_p \frac{\pi d_c^2}{4} \sqrt{2\Delta p \varrho_\varkappa};$$

μ_a is the atomizer discharge coefficient.

After simple transformations in (2.37):

$$\beta^* = 1 + \frac{\mu_p \varrho_\varkappa V_1 R T_1}{2 \frac{y^*}{d_c} \frac{z^*}{d_c} W_1 p_1}$$

(2.38)

and substitution of the values for the ordinates y^*/d_n and z^*/d_n, we obtain a working formula connecting β^* with the basic flow parameters:

$$\beta^* = 1 + \frac{\mu_p \sqrt{\varrho_\varkappa} \sqrt{R T_1} k_1^{\frac{1}{4}}}{\sqrt[4]{2}\, 4.3 \cdot 10 (\Delta p \cdot p_1)^{\frac{1}{4}} M_1^{\frac{1}{16}}} = 1 + \frac{\mu_p \sqrt{\frac{\varrho_\varkappa R T_1}{p_1}} k_1^{\frac{1}{4}}}{43 \sqrt[4]{2} \left(\frac{\Delta p}{p_1}\right)^{\frac{1}{4}} M_1^{\frac{1}{16}}}.$$

(2.39)

Thus, the concentration β^* does not depend on the nozzle-orifice diameter d_n, depends little on the free-stream Mach number M_1, and is determined basically by the number $\Delta p/p_1$ (which can vary over a broad range) and by the number $\varrho_\ell R T_1/p_1 = \varrho_\ell/\varrho_1$; $k_1 = c_{p_1}/c_{v_1}$ being the adiabatic exponent in the free stream. Curves of β^* appear in Figure 2.11.
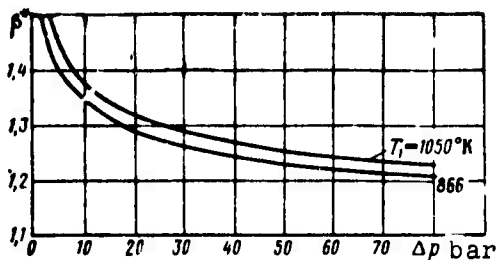
Figure 2.11. Liquid concentration in spray cone (M_1 = 2.85; p_1 = 1 bar; k_1 = 1.33).

With the formulas given above, we can estimate the cross-sectional areas of the cone and wave at a given x. The area ratios, together with the factor β^*, will emerge as important parameters in subsequent analysis of the processes in the evaporating cone.

In conclusion, we present an experimental formula for the range x_{lim} of a spray cone from a straight-cone nozzle against a supersonic stream. It may be used, for example, for protection of structural members, channel edges, etc., against heat:

$$\frac{x_{up}}{d_c} = 10 \left(\frac{\varrho_{\ast} V_1^2}{\varrho_1 W_1^2} \right)^{2/3}. \tag{2.40}$$

The experiments were carried out in a stream with M_1 = 2.9; p_{01} = 12 — 18 bar; T_{01} = 253° K; d_n = 0.8 — 1 mm; Δp = 5 — 40 bar (Figures 2.12 and 2.13).

§3. Model of Flow in Spray Cone

A number of interrelated elementary processes develop on a comparatively short interval of the spray cone between the injection point and the point of total vaporization. Following the decay of the liquid cone, the drops are entrained by the gas, and subjected to heating and dynamic vaporization. Heat, mass, and mechanical energy are exchanged between the two phases. Generally speaking, the various physical processes unfold almost simultaneously, but from the standpoint of intensity and effect on the final result (total vaporization) they can be separated in space and time.
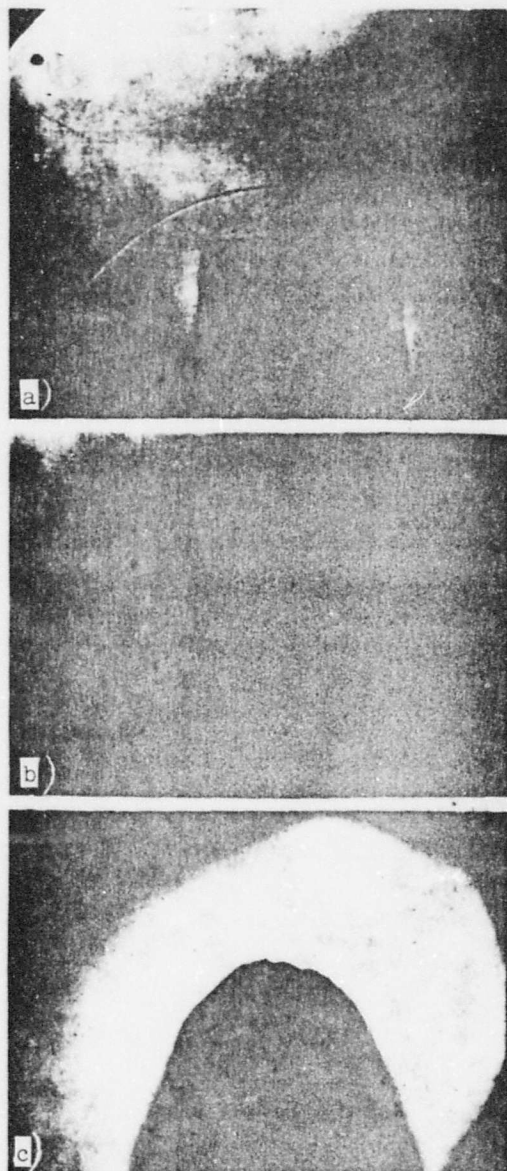
Figure 2.12. Spark photomicrographs of tip of spray cone (alcohol, M_1 = 2.9; p_0 = 15 bar; d_n = 0.8 mm; magnification 8.5 X).

a — Δp = 0; b — Δp = 5 bar; c — Δp = 10 bar.

We divide the spray cone arbitrarily into three successive segments along the ox axis: initial, main, and accelerating, in accordance with the most characteristic phenomena in each (Figure 2.14). The initial segment (with exit-section area F") has a short length x' on the order of the range on the cone, i.e., the ordinate y^* of the asymptote of the "cold" cone. Vaporization cannot yet be significant at this point owing to the very high drop concentration and the inadequate temperature to which they are heated, which rises appreciably only toward the end of the segment (for conditions in which the liquid delivered is at comparatively low, room temperatures). Photographs of liquid cones in a stream heated to 1000° K and above show an appreciable bow segment that differs little in shape and contour from the corresponding "cold-cone" segment. Sharp differences are observed on the interval that follows.

The initial segment is distinguished by strong depletion of mechanical energy from the gas. This energy is expended on deformation and decay of the
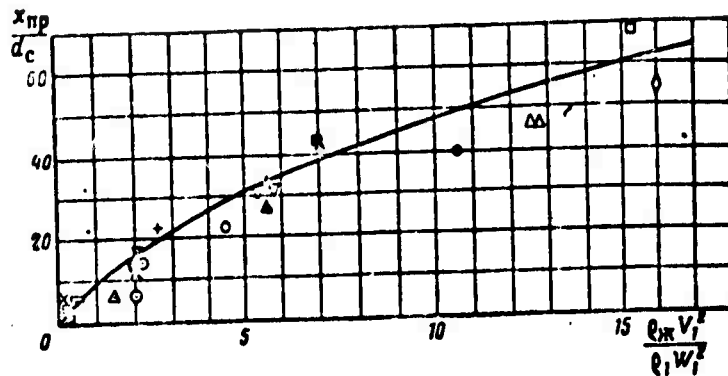
86

Figure 2.13. Range of cone in contra-stream injection (alcohol, M_1 = 2.9).

cone and on breakup of the drops, but for the most part it imparts kinetic energy to the mass of liquid particles. The drops are accelerated from comparatively low injection velocities of $V_1 \approx 40 - 120$ m/sec to the high velocities W' of the gas at the end of the segment. The streamlines and particle trajectories on this segment are extremely complex and disorganized: the flow behind the shock wave is distinguished by highly nonuniform distribution of the parameters.

Passing through the dense "liquid grid" of drops, which tends to level out the parameter field, the stream approaches more or less organized and uniform flow. The initial segment is followed by the main segment with entrance cross section 1' — 1', area F' and length x_v. In our opinion, the dominant process here is strong vaporization of the bulk of the liquid, accompanied by substantial withdrawal of heat from the gas and drops.
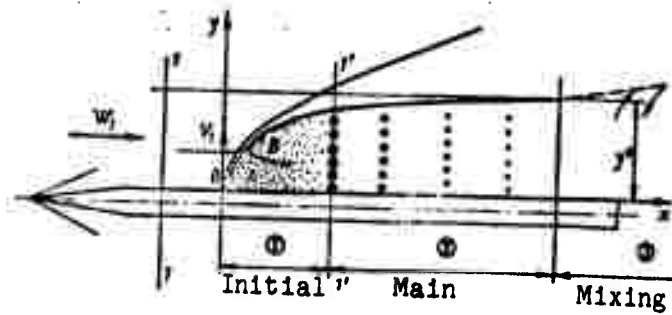
Figure 2.14. Characteristic segments of flow in spray cone.

Following the terminology of one-dimensional gasdynamics, it can be said that the initial segment "works" primarily as a mechanical nozzle, and the main segment as a combination nozzle (removal of heat and mass, and exchange of mechanical energy between the phases). Let us assume that the drops are uniformly distributed here and in motion as individual particles along a system of ordered and rather flat trajectories near parallels to the ox axis. Then the processes on the main segment can be described approximately by the theory of one-dimensional two-phase flow set forth in Chapter I. The initial conditions for the corresponding equation system must be assigned in terms of the parameters of cross section 1' -- 1', which are determined by the flow at the exit from the initial segment. In the general case, the vaporization parameters, for example, the length x_v, are influenced by two factors: the initial condition shaping the stream, i.e., the parameters W', T', β', and p', and the subsequent mixing of the flows within the cone and surrounding it.

For conditions with strongly developing phase transitions — in which atomization is quite fine (as is characteristic for supersonic flows), the fuel (for example, gasoline, alcohol) is thoroughly evaporated and the temperature of the free-stream gas is not particularly low ($T_1 \geq 700 - 800°$ K) — the first factor may be assumed to dominate. When mixing comes into play, the bulk of the liquid has already been vaporized. Calculation of the two-phase flow in all its complexity, with consideration of exchange of properties between the

88

two streams, is extremely difficult at the present time. The real process must be replaced by a crude idealization, whose purpose is to give some measure of the total-vaporization interval of the cone. This process might be called the "corresponding regime"; it represents a one-dimensional two-phase flow in a cylindrical pipe without friction (or in unbounded space) with the average entrance cross section parameters F', W', T', β', and p'. The drops have equal diameters — the a_{max} of the atomization spectrum. The isolated flow under consideration here will resemble the real flow more closely the smaller the relative (but not absolute) length of the vaporization interval in "calibers" of the cone $(x + x_u)/y^*$.

The correctness of the model adopted, in which the interactions taking place inside the cone are regarded as basic, must be determined by experiment. At this moment, we can state only the following. The effects of external mixing make themselves felt first of all on peripheral layers of the cone, while the bulk of the particles are in motion inside it. In particular, the effect in which the gas is sharply decelerated by the particles, which was brought out by the calculations for $M < 1$ in Chapter I, should occur in the zone of maximum concentration around the axis of the stream. The influence of expansion of the cone's free boundaries is not, according to certain calculations, particularly important. We refer, for example, to calculations of two-phase flow with consideration of pressure equalization between the free flow inside the cone and the surrounding gas. By the end of vaporization, the cross-sectional area of the cone has increased by about 10 — 25%, and the corresponding change in the gasdynamic variables has little influence on the length of the vaporization interval (as compared to the calculation without consideration of the expansion).

The main segment of the cone is followed by an accelerating or mixing segment. Much of the fuel has already been vaporized by the time it reaches the beginning of the segment. Mass, heat, and momentum exchange between the two gaseous media — the vapor-air mixture inside the cone and the surrounding stream — are the principal processes here.

89

In certain special cases, it may happen that vaporization is not yet complete at the beginning of the third segment, e.g., when local saturation intervenes in the "peak" concentration zone. Then intensive exchange at high velocity gradients and other parameters (if it involves most of the thickness of the cone) completes the vaporization quickly. In the present study, we are concerned with processes taking place only on the main and initial segments, since they determine the total-vaporization interval. We shall now consider the nature of the flow on the initial segment of the cone in detail, and submit certain qualitative arguments. The gas flow directly behind the segment with the strong shock wave (which is closely adjacent to the surface of the cone) contains a rather highly developed sub-critical layer A with M' < 1 (see Figure 2.14). To judge from the slopes of the wave in the xoy plane, its height is approximately 1/3 of y^* (for flow conditions with M_1 = 2.9). Evidently, most of the drops move in this zone.

Above layer A, behind a weaker wave, we have a supercritical flow B with M' > 1; they are separated by a certain surface on which M' = 1. Thus far, one type of gasdynamic effect predominates — removal of work from the gas to the drops;[*] the average (over the cross section) Mach number of the gas M' = $W'\sqrt{kRT'}$ increases in stream A, approaching 1 from below, while the Mach number of stream B decreases, approaching 1 from above. The large initial values of the pressure p'_A and temperature T'_A in the subcritical layer decrease, and the small quantities p'_B, T'_B in the supercritical layer increase. Conceivably, somewhere toward the end of the initial segment of the cone, the total stream A and B will tend to a limiting critical cross section with an average M' near 1.

---

[*]It is assumed that, beginning with a certain transverse cross section, the stream filaments are for the most part really cylindrical and the effect of their expansion is not decisive. The visible broadening of the cone with increasing distance from the injection point occurs chiefly because of the arrival of new gas filaments in the zone of the cone. The effects of exchange between streams A and B are also considered immaterial on the short segment under consideration.

Here we consider the so-called frozen Mach number of the gas, which is analogous to the M' introduced in Chapter I for one-dimensional two-phase flow. M' is formed from the average parameters W' and T' in the cone cross section corresponding to the equivalent one-dimensional flow (for details, see below). Generally, the bulk of the gas on the initial segment of the cone can move with M' < 1 and M' > 1. However, we may assume that there exists a certain class of flow conditions in which the flow is, on the average, subcritical over the entire initial segment, i.e., the gas inside the "liquid grid" is sharply decelerated and flows with increasing but comparatively small Mach numbers M' < 1 (everywhere except, perhaps, in the region of low particle concentrations in zone B at the periphery of the cone).

Details of the flow of gas with drops in stream B are unknown. A shock-free deceleration scheme is apparently more natural. Let us turn to the results of calculation of the kinematics of a single drop behind a curved cone shock wave (see Chapter I). In its relative motion, a subsonic stream flows around the drop, i.e., the (absolute, difference between the particle and gas velocities remains quite far below the speed of sound even until the stream has been accelerated beyond the supercritical level. The presence of a whole swarm of drops should lower the relative velocities even further, i.e., leave our conclusion in force. Thus, the initial supersonic gas stream B[*] may become subcritical inside the cone with no additional wave losses. It is also possible for flow B to be transformed via a system of many microscopic discontinuities on the drops. Then the average Mach number would still be near unity (but evidently smaller than unity), since the discontinuities become increasingly weak from one layer of drops to another.

Thus, no matter what the actual mechanism of the process, we assume conditions under which the average flow remains subcritical in the frontal zone of the cone. It is accelerated on an initial segment whose length is on the order of the cone scale, approaching

─────────────────────────

[*]Which follows the shock wave.

a critical cross section in which the Mach number is around unity and appreciable phase transitions may already have begun. The above arguments have a corollary of practical interest. If the vaporization process begins to develop in the region of subcritical flow (toward the end of the initial segment or at the beginning of the main segment), the gas is strongly decelerated as a result of phase transitions even on the main segment. This increases the liquid-particle stay time and gives a shorter total-vaporization interval accordingly. If, on the other hand, vaporization "gets stuck" at supercritical flow parameters, the phase transitions will accelerate the gas, shorten the stay time of the drops on the main segment, and extend the vaporization interval significantly. Calculations of two-phase flows in accordance with the theory set forth in Chapter I yield precisely this result (in a broad range of variation of the initial data). The to'al-vaporization interval x_v is much shorter with subcritical parameters $M_1 < 1$ than at supercritical parameters $M_1' > 1$.

Thus, the question as to the existence of subcritical flow over a rather long initial segment of the cone is related to the selection of a rational injection system that insures vaporization on a comparatively short length of the chamber. The stream of gas with liquid particles, not having been accelerated to supercritical parameters in the initial segment, then begins to slow down again in the zone of phase transitions, remaining subcritical to the end of vaporization. Subsequent acceleration of the vapor-gas mixture occurs only on the mixing segment. At large x' in a "cold" cone, in which vaporization is negligible, the transition through the critical state is completed closer to the injection point. It will be governed by the reversal of signs of the gasdynamic effects on the mixing segment due to property exchange between the streams inside and outside of the cone.

The qualitative arguments set forth here lead to a working hypothesis that might be called the hypothesis of the critical cross section. For a certain class of regimes, subcritical flow with $M' < 1$ occurs in an initial segment of the cone of length $x' \approx y^*$. Conditions approaching those of the critical cross section are created at the

exit from the initial segment, where M' approaches 1. In this case, vaporization of the bulk of the drops begins (in the main segment) at subcritical parameters with $M' \approx 1$. A certain near-unity value, e.g., $M' = 0.95$, can be used in calculations.

The subcritical-flow regimes should be characterized by a strong deceleration of the free stream in the shock wave, i.e., by quite high M_1 (strong wave) and liquid concentration β^*. There is no need for accurate determination of the coefficient of the critical cross section or the corresponding exact value of the critical Mach number M'. A mathematical singularity (non-single-valued solution) occurs in this cross section (as in that of Chapter I), and the sign of the generalized gasdynamic effect is reversed. The term "subcritical" as used here and below, signifies only flow of gas with $M' < 1$. The existence of subcritical flows will also be supported later on with analytical considerations.

In concluding this section, let us briefly discuss another limit model of the phase transitions in the heated cone.

As we have stated, the shock wave applies very closely to the cone on a certain segment. The pressure within the particle swarm directly behind the wave may reach comparatively high values, several times higher than the pressure in the surrounding stream. It should then drop quickly along the ox axis from the pressure behind the normal shock to pressures on the order of those in the free stream. For $M_1 = 2.9$ and $p_1 = 1$, $k = 1.4$, for example, the pressure drops by a factor ˜ approximately 10 (from 9.6 to 1 bar). If a drop manages to acquire a high enough temperature in the high-pressure zone, it may be overheated in the zone of low p, i.e., it may have a temperature above the local boiling point. This is possible for a preheated liquid.

Thus, a certain mass of drops should boil. The intensity of vaporization in this process will be very high, since the boiling drops are subjected to secondary breakup into extremely minute particles. The decay criterion in this case will be the ratio of the

saturation vapor pressure at a given point of the medium to the surface-tension pressure p_v/p_σ of the liquid.* The deformation and decay mechanism will be related to the effect of the vapor pressure inside the drop. When $p_v/p_\sigma \gg 1$, the secondary atomization will be very fine and there will be a large increase in liquid-surface area. However, the scheme considered above appears improbable for ordinary flow conditions, under which the initial liquid temperature T_{l1} is much lower than that in the free stream. Subsequent calculations (see §4) will indicate that the average effective parameters of the gas in the initial segment are far from the values directly behind the shock wave. We may not, therefore, expect high initial gas pressures that would overheat in a substantial fraction of the liquid. Boiling may start if the temperature of the liquids, for example, in the tank or cylinder (where the pressure is quite high) exceeds the boiling point of the medium into which the liquid is injected. In this regime, we may expect a considerable decrease in the range of the spray cone, which is transformed immediately after injection into a jet of vapor.

§4. The Initial-Parameter Problem in the Spray Cone

1. Fundamental Equations for the Initial Segment

At the present level of our knowledge, calculation of the gas flow entering a dense swarm of drops behind a shock wave is extremely difficult. Statement of the general problem of an arbitrary swarm of particles requires detailed study of highly complex internal processes of aerodynamic and thermal interaction between the gas and the particles, whose trajectories change under the influence of turbulent diffusion, collisions, atomization, etc. All of these processes determine the profiles of the parameters and the boundary contours of the complex two-phase flow. However, the experimentally

---

*We do not consider here the effect of surface tension itself on vapor pressure, which may be substantial for drops several orders smaller than typical spray-spectrum particles.

established boundary shapes of the cone (swarm of drops) and shock
wave and the coarseness of atomization should facilitate construction
of a semiempirical theory. This will enable us to confine ourselves,
in accordance with the one-dimensional flow scheme, to consideration
of resultant effects — the significant expenditure of stream energy
on entrainment of the drops and the amount of heat removed to heat
them (which is comparatively small until phase transitions begin).

Leaving aside detailed analysis of the inhomogeneous flow within
the bow zone of the cone, we shall determine average effective values
in cross section 1' — 1'. These parameters are the velocity W',
pressure p', temperature T', and liquid concentration β', and must be
subject to the general equations of conservation for the gas-and-drop
stream. Solution of this system has certain distinctive aspects and
requires the introduction of certain physical assumptions and hypo-
theses.

Let us consider the interval between cross section 1 — 1 with
the free-stream parameters W_1, p_1, and T_1 and the cross section
1' — 1' in the initial segment of the spray cone (Figure 2.15).
Liquid is injected at point o. We shall use the equations of
conservation of flow rate, energy, and momenta and the equation of
state of the gas for a one-dimensional stationary flow containing
liquid particles. Let us introduce the simplifying assumptions.

1. In accordance with the model adopted in §2, we neglect
phase transitions on the initial segment ox' of the cone. Actually,
vaporization may already have begun on segment ox', but it is
assumed that the small percentage of vaporized matter (which is
extremely hard to estimate) has no appreciable effect on the shape
of the frontal segment of the cone and the flow there.

2. We shall not consider exchange of mass, heat, and energy
between stream I, which enters the spray cone, and stream II, which
flows around it on the outside.

95
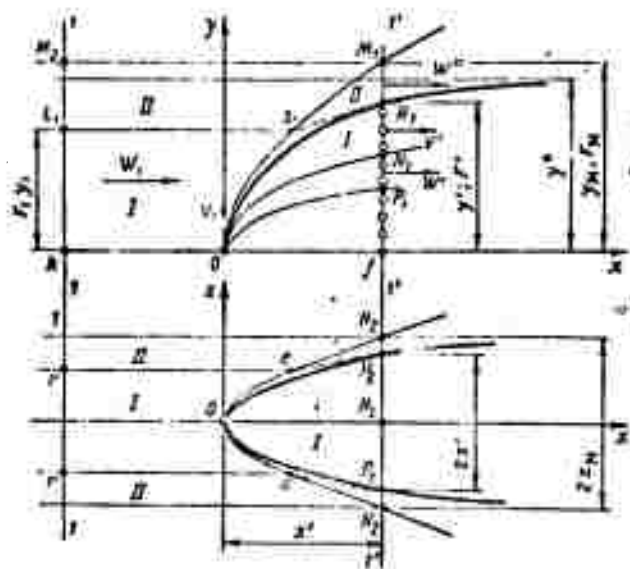
Figure 2.15. Diagram of flow in initial segment of spray cone (non-closed problem).

3. We shall assume that the gas streamlines and particle trajectories assume horizontal directions in cone cross section F', neglecting the vertical velocity components at the exit from the initial segment. The outer boundaries of the cone (from which infer-ences can be drawn as to the peripheral drop trajectories) very quickly approach horizontal lines, although they do not coincide exactly with them. Within the cone, however, and especially in the zone of liquid-concentration maximum, the hypothesis of horizontal flow is evidently close to the truth.

4. We shall neglect frictional forces acting on the reference surfaces bounding the stream under consideration. This is legitimate in view of the short lengths of the initial segment.

5. As in Chapter I, we shall disregard the area decrease of the flow section F' in the cone due to the presence of the drops (estimates indicate that this area can be reduced by about 2 — 6%).

This last constraint is not mandatory, and can be dispensed with by introducing a special area-correction factor. Selection of the initial-segment length x' of the spray cone, i.e., the position of cross section F', is, to a certain degree, arbitrary. On the one hand, the segment x' must be short enough to conform to the hypotheses of insignificant liquid vaporization, a weak effect of the interaction between the streams, and small frictional forces. At the same time, it must be long enough so that the slopes of the gas and drop velocity vectors to the ox axis will be small.

Examination of a series of shadow and Töpler photographs of the cone indicates that these conditions are approximately satisfied on an interval $0.6y^* \gtrsim x' \leq 1.5y^*$. These estimates are based on examination of the frontal segment, in which the configuration of the spray cone shows no sharp differences in hot and cold streams for a given set of initial data (which equal M, d_n, and velocity-head ratios between the free stream and the liquid). Appreciable differences may appear at larger $x'(x'/y^*)$ in a heated stream in the form of a sharp change in the boundary contour and a decrease in the range of the cone. The inclination of the cone boundary to the horizontal (at points R_1, p_2 in Figure 2.15) is small, usually ~6 — 10°, and the inclination of the shock wave approaches the Mach angle. Knowledge of the specific x' is not necessary in writing the initial equation system and introducing the dimensionless variables.

Below we shall give a method for a single-valued determination of the initial-segment effective length x' or x'/y^*. The control surface kM_3M_1fk and $k\mathcal{l}_1s_1R_1fk$ is selected as shown in Figure 2.15, and the outer normal to this surface is considered positive. It can be assumed that the dense swarm of drops acts as a liquid grid, i.e., that it offers a certain aerodynamic resistance to the free stream. As it flows around the bow of the cone, the gas splits into two streams: one stream I passes into the cone, while the other, II, flows around its periphery. The stream $k\mathcal{l}_1s_1R_1fk$ and reP_2P_2er is determined by five parameters: W', p', T', ϱ', and F_1. The cross-sectional area F_1 is not known for a given length x'; the corresponding

97

flow rate $m_1 = \rho_1 W_1 F_1$ is an unknown fraction of the total flow $\rho_1 W_1 F_m$ (F_m is the area in cross sections 1 — 1 and 1' — 1') passing through the initial segment of the cone. In zone II, $l_1 M_3 M_1 R_1 s_1 l_1$, the flow moves with the exit parameters W", p" = p', T", ρ", flowing around the cone in the space between its boundaries and the shock wave. Here we assume equality of the pressures over the entire cross section 1' — 1', a condition often used for unconfined streams in contact.

The gas variables of zone I can be related to one another by the equations of flow rate, state (Clapeyron equation) and energy conservation of the two-phase mixture (according to our assumptions, no energy flows across the lateral boundaries of the stream). The momentum equation cannot be used here, since the pressure distribution on surface segment $s_1 R_1$ is unknown.

For the zone of stream II, we can write the flow rate and energy conservation equations and the equation of state of the gas. We can also write the momentum equation for the entire two-phase streams I and II within the boundary surfaces $kM_3 M_1 fk$. In all, we have 3 + 4 = 7 relationships in the 5 + 3 = 8 unknowns that appear in them. We have therefore obtained a non-closed equation system. From this point, the theory can be developed in either of two possible directions.

1. Solution of the non-closed problem with the aid of an additional physical hypothesis.

2. Solution of the complete closed problem, in which the number of equations must equal the number of unknowns.

In the former case, the seven fundamental equations can be solved numerically and the unknowns expressed in terms of some single free parameter.

Thus, we obtain a set of solutions for streams I and II that corresponds to a whole range of values of one independent variable. Let us take as this free parameter the average (frozen) Mach number of stream I: $M' = W'/\sqrt{k' R T'}$ and revert to the hypothesis of the

"critical cross section" with $M' \approx 1$ that was formulated in §3 of this chapter. The flow in the initial segment of the cone will have Mach numbers that do not vary in a very broad range $M'_{n.s} < M' \le 1$ (here $M'_{n.s}$ is the Mach number·behind the normal shock), so that the orders of magnitude of the unknown functions do not depend very strongly upon the choice of M'. This approach yields a simplified method of closing the equation system and finding a unique solution.

Let us now examine the second, more complicated approach. It requires an additional integral equation and does not require the hypothesis that the flow is subcritical. We shall use the equation for the entropy flux in the single-phase flow II between the extreme cross sections 1 — 1 and 1' — 1'. We shall assume (in accordance with our earlier remarks on the weak influence of friction) that the flow outside the cone behind the shock wave — to cross section 1' — 1' — remains isentropic on a comparatively short segment ox'. In other words, the entropy increment of stream II is fully determined by the wave in front of the cone. This approach calls for more complete information on the shock wave.

To write the equations under point 1 above, we needed only the relationships for the area ratios of certain characteristic cross sections of the cone and wave. Here, however, we need data on the total heads behind the wave or on its slope angles. The effective values of the total heads behind the wave, defined by the projections onto the yox and zox planes, can be estimated approximately. The region of the wave under consideration is smooth and approaches the characteristic cone, so that the estimates are easier to obtain. We proceed with a concrete analysis.

We return first to the solution of the non-closed problem. We write the system of equations determining the flow variables in zone I.

Equation of conservation of gas flow rate

$$m_1 = m'; \quad F_1 W_1 \varrho_1 = F' W' \varrho'. \tag{2.41}$$

Equation of energy conservation for the two-phase mixture in enthalpy form

$$m_1 \left[i_1 + \frac{w_1^2}{2} \right] + m_{\varkappa 1} \left[i_{\varkappa 1} + \frac{v_1^2}{2} \right] =$$

$$= m' \left[i' + \frac{w'^2}{2} \right] + m_{\varkappa 1} \left[i'_{\varkappa} + \frac{v'^2}{2} + \varepsilon_\sigma \right] = 0. \tag{2.42}$$

Here the i terms are the specific enthalpies of the liquid and gas and ε_σ is the specific surface energy of the drops, which is related to the increase in liquid-surface area on decay of the injected jet. The enthalpies are computed from the usual formulas

$$i = \int_{T_\mathfrak{n}}^{T} c_p \, dT = \bar{c}_p (T - T_\mathfrak{n}).$$

It will be more convenient later to express them in terms of the average heat capacities $\bar{c}_p$ in a given temperature range. We neglect the influence of pressure on c_p. In our case, the heat capacities of the liquid vary comparatively little with temperature, and we may assume that

$$c_{\varkappa 1} \approx c'_{\varkappa} = c_{\varkappa}:$$

$$i_1 = \bar{c}_{p1}(T_1 - T_\mathfrak{n}); \quad i_{\varkappa 1} = c_{\varkappa}(T_{\varkappa 1} - T_\mathfrak{n});$$

$$i' = \bar{c}'_p(T' - T_\mathfrak{n}); \quad i'_{\varkappa} = c'_{\varkappa}(T'_{\varkappa} - T_\mathfrak{n}),$$

where T_{l1} is the temperature of the liquid to be injected, T'_l is the temperature of the liquid in cross section F', T_I is the initial reference temperature for the enthalpies, $\bar{c}_{p1}$ and $\bar{c}'_p$ are the average heat capacities in the corresponding temperature range,* $\varepsilon_\sigma = 6\sigma/a\varrho_l$

*For simplicity, we may use a linear relation for the heat capacities as functions of temperature, in which case $\bar{c}_{p1}$ and $\bar{c}'_p$ will be functions of the average temperatures $T_{av1} = T_v + T'/2$ and $T'_{av} = T_v + T'/2$.

100

(a is the averaged drop diameter). The numerical value of this term
is several orders smaller than the others even for the conditions of
a fine spray in a supersonic stream and liquids such as water, alcohol,
etc. We link the absolute drop velocity V' to the relative velocity
U' with the velocity-addition equation

$$U' = W' - V'. \qquad (2.43)$$

Equation of state of the gas

$$\frac{p'}{\varrho'} = RT'. \qquad (2.44)$$

Let us transform the equation system written out above. We
eliminate from it the density ϱ' and the temperature T' (which appears
as an explicit parameter). Thus, we reduce the system for zone I to
a single algebraic relation. Let us carry through certain auxiliary
transformations. The quantity β' characterizes the average liquid
concentration in cross section 1' — 1', where the gas flow rate m' =
$F'W'\varrho' = F_1 W_1 \varrho_1$:

$$\beta' = \frac{m' + m_{\rm m}}{m'}. \qquad (2.45)$$

Thus, the new unknown β' replaces the unknown F_1 (or m_1) and is
uniquely related to it. The concentration β' in cross section F' can
be expressed in terms of the minimum concentration in the cone, β.*
From the formulas

$$\frac{m_{\rm m}}{m'} = \beta' - 1 \qquad (2.37)$$

and

$$\frac{m_{\rm m}}{m^*} = \beta^* - 1 \qquad (2.45)$$

---

*The unknown β' is readily expressed in terms of the unknown F_1
from (2.41) and (2.42): $(\beta' - 1) = (\beta^* - 1)(F^*/F_1)$.

we obtain

$$\beta' - 1 = (\beta^* - 1) \frac{F^*}{F'} \frac{W_1}{W'} \frac{\varrho_1}{\varrho'} \cdot \qquad (2.46)$$

We introduce, as noted, the parameter M' — the effective Mach
number of the gas in cross section 1' — 1', defined by the relation

$$M' = \frac{W'}{\sqrt{k' R T'}}. \qquad (2.47)$$

We use an obvious identity to eliminate the density ϱ' from the
expression for $(\beta' - 1)$:

$$\frac{\varrho_1 W_1}{\varrho' W'} = \frac{p_1}{p'} \left(\frac{M_1}{M'}\right)^2 \frac{W'}{W_1} h_1,$$

$$h_1 = \frac{k_1}{k'} = \frac{c_p' - R}{c_{p1} - R} \cdot \frac{c_{p1}}{c_p'}. \qquad (2.48)$$

Here k_1 and k', c_{p1}, c_p' are the adiabatic exponents and heat capacities
of the gas in cross sections 1 — 1 and 1' — 1' (their ratio can be
written with the aid of the equation relating the heat capacities at
constant pressure and volume). From (2.46) and (2.48), we obtain an
auxiliary relation for the transformations to follow:

$$(\beta' - 1) = (\beta^* - 1) \frac{p_1}{p'} \left(\frac{M_1}{M'}\right)^2 \frac{W'}{W_1} \frac{F^*}{F'} \frac{h_1}{k'}. \qquad (2.49)$$

We reduce the energy equation (2.42) to dimensionless form by
normalizing all terms to the respective initial parameters. We then
apply the constant-flow rate relation (2.41) and, eliminating β' and
T' with the aid of (2.47) and (2.49), we finally obtain a third-degree
equation in the unknown parameter W'/W_1:

$$B_1\left(\frac{W'}{W_1}\right)^3 \frac{p_1}{p'} + \left[B_2 - B_3 \frac{p'}{p_1}\right]\left(\frac{W'}{W_1}\right)^2 - B_1 B_4 \frac{p'}{p_1}\left(\frac{W'}{W_1}\right) - B_5 =$$

$$= \varphi\left(\frac{W'}{W_1};\ \frac{p'}{p_1};\ M'\right) = 0. \tag{2.50}$$

The coefficients of this equation will contain the quantities p'/p_1 and M'. They are expressed by algebraic relations:

$$B_1 = (\mathfrak{p}^* - 1)\left(\frac{M_1}{M'}\right)^2 \frac{F^*}{F'} h_1;\quad B_2 = \frac{2 h_2 \nu_2}{(k_1 - 1) M'^2} + 1.$$

where

$$h_2 = \frac{c_p' - R}{c_{p1} - R} = h_1 \frac{c_p'}{c_{p1}},\quad \nu_2 = \frac{\overline{c}_p'(T_{cp}')}{c_p'(T')};\quad B_3 = 2 B_1 \frac{U''}{W_1};$$

$$B_4 = \frac{c_{\varkappa1}(T_{\varkappa1} - T_{\varkappa}')}{c_p' T_1} \cdot \frac{2\nu_1}{(k_1 - 1) M_1^2} + \frac{12s}{c_{\varkappa1} a_1 W_1^2} + \left(\frac{V_1}{W_1}\right)^2 - \left(\frac{U_1}{W_1}\right)^2;$$

$$B_5 = \frac{2\nu_1}{(k_1 - 1) M_1^2} + 1.$$

where

$$\nu_1 = \frac{\overline{c}_{p1}(T_{cp1})}{c_{p1}(T_1)}.$$

Relation (2.50) is the defining equation for the flow parameters in zone I.

The correction factors h_1 and h_2 appear because of the different heat capacities and adiabatic exponents of the gas in cross sections 1 — 1 and 1' — 1' (owing to the change in the temperature of the medium). The multipliers ν_1 and ν_2 are the ratios of the average heat capacities to the absolute ones in the respective cross sections.

Thus, the temperature T', which no longer appears explicitly in (2.50), is contained only in these correction factors, and its influence is comparatively weak. Let us estimate the quantities U' and T'_l, which pertain to the liquid particles and enter into the coefficients of Equation (2.50). The terms containing U' and T'_l are

comparatively unimportant, since the enthalpy of the drops and their kinetic energy are small in the relative (but not the absolute) motion compared to the enthalpy and kinetic energy of the gas in cross section 1' — 1'. This does not by any means imply that the presence of the drops can be neglected in deriving equations in which the important term containing the absolute drop velocity V' appears. It means only that in estimating V' = W' + U', we assume an approximate choice of U_1', since V' and W' are similar in order of magnitude.

It is assumed that by the time the two-phase flow reaches cross section F', all processes of jet decay and atomization of the drops have been completed. Then the relative velocity U' of drops a_1 cannot exceed the limit U_{max} permitted by the atomization number

$$\frac{\varrho' U_{max}^2 a_1}{\sigma'} = D_{a_1} \tag{2.51}$$

D_a = 10.7; 14;

$$U_{max} = \sqrt{\frac{D_a \sigma'}{a_1 \varrho'}} \approx \sqrt{\frac{D_a \sigma_1}{a_1 \varrho_1}}. \tag{2.52}$$

Replacement of the surface tension and density σ' and ϱ' of the medium in cross section 1' — 1' by the corresponding values of $\sigma(T_1)$ and ϱ_1 in cross section 1 — 1 and the use of either of the two numerical values of the atomization number D_a do not seriously affect the order of magnitude of U'. Thus, U' may vary in the range $0 \leq U' \leq U_{max}$, the regime with full entrainment of the drops (U' = 0) and the regime of maximum relative velocity with breakup (evidently, small relative velocities U' on the order of the turbulent fluctuation velocities of the gas will be more realistic for most drops). In the actual calculations, we shall assume $U' \approx U_{max}/2$:

$$U' = \frac{1}{2} \sqrt{\frac{\sigma \cdot 10.7}{\varrho_1 a_1}}. \tag{2.53}$$

The drop size a_1 in the initial cross section can be estimated from the diameters a_{max} or a_M. Usually, they differ by a factor of about two in the spray spectra. Evidently, drops with diameter a_M will be entrained even before cross section F', and it is more correct to use a_{max} in the calculations. The temperature T'_l lies in the range $T_{l1} < T'_l < T_b$, where T_b is the boiling point of the given liquid in cross section 1' — 1' (it is comparatively close to the boiling point in the initial segment, since, according to the results of the calculations to follow, the pressure does not vary too strongly). Selection of this temperature range is consistent with the remarks in §3 concerning the improbability of heating of the liquid of the initial segment. It can be assumed without incurring any large error that

$$T'_{\text{a}} \cong \frac{T_{\text{a}1} + T_{\text{кип}}}{2},$$ (2.54)

calculating the boiling point from the free-stream parameters. The term $12\sigma/\varrho_l a_1 W_1^2$ in the coefficient B_3, which depends on the surface energy of the drops, can, according to the estimates, be left out of account (the surface energy amounts to ~1% of the enthalpy of the drops). Let us turn now to the task of writing the equation defining the flow in zone II, between the boundary of the cone and the surface of the shock wave.

Equation of conservation of gas flow rate

$$m_{\text{м}} = m' + m'' = m_1 + m''.$$ (2.55)

Here m_M and m" are the gas flow rates across cross sections $F_M(M_1 f)$ and F_M — $F'(R_1 M_1)$ (see Figure 2.15).

The equation of flow rate conservation can be written

$$F_{\text{м}} \varrho_1 W_1 = F' \varrho' W' + (F_{\text{м}} - F') \varrho'' W''.$$ (2.56)

Equation of energy conservation in enthalpy form

$$l_1 + \frac{W_1^2}{2} = l'' + \frac{W''^2}{2}; \quad l'' = \bar{c}_{pl}(T'' - T_{\text{a}});$$ (2.57)

105

$\bar{c}''_p$ is the average heat capacity of the gas on the temperature interval T_r, T''.

As in the case of flow I, the momentum equation cannot be written here, since the pressure distribution on the interface s_1R_1 is unknown. However, this equation can be written for the entire space of streams I and II.

Momentum equation of resultant two-phase flow I + II

$$p_1 F_{\text{u}} + m_{\text{u}} W'_1 + m_{\text{u}} V_{1k} = m'W'' + m_{\text{x}} V' + m''W'' + p'F_{\text{u}},\qquad(2.58)$$

where $V_{1k} = V \cos \alpha_1$ and $m_l V_1 x$ are the horizontal momentum components of the two-phase jet. In the particular case of injection (the one most commonly encountered in practice) perpendicular to the stream, $\alpha_1 = 90°$ and $V_1 x = 0$.

We shall also use the equation of state for gas II.

Equation of state of the gas

$$\frac{p'}{\varrho^\circ} = RT''.\qquad(2.59)$$

We transform Equations (2.56), (2.57), and (2.58) to dimensionless form (as was done for the equations of stream I) by normalizing the respective terms and eliminating ϱ''. The appearance of the ratio m_l/m' during the transformations results in introduction of the parameter β':

$$C_1(\beta' - 1)\left(\frac{W^\circ}{W_1}\right)\left(\frac{p'}{p_1}\right) + C_2\left(\frac{T^\circ}{T_1}\right) - (\beta' - 1)\left(\frac{T^\circ}{T_1}\right) = 0;\qquad(2.60)$$

$$\left(\frac{W^\circ}{W_1}\right)^2 + C_3\left(\frac{T^\circ}{T_1}\right) - C_4 = 0;\qquad(2.61)$$

$$(\beta' - 1)\frac{W''}{W_1} - C_6 \frac{W''}{W_1} + C_5 \frac{W'}{W_1} + C_7(\beta' - 1)\frac{p'}{p_1} - C_8(\beta' - 1) = 0. \qquad (2.62)$$

The coefficients C_1 of the equation have the form

$$C_1 = 1 - \frac{F'}{F_M}; \quad C_2 = C_5' = (\beta^\circ - 1)\frac{F^\circ}{F_M}; \quad C_3 = \frac{2h_3 v_3}{(k_1 - 1)M_1^2};$$

$$h_3 = \frac{C_p^\circ}{C_{p1}}; \quad v_3 = \frac{\bar{C}_p'(T_{cp}')}{C_p'(T'')}; \quad T_{cp} = \frac{T_M + T''}{2}; \quad C_4 = \frac{2v_1}{(k_1 - 1)M_1^2} + 1;$$

$$C_6 = (\beta^\circ - 1)\frac{F^\circ}{F_M}; \quad C_7 = \frac{p_1}{\varrho_1 W_1^2} = \frac{1}{k_1 M_1^2};$$

$$C_8 = (\beta^\circ - 1)\frac{F^\circ}{F_M}\left[\frac{U''}{W''} - \frac{V_{1x}}{W_1}\right] + 1 + \frac{1}{k_1 M_1^2}.$$

On completing all of the transformations, we obtain a defining equation with the single unknown W'/W_1; its coefficients will depend on M'. Let us combine Equation (2.50) and Equations (2.60), (2.61), and (2.62). From relations (2.49), (2.60), (2.61), and (2.62), which contain W'/W_1, p'/p_1, W''/W_1, T'/T_1, and β', we eliminate W''/W_1, T''/T_1, and β' and find the relation $p'/p_1 = \varphi(W'/W_1)$. Substituting p'/p_1 into (2.50), we obtain a sixth-degree defining algebraic equation. It is quite complex and must be solved numerically, but it is much simpler to work with than the initial system of seven nonlinear algebraic equations.

Equation (2.63) can be written in the form of a monomial in certain combinations S and H composed of the coefficients B, C, and the unknown W'/W_1 (to avoid unwieldly expressions, we shall not write the equations out in the usual form in order of decreasing powers of W'/W_1):

$$F\left(\frac{W'}{W_1}; \quad M'; \quad \frac{x}{y^*}; \quad \frac{T'}{T_1}; \quad \frac{T''}{T_1}\right) = S_1^2 H_3 + S_2 H_1^2 + S_1 H_1 H_2 = 0. \qquad (2.63)$$

The combinations S and H have the form:

107

$$S_1 = \left(\frac{W'}{W_1}\right)^2 - 2\frac{U'}{W_1}\left(\frac{W'}{W_1}\right) - B_4;$$

$$S_2 = \left[C_6\frac{W'}{W_1} - C_6\right]^2 - C_6; \quad H_1 = B_6 - B_2\left(\frac{W'}{W_1}\right)^2;$$

$$H_2 = [2C_6 - B_1(2C_7 - C_1C_3)]\frac{W'}{W_1}\left[C_6\left(\frac{W'}{W_1}\right) - C_8\right] + 2C_2C_6;$$

$$H_3 = \left(\frac{W'}{W_1}\right)^2(C_6 - C_7B_1)[(C_6 - C_7B_1 - B_1C_1C_3)] - C_4C_3^2.$$

The constants B and C contain the ratios of the areas of the characteristic cone and wave cross sections F^*/F', F'/F_M, and F^*/F_M (which depend on x/y^*), the liquid concentration β^*, the initial flow parameters M_1 and T_1, ..., the velocities and temperatures of the drops U'; T'_l, ..., the correcting factors h_1, ν_1 (which depend on T' and T"), and, finally, the free parameter M'. The characteristic-section area ratio and β^* are calculated from the formulas of §2 of the present chapter, (2.35), (2.36), and (2.39), and the procedure for estimation of U' and T'_l was indicated above.

The correcting factors h_1 and ν_1 have values comparatively close to unity; in the first-approximation solution, they can be determined on the assumption that the adiabatic exponent and the corresponding heat capacities are constant, so that $h_1 = h_2 = h_3 = 1$ and $\nu_1 = \nu_2 = \nu_3 = 1$. Thus, the variables T'/T_1 and T''/T_1 in Equation (2.63) are comparatively insignificant. The defining equation is written in the form

$$F\left(\frac{W'}{W_1};\ M';\ \frac{x}{y^*}\right) = 0.$$

After the first-approximation solution, in which we find definite values for T' and T", we can calculate new values of h and ν and carry out the second-approximation solution, this time without the hypothesis of constant heat capacities. We observe in advance that this method generally gives fast convergence. Having the found the solution for W'/W_1, it is easy to calculate all of the remaining unknowns. To determine the concentration, we use the expression

$$\beta' - 1 = \frac{H_2}{2S_2}\left[-1 + \sqrt{1 - \frac{4H_3 S_2}{H_2^2}}\right]. \tag{2.64}$$

Only the value corresponding to the plus sign has physical significance, corresponding to the condition $\beta' > \beta^*$ ($m' > m^*$). Thus, each root of the defining equation yields a fully defined (for a selected M') group of sought parameters:

$$\frac{p'}{p_1} = \frac{B\frac{W'}{W_1}}{\beta' - 1}; \tag{2.65}$$

$$\frac{T'}{T_1} = \left(\frac{W'}{W_1}\right)^2 \left(\frac{M_1}{M'}\right)^2; \tag{2.66}$$

$$\frac{W''}{W_1} = \frac{(\beta' - 1)\left[C_8 - C_7\frac{p'}{p_1} - C_6\frac{W'}{W_1}\right] - C_6\frac{W'}{W_1}}{(\beta' - 1) - C_5}; \tag{2.67}$$

$$\frac{T''}{T_1} = \frac{C_4 - \left(\frac{W''}{W_1}\right)^2}{C_3}; \tag{2.68}$$

$$\frac{F_1}{F'} = \frac{W'}{W_1}\frac{\frac{p'}{p_1}}{\frac{T'}{T_1}}. \tag{2.69}$$

The last relation expresses the initial area F_1 of stream I, which flows into the frontal segment of the spray cone; the Mach numbers M" of the gas in stream II are

$$M'' = \frac{W''}{\sqrt{k'' R T''}}.$$

were $k'' \approx k_1$ (first approximation).

109

TABLE 2.6

$M_1 = 2.85$; $T_1 = 1050°$ K; $x/y* = 1.0$; $\Delta p = 40$ bar; $p_1 = 1$ bar; $d_n = 1$ mm; $T_{\mathcal{l}1} = 293°$ K

No.	Approximation	Root	M_1	$\dfrac{W'}{W_1}$	$\dfrac{p'}{p_1}$	$\dfrac{T'}{T_1}$	$\vartheta'-1$	$\dfrac{F_1}{F'}$	$\dfrac{W''}{W_1}$	$\dfrac{T''}{T_1}$
1	1	1	1,0	0,467	2,01	1,85	1,08	0,509	0,914	1,25
2	1	II	1,0	0,492	2,19	2,03	1,03	0,531	0,882	1,34
3	2	1	1,0	0,455	1,94	1,74	1,11	0,507	0,926	1,21
4	2	II	1,0	0,475	2,11	1,89	1,07	0,527	0,898	1,29
5	1	1	0,7	0,345	2,10	2,05	1,54	0,354	0,929	1,21
6	1	II	0,7	0,361	2,24	2,24	1,51	0,362	0,907	1,27
7	2	1	0,7	0,332	2,04	1,89	1,58	0,356	0,939	1,18
8	2	II	0,7	0,345	2,16	2,05	1,56	0,364	0,921	1,23

We turn now to computer solution of the defining equation. The sixth-degree polynomial forming the left-hand side of the equation has two real roots whose values differ only slightly (over the entire range of coefficient variation considered here). Two closely similar solutions for all of the unknown parameters correspond to them (Table 2.6).

The case of atomization of gasoline in air at $T_{\mathcal{l}1} = 293°$ K was considered. The accuracy of the calculation permitted separation of the two closely similar roots (W'/W_1) and the step Δ (the difference between two successive values of the argument of the polynomial) was usually taken smaller than the difference between the roots. A further increase in accuracy to $\Delta = 10^{-5}$ had practically no influence on the result (and did not change the number of roots of the polynomial). The solution was carried out both for the first approximation, in which the heat capacity and adiabatic exponent in cross section 1 — 1 were assumed constant (equal to their values in the free stream), and with consideration of the temperature dependence of the heat capacities (second approximation). The latter was carried out by the method of successive approximations.
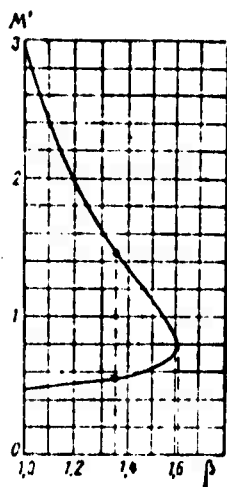
Figure 2.16. Illustrating flow of two-phase mixture in cylindrical pipe (two-valued nature of solution).

The two calculations give comparatively similar results (see Table 2.6), and we shall henceforth limit ourselves to the first approximation for simplicity. A brief remark on the origins of the two roots is in order. It is known that they appear on solution of the equations of one-dimensional flow in a channel, giving rise to a quadratic equation in one of the variables for $M_1 > 1$; one corresponds to continuous shock-free flow, and the other to the subsonic flow behind a normal shock. The same result is obtained in the elementary problem of transverse injection, solved in the scheme of one-dimensional gas flow with drops in a cylindrical pipe on premises similar to those adopted for stream I inside the cone (nonvaporizing drops, absence of friction against the wall, etc.).

Omitting the elementary transformations, we indicate the scheme and certain results of the solution for the parameters in the total-particle-entrainment cross section, where $V' = W'$. From the three conservation equations — energy, momentum, and flow rate — and the equation of state, we obtain a quadratic equation in the unknown variable $W'/W_1 = f(\beta^*) = 0$, which includes, in addition to the initial data, the concentration of the drops. Two roots W'/W_1 (and two values of all other parameters) correspond to a fixed value of β^*, converging with increasing β^*.

Let us examine (Figure 2.16) the curve of the gas Mach numbers $M' = W'/\sqrt{kRT'}$ vs. the parameter β^*; for a certain large $\beta^* = 1.62$, there is no solution (the roots are complex). The existence of a region in which both roots M' are near and smaller than unity (with quite large β^*) is interesting. This is an analogy to the two closely similar subcritical roots that were obtained in the problem of the cone for a whole series of regimes. The upper branch (as far as the vertex A) corresponds to shock-free flow, and the lower branch, to a
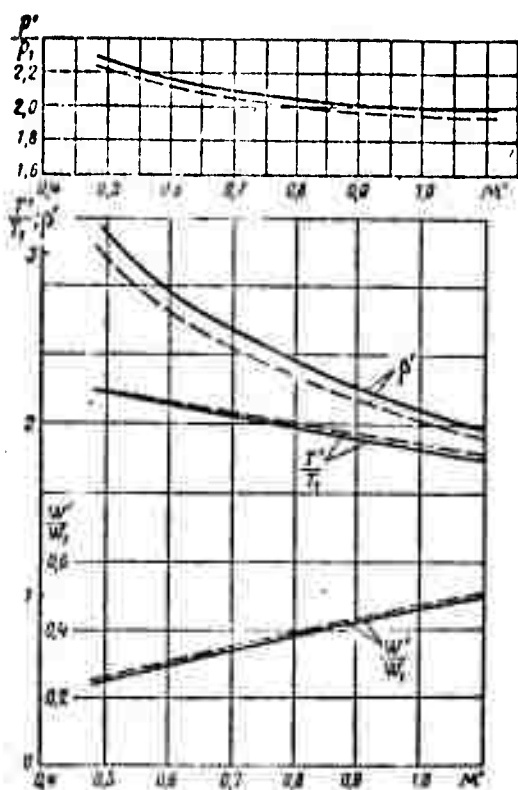
111

Figure 2.17. Results of solution of the non-closed problem with various values of the parameter M': ($M_1 = 2.85$; $x/y^* = 1$; $p_1 = 1$ bar; $\Delta p = 40$ bar; $d_n = 1$ mm).
—— $T_1 = 1050°$ K; --- $T_1 = 866°$ T.

normal shock in front of the drops in the initial cross section. The roots merge for $M' \approx 0.8$. As $\beta^* \to 1$ (absence of drops), we obtain the respective points M_1 and $M_{n.s}$ (the Mach number behind the normal shock). The solution was carried through for $M_1 = 2.9$, $T_1 = 1050°$ K, $p_1 = 1$ bar, $\Delta p = 40$ b, $T_{l_1} = 293°$ K, and $T'_{\cdot} = 340°$ K. This illustrates the singularities of the solution of the conservation equations, with the appearance of two roots.

Turning to our problem of the initial spray cone parameters, we note that selection of one root or the other is numerically immaterial. As a convention, we shall take in all cases the solution of the non-closed problem according to the first, smaller root W'/W_1. As an example, the diagrams of Figure 2.17 present curves of the fundamental gasdynamic parameters for the typical regime with $M_1 = 2.85$; $\Delta p = 40$ bar, and $p_1 = 1$ bar at two temperatures $T_1 = 1050$ and $866°$ K and $x/y^* = 1$, $d_n = 1$ mm, and $T_{l_1} = 293°$ K. They show how these quantities vary on arbitrary variation of the free flow parameter M.

At any of the values of M' in this interval, the unknown gas-dynamic variables within the cone differ very substantially from those in the free stream; the velocities drop, and the temperatures increase:

$$W' \approx 0.4 W_1; \quad T' = 2T_1; \quad p = 2p_1; \quad \beta' \approx (2 \div 2.5)\beta^*.$$

112

TABLE 2.7

$(M_1 = 2.85;\ d_n = 1\ \text{mm};\ x/y^* = 1;\ p_1 = 1\ b)$

$\dfrac{\Delta p}{b}$	$\dfrac{W'}{W_1}$	$\dfrac{p'}{p_1}$	$\dfrac{T'}{T_1}$	β'		$\dfrac{\Delta p}{b}$	$\dfrac{W'}{W_1}$	$\dfrac{p'}{p_1}$	$\dfrac{T'}{T_1}$	β'
	$T_1 = 1050°K$					$T_1° = 866°K$				
20	0,4658	2,302	1,625	2,168		20	0,4678	2,209	1,840	2,114
40	0,4688	2,005	1,850	2,073		40	0,4700	1,940	1,863	2,013
60	0,4708	1,872	1,864	2,009		60	0,4728	1,820	1,880	1,949
70	0,4718	1,829	1,872	1,983		70	0,4738	1,779	1,888	1,724

This is a result of deceleration of the gas as it strikes the initial segment of the cone. The parameters on the curve of Figure 2.17, which correspond to $M' = 1$, give the solution of the non-closed problem. Table 2.7 presents the analogous results for various Δp and T_1.

The curves of Figure 2.18 illustrate the effects of the choice of U_1 and T'_l. The relative velocity of the particles (plotted against the ox axis) varies in an extremely wide range ($0 \leq U' \leq U'_{max}$) (for hydrocarbon fuels). The calculations indicate that U' has comparatively little influence on the unknown parameters.

The coarseness of the individual drops, which has an effect through the factor U' on the initial segment, plays a relatively minor role. Physically, this is natural: the processes on the initial segment (vaporization is not significant here) are determined not by the individual particles, but by the entire dense swarm of drops. The curves in Figure 2.18 illustrate the role of T'_{l_1}, which varies from room temperature to a value on the order of the boiling point (of benzene and alcohol under standard conditions).
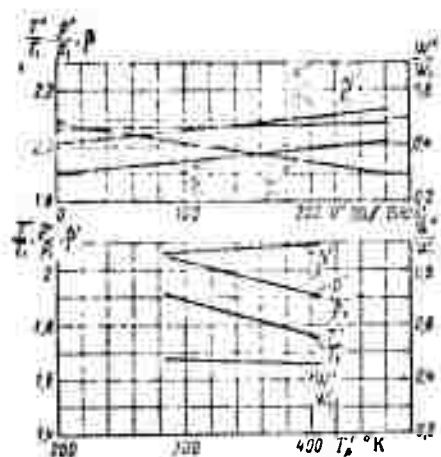
Figure 2.18. Results of solution of the non-closed problem with various values of u' and T'_l.
(M_1 = 2.85; x/y* = 1; M' = 1; T_1 = 1050° K; p_1 = 1 bar; Δp = 40 bar; d_n = 1 mm).

Thus, variation of the specific values of U' and T'_l does not substantially affect the values of the unknown parameters. For the typical regime mentioned above, we have, in particular,

$$U' \approx 120 \frac{M}{sec}; \quad a_{max} = 13 \ \mu; \quad T_{M} = 328° \, K.$$

Figure 2.19 shows the unknown parameters as functions of the free-stream Mach number M_1 for Δp = 40 bar, p_1 = 1 bar, T_1 = 1050° K, and x/y* = 1 and two fixed values of M' = 1 and 0.75. With increasing M_1, the values of $\bar{W}'$, $\bar{p}'$, $\bar{T}'$, and β' differ more and more strongly from the initial data in the free stream.

A similar calculation for various M_1 and constant stagnation parameters T_{01}, p_{01} yields results similar to those shown in Figure 2.19.

Let us state the scheme and write the successive items of the solution carried out on the non-closed problem of the effective parameters in the main segment of the spray cone. The initial data on which the unknown gasdynamic variables W'/W_1, p'/p_1, T'/T_1, β', and F'/F_1 (parameters inside the cone, zone I) and W''/W_1, p''/p_1 = p'/p_1, T''/T_1 (parameters of the flow around the cone, zone II) depend are:

(a) the parameters of the free gas stream W_1, p_1, T_1, $k_1 = c_{p_1}/c_{v_1}$ or M_1, T_{01}, p_{01}, k_1;

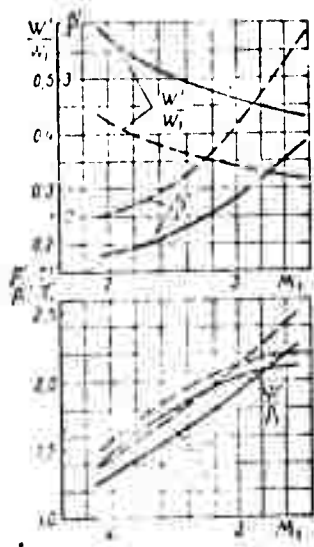(b) the injection parameters Δp, d_n, θ_{l1}, μ_a, σ, c_{l1}, T_{l1}, $T_b = f(p_1)$; n_1.

114

Figure 2.19. Results of
solution of the non-closed
problem with various M_1
($x/y^* = 1$; $T_1 = 1050°$ K;
$p_1 = 1$ bar; $\Delta p = 40$ bar;
$d_n = 1$ mm)
—— $M' = 1$; --- $M' = 0.7$.

1.   The calculation begins with determination of the ratios of the characteristic cross sections in the jet and the shock wave F^*/F', F^*/F_M, F'/F_M from Formulas (2.35) and (2.36) of §2, i.e., calculation of the dimensionless coordinates y/y^* and z/z^* of the cone and y_w/y^* and z_w/z^* of the wave from Relations (2.15), (2.17) and (2.23), (2.23') or (2.24), and (2.33). This requires a fixed value of the independent variable $x/y^* = 1$. For convenience in the calculation, we shall retain the single universal scale y^* and the variable x/y^*, eliminating z^* with the aid of (2.19). For this purpose, we calculate the ratio of velocity heads $\rho_l V_1^2/\rho_1 W_1^2$ from (2.2).

2.   The minimum liquid concentration β^* is calculated from Formula (2.39); we find the velocity V_1 of liquid injection from the delivery pressure.

3.   We then calculate the drop size $a_1 \approx a_{max}$ from the experimental formulas and from the values of U' according to (2.53); the values of T'_l are determined from (2.54).

4.   The parameters found under points 1, 2, and 3 can be used to evaluate the coefficients of the defining equation (2.63), i.e., the combinations H and S. These combinations contain the dimensionless constants C and B, the formulas for which were given above; they take the following forms:

115

$$C_1 = f_1\left(\frac{F'}{F_M}\right); \quad C_2 = C_4 = f_2\left(\frac{F^\bullet}{F_M}; \beta^\bullet\right) = f_5;$$

$$C_3 = f_3(M_1; k_1; h_2; v_2); \quad C_4 = f_4(M_1; k_1; v_1);$$

$$C_6 = f_6\left(\frac{F^\bullet}{F_M}; \beta^\bullet\right); \quad C_7 = f_7(M_1; k_1);$$

$$C_h = f_8\left(M_1; \frac{F^\bullet}{F_M}; \beta^\bullet; k_1; \frac{U''}{W_1}; \frac{V_{1s}}{W_1}\right);$$

$$B_1 = z_1\left(M_1; \frac{F^\bullet}{F'}; \beta^\bullet; M'; h_1\right); \quad B_2 = z_2(k_1; M'; h_2; v_2);$$

$$B_3 = z_3\left(M_1; \frac{F^\bullet}{F'}; \beta^\bullet; M'; \frac{U''}{W_1}; h_1\right);$$

$$B_4 = z_4\left(M_1; k_1; \frac{c_{A1}[T_{A1}-T_A]}{c_p T_1}; \frac{\sigma}{\varrho_A c_1 W_1^2}; \frac{V_1}{W_1}; \frac{U_1}{W_1}\right);$$

$$B_5 = z_5(M_1; k_1; v_1).$$

As we have noted, the correction factors that take account of the change in the heat capacities of the gas on the initial segment can be assumed equal to 1 in first approximation. The coefficients contain the unknown free parameter M', which can, generally speaking, be varied in the range $M_{n.s} \leq M' \leq 1$.

5. The roots of the determining equation (2.63) are then found numerically (according to the familiar theorem of algebra, solution in radicals is possible only for an equation of degree no higher than the fourth). For each fixed value of M' and x/y* = 1, the solution yields two real roots W'/W_1 with closely similar absolute values; the solution corresponding to the smaller root W'/W_1 is chosen. When M' ≈ 1 (e.g., M' = 0.95), we obtain the proper solution of the non-closed problem ("critical cross section hypothesis").

6. Knowing W'/W_1, we find all of the other unknown parameters with the simple formulas (2.64), (2.65), (2.66), (2.67), (2.68), and (2.69):

$$\beta'; \frac{p'}{p_1} = \frac{p''}{p_1}; \frac{T'}{T_1}; \frac{F_1}{F'}; \frac{W^\bullet}{W_1}; \frac{T''}{T_1}; \frac{F'}{F_1}; M''.$$

116

To estimate the extreme limits of the unknowns, we can analyze an entire group of solutions; values of $M' < M_{n.s}$ are physically impossible when the fuel is delivered at a 90° angle and there is no boundary-layer-separation zone, i.e., in the presence of a normal-shock element at the injection point. The position of the exit cross section F' can be varied similarly, for example, $0.8 \leq x/y^* \leq 1.2$. In many cases, the variation of M' is comparatively small in the range from 0.7 to 1. Estimates indicate that for liquids such as gasoline, kerosene, alcohol, and water, the physical constants of the atomized substances have little influence on the result under the conditions of atomization at $T_{l1} = 350°$ K; $M_1 = 2 - 3.5$; $d_n \approx 0.5 - 2$ mm.

The entire calculation is performed in dimensionless parameters; in finding the values of W', p', T', ..., the ratios obtained are multiplied by the corresponding initial values W_1; p_1; T_1, and determination of the length of the interval $x' = (0.8 - 1.5)y^*$ on our assumption that $x' = y^*$ requires calculation of the ordinate of the asymptote by Formula (2.12). Taking for simplicity the case of the first approximation $k_1 = k'' = k'$, we obtain the following general form of the solution for all of the unknowns W'/W_1; T'/T_1; p'/p_1; β', e.g.,

$$\frac{W'}{W_1} = F_1\left(M_1; \frac{F'}{F^*}; \frac{F^*}{F_M}; \beta^*; \frac{V_1}{W_1}; \frac{V_{1s}}{W_1}; k_1; \frac{U'}{W_1}; \frac{c_{x1}[T'_x - T_{x1}]}{c_{p1}T_1}; \frac{\bullet}{\varrho_{x1}a_1 W_1^2} \right).$$

where U' and T'_l are determined from the initial data.

As we have stated, for the conditions considered here and most regimes of practical importance, the parameters

$$\frac{V_1}{W_1}; \frac{V_{1s}}{W_1}; \frac{U'}{W_1}; \frac{c_{x1}[T'_x - T_{x1}]}{c_{p1}T_1} = \frac{l_{x1}}{l_1}; \frac{\bullet}{\varrho_{x1}a_1 W_1^2} \ll 1$$

have comparatively little influence on the result. If we also neglect k_1 (taking it consistently for some constant temperature, for example, $T_1 = 1000°$ K), we write in approximation $W'/W_1 \approx F_2(M_1; F'/F^*; F^*/F_M, \beta^*)$. Substituting the values of the characteristic-section ratios here, we obtain $W'/W_1 \approx F(M_1; \varrho_l V_1^2/\varrho_1 W_1^2; x/y^*; \beta^*)$. This applies to all other unknown parameters. Thus, the most significant physical

117

criteria are M_1; $\rho_l V_1^2 / \rho_1 W_1^2 = 2\Delta p / k_1 M_1^2 p_1$; β^*; and x/y^*, i.e., the free stream Mach number, the velocity-head ratio of the gas and liquid, the nominal liquid concentration, and the dimensionless coordinate. The last expression can be written

$$\frac{W'}{W_1} \approx F_4\left(M_1; \frac{\Delta p}{p_1}; \frac{\rho_* RT_1}{p_1}; \frac{x}{y^*}\right). \qquad (2.70)$$

Here the combination $\rho_l RT_1 / p_1 = \gamma_l / \gamma_1$ came from the expression for β^* and (assuming $\mu_a \approx$ const), $x/y^* = 1$. The combinations obtained can be designated the fundamental system of criteria determining the parameters at the exit from the initial segment of the spray cone.

We shall henceforth retain the same system of dimensionless numbers for general solution of the closed problem; the quantity x/y^* may assume other numerical values.

Solution of the Closed Problem

Here we shall set forth a solution of the closed problem that does not involve the critical cross section hypothesis. An additional relation for the flux of entropy in the single-phase flow II is used to close the general system. If the surface of the shock wave in the free stream is assigned, all parameters are found from the familiar formulas of gasdynamics, including even the entropy change behind the shock wave. We therefore have an opportunity to calculate the entropy-flux increment between cross sections $1 - 1$ and $1' - 1'$ for zone II on the assumption that entropy does not change on a comparatively short interval behind the shock wave. Then the general scheme of the solution will be as follows.

1. All operations of solving the non-closed problem are carried through for any fixed coordinate x/y^* in an arbitrary (sufficiently wide) range of variation of the free parameter M'. Then the total head $\bar{p}_0''$ is calculated for all values of the parameter M' by the conventional gasdynamic formulas for single-phase flow:

$$\bar{p}_0 = \frac{\dot{p}_0}{p_{01}} = \frac{p''}{\Pi(M'')} \cdot \frac{\Pi(M_1)}{p_1} = \frac{p'}{p_1} \cdot \frac{\Pi(M_1)}{\Pi(M'')} = \bar{t}_1\left(M'; \frac{x}{y^*}\right). \qquad (2.71)$$

where $\Pi(M_1)$ and $\Pi(M'')$ are the corresponding gasdynamic functions. The pressure $\bar{p}_0''$ is a certain effective value on the segment of cross section $1' - 1'$ of stream II (with area $F_M - F'$) that corresponds to the parameter M''. The values of M'' and p'/p_1 (like all of the unknown parameters in cross section $1' - 1'$) are determined in terms of the unknown M' after solution of the non-closed problem:

$$M'' = \frac{W''}{\sqrt{k'' R T''}}.$$

In first approximation, we may neglect the variation of the adiabatic exponents, assuming, as was done earlier, that $k'' \approx k_1$; the change in the exponents can be taken into account in the second-approximation calculations. (We note that stream II passes through a segment of a comparatively weak shock wave, and that the temperature T'' differs little from the initial temperature T_1.)

2. After solving the non-closed problem for an arbitrary value of x/y^*, the initial cross section $F_M - F_1$ is isolated in the free stream and in the area of the shock wave through which stream II passes with flow rate G^*. It is then possible to calculate the entropy flux and, consequently, the total head $\bar{p}_0'' = p_0/p_{01}$ by averaging over all streamlines behind the wave, i.e., over the local entropy and flow rate values.[*]

An auxiliary equation for the total head is obtained:

$$\bar{p}_{0cp} = \frac{\dot{p}_{0cp}}{p_{01}} = \varphi_2(M'). \qquad (2.72)$$

_____

[*]The entropy variation of the inhomogeneous flow behind the shock wave is small after averaging (mixing effect) compared with the entropy change on the shock wave.

119

Thus, equating φ_1 and φ_2, we obtain an additional relation for M' (for any parameter x/y^*):

$$\varphi_1 = \varphi_2, \qquad (2.72')$$

which closes the problem and the general system of eight conservation equations [see below for the form of Equation (2.72')]. Numerical (computer or graphical) solution of Equation (2.72') enables us to chose a single value of M' (Mach number of choice) and isolate one definite group of eight flow parameters in cross section 1' — 1' from the entire diversity of solutions. The difficulty of writing the equation for entropy flux and relation (2.72) consists in the need for approximate estimation of $\bar{p}_0$" behind the appropriate segment of the shock wave. This requires reconstruction of the shape of the surface from quite limited data on the contours of the wave's projection onto the two coordinate planes xoy and zoy.

Using certain simplifying assumptions, let us turn to determination of $\bar{p}_0$. As we know, the total head of the gas in the stream is averaged by calculating the mass-averaged entropy by the familiar formula

$$\Delta S = R \ln \left(\frac{p_{01}}{p_0} \right). \qquad (2.73)$$

Figure 2.20 gives a schematic representation of a segment of the shock wave and cone in their projections onto the coordinate planes, bounded by the exit cross section 1' — 1'. Line oM is the contour (projection) of the wave in the plane of symmetry yox of the cone and is described by the equation $y_w = f_1(x)$. Line oN_2 is the projection of the wave in the vertical plane zox (the line of maximum spans oN_1, which determines the width of the wave, is projected in this plane) and has the equation $oN_2 : z_w = f_2(x)$. The entropy-flux increment of gas II after passage through the shock wave is written
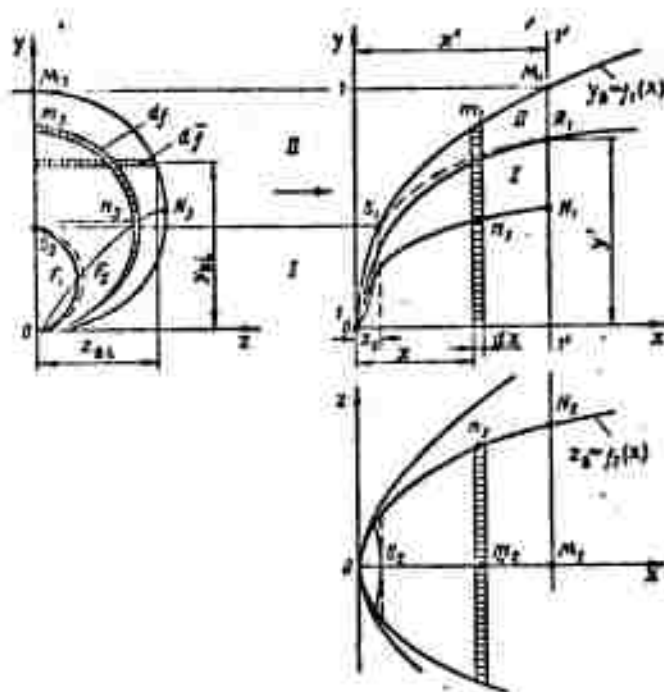
120

Figure 2.20. Diagram of flow in initial section of cone (closed problem).

$$\Delta S m'' = \int_{\vec{f}} \Delta s \, dm'' = \int_{f_i} \Delta s \varrho_1 W_1 \, df, \qquad (2.74)$$

where f is the area of the shock-wave surface zone under consideration, $m'' = \varrho_1 W_1 f = \varrho_1 W_1 (F_M - F_1)$ is the gas flow rate in stream II and is determined by the area $f = F_M - F_1$ of the projection of the corresponding shock-wave segment onto plane yoz (the area between the two eccentric ovals with the common symmetry axis oz), and df is the area of the wave-surface element in projection.

Then

$$\Delta S = \frac{1}{F_M - F_1} \int_{F_M - F_1} \Delta s \, df, \qquad (2.75)$$

where $\Delta S = S_{av} - S_1$ is the increment in the mass-average entropy of gas stream II and S_1 and S_{av} are the entropies in the initial cross section and behind the shock wave.

121

The same entropy increment will (according to the assumption
adopted) correspond to the interval between the initial cross section
and segment M_1R_1 of cross section 1' — 1' (see Figure 2.20).

Δs are the local entropy increments in stream filaments on
elements of the wave.

The segment of the wave under consideration here represents a
doubly connected closed surface that is bounded by two lines. The
inner space curve (the contour of the "orifice" oS_1) is the geometric
locus of the points at which the wave meets the streamlines of the
oncoming gas. These lines, which bend at the wave, separate streams
I and II (for example, S_1R_1). The projection of curve oS_1 (whose
equation is not known) onto the initial plane yoz forms an oval figure
(the solid line on the drawing) with the area F_1, which is determined
after solution of the non-closed problem. The outer curve will be an
elliptical contour bounding the area F_M in cross section 1' — 1'.

For simplicity in evaluation of the integral of (2.75), it can
be written in the form of two summands

$$\Delta S = \frac{1}{F_M - F_1}\left[\int_{F_s - F_1} \Delta s\, df + \int_{F_M - F_s} \Delta s\, df\right].$$

Here F_s is the cross-sectional area cut out by the shock wave on
the plane x_s = const (see Figure 2.20). The vertical axis y_s of the
resulting oval coincides with the vertical axis y_1 of cross section
F_1, but the horizontal axis is slightly longer than its counterpart.
For the interval of the coordinate $x'/y^* \geq 0.6$ — 0.7 that is of
interest, the areas of the two ovals F_1 and F_s are similar to one
another and much smaller than the area F_M, i.e., $F_s \approx F_1$. We can
then take

$$\Delta S \approx \frac{1}{F_M - F_1}\int_{F_M - F_s} \Delta s\, \Delta f.$$

122

As the surface element of the wave, we take the angular strip
shaded on all three projections in Figure 2.20 (it is cut out by two
closely spaced cross sections at x and x + dx, which are parallel to
the yoz plane). The element of integration df here is its projection
onto this plane. Let us attempt to evaluate the average entropy
increment Δs_i for an arbitrary i^{th} elementary strip.

The change in the parameters of the free stream gas, including
its entropy, at the points of the ring will be larger, the larger the
angle at which the streamlines meet the surface.

As we stated, the strong-shock zone in which the angles of
encounter are large, lies in the vicinity of the boundary $y_w = f_1(x)$.
The weak-shock zone with small encounter angles approaching the slope
of the characteristic is situated at the line of the largest trans-
verse spans $z_w = f_2(x)$. The surface of the wave is smooth everywhere
(except perhaps for a small singular region around the atomizer tube,
which cannot be considered in the calculation). The angles of encounter
of the stream with the wave at points of the elementary ring between
m_1 and n_1 (see Figure 2.20) decrease monotonically from the maximum
slope at point m_1 to the minimum at n_1. From point n_1, they again
rise monotonically up to the xoz plane. This type of variation, and
the transition from stronger wave segments to weaker wave segments,
appears physically natural.

The maximum drop density, i.e., the largest center of perturbation
of the stream, lies in the zone of the symmetry plane yoz of the spray
cone, on the axis of the liquid jet. Elements of the ring near the
plane of symmetry should be stronger wave segments; elements farther
from this plane should be weak wave segments. The slopes of the wave
and the values of Δs will be largest at point m_1 in the plane of
symmetry, and smallest at point n_1, which is fartherest from plane xoy.
In other words, lines oM_1 and oN_1 are the geometric loci of the points
of largest and smallest entropy change (smallest and largest total-
pressure recovery factors), respectively, on the shock wave surface.

123

The value of Δs_1 for the isolated annular element can be estimated in three ways — from the maximum, from the minimum, and from a certain mean value between them. Taking the entropy value at the frontal point m_1 at the boundary $y_w = f_1(x)$ (line oM_1) for all elements of the ring, we obtain $\Delta s = \Delta s_{max}$; taking for its elements the entropy values at a lateral point n_1 (line oN_1), which is projected onto the curve of the boundary $z_w = f_2(x)$ in plane xoz, we obtain $\Delta s = \Delta s_{min}$ and, finally, writing $\dot{\Delta s} = \Delta s_{max} + \Delta s_{min}/2$, we give a certain intermediate value. Thus, instead of the unknown entropies Δs on the surface of the wave, we take the entropies at the corresponding points on the minimum and maximum lines of the entropies $\Delta s(y, z)$. Substituting these values into the integral of (2.75), we can accordingly calculate three values of the total-entropy increment behind the shock wave: ΔS_{max}, ΔS_{min}, $\Delta \bar{S}$. We write an approximate expression for the area element df under the integral sign, using the assumption of elliptical cross section shapes that we adopted earlier:

$$df \cong d\left(\pi \frac{y_\bullet}{2} z_\bullet\right) = \frac{\pi}{2}\left[\frac{dy_\bullet}{dx} z_\bullet + \frac{dz_\bullet}{dx} y_\bullet\right]dx, \tag{2.76}$$

where $y_w/2$ and z_w are the semiaxes of the ellipse.

Relation (2.76) expresses the area difference between two nearby ellipses for the wave cross section (x, x + dx). Generally speaking, the cross sections of the shock wave are certain ovals:

$$f = k_f y_\bullet z_\bullet,$$

where k_f is an area coefficient near $\pi/2$ (in rougher estimates, the ellipses can be replaced by circles). Using the expression for df, we transform the area integral into an ordinary integral:

$$\Delta S \cong \frac{\frac{\pi}{2}}{F_u - F_1} \int_{x_a}^{x'} \Delta s\left[\frac{dy_\bullet}{dx} z_\bullet + \frac{dz_\bullet}{dx} y_\bullet\right] dx. \tag{2.77}$$

124

Here x_s is the abscissa of the cross section with area F_s. The lower limit of integration x_s is near zero (the region around the coordinate origin) and considerably smaller than the upper limit x'. Practical calculations yield the orders of magnitude $x_s/y^* < 0.01$ — 0.05, while $x'/y^* > 0.6$ — 0.7. Hence the error of estimation of x_s is comparatively unimportant.

We shall assume that the oval cross sections F_1 and F' of stream I are geometrically similar. We can then write the ratios of the axes of these ovals:

$$\frac{y_1}{y'} = \frac{z_1}{z'} = \sqrt{\frac{F_1}{F'}}.$$

Hence, knowing y' (for a given x') and the ratio F_1/F', we find

$$y_1 = y_s; \quad \eta_1 = y' \sqrt{\frac{F_1}{F'}}. \tag{2.78}$$

From the value of the ordinate $y_s = y_w = f_1(x_s)$, we calculate the unknown abscissa x_s from the equation of the shock-wave boundary (solving the equation for the argument x):

$$\frac{F_1}{F'} = \frac{F_1}{F^*} : \frac{F'}{F^*}.$$

We reduce expression (2.77) to dimensionless form (dividing and multiplying the right side by the constant y^*z^*):

$$\Delta S = R \ln \left(\frac{p_{01}}{p_0} \right) = \frac{1}{\frac{F_w}{F^*} - \frac{F_1}{F^*}} \int_{X_s}^{X'} \Phi(X) dX = F\left(M'; \frac{x}{y^*} \right). \tag{2.79}$$

where

$$\Phi(X) = \Delta s(X) \left[\frac{dY'_s}{dX} Z_s \cdot \frac{dZ_s}{dX} Y_s \right].$$

125

The integrand

$$d\Phi = \Phi(X)\,dX = \frac{\Delta s\,df}{\frac{\pi}{2}\,y^* z^*} = \frac{\Delta s\,dm^*}{F^* \rho_1 W_1}$$

is the entropy-flux increment behind the wave-surface element, referred to the mass of gas that has passed through the cold cone. It includes the dimensionless functions $Y_w = y_w/y^*$; $Z_w = z_w/z^*$ of the independent variable $X = x/y^*$. The limits of integration are

$$X = \frac{x'}{y^*}; \quad X_s = \frac{x_s}{y^*};$$

$$dX = \frac{dx}{y^*}.$$

The ratio F_M/F^* and the integrand are known for given flow parameters and the collected value of the coordinate x'/y^*. Determination of F_1/F^* requires assignment of M', after which the results of solution of the non-closed problem, where this ratio is obtained as a function of M', can be used. The local increment to the entropy s, which appears under the integral sign, is calculated from the total-head ratios at the selected points (as described above):

$$\Delta s_{max} = R \ln \left(\frac{p_{01}}{p_0} \right)_{m_1}; \quad \Delta s_{min} = R \ln \left(\frac{p_{01}}{p_0} \right)_{n_1}. \tag{2.80}$$

These total-head ratios are found from the local angles of encounter of the wave with the free stream with the aid of the gas-dynamic functions (details follow). Relations for the dimensionless coordinates Y_w and Z_w were obtained earlier:

$$Y_w = F_6(X; M_1); \quad Z_w = F_7\left(\frac{x}{z^*}; M_1 \right) = \bar{\varphi}\left(X; M_1; \frac{\rho_n V_1^2}{\rho_1 W_1^2} \right);$$

$$\frac{x}{z^*} = \frac{x}{y^*} \cdot \frac{y^*}{z^*} = X \frac{y^*}{z^*}.$$

126

The scale ratio $y*/z*$ is a function of the velocity-head ratio between the liquid and the gas. After evaluation of the integral in (2.79), e.g., with a computer, we obtain three total-entropy increments ΔS and three corresponding total-head ratios in stream II behind the wave. We find them from the formulas

$$\Delta S_{max} = R \ln \left(\frac{p_{01}}{p_0} \right)_{min} ; \quad \Delta S_{min} = R \ln \left(\frac{p_{01}}{p_0} \right)_{max} ; \qquad (2.81)$$
$$\Delta S_{cp} = R \ln \left(\frac{p_{01}}{p_0} \right)_{cp} .$$

The first estimate corresponds to the hypothesis of maximum wave losses in the stream flowing around the cone, the second to the hypothesis of smallest losses, and the third yields a certain intermediate loss value. These estimates have a simple geometric interpretation. In the first case, the actual shock wave is replaced by a cylindrical surface with generatrices parallel to the oz axis and passing across the curve $y_w = f_1(x)$, and in the second case the wave is replaced by a cylindrical surface with generatrices parallel to the oy axis and the curve $z_w = f_2(x)$ in the base.

Thus, the first case corresponds to the stream passing through the cylindrical element of maximum curvature for all points of a given cross section of the wave, and the second-to a stream passing through the cylindrical element of minimum curvature in the given cross section.

A few words on valuation of the integral (2.79) are in order. The bulk of the gas whose entropy flux is being calculated here passes below the contour with area F_1 [the area F_1 represents a comparatively small fraction of F_M approximately equal to $(0.2 - 0.3)F_M$]. Hence the estimate of the shape of cross section F_1 and x_s has little influence on the small region around the origin O, and may be made quite roughly with assumptions of the type of (2.78).

127

We take note of the following: when $x/y^* \approx 0.8 - 1.5$ and $M_1 > 2$, the various assumptions and errors connected with estimation of the wave cross-sectional shape and Δs do not greatly affect the resultant value of p_0''/p_{01} for the cross sections $x' =$ const of interest to us, which are comparatively far from the coordinate origin. This is explained by the approach of the shock wave surface to the characteristic cone, with the result that the bulk of gas II passes through segments of the wave on which the value of p_0'' differs comparatively little from the free stream value p_{01}.

Thus, the equation for the entropy-flux increment can be attached to the system of initial conservation equations (see §4). This closes the problem of determining the parameters in the initial segment of the spray cone. Turning to the total heads, we write an expression for p_0''/p_{01}:

$$\frac{\dot{p_0}}{p_{01}} = e^{-\frac{1}{R\left(\frac{r_\pi}{r^*} - \frac{r_1}{r^*}\right)} \int\limits_{X_s}^{X'} \Phi(X)\,dX} = \tau_2\left(M'; \frac{x}{y^*}\right). \tag{2.82}$$

Returning to (2.71), we use the expression obtained earlier for the same quantities p_0''/p_{01}. Thus, we can write the aforementioned functional equation (2.73) in a concrete form, where the function φ_1 is known from the solution of the non-closed problem and φ_2 is determined (after making the estimate given above) from Equation (2.82).

Returning from the total heads to the variables that we have adopted, we write the auxiliary equation (2.83) for the closed problem in the form

$$\frac{p'}{p_1}\frac{\pi(M_1)}{\pi(M')} = e^{-\frac{1}{R\left(\frac{r_\pi}{r^*} - \frac{r_1}{r^*}\right)} \int\limits_{X_s}^{X_1} \Phi(X)\,dX} \tag{2.83}$$

Having found the root $M' \equiv M_{ch}$ after solution of the closing equation (2.83), we calculate (as was done in the non-closed problem) all unknown parameters in a given cross section 1' — 1' of the spray cone; the parameter $x'/y*$ determines the cross section of the cone.

We turn now to the actual computing technique for the unknown local entropy increments Δs at selected points of the wave for evaluation of the previously discussed integral in the equation. The total-head recovery factor $\sigma = p_{02}/p_{01}$ can be determined at various points of the shock wave with the usual formulas of one-dimensional gasdynamics, see, for example, [16]. For this it is necessary to know the angle of encounter of the stream with the wave. A velocity coefficient λ_p corresponding to the stream component normal to the shock wave is usually introduced in the calculations. For simplicity, we shall consider the case of a constant adiabatic exponent on either side of the wave: $k = k_2 = k$. In the scheme of stream II (and M_1 not very large), this simplification will apparently not introduce any substantial errors, since the thermodynamic temperature at the passage through the wave changes insignificantly for most filaments, as we have noted: $T'' \approx T_1$ (zone of the strongest wave corresponds to stream I, which enters the interior of the cone). However, calculations can also be carried out in the case $k_1 \neq k_2$ (although the formulas are slightly more complex). From the flow rate equation* (in a stream filament passing through the wave)

$$\frac{p_{01} q(\lambda_1)}{\sqrt{T_{01}}} = \frac{p_{02} q(\lambda_2)}{\sqrt{T_{02}}} \tag{2.84}$$

($T_{01} = T_{02}$ — constancy of stagnation temperature in stream II), we obtain

$$\sigma = \frac{p_0''}{p_{01}} = \frac{p_{02}}{p_{01}} = \frac{q(\lambda_{1n})}{q(\lambda_{2n})}. \tag{2.85}$$

---

*For symmetry in writing the formulas, the double prime for parameters behind the shock wave is replaced in this paragraph by the index "2", as the index "1" refers, as before, to the free stream.

Figure 2.21. Illustrating estimation of total heads behind shock wave.
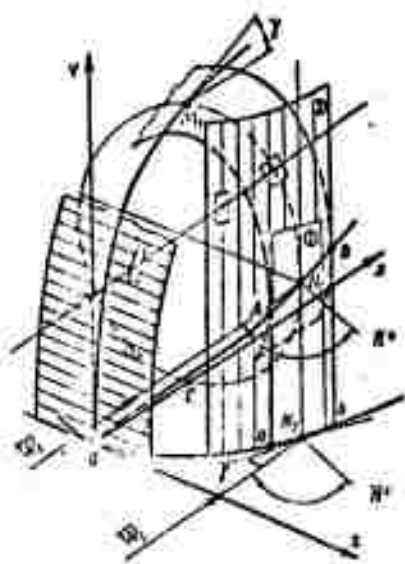
Here, according to the known formula

$$\lambda_{n1}^2 = \frac{\lambda_1^2}{\left(1 - \frac{k-1}{k+1}\lambda_1^2\right)\text{ctg}^2 a + 1}, \quad (2.86)$$

where $q(\lambda_{1p})$ and $q(\lambda_{2p})$ are the gasdynamic flow rate functions on either side of the shock wave surface and

$$\lambda_{n2} = \frac{1}{\lambda_{n1}}. \quad (2.87)$$

The velocity coefficient is related to the Mach number by

$$\lambda_1 = \sqrt{\frac{\frac{k+1}{2}M_1^2}{1 + \frac{k-1}{2}M_1^2}}; \quad (2.88)$$

a is the inclination angle of the shock wave to the ox axis at the surface point under consideration.

Let us show that for the lines oN_1, oM_1 on the surface they are are the angles of inclination γ, γ' at the corresponding points N_2 and M_1 on the profile and vertical boundaries of the wave in the yox and zox planes (Figure 2.21) and that they can be calculated from the formulas

$$\text{ctg}\,\gamma = \frac{1}{\frac{dY_s}{dX}} \quad \text{or} \quad \text{ctg}\,\gamma' = \frac{1}{\frac{dZ_s}{dX}}. \quad (2.89)$$

The geometrical reasoning is simple. It becomes clear from it that the angles between the direction of the free stream (ox axis) and the surface of the shock wave at points on line oN_1 (the angles between the horizontal and the vectors $\bar{n}^\circ$ of the surface normal) project without distortion onto the xoz plane and can be determined

130

from the projection of this line $z_w = f_2(x)$ onto the plane indicated.
Consider the length of shock wave surface with segment AB on the
maximum-span line oN_1. Its projection on the horizontal plane is
segment ab of the line $z_w = f_2(x)$ (the vertical projection of the shock
wave contour onto plane xoz).

At point N_1, we place plane (1) tangent to the wave; this plane
will contain the vertical N_1N_2 (the cross section $M_1N_1CM_1$ of the wave
also has its vertex at point N_1). Consequently, the normal $\bar{n}^o$ to the
wave at point N_1 is parallel to the xoz plane. Curve ab will be
tangent to plane I at point N_2; hence it is the base of the projecting
cylinder 2, which is tangent to plane I. Consequently, the normal
$\bar{n}'$ to the curve at point N_2 is parallel to normal $\bar{n}$.

Thus the angle of vector $\bar{W}_1$ to the wave surface at point N_1
equals the angle between this vector and the curve $z_w = f_2(x)$ at the
projection of this point N_2. The analogous result, that the angles at
points of the surface and corresponding points of the curve are equal,
is obvious for the profile boundary $y = f_1(x)$ (the curve coincides
with its projection).

Thus, the angles of encounter of the stream with the wave surface
at the points of curves oM_1 and oN_1 are equal to the angles of
encounter of the stream at the corresponding points with the projec-
tions of these curves $y = f_1(x)$ and $z = f_2(x)$. Thus knowing M_1 and
the angles of inclination γ and γ' to the wave boundaries at each
point, we calculate the local pressure recovery ratio by Formula
(2.85).

Let us summarize the simple reasoning and geometrical assumptions
on which calculation of the resultant total-pressure coefficient
$(p''_0/p_{01})_{av}$ behind the shock wave in stream II is based.

131

1. The increment in the elementary entropy flux at each point of an annular element of the wave surface, or the corresponding local total-head recovery factor, is replaced by a certain constant value that is effective for the entire ring; we estimate it from the maximum or minimum or the mean value between them (as set forth above).

2. The vertical boundary $y_1 = f(x)$ — the geometric locus of the greatest wave height in the symmetry plane yox of the spray cone — is the line of maximum total-head losses (the line of maximum entropy increment) over the entire wave cross section.

The geometric locus of the points of maximum wave span in the direction of the oz axis is the line of minimum total-head losses (the line of minimum entropy increment) over the entire wave cross section. It projects into the curve $z = f_2(x)$ on the zox plane.

3. We calculate the areas of the wave cross sections cut by planes parallel to yoz as the areas of ellipses with semiaxes $y_w/2$ and z_w (elliptical-section hypothesis).

4. In evaluating the integral determining the entropy-flux increment, we replace the area of the surface (across which the gas flows) that is bounded at the entrance by a space curve, with a closely similar segment with a plane oval curve.

5. We make the following assumption in finding the lower limit of this integral. The figure with area F_1 and semiaxes $y_1/2$, z_1 in the initial cross section 1 — 1 of stream I is similar to the figure with area F' and semiaxes $y'/2$, z' in cross section 1' — 1' of the same stream I.

The hypothesis of constant adiabatic exponent is not mandatory, and evidently has little influence on the result. We note that the most important quantities — the wave inclination angles (from which the local values of the total heads and entropies are found) — are unrelated to the elliptical-cross section hypothesis, which is needed

only for calculation of the area of the elementary ring. These
angles are determined directly from the equation of the experimental
curves — the boundaries of the wave $y_w = f_1(x)$ and $z_w = f_2(x)$.

In conclusion, we indicate the sequence of operations in carrying
out actual calculations of the resultant quantity p''_0/p_{01}.

1. From the initial flow parameters, we find the coefficients
of the dimensionless functions describing the boundary of the shock
wave in accordance with Equations (2.20), (2.21) (see Table 2.4).

Experience in the calculations has shown that the power-law
approximation is usually used up to $X \leq 0.1$, and that the exponential
approximation is chosen for $X > 0.1$.

2. We establish the number of divisions along the ox axis, i.e.,
the values of Δx or Δy and, accordingly, the number of elementary
strips on the shock wave surface (and in plane yoz), i.e., the number
of terms in the integral of (2.79).

According to machine calculations, $\approx 20 - 30$ subdivisions are
usually enough.

3. For each value of x, we calculate the angles of inclination
at points on both boundaries of the curve and use Formulas (2.88),
(2.86), (2.87) and (2.85) to find the local total-head loss coefficients
at these points.

4. Using a logarithmic expression of the form (2.80), we deter-
mine the values of $\Delta s(x)$ under the integral sign.

5. Using the approximating formulas for the boundaries of the
wave, we calculate the area element df (or $d\bar{f}$), which are factors with
Δs under the integral (2.79). Returning to the formulas cited earlier,
we determine the ratios of the characteristic cross sections F_M/F^*
and F'/F^*.

6. For a given set of flow parameters and a fixed $X' = x'/y^*$, we find the values of F_1/F' (or F_1/F^*) from the preceding solution of the non-closed problem for a selected range of variation of the free parameter M'. Knowing F_1/F', we determine the limit X_s (see 2.78) and the relation $y_w = f_1(x)$ from y_s.

7. Having thus determined the values of the terms under the integral sign and the limits of integration, we calculate the value of the integral by Formula (2.79). This will give the total entropy increment.

8. From the logarithmic formula (2.81), we find three values of the total loss coefficients (p''_0/p_{01}) in stream II behind the shock wave.

For subsequent calculations, we shall use the arithmetic mean value enclosed between the maximum and minimum total-head recovery coefficients behind the wave:

$$\left(\frac{p'_0}{p_{01}}\right)_{min} \leqslant \frac{p'_0}{p_{01}} \leqslant \left(\frac{p'_0}{p_{01}}\right)_{max}.$$

The above total-pressure estimate is, of course, highly approximate, but the orders of magnitude of the unknown parameters are not very sensitive to these errors, especially for the most interesting sub-critical flow regimes with $M' < 1$; as before, we operate with the first root of the defining equation (the results for the two roots are similar).

Figure 2.22 illustrates the solution of the closing equation (2.83) (lower left). The resultant recovery factor $(p''_0/p_{01})_{av}$ behind the wave depends weakly on the present value of the parameter M' and approaches unity, while p_0'' approaches the initial value simulating p_{01}. At $x/y^* = 1$, therefore, the most substantial "contribution" to the entropy flux comes from the region of the shock wave near the characteristic. The intersection point of the curves of $p''_0/p_{01} = \varphi(M')$ and $p''_0/p_{01} = \varphi_2(M')$ determines the Mach number M' of the gas in the particular cone cross section F' (the Mach number M' of choice) and all of the unknown parameters.

134

Figure 2.22. Region of subcritical flow in initial segment of spray cone ($M_1 = 2.85$; $p_1 = 1$ bar; $d_n = 1$ mm). Illustrating solution of closing equation (determination of M'_{ch}): $x/y^* = 1$; $T_1 = 1050°$ K; $\Delta p = 40$ bar:

$$\frac{\rho_l RT_1}{p_1} = 1940; \quad \text{---} \quad \frac{\rho_l RT_1}{p_1} = 2350.$$
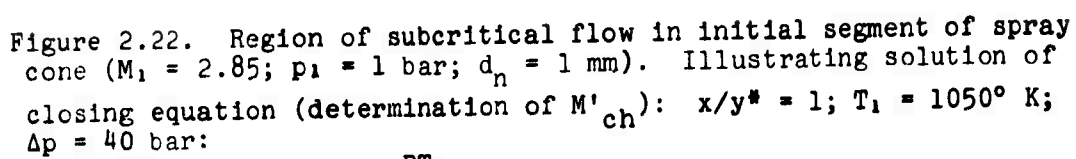
The plots in Figure 2.17 indicate that determination of M' from the curves corresponding to the extreme possible limits $(p''_0)_{min}$ and $(p'_0)_{max}$ does not affect the unknown parameters very significantly. This provides some justification for the approximations adopted in this section.

Solution of the closed problem for one regime requires 1 — 3 minutes of M-20 machine time when the above scheme is used: this is quite acceptable in practice and makes it possible to operate comfortably with the method proposed.

§5. Flow Relationships in the Initial Segment of the Spray Cone

The preceding section set forth in detail a method of solving the closed problem. Let us proceed to an analysis of its results. We shall first consider the possibility of replacing the real flow with a one-dimensional flow. The solution reduces to determination of two contacting one-dimensional flows, a two-phase flow I within the

135

cone with a varying stagnation temperature $T'_0 < T_0$; and a single-phase flow II that flows around the outside of the cone with constant stagnation temperature $T''_0 = T_{01}$ (see Figure 2.15). The cross-sectional areas of flows F' and F_M - F' (where all parameters are sought) are known. The two flows should be equivalent (in the sense of description by the integral equations of conservation) to the complex inhomogeneous flow in the frontal part of the cone. In the gasdynamics of single-phase flows, a similar problem was analyzed, for example, in [17]. It was found in the general case that a one-dimensional flow equivalent to a given inhomogeneous flow does not always exist. In other words, it is not always possible to find a one-dimensional flow with initial constants, mass flow rate, energy, and momentum stated beforehand. The problem examined here corresponds to a process in which mass, momentum (of the combined streams I and II) and energy are conserved, but entropy increases.

No attempt has been made to find a general analytical condition for the existence of the two one-dimensional flows I and II in explicit form. The limits of the parameters at which the one-dimensional solution fails have been determined by machine calculation.

The closed problem (determination of M' and all other quantities) was solved with assigned initial conditions M_1, T_1, p_1, Δp, ..., or the corresponding fundamental dimensionless numbers M_1, $\Delta p/p_1$, and $\rho_1 RT_1/p_1$ for rather closely spaced values of the variable abscissa x or x/y^*; $\delta(x/y^*) \approx 0.05 - 0.1$. It was shown that there always exists a point with a sufficiently small $x'_{l.b}$; $(x/y^*)_{l.b}$ (we shall call it the lower-boundary coordinate) at which there is no solution of the problem for all $x < x_{l.b}$ and $x/y^* < (x/y^*)_{l.b}$ and a solution always exists for $x \geq x_{l.b}$; $x/y^* > (x/y^*)_{l.b}$ (even for large $\dot{x}$ exceeding the limits imposed by the initial physical premises). Disappearance of the solution corresponds to the absence of an intersection point of the φ_1 and φ_2 curves in Figure 2.22.
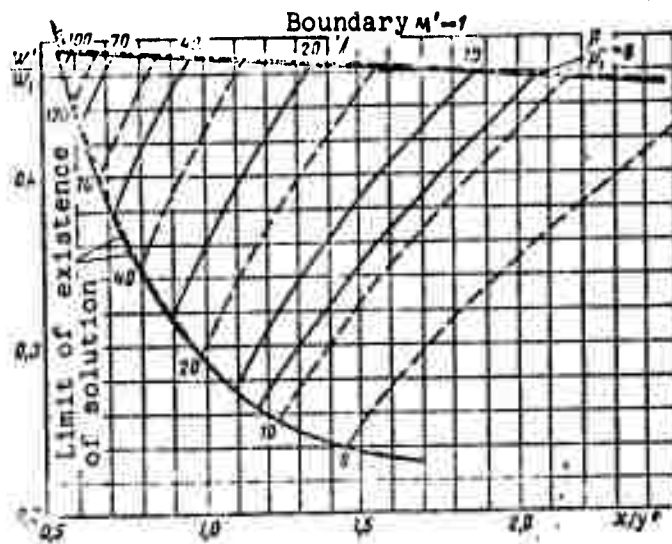
Figure 2.23. Range of subcritical flow in initial section of spray cone. ($M_1 = 2.85$; $p_1 = 1$ bar; $d_n = 1$ mm):

$$\underline{\qquad} \frac{\varrho_l RT_1}{p_1} = 1940; \quad \text{---} \quad \frac{\varrho_l RT_1}{p_1} = 2350$$

After finding the Mach number $M'_{l.b}$ at a point on the lower boundary, we calculate the corresponding gasdynamic parameters in the usual manner. Thus, the equivalent one-dimensional flows II and I, where stream I is the two-phase flow in the bow zone of the cone of interest to us, exist only up to a certain limit in M' and the coordinate x/y^*. Varying the basic initial parameters, e.g., $\Delta p/p_1$ and $\varrho_l RT_1/p_1$, we obtain the entire geometric locus of the points, i.e., the lower-boundary curve.

Together with the lower boundary, beyond which the one-dimensional solution vanishes, it is helpful to consider also the upper boundary, where $M' = 1$. Thus, we isolate a region of values of all parameters between the lower and upper boundaries that corresponds to subcritical flow conditions. A series of calculations has indicated the existence of such a region for a rather broad range of injection conditions. This result corresponds to a model of the phenomenon on the initial segment of the cone that leads to a picture of subcritical (in the mean) flow in the frontal zone of the cone.
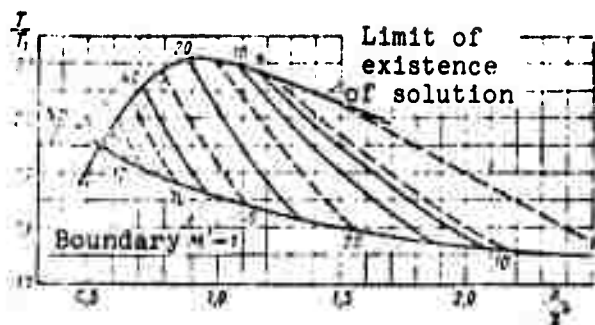
137
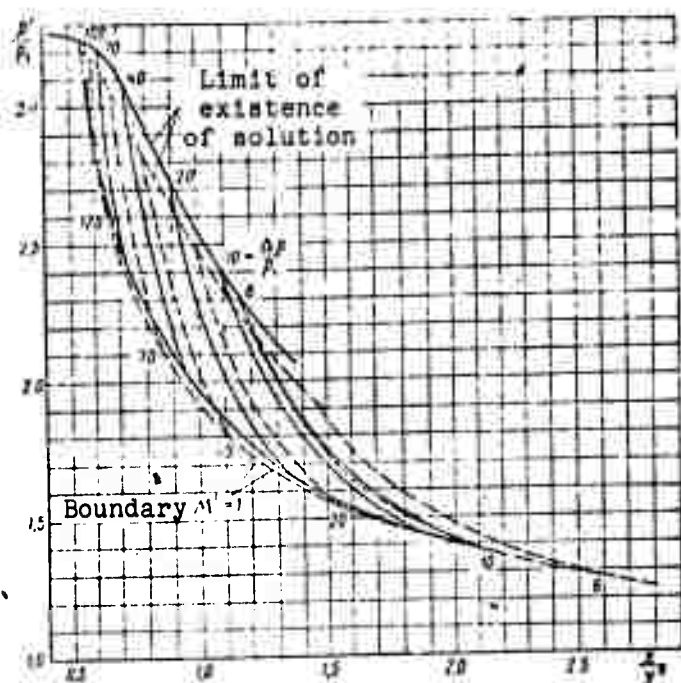
Figure 2.24. Subcritical-flow region in initial segment of spray cone ($M_1 = 2.85$; $p_1 = 1$ bar; $d_n = 1$ mm):

$$\frac{\rho_l RT_1}{p_1} = 1940; \quad --- \quad \frac{\rho_l RT_1}{p_1} = 2350$$

Let us consider the corresponding regions for the unknown parameters M'; W'/W_1; T'/T_1; p'/p_1; and β' in Figures 2.22, 2.23, 2.24, 2.25, and 2.26, as obtained with $M_1 = 2.85$; $d_n = 1$ mm; and $T_{l_1} = 293°$ K and various values of the combinations $\Delta p/p_1$; $\rho_l RT_1/p_1$; x/y^*.

The plane of the values of all parameters is subdivided into three characteristic zones. The points within the region (between their boundaries) correspond to subcritical flow conditions with $M' < 1$, while the points on the upper boundary of the flow correspond to flows with $M' = 1$. Below the lower boundary (small x/y^*), we have a region that "does not compute," in which it is impossible to use the principle of the equivalent one-dimensional flow,* and the zone above the upper boundary corresponds to supercritical flows with $M' > 1$.

_____

*The bulk of the gas will move here at "local" subcritical velocities with complex parameter profiles.

138

Figure 2.25. Subcritical-flow range in initial segment of spray cone ($M_1 = 2.85$; $p_1 = 1$ b; $d_n = 1$ mm):

$$\frac{\rho_l RT_1}{p_1} = 1940; \quad \text{---} \quad \frac{\rho_l RT_1}{p_1} = 2350$$

At a given free-stream Mach number, the lower boundary in the coordinates M'; x/y^* (see Figure 2.22, upper right) is practically independent of the other criteria in the range studied (at the computing accuracy indicated); its equation takes the form

$$M'_{n.r} \cong f\left(\frac{x}{y^*}\right). \tag{2.90}$$

We note that the curve of (2.90) makes an asymptotic approach to the horizontal line $M' \equiv M'_{n.s} = $ const, where $M'_{n.s}$ is the gas Mach number behind the normal shock and equals approximately $0.47 - 0.468$ at $M_1 = 2.85$ and $\rho_l RT_1/p_1 = 1940 - 2350$.[*] Thus, the average Mach number M' in the spray cone cannot assume values smaller than $M_{n.s}$ on the segment being computed. In the region under consideration, inclusive of its boundaries, therefore, the effective Mach number in the cone lies in the range

$$M_{n.c} \leqslant M_{n.r} \leqslant M' \leqslant 1,$$

as $x/y^* \to \infty$ $M_{l.b} \to M_{n.s}$.

---

[*]The slight difference in the asymptotes, i.e., $M_{n.s}$, is explained by a minor difference between the adiabatic exponents $k_1 = f(T_1)$.
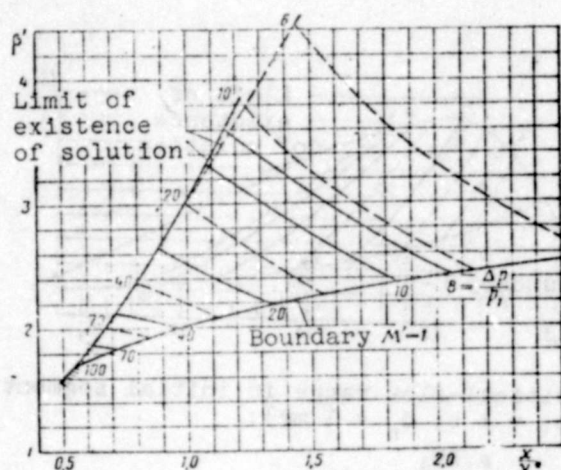
Figure 2.26. Subcritical-flow range in initial segment of spray cone (M_1 = 2.85; p_1 = 1 bar; d_n = 1 mm):
— $\dfrac{\rho_l RT_1}{p_1}$ = 1940; --- $\dfrac{\rho_l RT_1}{p_1}$ = 2350.

The limits of the other parameters W'/W_1, p'/p_1, T'/T_1, β' "stratify" slightly with respect to the dimensionless number $\rho_l RT_1/p_1$ (this is more noticeable with respect to p'/p_1). The assumed accuracy of calculation of the boundaries is quite acceptable for the analysis to follow. With fixed dimensionless numbers M_1 and $\rho_l RT_1/p_1$ and variation of the combinations $\Delta p/p$, we obtain a family of lines — subcritical-flow segments passing from the lower to the upper boundary within the region (solid and dashed curves). The subcritical-flow interval in the cone, i.e., the length $\Delta(x/y^*)$ of these lines, decreases with increasing parameter $\Delta p/p_1$ and decreasing $\rho_l RT_1/\rho_1 = \rho_l/\rho_1$. The subcritical-flow region with $M' < 1$ becomes shorter and moves closer to the point of injection if distance is measured in cone "calibers" x/y^*. This result is physically quite natural, since the indicated change in the combinations corresponds to a decrease in drop concentration β^*, i.e., weaker deceleration of the incoming gas in the cone.
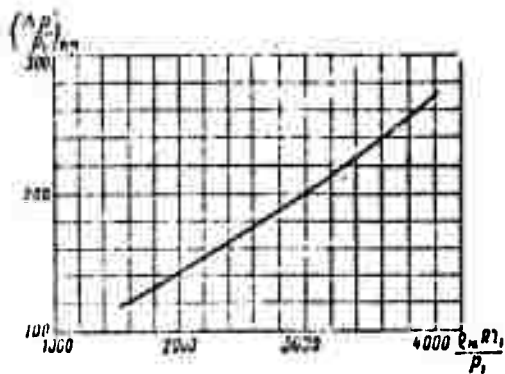
140

Figure 2.27. Limiting parameter $(\Delta p/p)_{lim}$ of subcritical flow in initial segment of spray cone $(M_1 = 2.85; d_n = 1$ mm$)$.
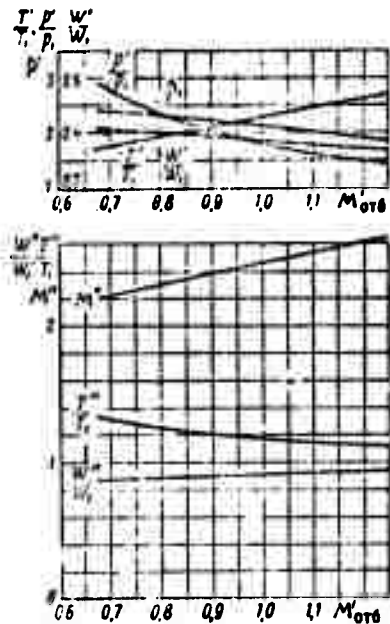

Figure 2.28. Variation of flow parameters along initial segment of cone as functions of M'_{ch} $(M_1 = 2.85; \Delta p = 40$ bar; $T_1 = 1050°$ K; $d_n = 1$ mm$)$.

Each of the regions on these figures has a characteristic corner point at which the boundaries intersect, and at which the subcritical-flow range contracts to o (for example, point A in Figure 2.22). The corner point corresponds to a certain rather large value $(\Delta p/p_1)_{lim}$ for each value of $\rho_1 RT_1/p_1$ and a certain minimum value $(x/y)_{lim} \approx 0.55.$* When $\Delta p/p_1 \geq (\Delta p/p_1)_{lim}$, the computing interval of the flow in the initial segment of the cone becomes supercritical, $M' \geq 1$, i.e., the cone has no zone in which the flow is subcritical in the mean.

Figure 2.27 shows the limiting number $(\Delta p/p_1)_{lim}$ as a function of the number $\rho_1 RT_1/p_1$. We see from the plot in Figures 2.22, 2.23, 2.26, 2.25, and 2.24 that the parameters M' and W'/W_1 increase and

* For $\frac{x}{y^*} < \left(\frac{x}{y^*}\right)_{lim}$, there is only one lower boundary dividing the parameter region into 2 zones: existence and absence of equivalent one-dimensional flow.

T'/T_1, p'/p_1, and β' decrease along each curve $\Delta p/p$ = const, i.e., the averaged gas flow inside the cone is accelerated in much the same way as the flow in a certain conventional gasdynamic nozzle.

The curves in Figure 2.28 relate the variations of the fundamental quantities with the Mach numbers M' in various cross sections of the cone for a typical regime.

All of the curves presented here indicate (like the results obtained previously for the non-closed problem) that the flow parameters in the frontal zone of the cone differ substantially from the corresponding values in the free stream over the entire range of x/y^*. The velocity W' may be approximately 1/2 to 1/4 of the initial velocity W_1, the temperature T' may exceed T_1 by a factor of 1.75 — 2.1, p' may be 1.3 to 3 times p_1, and the drop concentration β' may exceed the nominal value β^* by a factor of 1.3 — 3.5. The increase in liquid concentration β' is due to the fact that an appreciable portion of the incoming gas flows around the bow zone of the cone without penetrating into the "liquid grid."

Figure 2.29 shows the relationships for the basic parameters at various free stream Mach numbers M_1 = 2, 2.85 and 3.5 and x/y^* = 1; $\Delta p/p$ = 40; $\rho_l RT_1/p_1$ = 2350; d_n = 1 mm. Figure 2.30 shows the subcritical-flow intervals for M_1 = 2, 2.85, and 3.5; their lengths decrease with increasing M_1, i.e., with the transition to weaker shock waves. The gas in a given cross section x/y^* = const is found to be stagnated and heated the more strongly and to contain higher particle concentration the larger the free stream Mach number M_1.

We now touch briefly upon the problem of the stagnation temperature and pressure of the gas within the initial segment. The flow here is distinguished by the highest concentration β' and the strongest removal of mechanical energy from the gas to the particles. To a certain degree, the parameters determine the energy loss of the gas due to atomization and formation of the "cold" cone. They are not sufficient to characterize all types of losses, but they are found
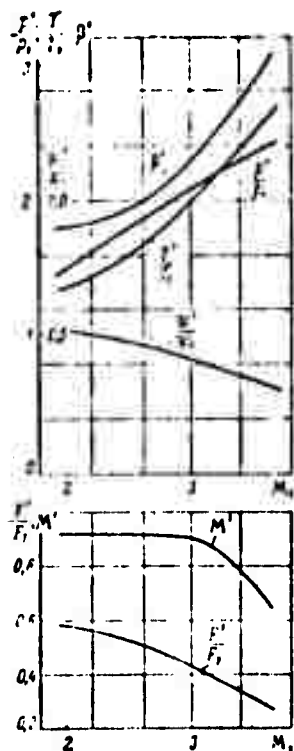
Figure 2.29. Flow parameters on initial segment of spray for various M_1 ($\Delta p/p_1 = 40$; $T_1 = 1050°$ K; $x/y^* = 1$; $d_n = 1$ mm).
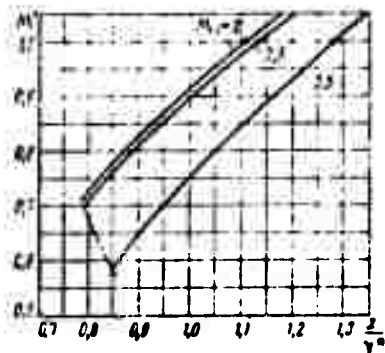

Figure 2.30. Intervals of sub-critical flow for various M_1 ($\Delta p/p_1 = 40$; $\rho_l RT_1/p_1 = 2350$; $d_n = 1$ mm).

helpful in estimating the losses due to subsequent combustion and mixing in the chamber and nozzle, where there is a whole system of spray zones. Allowance for this large-scale inhomogeneity in the stream would, of course, require a special analysis, but this is beyond the scope of the present work.

By the stagnation temperature and pressure T'_0 and p'_0 of the gas, we shall mean the temperature and pressure obtained on adiabatic deceleration of a gas without liquid particles from a given state with the parameters W', T', p', and M'. The results of simplified calculations that are given here, give a notion as to the orders of magnitude of the stagnation parameters and the manner in which they depend on various factors. The gas stagnation pressure and temperature are calculated with the simplified hypothesis that the adiabatic exponent does not vary, $k'' = k' = k_1$:

$$p_0' = \frac{p'}{\pi(M')}; \quad T_0 = \frac{T'}{\tau(M')};$$

(2.91)

$$p_0' = \frac{p''}{\pi(M'')} = \frac{p'}{\pi(M'')}; \quad T_0 = \frac{T''}{\tau(M'')}.$$

(2.92)

Calculations that take account of the temperature dependence of the adiabatic exponent can be carried out by the method of successive approximations. The stagnation temperature T_0' can be determined from the enthalpy equation (2.93) for stream I without using the gasdynamic functions; it is the upper limit of the values of T', $T' \le T_0'$ (we consider the case with $T_l \ll T'$):

$$\bar{c}_p' T_0' = \bar{c}_p' T' + \frac{W'^2}{2} = \bar{c}_p T_1 + \frac{W_1^2}{2} - (\beta' - 1)\left[i_x' - i_{x1} + \frac{1}{2}(V'' - V_1^2) + i_e \right] =$$

$$= \bar{c}_{p0} T_{01} - (\beta - 1)\left[i_x' - i_{x1} + \frac{1}{2}(V'' - V_1^2) \right];$$

(2.93)

$$i_e \cong 0.$$

For most real flow cases, $i_l > i_{l_1}$, $V' > V_1$, and the stagnation temperature T'_0 in cross sections of the initial segment is smaller than T_{01} as a result of withdrawal of heat and work from the gas to the particles.

Recognizing that $W_1^2/2 = M_1(k_1 - 1)$, we obtain a working formula from Equation (2.93):

$$\frac{T_0'}{T_1} = \frac{\bar{c}_p'}{\bar{c}_{p0}'} \frac{T'}{T_1} + \frac{c_{p1}}{c_{p0}} \frac{k_1 - 1}{2} M_1^2 \left(\frac{W'}{W_1}\right)^2.$$

(2.94)

The average heat capacities of the gas appearing in this expression depend on the corresponding temperatures:

$$c_{p1} = f(T_1); \quad \bar{c}_p' = f(T_{c0}'); \quad \bar{c}_{p0}' = f(\bar{T}_{cp0}'); \quad \bar{c}_{p0} = f(\bar{T}_{cp0}).$$

We may assume in approximation (in calculating the heat capacity) that

$$T_{cp}^{'} = \frac{T_* + T'}{2}; \quad T_{cp0}^{'} = \frac{T' + T_0^{'}}{2} \approx T_{cp0} = \frac{T_1 + T_{01}}{2}. \tag{2.95}$$

The change in the total head $p_0{}'$ of the gas on the initial segment of the cone is composed of wave losses and losses due to removal of energy during entrainment of the drops. In calculating the overall total-head-recovery coefficient $\sigma\Sigma = \bar{p}_0{}'$, therefore, it is interesting to divide this quantity into two parts corresponding to the losses on the shock wave and in the flow around the swarm of drops (for brevity, we shall use the term "recovery coefficient"):

$$\sigma_{\Sigma} = \frac{p_0^{'}}{p_{01}} = \frac{p_{0n}^{'}}{p_{01}} \cdot \frac{p_0^{'}}{p_{0n}} = \sigma_n \sigma_{\mu}. \tag{2.96}$$

The flow between the surface of the waves and the boundary surface of the cone is assumed isentropic:

$p'_{0w}; \; \sigma_w = p'_{0w}/p_{01}$ are the total pressure and the recovery coefficients behind the shock wave in front of the cone;

$\sigma_d = p''_0/p_{0w}$ is the total-head coefficient in the drop zone.

The quantity σ_w is determined by the method set forth above from the entropy-flux increment in the gas flowing inside the cone. Integration extends over segment os on the surface of the wave (as in 2.79):

$$\Delta S = R \ln\left(\frac{p_{01}}{p_{0n}}\right) = \frac{2}{\pi \frac{F_1}{F^{\bullet}}} \int_0^{X_s} \Delta s \left(\frac{dY_0}{dX} Z_* + \frac{dZ_0}{dX} Y_*\right) dX \tag{2.97}$$

or, if the area F_1 is subdivided by another method,

$$\Delta S = R \ln\left(\frac{p_{01}}{p_{0n}}\right) = \frac{2}{\pi \frac{F_1}{F^{\bullet}}} \int_0^{Y_1} \Delta s Z \, dY. \tag{2.98}$$

145

The coefficient σ_d is calculated from $\sigma\Sigma$ and σ_w:

$$z_x = \frac{\sigma_x}{\sigma_0}. \qquad (2.99)$$
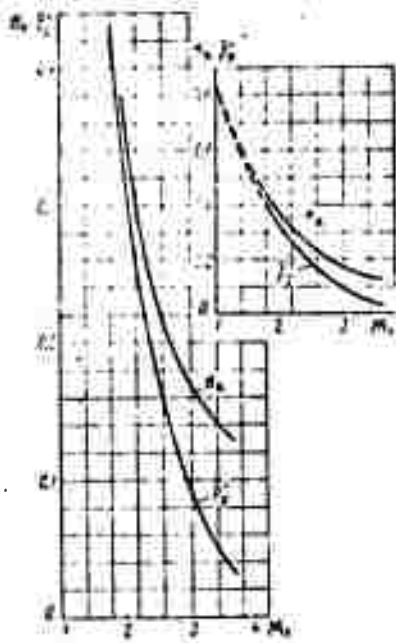
Figure 2.31. Total pressure coefficient in initial segment of spray cone for various M_1 ($x/y^* = 1$; $T_{01} = 2400°$ K; $p_{01} = 35$ bar; $\Delta p = 40$ bar; $d_n = 1$ mm).

The plot in Figure 2.31 reflects the dependence of the overall coefficient $\sigma \equiv p'_0/p_{01} = \bar{p}'_0$; σ_d and the loss coefficient related only to the particles on the free stream Mach number M_1 for $T_{01} = 2400°$ K; $p_{01} = 35$ bar; $\Delta p = 40$ bar; $d_n = 1$ mm; $T_{Z_1} = 293°$ K in a fixed cross section $x/y^* = 1$. At small Mach numbers $M_1 \leq 2 - 2.5$, the values of $\bar{p}_0'$ and σ_d are similar, i.e., the overall losses (which equal $1 - \sigma\Sigma$) are governed basically by the "liquid grid."

With increasing M_1, the wave-loss percentage becomes appreciable, approaching the size of the losses on the drops (the values of $\bar{p}_0$ and σ_d diverge). Extrapolation to the condition $M_1 = 1$ (Figure 2.31), which is, of course, very rough (and done only for orientation), indicates the following: in the subsonic stream, where the wave drag vanishes, the smallest total-head recovery coefficient (it will be larger for $M' < 1$ than for $M' = 1$) may be on the order of 0.8; consequently, the static-pressure ratio must also be smaller: $p'/p_1 \approx p'_0/p_1 < 0.8$.

A number of experiments have indicated the existence of an under-pressure inside a spray cone in a subsonic stream or a stationary medium. It is manifested in inflow of air into the cone from the surrounding space. Figure 2.32 shows the dependence of p'_0/p_{01} and
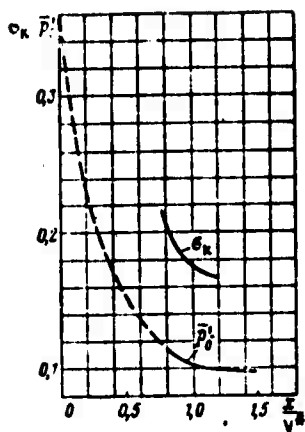
146

Figure 2.32. Total
pressure coefficient
in initial segment
of cone (separation
of losses), $M_1 = 2.85$.

σ_d on the coordinate x/y^* for a flow regime
with the same Δp, p_{01}, T_{01}, $d_n = 1$ and
$M_1 = 2.85$. The recovery coefficients
decrease along the length of the cone due
to the increase in the losses in the
accelerated two-phase stream.

At $x/y^* \geq 1 - 1.2$, the curves
indicate little variation of the parameters.
On the oy axis, we note the value of the
total-head recovery coefficient behind
the normal shock $\sigma_{n.s}$ (as $x/y^* \to 0$ p'_0/p_{01}
$\to \sigma_{n.s}$). The results of solution indicate
a drop in the stagnation temperature T_0' within the cone due to the
energy transferred to the drop. For example, for $M_1 = 2.85$, $T_1 = 1050°$ K, $p = 1$ bar, $\Delta p = 40$ bar, $d_n = 1$ mm, $T_{l1} = 293°$ K, and $x/y^* = 1$,
the stream yields approximately 15% of its total energy to the drops
and $T_0' \approx 0.9\ T_{01}$ (the stagnation temperature is lowered in stream II
above the cone).

The above data permit calculation of the overall total-head
recovery coefficient σ_c in cross section 1' — 1' of the spray cone.
The entropy-flux increment of the gas* (after its passage through
the shock wave and the zone of the cone) will be written as follows
for the cross section with area F_M:

$$\rho_1 W_1 F_1 \Delta S_1 + \rho_1 W_1 (F_M - F_1) \Delta S_{11} = \rho_1 W_1 F_M \Delta S_c.$$

Here ΔS_I, ΔS_{II}, ΔS_c are the entropy increments in the gas streams I
and II and the total increment for the entire cross section F_M.
Using the logarithmic relation between entropy and total head, we obtain

---

*Streams I and II are regarded as an isolated system from which
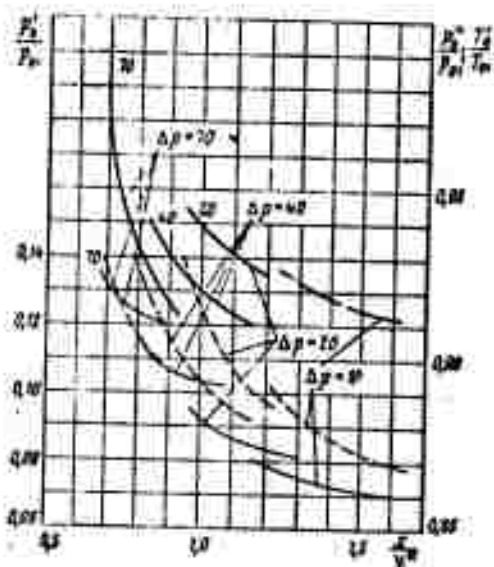mechanical and thermal energy is transferred to the drops.

Figure 2.33. Total-heads and stagnation temperatures of gas in initial segment of cone for various Δp ($M_1 = 2.85$; $p_1 = 1$ bar; $d_n = 1$ mm):
—— p'_0/p_{01}; —— p''/p_{01}; --- T'_0/T_1

$$\sigma_\phi = \left(\frac{p_0}{p_{01}}\right)_\phi = \left(\frac{p'_0}{p_{01}}\right)^{\frac{r_0}{r_u}}\left(\frac{p'_0}{p_{01}}\right)^{1-\frac{r_1}{r_u}} . \quad (2.100)$$

For the set of conditions cited above, $\sigma_c = 0.6$, Figure 2.33 shows the stagnation parameters $\bar{p}'_0 = p'_0/p_{01}$ and $\bar{T}'_0 = T'_0/T_{01}$ along the cone for various $\Delta p/p_1$. The losses $1 - \bar{p}'_0$, $1 - \bar{T}'_0$ of total-head and total energy of the gas in the cone increase with increasing coordinate x/y^* and with decreasing $\Delta p/p_1$, i.e., with decreasing range of the cone and, accordingly, increasing drop concentration. In the external flow, on the other hand, the total-head losses $1 = \bar{p}''$ decrease with decreasing $\Delta p/p_1$, i.e., with decreasing volume of the cone on which the shock wave forms.

Let us consider certain distinctive properties of the closed problem. Earlier, in determination of the parameters in the non-closed problem, whose solution exists for any coordinate, we assumed in approximation that $x/y^* \approx 1$.

In the present case, we obtain a fully defined relation between all of the quantities M', W', ..., and the coordinate x/y^* over the entire range of its values. The question again arises regarding the choice of effective parameters for the frontal segment for use as initial data in calculating the vaporization. We may assume that on the "noncomputing" segment (next to the point of injection), where $x/y^* < (x/y^*)_{l.b}$, there is practically no vaporization because of the high density of the swarm of insufficiently heated particles (which should be even higher than the values β' obtained in the calculation).

148

The calculations indicate that, for example, with $T_1 = 1050°$ K, $p_1 =$ 1 bar, $M_1 = 2.85$, $d_n = 1$ mm, $\Delta p = 40$ bar, $a_{max} = 13$ μ, and $(x/y^*)_{lim} \approx$ 0.72, the absolute value of the length of the "noncomputing" segment $x_{lim} = 11.3$ mm. With $8 \leq \Delta p/p_1 \leq 100$, $\rho_l RT_1/p_1 = 1940°$ K, $10.6 \leq a_{max} \leq$ 14.6 μ 8 mm $\leq x_{lim} \leq 14$ mm. It can be assumed that vaporization should still be insignificant on such short intervals in a swarm of drops with these diameters after a gas temperature on the order of 1000 — 2000° K. Vapor production may become appreciable on the approach to the upper limit of the interval, when its length is increased by a factor of two or more and the drop concentration decreases.

The small amount of vaporization on the initial segment of the cone, which the theory leaves out of account, tends to broaden slightly the subcritical-flow interval that results. To a minor degree, it slows the acceleration of the stream (the increase in M' over the coordinate x'/y^*) due to removal of heat to the drops. For the effective coordinate, i.e., the length of the initial segment, we take the average value of x/y^* on the computing segment:

$$\left(\frac{x}{y^*}\right)_{cp} = \frac{1}{2}\left[\left(\frac{x}{y^*}\right)_{x.r} + \left(\frac{x}{y^*}\right)_{a.r}\right], \qquad (2.101)$$

where $(x/y^*)_{l.b}$ and $(x/y^*)_{v.b}$ are the ordinates of the lower and upper boundaries of the subcritical-flow regime.

The corresponding calculations indicate that for most regimes with $M_1 = 2.85$, i.e., for $10 \leq \Delta p/p_1 \leq 120$, $\rho_l RT_1/p_1 = 1940 - 2350$, the influence of the second criterion is comparatively small and that $(x/y^*)_{av}$ is of the order of unity, and, as before, we take $x/y^* \approx 1$ to evaluate the total length of the cone from the injection point to the total-vaporization cross section. We could also take the effective value of $(x/y^*)_{av}$ from the average M_{av} determined from the values of the Mach number at the ends of the subcritical-flow interval:

$$M_{cp} = \frac{M_H + M_a}{2} = \frac{M_H + 1}{2}, \qquad (2.102)$$

149

where M_l and M_u are the values corresponding to the lower and upper boundaries.

Calculations show that the two methods of determining $(x/y^*)_{av}$ yield very similar results because the "isobars" $\Delta p/p_1$ in Figure 2.22 are comparatively close to the linear relations.

We should note in general that for many regimes, the orders of magnitude of the unknown normalized variables W'/W_1, p'/p_1, T'/T_1, and β' do not vary too strongly* as M' is varied on the computing interval in the range $M_{l.b} \leq M' \leq 1$. Hence the variations of the absolute values of W', p', T', β' are determined to a greater degree by the initial regime parameters than by the method of choosing the average effective parameter inside the initial interval.

According to the scheme adopted above, in which the cone is sub-divided into characteristic zones, vaporization develops strongly on the main segment of the cone. On the above basis, we shall calculate the vaporization in the closed problem for initial parameters W', p', T', β' determined from the average value $(x/y^*)_{av}$ according to formula (2.101). Earlier, we demonstrated the existence of "translimit" regimes in which $\Delta p/p_1 > (\Delta p/p_1)_{lim}$ (they are not considered in detail here). In this case, the flow is supercritical for all x/y^*, and for evaluation of the initial parameters we must choose the smallest value of the coordinate corresponding to an equivalent one-dimensional flow, i.e., the lower-boundary coordinate.

Let us now compare the results of solution of the closed and non-closed problems. As we have noted, the parameters W'/W_1, T'/T_1, etc., obtained in the solution of the non-closed problem will satisfy all conservation equations except the condition of entropy-flux increase. But the numerical differences between the parameters found by solving the two problems are comparatively small for a definite

*From the standpoint of the vaporizability calculation.

range of flow conditions. For example, for the typical regime $\Delta p/p_1 = 40$, $\theta_l RT_1/p_1 = 2350$, $x/y^* = 1$ ($T_{l_1} = 293°$ K, $d_n = 1$ mm), solution of the closed problem yields the parameters M' = 0.9; $\overline{W}'$ = 0.43; $\bar{p}'$ = $\bar{p}''$ = 2.03; T' = 1.91; β' = 2.2; M" = 2.41; $\overline{W}''$ = 0.92; T'" = 1.23; the same parameters in the non-closed problem have the values M' = 1; x/y^* = 1; $\overline{W}'$ = 0.469; $\bar{p}'$ = $\bar{p}''$ = 2.07; T' = 1.85; β' = 2.07; M" = 2.37; $\overline{W}''$ = 0.91; T'" = 1.25.

Comparing the parameters of the closed problem in respect to the average (effective) length $(x/y^*)_{av}$ of the initial interval with the parameters of the non-closed problem at $x/y^* = 1$, the two results may be considered relatively close in the following ranges:

$$1)\ M_1 = 2{,}85;\quad 20 < \frac{\Delta p}{p_1} < 50;\quad \frac{\varrho_* RT_1}{p_1} = 2350;$$

$$2)\ M_1 = 2{,}85;\quad 16 < \frac{\Delta p}{p_1} < 36;\quad \frac{\varrho_* RT_1}{p_1} = 1940.$$

Then the percentage differences between the corresponding parameters will be

$$1)\ \Delta\overline{W}' = \left| \frac{\overline{W}'_{замк} - \overline{W}'_{незамк}}{\overline{W}'_{незамк}} \right| = 10 \div 20\%;\quad \Delta\bar{p}' = 6 \div 27\%;$$

$$\Delta\overline{T}' = 1 \div 5\%;\quad \Delta\beta' = 3 \div 17\%;$$

$$2)\ \Delta\overline{W}' = 10 \div 18\%;\quad \Delta\bar{p}' = 12 \div 24\%;$$

$$\Delta\overline{T}' = 1 \div 4\%;\quad \Delta\beta' = 4 \div 15\%.$$

These discrepancies are not particularly significant for the subsequent calculation to determine the total vaporization interval x_v, and we may therefore use a simpler method based on solution of the non-closed problem in the range indicated.

In the broader ranges of values

$$20 < \frac{\Delta p}{p_1} \leqslant 70 \quad \text{at} \quad \frac{\varrho_* RT_1}{p_1} = 2350;$$

$$16 < \frac{\Delta p}{p_1} \leqslant 70 \quad \text{at} \quad \frac{\varrho_* RT_1}{p_1} = 1940,$$

151

the a sagreement increases, but the hypothesis $M' \approx 1$ can still be used for rougher estimates of the interval x_v.

Closely similar results are naturally obtained in this comparison when the Mach number M' of the chosen solution does not differ greatly from unity. Since these values of M' (other conditions the same) approach unity with decreasing free stream Mach number M_1, the agreement of the results of the two problems improves ($M_1 \leq 2.83 - 3$). As M_1 increases, on the other hand, the differences become larger.

A typical flow in the evaporating cone can be described as follows on the basis of the computing scheme adopted: the subcritical stream is accelerated on the initial segment. It can be compared to a practically nonvaporizing mixture of gas and particles flowing in the tapering section of a kind of "liquid Venturi tube" or in a "liquid nozzle" (closed problem where the stream makes a close approach to the critical cross section without reaching it. Then, with subcritical parameters, the flow enters the main cylindrical section, where phase transitions develop vigorously and go to completion.*

The critical cross section hypothesis simplifies the computer program to some degree and requires the use of a smaller volume of experimental information in the initial data. However, solution of the closed problem gives more complete and fundamentally new results:

(1) it confirms by calculation (for a broad class of conditions) the intuitive hypothesis that developed subcritical gas flow exists at $x/y^* \approx 1$ on the initial segment of the cone. This explains the observed short total-vaporization intervals when fuel is delivered into the chambers, nozzles, and other devices with stream Mach numbers $M_1 > 1$;

---

*In the cold stream, in the absence of vaporization, the gas with the particles passes through the critical cross section in the cone and is then accelerated to the supercritical parameters of the surrounding stream.

152

(2) it indicates a region of existence of the equivalent one-dimensional flow of the two-phase mixture. It satisfies the conservation equations for streams I and II in the cones and outside of them and the condition of increasing gas entropy flux on the shock wave (gas II). It shows a "noncomputing" region in which plotting of this flow is impossible, and a region of translimit flows where liquid may be vaporized under supercritical-flow conditions ($M' > 1$);

(3) relationships are obtained for the gasdynamic parameters and the liquid concentration in the dense (bounded) swarm of drops (the spray cone). They may be useful in analysis of the interaction between the gas and the drops in other cases (for example, injection from a surface, accompanied by a large zone of boundary-layer separation). As we know, no definitive theory of the dense particle swarm (a further development of two-phase flows) has as yet been created.

In concluding this section, we discuss briefly the possibilities of using the method developed here in a related problem.

The cone initial parameters determined in this section are computed in a simplified scheme of the flow that is not complicated by boundary-layer detachment phenomena (as is admissible for analysis of phase transitions). However, the method can also be used in analysis of other problems, e.g., in determination of the pressures on the wall behind the injection zone (the problem of thrust-vector control at outflow from the exhaust nozzle of a jet engine).

This study does not deal specifically with the problem of computing the forces on the surface in the injection zone. We present only certain physical considerations pertaining to it, with reference, for example, to the results of F. I. Sklyar [18]. They point up the importance of determining the parameters of a two-phase flow developing directly over the layer next to the wall.

153

This study presents typical experimental curves of static pressure plotted against the symmetry-line coordinate of the cone behind the point of injection on a plate.

Liquid (practically nonvaporizing) jets and a jet of gas were delivered into supersonic streams, and, for comparison, the flow around a solid "semi-infinite" cylinder* whose axis was perpendicular to the plate was studied for comparison. The analysis indicated much higher pressures in the first case as compared with the other two.

A weight cavity and boundary-layer detachment usually develop in the wall region (behind the delivery orifice and the solid cylinder), as a result of the bluff-body flow. The undecayed segment of the liquid jet ("liquid leg") is such a body. (For the gas jet, the cavity zone is enlarged considerably as a result of injection of gas from its volume by the surrounding high-velocity stream.)

The cavity** is suppressed by the larger external forces; this determines the boundary conditions at the surface of the wall region and increases the pressure on the plate. This provides an explanation for the marked difference in the static pressures measured for liquid and gas jets.

In the former case, the external gas stream behind the shock wave strikes the dense swarm of particles and acquires a higher pressure. The process unfolds here in much the same way as that studied in the present chapter, where calculation indicates an increase in p' on the initial segment of the cone as compared with the free stream p_1. The increased pressure in the external flow also increases the pressure on the wall. Here we observe a smaller drop in p' along the plate as compared with the case of the gas jet. The results for two liquids that differ only in their physical constants are interesting.

_____

*A rod of sufficient length.

**Characterized as an effect of underpressure.

154

The first liquid, a solution of alcohol in water, has a lower surface tension and a lower viscosity than the second, ethylene glycol. Hence the first case is distinguished by a shorter decay segment (a short "liquid leg") and a smaller cavity zone; here the swarm of drops moves up closer to the wall surface. The two factors act in the same direction, increasing pressure for the case of the alcohol solution, and this is indicated by the experiments referred to.

The above interpretation of the experimental data permits the following hypothesis: for conditions under which there is rapid decay near the injection points (as is characteristic for most liquids used in practice), it is the external stream that makes the main "contribution" to the pressure on the plate (in any event in its initial zone). It flows directly behind the wave in the swarm of liquid particles and presses on the surface of the cavity. In the presence of vaporization (on later segments of the cone), the pressure in the subcritical zone may rise (as compared with the case in which there are no phase transitions). The case of the infinite solid cylinder is, in accordance with the experiments, intermediate between the liquid and gas jets. The wall cavity (and the pressure-drop effect) is smaller here than in the case of gas injection, in which the jet expands sharply in highly noncomputable conditions, ejecting gas from the cavity zone.

The experiment indicates that in the case of prevalence of the pressure effect of the wall layer itself (gas, solid cylinder), the interval on which static pressure is equalized is a short one, amounting to a few diameters of the delivery orifice. If the effects of the external two-phase flow around the cavity predominate, the p' equalization interval is longer and measured in larger scale units, i.e., the characteristic dimensions of the drop swarm ($\sim y^*$).

Having data (e.g., from an experiment) on the shapes of the cone and wave, we can develop the above method for calculation of the pressures in the atomized-liquid zone in the case of injection from the walls of a nozzle. This pressure is decisive in many cases. Here it will be important to resolve the question as to the existence of a

155

subcritical-flow region in the initial segment of the spray cone with $M' < 1$ (in analogy to the discussion given here). This will permit correct selection, for example, of the point and Δp of injection to obtain the highest possible pressures (especially for vaporizing liquids).

Under this heading, we have given only general qualitative considerations as to the relation and definite analogy between the problem considered in this work and the problem of the controlling forces that arise when liquid is injected from holes on the surface of a nozzle wall.

§6. Total Vaporization Interval in the Spray Cone. Comparison of Theoretical and Experimental Results

In this section, we describe a method and results of experimental investigation of liquid injection into a heated supersonic stream.

The total-vaporization interval l_e was determined in spray cones in which strong phase transitions were observed.

The theory of the individual stages in the process that was set forth in the preceding sections made it possible to devise a consistent computing technique (see below). It was used to compute all characteristics of the two-phase flow in the cone and the fundamental parameter — the liquid-vaporization length x_v.

The results of experiment and theory were compared for various injection regimes. The experiments were run on a special setup (Figure 2.34). In it, an air-fuel generator was used to form the heated stream. The exit end of the device terminated in a gasdynamic nozzle with open working section.
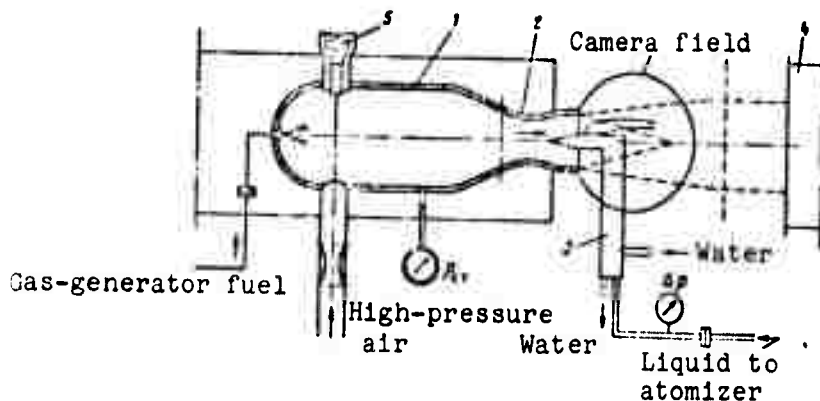
156

Figure 2.34. Diagram of experimental setup.
1 — gas generator; 2 — gasdynamic nozzle; 3 — cooled atomizer;
4 — exhaust pipe; 5— starting unit.

In steady-state operation, high-pressure air from cylinders was fed into the generator, where it was heated by the combustion of kerosene with an excess-air ratio $\alpha_T \approx 1 - 2$ and a combustion efficiency of approximately 0.93 — 0.97. Ignition of the fuel-air mixture was initiated at low pressure and sustained by a special antechamber, which was then shut off. The pressure in the generator was raised to the desired level with a regulating valve, with a simultaneous increase in the flow rate through the fuel nozzle.

The heated air (mixed with combustion products) flowed out of a supersonic nozzle whose critical- and exit-section diameters $D = 15$ and 35 mm. A special cooled atomizer was mounted at the exit from the nozzle, and the injection orifice and the initial segment of the cone were situated in the rhombus of equal free-jet parameters. The hot gas carrying the atomized liquid was then diverted into an exhaust pipe. The measuring system of the bench permitted determination of the usual parameters: the flow rate of the air entering the generator (Venturi tube), pressures in the generator chamber and the critical section of the supersonic nozzle, the flow rate of the fuel supplied to the generator, and the flow rate, temperature, and pressure of the liquids injected through the atomizer.

157

The setup could produce a supersonic stream with $M_1 = 2.85$ (geometrical Mach number) at near-nominal outflow $p_1 \cong p_{at}$ (where p_{at} is the atmospheric pressure) for two preheats $T \approx 1050$ and $866°$ K, and outflow velocities $W_1 = 1754$ and 1612 m/sec (total temperatures in gas generator, 2200 and $1700°$ K). The flow variables of the stream were determined by the familiar method:

(1) the excess-air ratio in the generator was calculated from the measured air and fuel flow rates m_a and m_T;

(2) assuming 100% combustion efficiency (and known compositions and enthalpies of the combustion products), the adiabatic exponent k and the gas constant R in the generator chamber were found from IS and RT diagrams (see, for example, [19]);

(3) the stagnation temperature was determined from the equation of the flow rate through the critical cross section of the generator nozzle with area F_{cr}:

$$T_0 = k \left(\frac{2}{k+1} \right)^{\frac{k+1}{k-1}}; \quad F_{кр}^2 \left(\frac{p_0}{m_a + m_T} \right)^2 \frac{1}{R},$$

were p_0 is the pressure in the generator;

(4) all other parameters of the flow in the nozzle exit section were calculated from the formulas of one-dimensional gasdynamics (the average value of the adiabatic exponent in the interval between the generator and the exit section was taken $k_2 = 1.25 - 1.28$). The experiments consisted of shadow or Töpler photography of the gas jet and spray cone under hot and cold conditions (with the generator on and off). The appropriate instrument panels (scales) were photographed simultaneously to record the readings determined by the flow parameters.
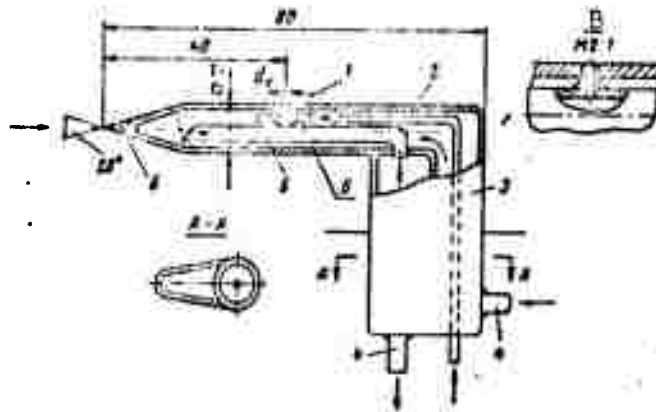
Figure 2.35. Cooled atomizer.
1 — exit channel of cylindrical atomizer; 2 — liquid supply for atomization; 3 — atomizer casing; 4 — cooling-water inlet and outlet; 5 — straightener tube; 6 — heat-resistant atomizer tip.

One of the major difficulties of the experiment consisted in the design of a nozzle with comparatively small dimensions and resistance combined with high thermal stability. It had to withstand exposures to high temperature for a considerable time (at least one hour) and should, to the extent possible, introduce no major disturbances into the flow around the spray cone. The problem was solved by the use of an atomizer of compact design with water cooling (Figure 2.35). The cooling-water temperature was monitored during the experiments. It was necessary to use tungsten for the thermally most stressed part of the atomizer — its tip, which tapered at an angle of ~28° (creating a weak shock wave similar to the characteristic), and to make it interchangeable. Visual observation showed that the fuel never flared up and that the spray cone was clearly visible, with steady boundary outlines, in reflected illuminator light.

The heated-stream experiments produced quite satisfactory photographs, examples of which appear in Figures 2.36 and 2.37. They can be used to determine the shape of the cone and the outlines of the shock wave in the frontal zone and total-vaporization interval. Because of the comparatively small field of the camera, the tail section of the vaporizing cone was sometimes cut off. In such cases, the camera was so set so that its field would cover the area of the spray cone tail section.

Figure 2.36. Vaporizing spray cone in supersonic flow (gasoline, M_1 = 2.85; T_1 = 1050° K; d_n = 0.8 mm; magnification 0.58 X).
a — Δp = 40 bar; p_0 = 46 bar, cold stream; b — Δp = 20 bar; p_0 = 40 bar; c — Δp = 78 bar; p_0 = 40 bar.

Photographs of cold stream regimes showed a continuous cone with uniform density over the entire length accessible to observation. (~250 — 300 mm), since there was practically no vaporization in this case. The range of the "hot" cone on a certain initial segment on which vaporization is still slight is practically the same as the range corresponding to "cold" cones.[*] With increasing distance from the injection point, the shape of the "hot" cone changes appreciably under the influence of phase transitions.

On certain photographs, the "hot" spray cone has a kind of "foxtail" shape in which the outer boundary slopes off to a tapered end. This is apparently to be explained by the distribution of liquid-phase concentration, which has a maximum somewhere inside the cone (an effect of the non-one-dimensional character of the two-phase flow). The weak shock waves observed on some of the photographs, for example, at the elbow of the atomizer, are close to the gasdynamic characteristic and have no appreciable influence on the shape of the cone. Gauging of the negatives (the experiment was repeated twice for each regime) showed fully satisfactory reproducibility of the results.

---

[*]Strictly speaking, cones with equal M_1; $\rho_l V_1^2 / \rho_1 W_1^2$; x/y^*, which determine shape on the initial segment, should be compared. For the experiments described, this means practical equality, accurate to $k_1(T_1)$, of the pressures Δp and p_1.
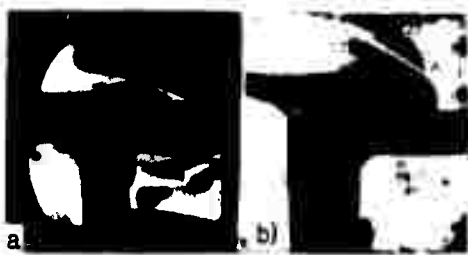
Figure 2.37. Vaporizing spray cone in supersonic flow (gasoline, $M_1 = 2.85$; $d_n = 1$ mm; magnification 0.58 X).

a — $\Delta p = 40$ bar; $p_0 = 45$ bar, bar, cold stream; b — $\Delta p = 38$ bar; $p_0 = 37$ bar; $T_1 = 866°$ K.

The main experiments were performed with gasoline at atomizer diameters $d_n = 0.6$, 1.0, and 1.45 mm and pressure drops $\Delta p = 19.6$ — 75.5 bar and alcohol with $d_n = 1$ mm and $\Delta p = 8$ — 56 bar. The spray cones that appeared on the photographs sometimes slightly exceeded the limits of the equal-velocity rhombus of the free jet as distance from the initial segment increased. The corresponding corrections were not introduced in computing the average parameters in the cone. As we noted above, the method used is based on the assumption that the rapid vaporization process is complete on a comparatively short interval. It depends primarily on the parameters of the stream shaped on the initial segment of the cone. The influence of mixing with the surrounding gas is considered secondary. The general procedure for calculation of the processes in the cone is based on the results set forth in this and the preceding chapter. It consists of three parts, which correspond to the main stages of the complex mixing process on the initial and main segments of the cone, where the liquid fuel is converted to vapor. We recall that these stages are:

(1) decay of the liquid jet and the appearance of a drop-size spectrum in the zone at the root of the cone;

(2) formation of a dense swarm of particles in chaotic motion on the initial segment of the cone behind the shock wave. Gas flows around it as it flows around a kind of semipermeable body, with a resulting sharp change from the initial parameters of the free stream after their penetration into the cone;

(3) an ordered two-phase flow of gas and drops with rapid vaporization. This takes place on the main segment of the zone and is likened (roughly) to the flow in an isolated channel; here we have processes of heat and mass exchange between the gas and drops, which have different velocities and temperatures (thermal and dynamic nonequilibrium). The complete calculation is also broken up into three items:

1. Determination of the coarseness of atomization from the free stream and injection parameters. The maximum particle diameter a_{max}, the average (median) diameter a_M, or the entire diameter spectrum is calculated using the aforementioned empirical dimensionless formulas. As we have stated, the decay of the liquid jet and the atomization of the drops in the supersonic stream take place very quickly and are complete on a small segment from fractions of a millimeter to a few millimeters in length. We can evidently disregard heating of the jet and calculate the physical constants of the liquid from its initial temperature T_{l1}. The effects of the fuel's initial enthalpy on the nature of the decay itself will be substantial if the liquid has first been heated to a high temperature, e.g., to near the boiling point (a case that is not considered here).

The following initial values are assigned for calculation of drop size: d_n; Δp; θ_l; σ; W_1; T_1; ρ_1; η_1; c_{p1}; c_{V1}; R, from which the dimensionless numbers

$$M_1 = \frac{W_1}{\sqrt{k_1 R T_1}}; \quad Re = \frac{W_1 d \rho_1}{\eta_1}; \quad We \approx \frac{\eta_1 W_1^2 d}{\sigma}; \quad \frac{V_1}{W_1}; \quad \frac{a_1}{d_e},$$

which appear in the drop-size formulas, are calculated.

2. The effective parameters W'; p'; T'; β' in the initial segment are calculated by computer solution of the fundamental conservation equations (as set forth in detail earlier) for the flow in the frontal segment between cross sections 1 — 1 and 1' — 1'. Here either the non-closed or closed problem can be solved, depending on the corresponding range of the parameters (see above). In our case,

162

the closed problem was solved for comparison with the experimental data (the results were similar to those of the non-closed problem). The calculation "converts" the initial free stream gas parameters to initial data for the equations of two-phase flow in the main segment of the cone. Here the following quantities are assigned: the drop size $a_1 = a_{max}$, the injection parameters Δp; d_n; $T_{l.l}$; T_b; ρ_l; μ_a (atomizer discharge coefficient), c_{l_1}, σ, and the gasdynamic parameters W_1; T_1; p_1; c_{p_1}; c_{v_1}; R (or M_1; T_{01}; p_{01}; $k_1 = c_{p_1}/c_{v_1}$). We note that for this stage in the calculations, the parameters a_1; σ; c_{l_1}; T_{l_1}; T_b; ρ_l are of little importance and can be estimated quite roughly.*

3. The concluding calculation of the processes with phase transitions on the main segment of the cone, and determination of the total-vaporization interval x_v. A computer is used to solve the equation system of two-phase flow (see Chapter I), with the initial values of the gasdynamic parameters and liquid concentration W'; T'; p'; β' and the drop size a_1 obtained under items 2 and 1 of this procedure, respectively. The coarseness of atomization is highly important in calculating the total-vaporization interval x_v. Here we take a_{max}, the largest diameter in the spray spectrum, with whose vaporization the phase transitions in the cone culminate.

This method uses the formulas for atomization coarseness that were obtained in the experiments of [15]. They express the median and maximum diameters of the spectrum:

$$\frac{a_{\mu}}{d_c} = 1.35 \frac{\left(\frac{M^2}{Re}\right)^{\frac{1}{5}}\left(\frac{V_1^2}{W_1^2}\right)^{\frac{1}{6}}}{\left(\frac{\rho_1 d_c W_1^2}{\sigma}\right)^{\frac{1}{5}}}; \quad \frac{a_{m_{21}}}{d_c} = 1.9 \frac{\left(\frac{M^2}{Re}\right)^{\frac{1}{9}}\left(\frac{V_1^2}{W_1^2}\right)^{\frac{1}{6}}}{\left(\frac{\rho_1 d_c W_1^2}{\sigma}\right)^{\frac{1}{5}}}.$$

---

*This applies to many practically important flow regimes, in which liquids such as gasoline, kerosene, alcohol, and water are atomized at small initial preheats, and when p_1 does not differ sharply from atmospheric pressure.

The basic dimensionless criterion is the Weber number $We = \rho_1 d_n W_1^2/\sigma$; the Mach number $M = W_1/a_{sd_1}$; the Reynolds number $Re = d_n W_1 \rho_1/\eta_1$. Reference [1] shows how to obtain an approximating formula for the spray spectrum from the values of a_M and a_{max}. The value of a_{max} corresponds to the condition that drops with sizes $a \leq a_{max}$ compose 95% of the entire mass of the liquid. Approximately 99% of all of the liquid is assumed to have evaporated at the instant of total vaporization of a particle with a_{max}. It has already been said that the calculation is performed for a one-dimensional isolated flow in a cylindrical pipe. It is regarded as a kind of "corresponding regime," which yields a measure of the vaporization interval in the real cone.

We take note of a peculiarity of this idealization. One of its consequences is that the calculated x_v is the upper limit of the total-vaporization range.

The effect of mixing between the flow inside the cone and the flow surrounding it, which the method does not take into account, should be to intensify the real vaporization process. Mass exchange (vapor leaving the cone and air entering it) lowers the concentration c_∞ of the vapor phase, increasing the rate of vapor production. Heat exchange takes place in more complex fashion. At the beginning of the main segment, the temperature in the space inside the cone exceeds the ambient temperature: $T' > T''$ (T'' near T_1). But then, under the influence of vaporization of the liquid, the mixture temperature T drops rapidly and, as the calculations show, falls below the free stream temperature, $T' < T_1$. This effect is more substantial, the higher the heat of vaporization that the liquid must absorb.

At the end of the vaporization interval of alcohol, for example, the temperature T_v in the cone is 100 — 300° C below ambient. Consequently, heat must flow into the cone from the outside. To this we should add that the vaporizability z_v rises sharply at the beginning

of the segment (the derivative dz_v/dx has a large value) and has low
sensitivity to temperature disturbances. To the contrary, at the end
of the main segment, where dz_v/dx is small, the vaporizability curves
$z_v = \varphi(x)$ are usually prolonged conspicuously along the x axis under
the influence of the decrease in ambient temperature.

Finally, exchange of momentum (acceleration of the two-phase flow
by the external stream) should result in sharp velocity gradients inside
the cone and strong turbulization, which intensifies the processes
of heat transfer between the phases. The large stream velocity gradi-
ent may cause secondary atomization of the drops and produce a larger
liquid surface. All of these effects will be stronger, the more diffi-
cult it is to vaporize the liquid. In comparing theoretical and
experimental results, therefore, the relative values of l_e/y^*, i.e.,
cone length measured in cone "calibers," should be taken into account,
since the mixing process over the length of the cone is determined by
this coordinate.

Selection of the maximum diameter a_{max} as the diameter defining
particle coarseness also corresponds to estimation of the liquid-
vaporization interval at the upper boundary. In performing actual
calculations of the phase-transition process and the total-vaporization
interval x_v in the last item of the procedure, use may be made of the
data obtained in Chapter I and plotted on the appropriate diagrams.
They are useful for a rather broad range of variation of the gasdynamic
parameters of the air in the initial cone segment and the drop sizes
that may be encountered in practice.

The possible error due to the difference between the physical
constants of the air and the product of combustion of hydrocarbon
fuels in air (heating of the stream under the experimental conditions)
is comparatively small and need not be considered (differences in heat
capacities, adiabatic exponents, etc.). The corresponding estimates
indicate that for regimes in which the initial effective gas pressure
p' and the liquid temperature T'_l of the cone do not differ strongly

165

from those under normal conditions ($p'/p_1 \approx 1.5 - 2.3$; $p_1 = 1$ b; $290 \leq T'_l \leq 320° K$), the vaporization interval can be calculated for simplicity for $p' = p_1 = 1$ bar and $T'_l = T_{1l} = 293° K$ (here the deviation would be $3 - 10\%$ if $T_1 \geq 800° K$).

Turning to a comparison of the theoretical and experimental results, we note once again the highly complex structure of the phenomenon being studied, in which at least three independent processes are interwoven into a single complex: decay of the liquid jet into drops, flow around the dense swarm of particles that results, and organized flow of gas with evaporating drops under conditions of dynamic and thermal nonequilibrium. To the best of our knowledge, this is the first attempt of its kind to penetrate consistently into a physical object as complex as the spray cone with phase transitions in a supersonic stream to obtain a single engineering method of calculation. Needless to say, all of this has been done at the cost of a rather crude idealization and a number of simplifying assumptions.

This combined calculation procedure is a first approximation. It may be improved later. Some opportunities for such improvements are inherent in the initial model. Tables 2.8 and 2.9 present calculated and experimental results for gasoline and alcohol.

The first six columns indicate the initial stream and injection parameters for the experimental regimes, then the drop diameter a_{max} and the determining parameters W', T', β' at the entrance to the main segment of the cone, from which the vaporization process is computed. According to calculations (§5), the orders of magnitude of W'/W_1 and T'/T_1 do not vary very strongly within the frontal segment. Estimating the effective values W' and T' at the center point of the interval (by the method adopted), we obtain comparatively large values in different regimes; the concentrations β' vary more strongly. What is significant is the fact that all of these effective parameters differ strongly from the parameters of the free supersonic stream.

166

TABLE 2.8

GASOLINE M = 2.85

	Flow Parameters						Drop Size	Initial Data in Cone			Theory					Experiment
No.	T_1 °K	W_1 m/sec	β°	d_c мм	Δp bar	V_1 m/sec	q_{max} μ	W' m/sec	$T_к$ °K	β'	$Y°$ мм	Δ %	$\frac{x_в+y*}{y*}$	$x_в$ мм	$x_в+y*$ мм	l_e мм
1	1050	1780	1.30	0.6	44	109	10	730	2040	2.2	10	7.8	4.4	34	44	46
2	1050	1780	1.25	0.6	76.5	137	10.6	765	2041	1.94	13	10.4	3.7	37	51	50
3	1050	1780	1.30	1.0	40	100	13	723	2040	2.24	16	5.2	4.2	52	68	72
4	1050	1780	1.25	1.0	64	126	14	775	2037	2.00	21	10.8	3.8	55	76	70
5	1050	1780	1.30	1.45	39	100	16	739	2021	2.54	23	11	4.0	70	93	84
6	1050	1780	1.50	0.6	19.6	70	9	687	2043	2.64	7	33	5.1	28	35	53
7	1050	1780	1.50	1.0	19.6	70	12	696	2031	2.63	11.4	10.5	4.9	45	56	63
8	1050	1780	1.50	1.45	19.6	70	14.7	700	2030	2.61	17	7.5	4.76	62	78	73
9	866	1610	1.30	0.6	39	100	10.6	676	1692	2.10	10	0.73	5.2	41	51	51
10	866	1610	1.25	0.6	75.5	135	11	725	1709	1.94	13	2.7	4.3	45	58	60
11	866	1610	1.30	1.0	39	100	12.7	695	1697	2.07	16	5.2	4.4	55	71	75
12	866	1610	1.25	1.0	65	126	13.6	728	1690	1.98	21	2.7	3.9	60	81	79
13	866	1610	1.30	1.45	39	100	16	692	1680	2.04	23	10.6	4.3	76	99	111

TABLE 2.9

ALCOHOL M_1 = 2.85

	Flow Parameters						Drop Size	Initial Data in Cone			Theory					
No.	T_1 °K	W_1 m/sec	β°	d_c мм	Δp bar	V_1 m/sec	q_{max} μ	W' m/sec	$T_к$ °K	β'	$Y°$ мм	Δ %	$\frac{x_в+y*}{y*}$	$x_в$ мм	$x_в+y*$ мм	l_e мм
1	1050	1780	1.7	1.0	10	49	10.7	650	2013	2.95	8.1	47	12.7	95	103	70
2	1050	1780	1.5	1.0	19.5	70	11.7	632	2040	2.64	11.4	43	10.0	103	114	80
3	1050	1780	1.3	1.0	40	100	12.4	643	2042	2.24	16.3	52	6.7	93	109	72
4	866	1610	1.7	1.0	8	44	10.5	604	1670	2.75	7.3	56	13.5	91	98	63
5	866	1610	1.5	1.0	20	70	11.5	645	1690	2.40	11.5	57	9.3	95	107	69
6	866	1610	1.3	1.0	39	100	12.4	693	1700	2.10	16.1	45	7.2	100	116	90
7	866	1610	1.25	1.0	56	119	13.0	717	1740	1.95	19.3	24	6.6	109	128	100

The chief unknown is the length of the main segment of the cone — the total-vaporization interval x_v; the table also gives the length $x' = y*$, which characterizes the extent of the initial cone segment. A comparison is drawn between the theoretical value of the total vaporization interval $x_v + x' \approx x_v + y*$ — the segment on which a liquid phase exists — and the value of l_e measured directly on spray cone

photographs (last two columns of the table). The order of magnitude obtained for l_e in the experiment suggests rather short vaporization intervals. That the process develops in this manner is explained by the high dispersion of the liquid particles, $a_{max} \sim 9 - 16 \mu$, and the significant increase in temperature and decrease in velocity in the initial segment of the cone as compared with the free stream parameters $T' > T_1$ and $W' < W_1$. The latter makes for comparatively long stay times of the drops in the cone.

We note in passing that the absence of ignition of the fuel in the experiments can be explained (apart from the induction-period factor) by the high fuel concentration $\beta' \approx 2 - 2.5$, i.e., by the very low excess-air ratios $\alpha_a < 0.1$ on the vaporizing segment of the cone. The figures given here make it possible to report quite satisfactory agreement between calculation and experiment for gasoline (see Table 2.8); the average deviation is

$$\Delta = \left| \frac{(x + y^\bullet) - l_\bullet}{l_\bullet} \right| \approx 7 \div 12\%.$$

The drop diameter a_{max} is one of the principal parameters, an increase in which increases l_e and x_v.

In the case of experiments with alcohol (see Table 2.9), the agreement is poorer and is characterized by a $30 - 55\%$ excess of the calculated values over the experimental ones. Let us analyze the results of comparison of theory and experiment for these two liquids. The calculated interval $(x_v + y^*)$ is found to be $30 - 50\%$ smaller in the case of gasoline than for alcohol.

Comparing, for example, regime No. 7 from Table 2.8 (gasoline) with regime No. 2 from Table 2.9 (alcohol), we see that they have closely similar initial conditions. The difference between the intervals is obtained at $(114 - 56)/114 \approx 40\%$, since alcohol is comparatively difficult to vaporize, with a latent heat approximately 2-1/2 times that of gasoline. However, the experiment shows that the difference
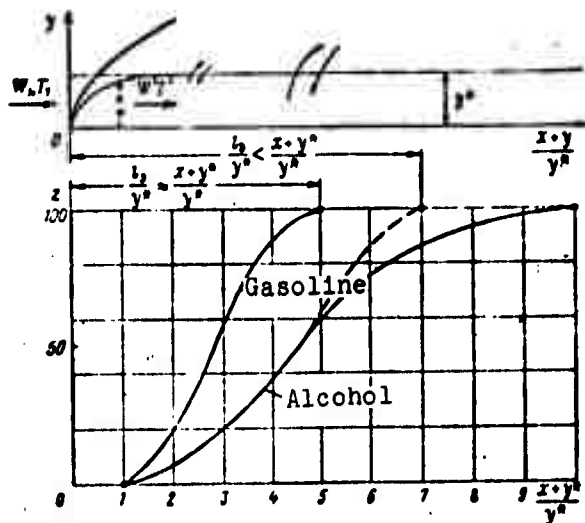
Figure 2.38. Vaporizability along spray cone:

—— calculated; --- real process.

between the true vaporization intervals of the two liquids is significantly smaller [(80 - 63)/ 80 ≈ 20% for the same regimes]. This can be explained by the peculiarities of the computing technique that were mentioned in this section. On a short cone of relative lengths $l_e/y^* < 3 — 5$, the real process follows the idealized process closely, since mixing has not yet made itself felt. For easily vaporized liquids such as gasoline, the calculation agrees with theory [sic]. But if the idealized process is not completed at these relative lengths, the intensifying effects of mixing, which we discussed in this section, come into play. Their influence is strong enough to vaporize the rest of the liquid alcohol on an additional short segment.

Thus, the mixing processes have a tendency to level the vaporizabilities of liquids with different physical constants. It can be assumed, from the data given in the table for gasoline, that the mixing factors are superimposed on the idealized process beginning at $(x + y^*)/y^* \geq 4 — 5$.

All of the above is illustrated by Figure 2.38, which shows the calculated vaporizability curves for gasoline and alcohol in a comparison with the experimental intervals of l_e/y^* for the regimes cited.

While the gasoline has been almost completely vaporized under conditions close to those of the isolated flow, only 60% of the alcohol has evaporated by this time. The remaining 40% (see the conditional dashed line) is vaporized in accelerated fashion (as compared with the theory) under the influence of mixing effects. The theory should

169

determine the interval x_v more correctly, the smaller the ratio

$(x_v + y^*)/y^*$, i.e., the longer the range y^* and the shorter the

vaporization interval. We note that the calculation of the vaporiza-

tion interval in which the free stream parameters ($W' = W_1$ and $T' = T_1$)

were taken as the initial data yields x_v, 2 — 5 times the experimental

values at the same drop size. Considering the complexity and the

limited extent of our knowledge of phase transitions in supersonic

streams, it should be acknowledged that the approximate theory proposed

here correctly describes the phenomenon in its general features and

agrees satisfactorily with experiment. It yields the upper limit of

the total-vaporization interval x_v for liquids of the type of benzene

and alcohol in the range of parameter variation considered.

§7. Mathematical Design of Injection
System and Calculation of Mixing
Parameters in an Ideal Chamber

Using a simple example, let us illustrate certain applications

of the theory of the spray cone in supersonic flow. They concern

calculation of the mixing segment of an idealized chamber with super-

sonic flow, the parameters of the injection system, the length of the

fuel-vaporization segment x_v, and the total head loss. As we noted

in §5, the total head loss is a conventional quantity; the calculation

is concerned with the "cold" losses involved in the injection process

itself (formation of the shock wave in front of the cone and motion

of the two-phase flow in the zone behind the wave).

To study all phenomena in the chamber, of course, it is necessary

to add the losses to friction (against the wall) and those due to

mixing and combustion.* Combustion develops after the mixing zone in

a whole series of cases (the problem of calculations for the entire

chamber is not posed in this chapter, although the material presented

is needed in solving it). The injection system will be characterized

*The overall total head losses are needed in calculations of
engine thrust (chamber and nozzle).

by the delivery pressure Δp and the diameter d_n and number n of atomizer orifices. The fundamental computing procedure is retained in the case of a real chamber with an annular or any other cross section. The formulas may be modified to take account of the particular shape and arrangement of the atomizers and other design features.

By "ideal chamber," we shall mean a cylindrical chamber without losses to friction of the gas against the wall, without consideration of the losses in flow around the atomizers themselves, and without interaction between inidividual spray cones. In real flows in chambers and at excess-air ratios $\alpha_T \geq 0.8 - 1$, the individual fuel cones do not overlap and their boundaries lie at a certain distance from one another, on the order of several lengths y^*. In particular, the effects from intersection of the shock waves of individual cones are left out of account; it is assumed that they damp out comparatively quickly and merge with the characteristics beyond the initial segment. The fuel sources are uniformly distributed on the cross-sectional area F_c of the chamber, and each of them controls its own zone of area f_T.

The problem is stated as follows: given the parameters of the gas at the entrance to the chamber M_1; T_1; and p_1 (or T_{01} and p_{01}), the specific gravity γ_T of the fuel; the excess-air ratio α_T; and the chamber diameter D_c. Find x_v; d_n; n; Δp; $\sigma_c = (p_0/p_{01})_c$. First we write the simple relations linking d_n; n; Δp. In partitioning the chamber into zones in accordance with the number of sources, it is convenient to introduce the partitioning coefficient k_T, which equals the ratio of the chamber area F_c to the total cross-sectional area of the spray cones. Characterizing the cross-sectional area of the cone by the limiting value F^*, we obtain

$$nf_{\tau} = nk_{\tau}F^* = F_{c}. \qquad (2.103)$$

The quantity $\sqrt{k_1} = D_c/\sqrt{nY^*2z^*} = D_c/d_c\sqrt{n}$ gives a measure of the linear expansion of all fuel cones to fill the chamber cross section. It indicates approximately (with "close-packing" accuracy) the factor by which the average cone diameter d_c in cross section F^* must be increased for the boundaries of neighboring cones to touch.[*] At $k_T \geq 1$, the liquid cones do not overlap anywhere. Substituting the expression $F^* = F(d_n; \Delta p/p_1; M_1; k_1)$ into (2.103), we obtain

$$n d^2 \Delta p^{\frac{3}{4}} k_1 = \frac{2^{\frac{1}{4}}}{4.3 \cdot 10} (k_1 p_1)^{\frac{3}{4}} M^{\frac{9}{16}} \frac{D_c^2}{4}. \tag{2.104}$$

From the condition for maintenance of the assigned excess-air ratio

$$a_T = \frac{G_a}{G_T L_T}$$

(L_T is the stoichiometric ratio for the particular fuel and G_a and G_T are the air and fuel flow rates) and the formula for the flow rate of liquid fuel through a single atomizer, G_{T1},

$$G_T = G_T n = \mu_p \frac{n \pi d_c^2}{4} \sqrt{2 \Delta p \gamma_T},$$

where μ_a is the discharge coefficient of the straight-jet atomizer, we obtain

$$n d_c^2 \Delta p^{\frac{1}{2}} = \frac{4 G_a}{\pi a_T L_T \mu_p \sqrt{2 \gamma_T}}. \tag{2.105}$$

The air flow rate through the chamber can be written

$$G_a = \frac{\pi D_c^2}{4} \frac{p_1}{\sqrt{R_1 T_1}} M_1 \sqrt{k_1}.$$

Solving Equations (2.104) and (2.105) for n and Δp, we obtain dimensionless relationships for determination of the parameters of

---

[*]The conditions that insure, to a certain degree, good large-scale mixing of the liquid fuel with air.

172

the fuel delivery system:

$$k_r = \frac{a_r L_r \mu_p \sqrt{\sqrt{\frac{RT_1 \tau_1}{p_1}} k_1^{\frac{1}{4}}}}{2^{\frac{5}{4}} \cdot .43 \cdot M_1^{\frac{1}{16}} \left(\frac{\Delta p}{p_1}\right)^{\frac{1}{4}}};$$

(2.106)

$$n = \frac{M_1 \sqrt{k_1}}{\sqrt{2} a_r L_r \mu_p \sqrt{\frac{RT_1 \tau_1}{p_1}}} \cdot \frac{1}{\left(\frac{\Delta p}{p_1}\right)^{\frac{1}{2}} \left(\frac{d_c}{D_u}\right)^2}.$$

(2.107)

In performing an actual calculation, it is necessary to assign two quantities, e.g., Δp and d_n (or d_n and k_T), after which the other two parameters are easily determined. To prevent fouling, the diameter of the atomizer nozzle orifice must not be too small, nor must it be too large from the standpoint of improving spray coarseness and lengthening the total-vaporization interval. It is recommended that the diameter d_n be in the range $0.4 — 0.5 \le d_n \le 2.5 — 3$ mm.

Other conditions the same, the factor k_T is uniquely determined by the fuel delivery pressure. The larger k_T, the greater, for the chosen d_n (and other conditions the same), will be the number of sources n and the better the conditions for subsequent mixing of the vapor with air. Knowing d_n and Δp, we determine the total-vaporization interval in the cones in accordance with the theory set forth above.

We turn now to determination of the total-head recovery factor in the ideal chamber. Following the derivation of the relation for the single cone in §5, we obtain, in perfectly similar fashion, a formula for the coefficient on the initial mixing segment of the chamber (Figure 2.39). The flow is partitioned into 3 zones with areas nF_1 for stream I, $n(F_M - F_1)$ for stream II, and $F_c - F_M n$ for the remaining stream III in the chamber:

173
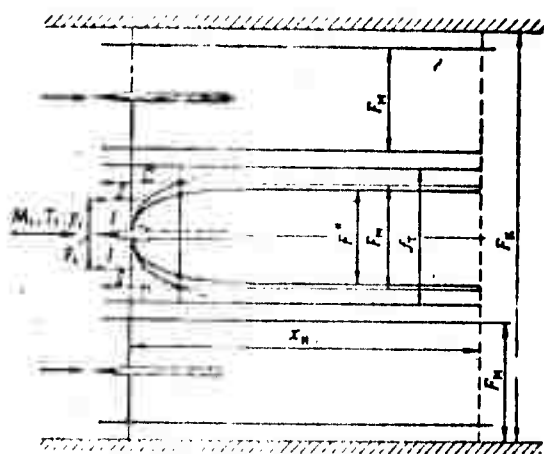
Figure 2.39. Illustrating calculation of ideal chamber.

$$\sigma_{\text{к.м}} \equiv \left(\frac{p_0}{p_{01}}\right)_{\text{к.м}} \doteq \qquad (2.108)$$

$$\left(\frac{\dot{p_0}}{p_{01}}\right)^{n\left(\frac{F_1}{F_{\text{к}}}\right)}\left(\frac{\dot{p_0}}{p_{01}}\right)^{\left(\frac{F_{\text{м}}-F_1}{F_{\text{к}}}\right)}\left(\frac{\ddot{p_0}}{p_{01}}\right)^{1-\frac{F_{\text{м}}}{F_{\text{к}}}}.$$

The quantity p'''_0/p_{01} corresponds to the zone of stream III, where the shock wave is near the characteristic. Hence the total pressure p'''_0 can be estimated roughly as the mean between p''_0 and p_{01}; $p'''_0 \approx (p''_0 + p'_{01})/2$ (usually $p''_0 \a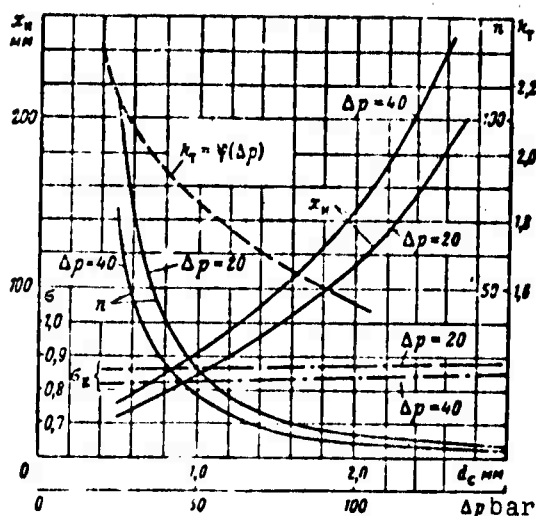pprox 0.93 - 0.99$). Even better accuracy can be obtained in calculating p'''_0 by using the equation for the shock wave boundaries. The area ratios in the exponents are conveniently determined from the relations

$$\frac{F_1}{F_{\text{к}}} = \frac{\frac{F_1}{F^{\bullet}}}{\frac{F_{\text{к}}}{F^{\bullet}}} = \frac{\frac{F_1}{F^{\bullet}}\cdot\frac{F'}{F^{\bullet}}}{\frac{F_{\text{к}}}{F^{\bullet}}}; \quad \frac{F_{\text{м}}}{F_{\text{к}}} = \frac{\frac{F_{\text{м}}}{F^{\bullet}}}{\frac{F_{\text{к}}}{F^{\bullet}}}.$$

The quantities F'/F^*; F_M/F^*; and F_c/F^* are calculated from the initial data for a fixed value of x/y^*, and F_1/F^*; F_1/F' are obtained after solution of the parameter problem for the initial cone segment.

The total-head ratio σ_c is calculated from formula (2.108) for $x/y^* = 1$. As a specific example, let us consider an ideal chamber in which gasoline is delivered into a stream of air (the only appreciable difference in the case of alcohol or kerosene would be in the calculation of x_v; the remaining parameters would remain almost the same as in the case of gasoline). We take the following initial data for the chamber: $M_1 = 3$; $p_1 = 1.2$ bar; $T_1 = 1200^\circ$ K; $\alpha_T = 1$; $D_c = 150$ mm (this corresponds to flight at $M_T = 8$ at a height $H = 30$ km). We assign the delivery pressure gradient $\Delta p = 40$ bar; $\mu_a = 0.7$ and find $k_T = 1.95$ from (2.106); each atomizer services an area of about twice the cross-sectional area F^* of the spray cone.

174

Figure 2.40. Total-vaporization interval x_v, number of atomizers n, and coefficients k_T and σ_c in ideal chamber:

—— n; --- k_T; -·-·- σ_c.

Putting the nozzle-orifice diameter at $d_n = 1$ mm, we obtain the number of fuel orifices from (2.107) at n = 18.5 ≈ 18. Using formula (2.108), where

$$\frac{p_0^{'}}{p_{01}} = 0.037; \quad \frac{p_0^{''}}{p_{01}} = 0.945; \quad \frac{p_0^{'''}}{p_{01}} = 0.975;$$

$$\frac{F_1}{F_{\kappa}} = 5.5 \cdot 10^{-3}; \quad \frac{F_{\mu}}{F_{\kappa}} = 26 \cdot 10^{-3},$$

we calculate $\sigma_c = (p_{01}/p_{01})_c = 0.77$.

We present the corresponding results for various values of $0.5 \leq d_n \leq 3$ and $\Delta p = 40$ and 20 bar.

Figure 2.40 presents curves of k_T against Δp, and curves of the number of atomizers n, the total vaporization interval x_v, and the ratio σ_c against d_n for the two delivery-pressure values. For the most part, the substantial increase in the parameter x_v is due to an increase in spray coarseness with increasing diameter d_n.

For the assigned flow regime in the chamber and a fixed $x/y^* = 1$ (with $d_n = 1$ mm and $\Delta p = 40$ and 20 bar; x' = y^* = 16 and 11 mm) the value of σ_c depends comparatively weakly on d_n and increases with decreasing Δp, i.e., with increasing coefficient k_T (spacing between atomizers).

On the whole, the calculation shows that fuel can be vaporized on intervals of the chamber that are quite acceptable from the design standpoint. The diameters d_n and gradients Δp are within the usual range for jet-engine injection systems. The total-head losses at fuel injection are found to be comparatively small.

175

Thus, there are no particular technical obstacles to delivery of fuel into supersonic chambers or its vaporization.

REFERENCES

1. Раушенбах Б. В., Белый С. А., Беспалов И. В., Бородачев В. Я., Волынский М. С., Прудников А. Г. Физические основы рабочего процесса в камерах сгорания воздушно-реактивных двигателей. М., «Машиностроение», 1964.
2. Баррер, Жомотт, Вебек, Вандеркеркхове. Ракетные двигатели. М., Оборонгиз, 1962.
3. C. J. Grun, F. Mac Gullough. Liquid Injection Thrust Vector AJAA, Jornal 1963, vol. 1, No 3.
4. Основы газовой динамики под редакцией Эммонс. М., ИЛ, 1963.
5. Волынский М. С. Исследование распыливания жидкости в сверхзвуковом потоке. Третье всесоюзное совещание по теории горения. М., Изд. АН СССР, 1960, том II.
6. Олевский В. А. Сборник научно-исследовательских работ научно-исследовательского и проектного института механической обработки полезных ископаемых, 1953, № 8, стр. 7—43.
7. Дубовкин Н. Д. Справочник по углеводородным топливам и их продуктам сгорания. М., Госэнергоиздат, 1962.
8. Reid R. The Propertis of Gases and Liquids their estimation and correlation, Mecrow Hill Book Company, 1958.
9. Зулис Л. А. Термодинамика газовых потоков. М., Энергоиздат, 1950.
10. Абрамович Г. Н. Прикладная газовая динамика. ГТТИ, 1953.
11. Седов Л. И. Методы подобия и размерностей в механике. М., «Наука», 1968.
12. Гухман А. Л. Введение в теорию подобия. М., «Высшая школа», 1963.
13. Бородин В. А., Дитякин Ю. Ф., Клячко Л. А., Ягодкин В. И. Распыливание жидкостей. М., «Машиностроение», 1967.
14. Jesiki N. Teoretical and experimental Study of Atomization of Liquid Drop in high Speed gas Stream Kep Transp. Techn. Research Just, 1959, p. 35.
15. Волынский М. С. Распыливание жидкости в сверхзвуковом потоке. Изв. АН СССР. «Механика и машиностроение», 1963, № 2.
16. Вишневецкий С. Л. О некоторых свойствах систем плоских косых скачков уплотнения. Изв. АН СССР, «Механика и машиностроение», 1960, № 6.
17. Седов Л. И. Методы подобия и размерности в механике. Изд. 6. М. «Наука», 1967.
18. Скляр Ф. И. О структуре струи при поперечном впрыске в сверхзвуковой поток. Изв. АН СССР, МЖГ, 1967, № 1.
19. Щетинков Е. С. Физика горения газов. М., «Наука», 1965.

Part 2

Turbulent Mixing and Combustion Processes in Jet Flows

CHAPTER I

MIXING IN TURBULENT FLOWS

There are two extreme trends, practically unrelated to one another,
in the development of the theory and calculation methods of turbulent-
mixing problems. The first is the traditional semiempirical theory
of turbulence, a trend based on the elementary physical models and
mathematical hypotheses of Boussinesq, Prandtl, Taylor, Reichardt,
and others, with which it is simplest to close the gasdynamic equa-
tions averaged over turbulent fluctuations, which are known as the
Reynolds equations. A detailed survey of these papers is given in
the monographs [1], [2], and [3].

The second trend, statistical fluid dynamics, was shaped for the
most part in the pre-war and post-war years on the basis of the fun-
damental theoretical studies of Karman, Taylor, Kolmogorov, and others.
Among the works on statistical fluid dynamics, we cite for reference
several books that are well known to a wide circle of readers special-
ized in turbulent fluid dynamics: those of Batchelor [19], Townsend
[20], Hintze [21], and A. S. Monin and A. M. Yaglom [22].

Among the problems of statistical gasdynamics, those of the internal gasdynamics of the jet engine are distinguished by three characteristic properties: The nonlocal nature of the scale and velocity parameters of the turbulence, the need to take account of the inhomogeneity of turbulent mixing (with consideration of the convective and gradient mixing components for problems with evolution of heat, etc.), and the substantial difference between and variation of the densities of the media being mixed ($\rho_1/\rho_2 \approx 4 - 15$).

The nonlocal nature of the turbulence is a general property of most jet problems. In the limit, nonlocality of turbulence means that the scale of the vortices that receive energy from the average streams is equal to the scale of the mixing layer of the streams, while the velocity scale of these vortices equals the difference between the average longitudinal velocities of these streams. This circumstance has been taken into account in the modern Prandtl hypothesis for determination of the eddy diffusivity.

At the same time, the nonlocal nature of turbulence casts doubt on the possibility of determining the correlation moments in the Reynolds equations in terms of any local stream parameters, or, in other words, on the possibility of approximating the turbulent exchange with differential equations. For this reason, averaged integral relations and physical models that take account of the nonlocal property of turbulent exchange have been used as a basis for analytical description of jet currents. The general solutions developed on the basis of these models subsequently made it possible to determine the general form of the correlation moments in a number of cases from the appropriate averaged differential equations of gasdynamics.

Mixing inhomogeneity is also inherent to most jet problems, since it is a consequence of the nonlocality and cascade decay of vortices. The inhomogeneity of mixing is found to be strongest in large vortices, where molecular exchange is negligible, and weakest in small vortices. However, it is not always necessary to take mixing inhomogeneity into consideration: it manifests itself strongly

178

only in problems of mixing of gases or liquids with a large density difference and in cases in which the gases react chemically or the radiation from the jets being mixed is to be calculated, i.e., wherever the fluctuations of density, composition, or temperature are of importance in addition to their average values. The physical models proposed in this book also take account of the property of the turbulent exchange.

Large density (temperature) differences and nonlocality and inhomogeneity of mixing result in the appearance of strong density and temperature fluctuations that must be taken into account, not only in the correlation moments of the Reynolds equations, but also in the time-averaged equation of state at an arbitrary point in the flow. It is not possible at the present time to determine these moments without additional constants, either with the equations of the semi-empirical theory or with the existing equations of the more rigorous statistical theory.

However, these difficulties are surmounted in analysis of physical models describing the phenomenon of turbulent exchange on the whole over the mixing layer. The present chapter considers two elementary models: the vortex model and the more formal diffusion model. The vortex model gives a physically more lucid picture of the phenomenon, the nature of the mixing inhomogeneity, the disagreement of the velocity and temperature profiles in a free or confined layer, etc. But there are more difficulties in the way of development of its mathematical apparatus, so that it promises fewer conveniences for the development of a practical method for solution of the various problems.

The diffusion model operates with the "usual" statistical characteristics: the dispersion and mean value of a liquid volume. It enables us to apply the familiar equations of statistical diffusion theory (the Fokker-Planck-Kolmogorov equations, §2, subsection 1, Chapter I), extending them only to the case of turbulent flows with transverse shear. In other words, the proposed approach uses a mathematical formalism that is, for the most part, borrowed from the

known results of the statistical theory of turbulent diffusion. No attempt is made here to fill the logical gaps in the reasoning behind the use of the Fokker-Planck-Kolmogorov equation for a process with an aftereffect and a single dispersion parameter for the mixing layer, or to justify its validity for the case of various sample-averaged velocities of portions of the media being mixed, in consideration, on the one hand, of the aforementioned inaccuracy of approximation of the conservation laws by differential equations in general and especially for the velocity and entropy fields and, on the other hand, taking consistent account of the integral relations which smooth out all of the possible inaccuracies of any specific solution in the overall balance of mass, energy, and momentum. An attempt was made in §2, subsection 2, Chapter I to defend the "legitimacy" of the differential equation of diffusion for microturbulent (gradient) exchange.

The basic definitions are introduced on the basis of the models, and a mathematical formalism is developed for the so-called diffusion model, which can be used to calculate the turbulent mixing of streams with different velocities, densities, and temperatures.

§1. Models of Turbulent Mixing

1. Vortex Model of Development of Turbulent Mixing Layer. Physical Concepts and Definitions

Let us consider certain characteristic features in the development of flows with transverse shear of longitudinal velocities, using a plane-parallel turbulent mixing layer as an example. This analysis will enable us to clarify the physical significance of the parameters to be introduced below. Figure 1.1a shows the elementary scheme of the vortex model of the turbulent layer.

As we know, the interface between two streams of gas moving at different velocities is unstable [26]. Any random small disturbance builds up exponentially. The rate of buildup depends on the wavelengths of the disturbance and has a maximum for a definite wavelength [27], [28]. The distribution of the disturbance increment λ_x as a
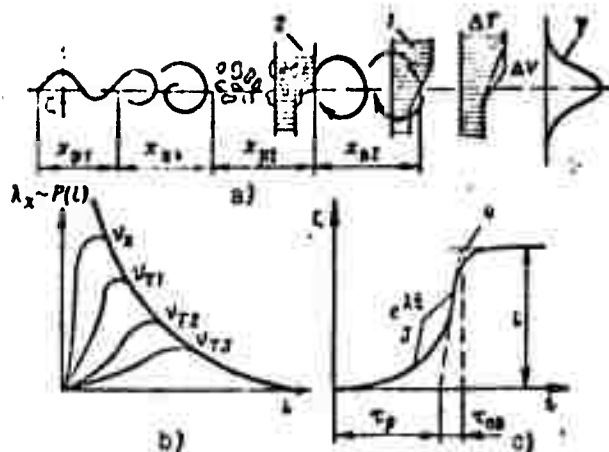
Figure 1.1. Vortex model (free mixing layer).

a — diagram of vortex model of turbulent layer; b — qualitative
time variation of ξ; c — distribution of disturbance increment λ_x
for various viscosity values; 1 — velocity profile in large
vortex; 2 — velocity profile in decay wake; 3 — increase in ampli-
tude of surface of discontinuity; 4 — model approximation.

function of wavelength is shown in Figure 1.1c for various viscosities,
including $\nu = 0$. The envelope of all of these curves is a hyperbola:

$$\lambda_z = \frac{\sqrt{\varrho_1 \varrho_2}\,(u_2 - u_1)\,\pi}{(u_1 \varrho_1 + \varrho_2 u_2)\,2 l_\bullet},\tag{1.1}$$

which corresponds to an infinitesimally thin tangential-discontinuity
surface with $\nu = 0$ ($u_1 \varrho_1$; $u_2 \varrho_2$ are the velocity and density of the
first and second streams, respectively; l_v is the radius of the vortex,
which is approximately equal to half the wavelength of the disturbance).

Experiment [23] has shown that the wave amplitude of a shear-
discontinuity disturbance increases to values on the order of the
radius of the vortex $\zeta(t) = l_v$, after which the wave curls into the
vortex. The manner in which ζ varies in time is shown in Figure 1.1b,
which also shows the simplest approximation for it (without considera-
tion of Landau's "nonlinearity" [26]). Two characteristic scales can
be seen on the $\zeta = f(t)$ curve (Figure 1.1b): the lifetime τ_d of the
discontinuity and the time for formation of the vortex $\tau_{v.f}$ which

181

satisfy the following relations:

$$\tau_p \simeq \frac{1}{\lambda_\tau} \ln\left(\frac{l_0}{\zeta_0}\right) \quad \text{and} \quad \tau_{0.0} \simeq \frac{1}{\lambda_\tau},$$ (1.2)

where λ_τ is the time increment of the determined wave in a coordinate system bound to the wave, and ζ_0 is the amplitude of the initial interface surface disturbances.

The transition to the corresponding length scales in the nonmoving coordinate system is accomplished with the relations

$$x_p = v_\phi \tau_p; \quad x_{0.0} = v_\phi \tau_{0.0} \quad \text{and} \quad v_\phi \lambda_x = \lambda_\tau$$

(v_p is the phase velocity of a disturbance wave of the "drift" type).

Like the scale l_v, the quantities ζ_0 are random functions, so that the scale τ_v is also a random function. We obtain its average value by substituting the expression for ζ_0 in terms of the velocity fluctuation from [26] on the initial segment $(u_2 - u_1)\frac{\partial \zeta_0}{\partial x} = (v_2 - v_1)$ and averaging:

$$\bar{x}_p = \frac{1}{\lambda_x} \ln\left(2\sqrt{1 + \frac{(\Delta u)^2}{\varepsilon_1^2 u_1^2 + \varepsilon_2^2 u_2^2}}\right),$$ (1.3)

where λ_x is the increment for a disturbance wave of the "drift" type and $\Delta u = u_2 - u_1$ is the difference between the average longitudinal velocities.

The experiments of [23] indicate that the maximum "noise" level does not, under ordinary conditions, exceed $\varepsilon_1 \simeq \varepsilon_2 \simeq \varepsilon_{max} = 0.25$, so that

$$\frac{\bar{x}_p}{x_{0.0}} \approx 3,$$ (1.4)

i.e., is nearly constant and considerably larger than unity. A similar condition, but with absolute independence of the initial conditions, can also be obtained with consideration of the "nonlinearity" of the surface-disturbance buildup during the last phase (according to Landau [26]).
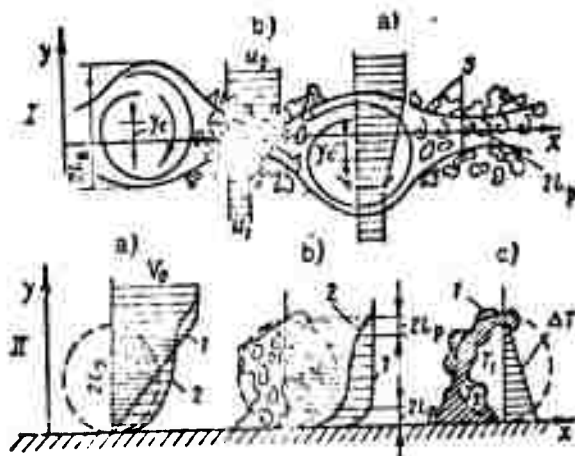
Figure 1.2. Velocity diagrams in free mixing layer (I) and in wall layer (II).

a — velocity profile in large vortex; 1 — without slip; 2 — with slip; 3 — boundary streamlines; b — velocity profile in decay wake; 1 — with restructuring; 2 — without restructuring; c — temperature profile in large vortex and decay wake; 1 — line of contact discontinuity.

In virtue of condition (1.4), the vortex forms "almost" instantaneously, which is equivalent to an inelastic collision of two liquid parcels, one "above" the disturbance wave and one "below" it. The laws of conservation of angular momentum and the position of the center of mass for the vortex before and after the "collision" yield the following values for the angular velocity ω of the vortex, the velocity v_v of its center of mass, and the ordinate y_c of the center of mass:

— for a free boundary layer (center of disturbance wave on the x axis of Figure 1.2, I)

$$\omega = \frac{\varrho_1 \varrho_2 l_\theta \Delta u}{\varrho_{cp}^2 4 l_i^2} ; \qquad \text{(a)}$$

$$v_\theta = \frac{\varrho_1 u_1 + \varrho_2 u_2}{\varrho_1 + \varrho_2} ; \qquad \text{(b)} \qquad\qquad (1.5)$$

$$y_c = \left(\frac{\varrho_1 - \varrho_2}{\varrho_1 + \varrho_2}\right) \frac{l_\theta}{2} , \qquad \text{(c)}$$

where $\varrho_{av} = (\varrho_1 + \varrho_2)/2$, l_1 is the radius of inertia of the vortex, and

$$\Delta u = u_2 - u_1.$$

— for a wall layer (vortex center at a distance l_v from the wall):

$$w_* = \frac{l_2}{l_1}\frac{\sigma_*}{2l_1} \qquad \text{(a)}$$

$$v_* = \frac{\varrho_1 u_1}{\varrho_1 + \left(\dfrac{l_2}{2l_* - l_2}\right)\varrho_2} \qquad \text{(b)} \qquad\qquad (1.6)$$

$$y_c = l_{*}. \qquad \text{(c)}$$

where ϱ_1 and u_1 are the density and velocity far from the wall, ϱ_2 is the density at the wall, and l_2 is the momentum-loss thickness in the boundary layer prior to the formation of the large vortex.

We see from (1.5) and (1.6) that the large vortex moves practically without "collision" in the free layer (the longitudinal-velocity profile has the form of Figure 1.2a), while in the boundary layer, since $l_1 \sim l_v \gg l_2$, the vortex moves with slip, forming a laminar underlayer below it and a laminar overlayer above it.

In the vortex, the interface is twisted into a "surface of contact discontinuity" (Figure 1.1c). The vortex that has formed is separated, as a single liquid parcel (mole) from the rest of the stream by a surface of tangential discontinuity, which, in turn, is unstable, since there are also two characteristic scales for the vortex: the lifetime τ_v of the vortex and its decay time $\tau_{v.d}$ and, accordingly, the scales $x_v = v_v\tau_v$; $x_{v.d} = v_v\tau_{v.d}$ (v_v is the velocity of the motion of the center of mass of the vortex).

We shall use the term "decay wake" for the volume of a decayed large vortex when it is occupied by small-scale turbulence. Turbulence in decay wakes is nearly homogeneous and isotropic [20]. On transitional segments from laminar to turbulent flow, decay wakes do not pack the entire space, and they are recorded by sensors in the form of "turbulence spots."

The problem of cascade decay of a large vortex into a series of small vortices with a trend toward homogeneous and isotropic distribution is in many respects identical to the problem of turbulence behind a grid. Hence the corresponding values of such parameters as

$\sqrt{\overline{(v_d')^2}}$, the rms fluctuation velocity in the decay wake after a time
t has elapsed since the decay of a large vortex, and $v_{MT} \simeq D_{MT}$, the
microturbulent viscosity (eddy diffusivity) in the decay wake, can
be taken for the time being from the corresponding experiments for
turbulence behind grids [19], [14]:

$$\overline{v_p'^2}/(\Delta u)^2 = f\left(\frac{\overline{v_p'}}{l_a}\right); \quad \frac{\Delta u l_a}{D_T} = \frac{\Delta u l_a}{v_{MT}} \approx Re_{l_a} \qquad (1.7)$$

where $\bar{v}_d$ is the average velocity of the motion of the decay wake and
$\Delta u = u_2 - u_1$ is, as before, the difference between the initial average
velocities of the two streams.

On decay of the large vortex, the average-concentration (tempera-
ture) profile in the decay wake is not restructured, but continues to
broaden in time under the influence of microturbulent (gradient)
diffusion with the coefficient D_{MT}. While the longitudinal-velocity
profile is not necessarily restructured on decay of the large vortex
(for example, for a wall layer), it can, in principle, be restructured
in such a way that, in accordance with the laws of conservation of
momentum and angular momentum, the upper part of the volume of the
decayed large vortex again begins to move at the velocity of the upper
stream ($V_{d1} \approx v_2$), while the lower part goes into motion at the velo-
city of the lower stream ($V_{d2} \approx v_1$), i.e., after the decay of a large
vortex, the longitudinal-velocity field can, in principle, return to
its original state in full consistency with conservation of momentum
and angular momentum, provided that the isotropic and homogeneous
distribution of the small vortices yields a zero resultant momentum
about the center of mass about the decay wake.

If it is assumed that the original average-velocity interface is
restored in the decay wake for a free boundary layer, a new large
vortex will be formed as a result of the instability of this discontin-
uity of finite thickness δ_d. The following trend is observed with
increasing distance x from the beginning of the layer: the most
probable size of the forming large vortex is found to be proportional
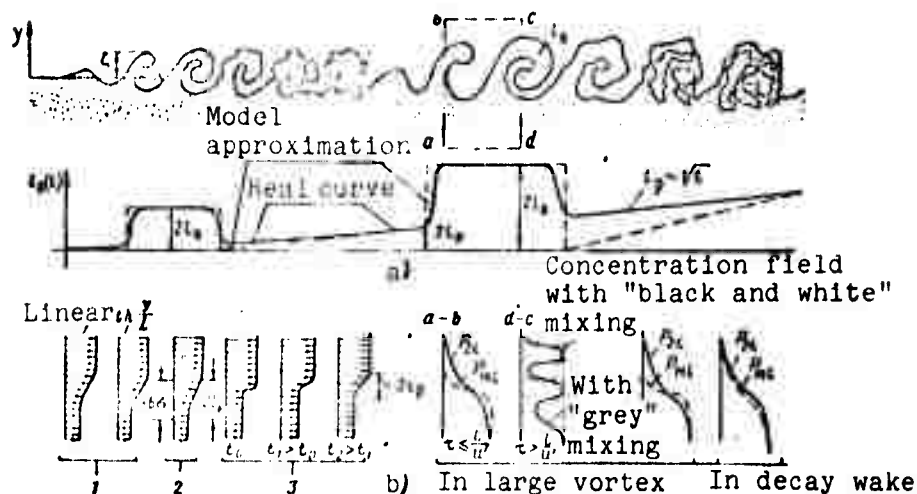
Figure 1.3. Vortex model of "black and white" mixing at large Re (a)
and the velocity and concentration fields (b).
$l_n(t)$ are the scales of instantaneous vortices in the model mixing
layer; P_{2l} is the volume-concentration distribution; P_{Ml} is the
mathematical expectation of intermediate compositions.

(in virtue of the results of linear instability theory) to the instan-
taneous boundary-layer thickness δ_d, which increases from discontinuity
to discontinuity owing to the increase in microscopic eddy viscosity
ν_{MT} in the decay wake and the increased discontinuity lifetime τ_d, so
that the size l_v of the vortex increases with increasing x (Figure
1.3). It is also necessary to remember the essentially statistical
nature of the phenomenon and, in particular, the dispersion of both
the scales l_v and the scales x_v, x_d, and y_c. Because of the sub-
stantial dispersions of the l_v, x_v, x_d, and y_c distributions, the
places of the decay wakes on the figure may be occupied by vortices
and vice versa.

The behavior of the various parameters of the turbulent mixing
layer can be evaluated quantitatively with the aid of the following
considerations.

The probability of appearance of an instantaneous value of velocity, temperature, pressure, etc., at an arbitrary point of the turbulent mixing layer and, in particular, the average-value profiles of these parameters are determined on the one hand by the instantaneous distributions of the particular parameter in the vortex and in the decay wake [relations of the type of (1.5) and (1.6)], and, on the other hand, by the form of the function $p(l)$ — the probability density distribution of the vortex scales l — and by the probability P_v of appearance of a large vortex in an arbitrary cross section x or the probability P_d of the appearance of a decay wake. The functions $P_v(x, Re_\Delta)$ and $F_d(x, Re_\Delta)$ are quite complex for small values of x and Re_Δ. However, with increasing x and Δu, when $Re_\Delta = \Delta u l/\nu$ becomes quite large and the probability that "laminar spots" will appear becomes quite small, these functions assume the form

$$P_{\bullet} = \frac{\bar{\tau}_{\mathbf{o}\,l}}{\bar{\tau}_{p\,l} + \bar{\tau}_{\mathbf{o}\,l}} \quad \text{and} \quad P_p = \frac{\bar{\tau}_{p\,l}}{\bar{\tau}_{p\,l} + \bar{\tau}_{\mathbf{o}\,l}} \tag{1.8}$$

or

$$P_{\mathbf{o}} = \frac{\bar{x}_{\mathbf{o}}}{\bar{x}_{\mathbf{o}} + \bar{x}_{p}} \quad \text{and} \quad P_p = \frac{\bar{x}_{p}}{\bar{x}_{p} + \bar{x}_{\mathbf{o}}},$$

where $\bar{\tau}_{v\,i}$; $\bar{\tau}_{d\,i}$ are the average lifetimes of the vortex and decay wake in the $i\underline{\text{th}}$ cross section of the layer and

$$\bar{x}_{\mathbf{o}} = V_{\mathbf{o}}\tau_{\mathbf{o}}; \;\; \bar{x}_{p} = V_{\mathbf{o}}\tau_{p}.$$

A number of indirect experimental observations and considerations that proceed from the linear theory permit the assumption that P_d and P_v are of the same order.

In fact, relations (1.1) and (1.2) yield a relation for the average lifetime of the discontinuity:

$$\tau_{pl} \sim \frac{1}{\lambda_{\tau_i}} \sim \frac{l_{\mathbf{o}}}{\Delta u} \sim \frac{l_1}{a_1}, \tag{1.9}$$

where l_1 and u_1 are the characteristic dimension and velocity of the first-order or first-cascade vortices.

In turn, the lifetime of the first-order vortices is determined basically by the time for second-order disturbances to build up to the scale l_2, since the formation of vortices of all subsequent orders has already occurred during the existence of the decay-wake average-velocity profile, i.e.,

$$\tau_1 \sim \frac{1}{\lambda_{l2}} \sim \frac{l_2}{u_2}.$$ (1.9a)

We note that in this definition of the time scales, the proportionality coefficient is the same in both relations. The question as to the size and velocity of the second-order vortices still remains open due to the lack of analogous linear equations for the vortices. However, if Prandtl's law operates in the particular process, we have

$$u_{i+1} \approx \frac{\partial u_i}{\partial r} l_{i+1} \text{ or } \omega_{i+1} \approx \frac{u_{i+1}}{l_{i+1}} \approx \omega_i \approx \omega_1 \approx \frac{\Delta u}{2 l_1},$$

(1.10)

$$\text{i.e., } \tau_i \approx \tau_{i+1} \approx \tau_1.$$

Here, r is the present radius of the vortex.

It is seen from (1.9) and (1.10) that the condition

$$P_1 \approx P_p = 0.5.$$ (1.11)

is satisfied with the same accuracy as that of Prandtl's law.

The function $p(l)$ has a shape resembling the Maxwellian distribution: it is either proportional to the increment function for the buildup of "drift-type" disturbances from wavelength L, i.e., $p(l_v) = \lambda_x(aL)$ (a is a form factor on the order of unity; preliminary estimates [28] give $a \approx 0.3 - 0.5$), or is a function of this increment that depends on the form of the initial disturbance spectrum. The features

of the $p(l)$ curve are such that the highest probability will occur at a scale l_m with an increment near the maximum value λ_{max}, the value of which decreases with increasing microturbulent viscosity ν_{MT} along the envelope corresponding to the increment of an infinitesimally thin tangential-discontinuity surface [see (1.1) and Figure 1.1c]. As a result, the average value of the scale $l \approx l_m$ for the free layer satisfies the relation

$$\frac{d\bar{l}}{dx} \approx \frac{l_{i-1} - l_i}{\bar{x}_{\text{в }i} + \bar{x}_{\nu i}} = \frac{\bar{l}_i}{\bar{x}_{\nu i}}\left(\frac{\text{Re}_\lambda}{\text{Re}_\tau} - 1\right)P_\text{в} \sim \frac{\Delta u \, \sqrt{n}}{2u_{cp}(n+1)}\left(\frac{\text{Re}_\lambda}{\text{Re}_\tau} - 1\right)P_\text{в}, \tag{1.12}$$

where $n = \rho_1/\rho_2$

$$u_{cp} = \frac{\rho_1 u_1 + \rho_2 u_2}{(\rho_1 + \rho_2)};$$

$$\frac{1}{\bar{x}_{\nu i}} \approx \frac{\lambda_{x i}}{3} \approx \frac{\sqrt{n}\Delta u \pi}{(n+1)u_{cp}\delta l_i}.$$

from Relation (1.1).

According to [19], the quantity $\dfrac{\Delta u l_i(x)}{\nu_{MT i}} \approx 250 \div 290$ for turbulence behind a grid (provided that $\nu_{MT} = D_{MT}$ and $l_i \approx M$ (M is the characteristic dimension of the grid mesh); $\text{Re}_\lambda = \dfrac{\bar{l}_{i-1}\Delta u}{\nu_{MT i}} \approx 380$ according to results of processing of the solutions in [28] for $n=1$, $\dfrac{u_1}{u_2}=0$ and the laminar thickness of the surface of discontinuity ($\nu_{MT i}=\nu$).

Substituting the values $n = 1$ and $u_1 = 0$ for a submerged isothermal semi-infinite jet, the value $P_d \approx P_v \approx 0.5$ and the values given above for Re_λ and Re_T into (1.12), we obtain a range of values for the average slope of the expansion of the jet:

$$\frac{d\bar{l}}{dx} \approx 0.06 - 0.09.$$

In view of the random nature of the value taken for Re_λ and Re_T and the approximate nature of the numerical-coefficient estimates in (1.12), this value should be recognized as in reasonable agreement with the direct experimental value ≈ 0.1 (see Chapter III).

In (1.12), the dependence on n is significant only for the first large vortices $(x \leq x_d)$; in subsequent formation of large vortices from decay wakes, n is near unity in virtue of the sufficient homogeneity of composition at the center of the wake $(\rho_1 \approx \rho_2 \approx \rho_{av})$.

The average velocity and temperature (concentration) profiles are determined by relations of the form

$$\bar{u} = P_s \bar{u}_s + P_p \bar{u}_p = P_s \int_0^\infty \bar{u}_{s,l} \frac{l}{\bar{l}} p(l)\,dl + P_p \int_0^\infty \bar{u}_{p,l} \frac{l_p}{\bar{l}_p} p(l)\,dl;$$

(1.13)

$$\bar{T} = \bar{T}_s P_s + \bar{T}_p P_p = P_s \int_0^\infty \bar{T}_{s,l} \frac{l}{\bar{l}} p(l)\,dl + P_p \int_0^\infty \bar{T}_{p,l} \frac{l_p}{\bar{l}_p} p(l)\,dl,$$

where (1)
$$p(l)\,dl = \lim_{N_o \to \infty} \frac{n(l)\,dl}{\int_0^\infty n(l)\,dl} \approx \frac{2}{\sqrt{2\pi}(\bar{l})^{3/2}} l^2 e^{-\frac{l^2}{2\bar{l}^2}}\,dl;$$

(2) $N_o = \int_0^\infty n(l)\,dl$ is the total number of vortices passing through the cross section x during an infinitely large time;

(3) $\bar{l} = \int_0^\infty l p(l)\,dl;$

(4) $\frac{l}{\bar{l}} = \frac{2l \cdot \tau_V}{2\bar{l} \cdot \tau_V}$ is the relative time for passage for a vortex of dimension $2l$ across cross section x, $\bar{u}_{vl}$ and $\bar{T}_{vl}$ are, respectively, the average longitudinal-velocity and temperature profiles at points $\bar{x}$ from large vortices of dimension $2l$; $\bar{u}_{dl}$; and $\bar{T}_{dl}$ are the corresponding velocities and temperatures in the decay wake.

The exact shape of the instantaneous $\bar{u}_{v\ell}$ and $\bar{u}_{d\ell}$ is immaterial because of the broad spectrum of scales ℓ and y_c. In the free layer, therefore, we can approximate them, for example, by a linear distribution of velocities from $\bar{u}_1$ to $\bar{u}_2$ over the respective width $\sim 2\ell_v$ and $\sim 2\ell_d$ or even take a constant value $(\bar{u}_2 + \bar{u}_1)/2$.

In the limit, since $\ell_d \ll \ell_v$, the profile $\bar{u}_{d\ell}$ can be replaced by a discontinuity at a random level $\sim y_d$. In the wall layer, the profiles $\bar{u}_{v\ell}$ and $\bar{u}_{d\ell}$ can be assigned in the form of three straight lines: a line in the vortex or decay wake with a slope that determines the angular velocity ω according to a relation of the type (1.6a) and lines in the laminar underlayer and overlayer, whose thicknesses are respectively $\delta_v \sim \sqrt{\nu \tau_v}$ and $\delta_d \sim \sqrt{\nu_{MT} \tau_d}$ where ν_{MT} is the microscopic eddy viscosity in the decay wake.

In the free mixing layer, the longitudinal average velocity profile is S-shaped across the layer, basically because of the function $p(\ell)$ for the large vortices. The inflection point of the S-curve lies in the region of the statistical average value of the large-vortex center coordinate $\bar{y}_c$ and the shear surfaces $\bar{y}_d$ of the decay wake. An illustration of the degree to which such curves agree with experimental data for free mixing layers will be given in Chapter II.

Figure 1.4 presents a profile calculated for the average longitudinal velocity at the wall for the case of maximum velocity restructuring during decay of the vortex and an experimental profile according to [29]. We see from Figure 1.4 that the calculated profile agrees with the experimental one with appropriate definition of the average scale $\bar{\ell}$ of the large vortices. At the very small dispersions of the scale ℓ_v that are usually observed at the beginning of the layer for the first large vortices, the main contribution to the main profile of the velocity $\bar{u}$ comes from the profile of $\bar{u}_{v\ell}$, which has, for a wall layer, a characteristic inflection point (see Figure 1.2a) that is clearly observed in experiments [29], [30]. With increasing
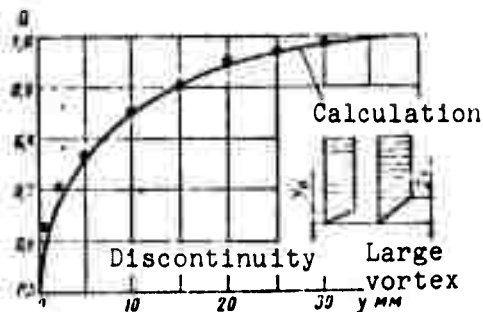
Figure 1.4. Turbulent boundary layer.

$$\bar{u} - \mu_p \left\{ \sqrt{\frac{\pi}{2}} \frac{y}{2 s_p} \left[1 - \Phi \left(\frac{y}{2 s_p} \right) \right] + 1 - e^{-\frac{y^2}{8 s_p^2}} \right\} +$$

$$+ (1 - \mu_p) \left\{ \sqrt{\frac{\pi}{2}} \frac{y}{2 s_e} \left[1 - \Phi \left(\frac{y}{2 s_e} \right) \right] + 1 - e^{-\frac{y^2}{8 s_e^2}} \right\}$$

Townsend experiment: $x = 76$; $u_0 = 1280$ cm/sec; $\sigma = 0.605$ mm; $\sigma_e = 6.3$ mm; $P(y_d)$ and $p(l)$ are Maxwellian functions; $P_d = 0.67$.

dispersion of the scale l_v, the transverse velocity-gradient profile gradually becomes monotonic.

In determining the average-temperature profiles in the vortex and decay wake, T_{vl} and T_{dl}, we distinguish certain characteristic features of the turbulent mixing that are passive with respect to the turbulence. A large vortex that has formed transports parcels of both media purely mechanically (Figure 1.2c). Following the terminology proposed by Townsend [20], we shall call this case of turbulent exchange <u>volume convection</u>. Here the profile of the average volume concentration in a unit vortex, or the probability of appearance of the second medium,

$$P_{2l} = \frac{\overline{T}_{vl} - T_1}{T_2 - T_1} ,$$

has the form shown in Figure 1.3. It is easily seen that its characteristic width l_T is determined, just as for the velocity profile in the vortex, by the scale l_v of the large vortex. At the same time, if the parcels are sorted on the basis of mass-average concentrations and the concentration profile of the sorted parcels is drawn, it is found that the intermediate concentrations are practically absent. The characteristic width l_M of this molecular concentration distribution profile is much smaller than l_v.

In the second stage, when the vortex decays, the characteristic width of the profile P_{2l} does not change. However, owing to the appearance of strong small-scale turbulence and vigorous <u>gradient</u>

diffusion [20], the temperature (concentration) fluctuations about
the average values in the decay wake quickly become vanishingly small.
As a result, the characteristic width l_M in the decay wakes becomes
practically identical to l_v (see Figure 1.3).

We note that after decay, the temperature fluctuations quickly
become homogeneous and isotropic throughout the volume of the decay
wake and decay in time, in accordance with laws similar to those for
velocity fluctuation.

We can introduce the concept of the "degree of mixing homogeneity"
N to describe the proportion of mixing to the state of molecular
homogeneity in the overall mixing, defining this parameter as follows:

$$N = \frac{\bar{l}_M}{\bar{l}_o} = \frac{\bar{l}_{MB}(1 - P_p) + \bar{l}_{Mp}P_p}{\bar{l}_o} . \tag{1.14}$$

If we imagine that the medium moving at velocity $\bar{u}_2$ is colored
black and that the medium at $\bar{u}_1$ is white before the formation of each
large vortex, volume convection by large vortices constitutes the
case of "black and white mixing," while gradient diffusion in the decay
wake constitutes a case that approaches "grey mixing" in the limit.   In
accordance with this definition of the two extreme turbulent-mixing
mechanisms, the parameter N will be called the "degree of greyness"
for brevity.

In relation (1.14), as before, P_d denotes the probability of
observation of decay wakes (the relative time of appearance of decay
wakes in the center of the mixing layer). We note that for the
mixing layer, this quantity is similar in physical content and absolute
value to the intermittency coefficient in the center of the layer,
which was first measured by Townsend [20], and Corrsin [31].

Actually, a large vortex gives a velocity profile that differs insignificantly from the average-velocity profile only because of a certain dispersion of the vortex dimensions, so that the passage of large vortices is recorded by the thermoanemometer as the practical absence of velocity fluctuations (absence of turbulence). On the other hand, owing to the microscopic dispersion of the dimensions and angular velocities of small vortices, and because of the possible dispersion of the location of the discontinuity on the instantaneous average-velocity profile, decay wakes are sensed as flows with large velocity fluctuation (turbulence present).

If the times of existence of the vortices and the discontinuity on the instantaneous average-velocity profile in the decay wakes are approximately the same, and we recall that $\bar{l}_{Mv} \ll \bar{l}_v$ and $\bar{l}_{Md} \approx l_v$, we obtain an estimate of the possible "degree of greyness" from (1.14):

$$N \approx 0{,}5. \tag{1.14a}$$

A relation can be established in similar fashion between the average width l_T of the average-temperature (average-concentration) profile and the characteristic widths of the average-velocity profile (l_v).

As we noted above, the velocity distribution is determined with sufficient accuracy from the assumption that the vortex rotates as a rigid body around a certain center, so that in this case

$$l_{v\,s} \simeq l_s.$$

In free-layer decay wakes, where the initial average-velocity discontinuity is restored,

$$l_{v\,p} = \bar{l}_p \ll l_s.$$

The average characteristic length of the longitudinal velocity profile is determined here by the relation

$$\bar{l}_v = l_{v_e} P_e \div l_{v_p} P_p \approx \bar{l}_e P_e + \bar{l}_p P_p$$

If we introduce the turbulent Prandtl number as the ratio $\dfrac{\overline{l_v^2}}{\overline{l_T^2}} = \dfrac{D_v}{D_T}$, where D_V and D_T are the effective, resultant values of the diffusion coefficients for velocity and property (for details concerning D_V and D_T, see the diffusion model of mixing in §1, subsection 2), we obtain:

$$\mathrm{Pr} = \frac{\overline{l_v^2}}{\overline{l_T^2}} \approx \frac{\overline{l_v^2}}{\overline{l_e^2}} = P_e + \left(\frac{l_p}{l_e}\right)^2 P_p$$

or, with $P_v = P_d \approx 0.5$ and $l_d \ll l_v$, an estimate of the possible value of the Prandtl number for this mixing model:

$$\mathrm{Pr} \approx 0.5. \bullet \tag{1.15}$$

For the wall layer, irrespective of whether the average-velocity profile in the large vortex is destroyed partially or totally in its decay, the velocity and temperature profiles will be similar ($\mathrm{Pr} = 1$) in the visible part of the layer with thickness $2(l_v - l_d)$, if they are constructed in the form

$$\frac{\bar{u} - u_p}{V_1 - u_p} \approx \frac{T_p - \bar{T}}{T_p - T_1}, \tag{1.16}$$

where u_d and T_d are the average velocity and temperature on the average upper boundary of the lower sublayer (see Figure 1.2b and c). The only difference is in determination of the average values of u_d and T_d. For example, if the restructuring is such that the original velocity V_1 is restored in the decay wake except for a layer of

---

*A detailed analysis of other physical models of mixing, including the well-known Taylor "vorticity transport" model, is given in the monograph of G. N. Abramovich [1].

thickness $\delta_d \sim l_d$ that sticks to the wall for the time τ_d and in which $V_2 \approx 0$ and $T_1 \approx T_2$, while the large vortices roll along the wall without slip, i.e., $T_d \sim T_1$ and $V_v = 0$ in the large vortices (see Figure 1.2b and c), we have

$$
\begin{aligned}
u_\rho &\approx V_1 P_\rho + 0 \cdot P_a \approx 0.5 \cdot V_1; \\
T_\rho &\approx T_2 P_\rho + T_1 P_a \approx \frac{T_2 + T_1}{2} .
\end{aligned}
\tag{1.17}
$$

However, such extreme restructuring is improbable, since it would require the assumption of angular-momentum and momentum exchange between the vortices and decay wakes, as well as the existence not only of transverse, but also of large longitudinal gradients of longitudinal velocity directly at the wall. Another model of velocity restructuring in which the longitudinal velocity profile remains practically unchanged is evidently more probable: the only change is that as the large vortex decays, the laminar underlayer formed due to its slip against the wall also disintegrates in accordance with the individual angular-momentum and momentum-conservation law of the wake, and the microturbulent underlayer of the decay wake begins to increase (Figure 1.2b).

The parameters u_d and T_d are determined in more complex fashion in this case, but their values will evidently be close to those determined by (1.17). Here the friction is determined as the statistical average value of the friction of a laminar underlayer of length $\bar{x}_v$ and the friction of a microturbulent underlayer of length $\bar{x}_d$. We note that, strictly speaking, only the first large vortices formed from the laminar boundary layer will be strictly laminar, so that the underlayer of the "sliding vortex" will also be strictly laminar: all subsequent large vortices formed from decay wakes will have residues of the turbulence of these wakes.

It follows from the above discussion that there is a direct relation between the concentration and velocity profiles, but not for the momentum profile. The vortex is a single kinematic whole, so that the velocity at each point of space depends on the distance to the center of the vortex and not on the distribution of density or momentum in this vortex. In other words, if the turbulent exchange of momentum is described by the diffusion equations (see §2, subsection 3), it will be more advantageous to introduce the velocity diffusion coefficient rather than that for momentum.

Let us now dwell on the distribution features of the static pressure profile in a plane-parallel layer and the total-pressure loss along the layer. Without loss of generality, statistics on large vortices can be collected by an ensemble of "cylindrical vortices" of unit height.

Details as to the shape and direction of the real vortex filaments will be significant only for rigorous determinations of the velocity fluctuation field, and, in particular, of the fluctuations along the z axis.

For a "cylindrical vortex" with an angular-velocity vector parallel to the z axis, we obtain from the equation of momentum conservation written for the center of the vortex

$$\frac{\partial p}{\partial r} = \varrho \omega^2 r \quad \text{or} \quad p(r) = p(0) + \frac{\varrho \omega^2 r^2}{2}. \tag{1.18}$$

where $p(0) = p - (\varrho \omega^2 l_v^2/2)$ is the static pressure in the center of the vortex and p is the static pressure outside the turbulent layer.

Assuming that the average level of the static pressure in the decay wake is the same as the pressure outside the layer, we obtain

$$p(x, y) = P_n \int p_l(r) \frac{l}{l} p(l) dl + P_v p \approx 0.5 \left(p + \int \bar{p}_l \frac{l}{l} p(l) dl \right). \tag{1.19}$$

where $\bar{p}_l$ is the average pressure at an arbitrary point $\vec{x}$ of the layer from vortices of dimension l.

Total pressure is lost both on the formation of the large vortex and during the decay of the decay wake. The loss coefficient for formation of the large vortex is determined by a relation of the form

$$\sigma_0 = \frac{\dfrac{(v_1 p_{01} + v_2 p_{02}) V_0^2}{2} + \dfrac{J \omega^2}{2} + \int p(r)\, dv}{v_1 p_{01} + v_2 p_{02}},$$ (1.20)

where p_{01} and p_{02} are the total pressures of the first and second streams, v_1 and v_2 are the volumes of the first and second streams forming the vortex (if the center of the disturbance wave forming the vortex lies on a surface of tangential discontinuity, $v_1 = v_2$), $J = \int v r^2\, dS = (v_1 v_1 + v_2 v_2) l_v^2$ is the moment of inertia of the vortex, and $p(r)$ is the static pressure at a distance r from the center of the vortex.

The integral in (1.20), written for a unit length of the cylindrical vortex, equals

$$\int p\, dv = p(0)(v_1 + v_2) + \frac{\rho \omega^2}{2} \int_0^{l_v} r^2 2\pi r\, dr = p(0)(v_1 + v_2) + \frac{\rho \omega^2 \pi l_v^4}{4};$$

where $p(0)$ is the static pressure at the center of the vortex.

The rotational energy of a unit length of a cylindrical vortex equals

$$\frac{J \omega^2}{2} = \frac{\rho \omega^2}{2} \int_0^{l_v} r^2 2\pi r\, dr = \frac{\rho \omega^2 \pi l_v^4}{4}.$$

Therefore,

$$\int p\, dv + \frac{J \omega^2}{2} = \frac{\rho \omega^2 \pi l_v^4}{2} + \pi l_v^2 \left(-\frac{\rho \omega^2 l_v^2}{2} + p \right) = \pi l_v^2 p,$$ (1.21)

where $p(0) = p - (\rho \omega^2 l_v^2 / 2)$ from (1.18). Relation (1.21) indicates that the rotational energy is exactly equal to the integral static-pressure decrease in the vortex. In other words, when a large vortex forms, the total energy (potential plus rotational energies) is conserved, and some of it is lost only as a result of "inelastic collision" of the two volumes:

$$\epsilon_* = \frac{\frac{\rho_{cp} V_v^2}{2} + p}{g_1 \rho_{01} + g_2 \rho_{02}} \, , \, \, \, \tag{1.22}$$

where $\rho_{av} = g_1 \rho_1 + g_2 \rho_2$; $g_1 = \frac{v_1}{v_1 + v_2}$; and $g_2 = \frac{v_2}{v_1 + v_2}$ are the volume proportions of the first and second streams in the large vortex.

Specifically, when $p \gg \frac{\rho v^2}{2}$, we obtain from the condition of momentum conservation in the form $\rho_1 g_1 (V_v - u_1) = \rho_2 g_2 (u_2 - V_v)$

$$\epsilon_* = \left[1 - \frac{\rho_1 g_1 \cdot (\rho_2 g_2)(u_2 - u_1)^2}{(\rho_1 g_1 + \rho_2 g_2) 2p} \right] \tag{1.23}$$

or with $g_1 = g_2$ and $\rho_1 = \rho_2$

$$\epsilon_* = \left[1 - \frac{\rho (u_2 - u_1)^2}{8p} \right]. \tag{1.24}$$

As we know, the decay of large vortices into a series of small vortices is a cascade process [19], [26]. An estimate of the loss of total pressure in the decay wake can be given with the aid of the following elementary model of cascade decay. A large vortex of radius l_1 decays into isotropic second-order vortices (a cascade) of radius l_2. The total kinetic energy of the second-order vortices immediately after their formation in a volume of $\approx 8 l_1^3$ will be

$$\int \frac{3\rho \overline{V'^2}}{2} \, dv \approx \frac{3n \cdot i_2 \cdot \omega_2^2}{2}, \tag{1.25}$$

where i_2, ω_2 are the projections of the moment of inertia and angular velocity onto one of the coordinate axes for a second-order vortex and $n \approx \left(\frac{l_1}{l_2} \right)^3$ is the number of second-order vortices in a volume of $\approx 8l^3$.

If the beginning of large-vortex decay is described by the linear theory, the dimension l_2 is determined by the half-wavelength of the unstable disturbance that breaks up the vortex with the greatest speed. This energy is subsequently converted to heat and it is redistributed among higher-order scales.

Assuming that all of the energy acquired initially by the isotropic second-order vortices is converted practically completely to heat during the lifetime of the decay wake, we obtain, for a constant average static pressure $p \gg \rho v^2/2$ in the decay wake, an expression similar to (1.23) for the total-pressure loss coefficient σ_d:

$$\sigma_p \approx \left(1 - \frac{3\left(\frac{l_1}{l_2}\right)^3 l_2 \omega_2^2}{2\rho \frac{4}{3} \pi l_1^3}\right) \tag{1.26}$$

or for "round vortices" with

$$l_2 = \pi l_2 \int_0^{l_2} (l^2 - x^2)\, dx = \frac{8}{15}\pi \rho l_2^5$$

and $\omega_2 = \omega_1 = \frac{\Delta u}{2 l_1}$, we have

$$\sigma_p = 1 - 0.3\left(\frac{l_2}{l_1}\right)^2 \frac{\rho(u_2 - u_1)^2}{2\rho} \cdot \tag{1.27}$$

We see on comparing (1.23) and (1.26) that (if l_2 is an order smaller than l_1) the losses on formation of the large vortex exceed those in the decay wake by more than an order of magnitude.

The statistical average total-pressure loss coefficient at the center of the mixing layer is determined by the following considerations. Each elementary event — the formation of a vortex and subsequent decay — yields a loss coefficient equal to $\sigma_v \cdot \sigma_d$. If ndx of these events have taken place on a length dx (n is the number of events per unit length), the average relative change in the total pressure on this length will be:

$$\frac{p_0(x + dx)}{p_0(x)} = 1 + \frac{dp_0(x)}{p_0(x)} = 1 + \frac{d\sigma}{\sigma} = (\sigma_v \sigma_p)^{ndx} \approx 1 + n \ln(\sigma_v \sigma_p)\, dx, \tag{1.28}$$

where

$$\sigma = \frac{p_0(x)}{p_0(0)}; \quad n = \frac{1}{\bar{x}_v + \bar{x}_p} \cdot$$

After integration over x with the boundary condition ln σ(0) = ln 1 = 0 we obtain

$$\sigma(x) = (\sigma_\rho \sigma_\Delta)^{\int_0^x \frac{dx}{\bar{x}_v + \bar{x}_\rho}}. \tag{1.29}$$

In an approximation of the form $\bar{x}_v + \bar{x}_d \approx 0.5\,\bar{x}_v \approx 0.5(\bar{x}_{v_0} + kx)$, where $\bar{x}_{v_0}$ is the initial length of the layer filled with large vortices formed from the initial "laminar" surface of tangential discontinuity and

$$k = \frac{\bar{x}_{\rho\,l}}{x} = \left(\frac{Re_v}{Re_\tau} - 1\right)P_\bullet$$

we obtain from (1.12)

$$\sigma(x) = (\sigma_\bullet \sigma_\rho)^{\frac{0.5}{k}\ln\left(1 + \frac{kr}{x_{v0}}\right)}. \tag{1.30}$$

The volume fractions into which the large vortex is divided on total decay can be determined from the law of total-pressure conservation. In fact, we may write, accurate to the total-pressure loss to turbulence

$$\rho_\bullet \frac{V_\bullet^2}{2} \approx \frac{\rho_0}{2}\left[g_{1\rho}V_{1\rho}^2 + g_{2\rho}V_{2\rho}^2\right], \tag{1.31}$$

where $\rho_v = g_1\rho_1 + g_2\rho_2$; g_{1_d} and V_{1_d} are the volume fraction and average longitudinal velocity of part I of the decay wake, and g_{2_d} and V_{2_d} are the same quantities for part II of the decay wake.

Remembering that on total decay

$$V_{1\rho} = V_1; \; V_{2\rho} = V_2,$$

we obtain from (1.31)

$$\varepsilon_{1p} = (V_2^2 - V_\bullet^2)/(V_2^2 - V_1^2);$$
$$\varepsilon_{2p} = (V_\bullet^2 - V_1^2)/(V_2^2 - V_1^2).$$

(1.32)

We see from (1.32) that the reformed surface of tangential discontinuity has been shifted by the following amount from the center of the vortex in the direction of the faster stream:

$$\frac{y_c - y_p}{l_\bullet} \approx \varepsilon_{1r} - \varepsilon_{2p} = \frac{V_2^2 + V_1^2 - 2V_\bullet^2}{V_2^2 - V_1^2}.$$

(1.33)

Relations (1.5c) and (1.33) indicate that, in addition to the linear scale l_v, which determines the width of the layer, there exist at least two additional linear scales: the scale of the "velocity-profile center" (denoted by a_V) and the scale of the "concentration (temperature) profile center," subsequently denoted by a_T.

For a plane-parallel free mixing layer, the scale a_T is, by definition, equal to the mean-value ordinate of the contact discontinuity surface between the two media. For a round jet, the scale a_T is the radius or the mathematical expectation of the boundary of the initial volumes of the jet.

If the average position of the vortex centers for the free layer coincides with the average interface in the media, we have

$$\bar{a}_t \approx \bar{y}_c \quad \text{и} \quad \bar{a}_V = \bar{a}_t P_\bullet + \bar{y}_p P_p = \bar{a}_t - (\varepsilon_{1p} - \varepsilon_{2p}) P_p \cdot l_\bullet.$$

(1.34)

The relation between the statistical average values of the scales a_T and a_V and the width scale of the layer is most simply determined from the integral laws of mass- and momentum-flux conservation (see §2). For most of the length of the jet, these scales are, as a rule, much smaller than the width scale of the layer. For this reason, all

known semiempirical theories of the turbulent jet either leave them out of account altogether or take them into account implicitly in the form of additional empirical constants.

Without consideration of these scales, we find it impossible to obtain sufficient accuracy in solving problems related to the initial segment of the jet (for example, the wake-vacuum problem) or problems for which $\bar{a}_T \geq l$ always (for example, forcing of jets through porous wall under high pressure).

The elementary vortex model of the development of the turbulent mixing layer that we have set forth above can be used, in principle, to construct the probability distribution functions of any random parameter that appears in the familiar Reynolds equations, thus closing these equations. We may hope that the development of the mathematical formalism of this model will in the future make possible more accurate determination of such parameters as the characteristic vortex lifetime, the characteristic linear dimension of the mixing layer (size of large vortices for various boundary conditions), degree of greyness, Prandtl number, total-pressure loss coefficient, etc., which have thus far been determined approximately for the simplest case of the plane-parallel layer, as well as theoretical determination of other as yet undetermined parameters such as turbulent friction and mass-transfer rate.

For most engineering problems of turbulent flow with release of heat, use of even simpler approximations of turbulent exchange on the basis of diffusion models with empirical values of D_T, Pr, and N is found to be adequate. We recall for comparison that the Navier-Stokes hydrodynamic equations also represent a "diffusion-model approximation" of a complex molecular motion that is described more accurately by the Maxwell-Boltzmann equation [145]. Let us see what basis there is for this approximation in the case of turbulent flow. It is easily seen from Relation (1.13) and Figure 1.3 that the average-velocity and average-concentration distributions for a free mixing layer have S-curved profiles, which are closely approximated by solution of the

diffusion equation. Reduction of Michalke and Lessen's data [27], [28] indicates that even in a single large vortex (without averaging over an ensemble of vortices), the curves of p_{2_l} = tanh $y/\bar{L}$ (see Figure 1.3b, curve 1) are similar in form to diffusion-type solutions.

When the scales l and y_c are sufficiently dispersed, the distributions of concentration and velocity in the isolated vortex are of no fundamental importance: for simplicity in mathematical analysis, they can even be specified constant throughout the volume of the vortex. Here the "diffusion-type solution" is explained by the fact that the functions $p(l)$ and $p(y_c)$ have nearly normal form. The function $p(l)$ has a near-Maxwellian distribution (see Figure 1.1c) while $p(y_c)$ is nearly-Gaussian. In the case of the diffusion model, the parameter determining the width of the mixing zone is the "layer dispersion" scale σ (for details see §2), which is proportional to the average vortex dimension $\bar{l}$. However, like any other model, the diffusion model must also take account of the degree of mixing inhomogeneity, the difference between the mixing of velocity and the mixing of concentration (temperature). All of these differences are taken into account simply by selecting an appropriate dispersion scale (see Chapter II).

The diffusion model is not always sufficiently accurate for a wall layer. As we showed in Chapter II, it gives a good description of the concentration field for jet flows at a wall. However, the velocity and temperature profiles above a wall without heat insulation cannot be described by the solution of the diffusion equation with the aid of a single scale σ or, which is the same thing, with a single eddy diffusivity $D(\sigma^2 \sim D)$, since, according to what we said above, the velocity profile above a wall is determined not only by the scale $l \sim \sigma$ of the large vortices, but also by the underlayer-thickness scale. In the extreme case, this can be done for a vortex model with extreme restructuring of velocities, with the aid of two diffusion-coefficient values: a convective coefficient D_T for the average longitudinal velocity of large vortices moving without slip and a gradient coefficient D_{MT} for the longitudinal-velocity profile in the decay wake.

We note that the introduction of a diffusion coefficient that varies through the thickness of the layer is not only of no practical advantage, but also physically illegitimate, since the dimensions l_v of the large vortices are comparable to the total width of the layer, and the dimensions l_d of the decay-wake vortices are comparable with the thickness of the viscous underlayer.

The diffusion model can tell us little concerning the friction at the wall, the static-pressure distribution, or the distribution of total pressure (energy) over the thickness of the layer. To determine these parameters, it is necessary to use the vortex model directly. Nevertheless, the diffusion model yields the simplest and most lucid semiempirical (accurate to the values of D, Pr, and N) description of all or most of the engineering problems related to turbulent mass and momentum exchange in jet flows with heat release. All problems presented in the chapters that follow are solved with this model.

2. Diffusion Model of "Black and White" Mixing

Here, as previously, the parameters of the cocurrent stream are identified by the subscript "1." For example, V_1 is the initial velocity, T_1 — the temperature, and ρ_{01} — the initial density of the cocurrent stream. The corresponding parameters of the jet will be identified by the subscript "2." For brevity, we shall also call the material of the cocurrent stream "white" and that of the jet — "black."

As described above, the black and white substances are mixed as a result of turbulent mechanical displacements of volumes of gas and by molecular diffusion.

Let a volume whose linear dimensions are smaller than the scales of the smallest turbulent vortices be isolated around a certain point in space. Portions of gas entering this volume will sometimes consist entirely of molecules of the white substance and sometimes entirely of black molecules, and in some cases they will consist of molecules of both types. If the probability of finding portions of gas with

intermediate composition is negligibly small at each point in space
as compared with the probabilities of the initial compositions, i.e.,
if basically only volumes of white or black gas can be encountered at
each point, it is natural to speak of "black and white" mixing.

For the "black and white" mixing model, we introduce the notions
of the probabilities of the appearance of volumes of either original
medium at a point in space. These probabilities are the same as the
probabilities of appearance of the corresponding temperature or density.
For example, for stationary mixing, the probability of appearance of
volumes of black gas (P_2) is calculated as the limit of the ratio of
the stay time of medium with temperature T_2 to the total time of obser-
vation, provided that the latter tends to a sufficiently large value.

P_1, the probability that white volumes will occupy the same space
point, is calculated similarly. The probabilities P_1 and P_2 can also
be interpreted differently, as the average fractions occupied by
volumes of "white" and "black" gas in a unit volume isolated around
the point under consideration or as the relative length along the axis
on which the variation of the parameters is uniform.

By definition,

$$P_1 + P_2 = 1. \tag{1.35}$$

We obtain for the average values of the temperatures and densities:

$$\overline{T} = T_1 P_1 + T_2 P_2; \tag{1.36}$$

$$\overline{\rho} = \rho_{01} P_1 + \rho_{02} P_2. \tag{1.37}$$

The following relation between the dimensionless density and
temperature profiles follows from the above relations:

$$P_2 = \frac{\overline{\rho} - \rho_{01}}{\rho_{02} - \rho_{01}} = \frac{\overline{T} - T_1}{T_2 - T_1}; \tag{1.38}$$

it is valid only for the "black and white" mixing model.

At first glance, this relation contradicts the time-average equation of state, for which we may expect $\bar{\rho} \sim 1/\bar{T}$. Actually, it is not permissible to neglect the correlation moment $\overline{\rho' T'}$, which is equal in our case to

$$\overline{\rho' T'} = (\rho_1 - \bar{\rho})(T_1 - \bar{T})P_1 + (\rho_2 - \bar{\rho})(T_2 - \bar{T})P_2$$

or

$$\overline{\rho' T'} = (\rho_2 - \rho_1)(T_2 - T_1)P_1 P_2 \qquad (1.39)$$

in finding the relation between $\bar{\rho}$ and $\bar{T}$ with the equation of state.

It is easy to estimate the maximum possible error resulting from this neglect.

The equation of state at constant pressure in the mixing zone (and with equal molecular weights of the two gases) has the form

$$\overline{\rho T} = \bar{\rho}\bar{T} + \overline{\rho' T'} = \rho_{01} T_1 = \rho_{02} T_2. \qquad (1.40)$$

On the assumption of a vanishing correlation moment, we shall denote the density found from (1.40) by $\bar{\rho}_0$. Then the error introduced by formal use of the equation of state can be estimated from the ratio of the true average density $\bar{\rho}$ to the density $\bar{\rho}_0$. We obtain from expressions (1.39) and (1.40)

$$\frac{\bar{\rho}}{\rho_0} = 1 + \frac{(n-1)^2}{n} P_1 P_2, \quad \text{where } n = \frac{\rho_{01}}{\rho_{02}} = \frac{T_1}{T_2}. \qquad (1.41)$$

n	1	2	3	4	5	6	14.5
$\bar{\rho}$	1	1,12	1,33	1,56	1,8	2,04	4,14

This error increases rapidly with increasing initial-temperature ratio. The table given below gives an idea of the numerical values. The calculation was performed for $P_1 = P_2 = 1/2$.

The distribution of the probabilities P_1 and P_2 across the mixing zone can be calculated if the characteristic diffusion parameters of the jet are known.

To introduce the first of these parameters — the dispersion of the jet — let us consider what happens to a "black" elementary volume emerging from a point in the initial plane passed through the nozzle exit section. In the stream, this volume describes a certain rather confused trajectory that depends on the choice of the individual volume. However, if we average over the set of all trajectories beginning at a given fixed point, we obviously obtain a smooth curve of $Y_i(x)$ $(i=1, 2, 3...)$, which might be called the average trajectory of the volume.

Each individual trajectory deviates from the average, and the bundle of trajectories is scattered (smeared). The mean-square deviation of the trajectories in a given cross section from the average, $(Y_i - \bar{Y_i})^2$, is a measure of the scattering in each specific cross section of the jet. Understandably, the mean-square deviation (dispersion) of the volume will increase with increasing distance downstream. On averaging the dispersion over all volumes in a certain jet cross section, we obtain a quantity that characterizes its smearing in this cross section — the dispersion of the jet σ_T^2. It will be understood from physical considerations that the smearing of the concentration profile is determined basically by the law of displacement of the instantaneous interface between the "black" and "white" media. This law is related to the law of motion of gas parcels immediately adjacent to the interface. We may therefore identify the dispersion of the jet with the dispersion of the volumes emerging directly from under the edge separating the streams at time zero.

With this definition of the dispersion, it becomes clear that the scale σ is proportional to the average scale l of the large vortices, which is determined by a relation of the form of (1.12).

The specific manner in which the dispersion of the jet varies downstream depends on the initial conditions: on the velocity ratio $m = V_1/V_2$ (cocurrency parameter), on the initial turbulence level, etc.

At considerable distances from the nozzle exit, σ varies in proportion to the distance downstream (see Chapter II). The proportionality factor depends on the ratio of the initial velocities: it decreases as the parameter m varies from 0 to 1 and increases as m increases from 1 to ∞.

For the simplest case of two plane-parallel semi-infinite streams with zero initial boundary-layer thicknesses, the vortex model can be used to calculate the numerical coefficient in (1.12) or in the analogous relation for the corresponding scale σ, accurate to the experimental constant Re_T of the theory of homogeneous and isotropic turbulence. In principle, we might also attempt this for various more complex problems, e.g., for streams with finite dimensions, with non-zero initial boundary layers, etc. However, the complexity and reliability of these calculations would, at the present time, be such that the advantage would lie with direct experimental determinations of $\sigma(x)$ under various boundary conditions. Detailed experimental data on σ will be given in the next chapter for various sets of conditions.

Another important parameter that must be known is the average linear dimension $a_T(x)$ of the jet. Let us explain its physical sense once again with reference to the axisymmetric jet. If we pass a plane perpendicular to the axis of the jet, the instantaneous interface between the volumes of the jet and the cocurrent stream forms a certain complex curve. The average radius a_T in this case will be the radius of the circle whose area is equal to the area enclosed by the curve. In other words, the average radius of the jet is the same as the radius of the circle that is obtained by collecting all of the scattered turbulent vortices together in the particular cross section of the jet volume.

This statement, written in mathematical form, means that for a round jet

$$\int_0^{\infty} P_{\tau} r\, dr = \frac{a_{\tau}^2}{2}.$$ (1.42)

Let the initial average radius be a_0. After the jet has all but acquired the velocity of the cocurrent stream, the limiting value $a_{T\infty}$ of the average radius is found from the law of constant flux of the material of the jet:

$$\varrho_2 V_1 \pi a_{\tau\infty}^2 = V_x \pi a_0^2 \varrho_{02}$$

or, if $\varrho_2 \approx \varrho_{02}$

$$a_{\tau\infty} = \frac{1}{\sqrt{m}}\, a_0.$$ (1.43)

Thus, if the jet has an initial velocity exceeding the velocity of the cocurrent stream (m < 1), its average radius will increase. The average radius will decrease in the contrary case. Finally, when the velocities of the jet and cocurrent stream are equal, $a_{\tau}(x) = a_0$ (Figure 1.5).   e average radius of the jet can also be treated as the mathemat al expectation of the average jet boundary. We recall [see (1.34)] at the introduction of the dispersion averaged over the cross section of the jet and average radius is found to be possible in virtue of the fact that the characteristic transverse velocities are much lower than the longitudinal velocities, while the vortex scales are comparable with the transverse dimensions of the jet.

3.   Model of "Grey" Mixing

By "grey" mixing, we mean mixing in which the temperature or concentration fluctuations about the average values are quite insignificant. In contrast to the preceding case, we may assume here that the density and temperature values are related by the equation of state, and it is therefore unnecessary to draw a distinction between the instantaneous and average values of these parameters.
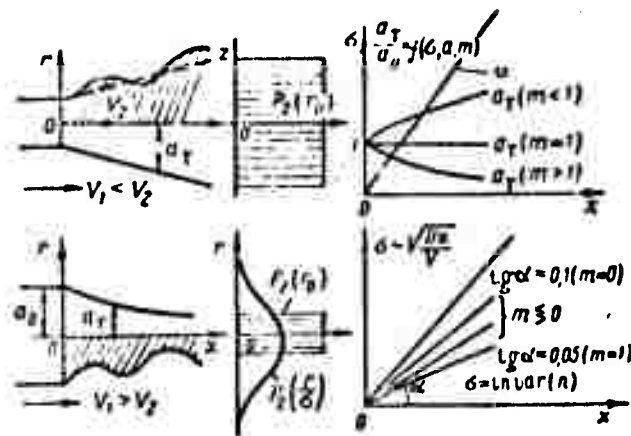
Figure 1.5. Statistical parameters of jet ($m = V_1/V_2$).

"Grey" mixing occurs when the scale of the transporting vortices in the turbulent stream is much smaller than the width of the average profile of the diffusing property. It can be assumed in this case that turbulent transport depends, on the average, on local conditions, and is proportional to the gradient of the diffusing property. For this reason, Townsend [20] proposed that this type of transport be called "gradient diffusion."

It must be noted that if the dispersion of the molecular transport in the process of laminar molecular diffusion is $y^2 = 2D_M t.$, where D_M is the molecular diffusion coefficient and t is the diffusion time, then the transport dispersion

$$\sigma_c^2 = 2D_M t$$

when gradient diffusion takes place in the turbulent stream; here D_{MT} is the coefficient of the so-called molecular-turbulent or microturbulent diffusion, which describes the acceleration of molecular diffusion under the influence of turbulence. This acceleration was first studied by Townsend [20], [32] and a number of other authors in application to isotropic turbulence [10], [22], [21]. The results of an investigation of this turbulence effect in nonisothermal jets will be given below in Chapter II.

In discussing the model of "black and white" mixing (§1, subsection 2), we introduced the concept of the probabilities of observing matter of the jet (P_2) and matter of the cocurrent stream (P_1). In the case under study, definition of the probabilities in terms of the fractions of the time during which objects of different species are observed is not feasible, for reasons that are readily understood. The natural assumption that the probability is proportional to the partial density of matter of the particular species at the particular point in space is a necessary generalization. For example, the partial density of jet substance, which equals the mass of jet substance in a unit volume, will be

$$\varrho_2 = \mu_2 n_2,$$

(1.44)

where μ_2 is the molecular weight of the jet substance and n_2 is the number of molecules of the particular species (with molecular weight μ_2) per unit volume.

Similarly,

$$\varrho_1 = \mu_1 n_1.$$

(1.45)

It is assumed below that

$$P_1 = \frac{\varrho_1}{\varrho_{01}} = \frac{n_1}{n_{01}} ; \quad P_2 = \frac{\varrho_2}{\varrho_{02}} = \frac{n_2}{n_{02}} ,$$

(1.46)

where the subscript "0" indicates that the parameters are taken in the initial cross section.

It is easily seen that at equal jet and stream temperatures

$$P_1 + P_2 = 1.$$

(1.47)

This result proceeds from the equation of state, which is conveniently written in the following form [146] (k is Boltzmann's constant):

$$n_1 + n_2 = \frac{p}{kT} .$$

(1.48)

Neglecting pressure fluctuations, we find that

$$n_1 + r_2 = n_{01} = n_{02}.$$

In the case of unequal jet and cocurrent stream temperatures, Relation (1.47) is equivalent to the hypothesis that the dimensionless temperature profiles and mass-average concentration profiles coincide, which means, with (1.46), that

$$-\frac{c_2}{c_1 + c_2} = \frac{P_2}{nP_1 + P_2} = \frac{T - T_1}{T_2 - T_1},$$

$$\left(n = \frac{T_2}{T_1} = \frac{c_{01}}{c_{02}}\right): \quad c_{01} > c_{02}.$$

$$(1.49)$$

Thus, the relation between the density and temperature profiles that was established for the model of "black and white" mixing [Formula (1.38)] no longer applies in the case of "grey" mixing with $n \neq 1$. Hence, the difference between the volume-average (convective) and mass-average (gradient) mixing will have a stronger effect on the average temperature profile, the greater the difference between n and unity.

As we know, the relation noted between the temperature and concentration profiles proceeds from the identity of the molecular-diffusion and heat-conduction equations with a Lewis* number equaling unity[[145], [146], i.e., at nearly equal molecular weights of the two mixing gases.

Since turbulent exchange (including gradient diffusion) is determined by the fluid-dynamic motions of medium and is not limited by the molecular exchange coefficients [10], Relation (1.49) should also be valid for gases with different molecular weights (but with equal adiabatic exponents).

---

* Translator's Note: This is a dimensionless characteristic number (Le) for flow phenomena involving both heat and mass transfer.

Let us explain the meaning of the reservation calling for equal adiabatic exponents or, what is the same thing, equal numbers of degrees of freedom of the molecules of the mixing gases.

Let the temperature at a certain point in space assume the value T as a result of equal distribution of the thermal energy between n_1 molecules of the cocurrent-stream substance and n_2 molecules of the substance of the jet.

If γ is the number of degrees of freedom of a molecule, the energy balance has the form

$$(\gamma_2 n_2 + \gamma_1 n_1)^{1/2} = n_1 \gamma_1 k T_1 + \gamma_2 n_2 k T_2$$

or

$$\frac{T}{T_2} - \frac{T_1}{T_1} = \frac{\gamma_2 n_2}{\gamma_1 n_1 + \gamma_2 n_2}.$$

Consequently, Relation (1.49) requires that $\gamma_1 = \gamma_2$. If $\gamma_1 \neq \gamma_2$, deviations from this relation are possible. Similar difficulties arise when $\gamma_1 \neq \gamma_2$ with the condition of pressure constancy across the mixing zone.

4.   Mixing in Real Flows

As we noted in §1, subsection 1, mixing in real flows is intermediate in nature between the "black and white" and "grey" mixing cases. As was explained in §1, subsection 1, therefore, it is necessary to introduce an additional parameter — the degree of "greyness" N $(0 \leq N \leq 1)$. The value $N = 0$ corresponds to the "black and white" mixing model, and $N = 1$ — to the "grey" model.

Nevertheless, the probabilities can be introduced even in the general case by means of relations such as (1.46), in which the average partial densities should be written:

$$P_1 = \frac{\rho_1}{\rho_{01}} = \frac{\bar{n}_1}{n_{01}}; \quad P_2 = \frac{\rho_2}{\rho_{02}} = \frac{\bar{n}_2}{n_{02}}. \tag{1.50}$$

Here, as before, we assume

$$P_1 + P_2 = 1. \qquad\qquad (1.51)$$

The diffusion parameters (average radius, dispersion of the jet) can also be used with appropriate refinements to their physical connotation. In defining the average radius a_T (§1, subsection 2), it is necessary to take account of dispersion of jet material both by convective displacements and as a result of accelerated molecular diffusion. In the general case, the dispersion of the jet σ^2 describes the mean square deviation of molecules of the jet substance from their average trajectories. The dispersion is determined by the concurrent advance of two processes: volume convection and gradient diffusion.

The somewhat complex character of the mixing can be described with the following simplified model [35], illustrated as it applies to the region of turbulent mixing of two plane-parallel streams (Figure 1.6). The grey-mixing layer is transported as a whole by large vortices, the scales of whose motion are greater than the characteristic width of this layer. In the layer itself, molecular mixing is intensified (accelerated)* by small-scale turbulence consisting of vortices whose dimensions are much smaller than the characteristic width.

If it is assumed that the mass transport processes governed by the small-scale turbulence and by the large vortices are statistically independent and are described by normal laws with the respective dispersions σ_g^2 and σ_T^2, then:

(a) the total transport is also described by a normal law;

---

*It must be noted that this acceleration implies only a more rapid increase in the amount of matter in the two streams that has been mixed to the state of molecular homogeneity, and does not by any means involve hypothetical variations of the laws of molecular statistics.
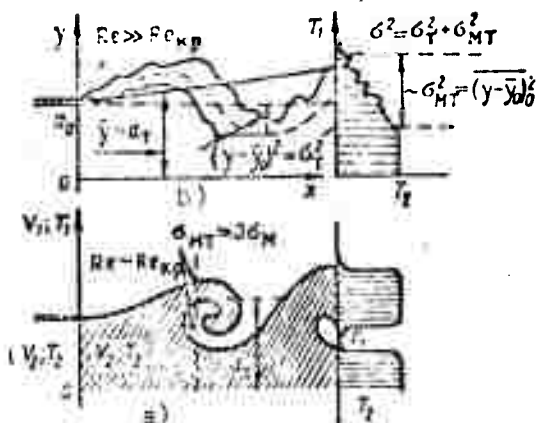
Figure 1.6. Models of turbulent mixing of streams.

a — model of "black and white" mixing ($\sigma_T \simeq \sigma$; $\sigma_{MT} \simeq \sigma M \ll \sigma$);
b — model of "grey" mixing ($\sigma_{MT} \approx \sigma$; $\sigma_T \sim 0$).

(b) the total dispersion is equal to the sum of the dispersions:

$$\sigma^2 = \sigma_c^2 + \sigma_T^2. \qquad (1.52)$$

(c) the degree of "greyness" N can be introduced as the ratio of the dispersion of grey mixing to the total dispersion:

$$N = \frac{\sigma_c}{\sigma}. \qquad (1.53)$$

These relations are also formally satisfied in other cases, e.g., in the other extreme case of small Re (see Figure 1.6), when microturbulence is absent and a statistical relation exists explicitly between the large vortices and the instantaneous mixing-layer thickness σ_M. In this case, we can write as before

$$(y_T' + y_M')^2 \approx \sigma_T^2 + \sigma_c^2,$$

where

$$y_T' = y_T - \overline{y_T}; \quad y_M' = y_M - \overline{y_M}; \quad \sigma_T^2 \approx \overline{y_T'^2}; \quad \sigma_c^2 \approx \overline{2 y_T' y_M'} + \overline{y_M'^2}.$$

Here the effect of the vortices will be not only positive (all cases: $\sigma_M, 3\sigma_M, 5\sigma_M$, etc., make contributions to the value of σ_c), but also negative (σ_M^2 may be much smaller than $\overline{y_M'^2}$ due to elongation of "surface of contact discontinuity").

Hence, a more general physical treatment of the parameters σ_c and σ_T is as follows. We sort the ensemble of intermediate compositions in order of their monotonic decrease, arranging the compositions along the y axis in the order of their most probable occurrence. Then the characteristic scale of the resulting distribution of most probable compositions will be σ_c, and the dispersion of the random distribution of this composition over the other values of y will be σ_T^2. As before, the parameters σ_c and σ_T are assumed constant for any composition. For an unbounded mixing layer with normal distributions, the composition $P_1 = P_2 = 0.5$ will be, by definition, most probable at the point $\bar{y} = a_T$.

The above model structure can be used to circumvent the difficulties noted in §1, subsection 2 as resulting from the use of the equation of state, to find the relation between the average values of density and temperature. It is also found possible to calculate not only the average values of the concentrations and temperatures, but also the corresponding probability densities for the occurrence of these values.

Let the probability density of displacement under the influence of convective motion of elements of the "grey" layer from the point $\vec{r}_0$ to the point $\vec{r}$ be equal to $p(\vec{r}, \vec{r}_0)$. Then, obviously, the average temperature profile will be given by the relation [see (1.49)]:

$$\frac{\bar{T}(\vec{r}) - T_1}{T_2 - T_1} = \int \frac{T(\vec{r}_0) - T_1}{T_2 - T_1} p(\vec{r}, \vec{r}_0) d\vec{r}_0 = \int \frac{P_{2c}}{nP_{1c} + P_{2c}} p(\vec{r}, \vec{r}_0) d\vec{r}_0. \qquad (1.54)$$

The symbol "c" indicates that the probabilities were calculated for "grey" mixing. (We shall call the corresponding profiles quasilaminar.)

The distribution of the root-mean-square temperature fluctuations is described by

$$\overline{T'^2(\vec{r})} = \overline{(T - \bar{T}(r))^2} = \int \left[\frac{\cdot P_{2c}}{nP_{1c} + P_{2c}} - \bar{T}(r) \right]^2 p(\vec{r}, \vec{r}_0) d\vec{r}_0. \qquad (1.55)$$

We also write a formula for the probability density of the appearance of a given partial density of jet matter at the space point $\vec{r}$:

$$p\left(\frac{\rho_2}{\rho_{02}} \right) d\left(\frac{\rho_2}{\rho_{02}} \right) = \int P_{2c}(r_0) \, p(\vec{r}, \vec{r}_0) dr_0 . . \qquad (1.56)$$

The integration is extended only over the region of space in which

$$\frac{\rho_2}{\rho_{02}} \leqslant P_{2c} \leqslant \frac{\rho_2}{\rho_{02}} + d\left(\frac{\rho_2}{\rho_{02}} \right).$$

§2. Fundamental Equations for Turbulent Jet Flows

1. Taylor Equation and Equation of Turbulent Diffusion for the Model of "Black and White" Mixing

It is shown in the statistical theory of turbulent diffusion that under certain conditions the probabilities P_1 and P_2 satisfy a certain partial differential equation [22], [36], [37].

Let us first examine the elementary case of diffusion in a field of homogeneous and isotropic turbulence. The distance covered by an isolated fluid particle during a time t in the direction of, say, the y axis is determined by the expression

$$Y_t = \int_0^t v'(\tau) d\tau, \qquad (1.57)$$

where v' is the component of the particle fluctuation velocity in this direction.

The mean square particle displacement $\overline{Y_\tau^2}$ — the dispersion of turbulent transport — plays an important role in the theory of turbulent diffusion.

The manner in which the dispersion changes with time is described by an equation that can be derived by multiplying both sides of (1.57) by $v'(t) = \frac{dY_\tau}{dt}$, transferring v'(t) under the integral sign, and then averaging both sides over the ensemble of statistically equivalent particles. This equation, which was derived by Taylor and bears his name, takes the form

$$\frac{1}{2} \frac{d\overline{Y_\tau^2}}{dt} = \int_0^t \overline{v'(t) v'(\tau)} \, d\tau.$$

For stationary (homogeneous) turbulence, the correlation moment $\overline{v'(t)v'(\tau)}$ depends only on the difference t - τ. Hence, the equation obtained above can be rewritten as follows:

$$\frac{1}{2} \frac{d\overline{Y_\tau^2}}{dt} = \int_0^t \overline{v'(t_0) v'(t_0 + \tau)} \, d\tau. \tag{1.58}$$

The Taylor equation has two limiting solutions. For small diffusion times

$$\overline{Y_\tau^2} \simeq \overline{v'^2} (t - t_0)^2. \tag{1.59}$$

For sufficiently large diffusion times

$$\overline{Y_i^2} \simeq 2 D_\tau (t - t_0), \tag{1.60}$$

where

$$D_\tau = \int_0^\infty \overline{v'(t_0) v'(t_0 + \tau)} \, d\tau$$

is the eddy diffusivity.

If we introduce a Lagrangian scale of length

$$l_L = \frac{\int_0^\infty \overline{v'(t_0)\, v'(t_0+\tau)}\, d\tau}{\sqrt{\overline{v'^2}}}.$$

we have

$$D_r = \sqrt{\overline{v'^2}} \cdot l_L. \tag{1.61}$$

It should be noted that, as will become clear below, the eddy diffusivity is the time-dependent quantity $\frac{1}{2}\frac{\overline{dY_r^2}}{dt}$. However, this term is often applied to the limiting value of $\frac{1}{2}\frac{dY_r^2}{dt}$ at $t \to \infty$, which equals (1.61), since it is only for this extreme case that the diffusion equation is justified with sufficient rigor.

Experiments indicate that if the probability of appearance of a particle in the interval $(y;\ y + dy)$ is written in the form $p(y)dy$, the probability distribution density has the normal form [22], [36]:

$$p(y) = \frac{1}{\sqrt{2\pi Y_r^2}}\, e^{-\frac{(y-y_0)^2}{2Y_r^2}}. \tag{1.62}$$

For small times at which Relation (1.59) is satisfied, the experimental fact that the turbulent-velocity field is also normally distributed speaks in favor of (1.62). In this case, the normal law of displacements is obtained from the normal law of velocities by simply multiplying the velocities by $(t - t_0)$.

The law (1.62) is also favored at large diffusion times by the fact that the resultant displacement of the particle is the sum of many small displacements that are statistically weakly related. Then the normal distribution may be simply a consequence of the familiar probability-theory theorem that states that the distribution functions of sums of a series of statistically independent terms converge (given

certain conditions) to a normal distribution law as the number of
terms is increased without limit [37].

It is easily seen that $p(y)$ satisfies the diffusion equation with
the diffusion coefficient

$$D = \frac{1}{2} \frac{\overline{dY_\tau^2}}{dt}; \quad \frac{\partial p}{\partial t} = \frac{1}{2} \frac{\overline{dY_\tau^2}}{dt} \frac{\partial^2 p}{\partial y^2}. \qquad (1.63)$$

Equation (1.63) is a particular form of the so-called Fokker-Planck
equation, one of the important equations of statistical physics. It
has been proven rigorously that the probability distribution density
of the random particle displacements satisfies an equation of this type
only for the so-called Markov random processes (processes without
aftereffect) [38]. This proof was obtained by A. N. Kolmogorov.

Needless to say, turbulent diffusion is not a Markov process.
Nevertheless, it can be assumed with certain stipulations that even
in the case of a process with an explicit prior history like turbulent
transport, the diffusion of liquid volumes is described by the Fokker-
Planck equation in its general form [14], [22], [34]:

$$\frac{\partial p}{\partial t} + \frac{\partial p \vec{u}_i}{\partial x_i} = \frac{\partial^2}{\partial x_i \partial x_j} D_{ij} p. \qquad (1.64)$$

where $p(\vec{r}_0, t_0, \vec{r}, t)$ is the probability that a unit volume that was at the
space point $\vec{r}_0$ at time t_0 will be at point $\vec{r}$ at time t; $\bar{u}_i(\vec{r}, t) = \frac{\partial \overline{Y_i}}{\partial t}$
is the average velocity of motion of the unit volume in the direction
of the coordinate x_1, and $D_{ij} = \frac{1}{2} \frac{\partial}{\partial t} \overline{Y_i Y_j}$ is the generalized diffusion
coefficient.

In a turbulized medium consisting of a certain gas, let another
gas occupy volume v_2 at time zero. We integrate Equation (1.64) over
the volume v_2 and recognize that

$$P_2 = \int_{v_2} p(\vec{r}, \vec{r}_0) d\vec{r}_0.$$

As a result, we arrive at the following equation for P_2:

$$\frac{\partial P_2}{dt} + \frac{\partial P_2 \overline{u}_i}{\partial x_i} = \frac{\partial^2}{\partial x_i \partial x_j} D_{ij} P_2.$$ (1.65)

The difference in the sampled average velocities, i.e., the velocities at the particular point averaged over the various classes of volumes, was considered immaterial in the derivation of Equation (1.65).

Exactly the same equation also applies for the probability P_1:

$$\frac{\partial P_1}{\partial t} + \frac{\partial P_1 \overline{u}_i}{\partial x_i} = \frac{\partial^2}{\partial x_i \partial x_j} D_{ij} P_1.$$ (1.66)

Adding Equations (1.65) and (1.66), we obtain the continuity equation

$$\frac{\partial \overline{u}_i}{\partial x_i} = 0.$$

Thus, despite the density difference between the mixing gases, the continuity equation for "black and white" mixing has the same form as for a homogeneous fluid.

Adding Relations (1.65) and (1.66) after first multiplying by ϱ_1 and ϱ_2, respectively, we obtain the mass conservation equation:

$$\frac{\partial \overline{\varrho}}{\partial t} + \frac{\partial \overline{\varrho u}_i}{\partial x_i} = \frac{\partial^2}{\partial x_i \partial x_j} D_{ij} \overline{\varrho}.$$

It should be noted that there are cases in which the sampled average velocities definitely differ from one another. This is exemplified by the jet of liquid in a gas. In this case, the diffusion of the gas and liquid volumes is determined by scattering of liquid drops with dispersion $\overline{Y}^2$. On the other hand, the average velocities averaged only over the volumes of gas or only over the drops will differ substantially.

2.   Equation of Gradient Diffusion ("Grey" Mixing Model)

Let us consider the case of gradient diffusion in a medium with low viscosity but a large molecular diffusion coefficient, which is the simplest from the standpoint of mathematical analysis but not the most important case. We note that the most rapid mixing occurs at decay of the large vortex (see Figure 1.3). At this time, there is a rapid equalization of the composition inhomogeneity through the entire volume of the vortex. At subsequent times (up to the formation of a new large vortex from the decay trace), gradient composition diffusion occurs at a rate much lower than the rate of mixing during decay.

The basic distinctive property of gradient diffusion is that the concentration fluctuations about the average values are small, just as their characteristic scales are small compared to the characteristic scale of variation of the average concentration $\bar{c}$. Consequently, the magnitude c' of the fluctuations is determined (accurate to quantities of second-order of smallness) by the average concentration gradient and can be written in accordance with the Boussinesq-Prandtl physical conception in the form

$$c' = (c - \bar{c}) = -\frac{\partial \bar{c}}{\partial x_j} l_j = -a_j l_j$$

$$\left(a_j = \frac{\partial \bar{c}}{\partial x_j} \right),$$

$$(1.67)$$

where $l_j = \int^{T(t)} u_j(t') dt'$ is a new random function whose rms value determines the length of the "turbulent mixing path," $u_j(t')$ is the average velocity of a turbulent micromole at time t' on the path from point x' to point x, and $T(t)$ is a new random function — the mixing time of the micromole.

The mixing time scale T must be small enough so that the maximum fluctuation amplitude l_j will not exceed the width of the mixing layer.

We note that the "mixing length" concept can be introduced only when the molecular diffusion coefficient is nonzero ($D_M \neq 0$), since it is only in this case that Condition (1.67) will not lead to the paradoxical conclusion that the random concentration fluctuation increases without limit. In other words, the "turbulent micromole" will dissolve in the surrounding medium before it has moved through a distance such that Condition (1.67) is no longer satisfied.

For sufficiently small mixing times, it can be assumed that

$$l_j = \int_0^{T(t)} u_j(t') \, dt' \simeq u_j(\vec{x}, t) T(t). \tag{1.68}$$

Condition (1.68) is similar in form to the known particular solution of the Taylor equation for the initial time of turbulent transport (diffusion), the only difference being that the Lagrangian velocity (particle velocity) appears in the Taylor equation and the random parameter $T(t)$ has been replaced by the simple time t.

In the case of "purely turbulent transport" ($D_M \simeq 0$), Condition (1.67) may not be satisfied, and by its very physical meaning, the parameter l_j is not equal to the Prandtl mixing length, which characterizes the length over which an inhomogeneity is transported during its "life." In fact, although the inhomogeneity is transported at $D_M = 0$, it retains its individuality in the process and does not dissolve in the surrounding medium. Physically, the parameter l_j becomes similar to the analogous parameter of Taylor turbulent composition (property) transport, except that it determines the transport in the Euler coordinate system. Establishment of a random function l_j that satisfies Condition (1.67) under any conditions (including at $D_M = 0$) would mean a theoretical rigorous justification of the turbulent gradient diffusion equation and determination of the relation between the Lagrangian and Euler diffusion characteristics of turbulence for this case.

Under this heading, we shall examine the much simpler case in which the molecular diffusion coefficient D_M is nonzero and so large that the mixing length conditions (1.67) and (1.68) are satisfied. In addition, the density in the gradient mixing layer is assumed practically constant.

In this case, the equations of fluid dynamics take the form

$$\frac{\partial c}{\partial t} + \frac{\partial c u_l}{\partial x_l} = D_u \frac{\partial^2 c}{\partial x_l^2}; \qquad (1.69)$$

$$\frac{\partial u_l}{\partial x_l} = 0; \qquad (1.70)$$

$$\frac{\partial u_l}{\partial t} + \frac{\partial u_l u_k}{\partial x_k} = -\frac{1}{\psi} \frac{\partial p}{\partial x_l} + \nu \frac{\partial^2 u_l}{\partial x_k^2}. \qquad (1.71)$$

Averaging Equation (1.69), we obtain

$$\frac{\partial \bar{c}}{\partial t} + \frac{\partial \overline{c' u_l}}{\partial x_l} = D_u \frac{\partial^2 \bar{c}}{\partial x_k^2}. \qquad (1.72)$$

Applying Equations (1.72) and (1.69), we reduce the diffusion equation to the form

$$\frac{\partial c'}{\partial t} + \frac{\partial (c' + \bar{c}) u_l}{\partial x_l} - \frac{\partial \overline{c' u_l}}{\partial x_l} = D_c \frac{\partial^2 c'}{\partial x_l^2}. \qquad (1.73)$$

With Relation (1.67), Equation (1.73) is written as follows

$$a_l \frac{\partial l_l}{\partial t} + a_l u_k \frac{\partial l_l}{\partial x_k} - u_l a_l - a_l \frac{\partial \overline{l_l u_k}}{\partial x_k} = D_u \frac{\partial l_l}{\partial x_k^2} a_l. \qquad (1.74)$$

In (1.74), we neglect the change in the parameter a_j as small compared to the change of the random parameter l_j.

Let us now apply the Friedman-Keller method of statistical turbulence theory [19]. To this end, we write Equation (1.71) at another point $\vec{x}'$, multiply it by $a_j l_j$ and add to Equation (1.74) after multiplying the latter by u'_i (the velocity at point x').

Averaging the sum, we find

$$a_j \frac{\overline{\partial l_j u_i}}{\partial t} + a_j \frac{\overline{\partial l_j u_i' u_k}}{\partial x_k} - \overline{u_i u_j a_j} + \frac{\overline{\partial u_i u_k' l_j a_j}}{\partial x_k} =$$

$$= D_u \frac{\overline{\partial^2 l_j u_i' a_j}}{\partial x_k^2} + \nu \frac{\overline{\partial^2 u_i' l_j}}{\partial x_k^{12}} a_j - \frac{1}{\varrho} \frac{\overline{\partial \bar{p} l_j}}{\partial x_i} a_j.$$

Applying (1.68), we assume

$$\overline{u_i l_j} \simeq \overline{u_j u_i} \bar{T}(t) = R_{ji}(\vec{r}, t) \bar{T}(t);$$

$$\overline{u_k u_i' l_j} \simeq \overline{u_k u_j u_i'} \bar{T}(t) = \Pi_{jki}(\vec{r}, t) \bar{T}(t),$$

where $\vec{r}$ is the radius vector drawn from the point $\vec{x}$ to the point $\vec{x}' (\vec{r} = \vec{x}' - \vec{x})$.

Recognizing that $\vec{r} = \vec{x}' - \vec{x}$ and, consequently,

$$\frac{\partial}{\partial x_i} = -\frac{\partial}{\partial r_i}, \quad \frac{\partial}{\partial x_i'} = \frac{\partial}{\partial r_i},$$

we find

$$a_j \frac{\partial R_{ji} \bar{T}}{\partial t} - \bar{T} a_j \frac{\partial \Pi_{jki}}{\partial r_k} - R_{ji} a_j + \bar{T} a_j \frac{\partial \Pi_{iki}(-r)}{\partial r_k} = \bar{T}(D_u + \nu) a_j \frac{\partial R_{ji}}{\partial r_k^2}. \qquad (1.75)$$

The term expressing the correlation of the pressure with l_j has been put equal to zero, since it is assumed that the vector of l_j is proportional to the velocity u_j and that the turbulence in the decay traces is practically homogeneous and isotropic.

The momentum equation (1.71) can be used by the same Friedman-Keller method to obtain the following dynamic equation for the correlation moments (see [19]):

$$\frac{\partial R_{jl}}{\partial t} = \frac{\partial}{\partial r_k}\left[\Pi_{jkl} - \Pi_{lkj}(-r)\right] + 2\nu\frac{\partial^2}{\partial r_k^2}R_{jl}.$$

Transforming (1.75) with the dynamics equation, we find

$$a_j R_{jl}\frac{\partial \bar{T}}{\partial t} + 2\bar{T}a_j\nu\frac{\partial}{\partial r_k^2}R_{jl} = a_j R_{jl} + \bar{T}(D_u + \nu)a_j\frac{\partial R_{jl}}{\partial r_k^2}.$$

or

$$a_j R_{jl}\frac{\partial \bar{T}}{\partial t} = a_j R_{jl} + (D_u - \nu)\bar{T}a_j\frac{\partial R_{jl}}{\partial r_k}.$$

We recognize further that only $a_n \neq 0$ in a plane-parallel mixing layer ($\vec{n}$ is the unit vector of the normal to the surface of the plane-parallel mixing layer, $u_n = \frac{\partial \bar{\varepsilon}}{\partial n}$)

Then

$$R_{nl}\frac{\partial \bar{T}}{\partial t} = R_{nl} + (D_u - \nu)\bar{T}\left(\frac{\partial R_{nl}}{\partial r_k^2}\right) \tag{1.76}$$

where, according to a relation known from the theory of isotropic turbulence [19],

$$R_{nl} = \frac{f-g}{r^2}r_l r_n n_k + g n_l.$$

Here f(r) is the longitudinal and g(r) the transverse coefficient of correlation for the velocity field at two points separated by a distance r.

In virtue of the limitations imposed by Conditions (1.67) and (1.68), the equation derived above is valid only in the neighborhood of r = 0.

In particular, substituting the expansions of the longitudinal and transverse correlation coefficients in the vicinity of zero:

$$f \simeq 1 - \frac{r^2}{2\lambda^2}, \quad g \simeq 1 - \frac{r^2}{\lambda^2}$$

where $\lambda^2 = -(1/f''_0)$ is the dissipation scale [19], we obtain, accurate to terms of higher orders of smallness

$$R_{nl} \simeq n_l; \quad \frac{\partial R_{nl}}{\partial r_k} \simeq \frac{\partial^2}{\partial r_k^2}\left(\frac{r_l r_k n_k}{2\lambda^2} + g n_l\right) \simeq -\frac{5 n_l}{\lambda^2},$$

since

$$\frac{\partial^2}{\partial r_k^2}\left(\frac{r_l r_k n_k}{2\lambda^2}\right) = \frac{n_l}{\lambda^2}; \quad \frac{\partial}{\partial r_k^2}\left(1 - \frac{r^2}{\lambda^2}\right)n_l = -\frac{5 n_l}{\lambda^2}.$$

Substituting these expressions into (1.76), we arrive at the equation sought for $\overline{T}$:

$$\frac{\partial \overline{T}}{\partial t} = 1 - 5\frac{D_M - \nu}{\lambda^2}\overline{T}. \tag{1.77}$$

It is evident from (1.77) that when $\lambda =$ const, the approximation (1.68) is accurate enough for all times, provided that $\text{Pr} = \nu/D_M \ll 1$. When $D \le \nu$, Condition (1.68) remains valid for $t < \frac{l_l^2}{s'}$, where l is the integral Lagrangian turbulence scale.

For $\lambda =$ const and $D \gg \nu$, the "mixing time" scale T becomes constant after a certain time and equal to

$$T = \frac{\lambda^2}{5(D_M - \nu)}.$$

The diffusion equations and the coefficient of microturbulent gradient diffusion will then have the form

$$\frac{\partial \overline{c}}{\partial t} = \left[D_{\text{M}} + \frac{u_n^2 \lambda^2}{5(D_{\text{M}} - v)} \right] \frac{\partial^2 \overline{c}}{\partial n^2} \sim D_{\text{M}} \left(1 + \frac{Re_T Pr^2}{5(1 - Pr)} \right) \frac{\partial^2 \overline{c}}{\partial n^2},$$

$$D_{\text{MT}} = \frac{u_n^2 \lambda^2}{D_{\text{M}} - v}. \tag{1.78}$$

where n is the coordinate along the normal to the one-dimensional mixing zone, $Pr = v/D_M$ is the laminar Prandtl number, and $Re_T = ul/v$ is the turbulent Reynolds number determined from the turbulent velocity u and the integral turbulence scale l, the latter defined, in turn, by the relation

$$\lambda = \sqrt{\frac{\overline{vl}}{u}}.$$

In the case of turbulence that decays in accordance with the law $u^2 = a(t - t_0)^{-n}$, the dissipation scale increases according to the law [19]

$$\lambda^2 = \frac{10v(t - t_0)}{n}. \tag{1.79}$$

Here the scale T and the microturbulent diffusion coefficient increase as follows according to (1.77) and (1.79):

$$T = \frac{t - t_0}{1 + \frac{n(D_M - v)}{2v}}, \quad D_{\text{MT}} = u^2 T = \frac{a(t - t_0)^{1-n}}{1 + \frac{n(D_M - v)}{2v}}. \tag{1.80}$$

In particular, for n = 1

$$D_{\text{MT}} = \frac{2a Pr}{1 + Pr}. \tag{1.81}$$

It is clear from (1.81) that, in the case of decaying turbulence, the approximation (1.68) is quite adequate for description of the microturbulent gradient diffusion coefficient D_{MT}.

Since a is approximately equal to $u\ell$ — the constant in the linear turbulence-decay law [19] — the equation takes the following form in this case:

$$\frac{\partial \bar{c}}{\partial t} = D_{\text{M}}\left(1 - \frac{2\,Re_\tau Pr^2}{1+Pr}\right)\frac{\partial^2 \bar{c}}{\partial n^2} = D_{\text{MT}}\frac{\partial^2 \bar{c}}{\partial n^2}. \qquad (1.82)$$

The values of D_{MT} in (1.78) and (1.82) are defined accurate to a coefficient on the order of unity, which we have introduced into the corresponding Reynolds number.

Both of the expressions for D_{MT} indicate that the microturbulent diffusion coefficient is physically equivalent to the molecular diffusion coefficient (simply proportional to it), but much larger in absolute magnitude than D_M — by a factor of about $Pr^2 Re_T$; for example, when $Pr = 0.7$, $D_{MT} \approx 0.6 Re_T$.

The results obtained indicate the possibility of describing gradient diffusion with the differential equation of diffusion, at least for times sufficiently large that the concentration fluctuations in the decay trace have become sufficiently small.

3.   Equations of Momentum Conservation in the "Black and White" Mixing Model

It is seen from examination of the models (§1) that momentum exchange between the two streams is of nonlocal nature. On the one hand, therefore, we should expect the momentum distribution in the layer to be described accurate to a single scale for the entire layer, but, on the other hand, it would be difficult to expect the turbulent mass and momentum fluxes in the familiar Reynolds equation to depend only on the local average gradients of these quantities, or on any function of many local variables, no matter how complex. This difficulty is circumvented to a certain degree for turbulent mass transport by introducing an equation of turbulent diffusion with a single scale σ_T that incorporates other more subtle features: the degree of mixing

homogeneity, inhomogeneity of turbulence along the stream, etc. Here the question as to the agreement of the solution of this equation with experiment remains open as before, and will therefore be examined in the next chapter.

The "diffusion approximation" of the turbulent momentum exchange is even more doubtful, both as a result of the dependence of the rate of momentum transport on the magnitude of the momentum transported and as a result of the clearly nonlocal nature of momentum transfer by pressure forces. However, experience has shown that for free-layer problems, the "diffusion approximation" with a single scale σ_V is also found to be quite adequate to obtain elementary solutions in a number of dynamic problems.

Let us formulate the corresponding equations of momentum transport for the first and second gases.

The change in the $j^{\underline{th}}$ momentum component of the first gas in a unit volume per unit of time equals

$$\frac{\partial}{\partial t} (c_1 u_j).$$

This change is governed: (a) by the momentum flux across the boundary of the volume due to mass transport; (b) the momentum flux associated with the action of the average static-pressure force gradients; (c) by the effect of volume interaction forces between the first and second gases.

The averaged momentum-conservation law takes the form

$$\frac{\partial}{\partial t} (\overline{c_1 u_j}) = -\frac{\partial}{\partial x_i} (\overline{c_1 u_i u_j}) - P_1 \frac{\partial \overline{p}}{\partial x_j} + F_{1j}, \qquad (1.83)$$

where F_{1j} is the force exerted by the second gas in the $j^{\underline{th}}$ direction on a unit length of the first gas.

Substituting the expressions $c_1 = \bar{c}_1 + c_1'; u_i = \bar{u}_i + u_i'; z_j = \bar{u}_j + u_j'$, into the correlation moment $\overline{c_1 u_i u_j}$, we find

$$\overline{c_1 u_j u_i} = \bar{c}_1 \bar{u}_j \bar{u}_i + \overline{c_1' u_i' u_j'} + \overline{c_1' u_i \bar{u}_j} + \overline{c_1' u_i' \bar{u}_i} + \overline{c_1 u_i u_j}.$$

In jet flows, there exists a direction in which the parameters vary slowly compared to their rates of change in other directions. If this is the $j^{\underline{th}}$ direction, the terms $\overline{c_1' u_j' \bar{u}_i}$ and $\overline{c_1' \bar{u} u_j'}$ can be neglected in the above expression for the correlation moment.

We transform the other terms with the aid of the Boussinesq-Prandtl hypothesis. That is to say, we assume that

$$\overline{c_1' u_{i1}'} = -D_T \frac{\partial \bar{c}_1}{\partial x_i}, \quad \text{where } \bar{c}_1 = \varrho_{01} P_1. \tag{1.84}$$

$$\overline{u_{i1}' u_{j1}'} = D_V \left(\frac{\partial \bar{u}_j}{\partial x_i} + \frac{\partial \bar{u}_i}{\partial x_j} \right) \simeq D_V \frac{\partial \bar{u}_j}{\partial x_i}, \tag{1.85}$$

where D_T and D_V are the turbulent diffusion coefficients for mass and velocity; the possible anisotropy of the diffusion coefficients is neglected for simplicity.

Thus:

$$\overline{c_1 u_i u_j} = \bar{c}_1 \bar{u}_i \bar{u}_j + \bar{\varrho} D_V \frac{\partial \bar{u}_j}{\partial x_i} + D_T u_j \frac{\partial \bar{c}_1}{\partial x_i}. \tag{1.86}$$

Substituting (1.86) into (1.83), we find the final form of the momentum-transport equation for the first gas:

$$\frac{\partial}{\partial x_i} (\bar{c}_1 \bar{u}_i \bar{u}_j) = \frac{\partial}{\partial x_i} \left(D_V \bar{c}_1 \frac{\partial \bar{u}_j}{\partial x_i} \right) + \frac{\partial}{\partial x_i} \left(D_T u_j \frac{\partial \bar{c}_1}{\partial x_i} \right) - P_1 \frac{\partial \bar{p}}{\partial x_j} + F_{1j}; \tag{1.87}$$
$$(\bar{c}_1 = \varrho_{01} P_1).$$

The time derivative is absent because of the assumed stationary nature of the flow. The equation for the second gas is derived in exactly the same way:

$$\frac{\partial}{\partial x_i}(\bar{\varrho}_2 \bar{u}_i \bar{u}_j) = \frac{\partial}{\partial x_i}\left(D_1 \bar{\varrho}_2 \frac{\partial \bar{u}_j}{\partial x_i}\right) + \frac{\partial}{\partial x_i}\left(D_1 u_j \frac{\partial \bar{\varrho}_2}{\partial x_i}\right) - P_2 \frac{\partial \bar{p}}{\partial x_j} + F_{2j}:$$

$$(\bar{\varrho}_2 = \varrho_{02} P_2).$$

(1.88)

Adding these equations with recognition of the fact that

$$F_{1j} + F_{2j} = 0,$$

we obtain the equation of average momentum transport:

$$\frac{\partial}{\partial x_i}(\bar{\varrho}\bar{u}_i \bar{u}_j) = \frac{\partial}{\partial x_i}\left(D_1 \bar{\varrho} \frac{\partial \bar{u}_j}{\partial x_i}\right) + \frac{\partial}{\partial x_i}\left(D_1 \bar{u}_j \frac{\partial \bar{\varrho}}{\partial x_i}\right) - \frac{\partial \bar{p}}{\partial x_j}.$$

(1.89)

For equal densities of the mixing gases, we arrive at an equation describing the diffusion of average velocity $\bar{u}_j$:

$$\frac{\partial}{\partial x_i}(\bar{u}_i \bar{u}_j) = \frac{\partial}{\partial x_i}\left(D_V \frac{\partial \bar{u}_j}{\partial x_i}\right) - \frac{1}{\varrho} \frac{\partial \bar{p}}{\partial x_j}.$$

If the densities differ, the velocity transport equation is more complex in form. To derive it, we divide Equation (1.87) by ϱ_{01} and Equation (1.89) by ϱ_{02} and add them:

$$\frac{\partial}{\partial x_i}(\bar{u}_i \bar{u}_j) = \frac{\partial}{\partial x_i}\left(D_V \frac{\partial \bar{u}_j}{\partial x_i}\right) + \frac{F_{1j}}{\varrho_{01}} + \frac{F_{2j}}{\varrho_{02}} - \frac{\partial \bar{p}}{\partial x_j}\left(\frac{P_1}{\varrho_{01}} + \frac{P_2}{\varrho_{02}}\right).$$

(1.90)

Thus, the velocity distribution is also described in this case by a diffusion equation, but with an additional term on the right that can be interpreted as a velocity source (or sink) governed by the volume forces.

Let us turn to determination of an expression for the volume forces that figure in the above equations.

For this purpose, we transform (1.87) with the relation

$$\frac{\partial}{\partial x_i}(\bar{\rho}_1\bar{u}_i\bar{u}_j) = \bar{u}_j\frac{\partial\bar{\rho}_1\bar{u}_i}{\partial x_i} + \bar{\rho}_1\frac{\partial\bar{u}_i\bar{u}_j}{\partial x_i} = \bar{u}_j\frac{\partial}{\partial x_i}D_\tau\frac{\partial\bar{\rho}_1}{\partial x_i} + \bar{\rho}_1\frac{\partial\bar{u}_i\bar{u}_j}{\partial x_i} \; .$$

As a result, we obtain

$$\frac{\partial\bar{u}_i\bar{u}_j}{\partial x_i} = \frac{\bar{u}_j}{\bar{\rho}_1}\frac{\partial}{\partial x_i}D_\tau\frac{\partial\bar{u}_j}{\partial x_i} + D_V\frac{\partial\bar{u}_j}{\partial x_i}\frac{\partial\ln\rho_1}{\partial x_i} + D_\tau\frac{\partial\bar{u}_j}{\partial x_i}\frac{\partial\ln P_1}{\partial x_i} - \frac{1}{\rho_{01}}\frac{\partial p}{\partial x_j} + \frac{F_{1j}}{\rho_{01}P_1} \; .$$

Exactly the same equation is established for the second gas.
Subtracting one equation from the other and substituting $F_{2j}=-F_{1j}$, we
find the sought expression for F_{1j}:

$$F_{1j} = -\frac{\rho_{01}\rho_{02}}{\bar{\rho}}(D_V+D_\tau)\frac{\partial\bar{u}_j}{\partial x_i}\frac{\partial P_1}{\partial x_i} - \frac{\rho_{01}-\rho_{02}}{\bar{\rho}}P_1P_2\frac{\partial p}{\partial x_j} \; . \tag{1.91}$$

Similarly:

$$F_{2j} = \frac{\rho_{01}\rho_{02}}{\bar{\rho}}(D_V+D_\tau)\frac{\partial\bar{u}_j}{\partial x_i}\frac{\partial P_1}{\partial x_i} + \frac{\rho_{01}-\rho_{02}}{\bar{\rho}}P_1P_2\frac{\partial p}{\partial x_j} \; . \tag{1.92}$$

The second term in the expression for the volume forces differs
from zero only when the densities of the mixing gases differ. It
results from the necessity of equalizing the accelerations of volumes
with different densities in the pressure-gradient field.

Let us illustrate this with reference to the simple example of
flow of a homogeneous "black and white" mixture in a one-dimensional
channel. Assuming that the sample-averaged velocities are not strati-
fied, the equation of motion takes the form*

$$\bar{\rho}\frac{d\bar{u}}{dt} = \frac{\partial\bar{p}}{\partial x} \; .$$

---

*The aerodynamic drag of the elementary volumes in motion relative
to one another is assumed to be so large that $\bar{u}_{1i}=\bar{u}_{2i}$.

Consequently, the average acceleration of the gases will be

$$a_1 = a_2 = \frac{1}{\varrho}\frac{\partial \bar{p}}{\partial x}.$$

On the other hand, we may write Newton's second law for each of the gases in the form

$$\varrho_{01} P_1 a = F_1 - P_1 \frac{\partial p}{\partial x}, \quad \varrho_{02} P_2 a = F_2 - P_2 \frac{\partial p}{\partial x}.$$

In this case, P_1 and P_2 denote the fractions of the lateral-face areas of the unit elementary volumes acted upon by the pressure p. From this we obtain

$$F_1 = -\frac{\varrho_{01} - \varrho_{02}}{\varrho} P_1 P_2 \frac{\partial p}{\partial x}, \quad F_2 = \frac{\varrho_{01} - \varrho_{02}}{\varrho} P_1 P_2 \frac{\partial p}{\partial x},$$

i.e., the second term on the right in (1.91).

The first term corresponds to the for e necessary to equalize the velocitie. of volumes of different classes in the presence of an average velocity gradient.

Substituting the expressions for the volume forces (1.91) into (1.90), we find the average-velocity transport equation in the form

$$\frac{\partial}{\partial x_i}(\bar{u}_i \bar{u}_j) = \frac{\partial}{\partial x_i}\left(D_V \frac{\partial u_j}{\partial x_i}\right) - \frac{1}{\varrho}\frac{\partial p}{\partial x_j} + (D_T + D_V)\frac{\varrho_{01} - \varrho_{02}}{\varrho}\frac{\partial u_j}{\partial x_i}\frac{\partial P_1}{\partial x_j}. \qquad (1.93)$$

The equation System (1.65), (1.93) can be used to find the density and velocity distributions if the values of the diffusion coefficients D_T and D_V are known. A possible physical interpretation of these parameters on the basis of a vortex model of the mixing layer was given in subsection 1 of §1.

4.   Integral Form of Conservation Laws

It is found convenient to base the development of engineering methods for jet calculations on the integral form of the mass and momentum conservation laws, which can be obtained either by integrating the differential transport equations given in subsection 3 of §2, or by direct analysis of the balance of the fluxes across an appropriately chosen control surface.

The integral conservation laws are also convenient in that questions as to the "differentialness" of the closed Reynolds equation, the accuracy of the various approximations of the these equations, etc., are not particularly relevant for them.

Let us consider the following three most typical types of flows: the mixing layer, the plane-parallel jet, and the axisymmetric jet.

For the mixing layer and plane-parallel jet, integration of Equation (1.65) over the transverse coordinate y yields (the flow is assumed stationary)

$$\frac{d}{dx} \int_{-\infty}^{\infty} \bar{u} P_s \, dy = 0, \tag{1.94}$$

where $\bar{u}$ is the longitudinal velocity (along the x axis).

In the axisymmetric case, the law of mass-flux conservation for the jet is

$$\frac{d}{dx} \int_{0}^{\infty} \bar{u} P_s r \, dr = 0$$

or

$$\int_{0}^{\infty} \bar{u} P_s r \, dr = V_s \frac{a_0^2}{2}. \tag{1.95}$$

We shall henceforth omit the averaging symbol.

The integral law of momentum-flux conservation proceeds similarly from (1.89). Here, however, this law will be derived by writing the balance of the momentum fluxes across an appropriate control surface.

Here we shall confine ourselves to the simplest case of free turbulent flows with zero pressure gradient.

Let us write the balance of the fluxes across control surface abcd for a mixing layer (see Figure 2.2). The distance y_0 from the x axis to the planes bc and ad is assumed to be so large that the longitudinal velocity along bc equals V_1, while that along ad equals V_2.

The momentum flux in the longitudinal direction across the surface ab is

$$S_{ab} = \varrho_1 V_1^2 y_0 + \varrho_2 V_2^2 y_0.$$

The momentum flux across surface cd is

$$S_{cd} = \int_{-y_0}^{y_0} \varrho u^2 \, dy.$$

The difference between S_{cd} and S_{ab} is equal to the momentum flux flowing into the elementary volume across surfaces bc and ad.

It is assumed that the transverse velocity equals zero or. one of the surfaces (for example, ad). (It may be assumed for the sake of concreteness that ad coincides with the symmetry plane of the plane-parallel jet.) Then the mass flux into the volume is

$$\int_{cd} \varrho u \, dy - \varrho_2 V_2 y_0 - \varrho_1 V_1 y_0 = \int_{cd} \varrho u \, dy - y_0 (\varrho_2 V_2 + \varrho_1 V_1).$$

This flux carries a momentum V_1 with it per unit of mass.

Hence the flux balance takes the form

$$\int_{-y_0}^{y_2} \varrho u^2 dy - V_1\left[\int_{-y_0}^{y_2} \varrho u\, dy - y_0(\varrho_2 V_2 + \varrho_1 V_1)\right] = \varrho_1 V_1^2 y_0 + \varrho_2 V_2^2 y_0.$$

We rewrite the balance condition in slightly different form:

$$\int_{y_0}^{0} (\varrho u^2 - \varrho u V_1 - \varrho_2 V_2^2 + \varrho_2 V_2 V_1) dy + \int_{0}^{\infty} (\varrho u^2 - \varrho u V_1) dy = 0.$$

Since the chosen y_0 is quite large, the law of momentum-flux conservation for the mixing layer assumes the following final form:

$$\int_{-\infty}^{0} (\varrho u^2 - \varrho u V_1 - \varrho_2 V_2^2 + \varrho_2 V_2 V_1) dy + \int_{0}^{\infty} (\varrho u^2 - \varrho u V_1) dy = 0. \qquad (1.96)$$

The laws of momentum conservation can be obtained in exactly the same way for a plane-parallel jet:

$$\int_{0}^{\infty} \varrho u (u - V_1) dy = \varrho_2 V_2 (V_2 - V_1) a_0 \qquad (1.97)$$

and for an axisymmetric jet

$$\int_{0}^{\infty} \varrho u (u - V_1) r dr = \varrho_2 V_2 \frac{a_0^2}{2}. \qquad (1.98)$$

We have written the momentum-flux balance without consideration of the fluctuation terms. It is assumed that the errors incurred by so doing are insignificant, especially when it is remembered that the fluctuation-term difference appears in the next approximation [20].

It is not possible to write the energy conservation equation formally in "diffusion form," since it includes not only the second moments, which admit of such approximation with certain reservations, but also the third moments, expression of which, in terms of the local average-parameter gradients, results in the appearance of new unknown

empirical "constants." The integral form of the conservation law is less sensitive to these "constants," but it must still take account of the total losses of total pressure as a result of turbulent mixing.

On the basis of the vortex-model concepts set forth in subsection 1 of §1, it is possible, in principle, to write a differential (or integral) equation that determines the average total pressure losses at an arbitrary point of the mixing layer, expressed in terms of the scale l or σ and in terms of the loss coefficient for the elementary event — the formation and decay of a vortex. An example of such an integral equation for the irreversible mixing losses was given in subsection 1 of §1 for a plane-parallel layer.

At the present time, the simplest approximation for subsonic jets, and one that is apparently sufficiently accurate, will be constant entropy of the mixing volumes not only outside of the mixing layer, but also at each point in it. In this case, the average entropy and its fluctuations are determined by the same equations as the temperature. If diffusional or homogeneous combustion takes place during mixing, the entropy jumps by a certain increment on a combustion front that is randomly distributed in the boundary layer (see Chapter IV).

CHAPTER II

COMPARISON OF THE DIFFUSION THEORY OF TURBULENT FLOWS WITH EXPERIMENTAL DATA

§1. Measurements of Average Parameters in Turbulent Mixing Zones

At this time, the bulk of experimental material pertaining to turbulent jets has been obtained with the Pitot tube, gas analysis, and the thermocouple. These methods of measurement have long response times and yield certain averaged values of the stream parameters. It is therefore appropriate to consider precisely how the average values are measured and how they relate to the statistical average values of the stream parameters discussed in the preceding chapter.

1.   Pitot-Tube Measurements

It is customary to assume that the difference between the total and static pressures, which is measured by the Pitot tube in a stream with velocity and density fluctuations, yields the time-averaged value of the velocity head $q = \frac{\overline{\rho u^2}}{2}$.

Since

$$\overline{\varrho u^2} = \overline{\varrho}\overline{u}^2 + \overline{\varrho}\overline{u'^2} + \overline{u}\overline{\varrho'u'} + \overline{\varrho'u'^2},$$ (2.1)

we may, assuming the discontinuity of the sampled longitudinal velocities (and, consequently, the correlation moment $\overline{\varrho'u'}$) to be small, write the following, accurate to terms of order $\varepsilon^2 = \dfrac{\overline{u'^2}}{\overline{u}^2}$

$$\overline{\varrho u^2} = \overline{\varrho}\overline{u}^2.$$ (2.1a)

Here it is necessary to clarify experimentally whether averaging with large density and velocity fluctuations is identical to statistical averaging.

Relation (2.1a) has been verified experimentally on an open inverted-cone turbulent flame jet behind a burner in an open stream of homogeneous mixture. In this case, since the average velocity is practically constant, the field of the measured velocity heads is similar to the average-density field, i.e.,

$$q(y) = q_1 \frac{\overline{\varrho}(y)}{\varrho_1} = q_2 \frac{\overline{\varrho}(y)}{\varrho_2}\,,$$ (2.2)

where q_1, ϱ_1 are the velocity head and density of the fresh mixture and q_2, ϱ_2 are the velocity head and density of the combustion products.

Constancy of the average velocities was tested, in particular, against the condition

$$\frac{q_1}{q_2} = \frac{\varrho_1}{\varrho_2} = \frac{T_2}{T_1}\,,$$ (2.3)

where the temperature ratio was determined from thermocouple readings and gas analysis.

Since it has been shown by experiment [92] that the thickness of the flame front surface is much smaller than the total thickness of the combustion zone, which is determined by the scale σ (see Chapter IV, §4), the average density is determined from the relations of the "black and white" mixing model.

In this case, using the probability of appearance of burned mixture P_2, relation (2.3) can be written

$$P_2(u) = \frac{1 - \dfrac{q(u)}{q_1}}{\dfrac{n-1}{n}} = \frac{q_1}{q_1 - q_2}\, \frac{q(u)}{q_1} .$$

(2.4)

If the Pitot tube provides correct averaging, the value of P_2 from (2.4) should agree with direct measurements of P_2. Direct measurements made by N. V. Kokushkin [92] with a low-lag resistance thermometer agreed fully with calculations according to (2.4).

Relation (2.2) is used much more frequently to calculate $\bar{u}$, with $\bar{\rho}$ determined from the average temperature $\bar{T}$, from the equation of state written in the form $\rho\bar{T} = \rho_1 T_1 = \rho_2 T_2$ and, consequently, the average velocity is determined as

$$\bar{u} = \sqrt{\frac{2q\bar{T}}{\rho_1 T_1}}$$

(2.5)

instead of

$$\bar{u}_0 = \sqrt{\frac{2q}{\rho_1 T_1 \left(\dfrac{1}{T}\right)}} ,$$

(2.6)

something that cannot be done in the presence of temperature and density fluctuations because $1/\bar{T} \neq (\bar{1}/T)$.

In a stream with fluctuations of maximum amplitude $(T_2 - T_1)$ neglect of this condition results in the largest error (as compared with all other types of fluctuations). The ratio of the velocity obtained from (2.5) to the true velocity $\bar{u}_0$ equals

$$\frac{\bar{u}}{\bar{u}_0} = \sqrt{\frac{\rho\bar{T}}{\rho_1 T_1}} .$$

(2.7)
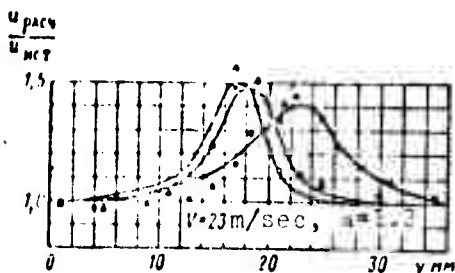
Figure 2.1. Distribution of relative error in average velocity measured with Pitot tube in an open flame jet (data of A. I. Lushpa)

● ┈┈ experiment;

— theoretical curve.

In the range in which temperature and density fluctuations are absent, $\bar{u}/\bar{u}_0 = 1$. Using the relations of Chapter I, §1 to determine $\bar{\rho}$ and $\bar{T}$, we obtain

$$\frac{\bar{u}}{u_0} = \sqrt{1 + \left(\frac{T_2}{T_1} + \frac{T_1}{T_2} - 2\right) P_2 P_1}, \quad (2.8)$$

where $P_1 = 1 - P_2$ is the probability of appearance of cold (fresh) mixture. Relation (2.8) was used to analyze experimental data on $\bar{u}$ for a flame jet in an open stream, including detailed curves of $\bar{u}(y)$ for various T_2/T_1 according to A. I. Lushpa [38], whose observed values of the average velocity in the combustion zone were much higher (up to 49%) (Figure 2.1). This overstatement is explained not only by the use of Formula (2.5), but also by the fact that the temperature distribution was determined with thermocouples, which give average-temperature values that are somewhat higher than the statistical average temperatures (see below).

Comparison of the calculations by Formula (2.8) with Lushpa's results indicates rather good agreement between the calculated hypothetical velocity overstatement and the experimental data; the maximum value of $\bar{u}/\bar{u}_0$ is reached at the point $P_2 = P_1 = 0.5$. At $T_2/T_1 = 6$, the theoretical maximum error reaches 43%, i.e., it is slightly smaller than in the experiments. When values of P_1 calculated from temperature profiles obtained directly from Lushpa's experiment are used in Formula (2.8), the experimental points fall directly on the theoretical curve. This agreement of theory with experiment indicates that Formula (2.8) must be used in calculating velocities from Pitot tube readings, and also that combustion in a homogeneous turbulent flame jet closely resembles surface combustion (the model of "black and white" mixing).

Thus, the presence of longitudinal-velocity "spikes" in the cone of an open turbulent flame jet behind a point burner does not reflect the true state of the stream. These "spikes" appear as a result of use of the incorrect formula (2.5), and their size is increased further owing to a certain overstatement of the average temperature $\bar{T}$ when measurements are made with thermocouples.

Formula (2.5) will also produce such errors in measurements made in turbulent boundary layers: the velocity profile obtained with (2.5) will be fuller than the true one.

In processing Pitot-tube readings, therefore, we may use the formula

$$q = \frac{\overline{\rho}\overline{u^2}}{2} .$$ (2.9)

But then it is necessary to write $\bar{\rho} = \rho_1 T_1 \cdot \overline{1/T}$ instead of $\bar{\rho} = \rho_1 T_1/\bar{T}$.

We note also that when the densities of the jet and the stream differ sharply (n > 10), Relation (2.9) may not be accurate enough without consideration of the correlation terms (2.1) [82].

2. The Thermocouple and the Resistance Thermometer

The dimensionless average temperature profile measured with a thermocouple differs from the profile of the true average temperatures by an amount on the order of ε^2, since, according to [113], the difference between them is proportional to $\frac{\overline{u'T'}}{u(T_2 - T_1)}$. Other error sources are sometimes found to be significant. In a turbulent flame, for example, there is yet another error source in addition to dissipation of heat at the ends and radiation losses. Measurements of the temperature fluctuations at the junction of a thermocouple placed in the variable-temperature zone of a turbulent flame jet showed that much slower cooling of the junction is observed, in many cases, in a stream of mixture that is capable of chemical reactions rather than in a stream of air (2.4). It is not known whether this is a result of action of the

junction and the stagnation zone behind it as a flame stabilizer or a result of the chemical reactions occurring at the heated surface of the junction. This effect depends strongly on the conditions of the experiment: the dimensions of the junction and the average temperatures and velocities of the stream. It thus happens that the average junction temperature is found to be somewhat higher than the average temperature at the particular point in the flame. Under ordinary conditions, this error is more significant than radiation and other losses. The effect was first recorded in [114]. Reference [92] describes a method of measuring average temperatures for the "black and white" mixing model on the basis of temperature-fluctuation oscillograms obtained with a low-lag resistance thermometer.

The probabilities P_2 determined in this way with a resistance thermometer in an open turbulent flame jet agree closely with the P_2 functions measured with the Pitot tube. This also suggests the possibility of using a low-lag resistance thermometer and Pitot tube for measurements in streams with temperature fluctuations.

Because of the important role of the concept of the probabilities of appearance of the substances to be mixed in the turbulent-mixing theory set forth here, the question arises as to the possibility of measuring them directly. For the "black and white" mixing mechanism — mixing of gas with liquid, of fresh mixture with combustion products in a homogeneous flame jet, etc. — determination of the probability of appearance of one of the initial substances reduces to the combination of the relative stay time of the particular substance at the sensor (low-lag resistance thermometer, thermocouple, cr any other initial-medium indicator). In the general case of gradient and convective diffusion, determination of the probability of appearance of a volume or mass fraction of an initial substance is a more complex problem.

The most general approach to its solution consists in the introduction of some indicator property that can be used to tag a substance of a given species without affecting its physical properties. For example, temperature can be used as such a property when the jet is

weakly heated $(n = T_2/T_1 \simeq 1)$. In fact, we obtain from (1.54)

$$\frac{\overline{T} - T_1}{T_2 - T_1} = \int \frac{P_{2e}}{nP_{1e} + P_{2e}} p(\vec{r}, \vec{r}_{a}) dr_{a} \simeq \int P_{2e} p(\vec{r}, \vec{r}_{a}) dr_{a} = P_{2}.$$

Thus, measurement of the average temperature is equivalent in this case to measurement of the observation probability P_2.

3. Gas Analysis

We indicated above that when two streams of different gases with equal temperatures are mixed, the probability profile coincides with the volume-concentration profile. Consequently, determination of the probability profiles can be reduced to measurement of a volume concentration by gas analysis methods.

In this context, it will be helpful to review the question as to interpretation of experimental results obtained by these methods.

Let us first discuss the case of equal temperatures of the gases being mixed (whose densities may be different). The gaseous mixture is usually tapped with a special probe and delivered through a sampling tube to a tank. Generally speaking, the tip of the probe introduces distortion into the stream; in particular, heavy and light gas volumes may be separated at the entrance of the sampling system. Separation can be avoided by using specially shaped (conical) probe tips [48], and we shall therefore not dwell further on this effect. Obviously, if the tubing is long enough and the sampling time large enough, a constant flow velocity will eventually be established in the sampling system. Hence the volume flow rate of the gas per unit time is constant.*

------

*This hypothesis will be invalid if the temperatures of different portions of the gas differ. In fact, the volumes of the portions of gas (and, consequently, their velocity in the sampling system) will vary in this case as a result of heating or cooling.

Thus, the total number of molecules of the first (n_1) and second (n_2) species arriving in the tank per unit of time is constant:

$$n_0 = n_1 + n_2.$$

The volume concentration in the tank is

$$c = \frac{\bar{n}_2}{\bar{n}_1 + \bar{n}_2} = \frac{\bar{n}_2}{n_0} = P_2.$$

The concentration by weight in the tank differs from the average weight concentration $\bar{g}_2$ in the stream, and equals

$$g_p = \frac{\mu_2 \bar{n}_2}{\mu_1 \bar{n}_1 + \mu_2 \bar{n}_2} = \frac{\bar{\varrho}_2}{\bar{\varrho}_1 + \bar{\varrho}_2},$$

while

$$\bar{g}_2 = \overline{\left(\frac{\varrho_2}{\varrho_1 + \varrho_2}\right)}.$$

where ϱ_1 and ϱ_2 are the partial densities of the two gases.

The difference between $\bar{g}_2$ and g_{tk} may be substantial. In the case of "black and white" mixing, for example,

$$\bar{g}_2 = P_2, \quad g_p = \frac{P_2}{nP_1 + P_2} \quad \left(n = \frac{\varrho_{01}}{\varrho_{02}} = \frac{\mu_1}{\mu_2}\right).$$

Incidentally, it follows from this that $\bar{g}_2 > g_{tk}$ when $\mu_1 > \mu_2$, and, conversely, that $\bar{g}_2 < g_{tk}$ when $\mu_2 > \mu_1$.

Thus, gas analysis can be used to measure the average volume concentration itself. The relation of this concentration to the average concentration by weight is established with the aid of the following considerations. The instantaneous value of the weight concentration takes the form

$$g_1 = \bar{g}_1 + g_1' = \frac{\mu_1 n_1}{\mu_1 n_1 + \mu_2 n_2}.$$

Let us rewrite this relation as follows:

$$\mu_1 n_1 \bar{c}_1 + \mu_2 n_2 \bar{g}_1 + \mu_1 n_1 g_1' + \mu_2 n_2 g_1' = \mu_1 n_1.$$

We now present n_1 and n_2 in the form

$$n_1 = \bar{n}_1 + n_1', \quad n_2 = \bar{n}_2 + n_2'$$

and recognize that because of the constancy of the sum $n_1 + n_2$

$$n_1' = - n_2'.$$

We obtain on averaging

$$\mu_1 n_1 \bar{g}_1 + \mu_2 n_2 \bar{g}_2 + \mu_1 \overline{n_1' g_1'} - \mu_2 \overline{n_1' g_1'} = \mu_1 \bar{n}_1.$$

Since $c_i = \dfrac{n_i}{n_0}$, we find at once [82]

$$\bar{g}_1 = \frac{\mu_1 \bar{c}_1 - (\mu_1 - \mu_2)\,\overline{c_1' g_1'}}{\mu_1 \bar{c}_1 + \mu_2 \bar{c}_2} . \tag{2.10}$$

Remembering that the correlation moment $\overline{c_1' g_1'}$ is always greater than zero in a turbulent flow, we can, in the general case, go directly from (2.10) to our earlier conclusion as to the relation between $\bar{g}_2$ and g_{tk}.

Since, on the other hand, the value of the correlation moment $\overline{c_1' g_1'}$ is unknown, it is not possible in the general case to convert numerically from a measured volume concentration to a concentration by weight.

From this we may conclude that gas analysis is incapable of accurate measurements of concentration by weight in turbulent streams. When gas analyses are made in streams that have different initial temperatures T_1 and T_2, interpretation of the sampling results depends on the ratio of two characteristic times. One of them is the time to heat (or cool) an element of gas that has entered the sampler from its initial temperature to the temperature established in the sampling system.

The other characteristic time is determined by the frequency of the temperature fluctuations in the turbulent stream.

Obviously, the first characteristic time describes the variation of sampling velocity at the sampler entrance cross section. If therefore, the temperature fluctuation frequency in the stream is very high, the sampling velocity at the sampler entrance remains practically constant. The volume concentration in the tank is then determined by the relation

$$c_\varrho = \frac{\bar{n}_2}{\bar{n}_1 + \bar{n}_2} = \frac{P_2}{\frac{T_2}{T_1} P_1 + P_2} \quad \left(\frac{n_{\varrho 2}}{n_{\varrho 1}} = \frac{T_1}{T_2} \right).$$

On the other hand, if the temperature fluctuations are very widely spaced, the sampler-entrance velocity ratio for portions of gas with temperatures T_1 and T_2 is T_1/T_2.[*] Therefore,

$$c_\varrho = \frac{\bar{m}_2}{\bar{m}_1 \frac{T_1}{T_2} + \bar{m}_2} = \frac{P_2}{P_1 + P_2} = P_2,$$

i.e., the volume concentration in the tank is the same as the observation probability.

In reality (when these characteristic-time values are comparable), the volume concentration lies between these extreme values.

§2. Free Turbulent Jets

1. Shapes of Density and Velocity Profiles

Density profile shapes are found by generalizing the solution obtained from study of mixing of streams with equal velocities to the case in which the jet and cocurrent stream have unequal velocities.

---

[*]It is assumed that the average flow velocity on the main length of the sampler is constant.
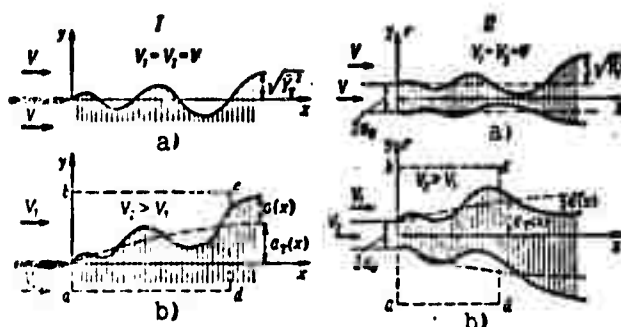
Figure 2.2. Mixing layer (I).
a — case of equal velocities; b — case of unequal velocities.
Plane (axisymmetric) cocurrent jet (II).
a — velocities of jet and stream equal; b — velocities unequal.

Let us examine the mixing at the interface of two streams with equal velocities and equal turbulence characteristics (D_T = const) (Figure 2.2). Since there are no transverse velocities in this case, the general diffusion equation assumes the form

$$V \frac{\partial P_2}{\partial x} = D_T \frac{\partial^2 P_2}{\partial y^2} .$$ (2.11)

In writing Equation (2.11), we have neglected longitudinal diffusion in virtue of the condition $v'^2 \ll V^2$.

Recognizing that

$$\frac{D_T}{V} = \frac{1}{2} \frac{d\overline{Y_T^2}}{dx} ,$$ (2.12)

we arrive at a diffusion equation in the form

$$\frac{\partial P_2}{\partial x} = \frac{1}{2} \frac{d\overline{Y_T^2}}{dx} \frac{\partial^2 P_2}{\partial y^2} .$$ (2.13)

The solution of (2.13) should be found for the following initial and boundary conditions.

$$x = 0, \; P_2 = 1 \; \text{for} \; y < 0; \; P_2 = 0 \; \text{for} \; y > 0;$$
$$y = -\infty, \; P_2 = 1; \; y = \infty, \; P_2 = 0.$$

It is easily seen that the corresponding solution will be

$$P_2 = \frac{1}{2}\left[1 - \Phi\left(\frac{y}{\sqrt{\overline{Y_1^2(x)}}}\right)\right],\qquad(2.14)$$

where $\Phi(x) = \frac{2}{\sqrt{2\pi}}\int_0^x e^{-\frac{t^2}{2}}dt$ is the probability integral.

The dispersion $\overline{Y_1^2(x)}$, which is the same for all liquid particles emerging at the plane $x = 0$, characterizes the dispersion of the particles about straight-line trajectories and increases with increasing distance according to the law [see (1.60)]:

$$\overline{Y_1^2} = \frac{\overline{v_1'^2}}{V^2}x^2 = \iota^2 x^2 \quad \text{for} \quad x < 2x_0 = \frac{D_1}{V\iota^2};$$

$$\qquad(2.15)$$

$$\overline{Y_1^2} = \frac{2D_1}{V}(x - x_0) \quad \text{for } x > 2x_0.$$

Accordingly, the probability profile, which originally took the form of a rectangular step of unit height, becomes increasingly eroded.

A fact, that must be noted here and will become important later on, is that Expression (2.14) can also be derived by a different approach based on the normal law (1.62). Here the probability P_2 is found by summing the probabilities that all volumes of the jet will arrive at a point under consideration:

$$P_2 = \int_{-\infty}^{0} p(y, y_0)\,dy_0 = \frac{1}{2}\left[1 - \Phi\left(\frac{y}{\sqrt{\overline{Y_1^2}}}\right)\right],$$

where

$$p(y, y_0) = \frac{1}{\sqrt{2\pi\overline{Y_1^2}}}\, e^{-\frac{(y-y_0)^2}{2\overline{Y_1^2}}}.$$

At any distance downstream in the plane y = 0, we have $P_2 = 1/2$, i.e., both volumes of the jet and volumes of the cocurrent stream will be encountered with equal probability in this plane.

When the jet and cocurrent stream have unequal velocities, the jet will be slowed down in the course of turbulent mixing (when $V_2 > V_1$). The line of equal probabilities $\left(P_1 = P_2 = \frac{1}{2}\right)$ is shifted upward (Figure 2.2b) and comes to occupy the position of $a_T(x)$.

As we have noted, the average boundary $a_T(x)$ corresponds physically to the interface that would be obtained between the gases if all particles of jet and cocurrent stream matter that have been dissipated by turbulent motions were reunited.

To find the probability P_2, it is necessary to know the statistical properties of the instantaneous fluctuations of the interface about its average position. If we assume that the scattering of these volumes around the average trajectory, i.e., around $a_T(x)$, is given by a normal law with dispersion $\sigma^2(x)$, we obviously arrive at the following formula instead of (2.14):

$$P_2 = \frac{\bar{c}_2}{c_{02}} = \frac{\bar{c} - c_{01}}{c_{02} - c_{01}} = \frac{1}{2}\left[1 - \Phi\left(\frac{y - a_T}{\sqrt{\sigma^2}}\right)\right]. \tag{2.16}$$

Reasons for using the normal distribution were stated in subsection 1 of §1 and subsection 2 of §1. Reference can also be made to an experimental investigation [12] of the behavior of a front separating turbulent from nonturbulent liquid, which confirmed the acceptability of the normal law even in the case of extremely inhomogeneous turbulence.

Some degree of deviation is possible only for very small diffusion times. This is indicated by the experiments of Hinze [21], who measured the thermal trace behind a thin hot wire placed in the combustion zone of a plane-parallel jet. The integral formula (2.16) gives practical accuracy even in this case, although the dispersion

$\sigma^2(x)$ that appears in (2.16) is now determined, when the initial-velocity difference of the streams is substantial, basically by the turbulence generated by transverse velocity shear.

For the dynamic problem, in virtue of the analogy between the processes of property and velocity field transport explained in subsection 1 of §1, we can formally write the velocity profile in the analogous form

$$P_{3V} = \frac{\bar{u} - V_1}{V_2 - V_1} = \frac{1}{2}\left[1 - \Phi\left(\frac{y_{,} - a_V}{\sigma_V}\right)\right]. \tag{2.16a}$$

Here $a_V(x)$ and $\sigma_V(x)$ are certain characteristic parameters, with the parameter $\sigma_V(x)$ related through an empirical constant (the Prandtl number) to the dispersion of the jet (see subsection 1 of §1):

$$\frac{\sigma_V^2}{\sigma^2} = Pr. \tag{2.17}$$

As we indicated in subsection 1 in §1, the turbulent Prandtl number is smaller than unity and approximately equal to 0.5.

In the case of the plane-parallel jet, Equation (2.13) should be solved with the following initial and boundary conditions:

$$x = 0, \quad -a_0 < y_0 < a_0, \quad P_3 = 1;$$
$$|y| > a_0, \quad P_3 = 0;$$
$$y = \pm \infty, \quad P_3 = 0.$$

The corresponding solution takes the form

$$P_3 = \frac{1}{2}\left[\Phi\left(\frac{y + a_0}{\sqrt{\overline{y_\tau^2}}}\right) - \Phi\left(\frac{y - a_0}{\sqrt{\overline{y_\tau^2}}}\right)\right]. \tag{2.18}$$

The integral relation is obtained by integrating (2.13) with respect to y:

$$\frac{d}{dx}\int_{-\infty}^{\infty} P_2 dy = \frac{1}{2}\frac{d\overline{Y_\tau^2}}{dx}\frac{\partial P_2}{\partial y}\Big|_{-\infty}^{\infty} = 0.$$

Or

$$\int_{-\infty}^{\infty} P_2 dy = const.$$

We thus have, with consideration of the initial conditions,

$$\int_{-\infty}^{\infty} P_2 dy = 2a_0. \qquad (2.19)$$

When the jet and cocurrent stream have different velocities, the probability profile can be obtained from the solution (2.18) by substituting $a_T(x)$ for a_0 and σ^2 for $\overline{Y}^2$:

$$P_2 = \frac{\bar{c}_2}{c_{02}} = \frac{\bar{c} - c_{01}}{c_{02} - c_{01}} = \frac{1}{2}\left[\Phi\left(\frac{y + a_\tau}{\sigma}\right) - \Phi\left(\frac{y - a_\tau}{\sigma}\right)\right]. \qquad (2.20)$$

The velocity profile is found in analogous form, but with the parameters a_V and σ_V:

$$P_{2V} = \frac{\bar{u} - V_1}{V_2 - V_1} = \frac{1}{2}\left[\Phi\left(\frac{y + a_V}{\sigma_V}\right) - \Phi\left(\frac{y - a_V}{\sigma_V}\right)\right]. \qquad (2.21)$$

Here, instead of (2.19),

$$\int_{-\infty}^{\infty} P_{2V} dy = 2a_V; \quad \int_{\bullet}^{\infty} \frac{\bar{u} - V_1}{V_2 - V_1} dy = 2a_V. \qquad (2.22)$$

At sufficiently great distances from the orifice, the dispersion is found to be considerably larger than the distance between the average boundaries, and the solutions (2.21) and (2.22) can be written in the following approximate forms:

$$P_2 \simeq \sqrt{\frac{2}{\pi}} \frac{a_T}{\epsilon} e^{-\frac{y^2}{2\epsilon^2}} \left(\frac{a_T}{\epsilon} \ll 1\right);$$

$$P_{2V} = \frac{\bar{u} - V_1}{V_2 - V_1} \simeq \sqrt{\frac{2}{\pi}} \frac{a_V}{\epsilon_V} e^{-\frac{y^2}{2\epsilon_V^2}} \left(\frac{a_V}{\epsilon_V} \ll 1\right). \tag{2.23}$$

From this

$$\frac{P_2}{P_{2m}} = e^{-\frac{y^2}{2\epsilon^2}}; \quad \frac{P_{2V}}{P_{2mV}} = \frac{\bar{u} - V_1}{u_m - V_1} = e^{-\frac{y^2}{2\epsilon_V^2}}. \tag{2.24}$$

where P_{2m} and u_m are the probability and velocity on the axis of the jet for all values of a_T/ϵ; a_V/ϵ_V:

$$P_{2m} = \Phi\left(\frac{a_T}{\epsilon}\right), \quad \frac{\bar{u}_m - V_1}{V_2 - V_1} = \Phi\left(\frac{a_V}{\epsilon_V}\right). \tag{2.25}$$

In virtue of (2.24), we have the following relation between the probability and velocity profiles:

$$\frac{P_2}{P_{2m}} = \left(\frac{\bar{u} - V_1}{u_m - V_1}\right)^{\frac{\epsilon_V^2}{\epsilon^2}}, \tag{2.26}$$

where, according to (2.17), the exponent is the Prandtl number.

Experience has shown that the numerical value of Pr is approximately constant, not only in the range in which the approximate formulas (2.23) are valid, but also over the entire length of the jet.

For the axisymmetric jet with equal velocities of the jet and cocurrent stream, the diffusion equation takes the form

$$\frac{\partial P_2}{\partial x} = \frac{1}{2} \frac{d\overline{Y_V^2}}{dx} \cdot \frac{1}{r} \frac{\partial}{\partial r}\left(r \frac{\partial P_2}{\partial r}\right). \tag{2.27}$$

The solution is sought with the initial and boundary conditions

$$x=0, \quad P_2=1 \quad (r \leqslant a_0);$$
$$P_2=0 \quad (r > a_0);$$
$$r=\infty, \quad P_2=0.$$

The method of finding the solution is set forth in [41] in the solution of the problem of diffusion of a vortex of finite initial size, which reduces to an equation of the type (2.27).

It is found that

$$\dot{P}_2 = \Pi\left(\frac{a_0}{\sqrt{\overline{r_\tau^2}}}, \quad \frac{r}{\sqrt{\overline{r_\tau^2}}}\right).$$

Here

$$\Pi\left(\frac{a}{\gamma}, \frac{r}{\gamma}\right) = \frac{1}{\gamma^2} \int_0^a e^{-\frac{r^2+r_0^2}{2\gamma^2}} I_0\left(\frac{r}{\gamma^2}\right) r_0 dr_0, \tag{2.28}$$

where I_0 is a zero-order Bessel function of an imaginary argument.

The function Π was tabulated in [42]. Integration of (2.27) over r from 0 to ∞ gives

$$\int_0^\infty P_2 r dr = \frac{a_0^2}{2}.$$

If the velocity of the jet differs from that of the cocurrent stream, jet particles collected in a certain cross section will no longer lie within a circle of radius a_0, but within a circle of radius $a_T(x)$ (Figure 2.2).

Use of the considerations set forth earlier in regard to the normal particle-displacement distribution yields the following expression for P_2:

$$P_2 = \frac{\bar{\varrho}_2}{\varrho_{02}} = \frac{\bar{c}-c_{01}}{c_{02}-c_{01}} = \Pi\left(\frac{a_T}{\bullet}, \frac{r}{\bullet}\right). \tag{2.29}$$

The velocity profile is assigned in the form

$$P_{2V} = \frac{\bar{u} - V_1}{V_2 - V_1} = \Pi\left(\frac{\sigma_V}{\sigma_V}, \frac{r}{\sigma_V}\right).$$ (2.30)

The applicable integral relations are

$$\int_0^\infty P_2 r \, dr = \frac{\sigma_2^2}{2}, \quad \int_0^\infty \frac{\bar{u} - V_1}{V_2 - V_1} r \, dr = \frac{\sigma_V^2}{2}.$$ (2.31)

The solutions of (2.29) and (2.30) are simplified on the axis of the jet $(r = 0)$:

$$P_{2a} = 1 - e^{-\frac{\sigma_2^2}{2\sigma^2}}, \quad \frac{\bar{u}_m - V_1}{V_2 - V_1} = 1 - e^{-\frac{\sigma_V^2}{2\sigma_V^2}}.$$ (2.32)

At large distances from the exit cross section, the probability and velocity profiles assume the form of Gaussian functions:

$$P_2 \simeq \frac{\sigma_2^2}{2\sigma^2} e^{-\frac{r^2}{2\sigma^2}} \quad \left(\frac{\sigma_2}{\sigma} \ll 1\right);$$

$$\frac{\bar{u} - V_1}{V_2 - V_1} \simeq \frac{\sigma_V^2}{2\sigma_1^2} e^{-\frac{r^2}{2\sigma_V^2}} \quad \left(\frac{\sigma_V}{\sigma_V} \ll 1\right).$$ (2.33)

As before, the parameters σ_V and σ are related via the turbulent Prandtl number [see (2.17)].

Since it is helpful in some problems to know the average transverse velocity v, it is expedient to cite the corresponding expressions. For the mixing layer, the continuity equation

$$\frac{\partial \bar{u}}{\partial x} + \frac{\partial \bar{v}}{\partial y} = 0$$ (2.34)

can be used to express the transverse velocity in terms of the longitudinal velocity:

$$\bar{v} = -\int_{-\infty}^{y} \frac{\partial \bar{u}}{\partial x}\, dy.$$

Since

$$\frac{\partial u}{\partial x} = \frac{\partial u}{\partial a_V}\frac{da_V}{dx} + \frac{\partial u}{\partial \sigma_V^2}\frac{d\sigma_V^2}{dx} \; ; \quad \frac{\partial u}{\partial a_V} = -\frac{\partial u}{\partial y} \; , \quad \frac{\partial u}{\partial \sigma_V^2} = \frac{1}{2}\frac{\partial^2 u}{\partial y^2}$$

[this last equality follows from the fact that when $a_V = 0$, the function u satisfies a diffusion equation of the form (2.13)], we have

$$v = \frac{da_V}{dx}\int_{-\infty}^{y}\frac{\partial u}{\partial y}\, dy - \frac{1}{2}\frac{d\sigma_V^2}{dx}\int_{-\infty}^{y}\frac{\partial^2 u}{\partial y^2}\, dy.$$

Finally,

$$v = \frac{da_V}{dx}(\bar{u} - V_2) - \frac{1}{2}\frac{d\sigma_V^2}{dx}\frac{\partial u}{\partial y} \; , \tag{2.35}$$

where the profile of $\bar{u}$ is given by (2.16a).

Integration of the continuity equation in the case of a plane-parallel jet yields

$$\bar{v} = -\int_{0}^{y}\frac{\partial \bar{u}}{\partial x}\, dy = -\int_{0}^{y}\frac{\partial u}{\partial a_V}\frac{da_V}{dx}\, dy - \int_{0}^{y}\frac{\partial u}{\partial \sigma_V^2}\frac{d\sigma_V^2}{dx}\, dy.$$

In virtue of (2.21)

$$\frac{\partial u}{\partial a_V} = \frac{V_2 - V_1}{2}\frac{\partial}{\partial y}\left[\phi\left(\frac{y + a_V}{\sigma_V}\right) - \phi\left(\frac{y - a_V}{\sigma_V}\right)\right].$$

In addition,

$$\frac{\partial u}{\partial \sigma_V^2} = \frac{1}{2}\frac{\partial^2 u}{\partial y^2}\cdot$$

In the plane-parallel jet, therefore,

$$v = -\frac{V_2 - V_1}{2}\left[\Phi\left(\frac{y + a_V}{c_V}\right) + \Phi\left(\frac{y - a_V}{c_V}\right)\right]\frac{da_V}{dx} - \frac{1}{2}\frac{\partial \bar{u}}{\partial y}\frac{dc_V}{dx}. \qquad (2.36)$$

Finally, for the axisymmetric jet

$$\frac{\partial \bar{u}}{\partial x} + \frac{1}{r}\frac{\partial}{\partial r}(r\bar{v}_r) = 0. \qquad (2.37)$$

Integrating, we find

$$rv_r = -\int_0^r \frac{\partial u}{\partial x} r_0 dr_0 = -\frac{da_V}{dx}\int_0^r \frac{\partial u}{\partial a_V} r_0 dr_0 + \frac{dc_V^2}{dx}\int_0^r \frac{\partial u}{\partial c_V^2} r_0 dr_0.$$

Since

$$\frac{\partial u}{\partial a_V} = \frac{V_2 - V_1}{c_V^2} e^{-\frac{a_V^2 + r_0^2}{2c_V^2}} I_0\left(\frac{a_V r_0}{c_V^2}\right) a_V;$$

$$\frac{\partial u}{\partial c_V^2} = \frac{1}{2}\frac{1}{r_0}\frac{\partial}{\partial r_0}\left(r_0 \frac{\partial u}{\partial r_0}\right),$$

we have

$$\int_0^r \frac{\partial u}{\partial a_V} r_0 dr_0 = \frac{V_2 - V_1}{c_V^2}\int_0^r e^{-\frac{a_V^2 + r_0^2}{2c_V^2}} I_0\left(\frac{a_V r_0}{c_V^2}\right) a_V r_0 dr_0 =$$

$$= (V_2 - V_1)a_V \Pi\left(\frac{r}{c_V}, \frac{a_V}{c_V}\right);$$

$$\int_0^r \frac{\partial u}{\partial c_V^2} r_0 dr_0 = \frac{1}{2}\int_0^r \frac{1}{r_0}\frac{\partial}{\partial r_0}\left(r_0 \frac{\partial u}{\partial r_0}\right) r_0 dr_0 = \frac{r}{2}\frac{\partial u}{\partial r}.$$

Thus, the radial velocity distribution has the following form in an axisymmetric jet:

$$rv_r = -\frac{1}{2}\frac{da_V^2}{dx}(V_2 - V_1)\Pi\left(\frac{r}{c_V}, \frac{a_V}{c_V}\right) - \frac{r}{2}\frac{dc_V^2}{dx}\frac{\partial \bar{u}}{\partial r}. \qquad (2.38)$$

2.   Determination of Integral Parameters of Jet

The density and velocity profiles are described with the four
parameters: σ, σ_V, a_T, and a_V.

The physical significance of the parameters a_T, σ, a_V and σ_V was
discussed earlier, in subsection 1 of §1.

One relation among these parameters is found by introducing the
Prandtl number (see (2.17)). Two other relations are established
with the aid of the momentum-flux and mass-flux conservation laws
(see subsection 2 of §1).

The density and velocity are to be substituted into these laws
in the form

$$\bar{\varrho} = \varrho_{01}(1 - P_2) + \varrho_{02}P_2 \qquad (2.39a)$$

$$\bar{u} = V_1 + (V_2 - V_1)P_{2V}. \qquad (2.39b)$$

where P_2 and P_{2V} have the respective functional forms indicated in

subsection 2 of §2 for the mixing layer, plane-parallel jet, and
axisymmetric jet.

The integrals can be evaluated in analytic form only when the
jet and cocurrent stream densities are equal (n = 1). All of the
calculations appear in the Appendix; only the final results are stated
here.

Mixing layer of two semiinfinite streams

Substitution of the boundary layer profiles of two semiinfinite
streams [(2.15), (2.16a)] into the mass-flux conservation law (1.94)
yields a relation that is valid for arbitrary n:

$$\frac{a_\gamma}{\sqrt{s^2+\sigma_V^2}}-(1-m)\psi\left(\frac{a_\gamma-a_V}{\sqrt{\sigma^2+\sigma_V^2}}\right)=0,\qquad (2.40)$$

where

$$\psi(x)=\frac{x}{2}[1+\Phi(x)]+\frac{1}{\sqrt{2\pi}}\,e^{-\frac{x^2}{2}}.$$

Use of the momentum-flux conservation condition (1.96) enables us to obtain the following relation among the diffusion parameters of the jet:[*]

$$\psi(\zeta)=\frac{nm+(1-m)(1-n)\psi(r)-mn\sqrt{\dfrac{\Pr}{\pi(1+\sigma_V^2/\sigma^2)}}}{(1-2m+mn)\sqrt{\dfrac{1+\Pr}{1+\sigma_V^2/\sigma^2}}},\qquad (2.41)$$

where

$$\zeta=\frac{a_\gamma-a_V}{\sigma\sqrt{1+\Pr}},\quad r=\zeta\sqrt{\frac{1+\Pr}{1+\sigma^2/\sigma^2}}+\sqrt{\frac{\Pr}{\pi(1+\sigma_V^2/\sigma^2)}}$$

and we have introduced the notation

$$\frac{\sigma_\gamma^2}{\sigma^2}=\frac{e^{\frac{1}{\pi}\Pr}}{[1+\Phi(1/\sqrt{\pi})]^2}\simeq0.67\,\Pr$$

$$\left(m=\frac{V_1}{V_2},\quad n=\frac{\rho_{01}}{\rho_{02}}\right).$$

For example, we have when $n=1$

$$a_V=\frac{1-m}{\sqrt{\pi}}\,\sigma_V.\qquad (2.42)$$

---

[*]For $0\leqslant\zeta\leqslant0.8$, Formula (2.41) can be replaced with sufficient accuracy by the following formula ($\Pr=0.5$):

$$\zeta=\frac{0.344n(1-m)+0.625(1-m)(1-n)-0.403(1-2m+mn)}{0.753(n-m)-1.06n}.$$

Figure 2.3. Influence of turbulent Prandtl number on concentration in plane y = 0 (m = 0 and n = 1).

$$1 - \mu_1; \quad 2 - \frac{a_T}{\sigma}$$
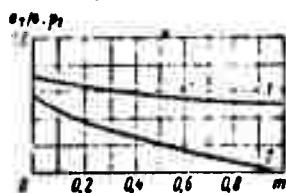
Figure 2.4. Influence of cocurrency parameter on concentration on y = 0 (Pr = 0.5 and n = 1).

$$1 - \mu_1 - \frac{1}{2}\left[1 - \phi\left(\frac{a_T}{\sigma}\right)\right]; \quad 2 - \frac{a_T}{\sigma}$$

Equations (2.40) and (2.42) yield the universal functions a_T/σ and a_V/σ of m, n, and Pr. Curves of the functions are plotted in Figures 2.3, 2.4, and 2.5.

Figure 2.3 shows that the ratio a_T/σ depends weakly on Pr over a rather broad range of the latter. The influence of the cocurrency parameter m is, on the other hand, quite substantial (Figure 2.4).

These relations were obtained for n = 1. Figure 2.5 shows a_T/σ and a_V/σ as functions of n for a submerged mixing layer (m = 0).

We see that the trends of a_T/σ and a_V/σ are opposite: a_T/σ increases with increasing n and a_V/σ decreases. Physically, this is explained by the fact that the lighter jet is more strongly decelerated by the heavy stream (the increase in a_T is faster). At the same time, the rate of velocity transfer to heavy volumes of the cocurrent stream decreases (slower increase in a_V).

Plane-parallel jet

The profiles (2.20) and (2.21) should be substituted into the mass-flux conservation law (1.94). Integration gives
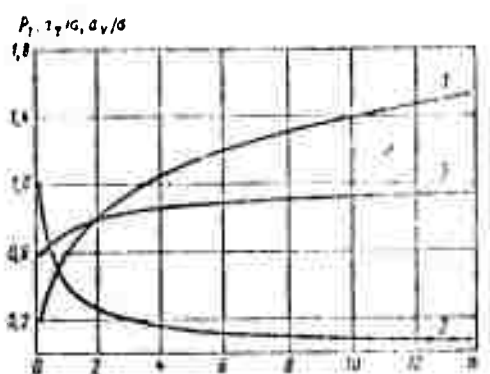
Figure 2.5. Influence of density ratio (Pr = 0.5; m = 0).

$1 - \frac{a_T}{\sigma}$; $2 - \frac{a_V}{\sigma}$; $3 - \rho_1$

$$m \frac{a_T}{\sqrt{\sigma^2 + \sigma_V^2}} + (1-m)\left[\varphi\left(\frac{a_T + a_V}{\sqrt{\sigma^2 + \sigma_V^2}}\right) - \varphi\left(\frac{a_T - a_V}{\sqrt{\sigma^2 + \sigma_V^2}}\right)\right] = \frac{a_0}{\sqrt{\sigma^2 + \sigma_V^2}}; \quad (2.43)$$

where

$$\varphi(z) = \frac{z}{2}\,\Phi(z) + \frac{1}{\sqrt{2\pi}}\,e^{-\frac{z^2}{2}}.$$

With equal densities of the jet and cocurrent stream, the momentum-flux conservation law (1.97) gives

$$m\frac{a_T}{\sigma_V} + (1-m)\left[\sqrt{2}\varphi\left(\frac{a_V}{\sigma_V} + 2\right) - \frac{1}{\sqrt{\pi}}\right] = \frac{a_0}{\sigma_V}. \quad (2.44)$$

In the range in which a_T/σ and a_V/σ_V are small, i.e., where the approximate expressions for P_2 and P_{2V} (2.23) are valid, we have the following expansion (the error is smaller than 7% for $z < 0.7$):

$$\varphi(z) \sim \frac{1}{\sqrt{2\pi}}\left(\frac{z^2}{2} + 1\right).$$

Thus, instead of (2.43) and (2.44), we have

$$m\frac{a_T}{\sqrt{\sigma^2 + \sigma_V^2}} + (1-m)\frac{4}{\sqrt{2\pi}}\frac{a_T a_V}{\sigma^2 + \sigma_V^2} = \frac{a_0}{\sqrt{\sigma^2 + \sigma_V^2}}; \quad (2.43')$$

$$m\frac{a_T}{\sigma_V} + (1-m)\frac{1}{\sqrt{\pi}}\frac{a_V^2}{\sigma_V^2} = \frac{a_0}{\sigma_V}. \quad (2.44')$$

For the submerged jet (m = 0) in particular

$$a_V^2 \sim \sqrt{\frac{\pi}{Pr}}\,a_0\sigma, \quad a_T^2 \sim a_0\frac{1 + Pr}{\sqrt{Pr}} \cdot \frac{\sqrt{\pi}}{2}\sigma.$$
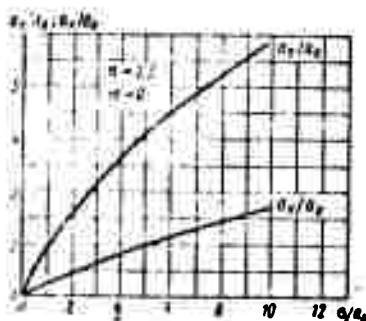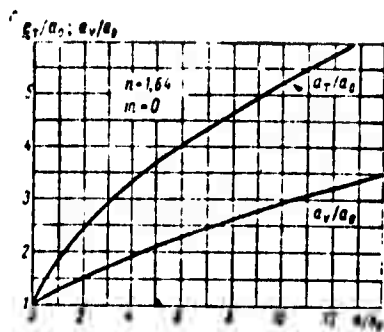
Figure 2.6. Average radii in plane-parallel jet.

Curves of a_T and a_V for $m = 0$ appear in Figure 2.6.

Hence the axial concentration and velocity values take the form

$$P_{2m} \simeq \sqrt{\frac{1+Pr}{\sqrt{\pi\,Pr}} \frac{a_0}{\sigma}}, \quad \frac{u_m}{V_2} = \sqrt{2\frac{a_0}{\sigma}\frac{1}{\sqrt{\pi\,Pr}}}.$$

Consequently,

$$V_2 \frac{P_{2m}}{u_m} = \sqrt{\frac{1+Pr}{2}}.$$

Since $Pr < 1$, the concentration on the axis drops off more rapidly than the velocity.

When the densities of the jet and cocurrent stream are unequal, the integrals in (1.97) can no longer be taken in analytic form.

It is convenient to use an approximate method to find the shape of the $a_T(\sigma)$ and $a_V(\sigma)$ curves for arbitrary values of the parameters m and n.

This method is essentially as follows. Large values of the ratio $\frac{a}{\sigma}\left(\frac{a}{\sigma} > 3\right)$ correspond for various boundary conditions to the conditions in the mixing boundary layer of two semiinfinite streams. The solution for this case was given above. For small a/σ, on the other hand, the profiles are Gaussian, so that the integrals are also taken in this case. Consequently, the $a(\sigma)$ relation can be found for both small and large σ. For the intermediate range of σ, the solution is found by extrapolation.

The final results take the following forms.

For $\sigma > \sigma_2$ such that the ratio $\dfrac{a_V}{a_V} \leqslant 0{,}7$:

$$\frac{a_0}{\sigma} = m\,\frac{a_T}{\sigma} - \frac{1}{2}\left[mn\,\sqrt{\pi\,\mathrm{Pr}}\,\frac{c}{b} - \sqrt{\pi\,\mathrm{Pr}}\,\frac{c^2}{b}\,(2m - mn - 1)\right] +$$
$$+ \sqrt{\frac{1}{4}\left[mn\,\sqrt{\pi\,\mathrm{Pr}}\,\frac{c}{b} + \sqrt{\pi\,\mathrm{Pr}}\,\frac{c^2}{b}\,(2m - mn - 1) + \right.}$$
$$\overline{ \frac{c^2}{b}\,\frac{a_T}{\sigma}\,\sqrt{\pi\,\mathrm{Pr}}\,m\,(1-m);}$$
$$\frac{a_V}{\sigma} = \frac{\dfrac{a_0}{\sigma} - m\,\dfrac{a_T}{\sigma}}{(1-m)\,c}, \tag{2.45}$$

where

$$b = n + (1-n)\,\Phi\!\left(\frac{a_T\,\sqrt{2}}{\sigma\,\sqrt{2+\mathrm{Pr}}}\right);$$
$$c = \Phi\!\left(\frac{a_T}{\sigma\,\sqrt{1+\mathrm{Pr}}}\right).$$

It follows from (2.45) that in all cases

$$a_T < \frac{1}{m}\,a_0 = \frac{V_2}{V_1}\,a_0.$$

The approach to the limit

$$a_T = \frac{V_2}{V_1}\,a_0$$

signifies that the stream velocities have become practically equal.

It is easily verified that at great distances downstream

$$a_V = \int_0^\infty \frac{\bar{u} - V_1}{V_2 - V_1}\,dy \to \frac{1}{mn}\,a_0.$$

In the range $0 \leqslant \sigma \leqslant \sigma_1\left(\dfrac{a_V}{a_V} \geqslant 3\right)$, the differences $a_V - a_0$ and $a_T - a_0$ are simply proportional to σ, and the problem reduces to determination of the proportionality factors with relations (2.40) and (2.41), which were derived for the mixing layer.

Finally, the following interpolation formula is proposed in the range $\sigma_1 \leqslant \sigma \leqslant \sigma_2$:

$$\sigma = \left(\frac{a-a_1}{a_2-a_1}\right)^2 \left[\sigma_2 - \sigma_1 - \frac{a_1}{a_1-a_0}(a_2-a_0)\right] + \frac{a-a_1}{a_1-a_0}\sigma_1 + \sigma_1. \tag{2.46}$$

Axisymmetric jet

Substitution of the velocity profile (2.30) and the probability profile (2.29) into the mass-flux conservation law (1.95) yields the following relation linking the diffusion parameters:

$$
\begin{aligned}
ma_T^2 + (1-m)&\left[a_T^2\Pi\left(\frac{a_V}{\sigma^2+\sigma_V^2},\ \frac{a_T}{\sqrt{\sigma^2+\sigma_V^2}}\right) + \right.\\
&+ a_V^2\,\Pi\left(\frac{a_T}{\sqrt{\sigma^2+\sigma_V^2}},\ \frac{a_V}{\sqrt{\sigma^2+\sigma_V^2}}\right) - \\
&\left. - a_V a_T e^{-\frac{a_T^2+a_V^2}{2(\sigma_V^2+\sigma^2)}} \cdot I_1\left(\frac{a_V a_T}{\sigma^2+\sigma_V^2}\right)\right] = a_0^2,
\end{aligned}
\tag{2.47}
$$

where I_1 is a first-order Bessel function of an imaginary argument.

For equal densities of the jet and cocurrent stream, the momentum-flux conservation law yields a second relation between the parameters a_V and σ_V:

$$
\begin{aligned}
ma_V^2 + (1-m)&\left[2a_V^2\,\Pi\left(\frac{a_V}{\sigma_V\sqrt{2}},\ \frac{a_V}{\sigma_V\sqrt{2}}\right) - \right.\\
&\left. - a_V^2\,e^{-\frac{a_V^2}{2\sigma_V^2}}\,I_1\left(\frac{a_V^2}{2\sigma_V^2}\right)\right] = a_0.
\end{aligned}
$$

At small a/σ, i.e., at great distances downstream, the functions that appear in formulas (2.47) and (2.48) can be expanded in Taylor series in powers of the ratios a_T/σ and a_V/σ. The equations are simplified as a result:

$$m\,\frac{a_T^2}{\sigma_2 + \sigma_V^2} + (1-m)\frac{a_T^2 a_T^2}{2(\sigma_V^2 + \sigma^2)} = \frac{a_0^2}{a_V^2 + \sigma^2}; \tag{2.47'}$$

$$m \frac{a_V^2}{\sigma_V^2} + (1-m) \frac{a_V^4}{4\sigma_V^4} = \frac{a_0^2}{\sigma_V^2}.$$

<div align="right">(2.48')</div>

For the submerged jet ($m = 0$):

$$a_V^2 = 2a_0 \sqrt{\text{Pr}},$$

$$a_\tau^2 = \frac{1 + \text{Pr}}{\sqrt{\text{Pr}}} a_0 \sigma.$$

The axial values of the concentration and velocity are respectively,

$$P_{\tau m} = 1 - e^{-\frac{a_\tau^2}{2\sigma^2}} \simeq \frac{a_\tau^2}{2\sigma^2} \simeq \frac{1 + \text{Pr}}{\sqrt{\text{Pr}}} \frac{a_0}{2\sigma};$$

$$\frac{u_m}{V_2} \simeq \frac{a_V^2}{2\sigma_V^2} \simeq \frac{a_0}{\sigma \sqrt{\text{Pr}}}.$$

Consequently,

$$V_2 \frac{P_{2m}}{u_m} \simeq \frac{1 + \text{Pr}}{2\text{Pr}},$$

which means, in agreement with experiment, a faster decrease in the axial concentration as compared to the axial velocity (Pr < 1).

At unequal jet and cocurrent stream densities, the computational difficulties are overcome just as in the case of the plane-parallel jet.

The formulas obtained in our discussion of the mixing layer can be used for small $\sigma(\sigma < \sigma_1)$. When σ is sufficiently large ($\sigma > \sigma_2$), a_V/σ_V is small, and then

$$P_{2V} = \frac{\bar{u} - V_1}{V_2 - V_1} \simeq \frac{a_V^2}{2\sigma_V^2} e^{-\frac{r^2}{2\sigma_V^2}}.$$

In the present approximation ($\frac{a_V}{c_V}$ small, but no limitations imposed on the ratio $\frac{a_\tau}{c}$), the law of mass-flux conservation takes the form

$$ma_\tau^2 + (1-m)a_V^2\left[1 - e^{-\frac{a_\tau^2}{2\left(c^2 + c_\tau^2\right)}}\right] = a_0^2. \tag{2.47''}$$

Let us dwell in greater detail on determination of the integral momentum-flux conservation condition (1.98):

$$\int\limits_0^\infty \frac{\varrho u}{\varrho_2 V_2}\frac{u - V_1}{V_2 - V_1} r\, dr = mn \int\limits_0^\infty P_{2V} r\, dr + n(1-m)\int\limits_0^\infty P_{2V}^2 r\, dr +$$

$$+ m(1-n)\int\limits_0^\infty P_{2V} P_2 r\, dr + (1-n)(1-m)\int\limits_0^\infty P_{2V}^2 P_2 r\, dr = \frac{a_0^2}{2}.$$

All of the integrals that appear here can be evaluated:

$$\int\limits_0^\infty P_{2V} r\, dr = \frac{a_V^2}{2}, \quad \int\limits_0^\infty P_{2V}^2 r\, dr = \frac{a_V^4}{2c_V^2},$$

$$\int\limits_0^\infty P_{2V} P_2 r\, dr = \frac{a_0^2 - ma_\tau^2}{2(1-m)}.$$

Finally,

$$\int\limits_0^\infty P_{2V}^2 K_2 r\, dr = \int\limits_0^\infty \frac{a_V^4}{4c_V^4} e^{-\frac{r^2}{2c_V^2}} P_2 r\, dr =$$

$$= \frac{1}{8}\frac{a_V^4}{c_V^2}\int\limits_0^\infty \frac{1}{(c_V/\sqrt{2})^2} e^{-\frac{r^2}{2(c_V/\sqrt{2})^2}} P_2 r\, dr =$$

$$= \frac{1}{8}\frac{a_V^4}{c_V^2} \Pi\left(\frac{a_\tau}{\sqrt{c^2 + c_\tau^2/2}}, 0\right) = \frac{1}{8}\frac{a_V^4}{c_V^2}\left(1 - e^{-\frac{a_\tau^2}{c_V^2 + 2c^2}}\right).$$

Consequently, the momentum-flux conservation law is written:

$$nma_V^2 + n(1-m)\frac{a_V^4}{4a_V^2} + m(1-n)\frac{a_0^2 - ma_T^2}{1-m} +$$

$$+(1-n)(1-m)\frac{1}{4}\frac{a_V^4}{a_V^2}\left(1 - e^{-\frac{a_T^2}{a_V^2 + 2a^2}}\right) = a_0^2. \tag{2.49}$$

We introduce the notation

$$d = 1 - e^{-\frac{a_T^2}{2a^2(1+Pr)}}; \quad f = n + (1-n)\left[1 - e^{-\frac{a_T^2}{a^2(2+Pr)}}\right].$$

Then the sought working relationships obtained by transforming (2.47") and (2.49), will be

$$\frac{a_V^2}{a^2} = \frac{\frac{a_0^2}{a^2} - m\frac{a_T^2}{a^2}}{(1-m)d}; \tag{2.50}$$

$$\frac{a_0^2}{a^2} = m\frac{a_T^2}{a^2} - 2mn\,Pr\,\frac{a^2}{f}(1-d) - 2\,Pr\,\frac{a^2}{f}(2m-1) +$$

$$+\sqrt{4m\frac{a_T^2}{a^2}Pr\,\frac{a^2}{f}(1-m) + \left[2mn\,Pr\,\frac{a^2}{f}(1-d) + 2\,Pr\,\frac{a^2}{f}(2m-1)\right]^2}. \tag{2.51}$$

We see from (2.51) that always

$$a_T < \frac{a_0}{\sqrt{m}} = \sqrt{\frac{V_2}{V_1}}\,a_0.$$

In the limit, when the stream velocities have become practically equal

$$a_T \to \sqrt{\frac{V_2}{V_1}}\,a_0, \quad a_V \to \frac{1}{\sqrt{mn}}\,a_0.$$
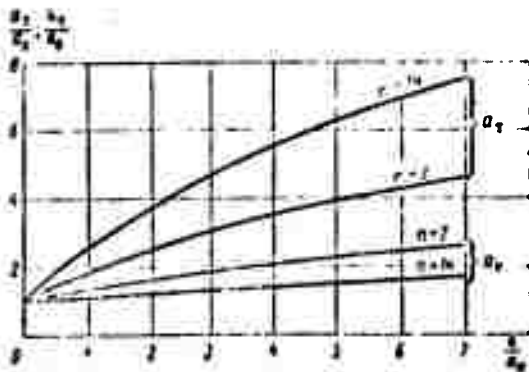
Figure 2.7. Average radii in
axisymmetric jet.

Formula (2.46) is used for inter-
polation into the range in which
$\sigma_1 < \sigma < \sigma_2$, as in the case of the
plane-parallel jet.

Figure 2.7 shows curves of a_T
and a_V plotted against σ for n = 14
and n = 2 with Pr = 0.5.

3. Calculation of Temperature Profiles

The relationships established in subsection 2 of §2 among the
diffusion parameters of the jet enable us to find density and velocity
profiles for a known law of variation of the dispersion $\sigma^2(x)$. As
we stated in §1, subsection 2, the equation of state cannot be used
formally to find a temperature profile from a known density profile.
Otherwise the error will be small at realistic degrees of greyness N
up to temperature ratios $T_{02}/T_{01} = 3 - 4$ (compare also the table
given in Chapter I, §1, subsection 2).

In the general case, it is necessary to use (1.54), which indi-
cates that an additional parameter — the degree of greyness $N = \frac{a_c}{e}$
— must be known in order to determine the temperature.

Let us state this formula specifically for cases with various
jet geometries, assuming that the probability distribution density
$p(\vec{r}, \vec{r_0})$ of turbulent volume displacements is described by a normal law
with dispersion σ_T^2.

The mixing layer

$$\frac{\bar{T} - T_1}{T_2 - T_1} = \int\limits_{-\infty}^{\infty} \frac{P_{2c}}{nP_{1c} + P_{2c}} \, p(y, y_0) dy, \qquad (2.52)$$

where

$$P_{2c} = \frac{1}{2}\left[1 - \Phi\left(\frac{y - a_\tau}{\sigma_c}\right)\right]$$

$$p(y, y_0) = \frac{1}{\sigma_\tau \sqrt{2\pi}}\, e^{-\frac{(y - y_0)^2}{2\sigma_\tau^2}}.$$

The plane-parallel jet

$$\frac{\bar{T} - T_1}{T_2 - T_1} = \int_{-\infty}^{\infty} \frac{P_{2c}}{nP_{1c} + P_{2c}}\, p(y, y_0)\, dy, \qquad (2.53)$$

where

$$P_{2c} = \frac{1}{2}\left[\Phi\left(\frac{y + a_\tau}{\sigma_c}\right) - \Phi\left(\frac{y - a_\tau}{\sigma_c}\right)\right];$$

$$p(y, y_0) = \frac{1}{\sigma_\tau \sqrt{2\pi}}\, e^{-\frac{(y - y_0)^2}{2\sigma_\tau^2}}.$$

The axisymmetric jet

$$\frac{\bar{T} - T_1}{T_2 - T_1} = \int_{0}^{\infty} \frac{P_{2c}}{nP_{1c} + P_{2c}}\, p(\vec{r}, \vec{r_0})\, d\vec{r_0}, \qquad (2.54)$$

where

$$P_{2c} = \Pi\left(\frac{a_\tau}{\sigma_c},\ \frac{r}{\sigma_c}\right),$$

$$p(\vec{r}, \vec{r_0}) = \frac{1}{2\pi\sigma_\tau^2}\, e^{-\frac{(\vec{r} - \vec{r_0})^2}{2\sigma_\tau^2}}.$$

An approximate method of evaluating the integrals of (2.52) — (2.54) can be given. Let us consider the axisymmetric jet as an example.
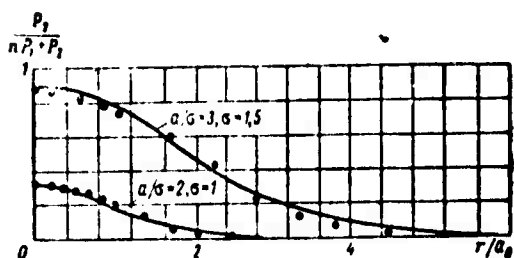
Figure 2.8. Approximation of the function $P_2/nP_1 + P_2$ by means of the function II (n = 14).

$$— \; - \frac{P_2}{nP_1 + P_2}; \quad \bullet - \blacksquare$$

Figure 2.9. Auxiliary curves for calculation of temperatures in axisymmetric jet.

Let us attempt to approximate one of the multipliers $\left(\dfrac{P_{2c}}{nP_{1c} + P_{2c}}\right)$ in the integrand by the function II but with different (effective) values of the average radius and dispersion a_{ef} and σ_{ef}:

$$\frac{P_{2c}}{nP_{1c} + P_{2c}} = II\left(\frac{a_{ef}}{\sigma_{ef}}, \; \frac{r}{\sigma_{ef}}\right). \tag{2.55}$$

The parameters a_{ef} and σ_{ef} are found by equating the functions $\dfrac{P_{2c}}{nP_{1c} + P_{2c}}$ and $II[(a_{ef}/\sigma_{ef}), \; (r/\sigma_{ef})]$ at two characteristic points: on the jet axis ($r = 0$) and at the point at which the first function has a value one-third as large as on the axis.

Figure 2.8 illustrates the agreement attained with the approximation (2.55) when the jet temperature is 14 times the cocurrent stream temperature. The agreement would, of course, be even better for $n < 14$.

Figure 2.9 shows plots of a_{ef}/a_T and σ_{ef}/σ_c against the ratio a_T/σ_c for various n. The limiting values of a_{ef}/a_T and σ_{ef}/σ_c at $a_T/\sigma_c \to 0$ are easily found from the following considerations.

271

For small a_1/σ_c

$$\frac{P_{2c}}{nP_{1c}+P_{2c}} \simeq \frac{P_{2c}}{n} \simeq \frac{a_r^2}{2n\sigma_c^2}\, e^{-\frac{r^2}{2\sigma_c^2}} = \frac{a_{\sigma\phi}^2}{2\sigma_{\sigma\phi}^2}\, e^{-\frac{r^2}{2\sigma_{\sigma\phi}^2}}.$$

Hence, at $\frac{a_r}{\sigma_c} \to 0$

$$a_{\sigma\phi} \to \frac{a_r}{\sqrt{n}}, \quad \sigma_{\sigma\phi} \to \sigma_c.$$

Using the approximation (2.55) instead of (2.54), we can write

$$\frac{\bar{T}-T_1}{T_2-T_1} \simeq \int_0^\infty \Pi\left(\frac{a_{\sigma\phi}}{\sigma_{\sigma\phi}}, \frac{r}{\sigma_{\sigma\phi}}\right) p(\vec{r},\vec{r_0})\, d\vec{r_0} = \Pi\left(\frac{a_{\sigma\phi}}{\sqrt{\sigma_{\sigma\phi}^2+\sigma_1^2}}, \frac{r}{\sqrt{\sigma_{\sigma\phi}^2+\sigma_r^2}}\right).$$

With sufficient accuracy (see Figure 2.9, lower diagram):

$$\sqrt{\sigma_r^2+\sigma_{\sigma\phi}^2} \simeq \sigma.$$

Finally, therefore,

$$\frac{\bar{T}-T_1}{T_2-T_1} = \Pi\left(\frac{a_{\sigma\phi}}{\sigma}, \frac{r}{\sigma}\right), \tag{2.56}$$

where a_{ef} is found from the upper diagram of Figure 2.9.

Analogous formulas can be obtained for the mixing layer and plane-parallel jet. A significant result of this analysis is that, according to (2.56), the total dispersion of the jet can be found with sufficient accuracy from temperature profiles.

Thus, the results obtained above indicate that the density, velocity, and temperature profiles and the concentration and temperature probability distribution functions can be calculated from knowledge of the jet dispersion σ^2, the degree of greyness N, and the turbulence Pr.
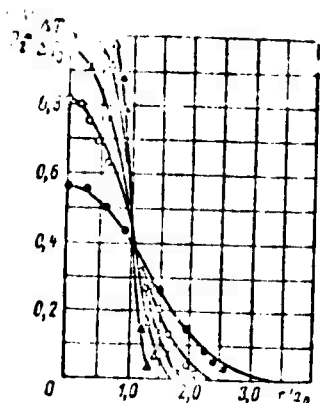
Figure 2.10. The function $\Pi\left(\frac{a_1}{\sigma}, \frac{r}{\sigma}\right)$ and experimental data (m = 0.38). Experiment:

$\blacktriangle - \frac{x}{d} = 2;\ \vartriangle - \frac{x}{d} = 4;\ x -$
$- \frac{x}{d} = 7;\ \text{--} - \frac{x}{d} = 10;\ \bullet - \frac{x}{d} = 15$

Our main source of knowledge as to the behavior of these parameters is still the experiment. It is found that the parameters N and Pr depend weakly on the initial conditions, and the hypothesis that they are constant is quite acceptable for practical calculations. The variation of the dispersion of the jet is more complex in nature and, in particular, highly sensitive to the cocurrency parameter m.

4. Comparison with Experiment

Homogeneous turbulent jets

The results obtained above in regard to the form of the average parameter profiles, the relationships established there among the diffusion parameters of the jet, and the corollaries of the relationships have been compared with experimental data on the mixing of turbulent streams with the purpose of testing the theory developed.

It should be noted that the possibility in principle of approximating the experimental profiles with Gaussian-type distribution has been noted more than once in the literature [3], [25], [44]. We may therefore expect the solutions proposed above to give a good description of experimental data.

For example, Figure 2.10 shows how successfully the Π function [see Formulas (2.29) and (2.30)] describes the continuous transformation of the profiles downstream on the basis of the experimental results of I. B. Palatnik [43], who studied the temperature and velocity distributions in a weakly heated ($\Delta T = 25°$ K) jet at various values of the cocurrency parameter. It must be remembered that the corresponding values of the average radius and dispersion were found from these same distributions.
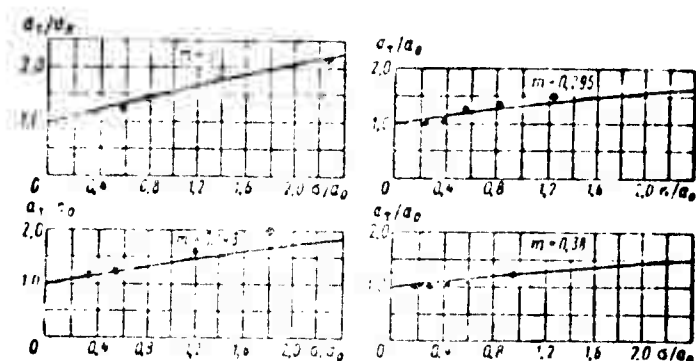
Figure 2.11. Comparison of results of solution of thermal problem with experiments for various m.

• — experiments of I. E. Palatnik; —— —— theory (Pr = 0.5).

Figure 2.11 presents a comparison of the $a_T(\sigma)$ relation established by processing the experiment with the theoretical relationship. We see that the agreement is quite satisfactory. The slight discrepancies are fully explained by the nonuniformity of the initial profiles, which was not considered in the calculations.

Figure 2.12 illustrates the agreement of theory with experiment for the mixing layer of a submerged jet (experiments of G. N. Abramovich [1]).

The dispersion was chosen following the recommendations given in Chapter III.

It is interesting that, unlike other calculation schemes that use the notion of the asymptotic boundary layer [3], [45], the present calculation does not require introduction of the additional empirical constant to characterize the displacement of the theoretical profile with respect to the experimental points.

In accordance with (2.40), the velocity in the plane y = 0 remains constant:

$$\frac{\bar{u} - V_1}{V_2 - V_1} = \frac{1}{2}\left[1 + \Phi\left(\frac{z_v}{\sigma_v}\right)\right] = \frac{1}{2}\left[1 + \Phi\left(\frac{1-m}{\sqrt{\pi}}\right)\right]$$
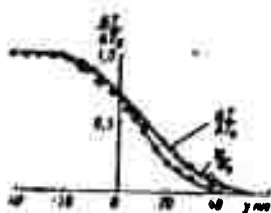
Figure 2.12. Velocity and temperature profiles in mixing layer.

•, ○ — experimental data of G. N. Abramovich (x = 250 mm); —— calculation (σ = 21 mm; Pr = 0.5).
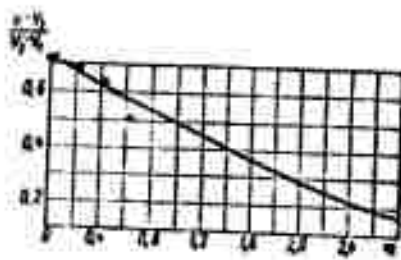
Figure 2.13. Velocity in plane y = 0 for various values of the cocurrency parameter m.

x — Reichardt's experiments; • — B. A. Zhestkov's experiments; —— theory.

Figure 2.13 shows that the relationship obtained gives a good description of the behavior observed in experiments (those of B. A. Zhestkov, R. V. Glazkov, and M. D. Guseva [1]). The discrepancy between theory and experiment at m = 0.64 is explained by the collapse of the average velocities in the trace behind the interface of the streams. This trough persists downstream for some time at large m.

Examining the proposed analytical expressions for the average parameter profiles, we can establish that in the appropriate dimensionless coordinates, these expressions become universal, i.e., they do not depend on the concurrency parameter or the distance downstream.

For example, on introduction of the characteristic scales

$$\Delta y_{\bullet} = y_{0.9} - y_{0.1}, \quad \Delta y_c = y - a$$

the mixing-layer velocity profile (2.16) is brought to the universal form

$$P_{2V} = \frac{\bar{u} - V_1}{V_2 - V_1} = \frac{1}{2}\left[1 + \Phi\left(2.56\frac{\Delta y_c}{\Delta y_\bullet}\right)\right]. \tag{2.57}$$

Here, $y_{0.9}$ and $y_{0.1}$ denote the points at which P_{2V} assume the respective values 0.9 and 0.1.
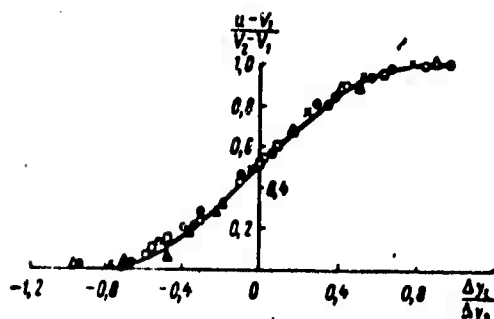
Figure 2.14. Illustrating universal nature of dimensionless velocity profiles in mixing layer.

Experiments of B. A. Zhestkov:
$\bigcirc - m=0,$ $\bullet - m=0.23;$ $\blacktriangle - m=0.43;$ $\triangle - m=0.64;$
Experiments of Albertson:
$\times - \frac{r}{2a_0} = 4;$ $\ominus - \frac{r}{2a_0} = 3;$ $C - \frac{r}{2a_0} = 2;$ $\square - \frac{r}{2a_0} = 1;$
—— theory.

It was taken into consideration in the transformation that

$$y_{0.1} - y_{0.9} \simeq 2.56 \, \sigma.$$

A plot of (2.57) appears in Figure 2.14. Also indicated here are the experimental points of B. A. Zhestkov, R. V. Glazkov, and M. D. Guseva (m = 0; 0.23; 0.43; and 0.64) and Albertson, which were plotted in [1] in the appropriate dimensionless coordinates. The full agreement between the theoretical curve of (2.57) and experiment is obvious.

For plane-parallel and axisymmetric jets, the profiles become universal only at sufficient distances downstream. For example, in the range in which the profiles are Gaussian [(2.23) and (2.33)]:

$$\frac{P_2}{P_{2m}} = e^{-\ln 2 \left(\frac{y}{y_{\frac{1}{2}}} \right)^2};$$

$$\frac{P_{2V}}{P_{2V_m}} = e^{-\ln 2 \left(\frac{y}{y_{\frac{1}{2}}} \right)^2}.$$

(2.58)

Here $y_{\frac{1}{2}} = \eta \sqrt{2 \ln 2} \simeq 1.18 \sigma.$

Figure 2.15 shows how the ratio P/P_{2_m} approaches the universal curve of (2.58) as a/σ decreases. The experimental results of V. Ya. Borodachev (m = 0) and A. Weinstein (m = 0.33; 0.5; 0.67) [46], who studied mixing in plane-parallel jets, are also entered here.

Similar results are also obtained for the axisymmetric jet. In Figure 2.16, the temperature profiles measured by I. B. Palatnik have been plotted against the dimensionless coordinate $r/r_{1/2}$. At m = 0.38, the experimental points fall onto the universal curve from approximately 1C calibers on.
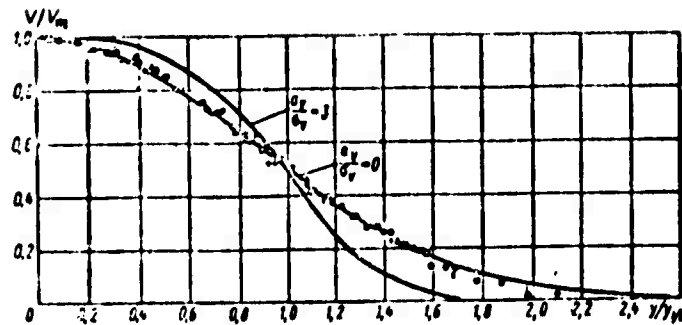
Figure 2.15. Universal nature of velocity profiles in plane-parallel jet at large distances from exit cross section.

Experiments of Weinstein

$\bullet - m \cdot 0.5$, $\blacksquare - m - 0.334$, $\bullet - m - 0.667$, $\square, \bigcirc - \frac{x}{2a} - 41.5$; $+ - \frac{x}{2a_0} - 16.5$,

$\triangle - \frac{x}{2a} - 33$.

Experiments of V. Ya. Borodachev:

$\bullet - \frac{x}{2a} - 25$, $\triangle - \frac{x}{2a} - 29$ —— theory

For comparison of theory with experiment on the jet axis, let us consider the data of Corrsin, Uberoi [47], and Forstall [40], which are most detailed.

Corrsin studied a weakly heated submerged air jet ($\Delta T = 15°$ K), while Forstall's experiments were concerned with a submerged water jet issuing into a still one-percent solution of sodium chloride, so that it was possible to construct concentration profiles for the material of the jet.

Figures 2.17 and 2.18 show that the theory gives a good description of the continuous concentration (temperature) and velocity decrease along the axis of the stream.

The following relation was taken for the dispersion, which was put into the calculation in accordance with results to be given in the next chapter:

$$\frac{a}{d} = 0.095 \left(\frac{x}{d} - 2 \right). \tag{2.59}$$
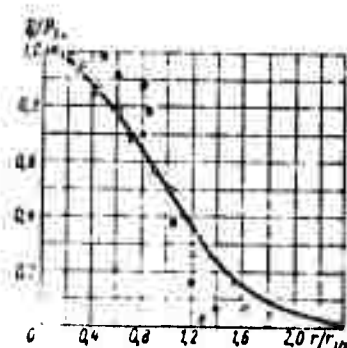
Figure 2.16. Transformation of temperature profiles in axisymmetric jet (m = 0.38). $\circ - \frac{x}{2a_o} = 2$, $\triangle - \frac{x}{2a_o} = 4$; $(- \frac{x}{2a_o} = 7$; $\times - \frac{x}{2a_o} = 10$; $\bullet - \frac{x}{2a_o} = 15$ (according to I. V. Palatnik); —— — curve of $e^{-\ln 2 (r/r_{v_2})^2}$

In conclusion, it is appropriate to compare the values measured by Corrsin and Kistler [31] for the average radius and dispersion of a jet with the amplitude (σ_f) and the average position of the turbulence front (R).

These investigators studied the so-called intermittency of the flow, which consists in the appearance of both turbulent (with large vorticity fluctuations) and non-turbulent liquid at a fixed point in space (see Chapter I, §1). The interface (turbulence front) between the turbulent and nonturbulent liquids is very thin and oscillates in random fashion, moving into the region of the nonturbulent liquid.

It follows from Figure 2.19 that the average position of the front exceeds the average radius $a_T(x)$ by a substantial margin. This becomes quite understandable when it is remembered that $a_T(x)$ increases only as a result of deceleration of volumes of the jet, while R is also increased as a result of entrainment of additional volumes of the cocurrent stream into the turbulent flow.

The dispersion σ_f^2 of intermittency is, to the contrary, much smaller than the total dispersion $\sigma^2(x)$, since the oscillations of the turbulent front are due to a motion set up by a group of large, slow vortices [20], which make an insignificant contribution to turbulent transport.*

---

*Because the data of [31] are the only ones of their kind, the question remains open as to the regularity or randomness of the result (Figure 2.19):

$$\bullet \approx \bar{R} \quad \text{and} \quad \bullet \sim a_r$$
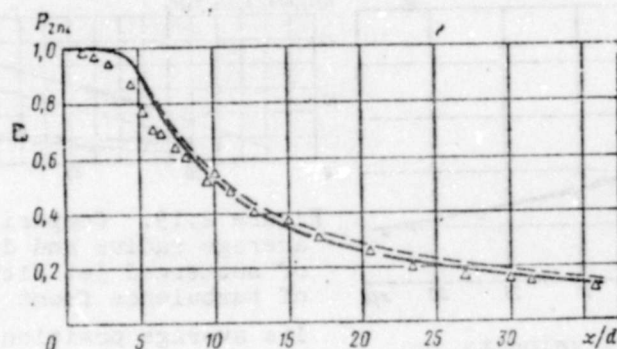
Figure 2.17. Axial temperatures and concentrations in axisymmetric jet.

--- — temperature (according to Corrsin); Δ — concentration (according to Forstall); — — theory.

Inhomogeneous turbulent jets

Experimental study of the mixing of turbulent streams with different physical properties is a highly complex task. For example, as we noted above, major difficulties are encountered in interpreting the readings from the measuring instruments. Another problem is the attainment of identity of the initial and boundary conditions on different experimental setups. These difficulties cause disagreement among the data of different authors, which have been discussed on several occasions in the literature [1], [3].

Thus, the acquisition of reliable data over a sufficiently broad range of variation of the parameters m and n is in large part a matter for the future. Nevertheless, the available results permit a comparison with the conclusions of the theory developed in Chapter I.

Let us begin with an analysis of the mixing of jets with equal temperatures but different densities (different molecular weights). Here interest attaches to the experiments of Alpinieri [48], who investigated the mixing of round jets of hydrogen (n = 17) and carbon dioxide (n = 0.7) with a cocurrent stream of air whose velocity was held constant at 198 m/sec.

279
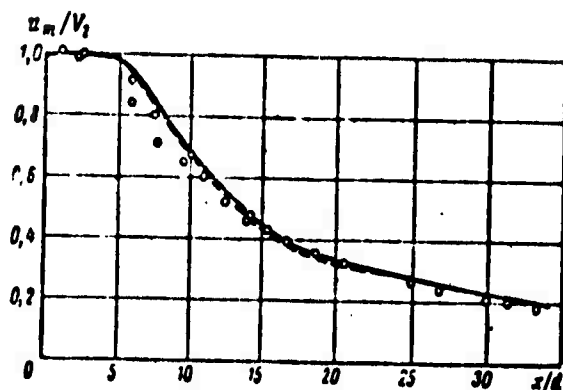
Figure 2.18. Axial velocity in axisymmetric submerged jet.

--- Corrsin; O — Forstall;
—— — theory.
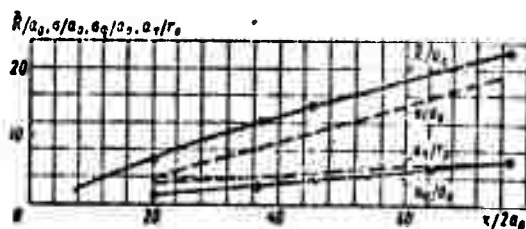
Figure 2.19. Comparison of average radius and dispersion of submerged jet with amplitude of turbulence front (σ_f/a_0) and its average position (R/a_0).

• — experiments of Corrsin and Kistler.

Figure 2.21 presents data on the profiles of concentration by weight at various distances downstream. The measurements were made at distances at which the stream velocities had become substantially equal. As was indicated in Chapter I, §2, we have in this case

$$a_1 \simeq \frac{1}{\sqrt{m}}\, a_0.$$

To construct the weight-concentration profile g_2, we use experimental data for the jet axis to determine the dispersion from the equality

$$\frac{1 - e^{-\frac{a_0^2}{2m_1^2}}}{u n e^{-\frac{a_0^2}{2m_0^2}} + 1 - e^{-\frac{a_0^2}{2m_1^2}}} = g_2(0).$$

This equality follows from the relation obtained in our analysis of the problem of gas-analysis data interpretation; it can be used to determine the function $\sigma(x)$ from the concentration distribution on the jet axis (see Figure 2.21).
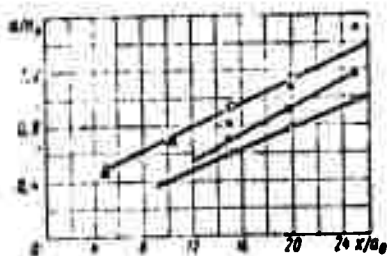
Figure 2.20. Dispersion of jets of gases with different densities in cocurrent air stream (according to Alpinieri's experiments).

$-m$ 1.25, $\blacksquare -m$ 1.54, $\triangle$ m 2.13 (CO₂):
$\bullet -n$ 0.8, $\blacktriangle$ m 1.05, $\bigcirc -m$ 1.57 (H₂)

Knowing the dispersion, we can construct the theoretical concentration profiles in Figure 2.20. As we see, the theoretical curve, which has been controlled with the experiment only at a single point on the axis, is in good agreement with experiment.

The dispersion in Alpinieri's experiments behaved in a highly unique fashion. In fact, the parameter σ increases practically linearly:

$$\sigma \simeq 0.04(x - x_0),$$

where x_0 depends on m and n.

On the basis of a generalizing analysis of the experimental data on σ that is given in Chapter III, it can be stated that this value corresponds to the case m ≈ 1, in which the turbulence of the outer stream is decisive, and the slope corresponds for small x to the intensity of the established pipe turbulence.

It will be shown that interest attaches to the similar variation of the dispersion observed in experiments by a whole series of American investigators [49] working on other installations to study the decrease in axial concentration at large distances downstream, where

$$\varkappa = \frac{P_{2m}}{nP_{1m} + P_{2m}} \simeq \frac{P_{2m}}{n} \sim \frac{a_r^2}{2n\sigma^2} = \frac{a_0^2}{2mn\sigma^2}. \qquad (2.60)$$

It follows immediately from this that, if the dispersion is independent of the properties of the jet (i.e., if it is determined by the turbulence generated outside of it), the law of concentration decrease depends on the combination
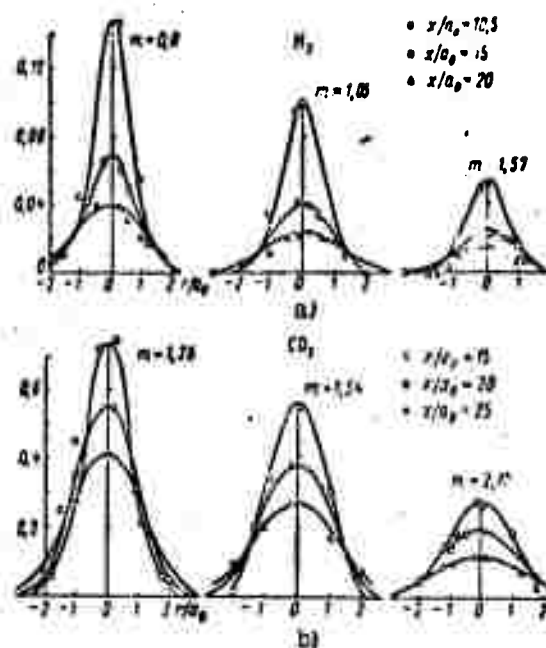
Figure 2.21. Concentration distribution in axisymmetric jets of hydrogen (a) and carbon dioxide (b) at various ratios of jet and cocurrent stream velocities.

O, □, Δ — according to Alpinieri's experiments; —— —— theory.

$$\lambda = \frac{1}{nm} = \frac{n_1 V_2}{n_{01} V_1}.$$

Precisely this fact was reported in [49] without notice of its implication of the presence of strong external generation of turbulence unrelated to the usual pattern observed in jets (Chapter III).

The formula proposed in [49] to describe the axial-concentration decrease,

$$\bar{g}_2 = \left(\frac{\frac{x}{a_1}}{22\sqrt{\lambda}} \right)^{-1},$$

agrees fairly well with the formula obtained using the dispersion law
reported from Alpinieri's experiments:

$$g_1 \simeq \frac{a_0}{2nm} \frac{1}{c^2} \simeq \frac{\varrho_{02} V_2}{\varrho_{01} V_1} \frac{a_1}{2(0,04\,x)^2} \simeq \left(\frac{\frac{x}{a_1}}{18\sqrt{\lambda}}\right)^{-2}.$$

The fact that the dispersion is independent of the density ratio
of the streams being mixed (see Chapter III) enables us to explain the
usefulness of the "jet equivalent radius" concept that has been intro-
duced by a number of authors [50]. They observed in analysis of their
experimental data that the rate of temperature decrease on the axis of
a submerged axisymmetric jet is a universal function (independent of
the initial-temperature ratio) of the dimensionless coordinate x/a'_0
where

$$a'_0 = a_0 \sqrt{\frac{\varrho_{02}}{\varrho_{01}}} = a_0 \sqrt{\frac{T_1}{T_2}}.$$

(Here we are concerned with nonisothermal jets whose molecular weights
are the same as those of the surrounding media.)

In fact, at large distances from the beginning of the jet, accor-
ding to (2.54),

$$\frac{\bar{T} - T_1}{T_2 - T_1} \simeq \frac{P_2}{n} = \frac{a_T^2}{2ns^2}.$$

On the other hand, in a submerged jet, according to (2.51) of
Chapter II:

$$\frac{a_0^2}{s^2} = 2\frac{d}{f},$$

where

$$d = \frac{a_T^2}{3s^2}, \quad f \simeq n.$$
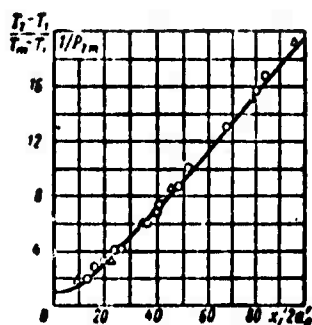
Figure 2.22. Temperature
variation along the axis,
expressed in terms of
equivalent mouthpiece
radius. $\triangle - \frac{1}{P_{2m}}$ $(n = 1;$ $\bigcirc - \frac{T_2 - T_1}{T_n - T_1}$ $(n = 2)$
(experiments of Sunavala);
— calculation.

From this

$$a_r^2 \sim \sqrt{n} a_0 \sigma$$

or

$$\frac{\bar{T} - T_1}{T_1 - T_1} \sim \frac{a_0}{\sqrt{n}\sigma} = \frac{a_0'}{\epsilon}. \qquad (2.61)$$

This universality proceeds
directly from (2.61) if the dis-
persion does not depend on n.

Reference [50] reports the
result of special experiments
designed to confirm the "equivalent

radius" concept. The axial concentration of the matter of an isother-
mal jet (P_{2m}) and the temperature of a nonisothermal jet $(n =$

$\frac{T_2}{T_1} = \frac{593°\,K}{298°\,K} \simeq 2)$ were measured.

In Figure 2.22, $1/P_{2m}$ has been plotted against x/a_0, and $\frac{T_2 - T_1}{T_m - T_1}$

against x/a'_0. The practical agreement between the two curves is
evident. The theoretical curve is also shown [plotted for $\sigma =$

$0,1\left(\frac{x}{a^0} - 10\right)\Big]$.

As we noted in Chapter I, §2, it is necessary in analyzing the
results of experiments pertaining to the mixing of streams with widely
different temperatures to take account of the complex nature of the
mixing $(0 < N < 1)$. On the other hand, these results permit indepen-
dent determination of a measure of mixing homogeneity — the degree
of greyness N — and comparison of this quantity with experimental
data obtained directly by the optical-diffusion method (see below,
Chapter III).

The experiments of V. Ya. Bezmenov and V. S. Borisov [51], who studied a submerged axisymmetric jet of air heated to 4000° K (n ≈ 14), are of special interest in this connection.

The idea of finding the degree of greyness from their data consists in the following.

The $a_T(\sigma)$ relation can be calculated theoretically (it was plotted in Figure 2.7 of Chapter II). On the other hand, it is known how the dispersion varies over length (see §3 of Chapter III):

$$\sigma \simeq 0.095\, x.$$

Consequently, a theoretical value of the average radius a_T can be determined in each cross section of the jet. The effective average radius a_{ef} is also found in each cross section from the experimental temperature profile (see Chapter II, §2, Figure 2.9). From the ratio a_{ef}/a_T and the diagram of Figure 2.9 in Chapter II, we can calculate a_{ef}/σ_c and then the ratio a_{ef}/σ. It is then easy to find the degree of greyness:

$$N = \frac{1}{\sigma}\,\frac{a_{ef}}{a_{ef}/\sigma_c} = \frac{\sigma_c}{\sigma}.$$

Clearly, the method set forth above for determination of N is valid if the jet temperatures are high enough (if n is much larger than 1), since otherwise, as Figure 2.9 shows, small errors in the numerical value of the ratio a_{ef}/a_T will result in wide scatter of the ratio a_T/σ_c. At the same time, we see from Figure 2.9 that when n < 1, i.e., when the temperature of the jet is lower than the temperature of the stream, the limitations are much less stringent.

The results of a rough calculation from the data of Bezmenov and Borisov appear in Figure 2.23. Also plotted are the points obtained by the optical diffusion method for nonisothermal jets. The agreement must be recognized as highly indicative.
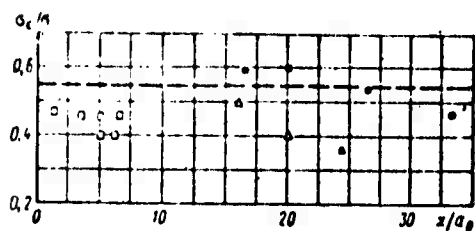
Figure 2.23. Degree of greyness in nonisothermal jets.

• — reduction of data of V. Ya. Bezmenov and V. S. Borisov; □ — d = 30 mm; n = 4 — 5; m = 0.8; Δ — d = 10 mm; n = 0.6 — 0.8; m = 0.46 — 0.6; experiments of N. A. Zamyatina.
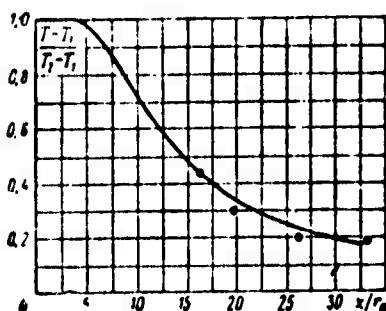
Figure 2.24. Axial temperature in nonisothermal jet (n = 14; m = 0).
—— — calculation; • — experiment.

In Figures 2.24 and 2.25, the theoretical curves for the decrease in the axial velocity-heads and axial temperatures agree with experiment.

The calculations were made with an average degree of greyness equal to 0.55. It was also found necessary to make a rough correction for the nonuniformity of the initial profiles. Namely, the integrals of the experimental dimensionless velocity-head profiles $\frac{\varrho u^2}{\varrho_{0i} V^2}$ were not equal to $\frac{a_0^2}{2}$, as it should be for rectangular initial profiles, but equalled $\frac{a_0'^2}{2}$, where $a_0' \simeq 0.83 a_0$. The calculations were therefore made for a jet with a fictitious initial radius a'_0.

To illustrate the differences in the density values found from experimentally known axial temperatures with different degrees of greyness, Figure 2.26 compares curves obtained by formal application of the equation of state for (N = 1) with those calculated for a number of specific values of N.

We see that the error is about 30% for realistic values of the degree of greyness. Since the magnitude of this error decreases sharply with decreasing n, the equation of state can be used with sufficient accuracy for temperature ratios that do not exceed 3 — 4.
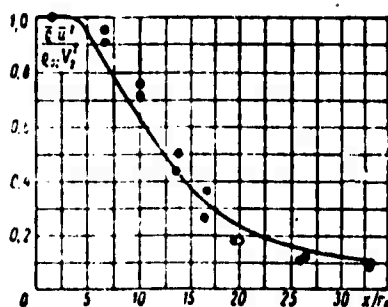
Figure 2.25. Axial values of velocity head in nonisothermal jet.

—— calculation; ● —— experiment.
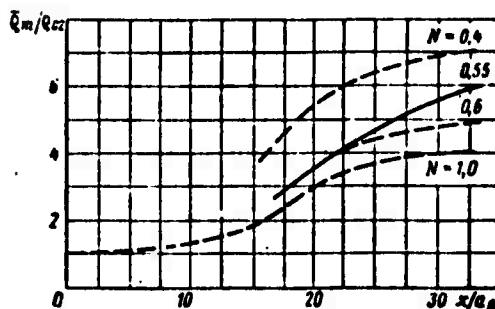
Figure 2.26. Influence of degree of greyness on axial density determined from known temperature (the solid curve represents a rough calculation from the experiments of V. Ya. Bezmenov and V. S. Borisov, $n = 14$, $N = 0.55$).

We take note of yet another interesting fact. It is found that the universality of dispersion (in the sense of independence of the density ratio) in the submerged jet is practically equivalent to the dynamic-pressure universality.

If we plot a theoretical curve of $\dfrac{\rho u^2}{\rho_{o2} V_2^2}$ in the mixing layer against the ratio y/σ, we find that the relation is expressed by the same curve for a jet of air ($n = 1$) and a jet of hydrogen ($n = 14.5$) (Figure 2.27). In the real coordinates (y, x), therefore, the velocity head profiles will be universal if the dispersion is universal.

In any event, if experimental velocity head profiles are plotted against the dimensionless coordinate y/σ, the experimental points should, according to the theory, lie on the same curve. This universality was indeed observed in the experiments of Sh. A. Yershin and Z. B. Sakipov [52] (Figure 2.27). They studied the initial segment of a nonisothermal jet ($n = 4 - 5.3$) emerging from a nozzle at a precompression ratio of 19 ($2a_o = 46$ mm) and the initial segment of a hydrogen jet issuing into the atmosphere through a nozzle 5 mm in diameter with a precompression ratio of 625. Experiments with a non-isothermal jet were also performed for comparison on the same installations. The outflow velocity was varied in the range from 30 to 120 m/sec.
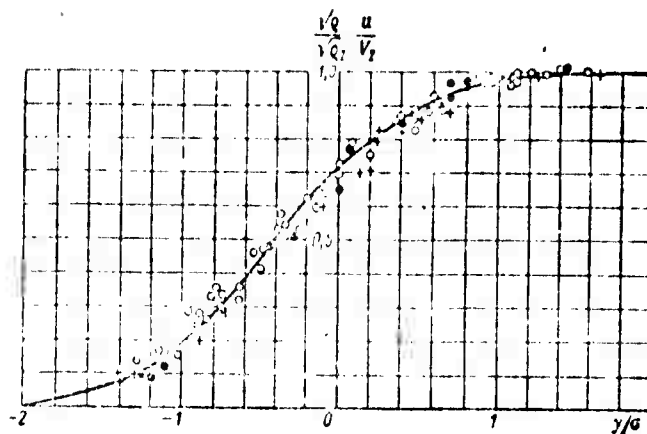
Figure 2.27. Universal profile of dynamic pressure in mixing layer.
● — isothermal jet (n = 1); + — nonisothermal jet (n = 1 — 4);
○ — hydrogen jet (n = 14.5) (experiments of Sh. A. Yershin and Z. B. Sakipov); — — theory (Pr = 0.5).

Self-similarity with respect to y/kx was observed in the experiments, indicating a linear increase of the parameter $\sigma = kx$. Here the coefficient k was left approximately constant for each of the installations: k = 0.11 — 0.13 for the first and k = 0.105 . r the second in the hydrogen experiments and k = 0.083 in the isothermal jet experiments. The scatter of the values of k may be either a consequence of the different initial conditions (which include different n), which are taken into account in this relation not through x_0, but through the different values of k, or a direct effect of the density ratio on σ for the transitional range of the jet ($x \geq x_0$).

The comparatively large k for the first installation can be explained, for example, by a higher level of the fluctuations due to fire preheating [53].

Quite analogous results are obtained on analysis of the decay of the dynamic pressures along the axis of a round submerged jet (Figures 2.28 and 2.29). In this case, although some stratification is evident (the dynamic pressure drops off more rapidly in the lighter jet), it will be understood that this stratification is within the limits of experimental error when the dispersions are equal.
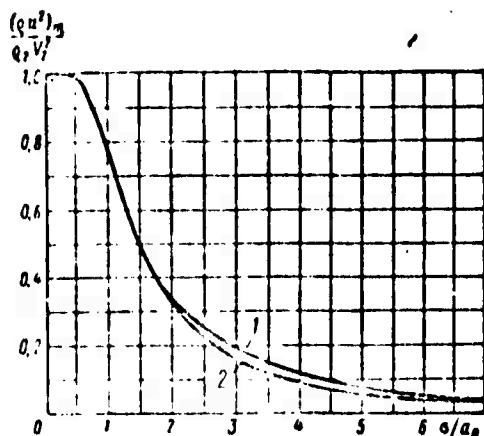
Figure 2.28. Variation of dynamic pressure along axis of submerged jet (calculation for Pr = 0.5).

1 — n = 1.0; 2 — n = 14.5.
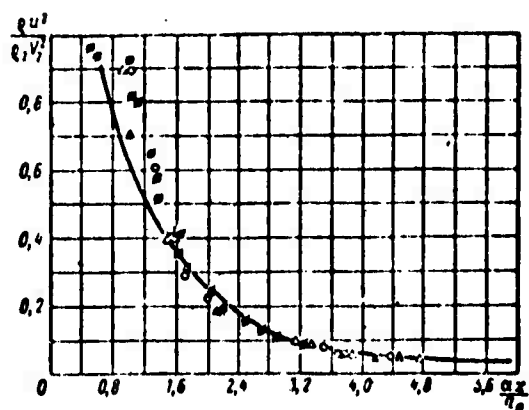
Figure 2.29. Universal nature of dynamic pressure on axis of submerged jet.

▲, ○, △ — experiments of L. A. Vulis and N. N. Terekhina (n = 1 — 14.5); —— — calculation for σ = 1.18x.

Thus, the conclusion of L. A. Vulis [53] to the effect that velocity head stratification is due solely to changes in the turbulent mixing characteristics (specifically, the dispersion of the jet) from one installation to another is confirmed in the particular case of the submerged jet.

In the light of the above, it is appropriate to consider the problem of conditions that minimize mixing in the jet. As we know, various authors disagree sharply on this question. Thus, it is stated in the work of G. N. Abramovich and his co-workers that this condition consists in equality of the stream velocities (m = 1) [1]. L. A. Vulis [53] proposes, to the contrary, that the dynamic heads must be equal (m^2n = 1). Finally, the significance of the combination λ = mn is noted in the work of American investigators.

Two different aspects of the problem are naturally distinguished here. First, there is the aspect related to the minimum-dispersion question. It will be shown in Chapter III that the dispersion is minimized at equal velocities of the jet and cocurrent stream. As the cocurrency parameter m increases, the dispersion decreases in proportion

to the multiplier 1 - m. It is also noted that, when the initial-turbulence level is high, the dispersion ceases to change even at m = 0.5 — 0.6, remaining constant all the way up to m = 1.5 — 2, after which it resumes its increase.

Secondly, there is the separate question as to the conditions for minimal mixing on the axis of the jet. The answer is to be found in the laws of variation of the ratio a_T/σ, since it is on this ratio that the axial concentration depends.

Let us analyze the trend of the ratio a_T/σ as the cocurrency parameter m varies (with the parameter n fixed). As a concrete example, we propose to consider a point on the axis of the jet at the very beginning of the main segment, where the relations obtained for the mixing layer can be used with sufficient accuracy. (This hypothesis corresponds to the experimental conditions of [3], in which it was observed that minimal mixing occurs when $m^2 n = 1$.)

Then when $m < m_0$ (m_0 depends on the level of the initial turbulence),

$$\frac{a_T}{\sigma} \simeq \frac{a_0}{\sigma} + (1-m)\psi \simeq \frac{a_0}{\sigma_0}\frac{1}{1-m} + (1-m)\psi. \qquad (2.62)$$

where σ_0 is the dispersion in the submerged jet and the function ψ reflects the influence of the density and velocity ratios on the increase of the average radius [see (2.40)].

For $2 - m_0 > m > m_0$:

$$\frac{a_T}{\sigma} \simeq \frac{a_0}{\sigma_{m0}} + (1-m)\phi. \qquad (2.62')$$

Here σ_{m0} is the smallest possible dispersion in this jet cross section.

It follows from (2.62) and (2.62') that a_T/σ increases* (mixing deteriorates) as m increases to m_0. The ratio a_T/σ then decreases and mixing becomes stronger. The mixing minimum will occur at m = m_0. Thus, for a low initial turbulence level ($m_0 \simeq 0.9 - 1$), the mixing minimum corresponds to equal velocities of the jet and cocurrent stream.

At a high level of initial turbulence and $m_0 \simeq 0.5 - 0.6$, the mixing-minimum condition, written in terms of the dynamic-pressure ratio, will take the form

$$(m^2 n)_{min} = m_0^2 n.$$

If n = 3 — 4, as in the experiments of I. B. Palatnik [3],

$$(m^2 n)_{min} \approx 1.$$

Thus, the results cited in [3] are evidently not of a general nature.

We may therefore state that the condition for minimum mixing depends not only on the parameters m and n, but also on the level of the initial turbulence in the streams whose mixing laws are being studied.

§3. Wall Jets in a Subsonic Stream**

The existing methods of solving problems of free turbulent jets and wall jets are based on the familiar methods of semiempirical turbulence theory [1] — [3]. But, as a rule, these methods are found to differ for different boundary conditions. The attempt by Spalding [4] to generalize the integral equations for turbulent flows with a

---

*This increase is due to the increase in the first term in (2.62), which is more rapid than the decrease in the second term when $\psi < -\frac{a}{a_{11}}$.

**The results of this section were obtained by E. P. Yukina [152].
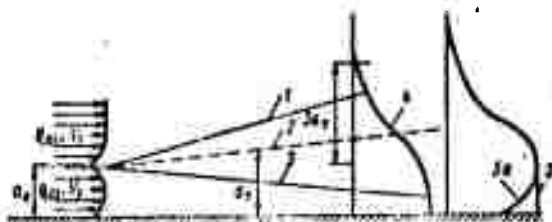
Figure 2.30. Diagram of mixing of semibounded jet.

1 — outer boundary of mixing zone; 2 — statistical average boundary of jet; 3 — inner boundary of mixing zone; 4 — P_2 — average concentration profile (excess-temperature profile in the case of a heat-insulated wall); 5 — excess-velocity profile for ideal wall according to diffusion model D_T = in var (x, y); 5a — real velocity profile.

broad class of boundary conditions reduces essentially to simultaneous use of two different solutions of the semiempirical theory for free and wall jets.

In the present section, we examine a method of computing concentration (temperature) and velocity profiles when gas is injected through a slit in a porous wall; it constitutes a generalization of the method based on the diffusion model for calculation of free turbulent jets. It is shown that when the dispersion $\sigma^2(x)$, obtained from laws similar to those of the free boundary vortex layer, is used as the determining parameter, satisfactory description of the experimental data becomes possible.

As a first example, let us consider a semi-bounded jet of density ρ_{02} issuing at velocity V_2 into a cocurrent stream of density ρ_{01} and velocity V_1 (Figure 2.30). We find the general solution of the diffusion equation with the initial and boundary conditions

$$P_2(0, y) = 1 \qquad 0 \leqslant y < a_0;$$
$$P_2(0, y) = 0 \qquad y > a_0;$$
$$\frac{\partial P_2}{\partial y}\bigg|_{y=0} = \frac{\partial P_2}{\partial y}\bigg|_{y=\infty} = 0$$

in the form of the relation

$$P_2 = \frac{1}{2}\left[\Phi\left(\frac{y + a_1}{\bullet}\right) - \Phi\left(\frac{y - a_1}{\bullet}\right)\right], \qquad (2.63)$$
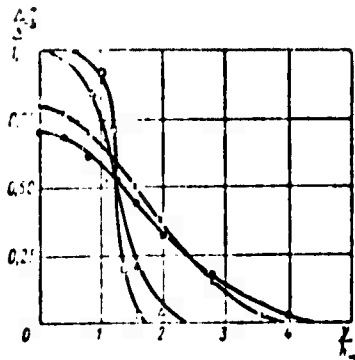
Figure 2.31. Temperature variation in cocurrent semi-bounded jet (workup of an experimental V. Ya. Borodachev) $(h_S = 5$ мм, $\Delta t_0 \; 6.0 \degree K$; $m = 1.5)$:

$\square - \frac{x}{h_S} = 4,$ $\triangle - 16;$ calculation

$\times - 64;$ $\bullet - 84$
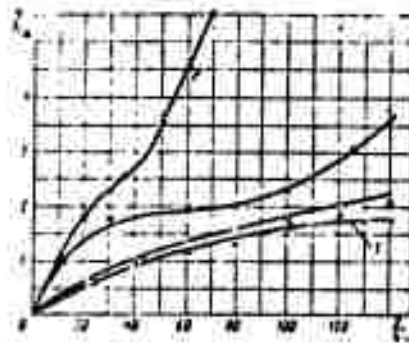
Figure 2.32. Change in dispersion of wall jet on initial and transitional segments (workup of data of B. A. Zhestkov, V. Ya. Borodachev, and A. T. Trofimenko).

1 — calculation from parameters of free stream pipe turbulence;

$\bullet - m = 0;$ $\square - m = 2.36;$ $\circ - m = 1.55;$ $\triangle - m = 0.075$

where $\Phi(x)$ is the probability integral: $\Phi = \frac{2}{\sqrt{2\pi}} \int\limits_0^x e^{-\frac{t^2}{2}} dt,$ and σ and a_T are the parameters in cross section x.

We note that the average convective flux of jet volumes in the transverse direction is implicit in the parameter a_T, while the diffusion flux across the jet is expressed by the parameter σ^2, with $\frac{d\sigma^2}{2\,dx} \approx \frac{D_t}{\bar{u}_{av}}$ and $\frac{da_t}{dx} \approx \frac{\bar{V}}{\bar{u}_{av}},$ where $\bar{V}$, $\bar{u}_{av}$, and D_T are, respectively, the transverse and longitudinal velocities averaged over the jet cross section and the eddy diffusivity.

The "displacement thickness" a_T of the jet is determined from the theoretical or experimental P_2 profile with the relation

$$a_t = \int\limits_0^\infty P_2 \, dy. \tag{2.64}$$
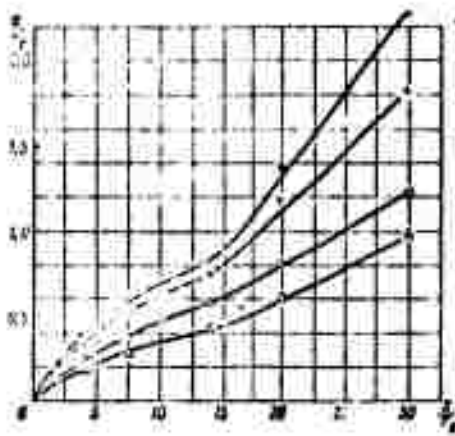
Figure 2.33. Change in dispersion of free jet on initial and transitional segments (workup of data of I. V. Palatnik).

$\bullet - m=0; \; + - m=0.145; \; \circ - m=0.296; \; \triangle - m=0.380$

It was shown earlier (see Chapter I) that for small overheats ($n \approx 1$), P_2 coincides with the dimen-cionless excess temperature profile. Thus, the agreement of Formula (2.63) with experiment can be illustrated by reference to the experimental temperature profile of a plane-parallel jet with small overheat over a heat-insulated wall. Such curves are plotted in Figure 2.31 according to the data of V. Ya. Borodachev and B. A. Zhestkov. Figure 2.32 gives values of the parameter $\sigma(x)$ for semi-bounded jets, as calculated from temperature profiles (heat-insulated wall) measured in [141] (submerged wall jet) and in the experiments of Borodachev and Zhestkov for the range of cocurrency range

$$m = \frac{V_1}{V_2} = 0.7 \div 2.36.$$

For comparison, Figure 2.33 shows values of the dispersions on the initial and transitional segments of a free jet according to the experimental data of I. B. Palatnik. We see on comparing Figures 2.32 and 2.33 that the manner in which $\sigma(x)$ varies over length and with respect to the cocurrency parameter m is the same for wall and free jets on the initial and transitional segments when the jet is semi-bounded. The absolute values of σ were different on the initial segment in the experiments (see Figures 2.32 and 2.33) because of the different levels of the initial perturbations in the boundary layers. In Palatnik's experiments, in contrast to the others, they were deliberately sharply reduced. In the experiments of Figure 2.32, the slope of $\sigma(x)$ at the transition to the main segment is found to be the same for given values of m much smaller than unity, as for the case of

developed free turbulent jets, and at $m \to 1$, the value of σ approaches the value corresponding to the level of developed cocurrent stream pipe turbulence.

On the initial segment of the jet, it is obviously only the free boundary (vortex) layer that makes the main contribution to the dispersion. On the main segment, when σ has become much larger than a_T, the wall begins to make itself felt. Its effect should be manifested in a change in the growth rate of free-layer vortices,* the value of $\bar{u}_{av}$ and, consequently, the effective value of σ. However, no such variation was observed in the experiments cited ($x/h \leq 150$).

Similarly, the excess velocity profile above an ideal surface is written

$$\frac{\bar{u}-V_1}{V_2-V_1} = \frac{1}{2}\left[\Phi\left(\frac{y+a_V}{\sigma_V}\right) - \Phi\left(\frac{y-a_V}{\sigma_V}\right)\right], \qquad (2.65)$$

where

$$a_V = \int_0^\infty \frac{\bar{u}-V_1}{V_2-V_1}\,dy;$$

σ_V is a parameter characterizing the diffuseness of the velocity profile.

The relation between the diffusion parameters a_T, a_V, σ, σ_V introduced above is assigned by two integral conservation laws.

The law of conservation for jet mass flux is

$$\int_0^\infty \bar{u}P_2\,dy = a_u V_2. \qquad (2.66)$$

The law of momentum conservation (without consideration of friction)

---

*Estimates of the growth rate of the boundary layer at the wall indicate that the vortices at the wall grow more slowly.
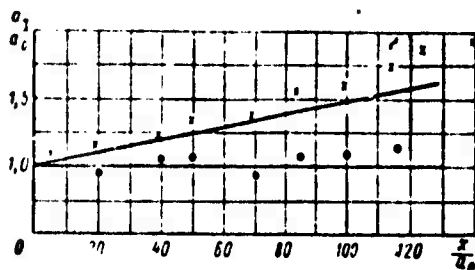
Figure 2.34. Comparison of calculated and experimental values of statistical average jet boundary $a_T(x)$.

$x - m = 0.643$; $\bullet - m = 1.0$; ——calculation without consideration of friction.

is

$$\int_0^\infty \bar{u}^2 \, dy = a_0 V_2^2 + J_1. \qquad (2.67)$$

Here J_1 is the initial momentum of the cocurrent stream.

Substituting the profiles (2.63) and (2.65) into (2.66) and (2.67), we obtain the relations:

$$a_0 = \frac{2m}{1+m} a_V + \frac{1-m}{1+m} \left[a_V \Phi \left(\frac{a_V}{\sigma_V} \sqrt{2} \right) + \frac{\sigma_V}{\sqrt{\pi}} \left(e^{-\frac{a_V^2}{2\sigma_V^2}} - 1 \right) \right]; \qquad (2.68)$$

$$a_0 = m a_T + \frac{1-m}{2} a_T \left[\Phi \left(\frac{a_V + a_T}{\sqrt{\sigma_V^2 + \sigma^2}} \right) + \Phi \left(\frac{a_V - a_T}{\sqrt{\sigma_V^2 + \sigma^2}} \right) \right] +$$
$$+ \frac{1-m}{2} a_V \left[\Phi \left(\frac{a_V + a_T}{\sqrt{\sigma^2 + \sigma_V^2}} \right) + \Phi \left(\frac{a_T - a_V}{\sqrt{\sigma^2 + \sigma_V^2}} \right) \right] +$$
$$+ \frac{1-m}{2} \frac{2}{\sqrt{2\pi}} \sqrt{\sigma_V^2 + \sigma^2} \left\{ e^{-\frac{(a_V + a_T)^2}{2(\sigma^2 + \sigma_V^2)}} + e^{-\frac{(a_V - a_T)^2}{2(\sigma^2 + \sigma_V^2)}} \right\}, \qquad (2.69)$$

where $m = V_1/V_2$.

Thus, assigning the dispersion σ^2 from experiment and taking the same turbulent $Pr = \frac{\sigma_V^2}{\sigma_T^2}$ as in the case of free jets ($Pr = 0.5$), we can use Formulas (2.68) and (2.69) to calculate a_T and a_V and, consequently, the concentration (temperature) and velocity profiles.

Figure 2.34 presents a comparison of the calculated and experimental values of the statistical average jet boundary $a_T(x)$. The disagreement with experiment that is observed at a distance of about 80 calibers can be explained by a marked decelerating effect of friction

x₀: present
coordinate of filament
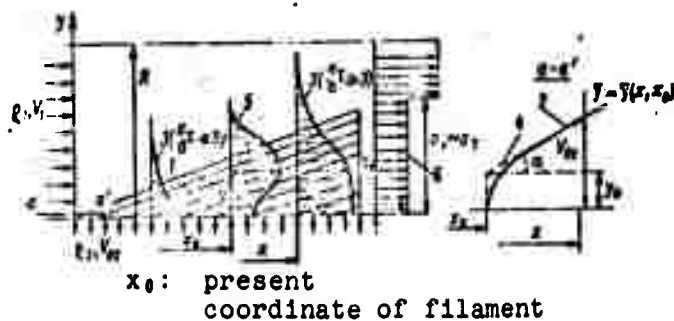
Figure 2.35. Mixing diagram for injection through porous wall.

1 — average trajectory of outflowing filament; 2 — average tra-
jectory of outflowing filament on initial segment a — a'; 3 —
profile of concentrations P₋ (probability of appearance of a volume
of the injected gas); 4 — approximation of average filament trajec-
tory; 5 — distribution density profile of probability of appearance
of outflowing filament $l[y, y(x_0, x)]$; 6 — profile of sample-averaged
velocities.

at great distances, which was not taken into account in the integral
momentum conservation law (2.67).

It is easy to construct similar solutions for the case in which
the jet does not lie against the wall but is lifted off it, for the
case of successive barrier-cooling wall jets, and for the case of a
plane-parallel jet between two walls. Similar solutions can also be
constructed for the more complex case in which the wall is not heat-
insulated and not ideal. In this case, the boundary values of the
temperature and velocity derivatives at the wall are assumed to be
given.

As a second example of wall diffusion of a jet, let us consider
diffusion of a gas in a pipe when it is injected through permeable
walls (Figure 2.35). The general solution for P_2 takes the form

$$P_2 = \int_0^{a_\tau} p(\vec{x}_0, \vec{x})d\vec{x}_0, \tag{2.70}$$

where $p(\vec{x}_0, \vec{x})$ is the probability distribution density for finding a
unit volume of an elementary filament from a point $\vec{x}_0$, which defines
the average position of the filament, at an arbitrary point $\vec{x}$. The

207

integration is extended over the entire range of the mathematical expectation of the diffusing gas "2" to the "displacement-thickness" boundary of the stream, "1" defined by the parameter a_T.

Replacing, for simplicity of integration, the average trajectory of the filament by two straight lines, as shown in Figure 2.35, and neglecting the longitudinal diffusion for $y \geq y_0$, we can approximate the probability density with the following function, which is a solution of the equation of diffusion from a point source with consideration of the impermeability of the wall:

$$p(\vec{x}_0, \vec{x}) \approx p(\vec{y}, \vec{y}) = \frac{1}{\sqrt{2\pi}\sigma(\xi)} \left[e^{-\frac{(y-\bar{y})^2}{2\sigma^2}} + e^{-\frac{(y+\bar{y})^2}{2\sigma^2}} \right]. \qquad (2.71)$$

Here $\xi = x - x_0$;

$$\bar{y} = y_0 + \operatorname{tg} u = y_0 + \frac{a_T(x)}{x} \xi;$$

a_T is the ordinate of the average position of the outermost filament, or the "displacement thickness" of cocurrent stream filaments;

$$\sigma = \sigma(\xi), \quad \text{where} \quad \sigma_{\xi=0} = \sigma(y_0) \neq 0,$$

i.e., $\sigma = \sigma(\xi) + \sigma(y_0)$.

Substituting (2.71) into (2.70), we obtain

$$P_2 = \int_{y_0}^{a_T} p(\bar{y}, y) d\bar{y} = \frac{a_T}{x} \int_0^{x\left[1-\frac{y_0}{a_T}\right]} p(\xi, y) d\xi \approx \frac{a_T}{x} \int_0^x p \, d\xi, \qquad (2.72)$$

(since $\frac{y_0}{a_T} \ll 1$).

For strong injection $\left(\frac{a_T}{\sigma} \geq 2.5 \right)$, for example, Relation (2.72) can be written in the simpler form

$$P_2(x, y) = \frac{1}{2} \left\{ 1 - \Phi \left[\frac{y - a_T(x)}{\sigma(x)} \right] \right\}$$

and

$$P_s(\dot{x}, 0) = \frac{1}{2}\left[1 + \Phi\left(\frac{a_T}{\bullet}\right)\right] \approx 1. \quad (2.73)$$
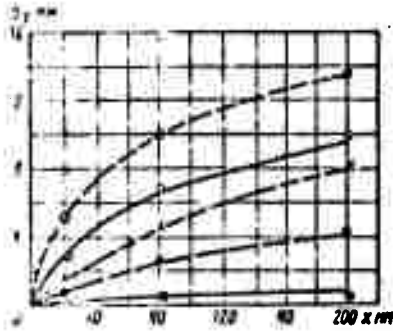
Figure 2.36. Variation of average jet boundary $a_T(x)$ in a pipe for various injection rates (workup of data of V. I. Bespalov and A. M. Gubertov).

$:-v,.\ 0.1;\ \bullet -v,.\ 0.07;\ \times -0.005;\ 0 -0.0192;$ $\blacksquare -0.0455;\ ----\ $ experiment; —— calculation.

Figure 2.38 presents experimental volume-concentration profiles measured by I. V. Bespalov and A. M. Gubertov for carbon dioxide injected through the porous wall of a round pipe, together with theoretical profiles constructed from Relations (2.72) and (2.73). The values of the parameters a_T and σ were determined from experimental profiles (Figures 2.36 and 2.37). The agreement of theory with experiment in Figure 2.38 illustrates the accuracy of the diffusion model for the particular case.

The experimental value of a_T is determined from the excess-concentration (temperature) profiles with the aid of (2.64).

The integral laws of conservation can be used for theoretical determination of the "displacement thickness" a_T as in the case of the semi-bounded jet.

Here the fundamental equations are the equation of mass conservation for the injected gas, written for a round pipe of radius $R \gg a_T$, in which the experiments were performed:

$$\int \bar{u} P_s \, dF = 2\pi R V_{sx} x, \quad (2.74)$$

(F is the area of the pipe).
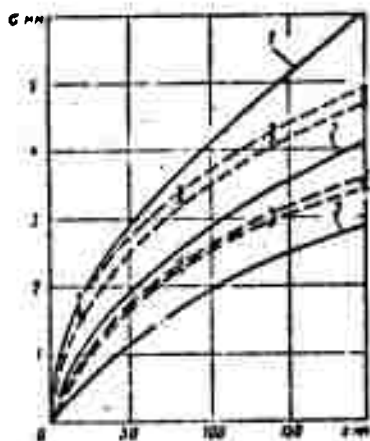
Figure 2.37. Injection of carbon dioxide through porous walls of pipe with $d_{pp} = 50$ mm (according to V. I. Bespalov and A. M. Gubertov).

1 — dispersion of coaxial jet at m = 2; 2 — dispersion of coaxial jet at m = 1; 3 — integral value of $\sigma = (m-1)/\sqrt{F}$ $\bullet - q_x = 0.1$; $\times - 0.05$; $0 - 0.019$; $\blacksquare - 0.004$; $+ - 0.0098$

Axis of pipe
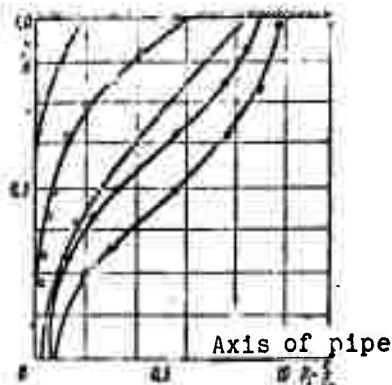
Figure 2.38. Concentration profile for various injection rates (experiments of I. V. Bespalov and A. M. Gubertov).

—— calculation;

$\times - q_x = 0.1$; $\bullet - 0.0567$; $\times - 0.0815$; $0 - 0.0192$; $+ - 0.0455$

$\frac{x}{d_{тр}} = 4.0$

The general mass conservation equation is

$$\int \bar{\varrho}\bar{u}\,dF = 2\pi R \varrho_1 V_{s4} c + \varrho_1 V_j F. \qquad (2.75)$$

The equation of momentum conservation is

$$\int \bar{\varrho}\bar{u}^2\,dF = \varrho_1 V_1^2 F + F\Delta p - F_{mp}, \qquad (2.76)$$

and the two energy equations for the injected gas and the cocurrent stream are, respectively,

$$\frac{\varrho_2 u_2^2}{2} - \frac{\varrho_2 V_{2n}^2}{2} = \Delta p; \qquad (2.77)$$

$$\frac{\varrho_1 u_1^2}{2} - \frac{\varrho_1 V_1^2}{2} = \Delta p. \qquad (2.78)$$

In these equations, the work done by one gas on the other is neglected for simplicity. V_{2n} is the injection velocity, $\bar{\rho}$ is the average density: $\bar{\rho} = \rho_1 \approx \rho_2$ (air and carbon dioxide), u_1 and u_2 are the sample-averaged longitudinal velocities of the air and the injected gas, $\bar{u} = \bar{u}_1 P_{1v} + \bar{u}_2 P_{2v}$; $P_{1v} + P_{2v} = 1$; P_{2v} is the probability of occurrence of the velocity of the injected gas, and Δp is the static-pressure difference between cross sections x and x_0. Instead of the pressure in the present cross section x_0, we might take the static pressure in front of the cross section at which injection begins and still obtain sufficient accuracy. F_{fr} is the force of friction, which depends on the injection parameter

$$B_0 = \frac{\rho_1 V_1}{\rho_2 V_{2n} c_{fn}}$$

(c_{fn} is the coefficient of friction in the absence of injection).

The function P_{2V} is written in the same way as P_2, except that a_V and σ_V are to be substituted instead of a_T and σ.

Equations (2.74) — (2.78) form a closed system with five unknowns: $\bar{u}_1, \bar{u}_2, a_T, a_V, \Delta p$. Figures 2.36 and 2.39 present the results of iterative calculation of the average jet boundary and the static pressure in the pipe for two injection rates: $q_w = \frac{\rho_2 V_{2n}^2}{\rho_1 V_1} = 0.0567$ and $q_w = 0.00455$. Here the parameter $\sigma(x)$ was calculated from the experimental profiles of carbon dioxide volume concentration measured by Bespalov and Gubertov. The Prandtl number was assumed equal to 0.5.

The preceding figures showed cases of wall jets with $n \approx 1$ (a jet of weakly preheated air or carbon dioxide), where the difference between the mass-average and volumetric probability profiles is not essential to the specifics of convective transport and gradient diffusion.
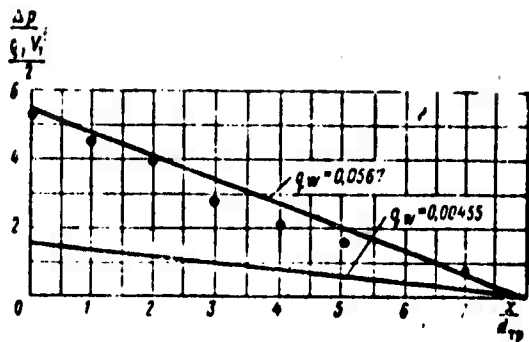
Figure 2.39. Variation of static
pressure over length of pipe.

• — experiment of I. V.
Bespalov and A. M. Gubertov,
$q_W = 0.049$; —— calculation.

Figure 2.40 shows the volume-
concentration profiles for two
gases with widely different densi-
ties (helium and carbon dioxide)
injected through the porous walls
of a pipe, for two different condi-
tions: q_W = const and V_2n/V_1 =
const. The dispersion was the same
in both cases, but the displacement
thicknesses were the same only at
equal injection velocities. Never-
theless, the calculation of the
volume concentration with Relation
(2.72) agrees satisfactorily with experiment in both cases.

Figures 2.41 and 2.42 give values of the displacement thickness
a_T and the parameter σ for various rates of injection through a porous
plate. Since the flow in this case has practically no pressure gradi-
ent along the stream, a_T varies in accordance with the law

$$a_T = \frac{V_{2n}}{V_1} x,$$

and the increase in the parameter σ along x is found to be stronger
at high injection rates than for injection at the same rates into a
stream bounded by walls. The agreement of the calculated and experi-
mental concentration profiles for various injection rates is demon-
strated in Figure 2.43. Let us dwell on the features of the dispersion
curve for injection in a pipe and on a plate (see Figures 2.37 and
2.42).

In contrast to the dispersion of a jet supplied from one source,
the dispersion in a jet with distributed delivery depends on a much
larger number of secondary factors: on the increase in longitudinal
velocity on delivery in a pipe, on the partial averaging of this
velocity not only over the cross section, but also over the length of
the stream (all filaments from o to the injection abscissa x contribute
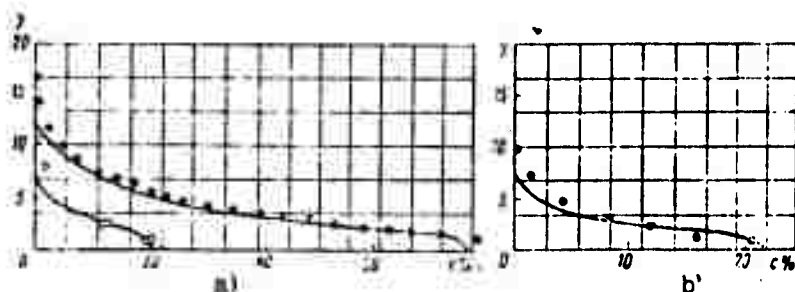
Figure 2.40. Concentration profiles for injection of gases with various densities through a porous pipe (data of I. V. Bespalov). a — stratification of volume concentrations of He and CO_2 at q_W = const; • — He, x = 200 mm; O — CO_2; q_W = 0.00454; — calculation by formula (2.72); $\sigma_{CO_2} \approx \sigma_{He}$ = 3.3 mm; a_T = f(n); n = ρ_g/ρ_a; b — agreement of volume concentrations at equal relative gas-delivery velocities (He, CO_2); • — He; CO_2; x = 200 mm; V_g/V_a = 0.003; — calculation by formula (2.72); $a_{T\ He}$ = $a_{T\ CO_2}$; $\sigma_{He} \approx \sigma_{CO_2}$ = 3.3 mm.

to the concentration field), on the boundary-layer parameters of the free stream, on the lengthwise variation of the cocurrency parameter, which is determined from the longitudinal velocity components of volumes of the two streams, on the manner in which these velocities are determined, and so forth. With this variety of influencing factors, it is most convenient to compare experiment with calculation on the basis of several extreme assumptions. Three calculated values of σ are plotted in Figures 2.37 and 2.42:

1. The value of σ for a free coaxial jet with m = 2, which corresponds approximately to the ratio of the stream velocity to the integral longitudinal velocity of the injected gas.

2. The dispersion of a coaxial free jet at m = 1 (the dispersion of steady-state turbulence in a pipe).

3. The dispersion of the jet for m = 1, but averaged over the time of diffusion from x = 0 to the x at the end of the injection length.
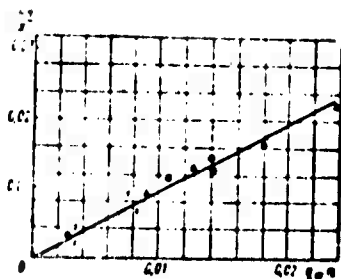
Figure 2.41. Variation of average boundary a_T for injection at various densities at a plate:

$$\frac{a_T}{x} = q_w n; \quad a_T = \int_0^\infty c(u)\, du, \quad q_w = \frac{c_w v_w}{\rho_i u_i};$$

$$\frac{Q_0}{v_T} = n; \quad \bullet\ \triangle - {}^{He} \text{(Bespalov, Bekritskaya)};$$
$$\times, \boxtimes - CO, \quad \text{(Bespalov, Yukina)}.$$
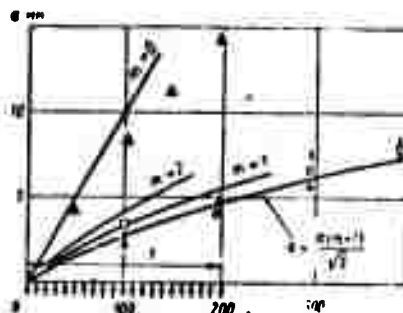
Figure 2.42. Variation of mixing parameter σ as a function of injection rate q_W for delivery of carbon dioxide through a porous plate:

1 — segment of porous plate;
$\triangle q_w = 0.03, \quad \times - c_w = 0.0051, \quad \square - q_w = 0.0059$
$\bullet - q_w = 0.0034;$ ——— calculation.

Figure 2.42 also gives values of σ for a submerged cocurrent stream ($m = 0$). It must be remembered in comparing the calculated σ with the experimental values that the experimental concentration profile at very small injection rates ($a_T/\sigma \ll 3$) is the result of averaging over the dispersions of all filaments, so that the effective value of σ is close to the value calculated in the form $\sigma = \sigma(m = 1)/\sqrt{2}$. With increasing injection rate ($a_T/\sigma \gtrsim 3$), the behavior of the variable part of the concentration profile is determined basically by the dispersion of the boundary filaments expelled in the region of $x \approx 0$: diffusion of the remaining filaments occurs in a range where the relative concentration is practically equal to one.

We see from comparison of Figures 2.37 and 2.42 that at large injection rates, the dispersions of streams with and without pressure gradients are found to differ. The injected gas is accelerated in the pipe as it moves along the stream, so that the effective value of m lies somewhere in the range from m = 1 to m = 2 (according to longitudinal velocity measurements), in agreement with direct measurements of σ.
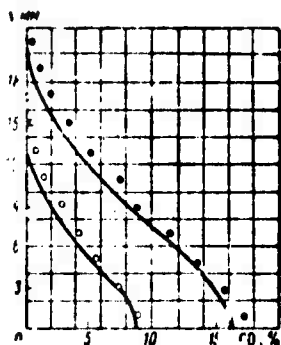
Figure 2.43. CO_2 concentration profiles for various injection rates on impermeable segment of plate, $x = 290$ mm (data of I. V. Bespalcv and E. P. Yukina). ● — $q_w = 0.001$; ○ — $q_w = 0.003$; —— calculation.

For plate flows, the entrainment of the gas decreases steadily with increasing injection rate, so that its cocurrency parameter tends asymptotically to infinity (the behavior of the cocurrent stream has as a limit the behavior of a submerged jet over an infinitely thick layer of gas that is at rest in the mean (see Figure 2.42 at $q_w \gg 0.03$).

Figure 2.44 shows the influence of the initial cocurrent stream turbulence on mixing rate. The turbulence intensity values ε indicated on the figure were measured at the initial cross section of injection. The relatively weak influence of the initial turbulence level is evident, and is explained by the ineffectiveness of local elevations and depressions of the turbulence above and below the pipe turbulence level. It is reported in the literature [14] that for a turbulizing grid that gives an initial ε = 15°, the average value of ε on a length $x \le 300$ mm (at calibers ≤17 M, where M ≈ b ≈ 18 mm are the characteristic dimensions of the grid) does not exceed 7 — 8%. Like ε, the eddy diffusivity behind a grid in technical pipes tends rapidly to a level determined by the size of the cocurrent stream (pipe diameter), so that its average value is no more than 40 — 60% greater than the corresponding steady-state value in the cocurrent stream. Here, according to the Taylor equation, the effective value of the free stream σ, which appears as a component in the dispersion of the injected gas, will also be 40 — 60% above the steady-state value of the initial segment and 20 — 30% higher on the diffusion segment proper. We may be guided by similar reasoning in determination of the effective value of σ for the case in which turbulence is suppressed behind a Vitoshinskiy nozzle or a grid damper.
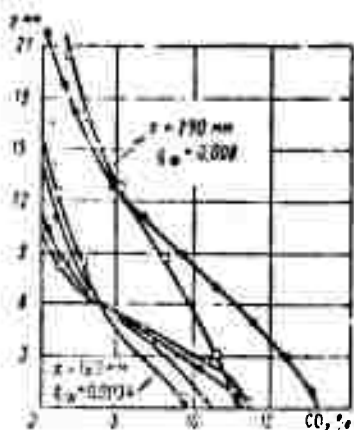
Figure 2.44. Shapes of concentration profiles for various free stream turbulence intensities.

$$O - \varepsilon \ 0.5 - 1.0\%; \quad \bullet - \varepsilon = 5\%; \quad X - \varepsilon = 7 + 8\%;$$
$$\square - \varepsilon = 15\%$$

§4. Flow of a Plane-Parallel Subsonic Jet Near a Deflecting Surface (Coanda Effect)*

When a jet of viscous gas flows in a submerged space at pressure p_H near a solid surface, the pressure decreases in the region between the jet and the wall as a result of a suction effect of the stream. The pressure drop formed at the boundaries of the jet deflects the jet toward the solid wall (Coanda effect). The flow becomes steady when the jet sticks to the wall and the back currents that have arisen make up for the mass carried out of the base region. The density of the jet gases is assumed to be the same in the base region and in the space surrounding it. The velocity profile at the exit cross section of the jet orifice is assumed rectangular. We shall approximate the trajectory of the jet with an arc of a circle whose radius is determined by the exit momentum J of the jet and the pressure drop across the boundaries of the jet $(p_H - p_b)$, which emerges in this case as a centripetal force. This assumption is quite obvious for subsonic jets; it has been used successfully in a number of similar problems [117].

We shall examine two flows: (1) flow of a jet from an exit orifice of width b over a rectangular step of height h and (2) the flow of a jet issuing from a wall at an angle α to the latter.

---

*The results in this section were obtained by S. Kh. Oganesyan.

The determining parameter is the base pressure p_b. A dimensional analysis in [117] showed that the dimensionless pressure coefficient $c_p = \frac{p_b - p_H}{\varrho u_{t_i}^2/2}$ depends only on the ratio h/b and the angle α in the first and second flows, respectively. Here it is assumed that the Reynolds number $\mathrm{Re} = u_0 b/\nu$ is sufficiently large and has no influence on the nature of the mixing or, consequently, on the base pressure. The dispersion of the submerged jet on the initial and transitional segments will be defined by the relation

$$a = kx, \qquad (2.79)$$

where the average value of k = 1/12 = 0.084 along the jet is henceforth assumed to obtain exact agreement of the calculations with experiment. We note that k = 0.09 on the main segment of the jet; x is the coordinate computed from the orifice exit cross section along the trajectory arc of the jet. It will be shown below how the results can be converted for other values of the empirical constant corresponding to other values of the cocurrency parameter (m ≠ 0), and for the case of flow of a jet over a step with an arbitrary angle between the walls. The momentum of the jet at the exit cross section of an orifice of width b is determined from the relation (for a unit length of the orifice)

$$J = \varrho u_0^2 b.$$

The trajectory of the jet centerline will, by hypothesis, be an arc of a circle with radius

$$R = \frac{J}{p_H - p_b}, \qquad (2.80)$$

where p_b is the static pressure in the stagnation zone. Strictly speaking, this is the pressure at the boundary of the zone (on the wall and directly below the jet). The pressure may be lower at the center of the zone owing to the rotating adjacent vortex. We take a coordinate system xoy such that the coordinate x is reckoned along the jet centerline and the y coordinate in the direction perpendicular to the arc, i.e., along the radius at each point of the arc (Figure 2.45).
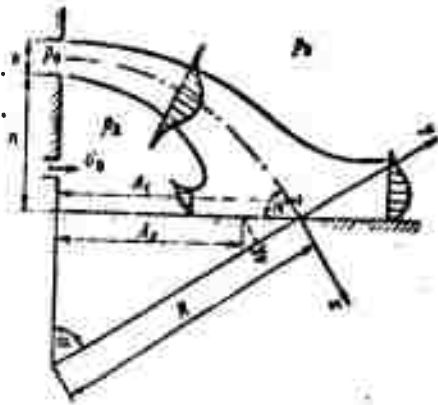
Figure 2.45. Diagram showing sticking of plane-parallel subsonic jet expelled parallel to a deflecting surface.

The angle α at which the jet meets the wall will be determined by the obvious geometrical relation

$$\cos \alpha = 1 - \frac{h}{R}.\qquad(2.81)$$

The path length on which mixing of the jet matter with the base gas and atmospheric gas occurs is equal to the arc length on the circle of radius R from the orifice exit section to the intersection with the wall:

$$S = R\alpha.\qquad(2.82)$$

According to (2.79), the dispersion of the mixing layer at the point at which the jet sticks and divides will be

$$\sigma = kS.\qquad(2.83)$$

The probability profiles P_1 for the atmospheric gases, P_2 for the jet, and P_b for the base region and the velocity profile, all written in terms of the dimensionless coordinate $\xi = \frac{y}{\sigma(x)}$, will have the respective forms

$$P_1 = \frac{1}{2}[1 - \Phi(\xi - \xi_r)]; \quad P_2 = \frac{1}{2}[\Phi(\xi + \xi_r) - \Phi(\xi - \xi_r)];$$

$$P_b = \frac{1}{2}[1 - \Phi(\xi + \xi_r)]; \quad u(\xi) = \frac{u_0}{2}\left[\Phi\left(\frac{\xi + \xi_V}{\sqrt{\mathrm{Pr}}}\right) - \Phi\left(\frac{\xi - \xi_V}{\sqrt{\mathrm{Pr}}}\right)\right].$$

Here ξ_T and ξ_V are the dimensionless coordinates of the statistical average boundaries of the density and velocity profiles. The empirically determined Prandtl number has little influence on the base pressure, and it was assumed that Pr = 0.5.

As in the other problem considered previously, the shape parameters ξ_T and ξ_V are determined by the conditions of jet mass and momentum conservation along the trajectory:

$$\rho u_0 b = \sigma \int_{-\infty}^{\infty} \rho P_2(\xi) u(\xi) d\xi \tag{2.84}$$

$$\rho u_0^2 b = \sigma \int_{-\infty}^{\infty} \rho u^2(\xi) d\xi. \tag{2.85}$$

We introduce the mixing-layer dividing-line coordinate ξ_0 below which all of the matter in the layer is turned into the base region, forming back currents.

In steady-state flow, the mass of the gas in the base region remains constant. The mass-balance equation takes the form

$$\sigma \int_{\xi_0}^{+\infty} \rho P_2(\xi) u(\xi) d\xi = \sigma \int_{-\infty}^{\xi_2} \rho [P_2(\xi) + P_1(\xi)] u(\xi) d\xi + Q_\bullet. \tag{2.86}$$

The amount of base gas carried downstream by the mixing layer from the base region has been written into the left side of the equation. The terms on the right describe, respectively, the amounts of atmospheric gas and jet gas present in the back currents and the amount of gas injected into the zone independently from an independent external source.

The dividing-line coordinate ξ_0 is determined by the approximate equation of conservation of the jet momentum component parallel to the wall; on impingement and division of the jet,

$$J \cos \alpha = \sigma \int_{\xi_0}^{+\infty} \rho u^2(\xi) d\xi - \sigma \int_{-\infty}^{\xi_2} \rho u^2(\xi) d\xi. \tag{2.87}$$

We shall neglect the momentum of the injected gas.
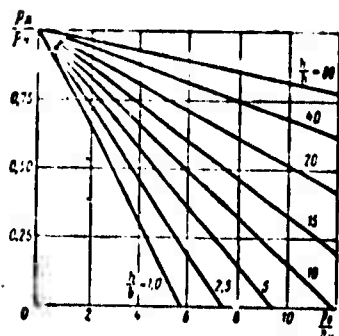
Figure 2.46. Base pressure in flow of a subsonic jet over a flat step (k = 1/12).

The equation is approximate because it does not take account of the pressure gradient in the sticking zone. It has also been assumed that the velocity profile is not deformed during the rotation.

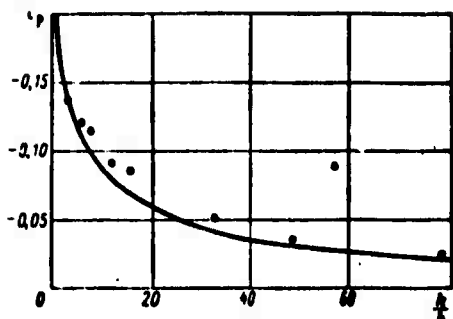The relations obtained above are sufficient for calculation of the base pressure. The calculation was performed in accordance with the following scheme. At given flow geometry h/b and jet momentum J, the base pressure is also given. Formulas (2.79) — (2.82) are used to find the radius of the jet centerline arc, the angle of impingement of the jet on the wall, and the dispersion in the sticking zone. The parameters ξ_T and ξ_V are determined from Equations (2.84) — (2.85), so that the concentration and velocity distributions are now known. Then Equation (2.87) is used to find the coordinate ξ_0 of the constant-mass line, and the mass-balance equation (2.86) to find the injection parameter value corresponding to the predetermined base pressure. The calculation to determine the base pressure at zero injection was performed by successive approximations.

The calculated results for zero injection appear in Figure 2.46. The abscissa is the ratio of the total-head of the jet $p_0 = p_H + \frac{\rho u^2}{2}$ to the static pressure in the surrounding space. We see that the base pressure tends linearly to zero for the flow model used. In fact, for $p_0/p_H > 2$ and small h/b, p_b will approach zero asymptotically in (2.87) because of the compressibility of the fluid and the large pressure gradients. Its determination is the object of another, more complex problem — that of the base vacuum [130], [131], [132], [133], [134], [135].

Figure 2.47. Pressure coefficient as a function of relative jet exit orifice dimension (k = 1/12).

Figure 2.47 presents the calculated curve in the form of $c_p = f(h/b)$. The same figure includes experimental points from [117], which corresponds to the lowest static pressures, as measured on the lower wall.

The proposed method of calculation can be used to determine the position of the dividing point of the jet on the wall. The distance of the point of intersection of the jet centerline and the wall from the corner of the step will be determined by the formula (see Figure 2.45):

$$A_c = R \sin \alpha.$$

At this point, as at the others, the oy axis coincides in direction with the radius of the arc. If the dividing-line coordinate is y_0, we have for the distance of the turning point from the corner of the step

$$A_0 = A_c - \frac{y_0}{\sin \alpha} = R \sin \alpha - \frac{e y_0}{\sin \alpha}. \tag{2.88}$$

A comparison with the experimental values of A_0 appears in Figure 2.48.

Calculated curves indicating the effect of gas injection on base pressure at a constant ratio h/b = 20 appear in Figure 2.49. The amount of injection is determined by the parameter $g_a = \Omega_a / \rho u_0 h$.

As we should expect, the base pressure rises on injection and decreases on suction (negative values of the parameter g_a).

311
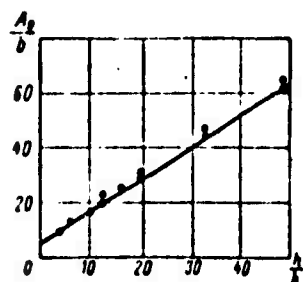
Figure 2.48. Position of
sticking point of jet on lower
wall at various ratios of exit-
orifice dimension to height of
step (k = 1/12).
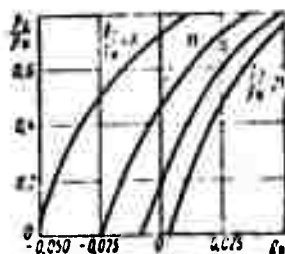
Figure 2.49. Base pressure in
flow of subsonic jet over a
flat step as a function of
injection rate in back current
zone (k = 1/12; h/b = 20).

The theoretical flow model for an incompressible jet expelled
from a wall at a certain angle α is constructed on the same assumptions
as were used in the case considered above. A diagram of the flow
appears in Figure 2.50. As before, the radius of the circle used for
approximate description of the jet trajectory is determined from the
condition (2.80). A consequence of the basic assumption as to the
shape of the jet is the fact that the angle of encounter of the jet
with the wall is exactly equal to the expulsion angle α. Thus it
is no longer necessary to determine the angle between the jet and the
wall in the sticking zone, since the expulsion angle is assigned in
advance and is the only geometrical parameter defining the flow
fully. As we noted above, it can be shown that the exit-orifice
width b has no influence on the pressure coefficient.

The length of the circle arc from the exit-orifice to the sticking
point on the wall is determined from the formula

$$S = R2a.$$ (2.89)

All other equations needed for the calculation are identical with
Equations (2.83) — (2.88).
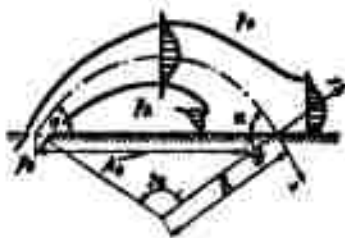
Figure 2.50. Diagram showing
sticking of subsonic jet expelled
from wall at a given angle.
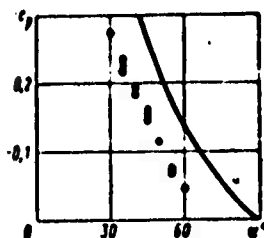
Figure 2.51. Pressure coefficient
in back current zone at various
jet expulsion angles.

The theoretical curve for zero injection appears in Figure 2.51.
We see that the agreement with experiment (the experimental values of
the minimum base pressure on the wall according to [117] are plotted)
is much poorer than in the case of jet flow over a rectangular step.
The same can also be said concerning the comparison of calculated and
experimental values of the distance of the jet dividing point from the
exit-orifice cross section (Figure 2.52).

The disagreement with experiment can be explained by several
factors that are not taken into account in the flow model. Chief
among these is the interaction of the back currents with the main jet.
In contrast to the problem of flow over a step, the back currents in
our case, which have a momentum comparable with that of the jets, are
directed straight into the root of the expelled jet and increase the
expulsion angle and, consequently, also the angle at which the jet
meets the wall. In addition, the pressure set up at the root of the
jet is appreciably higher than that around the zone in which the back
currents are generated, which results in an even greater increase in
the angle of impingement of the jet on the surface due to the increase
in the curvature of the trajectory with distance from the exit cross
section. The interaction of the jet with back currents cannot but
affect the quantitative mixing characteristics as well.

Thus, the agreement with experimental data can be improved by
introducing an effective jet expulsion angle or by adjusting the pro-
portionality coefficient determining the dispersion. It is shown in
[117], for example, that satisfactory agreements between theory and
experiment can be obtained by changing only the value of k.

313
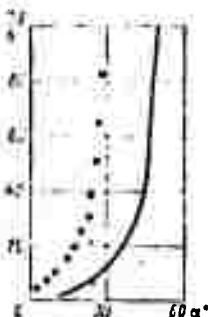
Figure 2.52. Distance of
sticking point from point
of jet expulsion at various
expulsion angles (k = 1/12).

In many cases, it may be found
helpful to calculate the base pres-
sure for various intensities of
mixing. In view of the difficulties
of evaluating the integrals in
Equations (2.84) — (2.87) (the
calculation was made on an electronic
digital computer), we present a
simple method of converting the $c_p(\alpha)$
relation obtained for k = 1/12 (see
Figure 2.51) for any other values
of the coefficient k.

Let us consider two jets that have equal exit-orifice widths $b_1 = b_2$, and are expelled from a wall at the same angle α (Figure 2.53a). Suppose that the radii of the approximating arcs are unequal because the momenta of the jets are unequal. The ratio of the mixing-layer lengths can be written

$$\frac{S_1}{S_2} = \frac{R_1}{R_2} = \frac{J_1}{\Delta p_1} \cdot \frac{\Delta p_2}{J_2} = \frac{c_{p2}}{c_{p1}} \cdot \frac{b_1}{b_2} = \frac{c_{p2}}{c_{p1}}. \tag{2.90}$$

Let us also assume that the mixing dispersion at the end of the layer is the same for both jets. This condition leads to the formula

$$k_1 S_1 = k_2 S_2$$

or

$$\frac{S_1}{S_2} = \frac{k_2}{k_1}. \tag{2.91}$$

We note also that in this case, the solutions of Equations (2.84) — (2.87) for zero injection will be identical for the first and second jets.
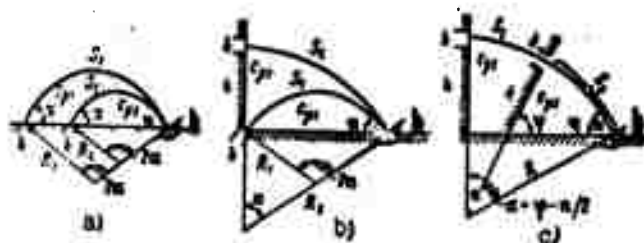
Figure 2.53. Diagrams for conversion of pressure coefficient in various cases of subsonic jet flow near deflecting surfaces.

Thus, we obtain finally from (2.90) and (2.91)

$$\frac{c_{p1}(\alpha)}{k_1} = \frac{c_{p2}(\alpha)}{k_2} = 12c_p\left(\alpha, k = \frac{1}{12}\right).$$ (2.92)

Having the calculated curve of $c_p(\alpha)$ for $k = 1/12$ (see Figure 2.51), we can construct a curve of $c_p/k = f(\alpha)$, with which it is easy to obtain the value of the pressure coefficient for a given angle α and a given mixing intensity. The universal curve appears in Figure 2.54.

The calculated $c_p(\alpha)$ relation obtained for a jet expelled from a wall can be used to find the $c_p(h/b)$ relation for the flat step at the same mixing intensity.

Let a jet of gas be blown out of an orifice of width b at an angle α to the wall. It is always possible to adjust the flow over the flat step in such a way that both jets will stick at the same angle. Here the widths of the jets are assumed equal, and the exit-orifice cross section of the second jet will be on the perpendicular erected from the center of the orifice of the first jet if the sticking points are placed in coincidence (see Figure 2.53c). It is easily seen that the lengths of the mixing layers are the same in this case and that the relation

$$\frac{R_2}{R_1} = \frac{c_{p1}b_1}{c_{p2}b_2} = \frac{c_{p1}}{c_{p2}} = 2$$

applies for the radii of the jets, or

$$c_{p2} = \frac{c_{p1}}{2}. \qquad (2.93)$$

To determine the parameter h/b, we write the geometrical equality

$$\left(\frac{h}{b} + \frac{1}{2}\right) = \frac{R_2}{b}(1 - \cos\alpha) = \frac{2R_1}{b}(1 - \cos\alpha).$$

Using the formula $R_1/b = 2/c_{p1}$, we finally obtain

$$\frac{h}{b} = \frac{4(1 - \cos\alpha)}{c_{p1}} - \frac{1}{2}. \qquad (2.94)$$
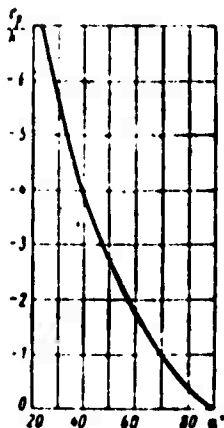
Figure 2.54. Universal relation between pressure coefficient, intensity of mixing, and angle of encounter of subsonic jet with wall.

Equations (2.93) and (2.94) can be used to calculate the $c_{p2}(h/b)$ relation if $c_{p1}(\alpha)$ is known for the same value of the coefficient k.

In turn, the relation $c_{p2}(h/b)$ for the rectangular step can be used to obtain the parameters of flow over a nonrectangular step with an angle φ between the walls.

Let us take two such flows with equal exit momenta J, equal orifice widths b, and equal ratios h/b. If the mixing coefficient is so adjusted that the sticking dispersions are also equal, all equations will be fully equivalent, and we obtain

$$P_{a1} = P_{a2} \quad \text{or} \quad c_{p2} = c_{p\varphi}. \qquad (2.95)$$

For the length ratio of the mixing layers, we have the geometrical
relation (see Figure 2.53c)

$$\frac{S_1}{S_2} = \frac{R\left(\alpha + \varphi - \frac{\pi}{2}\right)}{R\alpha} = 1 + \frac{\varphi}{\alpha} - \frac{\pi}{2\alpha}.$$

In virtue of Condition (2.91), the pressure coefficients of these
two flows will be equal if the coefficients determining the mixing
intensities satisfy the equation

$$\frac{h_2}{h_3} = 1 + \frac{\varphi}{\alpha} - \frac{\pi}{2\alpha}$$
$$(0 \leqslant \varphi \leqslant \pi). \qquad\qquad (2.96)$$

Thus, having the calculated curve (Figure 2.54), we can easily
use formulas (2.92) — (2.96) to determine the base pressure
in any of the above three flows for a given coefficient k.

CHAPTER III

EMPIRICAL DATA ON DIFFUSION PARAMETERS
OF TURBULENT JET FLOWS

§1.   Self-Similar Turbulent Flows

It is not possible at the present time to calculate the principal
diffusion parameter of the jet — its dispersion (see §1 of Chapter I)
— with sufficient rigor. However, there exists a class of turbulent
flows for which the behavior of the dispersion can be predicted
accurate to a coefficient.

The distinctive property of these flows is what is known as
self-similarity, which is characterized by similarity of the hydro-
dynamic fields in various cross sections downstream [20]. It is
natural to assume that self-similarity is established at sufficiently
large distances from the initial orifice when the specifics of the
initial conditions are no longer a factor. The self-similarity
hypothesis can be formulated as follows: for a stream to be self-
similar, it is necessary that the variation of any average quantity
in any cross section x = const be expressible in dimensionless form
in terms of appropriate scales l_0 and velocities u_0, in the form of
a certain universal function of y/l_0. The length and velocity scales
change from one cross section to another, but depend only on x.

If Reynolds number similarity is also observed, the shapes of the self-similar distributions of average velocity, fluctuation intensity, and other averaged characteristics of the turbulence, except dissipation, will be universal for all flows of a given type.

To obtain the conditions under which a flow can be self-similar, it is necessary to consider the equation of the average motion, which has the following form in the two-dimensional case [20]:

$$u\frac{\partial u}{\partial x}+v\frac{\partial u}{\partial y}+\frac{\partial(\overline{u^2}-\overline{v^2})}{\partial x}+\frac{\partial\overline{uv}}{\partial y}=v\frac{\partial^2 u}{\partial y^2}. \tag{3.1}$$

If a turbulent flow is self-similar, we have

$$u=u_1+u_0 f(y/l_0), \quad \overline{uv}=u_0^2 g_{12}(y/l_0); \quad \overline{u^2}=u_0^2 g_1(y/l_0); \quad \overline{v^2}=u_0^2 g_2(y/l_0). \tag{3.2}$$

where u_1 is the velocity of translational displacement of the entire flow.

Thus, the following dimensionless equation proceeds from (3.1) with consideration of the continuity condition [20]:

$$\frac{u_1}{u_0}\left[\frac{l_0}{u_0}\frac{du_0}{dx}f-\frac{dl_0}{dx}\eta f'\right]+\frac{l_0}{u_0}\frac{du_0}{dx}(f^2)-\frac{1}{u_0}\frac{d(u_0 l_0)}{dx}f'\int_{\eta_0}^{\eta}f(\eta_1)d\eta_1+$$
$$+2\frac{l_0}{u_0}\frac{du_0}{dx}(g_1-g_2)-\frac{dl_0}{dx}\eta(g_1'-g_2')+g_{12}'=\frac{v}{u_0 l_0}f''. \tag{3.3}$$

where $\eta = y/l_0$, and η_0 is the value of η for which $v = 0$.

It is assumed below that the Reynolds number $\frac{u_0 l_0}{v}$ is so large that the term on the right side of the equation is negligibly small.

Relation (3.3) is valid for all values of η and x. Since the coefficient of $g_{12}'(\eta)$ equals unity, it is easily seen that the remaining coefficients are either zero or constant.

Further analysis shows that for a nonzero value of u_1

$$u_0 = \text{const}; \quad l_0 \sim x - x_0,$$ (3.4)

where x_0 is a conventional "origin of the jet." This case corresponds to a mixing layer between two gas streams moving at different velocities.

If $u_1 = 0$, there is an additional possibility:

$$\frac{l_0}{u_0} \frac{du_0}{dx} = \text{const}; \quad \frac{dl_0}{dx} = \text{const}.$$ (3.5)

Condition (3.5) describes a plane-parallel jet. Application of the integral law of momentum conservation in a plane-parallel jet shows that the following should be chosen among the possible solutions of Equations (3.5):

$$u_0 \sim (x - x_0)^{-\frac{1}{2}}, \quad l_0 \sim x - x_0.$$ (3.6)

Fully analogous treatment of the axisymmetric jet leads to the conclusion that [22]:

$$l_0(x) \sim x - x_0, \quad u_0 \sim (x - x_0)^{-1}.$$ (3.7)

On the basis of the results obtained, we can study certain statistical properties of the displacement of a tagged parcel of fluid released from a given point in a turbulent stream with transverse shear and, in particular, establish the laws of variation of the dispersion with respect to the average position over a long time interval. We have already noted that simple results are obtained when the velocity of the particle is a stationary random time function. The basic hypothesis of the analysis originally given by Batchelor [54] is that the Lagrangian velocity of a fluid particle in free turbulent streams having similar structures in different cross sections downstream exhibits corresponding similarity and can be transformed

to a stationary random function by appropriate changes of the velocity and time scales. The Lagrangian velocity $w = dY/dt$ of the particle is not a stationary random function of time for arbitrary t.

It is also assumed that the Lagrangian velocity and time scales are proportional to the Euler scales:

$$w(t) \sim u_0 \sim \bar{x}(t)^{-q}; \quad \tau(t) \sim \frac{l_0}{u_0} \sim \bar{x}(t)^{1+q},$$ (3.8)

where q is a general symbol for the exponent, which, as was shown above, may be equal to 0, 1/2, or 1. (Here and below, we assume $x_0 = 0$. It is also assumed that $u_1 = 0$.)

Analytically, the hypothesis is that

$$\frac{u(t)}{w(t)} = F(\eta); \quad \frac{\tau(t)}{\bar{x}(t)} = G(\eta);$$ (3.9)

where $F(\eta)$ and $G(\eta)$ are stationary random functions of the new variable η, which takes the form

$$d\eta \sim \frac{dt}{\tau(t)}.$$ (3.10)

Relation (3.9) can be used to find the average longitudinal displacement of the particle as a function of its time in motion. In fact,

$$\frac{d\bar{x}(t)}{dt} = \bar{u}(t) = \overline{F(\eta)} w(t),$$ (3.11)

where $\overline{F(\eta)}$ is a constant.

Integrating (3.11) with (3.8), we find

$$\bar{x}(t) \sim t^{\frac{1}{1+q}}.$$ (3.12)

Further, it follows from (3.8) that $\tau(t) \sim t$

Hence it follows immediately that the independent variable η of (3.10) has the form

$$\eta = \ln t. \tag{3.13}$$

By definition, the dispersion equals

$$\sigma^2(t) = \overline{[y(t) - \bar{y}(t)]^2}.$$

Therefore,

$$\frac{d\sigma^2}{dt} = 2\,\overline{[v(t) - \bar{v}(t)][y(t) - \bar{y}(t)]}. \tag{3.14}$$

But

$$v(t) - \bar{v}(t) \sim t^{-\frac{q}{1+q}}[G(\eta) - \bar{G}(\eta)] \sim t^{-\frac{q}{1+q}} g(\eta),$$

where $g(\eta)$ is also a stationary random function of η.

The fluctuation of the particle displacement about its average position equals

$$y(t) - \bar{y}(t) = \int_0^t t'^{-\frac{q}{1+q}} g(\eta')\,dt' = \int_{-\infty}^{\ln t} e^{\frac{\eta'}{1+q}} f(\eta')\,d\eta'.$$

Making the substitution in (3.14), we obtain

$$\frac{d\sigma^2}{dt} \sim t^{-\frac{q}{1+q}} \int_{-\infty}^{\ln t} e^{\frac{\eta'}{1+q}} \overline{f(\eta)f(\eta')}\,d\eta' \cong$$

$$\cong t^{\frac{1-q}{1+q}} \int_0^{\infty} e^{-\frac{\zeta}{1-q}} R(\zeta)\,d\zeta. \tag{3.15}$$

where $\zeta = \eta - \eta'$ and $R(\zeta)$ is the correlation function of $f(\eta)$.

Integration of (3.15) leads to the conclusion that $\varkappa \sim l^{\frac{2}{1+q}}$.

Application of (3.12) then enables us to find the sought dependence of the dispersion on the longitudinal coordinate:

$$\sigma \sim x.$$

Thus, σ is, in the presence of self-similarity in either a mixing layer or a plane-parallel or axisymmetric jet, proportional to the distance downstream reckoned from some arbitrary origin:

$$\sigma \sim x - x_0. \tag{3.16}$$

However, the reasoning presented above does not make it possible to find the proportionality coefficient in (3.16). The answer to this question can be obtained only from an examination of the physics of vortex generation (see Chapter I, §1) or from experiment. Thus far, only experiment yields the dispersion for non-self-similar flows with sufficient accuracy and enables us to study the influence of cocurrency, the density ratios of the streams, and the other initial parameters. The corresponding data and the methods by which they are obtained are set forth in the sections that follow.

§2. Methods of Determining the Diffusion Parameters

1. Determination of σ_T, σ_V, and N from Average Temperature, Concentration, and Velocity Profiles

Before setting forth the laws of variation of the mixing characteristics in turbulent jets, it will be helpful if we dwell on methods for their determination from experimental data.

We showed above that the profiles of the average parameters are expressed in terms of the diffusion parameters σ_1, σ_V and N. Consequently, knowledge of the experimental profiles enables us to find the diffusion-parameter values that correspond to the experiment at hand.

To this end, it is convenient to use the analytical properties of the functions describing the profiles in the jets.

For example, the distribution of the average parameters in a mixing layer is described by the function

$$f = \frac{1}{2}\left[1 - \Phi\left(\frac{y-a}{\sigma}\right)\right].$$ (3.17)

(Here the subscripts σ and a have been omitted intentionally, since the function (3.17) corresponds equally to temperature, concentration, and velocity profiles [see Chapter II, §2].)

We see that the equality y = a is satisfied where f = 1/2. On the other hand, the distance between the points at which f = 0.1 and f = 0.9 is 2.56 σ.

Thus, having an experimental profile of, say, the velocity, $\frac{u-V_1}{V_2-V_1}$, we should find the value $y_{1/2}$ where $\frac{u-V_1}{V_2-V_1} = \frac{1}{2}$. This immediately enables us to find $a_V = y_{1/2}$. The distance between the points at which $\frac{u-V_1}{V_2-V_1} = 0.1$ and $\frac{u-V_1}{V_2-V_1} = 0.9$ can be used to calculate σ_V.

Another method can also be used to find σ, using the maximum derivative $(\partial f/\partial y)_{max}$. It is easily seen that

$$\sigma = \frac{1}{\sqrt{2\pi}\left(\frac{\partial f}{\partial y}\right)_{y=a}}.$$
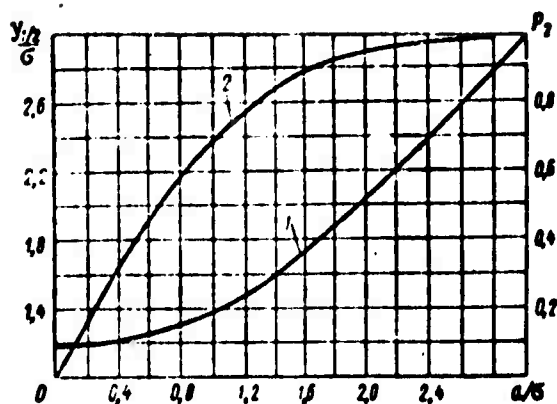
Figure 3.1. Half-boundary and probability on axis of plane-parallel jet as functions of a/σ.

$$1 \;-\; v_{1,2} \; 2-P_1 = \Phi\left(\frac{a}{\sigma}\right)$$
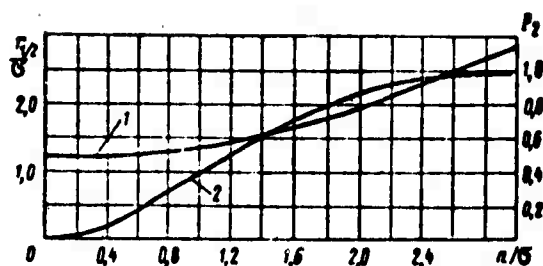
Figure 3.2. Half-radius and probability on axis of axisymmetric jet as functions of the ratio a/σ.

$$1 \;-\; r_{1,2} \; 2-P_1 = 1-e^{-\frac{a^2}{2\sigma^2}}$$

Similar information can be obtained by processing experimental temperature or concentration profiles.

To find the diffusion parameters of a plane-parallel jet, it is sufficient to have data on the variation of the measurand along the axis, together with the law of variation of the so-called half-boundary $y_{1/2}$ of the jet, which corresponds to the distance from the axis at which the measurand is half as large as its axial value.

If the axial values are known, the ratio a/σ can be determined [since $f_m = \Phi(a/\sigma)$ in Equations (2.20) and (2.21) and Figure 3.1].

Then σ can be found with the calculated plot of $y_{1/2}/\sigma$ against a/σ (also shown in Figure 3.1) and the experimental value of $y_{1/2}$.

The diffusion parameters for an axisymmetric jet are determined in exactly the same way. It is only necessary to remember that the dependences on the ratio a/σ for the axial values and the half-boundaries $r_{1/2}$ of the jet will be different (Figure 3.2).

It must be noted that use of the relations that follow from the integral conservation laws (see Chapter II, §2) yields the diffusion parameters either only for the axial values or only for data on the half-boundary of the jet. However, both sets of data are usually cited in practice, so that it is possible to avoid the rather unwieldly calculations involved in using the conservation laws.

At very great distances from the origin of the jet, where the profiles acquire the characteristic Gaussian form, the following relation may be used to determine the dispersion:

$$\sigma \simeq \frac{r_{12}}{\sqrt{2\ln 2}} \simeq 0.82 r_{12}. \tag{3.18}$$

Determination of the degree of greyness from temperature profiles is possible in accordance with the results of Chapter II, §2, when there is a substantial difference between the temperatures of the jet and the cocurrent stream.

In fact, having found a_{ef} and σ from experimental data, we can then calculate $a_T(\sigma)$ and find the ratio a_{ef}/a_T. Knowing this ratio, we can now easily determine σ_c or the ratio (degree of greyness) $N = \sigma_c/\sigma$, for example, with the diagrams (see Figure 2.9a in Chapter II). It is interesting that N is determined more accurately when n < 1 than when n > 1.

2. Optical-Diffusion Method of Determining the Dispersion

The method consists of the following: the dispersion is measured on photographs of a diffusion wake of glowing particles behind a source placed in the stream. Smoke produced by burning tobacco or wood or vapors of ammonia, hydrochloric acid, iodine, etc., can be used for cold streams. The smoke filament is photographed against a dark background with side lighting. Figure 3.3 shows one of the possible experimental setups for determination of dispersion by the optical-diffusion method.

To x-y unit
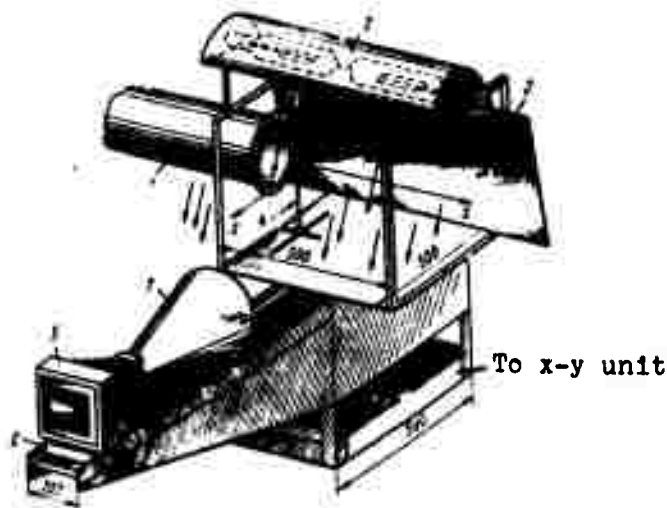
Figure 3.3. Diagram of experimental setup for investigation of cold streams by the optical-diffusion method.
1 — pipe; 2 — illuminating lamps; 3 — background (black velvet); 4 — source; 5 — camera; 6 — moving plate; 7 — lens barrel.

For hot streams (or flames), it is more advantageous to use vaporized salts of alkali metals: Na, K, Li, etc.

Using the results of turbulent-diffusion theory (see Chapter II), it can be shown that in the case of a low concentration of the glowing particles, the following relation is satisfied at large distances from the source [58]:

$$\bar{J}(x, y) = \bar{J}(x, 0) \exp\left[-\frac{y^2}{2\sigma_y^2}\right], \tag{3.19}$$

where $J(x, y)$ is the average intensity of the light incident on point x, y of the photographic plate and $J(x, 0)$ is the average luminous intensity incident on the axis of the image of the diffusion wake in cross section x.

The following coordinate system is chosen: the origin coincides with the source, the Ox axis is the axis of the jet, and the Oz axis is perpendicular to the plane of the photographic plate.

Relation (3.19) is valid for smoke and vaporized alkali-metal salts at large distances from the source: $a_T < \sigma$. We see from Expression (3.19) that the distribution of radiant intensity on the main segment of the jet is Gaussian. Thus, the dispersion is calculated from the radiant-intensity distribution $\frac{J(x,y)}{J(x,0)}$ in exactly the same way as from the average-concentration distribution $\frac{\bar{c}(x,y)}{\bar{c}(x,0)}$ (see subsection 2, §1, Chapter III).

The intensity distribution of the light incident on the photographic plate is determined from the relation [56]:

$$S(x, y) = \gamma \lg \bar{J}(x, y) + S_0,$$
(3.20)

where $S(x, y)$ is the density logarithm on the photographic-plate field, whose coordinates are x and y, S_0 is the density of plate areas not carrying image (the background), and γ is the development factor of the photographic plate.

We note that the dispersion σ^2 is more conveniently calculated directly from density profiles of the plate, which are obtained by processing it on the microphotometer. The working formula for the dispersion takes the form of (3.18), where $r_{i'} = y_{i'}$, the half-boundary of the jet, is found from a condition obtained from (3.19) and (3.20):

$$S(x, 0) - S(x, y_{1/2}) = \gamma \lg 2.$$
(3.21)

Figure 3.4a shows sample photographs of a jet of smoke in a cold stream behind turbulence-generating grids (from [58]: stream diameter d_1 = 200 mm, jet diameter d_2 = 1 — 2 mm, jet and stream velocities equal). Figure 3.4b shows photographs of a diffusion wake of glowing Na particles behind a point source based in a hot stream: the source diameter was 0.5 — 1 mm, the stream diameter d_1 = 100 mm, and the stream temperature T_1 = 1400 — 2300° K.

The optical-diffusion method can also be used to determine σ_c^2, the dispersion of "grey" mixing.
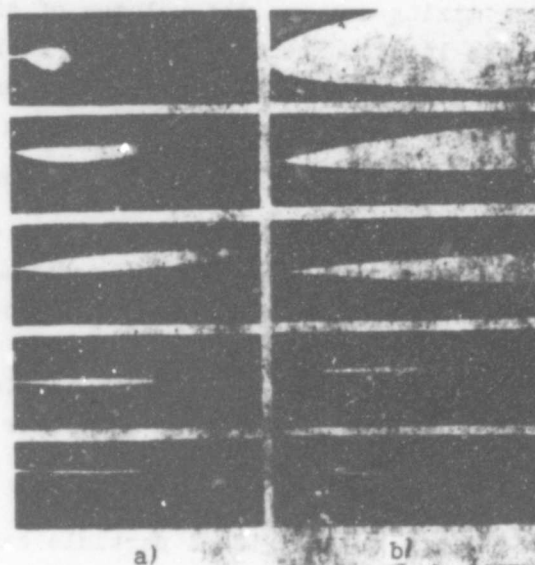
Figure 3.4. Photographs of smoke jet in cold stream (T ≈ 300° K) behind turbulizer grids (a).

$1 - t_1 \approx 33\%$; $2 - t_1 \approx 18 - 20\%$; $3 - t \approx 12\%$; $l_1 > 23$ мм; $l_2 = 7 - 8$ мм; $l_3 = 5$ мм; $4 - t_1 \approx 10\%$; $5 - t_1 \approx 4.5 - 5\%$; $l_1 = 5$ мм; $l_2 = 2 - 2.5$ мм

Photographs of diffusion wake of glowing particles behind a point source in a hot stream (b), (T ≈ 1400 — 2500° K).

$1 - t_1 \approx 40\%$; $l_1 \approx 10$ мм; $2 - t_1 \approx 16 - 17\%$; $l_1 \approx 4 - 4.5$ мм; $3 - t_1 \approx 10 - 12\%$; $l_1 \approx 3.5 - 4$ мм; $4 - t_1 \approx 7 - 8\%$; $5 - t_1 \approx 4.7\%$; $l_1 \approx 2 - 2.5$ мм; $l_2 \approx 3.5 - 4$ мм

A possibility for use of the optical-diffusion method to investigate molecular mixing of turbulent streams consists of the following. If a hot jet issuing into a cold stream contains atoms of the alkali metal Na, the jet will glow. If molecular mixing (physical mixing) were absent ($D_M \rightarrow 0$), only mechanical mixing of volumes would occur in the stream, with no change in their composition, temperature, or luminosity, and the resultant radiant intensity in a cross section would not vary from one cross section to another ("black and white" mixing model).

Since molecular mixing occurs, the volumes of the jet are cooled
and the jet emits less light. The change in the total radiant inten-
sity of the jet along its length can be used to determine the effective
molecular diffusion coefficient D_{MT} (in the sense in which it was
introduced for the jet in Chapter I) or the corresponding value of σ_c.

The radiation from each particle of the jet depends only on the local
concentration $\tilde{c}$* of alkali-metal atoms in the particle and on the particle
temperature $\tilde{T}$, and does not depend on the position occupied in cross
section x, i.e., the radiation of each particle and, consequently, the
total radiation of all particles in each cross section of the jet are
determined only by the rate of accelerated molecular mixing in the
jet.

The radiation J* from an individual particle can, in first
approximation, be written [56]

$$J^\circ = f\tilde{c}\exp\left[-\frac{h\nu}{k\tilde{T}}\right],$$ (3.22)

where f is a constant for the particular spectral line, h is Planck's
constant, k is Boltzmann's constant, and ν is the frequency of the
resonance radiation (wavelength for Na: $\lambda = 5893$ Å).

The values of $\tilde{T}$ and $\tilde{c}$, the temperature and concentration of the
Na atoms, are determined in the "grey" mixing model by the corres-
ponding dependence on σ_c and a_T.

The total radiant intensity A(x) of the jet in cross section x
equals

$$A(x) = \int\int_{-\infty}^{+\infty} J^\circ(x_0,\ y_0,\ z_0)\,dy_0\,dz_0.$$ (3.23)

_____

*The symbol ~ over a parameter signifies a local, instantaneous
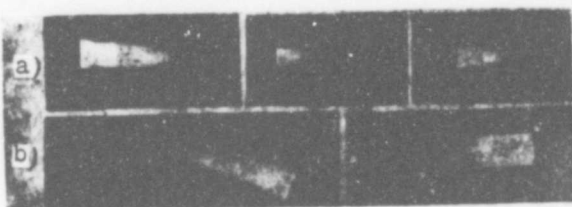averaging over microscopic nonuniformities within the limits of the
particle itself.

Figure 3.5. Photographs of luminous hot jet in cold cocurrent stream (initial segment).

a — subsonic jet; (d_0 = 30 mm, T_2 = 1600° K; V_2 = 80 m/sec; d_1 = 200 mm; $T_1 \approx$ 300° K).

1 — V_1 = 0; m = 0; 2 — V_1 = 48 m/sec; m = 0.6; 3 — V_1 = 80 m/sec; m = 1; b — supersonic jet (d_0 = 10 mm, M_2 = 1); 1 — θ = 0°; V_1 = 100 m/sec; T_{02} = 1500° K; 2 — θ = 45°; V_1 = 50 m/sec; T_{02} = 1600° K.

Figure 3.6. Photographs of luminous cold jet in hot cocurrent stream (d_1 = 400 mm; T_1 = 1550° K; V_1 = 100 — 150 m/sec).

$1 - d_0 = 10$ мм $T_2 = 1000°$K; $m = 0.6$; $2 - d_0 = 2$ мм $T_0 = 1310°$K; $m = 0.6$

If we substitute Relation (3.22) into Equation (3.23) with the appropriate expressions for $\widetilde{T}$ and $\widetilde{c}$ in terms of σ_c and a_T, we find that A(x) is a function of the grey-mixing dispersion $\sigma_c{}^2$ and the average jet radius a_T.

The total radiation of the jet in cross section x (the Ox axis is the jet axis) can be determined experimentally from photographs of the flowing jet, because

$$A(x) = \int\limits_{-\infty}^{+\infty}\int \bar{J}^0(x, y, z)\,dy\,dz, \qquad (3.24)$$

where $\bar{J}^0(x, y, z)$ is the time-averaged radiant intensity at point x, y, z of the jet.

We have from Relations (3.23) and (3.24)*

$$\int\limits_{-\infty}^{+\infty}\int \bar{J}^0(x_0, y_0, z_0)\,dy_0\,dz_0 = \int\limits_{-\infty}^{+\infty}\int \bar{J}^0(x, y, z)\,dy\,dz. \qquad (3.25)$$

---

*Relation (3.25) is a consequence of the fact that the total probability of convective displacements of a particle in the yz plane equals unity.

It follows from the above arguments that the left side of Relation (3.25) is a function of σ_c^2, while the right side of (3.25) can be determined experimentally from photographs of the glowing jet.

Figure 3.5 shows photographs of a "tinted" hot jet issuing into a cold cocurrent stream. Photographs of such a jet can be used to calculate σ_c only on the initial segment of the jet because of the rapid decay of its emission. Photographs of a "cold" tinted jet emerging into a hot cocurrent stream (Figure 3.6) can be used to calculate σ_c^2 and the total dispersion σ^2 on the main segment of the jet.

The photographs in Figures 3.5 and 3.6 were obtained on different experimental setups. The latter are shown schematically in Figure 3.7.

The working formulas for the two cases cited above will obviously be different. An analytic relation for the total radiation of the jet as a function of σ_c^2 was found for these two cases in [59] and [60].

The working relation for σ_c^2 on the initial segment of the jet (setup I) in terms of photographic density takes the form

$$S(0,0) - S(x,0) = \gamma \lg \frac{a_{c\delta}(x)}{a_{c\delta}(0)} = \gamma \frac{h\nu M}{kT_2}(n-1)e^{-\frac{a_{c\delta}^2}{2\sigma_c^2}}, \qquad (3.26)$$

where $M = \lg e$, $n = \frac{T_2}{T_1}\frac{\mu_1}{\mu_2}$, $S(x,0)$ — the density of the photograph on the axis of the wake — is determined in accordance with (3.20) by the relation

$$S(x,0) = S_0 + \gamma \lg J(x,0); \qquad (3.27)$$

$J(x,0)$ — the average intensity of the light incident at point $x, 0$ on the photographic plate — equals the sum of the intensities of the radiation from all glowing particles of the jet, projected to this point:
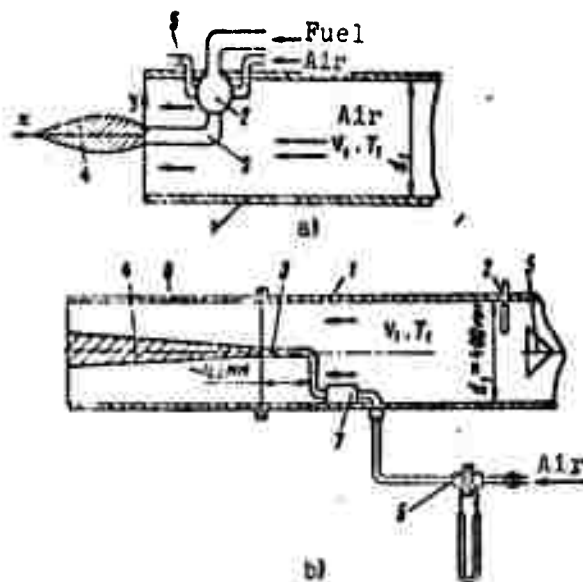
Figure 3.7. Diagrams of experimental setups for determination of grey-mixing dispersion σ_c by the optical diffusion method.

a — setup I for investigation of initial segment of jet: 1 — pipe; 2 — antechamber; 3 — nozzle tube; 4 — luminous jet; 5 — supply of alcoholic NaOH solutions; b — setup II for investigation of main segment of jet: 1 — pipe; 2 — plug; 3 — nozzle tube; 4 — luminous jet; 5 — stabilizer; 6 — flowmeter disk; 7 — NaNO₃ capsule; 8 — protective case.

$$J(x, 0) = \int\limits_{-\infty}^{+\infty} J^0(x, 0, z)\, dz; \qquad (3.28)$$

$a_{em}(x)$ — the half-width of the emission profile — is determined by the relation

$$\frac{J(x, 0)}{J(x, a_{c0})} = 2; \qquad (3.29)$$

a_{ef} is the effective emitting radius of the jet and is introduced in cases of nonuniform radiant-intensity distribution in the initial jet cross section:

$$\frac{a_c(x)}{a_c(0)} = \frac{a_T}{a_0}, \qquad (3.30)$$
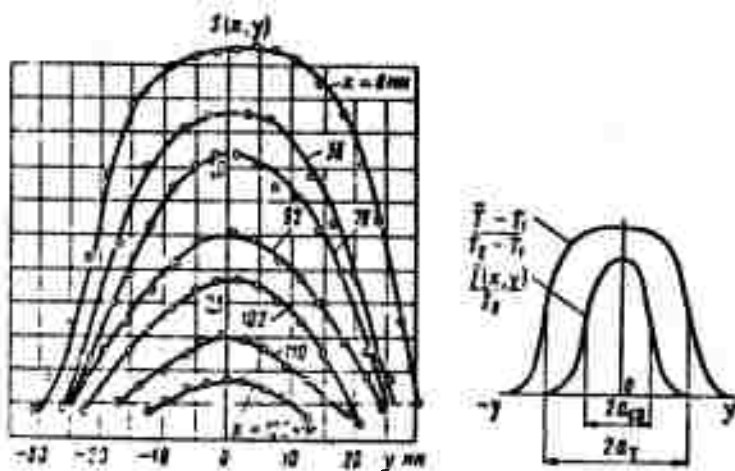
Figure 3.8. Photographic density profiles obtained from photographs of hot jet in cold stream (initial segment of jet) $d_0=30$ мм; $T_2=1600°$K; $V_2=60$ m/sec; $d_1=200$ мм; $V_1=90$ m/sec; $T_1=300°$K

where a_T is the statistical average radius of the jet, $a_c(0)$ is the half-width of the emission profile in the initial cross section, and a_0 is the initial radius of the jet.

The quantities a_T and σ are determined from average-temperature profiles measured with a thermocouple, using the formulas relating a_T and σ with $\bar{T}$ on the initial segment, while the quantities $S(0, 0)$, $S(x, 0)$, and $a_{em}(x)$, which appear in (3.26), are determined from gamma profiles across the wake. Figure 3.8 shows photographic-density profiles obtained by processing a photograph of a glowing hot jet in a cold cocurrent stream. The jet diameter d_0 = 30 mm, the jet temperature T_2 = 1600° K, and the velocity of the jet V_2 = 80 m/sec. The parameters of the cocurrent stream were d_1 = 200 mm, V_1 = 90 m/sec, and T_1 = 300° K.

We note that photographs of a hot glowing jet in a cold cocurrent stream can be used to determine only the "grey" mixing parameter σ_c^2; the dispersion σ^2 of the jet must be determined from average temperature profiles measured with a thermocouple.

Photographs of a cold jet in a hot cocurrent stream (see Figure 3.6) form a basis for calculating both σ_c^2 and σ^2 simultaneously.

As we noted earlier, the distribution of the radiant intensity $J(x, y)$ on the main segment is Gaussian in form [see (3.19)]. The dispersion σ^2 of the jet can therefore be calculated from photographs of a cold jet in a hot stream by the formulas given above.

The grey-mixing dispersion σ_c^2 is calculated by the formula given in [60]:

$$S'(\infty) - S'(x) = \gamma \lg \frac{\eta}{1 - e^{-\eta}} , \qquad (3.31)$$

where $S'(x) = S(x, 0) + \gamma \lg \sigma + \text{const};$

$$\eta = \frac{h\nu}{kT_1}\left(\frac{1}{n} - 1\right)\frac{a_\tau^2(\infty)}{2\sigma_c^2} ; \qquad (3.32)$$

$$a_\tau(\infty) = \sqrt{\frac{V_2}{V_1}}\, a_0; \quad n = \frac{T_2}{T_1}\frac{\mu_1}{\mu_2} .$$

The optical-diffusion method can be used at any Reynolds number, at high temperatures and at high stream velocities if there is no limit on the per-second flowrate of the glowing particles from the source. In practice, a filament of tobacco smoke emerging through a tube with a diameter of ~1 — 10 mm into a cold stream can be photographed reliably with an ordinary camera using an ordinary photographic plate up to free-stream velocities of ~50 m/sec, so that reliable measurements of the filament dispersion on the initial and main segments can be made for streams with diameters no smaller than 40 mm and no larger than 400 mm. The minimum pipe diameter is determined by the errors of turbulent-intensity measurements made with a tube ≥ 1 mm in diameter. The maximum pipe diameter is determined by the errors of measurement of D_T at large distances with a tube ≤ 10 mm in diameter. There are apparently no limits to the capacity of the Na-atom source, but there is a lower-limit free stream temperature: it may not be below 1200 — 1400° K.

3. Determination of Dispersion by the Toepler Method

Photographs made on photographic plates in a Toepler apparatus can also be subjected to photometric processing by the optical-diffusion method. However, in contrast to the direct optical-diffusion method, the intensity of the light from an arbitrary point in a mixing layer is, as we know, proportional not to the concentration (density) of the matter, but to the local, instantaneous density gradient. We shall dwell in somewhat greater detail on a method for determining the parameters a_T and σ for an axisymmetric jet, since processing of photographs of plane-parallel jets encounters no fundamental difficulty.

If the optical inhomogeneity to be studied is situated in a parallel light beam (with the direction of the rays coincident with the Oz axis), we may write with certain approximations for the deflection angles ε_x and ε_y from the Ox and Oy axes, respectively [62]:

$$\varepsilon_y = \frac{1}{n_0} \int_{z_1}^{z_2} \frac{\partial n(x, y, z)}{\partial y}\, dz; \qquad (3.33)$$

$$\varepsilon_z = \frac{1}{n_0} \int_{z_1}^{z_2} \frac{\partial n(x, y, z)}{\partial x}\, dz, \qquad (3.34)$$

$n(x, y, z)$ is the refractive index at point x, y, z of the inhomogeneity and n_0 is the refractive index in the undisturbed medium.

Knowing the deflection angle, we can determine the refractive index at any point of the inhomogeneous medium.

Using the Lorenz-Lorentz formula

$$\frac{1}{\varrho}\frac{n^2-1}{n^2+1} = k \quad \text{or for} \quad n \approx 1\; \frac{n-1}{\varrho} \simeq k, \qquad (3.35)$$

(where k is the specific refraction and depends on the wavelength of
the light and the nature of the substance), we can determine the
density field. A quantitative method of determining the field of the
average (nonfluctuating) density from Toepler photographs has been
developed only for a plane radiant field. There are approximate
methods of calculation for three-dimensional objects. References
[63] — [65] propose approximate methods of calculating the density
field for objects that do and do not have planes of symmetry. These
methods require taking a series of Toepler photographs of the inhomo-
geneity under study with the knife edge in various positions and are
quite time consuming.

An approximate method was proposed in [63] for calculations for
axisymmetric jets. The method requires Toepler photography of a known
optical inhomogeneity simultaneously with the photography of the jets.
These methods also call for high quality in the photographs.

Determination of the average density field in an axisymmetric
turbulent jet encounters another fundamental difficulty due to pecli-
arities of the averaging of the refracted light fluctuations over
time and space.

In time averaging of an infinite number of instantaneous gradients,
the average density gradient in the "black and white" mixing model may
differ substantially from the spatial average gradient of the "grey"
mixing model.

The fact that averaging of the refractive light in the Toepler
apparatus is practically identical to statistical averaging can be
demonstrated only by direct comparison of Toepler-photograph results
with data from other measurements made with a thermocouple or by direct
photography. A comparison made for density ratios no higher than n =
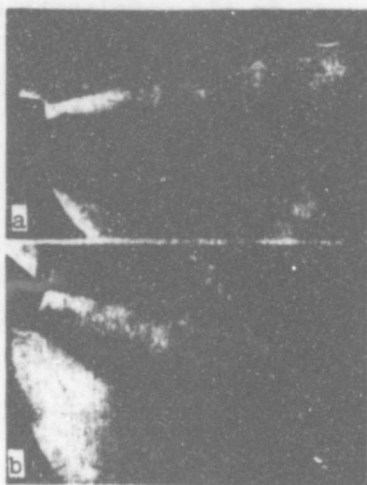6 indicates practically identical results.

Figure 3.9. Toepler photographs of supersonic jet in subsonic stream.

$a - M_1 - 1; \ d_o = 10 \ \text{mm}; \ \mathfrak{z} - 1.2; \ V_1 - 40 \ \text{m/sec}$
$\mathfrak{z} - 0^\circ; \ b - M_1 \ 1; \ d_o = 10 \ \text{mm}; \ \mathfrak{z} - 1.2; \ V_1 - 50 \ \text{m/sec}; \ \mathfrak{z} - 45^\circ$

Using the analytical relationships obtained above for the average density along the radius of the jet and the average radius a_T as functions of the dispersion σ^2 and the density ratio n, we can indicate a method for calculating the parameters of an axisymmetric turbulent jet from a single Toepler photograph.

Figure 3.9 shows typical Toepler photographs of a jet; an IAB-450 Toepler instrument was used to make the schlieren photographs.

A jet of gas with a density that differs markedly from that of the surrounding medium, placed in a parallel beam of light, will deflect the light rays. If the Oz axis is the propagation direction of the light illuminating the jet, the Ox axis is the jet axis, and the Oy axis is perpendicular to the knife edge and increases away from it, the jet will deflect the rays by an amount ε_y in the direction of the Oy axis (Figure 3.10). As a result, the illumination of the photographic plate will change by an amount ΔJ [62]:

$$\frac{\Delta J}{J_0} = \frac{F}{a} \varepsilon_{y}. \tag{3.36}$$

where F is the focal length, a is the width of the light beam that can pass above the knife edge, and J_0 is the intensity of the light in the absence of the optical inhomogeneity.

Substituting (3.33) into (3.36) and applying Relation (3.35), we obtain after averaging

$$\frac{\Delta \bar{J}}{J_0} \simeq \frac{Fk_1}{an_0} \int_{-\infty}^{+\infty} \frac{\partial \bar{v}(x, y, z)}{\partial y} \, dz. \tag{3.37}$$
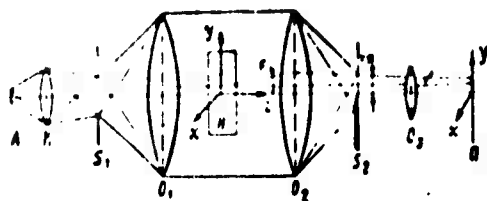
Figure 3.10. Scheme of operation of shadow instrument.

A — light source; K — condensor; S_1 — illuminator slit; O_1O_2 — main optical system; H — inhomogeneity; ε — beam deflection angle at exit from inhomogeneity; S_2 — knife edge; П — photographic plate; a — distance from knife edge to edge of slit image; O_3 — photographic-attachment lens.
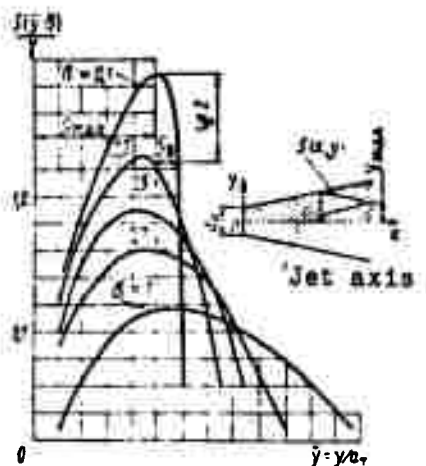

Figure 3.11. Photographic density distribution in cross sections of Toepler photograph of jet.

Substituting P_2 for the expression for the average density, we get

$$\frac{\Delta J}{J_0} \sim \int_{-\infty}^{+\infty} \frac{\partial P_2}{\partial y} \, dz. \tag{3.38}$$

We note that the difference between the P_2 profile and the average density is of the same order as the aforementioned differences between space and time averaging, and for this reason they are not taken into account (for $n \leq 6$). Use of this method for widely different densities naturally requires adjustment of the method and an independent verification by other methods.

Substituting the value of P_2 in the form (2.29) into (3.38), we obtain, after the necessary calculations, the following relation in terms of the logarithm of the plate density [67]:

$$\frac{S(\Delta J) - S_0}{\tau} = \lg 4 - \lg 3 - \frac{y^2 + a_\tau^2}{2\sigma} \lg e +$$

$$+ \lg \int_{-a_\tau}^{a_\tau} e^{\frac{z'^2}{2\sigma^2}} \operatorname{Sh}\left(\frac{a_\tau^2 - z'^2}{\sigma^2} \, y\right) d', \tag{3.39}$$

Figure 3.12. Illustrating calculation of jet parameters a_T and σ from Toepler photographs of jet.

where $S_\bullet$ is the background density of the plate;

$$S(\Delta \overline{J}) = \gamma \lg \Delta \overline{J}.$$

A plot of the experimental function $\Delta S/\gamma$ against $\overline{y} = y/a_T$ and $\overline{\sigma} = \sigma/a_T$ appears in Figure 3.11. The jet parameters a_T and σ are determined with the aid of the auxiliary characteristic parameters $\overline{y}_V$ and $\overline{y}_{max}$ of this function and the plots of k_a and k_σ in Figure 3.12. The calculating method is set forth in greater detail in [67]. There it is shown that $a_T = k_a y_{max}$ and $\sigma = k_\sigma y_V$ at $y_V/y_{max} \leq 0.95$.

The proposed method makes it possible to calculate the jet diffusion parameters a_T and σ from a single Toepler photograph and then to calculate the distribution of the average temperatures and densities from the appropriate formulas of the preceding chapter, with reference to tables of the functions P_2 [42]. A comparison of this method with others indicated full agreement of the results obtained by the various methods (see §§3 and 4, Chapter III). The method can be used to investigate the mixing of jets issuing into a cocurrent stream at all velocity ratios and all outflow velocities, including supersonic, in which case investigation by other methods is difficult.
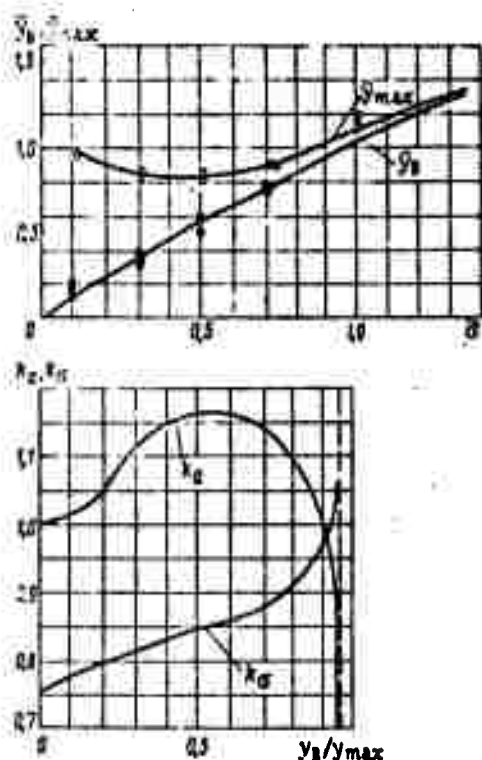
§3. Dispersion of Turbulent Diffusion on the Main Segments of Free Subsonic and Supersonic Jets

1. Total Dispersion

Subsonic Jet

Most papers devoted to experimental study of subsonic plane-parallel and axisymmetric jets have been investigations of the main segments of the jets. On its main segment, the jet flow acquires the same form as the flow from an infinitesimally small source. On this segment, the distribution of the average temperatures, concentrations, and velocities across the jet is accurately described by a Gaussian curve if the condition

$$\sigma > 0.7 a_1$$

is satisfied.

Let us begin with an examination of the main segment of a submerged nonisothermal jet and establish the influence of the density ratio $n = \rho_{01}/\rho_{02}$ on the parameter σ which characterizes the turbulent mixing of the jet.

Figure 3.13 presents values of σ at various n for a submerged jet, as calculated from the data of various authors.

The initial outflow parameters of the submerged jet are given in the table and Figure 3.13 for all of the experiments.

We see from Figure 3.13 that the parameter σ on the main segment of the submerged nonisothermal jet is closely approximated as a linear function of x (x is the distance from the nozzle exit cross section):
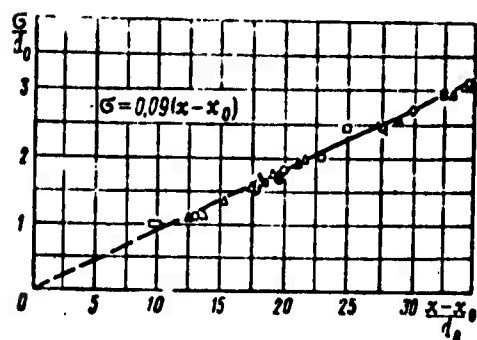
$$\sigma = k_1 (x - x_0). \tag{3.40}$$

$$\sigma = 0{,}09(x - x_0)$$

Figure 3.13. Dispersion of submerged jet plotted against density ratio on main segment:

Symbol	Author	d_0 mm	T_2° K	V_2 m/sec	ρ_1 ρ_2	Substance of Jet	Measured
O	Palatnik [43]	20	320	60	~1	air	Temperature; x/d_0=10 — 20
◊	Stark [68]	41.5	305	20	1.05	air	Temperature; x/d_0=5 — 35
×	Cleeves and Boelter [69]		860	17	~3	air	Temperature: x/d_0=2 — 13
Δ	Bezmenov and Borisov [51]	30	4000		~14	air	Temperature: x/d_0=12 — 18
Ø ⊕	Keagy and Weller [63]		293 293 293		7.2 1.03 0.67	Helium Nitrogen Carbon dioxide	Concentration: $x/d_0 \geq 16$
▫ ■	Abramovich et al. [82]	20 50	290 — 350	20 — 100	7.2 ~1	Helium Air Freon	Concentration, Temperature: x/d_0=10 — 50
▭	Setup I [60]	-10 — 30	1550	10 — 100	5.3	Air	Temperature

We note that the linear dependence of $\sigma \approx \sqrt{\dfrac{u'}{u_{av}} l \cdot x}$ on x for the submerged jet also follows from direct measurement of the turbulence parameters, the rms fluctuation velocity u', the turbulence scale l, and the average velocity along the jet [147].

The slope k_T remains independent of the density ratio $n = \dfrac{c_{01}}{c_{02}}$ as this ratio varies over a broad range:

$$0.67 \leqslant n \leqslant 14.$$

As we noted in Chapter I, this is a consequence of the fact that the instantaneous density of the gas is constant and near its average value in the regions of maximum turbulent shear of the developed vortex layer, where the new vortices are generated, so that the gas density is excluded in practice from relations of the type of (1.12) in Chapter I.

Figure 3.13 shows that k_T is also independent of the diameter and velocity of the jet when

$$Re = \frac{v_x d_0}{v_2} > 10^4.$$

Nonuniformity of the initial velocity distribution does not influence k_T: the values of k_T on a setup with "pipe" [60] and rectangular [43] initial velocity distributions are the same.

Within the limits of experimental error, the slope k_T can be put equal to

$$k_\tau = 0.09. \tag{3.41}$$

Figure 3.14 gives dispersion values for a submerged jet at various values of the initial jet turbulence intensity ε_2.

The values of σ were calculated from the average velocity distributions given in [73], using the formulas for the plane-parallel submerged jet.
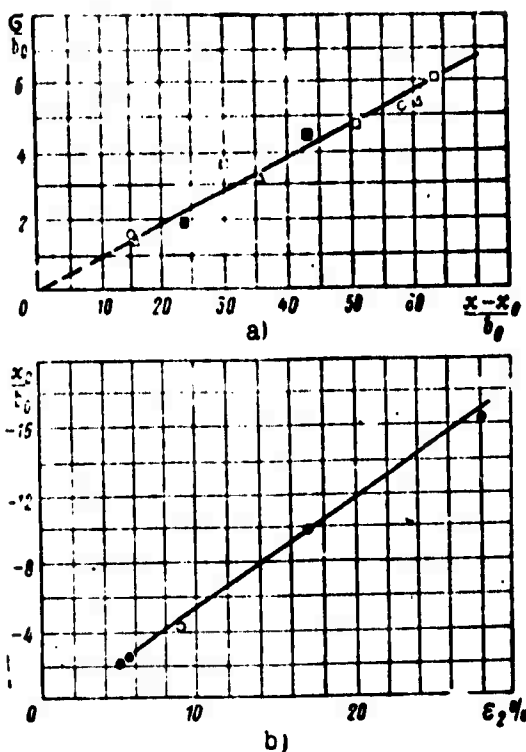
Figure 3.14. Total dispersion and pole of jet as functions of initial turbulent intensity of jet (after Yu. A. Shchebrina, m = 0).

a — dispersion of jet $\left(\frac{\sigma_0}{b_0} - 0.09\frac{x - x_0}{b_0}\right)$:

$\bigcirc - \epsilon_2 = 8\%;$ $\square - \epsilon_2 = 30\%;$ $\blacksquare - \epsilon_2 = 13\%;$ $\triangle - \epsilon_2 = 6\%;$

b — pole of jet $\bullet$ — according to Fahrtmann; $\bigcirc$ — estimates from data of [23].

The initial turbulence of the jet was deliberately varied in these experiments in the broad range from 0.05 to 0.3 by the use of turbulence-generating grids mounted in the nozzle 25 mm from its exit section.

We see from Figure 3.14 that, in spite of the sixfold variation of the initial intensity in the jet, the function σ satisfies Relation (3.40), with k_T independent of ϵ_2 and taking the "universal" value of 0.09.

Following the terminology used in the semiempirical theories, we shall call the coordinate x_0 the pole of the jet; its value characterizes the range of the jet. The parameter x_0 depends, in turn, on the shear Reynolds number $\Delta V \delta / \nu$ (ΔV is the difference between the initial velocities of the jet and the cocurrent stream, and δ is the characteristic scale of the initial boundary layer), on the levels of the acoustic and turbulent disturbances, and on other less important specific properties of the initial and boundary conditions of the jet. It depends weakly on the nonuniformity of the initial velocity distribution: $x_0 \approx 0$ for $n = 1$ and a rectangular velocity distribution; $x_0 = 0.5 d_0$ for $n = 1$ and a "pipe" velocity profile.

The quantity x_0 depends weakly on the density ratio: $x_0 = 8d_0$ for $n = 0.27$ and $x_0 = 4d_0$ for $n = 14$.

For a large initial turbulence x_0 takes a negative value and increases in absolute value from $2b_0$ to $18b_0$ (b_0 is the width of the plane-parallel jet) in accordance with the empirical formula (see Figure 3.14):

$$x_0/b_0 = -55\epsilon_2 + 1.6. \tag{3.42}$$

In engineering calculations, x_0 can be left out of account in a first approximation on the mixing segment of the jet. The other parameter, the average radius of the jet a_T, which describes the mixing of the jet on the average, depends not only on the velocity ratio, but also on the density ratio, as follows from the relations derived in Chapter I.

On the main segment of the submerged jet, this relation can be approximated by the simpler analytical relation

$$a_T \simeq a_0 \left(4.5 n \frac{c^2 \cdot x}{a_0^2} \right)^{1/4}; \qquad n = \frac{T_2}{T_1} \frac{\mu_1}{\mu_2}. \tag{3.43}$$

where a_0 is the initial radius of the jet.

According to (3.40) and (3.43), the volume-concentration variation on the jet axis is represented for $n > 1$ by

$$\frac{c(x, 0, 0)}{c(0, 0, 0)} = \frac{1.18 \vert \bar{n}}{\dfrac{x}{d_0} - \dfrac{x_0}{d_0}}. \tag{3.44}$$

The variation of the concentration by weight (mass fraction of jet substance) on the jet axis is determined by the relation

$$\kappa_2(x, 0, 0) \approx \frac{1}{n} \frac{c(x, 0, 0)}{c(0, 0, 0)} = \frac{1.18}{\sqrt{n} \left(\dfrac{x}{d_0} - \dfrac{x_0}{d_0} \right)}. \tag{3.45}$$

In first approximation, the dimensionless excess-temperature profile on the jet axis corresponds at large distances to the relative concentration by weight, and it can be calculated from (3.45).

Let us now discuss the dependence of the jet dispersion on the main segment on the cocurrency parameter $m = V_1/V_2$. Reports of experiments by various authors on the turbulent mixing of cocurrent jets are now available in sufficient numbers for determination of this dependence. This is no difficult matter even though the authors do not cite the raw experimental data on the profiles, but instead the distributions over the length of the jet — of the half-radius (half-width)of the jet, of the ordinate of the jet outer boundary, etc., in terms of the elementary relationships that hold between these parameters on the main segment (see Chapter III, §2).

We shall first examine the dependence of jet dispersion on the cocurrence parameter as obtained on a single setup under identical conditions during one series of experiments by the optical-diffusion method, and then confirm this relationship by reference to data of other authors.

Figure 3.7 showed a diagram of experimental setup II, on which these studies were made. The values of σ were calculated from photographic-density profiles obtained by microphotometer processing of the negatives.

Figure 3.15 presents values of the parameter σ for jets 10 and 4 mm in diameter and various m. The velocity ratio varied in the range from 0.3 to 1.3. Figure 3.15 also shows values of σ for a submerged jet (m = 0) from the diagram of Figure 3.13 and the data of Yu. A. Shchebrina [70], who used the same method to measure the dispersion function σ^2 with m = 1.

Values of σ corresponding to various jet diameters and two distances from the beginning of the jet — 180 mm and 430 mm — are plotted in Figure 3.16. We see from Figure 3.16 that the dispersion of the jet is independent of jet diameter within the limits of experimental error.
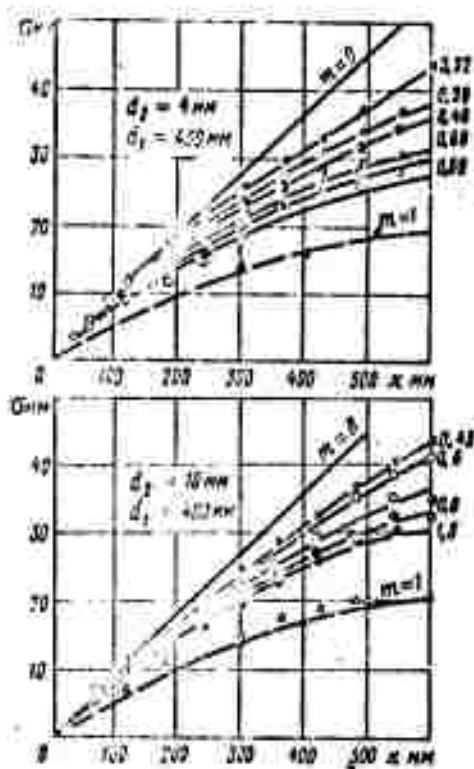
Figure 3.15. Plot of σ against ratio of jet and cocurrent-stream velocities ($m = V_1/V_2$) on main segment of jet.
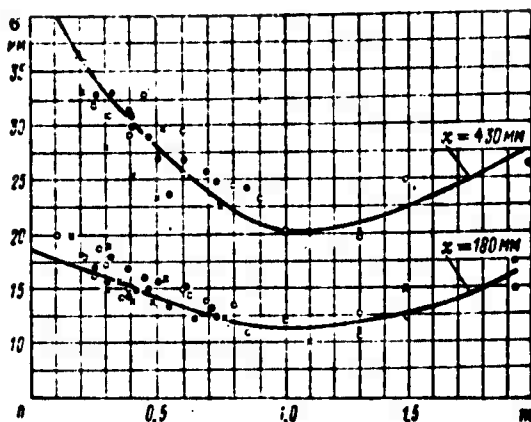
▲ — Shchebrina experiment.

Figure 3.16. Dispersion of jet independent of jet diameter on main segment:

— $d_1 = 10$ мм ● — $d_1 = 4$ мм × — $d_1 = 2$ мм

It follows from Figures 3.15 and 3.16 that σ reaches its largest value for the submerged jet (m = 0) and its smallest value for equal velocities of the jet and cocurrent stream: m = 1. The value of σ increases when the parameter m changes in either direction.

The function σ(x) may differ substantially from zero for equal jet and cocurrent stream velocities as a result of the initial turbulence of both streams. In this case, we mean by initial turbulence both the turbulence of the main stream and the jet and the turbulence of the boundary layers, as well as the turbulence that arises due to the initial velocity dip in the wake jet behind the edge of the source.

Let us consider the simplest case of the effects of initial turbulence — the case of a source of relatively small size ($d_2 \ll d_1$) situated on the axis of a long technical pipe. In this case, the dispersion is determined basically by the free stream turbulence,

the parameters of which are universal, for practically all values of $x \geq (20 - 25)d_2$. The initial turbulence from the source itself is important only on an initial segment whose absolute length is determined by the size of the source and the level of the measured cocurrent-stream turbulence.

Using the limiting particular solutions of the Taylor equation, we can write for $x \geq 20d_2$ (see Chapter I, §2)

$$\sigma^2 = \varepsilon_1^2 x^2 \qquad\qquad x < 2x';$$
$$\sigma^2 = \frac{2D_1}{V}(x - x') \qquad x \geq 2x', \tag{3.46}$$

where ε_1 and D_1 are the turbulence intensity and the eddy diffusivity of the cocurrent stream, $V = V_1 \approx V_2$ is the stream velocity, $x' = D_1/2V\varepsilon_1^2$ and $D_1/Vd_1 = 0.009$ and $\varepsilon_1 \approx 0.04 - 0.05$ according to thermo-anemometer and diffusion measurements.

The experimental value of D_1/Vd_1 for the pipe-turbulence level and stream Reynolds numbers $Re \geq 10^5$ was obtained by diffusion of carbon dioxide and by the optical-diffusion method [58] in long technical pipes with various diameters ($d_1 = 40$ mm; 100; 150; 200; and 400 mm).

In Figure 3.15, the curve for $m = 1$ corresponds to the calculation by Formula (3.46). It can be seen that the calculated and experimental values agree quite satisfactorily.

If we compare the value obtained for σ for $m = 1$ with the largest value of σ obtained earlier for the submerged jet, we see at once that their average proportionality coefficient differs from x by no more than a factor of two, i.e., that the role of the initial turbulence on the main segment of the jet is found to be quite appreciable, even for m near zero. The initial turbulence and, consequently, its contribution to the total dispersion may vary markedly with the diameter and initial converging effect of the cocurrent stream. The length of cocurrent stream pipe after an elbow, after a honeycomb

(turbulence-generating) grid, or after a turbulizing grid can have very little practical effect on σ if the distance between these elements and the source is more than 20 — 25 calibers of the characteristic scale of the initial cocurrent-stream average-velocity profile nonuniformity. For an elbow, this scale is the diameter of the pipe; for a honeycomb, it is the size of the cell, and so forth.

The increase in the parameters ε and D behind a deturbulizing grid (from the values determined by the hydraulics of the grid to the pipe-turbulence values) should also be figured in calibers with reference to the pipe diameter. For a source placed immediately after a Vitoshinskiy nozzle at the end of a long pipe with no grids or honeycombs, the value of σ at m = 1 will also be different (see §5, Chapter III).

Figure 3.17 presents values of σ/x (average values in the range x = (10 — 50)d_2) illustrating the effects of the initial conditions used by various authors.

It is seen from the data given here that appreciable stratification is observed even at m ≤ 0.5: the smallest value of σ/x corresponds to experiments in smooth small-diameter pipes (the experiments of Pabst and Forstall), and the largest value was obtained in large-diameter pipes.

If we assume in first approximation that the turbulent displacements of the medium due to the initial turbulence and to shear turbulence become statistically practically independent on the main segment of the jet, the dispersion of the jet can be written

$$\sigma^2 \approx \sigma_1^2 + \sigma_2^2 \approx \sigma_1^2 + k^2(x - x_0)^2, \qquad (3.47)$$

where σ_1^2 is the dispersion of the initial turbulence. In virtue of the assumption adopted, the value of σ_1^2 equals the total dispersion at m = 1; σ_2^2 is the transverse shear dispersion, which is determined by the turbulence generated in the free turbulent boundary layer, k
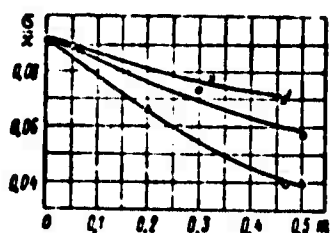
Figure 3.17. Influence of initial cocurrent stream turbulence on σ.

Symbol	d_2 mm	d_1 mm	V_2 m/sec	$T_2°$ K	Remarks	Author
●	20	300	60	293	Precompression $$\frac{F_{01}}{F_1} = 9;$$ $$\frac{F_{01}}{F_0} = 30$$	L. A. Vulis et al.
○	5	80	400	600	Smooth pipe	E. Pabst
Δ	6.4	102	70	293	Smooth pipe	Forstall, Shapiro
×	10	400	60	1500	$\epsilon_1 - \epsilon_1 - 0.05$	Setup II [60]

is a proportionality coefficient that depends less strongly on the
particular conditions of the experiment, and x_0 is the pole of the
jet.

Figure 3.18 shows $k = \sigma^2/(x - x_0)$ as a function of the velocity
ratio m according to various authors as this ratio varies through a
broad range. The values of σ_1 were calculated from Formula (3.46)
for the pipe-turbulence level of the cocurrent stream or were found
by extrapolation of available experimental data on m (for m → 1).

Analysis of the experimental data given in Figure 3.17 indicates
the practical universality of our relation (3.41), and that the same
value as in the submerged jet can be taken for x_0 for the Reynolds
numbers under consideration (Re > 10^5) and at all m.
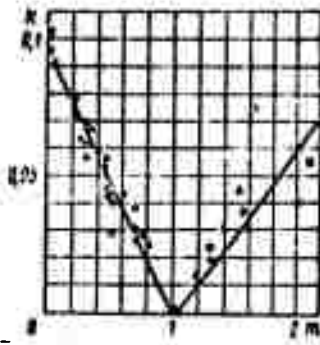
Figure 3.18. Illustrating calculation of dispersion of subsonic jet on its main segment.

Symbol	d_2 mm	d_1 mm	V_2 m/sec	$n = \rho_1/\rho_2$	Author
×	5	60	400	~2	E. Pabst
▢	6,4	102	70	~1	Forstall, Shapiro
⊠	50	210	50	14 5 0,66	Alpinieri
⊘	20 50	300 600	60 80	1 4,15	L. A. Vulis, et al.
■	4	400	28	~1	Yu. A. Shchebrina
△ ▲ ▽	2 4 10	400	65÷90	5÷5,5	Setup II [60]
●	3	200	60	0 66	[58]

The values of k (Figure 3.18) can be approximated by the relations

$$k(m) = k_1(1-m) \quad k_1 = 0{,}09 \; \text{for} \; m < 1;$$
$$k(m) = k_1(m-1) \quad k_1 = 0{,}06 \; \text{for} \; 2 \geqslant m > 1.$$

(3.48)

In relation (3.47) for the pipe-turbulence level of the free stream, the first term is small compared to the second for m = 0 — 0.3, and can therefore be left out of account in engineering calculations. But for m > 0.6, the first term in (3.47) becomes comparable to and even larger than the second, so that it may be assumed in first approximation that the total dispersion of the jet for these values of m is determined only by the initial turbulence. This is why mixing ceases to depend on the velocity ratio even for m ≈ 0.6 at a sufficiently high initial-turbulence level of the streams being mixed, such as usually prevails in the engineering devices and experimental setups that are investigated.

When the initial turbulence of the mixing streams is deliberately lowered, it is possible to observe a dependence of σ on m up to m ~ 0.9 [57].

Thus, the total dispersion σ of the jet on the main segment is composed at subsonic outflow velocities of the dispersion of the initial turbulence, which is most simply determined from the particular value of the dispersion at m = 1, and the dispersion of the turbulence generated by transverse longitudinal-velocity shear, as determined by the second term in relation (3.47).

Supersonic jet

The mixing of supersonic jets in subsonic cocurrent streams is of no lesser practical interest than that of subsonic jets, but this flow case has not yet been adequately studied. Most experimental studies of supersonic streams have been devoted to the mixing of the supersonic submerged jet on its main segment.

The total dispersion σ for supersonic jets can be determined from temperature, concentration, and velocity profiles just as in the case of subsonic jets. To investigate the behavior of σ in supersonic submerged jets as the jet Mach number (M_2) and the initial preheat $\left(n_0 = \frac{T_{0_2}}{T_{u1}}\right)$ were varied, we referred to the data of [67] and those of

B. A. Zhestkov, M. M. Maksimov, and N. N. Sakharov [1], V. Ya. Borodachev, V. S. Makaron, and R. Broer [75], A. Andersen and Johnson [143], N. Johannesen [76], and E. Pitkin and I. Glassman [77].

The experimental data indicate that the supersonic submerged jet is diffused more slowly than the subsonic jet, and that this effect becomes stronger with increasing Mach number. Nevertheless, the relation (Figure 3.19a)

$$\sigma = k_i(x - x_0). \tag{3.49}$$

is satisfied, as before, on the main segment for supersonic submerged jets. Here the coefficient k_T does not depend on the Mach number of the jet or its initial preheat, and agrees with the $k_T = 0.09$ for submerged subsonic jets.

The quantity x_0, which characterizes the range of the jet, is always positive and much larger than in the case of subsonic jets. The value of x_0 increases with increasing stability of the jet (increasing jet Mach number and decreasing initial preheat) (see Figure 3.19b). For design outflow of a jet, it can be approximated by

$$\frac{x_0}{d_0} = \frac{1}{1.4\,(n_0)^{0.7}} M_3^2 \tag{3.50}$$
$$\text{for } M_2 \leqslant 3.5, \ n_0 \leqslant 8,$$

where $n_0 = \frac{T_{02}}{T_{01}}$ is the stagnation-temperature ratio of the jet and the surrounding space.

Figure 3.19b presents experimental values of x_0; the solid curve represents the calculation by Formula (3.50).

To calculate the mixing of a supersonic jet in a subsonic cocurrent stream, it is possible, as a first approximation, to use relation (3.49), where x_0 is calculated from Formula (3.50), and the value of k_T from Formula (3.48).
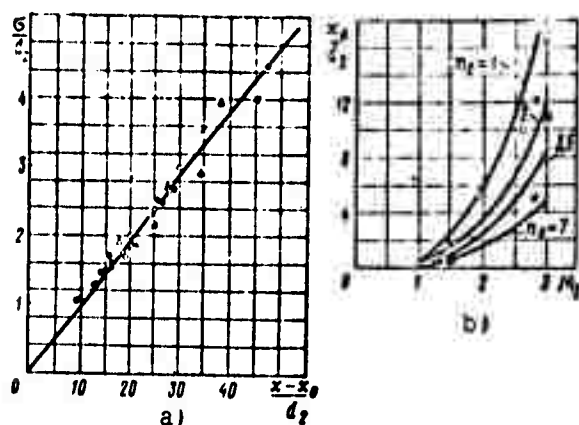
Figure 3.19. Influence of Mach number and preheating of jet on total dispersion of theoretical submerged supersonic jet.

Symbol	d_2 mm	M_2	$n_o - \frac{T_{o_2}}{T_{o_1}}$	Author
× • ⊙	5	1.41 1.93 2.9	1 1 1	V. Ya. Borodachev
■ ⊙ + □	8	1.5 1.5 3 3	2 1 1 1	B. A. Zhestkov
⊘ □ ◆	20 36	2.85 1.4 1.84	7.5 1 ~3.7	V. S. Makaron Johannesen Andersen

In most cases, the outflow of a jet from the exhaust nozzle of a rocket engine, which occurs at supersonic velocitites, is off-design. On emerging from the nozzle, the jet of gas forms a complex periodic structure with discontinuities, expansion flows, and a substantial change in cross-sectional area. After a series of "barrels," the static pressure in the so-called isobaric cross section of the jet equalizes with the ambient pressure, the periodic variations of the parameters cease, and the jet enters a segment on which mixing with the gas of the external medium is the determining process.

To calculate the mixing of the off-design jet on the main segment, it is necessary to know the parameters of the jet in the isobaric cross section: the area of the cross section, the velocity, density, and total-head loss.
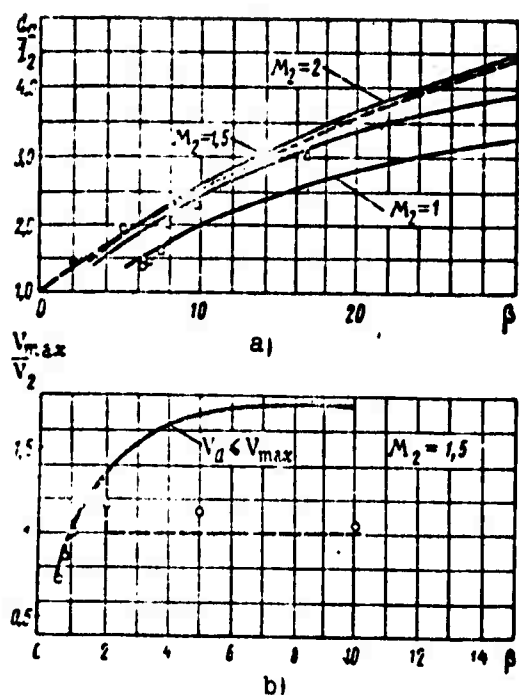
Figure 3.20. Diameter of
  isobaric cross section plotted
  against off-design factor of
  outflow (a).

—— calculation by Cherkez's
method [28]; --- calculation
by formula (3.51); □ — M_c = 2
(E. Love); Δ — M_c = 1.5 — 2
(T. Adamson); O — $M_c \approx$ 1 (G. A.
Akimov); • — M_c = 1 (setup III).

Comparison of calculated and
experimental velocity variation
along the axis of an off-design
jet issuing into a submerged
space (b).

—— calculation by Cherkez's
method; --- formulas (3.52) and
(3.53); O — data of B. A.
Zhestkov et al.

In [78], A. Ya. Cherkez prop-
posed a method for calculation of
jet parameters in the isobaric
cross section. For a constant
stagnation temperature T_{02} at all
points of the jet cross section
(a condition that is satisfied
when the jet does not mix with
the external medium on the off-
design segment), he found the
average values of the other para-
meters in the cross section of
the stream, which satisfy the
conditions of flow rate, total-
energy, and total-momentum con-
servation.

Values of the isobaric cross-
section diameter d_a calculated by
Cherkez's method are represented
by the solid line in Figure 3.20a
and agree closely with estimates
of this diameter from Toepler
photographs made by E. Love [79],
T. Adamson [80], and G. A.
Akimov [78].

As Figure 3.20a shows, the
values of d_a depend weakly on the
jet Mach number ($M_2 \leq 2$) and are
described by the approximate rela-
tion

$$d_a = d_2 \sqrt[3]{\beta},$$
(3.51)

where $\beta = p_n/p_H$ is the off-design factor of the jet — the ratio of the static pressure p_n in the jet at the nozzle exit section to the static pressure p_H in the surrounding space.

The result calculated from (3.51) is represented by the dashed line in Figure 3.20a.

Values of the velocity V_a in the isobaric cross section of the jet were calculated by the Cherkez method for various values of β and a nozzle Mach number of 1.5 and are plotted in Figure 3.20b. The open circles indicate the velocity values $V_{a\ max}$ on the axis of the jet in the isobaric cross section, as calculated from the experimental data of M. M. Maksimov, B. A. Zhestkov, and M. M. Sakharov. It is seen that the calculation by the Cherkez method overstates the velocity values in the isobaric cross section.

The cause of this disagreement between the calculated and experimental values appears to be the fact that the Cherkez method neglects the effects of the mixing process, which plays a decisive role in the shaping of the off-design and in the decay of the periodic structure.

The velocity in the isobaric cross section of the jet is usually calculated with the approximating relationships

$$V_a = V_s; \qquad \beta > 2; \qquad (3.52)$$

$$V_a = \dot{V}_s \sqrt{\bar{\beta}}; \qquad \beta_s < 2. \qquad (3.53)$$

Formulas (3.52) and (3.53) give a satisfactory description of experimental data of B. A. Zhestkov et al. [1] and V. I. Dmitriyev [81], which were obtained for a nonisothermal jet: $T_0 = 2800^\circ$ K, $M_2 = 1.5-2$.

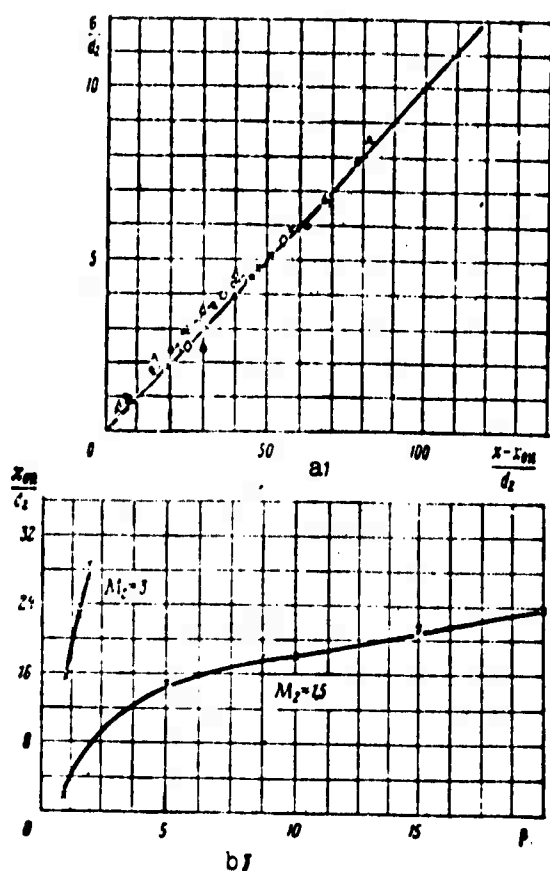Figure 3.21. Illustrating mixing of supersonic off-design jet on main segment (according to B. A. Zhestkov).

$M_2 = 1.5$	Symbol	□	⌐	△	·	▲	∅
	β	1	0.8	0.6	5	10	20
$M_2 = 3$	Symbol	▲	●	◊			
	β	1	1.5	2			

Figure 3.21 gives values of the dispersion σ calculated from the data of B. A. Zhestkov et al. for supersonic off-design jets for various values of the jet Mach number M_2 and the off-design factor β. We see from the plot in Figure 3.21a that the total dispersion of the off-design jet is approximated closely by a linear relationship, with the slope of the line the same as in the case of the subsonic jet:

$$\sigma = 0.09(x - x_{00}). \qquad (3.54)$$

The values of x_{00}, which characterize the range of the off-design supersonic jet, are considerably larger than the corresponding values of x_0 for the design jet and increase with increasing β (Figure 3.21b).

In first approximation, the value of x_{00} can be defined by the relation

$$x_{00} = x_0 + x_{01} \qquad (3.55)$$

where x_0 is the length of the off-design segment of the jet (the distance from the nozzle exit section to the isobaric cross section) and x_0 is the length characterizing the range of the design supersonic jet, and is calculated from (3.50), in which d_0 and M_2 must be replaced by d_a, the diameter of the isobaric cross section (3.51),
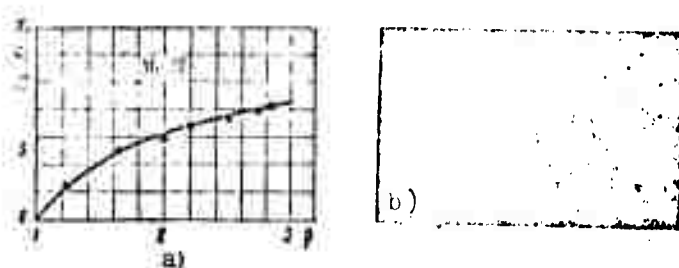
Figure 3.22. Influence of off-design factor of outflow on length of off-design segment (a) and Toepler photograph of off-design segment of jet (knife edge vertical) (b); $M_2 = 1$; $d_2 = 10$ mm; $\beta = 2.9$.

and the jet Mach number in the isobaric cross section. The latter is determined with (3.52) and (3.53). The length of the off-design segment for $M_2 = 1$ was estimated from Toepler photographs of a jet (Figure 3.22a), with the assumption that the isobaric cross section occurs immediately after the first invisible barrel (Figure 3.22b). The values of x_o determined in this way can be described by the empirical formula

$$\frac{x_{_H}}{d_2} = 30\beta^{-0.5}\ln\beta \quad \text{for} \quad \beta = \frac{p_c}{p_H} < 3; \quad M_2 = 1. \tag{3.56}$$

The position of the first shock (Mach disk) x_{sh} was determined in [79] and [80] from Toepler and shadow photographs of a jet (Figure 3.23). It is seen from the Toepler photographs [79] that the distance x_{sh} to the first shock is related to the length x_o of the off-design segment by the approximate relation

$$x_{_H} \simeq 1.25 x_{c_k} \quad \text{for} \quad M_2 < 3; \ 3 < \beta < 25. \tag{3.57}$$

Using relation (3.57) and Figure 3.23, which presents plots of x_{sh} against the Mach number M_2 and the off-design factor β, the variation of the off-design-segment length x_o can be approximated by the empirical formula

$$\frac{x_{_H}}{d_2} = 1.12 \sqrt{\beta} M_2^{0.9} \quad \text{for} \quad \beta \geqslant 3, \ M_2 < 3. \tag{3.58}$$
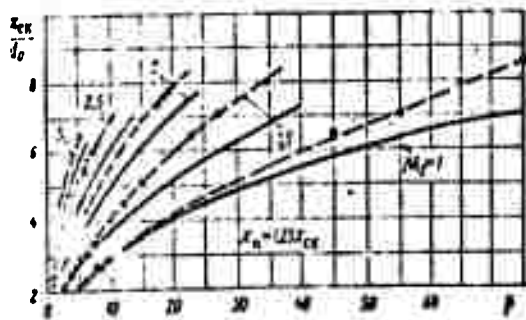
Figure 3.23. Influence of off-design factor of outflow and jet Mach number on position of first shock.

Δ — Donald's experiment [10];
—·—·— APL experiment [80];
——— NACA experiment [80].

Relations (3.51) — (3.58) can be used to calculate the mixing of off-design supersonic jets on their main segments.
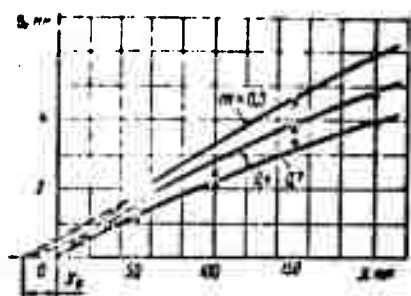
2. Molecular Mixing Dispersion on the Main Segment of the Jet

Mixing of jets to molecular homogeneity was investigated by the optical-diffusion method on three experimental setups. The main segment of the jet in the cocurrent stream was studied on the setup diagramed in Figure 3.7b. The investigations were made with the following initial parameters of the mixing streams: jet diameters d_2 = 10, 4, and 2 mm; the jet velocity V_2 was varied from 50 to 250 m/sec; jet temperature T_2 = 900 — 1300° K; substance of jet, air; cocurrent-stream diameter d_1 = 400 mm; stream velocity V_1 varied in the range from 50 to 90 m/sec; stream temperature T_1 = 1600 — 1750° K; cocurrent stream composed of gasoline combustion products.

The dispersion σ_c of molecular ("grey") mixing was calculated from photographs of the glowing jet in accordance with Formulas (3.31) and (3.32).

Values of σ_c for the main segment of the jet appear in Figure 3.24. We see that σ_c depends on the ratio m of the jet and stream velocities. The largest value of σ_c corresponds to the submerged jet (m = 0), and it decreases with equalization of the velocities as m → 1. The dispersion σ_c reaches its minimum value when the jet and cocurrent stream velocities are equal, m = 1. We see from comparison of the plots in Figures 3.15 and 3.24 that the grey-mixing dispersion σ_c^2 depends on the velocity ratio in much the same way as
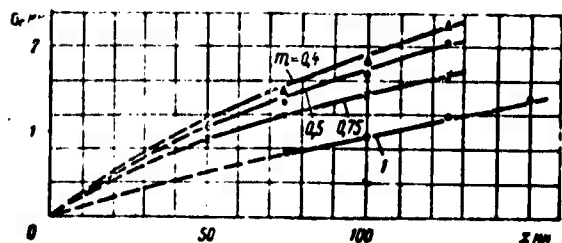
Figure 3.24. Variation of σ_c along jet axis.

$a - d_1 - 4$ мм. $d_2 - 400$ мм. $V_1 - 75$ m/sec; $b - d_1 - 2$ мм; $d_2 - 400$ мм. $V_1 - 60$ m/sec

does the total dispersion σ^2 of the jet.

The above is also illustrated by the diagram in Figure 3.25, which presents the ratio $\sigma_c/\sigma_{c(m)}$ for various m (compare with the diagram of Figure 3.16).

The absolute value of σ_c depends weakly on the initial turbulence of the jet (on its diameter) (see Figure 3.24), and this dependence becomes weaker with increasing distance; however, it is more pronounced than the dependence for the total dispersion (see Figure 3.15).

The value of σ_c on the main segment of the jet can be calculated with the aid of the curve in Figure 3.25 for a known σ_{1c} — the dission of "grey" mixing for equal jet and cocurrent-stream velocities (m = 1).

An analytical relation for σ_{1c} can be obtained from physical conceptions and dimension-theory considerations. At equal velocities, the dispersion σ_{1c} is determined by the sum of two statistically independent processes: the microturbulent diffusion determined by the initial parameters of the jet and the microturbulent diffusion determined by the relative (Lagrangian) parameters of the cocurrent stream, i.e.,

$$\frac{d\sigma_{1c}^2}{2\,dx} = \frac{D_{1c} + D_{2c}}{\bar{u}} \quad \text{for} \quad \bar{u}_1 = \bar{u}_2 = \bar{u}. \tag{3.59}$$
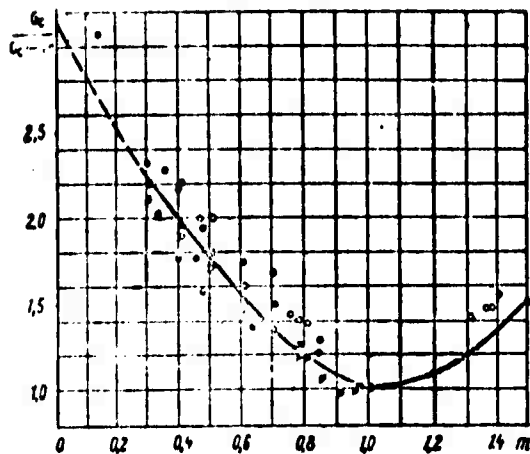
Figure 3.25. Dispersion of "grey" mixing plotted against velocity ratio on main segment of jet:

$\bigcirc - d_2 - 10$ мм $\bullet - d_2 - 4$ мм $\bullet - d_2 - 2$ мм

The coefficient of diffusion of the initial jet turbulence remains constant or even decreases, i.e.,

$$\frac{D_{2c}}{\bar{u}} \sim \frac{u_2'(x)\,l_2(x)}{\bar{u}} \sim \epsilon_2 d_2,\qquad (3.60)$$

where ϵ_2 is the initial turbulence intensity of the jet and d_2 is the initial diameter of the jet.

To the contrary, the coefficient D_{1c} of Lagrangian diffusion of the layer increases with increasing distance from the source, both as a result of the increase in the scale of the vortices entering the molecular layer and as a result of the increase in their velocity. From Richardson's law of local turbulence theory [22] and [26], which was first derived for the atmosphere, we have

$$\frac{D_{1c}}{\bar{u}} \approx (\epsilon)^{1/3}\, l_{1c}^{4/3},\qquad (3.61)$$

where $\epsilon = u'^3/l$ is the rate of turbulent energy dissipation; $(u_1',\, l_1$ are the integral velocity and integral scale of the cocurrent-stream vortices).

In such diffusion, the layer scale increases in accordance with the law $\sigma_c \sim x^{3/2}$. Under the combined influence of the initial turbulence of the jet and the turbulent microstructure of the cocurrent stream, the law of variation of σ_c will be more complex. On the main segment of the jet, it can be assumed linear for simplicity (see Figure 3.24); then $D_{1c} \sim x^{4/3}$, and the dispersion of the molecular-mixing layer σ_{1c}^2 will be written after integration (3.59) in the form

$$\sigma_{1c}^2 = A \varepsilon_1 D_2 x + B \varepsilon_1 \left(\frac{\bar{u}x}{D_1} \right)^{1.3} x^2.$$ (3.62)

where ε_1 and D_1 are the intensity and the total diffusion coefficient of the cocurrent stream turbulence. The empirical constants were determined as follows:

A = 0.07 from σ_c data for the initial segment of the jets (see §4);

B = $0.9 \cdot 10^{-3}$ (from values of σ_c for the $_{J\backslash}$ with the smallest diameter d_2 = 2 mm at x > $30d_2$).

By hypothesis in the derivation of (3.61), Relation (3.62) is valid for the x for which the inequality $D_{1c} \ll D_1$ or $\sigma_{1c} \ll l_1$ is satisfied; when $\sigma_{1c} > l_1$, D_{1c} tends to its limiting value, which is smaller than or equal to D_1.

We obtain the working relation for the steady-state stream in the pipe by substituting the empirical relations for D_1 and ε_1 (see §3, subsection 1):

$$\sigma_{1c}^2 = 3.5 \cdot 10^{-3} d_2 x + 4.5 \cdot 10^{-3} \left(\frac{x}{0.018 d_2} \right)^{1.3} x^2.$$ (3.63)

In solving certain problems, it is more convenient to use the parameter N = σ_c / σ. For the main segment of the jet, up to the x at which $D_{1c} \leq D_1$ and $\sigma \sim k(m)x$, the parameter N can be determined from the relation

$$N(m) = \frac{\sigma_c(m)}{\sigma(m)} = \frac{\sigma_c(m)}{\sigma_c(1)} \cdot \frac{\sigma(1)}{\sigma(m)} \cdot N(1),$$ (3.64)

where N(1) is the degree of greyness at m = 1.

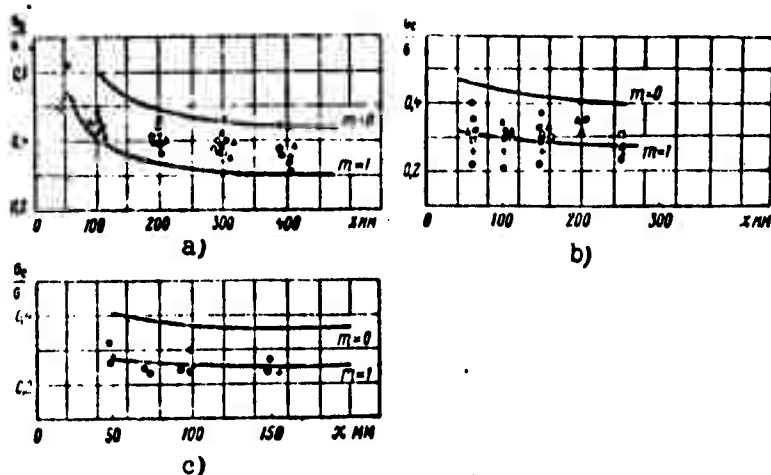Figure 3.26. Experimental values of mixing homogeneity for various values of the jet diameter and velocity ratio.

With σ and σ_c depending in practically identical fashion on the cocurrency parameter m, i.e., with $\sigma_c(m)/\sigma_c(1) \approx \sigma(m)/\sigma/(1)$, we obtain

$$N(m) = N(1),\qquad\qquad(3.65)$$

where

$$N(1) = \frac{1}{k(1)} \sqrt{\frac{A t_2}{\bar{x}} + B t_2 \left(\frac{x \bar{u}_1}{D_1}\right)^{1/3}}$$

$$\left(\bar{x} = \frac{x}{d_2}\right):\qquad\qquad(3.66)$$

k(1) is the average coefficient for σ at m = 1.

Figure 3.26 shows experimental values of N for jets with diameters of 10, 4, and 2 mm. The solid lines in Figure 3.26 represent the calculation by Formula (3.64) for the two limiting cases m = 0 and m = 1.
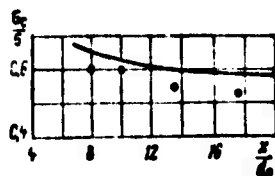
Figure 3.27. Homogeneity of mixing of submerged subsonic jet (d_0 = 30 mm).

—— calculation by formula;
• calculation from average-temperature profiles.

In §2, subsection 1 of Chapter III, we noted the possibility of computing N from the average temperature profiles of the jet if the initial preheat of the jet is large ($\frac{T_2}{T_1} \geqslant 10$). Figure 3.27 shows a calculation of N from the average temperature profiles of a submerged jet (T_2 = 4000° K; d_2 = 30 mm) (see Chapter II), and the solid curve indicates the calculation by (3.64).
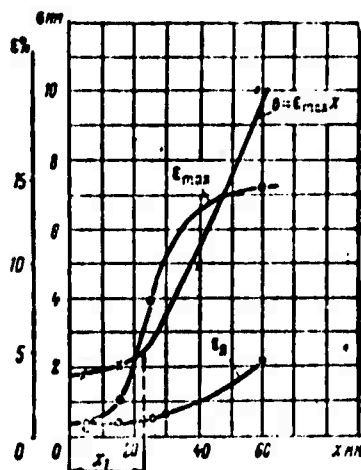

Figure 3.28. Variation of dispersion on initial segment (according to Yakovlevskiy and Sekundov).

$\varepsilon_m \cdot \varepsilon_c$ — intensity of velocity fluctuations in mixing zone (on jet axis); d_0 = 20 mm; Re_d = $1.1 \cdot 10^4$; air jet, m = 0.

§4. Dispersion on the Initial Segment of the Jet

1.   Subsonic Jet in Subsonic Stream

The formation of the turbulent boundary layer in the initial segment of a subsonic jet and, consequently, its total dispersion σ^2 are strongly influenced (apart from the velocity difference) by the outflow boundary conditions of the jet: the density difference, the thickness of the nozzle edge, and the initial boundary layers that are formed on the outer and inner surfaces of the nozzle.

The fact that mixing is influenced by many factors, some of which depend on specific features of the experimental setup, explains the quantitative disagreement among the results of many studies of turbulent mixing of cocurrent nonisothermal jets on their initial segments.

Nevertheless, studies of the initial segment of the jet have
made it possible to bring out a number of general qualitative laws
of motion and turbulent transport on this segment. Toepler photo-
graphs of jets at moderate Reynolds numbers on the initial segment
show three clearly distinguishable regions of flow: a region immedi-
ately adjacent to the nozzle (the segment on which instability develops)
with insignificant growth of the turbulent mixing layer; a region of
individual large vortices, and a region of developed turbulence (see
Chapter I, §1).

A sharp increase in the mixing zone thickness occurs at the end
of the developing-instability segment, whose length is x_1. Figure
3.28 presents values of σ, calculated for the initial mixing-layer
thickness of an air jet issuing into a submerged space (d = 20 mm,
V_2 = 7.5 m/sec, and $Re_2 = \rho_2 d_2 / V_2$ = 1.1·10^4 [82] and experimental
values of the turbulent intensity measured at the center of the layer
(ε_{max}) and on the jet axis (ε_0). This jet has an instability length
$x_1 \sim d_2$. On this length, the maximum value ε_{max} of turbulence inten-
sity in the mixing layer increases from 1 to 8%. It is seen from
Figure 3.28b that the value of σ on the developed turbulence segment
($x \geq x_1$) can be expressed approximately by the initial solution of
the Taylor equation:

$$\mathfrak{z} = \mathfrak{e} x,$$
(3.67)

where the value ε = 0.15 is, considering the various measurement
methods and the possible anisotropy of the initial turbulence, in
practical agreement with the maximum value of turbulence intensity
in the mixing layer. The universal nature of this relation is
difficult to verify at the present time because such experiments have
not been performed in sufficient numbers. However, the correlation
of the longitudinal fluctuation intensity with the transverse turbu-
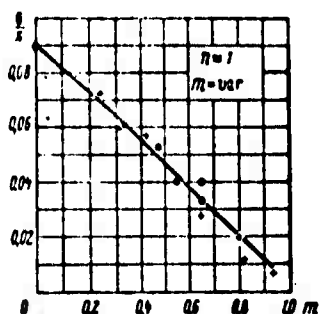lent displacements is clearly evident from the data given above.

Figure 3.29. Dispersion of subsonic jet on initial segment (dependence on stream velocity ratio).

Sym-bol	d_2 mm	d_1 mm	Remark	Author
+	40	306	$n = 1$; $\varepsilon_2 < 1\%$ grids at exit	Pavel'yev, Navoznov
•	65	320	$n = 1 — 1.5$, thrott-ling, grids	Willis, Glassman

It is also seen from [82] that the length of the instability segment x_1 is for practical purposes small even at $Re_2 \geq 10^2$. At a thickness $\delta_2 = 1$ mm of the boundary layer on the nozzle edge and $\varepsilon_1 = \varepsilon_2 = 1.5\%$, for example, $x_1 \approx d_0$ for a jet of air, and x_1 practically vanishes for jets of helium and Freon.

The dispersion σ depends strongly on the velocity ratio m on the initial segment of the jet, for $x > x_1$. Figure 3.29 presents values of σ/x for jets of equal density, as calculated from the experimental data of R. Willis and I. Glassman [83] and A. A. Pavel'yev and O. I. Navoznov [57]. The data were obtained on setups with low initial turbulence level (ε_1, $\varepsilon_2 < 1\%$) and zero boundary layer thicknesses at the merging point of the streams. This was accomplished by mounting grids in the stream and at the jet exit cross section, and, in the experiment of Willis and Glassman, also by multiple throttling of both streams.

Figure 3.29 shows that the same type of dependence of σ/x on the velocity ratio is observed under these conditions as for the main segment of the jet all the way to m = 0.9, i.e., for n = 1, Relations (3.46) and (3.47) remain valid even as $\sigma_1 \to 0$. Figure 3.30 shows values of σ/x for jets with various densities: jets of Freon, air, and helium. We should note that the dispersion σ of the jet is not a strictly linear function of x, and that for this reason the average value of σ/x on the segment $x = (0 — 10)d_0$ appears in Figure 3.30.
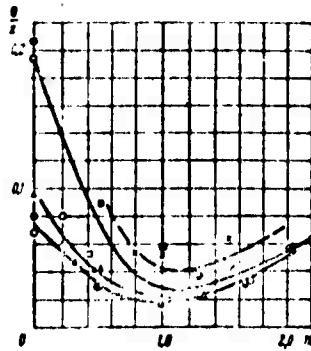
Figure 3.30. Influence of velocity ratio and density ratio on dispersion of jet (initial segment of jet).

Symbol	d_2 mm	d_{pp} mm	n	Re_d	Remarks			Author
● C	20 50	150	0,25 0,27	10^1 -10^6	Throttling Boundary layer			
▲ △	50	1'0	1 25 1,77	10^4	l_1 1,0)	u_1 0,32	d_1 ЛЛ 20	Abramovich et al.
■ □	20 50	150	7 25 8,2	10^4 -10^5	0,75 $u_1 \sim l_2 = 1,5\%$	0,5	;0	
∅ X	50,8	210	0,6) 14,5					Alpinieri

The manner in which the dispersion of the jet depends on the velocity ratio is the same as for the main segment of the jet, but in this case we observe only slight stratification of the curves with respect to the parameter n. It is not possible at the present time to submit an analytical relation for the dispersion of the jet as a function of the density ratio for various outflow conditions, both because of the lack of adequate experimental material and because of the complexity of theoretical analysis of this relationship for jets of limited size. However, because of the weak dependence of the parameter σ on r, the data given in Figure 3.30 are found to be quite sufficient for a correct choice of the value of σ on the initial segment for the appropriate value of n.

2. Supersonic Jet in Subsonic Stream

For supersonic streams, according to the linear theory, the surface of tangential discontinuity becomes stable as the Mach number increases [2]. This result is consistent with direct observations and measurements in supersonic nozzles and pipes, which indicate stability of the interface between the two streams and a decrease in the level of turbulence in the pipes with increasing Mach number [148]. In the general case, therefore, we should expect a decrease in the dispersion with increasing Mach number both for the initial turbulence (m = 1) and for shear turbulence (m $\neq$ 1).

However, there are two possible exceptional cases. In the case of flow with a pressure gradient that is positive in the mean (in a diffusor), the system of shocks, which is accompanied by boundary layer detachments on the walls and in zones of large transverse velocity shear, may produce a high initial turbulence level. In the case of an airplane (rocket) in supersonic flight, the dispersion of the jet engine exhaust at m = 1, which is determined basically by the initial turbulence parameters of the atmosphere, may also be rather large. In the former case, the diffusion due to the initial turbulence is measured independently in each specific case by one of the aforementioned methods (see §2); its characteristics depend on the specific geometry of the diffusor and are therefore of particular interest. To determine the "initial dispersion" in the latter case, we might, for example, use experimental data [149, 151], with the proviso that the data do not by any means exhaust all cases of atmospheric diffusion. Analysis of the data available for the atmosphere yields the relation

$$D_{u} = k_{z}^{1/3} l^{4/3}; \quad D_{\tau} = \frac{1}{l} \frac{d(z)^{2}}{dt}, \tag{3.68}$$

where l is the characteristic scale, $l \sim \sigma$; k is a constant ($k \approx 0.7$ under the conditions of lowered mass exchange for diffusion of H_2).

We note certain features of the variation of the supersonic-shear dispersion. The law of dispersion variation over the length of the free boundary layer can be written (see Chapter I)

$$\frac{d\mathfrak{z}}{dx} \sim -\frac{u'}{u_{cp}}\left(\frac{l}{\mathfrak{s}}\right),\tag{3.69}$$

where u', l, and u_{av} are the characteristic velocity, dimension, and average velocity of vorticity transport along the layer. We noted in Chapter I that for values of the initial longitudinal-velocity shear between two streams that meet the condition $u_2 - u_1 = \Delta u \ll a$ (a is the average velocity of sound in the layer), the scales u' and l have the following orders of magnitude:

$$u' \sim \Delta u \text{ and } l \sim \mathfrak{z}, \text{ with}$$
$$u'/l \sim \Delta u/\mathfrak{z}.\tag{3.70}$$

With increasing discontinuity (shear) Mach number $M_\Delta = \Delta u/a$, the velocity of rotation of the vortices will lag behind the increase in shear, since it has a limit determined by the zero pressure at the vortex center. For a "cylindrical" vortex with a constant angular velocity, this limit is determined from the condition of momentum conservation in the vortex, written in the form

$$\int_0^l \frac{v_n^2 dr}{r} \cdots \int_0^p \frac{dp}{\varrho} \text{ or } u'^2 \leqslant \frac{2a^2}{x-1},\tag{3.71}$$

where u' is the maximum linear velocity of the vortex and x is the adiabatic exponent.

Using an exponential relation to approximate the growth dynamics of vortex velocity, we obtain

$$u' = \sqrt{\frac{2}{x-1}}\,a\left(1 - e^{-\frac{\Delta u}{a}\sqrt{\frac{x-1}{2}}}\right) \text{ and } l \sim \mathfrak{z}\sqrt{\frac{2}{x-1}}\,\frac{a}{\Delta u}\left(1 - e^{-\frac{\Delta u}{a}\sqrt{\frac{x-1}{2}}}\right)$$

or

$$\frac{dz}{dx} \sim \frac{u'^2}{u_{cp}\Delta u} = \frac{2a^2}{(x-1)\Delta u u_{cp}} \left[1 - \exp\left(-\frac{\Delta u}{a}\sqrt{\frac{x-1}{2}}\right)\right]^2. \qquad (3.72)$$

The dispersion relation has two limiting forms:

(a)
$$\frac{dz}{dx} \sim \frac{\Delta u}{u_{cp}} \frac{\sqrt{\frac{2}{x-1}}}{\left(\sqrt{\frac{2}{x-1}} + M_{\Delta}\right)} \quad \text{for} \quad M_{\Delta} \ll \sqrt{\frac{2}{x-1}} \approx 2.24;$$

$$(3.73)$$

and (b)
$$\frac{dz}{dx} \sim \frac{2}{(x-1)M_{\Delta}M_{cp}} \quad \cdot \quad \text{for} \quad M_{\Delta} \gg \sqrt{\frac{2}{x-1}}.$$

It is clear from the first relation that at transonic shears, the increase rate of layer width depends on the shear in approximately the same way as for subsonic shears, although the numerical coefficient decreases with increasing shear Mach number. For hypersonic shears, according to the second relation in (3.73), we should expect the contrary dependence on shear. We note that since the vortex scale decreases monotonically with increasing shear Mach number, the mixing layer tends to be quasilaminar with a mixing inhomogeneity that tends monotonically to zero (see §4, subsection 4). In mixing of hypersonic and subsonic streams with nonzero initial boundary layer thicknesses, the integral scales u' and l' and the nature of the mixing over the thickness of the layer may differ appreciably. In the subsonic and transonic part, the development of the layer will follow laws of convective gradient diffusion such as (3.73a), while the hypersonic part will be subject to a gradient-diffusion law of the type (3.73b).

There are relatively few experimental data suitable for determination of the mixing dispersion of supersonic streams; the analogous data for hypersonic streams are practically nonexistent.
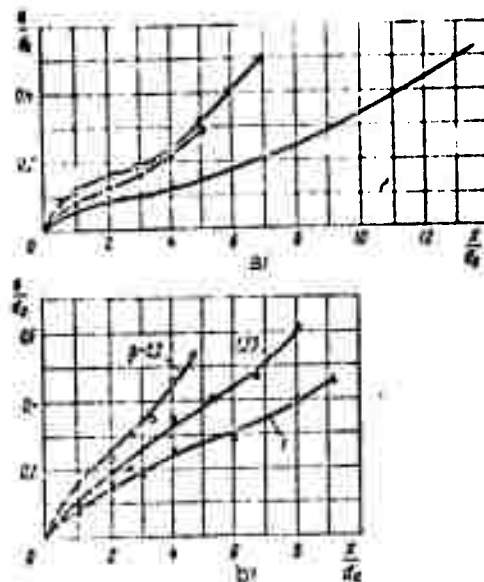
Figure 3.31. Dispersion of supersonic jets on initial segment.
a — submerged jet, $n_0 = 2$; $m = 0$; $\beta = 1$.

Symbol	M_a	Author
□	0 ?	Pabst
⊕	1 5	Zhestkov, Maksimov
×	3	Sakharov

b — jet in cocurrent stream

Symbol	M_2	ϑ	d_1 мм	d_a мм	V_1 m/sec	Remark
●	~1	1,53	~8,5	~10	5	Setup III
⊙	1	2.2	10	14.8	20	
△	1	1.0	10	10	30	

Figure 3.31 shows values of σ on the initial segment of a super-sonic jet under various jet-outflow conditions ($n = T_{02}/T_{01} = 2$; $M_2 = 0.8 — 3$; $\beta = 1 — 2.2$) according to various authors.

The values of σ were calculated from Toepler photographs of the jet by the method proposed in §2, subsection 3, Chapter III. We see from Figure 3.31 that the total dispersion σ of the jet is a nearly, but not quite, linear function of x. Hence the experimental data in Figure 3.31 can be approximated by
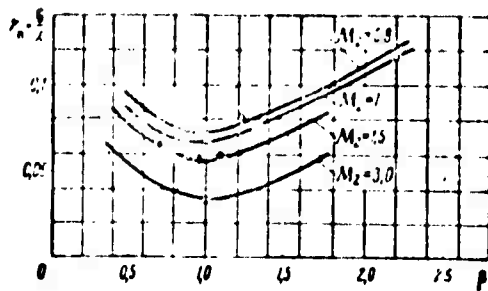
Figure 3.32. Influence of off-design factor of outflow on dispersion of supersonic jet (initial segment); $\theta = 0°$; $V_1 = 5 — 10$ m/sec.
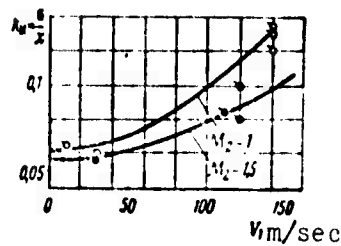

Figure 3.33. Influence of velocity of entraining stream on dispersion of supersonic jets (initial segment); $\beta = 1$; $\theta = 45°$.

$$\sigma = k_{\text{и}} x,$$

where

$$k_{\text{и}} = \frac{0.01 n_0 + 0.05}{\sqrt{M_2 + 1.4}}; \quad \text{for } M_2 < 3; \; n_0 < 5; \; \beta = 1. \tag{3.74}$$

Figure 3.32 shows k_0 as a function of jet Mach number and the off-design factor β. We see that σ increases as the parameter β deviates in either direction from unity.

Analysis of the experimental data indicates that the cocurrent subsonic stream has some slight influence on the mixing on the initial segment of a supersonic jet emerging at an initial angle $\theta \neq 0$ and that the mixing rate increases with increasing velocity of the cocurrent stream (Figure 3.33). This effect becomes weaker with increasing jet Mach number.

For calculation of σ with consideration of the effects of the parameters β and M_1 at $\theta \neq 0$, we propose the following empirical formula, which has been tested against experimental data in the range

$$0.7 < \beta < 3; \; M_2 < 3; \; n_0 < 5; \; M_1 < 0.45; \; \theta < 45°$$
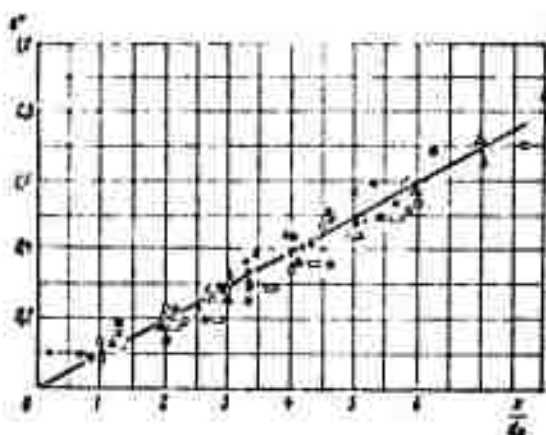
Figure 3.34. Dispersion of supersonic jet in initial segment for various values of the off-design factor and entraining-stream velocity:

$$d_j = d_1 \frac{\sqrt{M_1 + 1.4}}{(1 + 2.2|\lg \beta|)(1 + 8.3 \sin \theta \, M_1^2 : M_2^2)}$$

Symbol	⊥	■	▲	●	ɔ	⊙	⊀	✕	⊘	⊕	⌐	□	△	▵
M_1	1	1.5	1.5	1.5	1.5	1.5	1.6	1	1	1.5	1.5	1	1	1
β	1.33	0.72	0.75	0.95	1	0.95	1	2.2	1	0.76	0.72	1	1	1
θ°	0	45	45	45	45	0	45	0	0	0	0	45	45	45
V_1 м/сек	5	10	7	120	120	120	120	5	15	120	120	140	140	5
d_a мм	10	12.7	15	14.6	15	14.6	15	14.7	10	15	12.7	10	10	10

$$k_н = \frac{\sigma}{x} = \frac{0.01 n_0 + 0.05}{\sqrt{M_2 + 1.4}} (1 + 2.2|\lg \beta|)\left(1 + 8.3 \frac{M_1^2}{M_2^2} \sin \theta\right). \tag{3.75}$$

Values of the dispersion σ of a supersonic off-design jet are represented in Figure 3.34 by the solid line, which was calculated from Formula (3.75).

3. Jet in Supersonic Stream

There are not many experimental data on the mixing of supersonic jets with supersonic cocurrent streams. Data were recently published, for example, by J. Wilder and K. Hindersinn [84]. These authors investigated heated ($n_0 \leq 2$) supersonic ($M_2 \leq 1.4$) air jets and jets of carbon dioxide emerging into a supersonic cocurrent stream ($M_1 \leq 2.6$). They took samples from the CO_2 jet, measured stagnation temperatures, and photographed the jet with a Toepler instrument. The cocurrent stream was formed by a supersonic ejector tube into whose open entrance interchangeable flat nozzles were inserted to develop flows with Mach numbers of 1, 1.4, 8 and 2.6. The measurements were made near the nozzle. The data were used to determine the values of σ for various sets of conditions that appear in Figure 3.35. The data of Figure 3.35 indicate that the smallest total dispersion σ^2 is reached when the velocity of the jet and cocurrent stream are equal, $m = 1$, although the Mach numbers are then unequal.

In first approximation, the dispersion value can be approximated as a linear function

$$\sigma \sim b + kx,\tag{3.76}$$

where b characterizes the initial nonuniformity of the temperature profile; for this experiment,

$$b = 0.05h.$$

Here h is the height of the flat nozzle. The absolute value of b is smaller than the analogous values of other authors, but it appears larger against the background of the slow increase in σ. The mixing rate of the jet, which is determined by the value of k, is very low in these experiments (the smallest k equals 0.005). We note that this value is the smallest among other similar experimental figures, and that this can be explained as due to the low turbulence level of the streams in front of the nozzle (it appears that the turbulence level of the stream in front of the nozzle does not exceed the turbulence level in supersonic wind tunnels). The value of k decreases
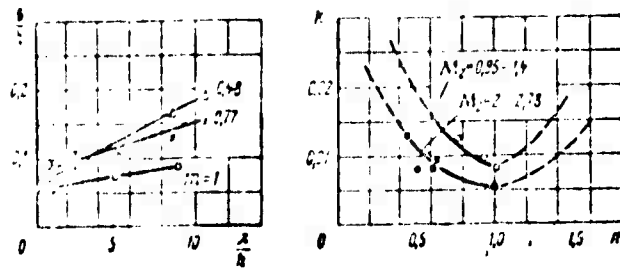
Figure 3.35. Spreading of supersonic jet in supersonic stream on initial segment (8.7 × 25-mm jet; cocurrent stream d ≈ 107 mm) (according to Wilder and Hindersinn).

Symbol	M_0	M_1	$T_{01}°k$	Remark
∆	2.73	1.6	590	
▲	1.23	1.35	590	Study of temperature fields (data of [84]), CO_2, sampling [84]
○	2	1.73		

with increasing M_2 in the same way as in the case of a supersonic jet in a subsonic stream (compare Figures 3.32 and 3.35).

Figure 3.36a presents values of σ calculated from the concentration distributions in subsonic jets of hydrogen and helium propagating in a supersonic cocurrent stream ($M_1 ≤ 3$). These data were borrowed from A. Ferry's survey paper [49].

The values of σ in Figure 3.36 were approximated by the formula σ = $k(x - x_0)$. The quantity k depends on the velocity ratio (see Figure 3.36a).

The quantity x_0 depends on the molecular-weight ratio $\frac{\mu_1}{\mu_2}$ approximately as follows:

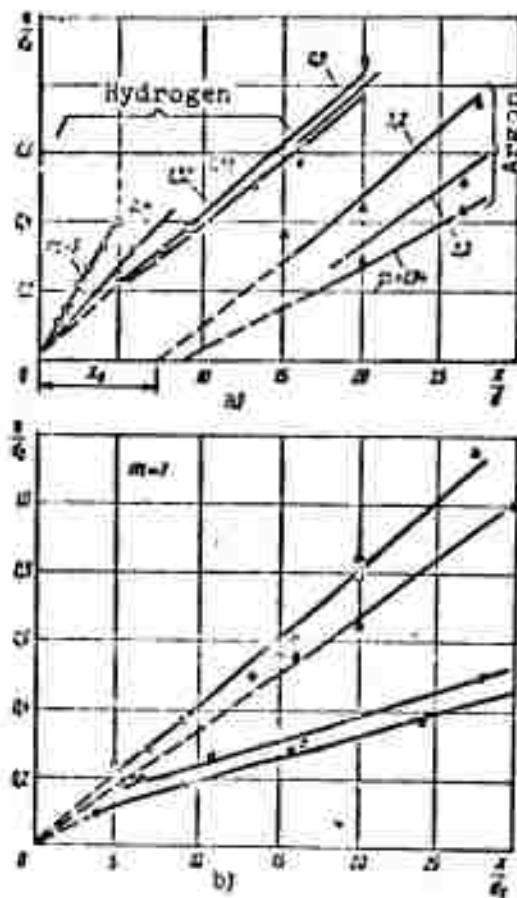$$x_0 \approx 8 \frac{\mu_2}{\mu_1} d_0. \tag{3.77}$$

Figure 3.36. Influence of velocity ratio on dispersion of subsonic jet in supersonic cocurrent stream ($M_2 < 1$, $M_1 > 1$):

Symbol	$\frac{d_i}{d_0}$	$\frac{d_1}{d_0}$	M_1	w_2	n	T_{01}°K	T_{02}°K	Substance	Author
O	7,6	—	~1.5	<1	~6	630	~0	Hydrogen	W. Zackey, B. Krause, S. Wu
△	7,6	—	~1.5	0,7	~4	30	370	Helium	
▲	3,9	—	1.3	~0.5	~10	200	~0	Helium	
⦿	50,8	~10	3	0.75	42	290	290	Hydrogen	Ferry, Libby, Zackey
●	20	70	1.5	2.8	2.0	1100	1100	Products of combustion of hydrogen, kerosene, and alcohol in air	Optical-diffusion method, data of Mal'tsev [150].

An explanation of this fact was offered in Chapter II, §2.

Figure 3.36a indicates that σ reaches its smallest value when the jet and cocurrent stream velocities are equal, m = 1, although the Mach-number ratio is not unity: $M_2 < 1$, $M_1 \simeq 1.3$.

Figure 3.36b gives values of σ for the case of equal jet and stream velocities but different cocurrent stream Mach numbers (M_1 = 1.5 and M_1 = 3). We see that with increasing Mach number M_1 of the cocurrent stream, the increase rate of the dispersion of the jet decreases, although the density ratio n = ρ_1/ρ_2 increases: n $\approx$ 4 — 10 for M_1 = 1.5 and n $\approx$ 42 for M_1 = 3, i.e., the density ratio does not depend strongly on the growth rate of jet dispersion in a supersonic stream.*

The influence of the jet-density ratio on the initial mixing parameters remains as before: the lighter the jet, the smaller the value of x_0 and the larger the limit of extrapolation of the function $\sigma(x)$ as x → 0.

Figure 3.37 shows values of the growth rate of the function σ of a subsonic jet in supersonic streams. The figure shows that the dependence on the velocity ratio remains qualitatively the same for $M_1 \leq 3$, although the absolute values of k decrease with increasing M_1.

4. Molecular-Mixing Dispersion on Initial Segment of Jet

The dispersion of molecular ("grey") mixing σ_c on the initial segment of a subsonic jet was determined by the optical diffusion method on the setup diagramed in Figure 3.7a (see also [59]). The study was made for the mixing of streams having the parameters indicated in Figure 3.38.

*Figure 3.36 also shows the value of σ recently obtained by A. I. Mal'tsev [150] at the Central Aero-Hydrodynamic Institute by the optical-diffusion method for m $\approx$ 1 and M_1 = 1.8, M_2 = 2.8, and n $\approx$ 2 for two axisymmetric coaxial streams. The jet was registered by tinting the products of combustion of hydrogen with air with an alcoholic solution of NaOH.
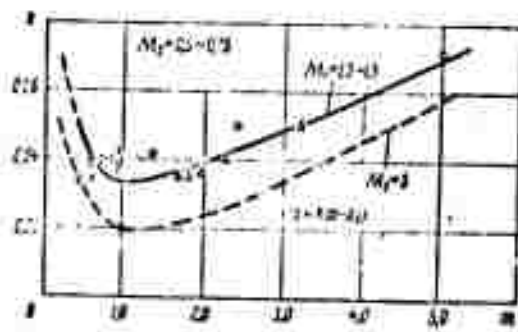
Figure 3.37. Influence of density ratio on dispersion of subsonic jet in supersonic cocurrent stream (velocities of jet and stream equal):

Symbol	Substance of Jet	$T_{01}°K$	$T_{02}°K$	M_1	M_2	n	Author
	Hydrogen	~0.	830	~1.3	<1	10-8	Libby, Krause, Wu
	Helium	200-820	200-110	~1.3	~1	7-4	
△	Argon			~1.4	<1	~0.7	
○	Hydrogen	290	290	~0	0.75	43	Ferry, Libby, Zackey

The jet was composed of the combustion products of a propane-air or gasoline-air mixture.

Values of σ_c for the initial segment of the jet appear in Figure 3.38. Figure 3.39 is a plot of $\sigma_c(m)/\sigma_c(1)$. We see that the dependence of the molecular (grey) mixing parameter σ_c on m on the initial segment of the subsonic jet is similar to that of the parameters σ_c and σ on the main segment: σ_c has its smallest value for equal velocities (m = 1) and its largest value for the submerged jet (m = 0). It also follows from the experimental data in Figure 3.38 that the dispersion values for a sonic nonisothermal jet ($M_2 = 1$, $T_{02} = 1500°$ K) agree, within the limits of experimental error, with the corresponding values for the subsonic jets. This particular result indicates that gradient diffusion on the initial segment of the jet, where the influence of the initial turbulence is strong, behaves in the same way up to a jet Mach number of unity.
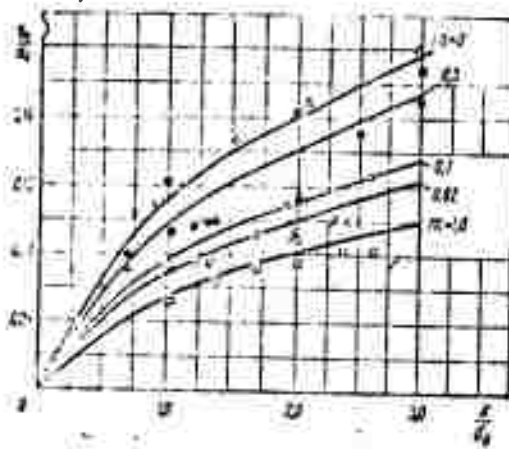
Figure 3.38. Dispersion of "grey" mixing on initial segment of jet.

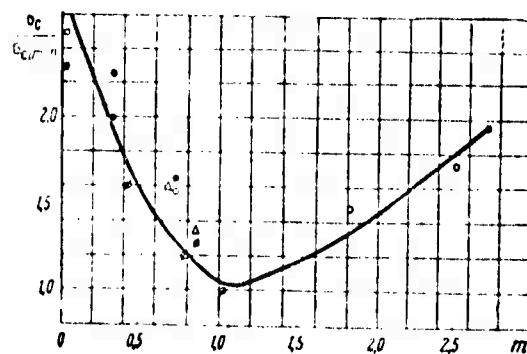| Symbol	d_2 мм	T_2°K	V m/sec	d_1 мм	T_1°K
× ⊕ ⊙ ●	25 60	1500–1700	15–20 15	100 200	300
▫ ▲ ▣ △	0 10		50–110 $M_1 = 1$	200 100	

Figure 3.39. Influence of velocity ratio on grey mixing dispersion (initial segment of subsonic jet):

Symbol	⊙	●	⊘	△
d_2, мм	10	26	30	60

On the initial segment of the jet, the value of σ_c increases as $\sqrt{x}$ with increasing distance from the nozzle exit cross section. The absolute value of σ_c increases as $\sigma_c \sim \sqrt{d_2}$ with increasing jet diameter, indicating that the initial turbulence of the jet is the dominant factor. It was noted previously, in Chapter III, §3, subsection 2, that the influence of the initial jet turbulence on the rate of molecular mixing at m = 1 can be expressed (accurate to an empirical constant) in terms of the initial turbulence ε_2 in the jet and the jet-vortex scale, which is proportional to the jet diameter d_2.

Here σ_c can be described by the following relation on the initial segment of the jet:

$$\sigma_{2c}^2 = \sigma_{c\ (m=1)}^2 = A_1 \varepsilon_2 d_2 x. \tag{3.78}$$

Remembering that for the experimental setup of Figure 3.7a, the initial turbulent intensity in the core of the jet is equal to the normal pipe-turbulence intensity $\varepsilon_1 = \varepsilon_2 = 0.05$, we find that the experimental values of σ_c for m = 1 satisfy relation (3.78) when A_1 equals 0.07. For arbitrary m, σ_c can be calculated from this relation and the diagram in Figure 3.39.

Figure 3.40 presents experimental values of N on the initial segments of subsonic and supersonic jets.* We see that up to M_2 = 2.8 and x/d ≤ 32, according to [150], the value of N fluctuates in the rather narrow range 0.30 — 0.55 with varying x and m.

It has not yet been possible to obtain data on the molecular mixing of supersonic jets at very large Mach numbers (M ≫ 3) in subsonic or supersonic cocurrent streams, since the optical diffusion method, the only one suitable for such conditions, still encounters

---

*The values of N for the supersonic jets were obtained by A. I. Mal'tsev [150] and the Central-Aero-Hydrodynamics Institute by computer processing of data obtained by the optical diffusion method.
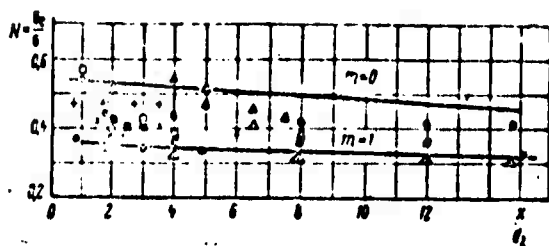
Figure 3.40. Degree of mixing homogeneity on initial segment of subsonic jet:

Symbol	○ ●	△	⅄ ⊙	▢	+	▣	▲	△	▰	◉
$\frac{d_i}{\mu_a}$	40	10	20		40		10	$d_i=20$ $d_i=10$	$d_i=20$ $d_i=70$	$d_i=20$ $d_i=70$
m	1.7 1.4	0	0.7 0.7	0	0,65	0,82	~0	0,945	1,04	0,97
v, m/sec	15–20	10	~30		80–100		$M_i=1$	$M_i=1,5$ $M_i=2,8$	$M_i=2,4$ $M_i=2,8$	$M_i=1,8$ $M_i=2,8$

insurmountable methodological difficulties due to the low temperatures of the streams (the low brightness of the light emitted by the gas particles being mixed). The only hope here is the possible development of a method for rendering the supersonic stream visible with the aid of the "cold luminescence" of intermediate radicals formed during mixing of the two streams [7]. As for extrapolation of the experimental data given above to very large shear Mach numbers, it would be most legitimate physically to extrapolate absolute values of σ_c, obtained on the initial segment of the sonic jet in accordance with the argument presented in §4, subsection 2. With increasing Mach number of the jet or cocurrent stream, the parameter N will increase monotonically, since the probability of appearance of convective diffusion decreases monotonically in this process.

Applying (3.72) and using a linear relation for first-order approximation of the decrease in mixing inhomogeneity, we obtain the following law of increase of the parameter N with shear Mach number:

$$[1-N(M_a)]=[1-N(1)]\frac{l}{e}=[1-N(1)]\sqrt{\frac{2}{x-1}}\times$$
$$\times\left(1-e^{-V\frac{x-1}{2}M_a}\right)\frac{1}{M_a}. \tag{3.79}$$

where $N(1) = 0.45 - 0.55$ is the degree of mixing homogeneity for $M_\Delta = 1$ (see Figure 3.40).

In this case, the characteristic vortex scale is defined in such a way that $l = \sigma$ at $M_\lambda = 1$.

§5. Behavior of Dispersion in Nozzles

1. Experimental Setup

Experiments were performed on the setup shown in Figure 3.41, where the arrows indicate delivery of air. Temperature profiles were measured in the mixing zone of a weakly preheated jet delivered from a heat-insulated cylindrical pipe 50 mm in diameter coaxially into a stream of cold air.

The diffusion characteristics of the stream in converging-nozzle flow were investigated in working segment I. Vitoshinskiy nozzles 200 and 400 mm long with entrance and exit diameters of 200 and 85 mm were used. The excess over atmospheric pressure in the cylindrical channel was varied in the range 0.3 — 1.2 bar in the experiments, to obtain exit-section Mach numbers in the range from 0.63 to 1.0.

The diffusion parameters of the initial flow were measured on working segment II in the cylindrical chamber at the same pressures.

The diverging segment of the nozzle, working section III, was a cone with entrance and exit cross sections of 85.3 and 90 mm and, at an excess pressure of 2 bars, provided supersonic conditions with $M = 1.0 - 1.4$; at an excess pressure of 0.3 bar, the flow was subsonic, at $M = 0.79 - 0.63$. The 200-mm-long converging section had a Vitoshinskiy profile.

The temperatures were measured in six cross sections with differential thermocouples whose moving junctions 1 were displaced simultaneously in 5-mm steps into the receiving ports 3 by electrical coordinator 2, while their stationary junctions (not shown on the
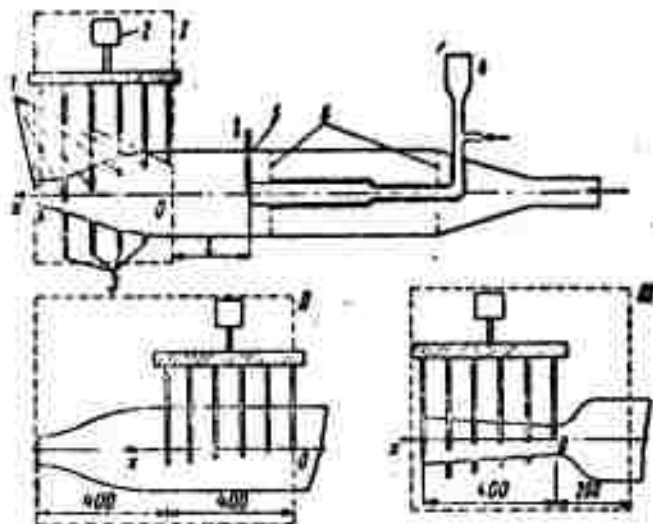
Figure 3.41. Diagram of experimental setup.

diagram) were mounted in the cross sections of interest at a distance
of 3 — 4 mm from the nozzle wall.

The temperature of the jet, which was measured with moving
thermocouple 5, was regulated by adjusting the flow rate ratio of the
air and gasoline combustion products in antechamber 4. The equalizing
grids 6, which were mounted in the cocurrent stream with their centers
9 mm apart, had apertures 6 mm in diameter.

2. Relation Between Measured Temperature Profiles and Diffusion Parameters

Let us consider the diffusion in a stream from a continuous
point source situated on the axis of an axisymmetric channel of
variable cross section.

In the case with $m \approx 1$ and $n \approx 1$, the velocity in the core of
the stream remains practically unchanged over the cross section of
the nozzle, and the turbulence is homogeneous.

The equation of turbulent diffusion for a central jet is written as follows in cylindrical coordinates:

$$\frac{\partial(\rho c \bar{u})}{\partial x} + \frac{1}{r}\frac{\partial}{\partial r}(\rho c \bar{v} r) = D(x)\frac{1}{r}\frac{\partial}{\partial r}\left(r\frac{\partial \rho c}{\partial r}\right). \qquad (3.80)$$

Here $\bar{u}(x)$ is the longitudinal velocity, $\bar{v}(x, r)$ is the transverse velocity, $\rho(x)$ is the density, $D(x)$ is the eddy diffusivity in the transverse direction, and c is the concentration of jet volumes.

If it is a property of the flow in the channel that the relative position of any averaged streamline r/r_c does not vary in the flow along the channel, the transverse velocity is related to the longitundinal velocity by

$$\bar{v} = \bar{u}\frac{r}{r_c}\frac{dr_c}{dx}, \qquad (3.81)$$

where $r_c(x)$ is the channel radius in the cross section of interest.

Let us also consider channel cross sections in which the material of the source has for all practical purposes not yet reached the walls (its concentration at the walls is negligibly small compared to the concentration on the axis). The mean square displacement in a certain fixed direction perpendicular to the channel axis is by definition equal to

$$\bar{r}^2 = \int_0^\infty c(r) r^2 2\pi r dr \left(\int_0^\infty c(r) 2\pi r dr\right)^{-1}, \qquad (3.82)$$

where $\bar{r}^2 = \sigma_y^2 + \sigma_z^2 = 2\sigma^2$.

In virtue of the constancy of the flow of material from the source, we also have

$$\bar{u}\rho\int_0^\infty c(r) 2\pi r dr = u_s \rho_s \pi r_s^2 = \text{const.} \qquad (3.83)$$

We substitute the expression for the transverse velocity (3.81) into the diffusion equation (3.80), multiply both sides of the equation by r^2, and integrate it over the area. Applying (3.82) and (3.83), we obtain the law of dispersion variation in the channel:

$$\frac{d\sigma^2}{dx} - \frac{2}{r_c} \frac{dr_c}{dx} \sigma^2 = 2 \frac{D}{\bar{u}} . \tag{3.84}$$

If we take r_c = const (then $\bar{v}$ = 0) the usual relation for the diffusion in a constant-section channel follows from (3.84):

$$\frac{1}{2} \frac{d\sigma^2}{dx} = \frac{D}{\bar{u}} \quad \text{or} \quad \frac{1}{2} \frac{d\sigma^2}{dt} = D. \tag{3.85}$$

In the other extreme case, in which there is no mixing (D = 0), we find

$$\sigma^2 = \frac{\sigma_I^2 r_c^2}{r_I^2} . \tag{3.86}$$

where r_I and σ_I^2 are the initial radius of the nozzle and the initial dispersion.

Since the dispersion varies not only as a result of diffusion in variable-section channels, but also as a result of the changes in cross-sectional area, we present (3.84) in the form

$$\frac{d\Sigma^2}{dx} = 2 \frac{r_I^2}{r_c^2} \frac{D}{u} . \tag{3.87}$$

where

$$\Sigma^2 = \frac{r_I^2}{r_c^2} \sigma^2.$$

To describe the turbulent mixing in the channel, it is expedient to introduce another parameter:

$$\underline{\Sigma}^2(x) = \underline{\Sigma}_0^2(x) - \underline{\Sigma}_H^2 = \frac{r_H^2}{r_c^2} s^2 - s_H^2.$$ (3.88)

This parameter vanishes identically in the absence of diffusion, and satisfies the relation

$$\frac{d\Sigma^2}{dx} = 2 \frac{r_H^2}{r_c^2} \frac{D}{u}.$$ (3.89)

The parameter Σ^2 does not depend on the dispersion at the entrance into the channel segment under investigation, and it determines the diffusion properties of the stream on that segment. We note that for diffusion from a central point source, which is subject to (3.80), the concentration distribution in each nozzle cross section is, as in the case of a cylindrical channel, described by a Gaussian curve. This can be verified directly by applying (3.81) and (3.84), the continuity condition, and the constancy of delivery from the source. In this case, therefore, the dispersion can be determined experimentally in each cross section from a characteristic width of the profile (usually its width at the level at which the concentration is half the concentration on the axis, which is the highest concentration in the cross section).

The source cannot be regarded as a point source in analyzing the results of these experiments. For diffusion from a round coaxial source, which is subject to (3.80), the concentration distribution in any cross section has in this case the form (in the absence of wall effects)

$$\frac{c(x, r)}{c_0} = H\left(\frac{a(u)}{z(x)}, \frac{r}{z(x)}\right) =$$

$$= \frac{1}{z^2} \exp\left(-\frac{r^2}{2z^2}\right) \int_0^{a(x)} \exp\left(-\frac{z^2}{2z^2}\right) I_0\left(\frac{r\varrho}{z^2}\right) \varrho \, d\varrho,$$ (3.90)

$$a(x) = a_0 \frac{r_c(x)}{r_0}.$$

Here c_0 is the concentration of the admixture from the source and a_0 and r_0 are the initial radius of the source and the radius of the channel in the cross section at which the gas is delivered. This can be demonstrated most simply as follows. In the dimensionless parameters $r' = \dfrac{r}{r_c}$ and $r' = \dfrac{a}{r_c}$, Equation (3.80) acquires, after application of (3.81), (3.84), and the continuity condition, the usual form of the diffusion equation for the axisymmetric case:

$$\frac{\partial c}{\partial x} = \frac{1}{2} \frac{da^{*2}}{dx} \cdot \frac{1}{r^*} \frac{\partial}{\partial r^*} r^* \frac{\partial c}{\partial r^*} . \tag{3.91}$$

The solution of this equation will be a function of the form $\Pi(a^*, r^*, r')$ or $\Pi\left(\dfrac{a}{a} ; \dfrac{r}{a}\right)^*$, as introduced earlier, in Chapter II.

The methods described in §2 were used to find the dispersion from the profile described by the Π-function.

In analysis of the results of experiments with weakly preheated jets, we used the excess stagnation temperature referred to the initial overheat of the jet as a parameter equivalent to concentration. It is also convenient to use the reduced dispersion $\Sigma^2(x)$ given by (3.88) in describing the mixing of nonisothermal jets, but then the combination Σ_I^2 will no longer always be constant along the nozzle. An expression for determining the behavior of $\Sigma_I^2(x)$ in the absence of mixing in the nozzle can be obtained from the condition of excess-enthalpy conservation.

Let us consider a flow with constant velocities at the entrance into the nozzle. In this case, the decrease in pressure along the nozzle (the pressure was assumed constant for each cross section) is accompanied by a transition from flow at constant velocity to flow with constant reduced velocities λ.

*Appropriate boundary conditions should be used if it is necessary to account for the wall effects in solving (3.91).

Approximating the shape of the stagnation temperature profiles along the nozzle by Gaussian curves (with certain effective parameters), we can find the limiting value of the dispersion Σ_I^2 that is attainable in cross sections with constant λ from the expression

$$\Sigma_{\text{в}}^2 = \frac{1}{2}\ln\frac{T_{01}}{T_{02}}\left[\left(\frac{T_{01}}{T_{02}}\right)^{\frac{1}{2}} - 1\right]^{-1}\sigma_{\text{в}}^2, \qquad (3.92)$$

and, in the transitional region at relatively low jet flow rates, from an asymptotic expression that is valid on the initial segment of the nozzle:

$$\Sigma_{\text{в}}^2(x) = \ln\frac{T_{01}}{T_{02}}\left[\frac{2 - \pi_{\text{к}}(x) - \pi_{\text{в}}}{2[1 - \pi_{\text{c}}(x)]}\ln\frac{T_{01}}{T_{02}} + \frac{\pi_{\text{к}} - \pi_{\text{к}}(x)}{2[1 - \pi_{\text{c}}(x)]}\left(\frac{T_{01}}{T_{02}} - 1\right)\right]^{-1}\sigma_{\text{в}}^2, \qquad (3.93)$$

where σ_I^2 is the dispersion at the beginning of the nozzle and T_{01} and T_{02} are the maximum and minimum stagnation temperatures at the beginning of the nozzle.

Theoretical analysis of the behavior of dispersion in flows in variable-section channels is possible only in the case of isothermal constant velocity flows. The behavior of the diffusion coefficient for such flows, which is related to the reduced dispersion Σ^2 by (3.89), can be found on the basis of the theory of homogeneous turbulence deformation [19].[*] In the extreme case of rapid deformation, the behavior of the eddy diffusivity in the transverse direction is subject to the relation

$$\frac{D_t}{D_{t0}} = 1 - \bar{c}\left[\frac{3c}{4} + \frac{3}{4c^2}\left(\frac{1}{2a^2} - \frac{1-a^2}{4a^3}\ln\frac{1+a}{1-a}\right)\right]^{-\frac{1}{2}},$$

$$a = 1 - \frac{1}{c^3}, \qquad c = \frac{u(x)}{u_{\text{в}}}\left(\frac{\varrho(x)}{\varrho_{\text{в}}}\right)^{\frac{1}{3}}, \qquad (3.94)$$

---

where ρ is the density and u is the average longitudinal velocity. The subscript "I" identifies the parameters in the initial cross section, in which the turbulence is assumed to be isotropic. In real flows, in which the length and diameter of the channel are of the same order, the hypothesis of rapid deformation, in which the inertial and viscous terms in the equation of motion are disregarded, is not satisfied. Analysis of flow deformation, during which there is time for the turbulence to become isotropic, has shown that the eddy diffusivity remains constant in flow along a channel. This result was obtained by V. M. Iyevlev with the aid of the familiar Friedman-Keller method. The forms of the nonlinear inertial and viscous terms were selected on the basis of dimensionality considerations in terms of the turbulence scale and fluctuation velocity. Here the proportionality coefficients were chosen such that in the absence of deformation, the calculated decay of fluctuation velocity would correctly describe the results of experiments behind grids, while the eddy diffusivity would remain constant in accordance with a certain experimental linear law (see Appendix II).

3.   Dispersion of Isothermal Jet

Figure 3.42 shows the distribution of the dispersion σ^2 along the cylindrical chamber (working section II, L = 250 mm) for absolute pressures of 1.3 and 2.2 bars. The approximating straight lines, which were plotted by the method of least squares, correspond under the experimental conditions to D_T/u = 0.12 cm or D_T/ud_1 = 0.0048, which is five times the level of steady-state pipe turbulence (see §3), apparently because of disturbances from the converging segment at the beginning of the cylindrical channel and, in the mixing zone, the effects of the boundary layer formed on the delivery pipe.

By way of example, Figure 3.43 presents the results of dispersion measurements in a converging nozzle with M = 0.87 at its exit section (L = 250 mm). The diagram shows σ^2 as measured and Σ_0^2 after reduction to the dimensions of the cylindrical chamber, together with σ_I^2 and Σ_I^2, which correspond to the case in which diffusion is absent. We see
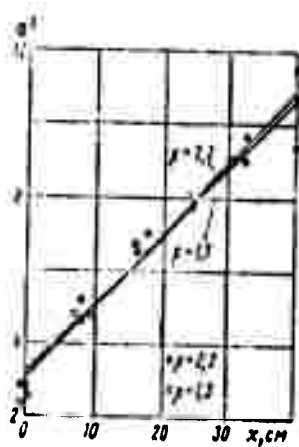
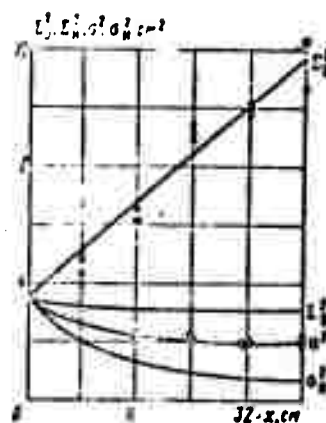Figure 3.42. Dispersion in cylindrical pipe (setup II).

Figure 3.43. Dispersion in tapering nozzle.

from the diagram that the absolute value of the squared dispersion, measured along the nozzle, decreases in spite of the presence of mixing.

Figure 3.44 shows the x distribution of the values obtained for Σ^2 according to (3.88) at $N = 0.63$ and 1.0 at the exit cross section, together with the theoretical curves: a for M = 0.63 and b for M = 1.0 and the experimental curve c for the cylinder. The theoretical calculation was made by graphical integration of (3.89), in which $u(x)$ was calculated from the geometry of the nozzle and $D(x)$ from Formula (3.94) for rapid deformation (curves 1) and D = const for slow deformation (curves 2).

Let us analyze these data. It follows from the solution of Equation (3.91) that for a given $\Sigma^2(x)$, mixing occurs at equal rates along the channel and along the nozzle, i.e., the maximum concentrations decrease in the same fashion along the axis of the jet, while the concentration profiles in sections with the same values of the longitudinal coordinate x are related to one another by an affine transformation of the transverse coordinate. Hence, it also follows that for an incompressible fluid at D = const, the relative intensity of mixing along an axisymmetric channel does not depend on the shape
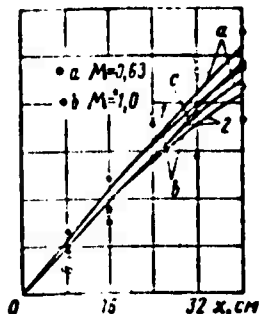
Figure 3.44. Experiment and
calculation for tapering
nozzle.

of its generatrix. For example,
the velocity increases if the
channel tapers, but there is a
corresponding decrease in the
distance to the wall that the
volumes of the jet must travel
to produce the same degree of
mixing.

For mixing of a compressible
gas in a nozzle, the density
decrease causes the velocity to
increase more rapidly than the area decreases, with the result that
the extent of mixing is lower at D = const.

It is evident from comparison of the values of the dispersion
Σ^2 shown in Figure 3.44, which were obtained in a cylinder, with the
theoretical calculations for a converging nozzle that with M = 0.63
and D = const, the effect of compressibility, which is to retard
mixing, is weak, and noticeable only on the last quarter of nozzle
length. For the rapid-deformation hypothesis, when D increases (in
the experimental data, by 15% at the end of the nozzle), mixing
takes place more intensively in the nozzle than in the cylinder.
According to th theory, the compressibility effect is more conspicu-
ous at the criti pressure drop. Figure 3.44 shows that in the
case of rapid deformation at M = 1, despite the increase in the
diffusion coefficient, mixing is practically the same as in the
cylinder, while it is slower for the case of slow deformation.
However, the stratification due to the compressibility effect on a
change in the pressure drop is slight, like the diffusion difference
in the cases of fast and slow deformation. We see from Figure 3.44
that the mixing process takes the same course in the converging nozzle
and in the cylinder within the limits of experimental error. This
is also confirmed by the fact that the curves representing the
decrease in the relative excess stagnation temperature ΔT_0 on the
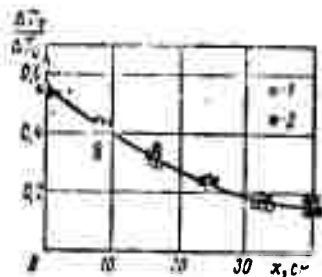jet axis do not separate for the nozzle and the cylinder.

Figure 3.45. Decrease in
stagnation temperature along
axis of jet in cylinder (1)
and nozzle (2).

By way of example, Figure
3.45 presents these data for
M = 0.63 [1 - cylinder; 2 - nozzle].

Figure 3.46. Experiment and
calculation for isothermal
jet in expanding section of
nozzle.

The results of the experi-
ments and calculations for the
diverging part of the nozzle (L = 150 mm) appear in Figure 3.46,
where curve 1 represents the rapid deformation calculation, curve 2-
the slow deformation calculation, Ia-supersonic flow, IIb-subsonic
flow, and c - the experiment in the cylinder. The dispersion was
converted to the dimensions of the cylindrical chamber and the value
of Σ_I^2, which is constant along the nozzle cone, was found from the
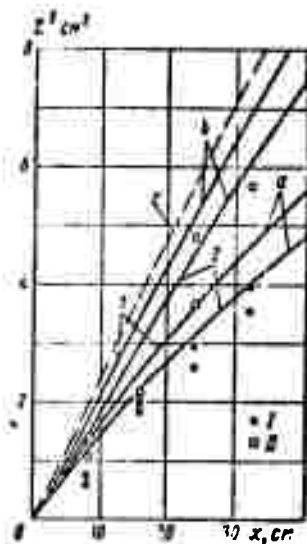value of the experimental straight line Σ_0^2 at the point x = 0.

As the diagram indicates, mixing takes place more slowly in the
cone than in the cylinder, especially for the supersonic flow. The
difference between the fast and slow deformations is larger in this
case (due to the preliminary variation of the diffusion coefficient
during rapid deformation in the converging segment), and, as is seen
from the diagram, the experimental points lie closer to the curves
calculated on the assumption of slow deformation. The rather good
agreement between experiment and theory indicates that the behavior
of the eddy diffusivity is determined under the experimental condi-
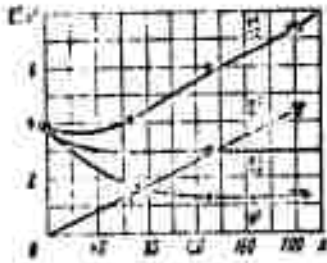tions basically by the deformation of the stream, while the influence

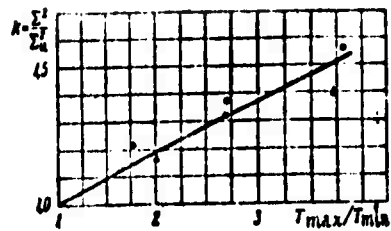Figure 3.47. Dispersion of nonisothermal jet in tapering nozzle.

Figure 3.48. Increase of mixing rates in tapering sections of nonisothermal nozzles.

$\bigcirc - L_{\Pi} - 200$ мм $\blacktriangle - L_{\Pi} - 400$ мм

of the walls and other factors goes practically unnoticed. As will be seen from the results to be given below, the diffusion in the nozzle may deviate from the theoretical results and take place more intensively than in the cylinder in the case of artificially suppressed turbulence [154], [155].

4. Dispersion of Nonisothermal Jet

The tests were run on a setup differing from that shown in Figure 3.41 in that the antechamber was mounted coaxially inside the cylindrical chamber, while the 0.3-meter-long pipe for delivery of the jet was smooth (without heat insulation).

The jet temperature was ≈2000° K, and the departure from isothermy at the entrance into the nozzle was adjusted by varying the distance between the beginning of the jet and the entrance to the nozzle (in the experiments, L = 170, 300, and 450 mm, and the pressure drop was critical). The values of a_T and σ were determined by the method indicated above; $a_T(0)$ was markedly smaller than the radius of the jet source and $\sigma(0)$ deviated appreciably from zero because of heat losses on the walls of the source.

It is interesting to note that for the nonisothermal jet, the experimental values of $\Sigma^2(x)$ in the nozzle also array themselves along a practically straight line (see Figure 3.47). However, the slope k increases with increasing temperature ratio, and is larger than in the cylinder. Figure 3.48 presents values of $k = \Sigma^2/\Sigma_u^2$ for two nozzle lengths $L_n = 200$ mm and $L_n = 400$ mm as they depend on the temperature ratio at the nozzle entrance. It follows from this plot that the slope increases in the nozzle with increasing temperature nonuniformity, indicating additional turbulence generation in the stream owing to the developing velocity shear in the nozzle flow.

The effect of intensified mixing of nonisothermal jets in flow in the nozzle is manifested to a much stronger degree when the turbulence level of the stream in the cylindrical chamber is lowered.

Figure 3.49 shows values of Σ^2 obtained under such conditions for mixing in a cylinder and converging nozzle (L = 400) at various jet temperatures. That the mixing intensity is strongly influenced by the nonisothermal nature of the stream is evident.

The experiments were performed on the setup shown in Figure 3.41. A honeycomb that filled the entire channel cross section was installed to lower the turbulence level at the entrance into the section to be studied (nozzle or cylinder). The honeycomb was fabricated from a long corrugated metal strip 0.5 mm thick and 40 mm wide, and had passages 2.5 mm in diameter.

It is interesting to note that in the case of a practically isothermal initial flow ($\Delta T_m \approx 75°$ at the entrance into the segment of the nozzle under study) and a low eddy-diffusivity level, mixing takes place more strongly in the nozzle than in the cylinder. This result is further confirmed by the fact that the maximum stagnation temperature decreases more rapidly in the nozzle. In other words, the disagreement of the experimental results with those of the theories of homogeneous turbulence deformation apparently results not only from the transverse shear developing due to the unequal accelerations of
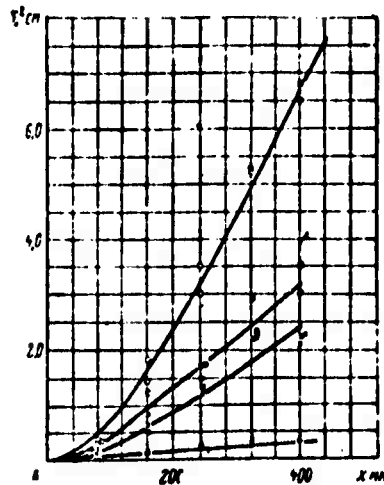
Figure 3.49. Behavior of reduced dispersion Σ^2 of nonisothermal jet with suppressed initial turbulence (subsonic flow):

			Method of determining Σ
$\bigcirc - \Delta T_0 = 1200°K$	$\Delta T_m(0) = 720°K$	nozzle	from half-widths and from
$\square - \Delta T_0 = 600°K$	$\Delta T_m(0) = 240°K$		ΔT_m
$\times - \Delta T_0 = 160°K$	$\Delta T_m(0) = 75°K$		
$\triangle - \Delta T_0 = 160°K$	$\Delta T_m(0) = 70°K$, cylinder		from ΔT_m

"cold" and "hot" volumes of gas in its flow along the nozzle, but also from longitudinal velocity shear on deviation of the real flow in the nozzle from one-dimensional, which also leads to turbulization of the flow that is not perceptible when the initial turbulent diffusion level is high. Figure 3.50 shows experimental results obtained in a supersonic flow in the diverging part of the nozzle with turbulence suppressed in the cylindrical chamber.

Let us examine the following physical explanation of the data obtained. At high initial turbulence, the influence of the additional velocity shear of the nonisothermal jet can be taken into account in the first approximation as an increment, proportional to ΔT, to the initial diffusion coefficient, i.e., we may set
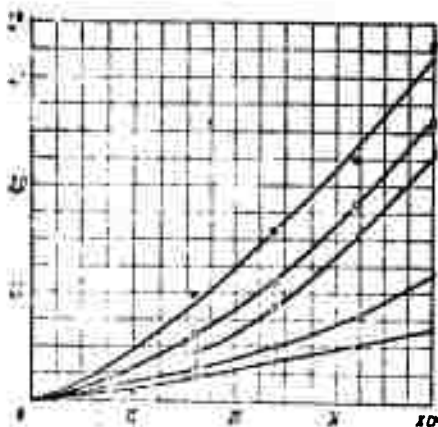
Figure 3.50. Behavior of reduced dispersion Σ^2 of nonisothermal jet with suppressed initial turbulence (supersonic flow).

$\blacksquare - \Delta T_m(0) - 900°K; \quad \square - \Delta T_m(0) - 550°K; \quad \bigcirc - \Delta T_m(0) - 370°K; \quad \triangle - \Delta T_m(0) - 210°K; \quad \times - \Delta T_m(0) - 60°K$

$$\Sigma^2 = \frac{2\left[D_0 + k_0\left(\frac{T_2}{T_1} - 1\right)\right]x}{u(0)}, \quad (3.95)$$

where, according to Figure 3.48, $k_0/D_0 = 0.13$.

With the relatively strong influence of velocity stratification in the nozzle, the total dispersion Σ^2 is more accurately determined as the sum of all dispersions.[*] Neglecting the dispersion due to secondary turbulization of the cocurrent stream in the nozzle, we can write

$$\Sigma^2 = \frac{2D_0}{u(0)}x + k_1^2\left[\frac{u_2(x) - u_1(x)}{u_2(x) + u_1(x)}\right]^2 x^2, \quad (3.96)$$

Since $n \cdot m(0) \cdot [u_1(x) - u_1(0)] = [u_2(x) - u_2(0)]$ from the momentum equation and $u_1(x)/u_1(0) = F_I \rho_1(0)/F_n(x)\rho_1(x)$ is given by the geometry of the nozzle, we can determine the behavior of the second term in (3.96) accurate to the value of the constant k_1. For example, we obtain for the subsonic part of the nozzle with $\rho_1 \approx$ const and $m(0) = \frac{u_1(0)}{u_2(0)} \approx 1$ and $F_I/F_n \leq 10$

$$\Sigma^2 = \frac{2D_0}{u(0)}x + k_1^2\left[\frac{(n-1)(F_n/F_c - 1)}{(n+1)F_n/F_c - (n-1)}\right]^2 x^2. \quad (3.97)$$

Substituting the values of n according to the data on $\Delta T_m(0)$ in front of the nozzle (see Figure 1.49), we obtain an average value $k_1 \approx 0.26$, which also takes implicit account of the increase in

_____

[*]Strictly speaking, the dispersions should be summed with consideration of the probability of appearance of each form of turbulence, for example, with all turbulence sources equiprobable with coefficient 1/N (N is the number of sources), which we did not do because the dispersions are determined accurate to an empirical constant.

cocurrent stream diffusion in the nozzle as compared to the cylindrical
pipe.

CHAPTER IV

HOMOGENEOUS COMBUSTION IN A TURBULENT STREAM

In the preceding chapters, we discussed the mixing of nonreacting jets of liquids and gases. For many engineering problems, however, interest attaches to turbulent flows with chemical transformations. When the reaction rates are high and mixing is the limiting process, it is natural to expect the ideas and methods developed above for analysis of turbulent mixing to be applicable. In certain engineering systems, the processes of mixing and combustion can be separated arbitrarily. In this case, combustion becomes a process of turbulent mixing of combustion products and a homogeneous fresh mixture with simultaneous reaction of the latter in molecular (grey) mixing layers. For brevity, this process is known as homogeneous combustion.

The present chapter deals with certain problems of turbulent homogeneous combustion.

§1. Models of Combustion

Historically, the first model of surface combustion made its appearance in the papers of G. Damköhler and K. I. Shchelkin [85], [86]. In this model, the increase in the combustion rate u_T in a turbulent stream as compared with the rate of normal combustion u_n in a laminar stream is explained simply by the increase in the area of the flame as a result of the curving effect of turbulent fluctuations.

Here it is assumed that the rate of combustion is constant along the normal to any element of the flame front and equal to the normal combustion rate.

During the decades that followed the appearance of the first studies [85], [86] of the surface combustion mechanism, dozens of papers by other authors, who expanded on this model, made their appearance. Most significant among these papers were those of Scurlock [97], Wohl [98], Karlovitz [100], A. V. Talantov [104], L. S. Kozachenko [142], and others. However, the development of conceptions of turbulence and of local turbulence in particular and the accumulation of experimental data made it possible to review and revise many established views as to the laws governing turbulent homogeneous combustion. In the light of our present knowledge, it could be expected that this model would give a quite realistic picture at small Reynolds numbers, at which only large vortices with dimensions many times greater than the width of the laminar flame are present in the stream. However, the calculations of A. M. Klimov [87] indicate that as a result of stretching of the combustion surface by large vortices, it becomes much thinner at the stretching points than the normal laminar front, and the combustion rate on this segment accordingly becomes appreciably smaller than u_n.

Experimental values of u_T and the average area of the combustion surface indirectly confirm this result. Thus, visual and direct measurements of the combustion surface [88] with simultaneous measurement of the statistical average values of u_T indicate that the average combustion rate over the surface may be much lower than u_n. This becomes especially conspicuous at very small Reynolds numbers, when the turbulent microstructure makes no contribution to u_T and the combustion macrosurface is found to be largest due to the long vortex lifetime.

The other extreme case is described by a three-dimensional model in which it is assumed that the structure of the turbulent flame is fundamentally no different from that of the laminar flame except for the value of the diffusion coefficient. The mechanism of this increase in combustion rate was also first noted in one of K. I. Shchelkin's papers [89]. It was later developed in various modifications in the work of Summerfield [90], Ye. S. Shchetnikov [91], and others.

Turbulent vortices with dimensions an order smaller than the width of the laminar front exist in a real stream at large Reynolds numbers (Re > 10^5), so that it is unnecessary to speak of preservation of the laminar combustion surface under such conditions. However, the conventional notion of the combustion surface is retained, since vortices much larger than the instantaneous thickness of the zone of microvolume combustion exist in the spectrum of turbulent scales of large combustion chambers.

In the model of microvolume combustion, which was first treated in detail in the papers of Ye. S. Shchetnikov [91], it is assumed that, in contrast to the hypothesis of the laminar surface model, the developed turbulent stream does not contain curved fronts propagating in accordance with the laws of the laminar flame. Because of the fast relative motion of the moles and the presence of a finite induction period, there is not sufficient time for these fronts to form on the boundaries between micromoles of fresh mixture and combustion products. In those moles in which the temperature is sufficiently high as a result of molecular mixing, the mixture burns rapidly in accordance with bulk-reaction laws. The resulting combustion products are again mixed with moles of fresh mixture, the bulk reaction again takes place, and combustion propagates through the fresh mixture in this way.

§2. Fluid-Dynamics Equations for a Turbulent Homogeneous Flame

The parameters of the medium in the turbulent combustion zone
are random functions of the space and time coordinates. On the other
hand, these parameters are continuous and differentiable functions of
these coordinates, so that the fluid dynamics equations are fully
applicable to them. The continuity and differentiability are explained
by the fact that molecular viscosity completely suppresses the
turbulent-motion components whose scales are comparable with the mole-
cular free path, so that the smallest turbulent fluctuation scales
of any of the above parameters are always much smaller than this path.
Hence it is always possible to neglect the molecular structure of the
fluid and treat it as a continuous medium. The applicability of the
fluid dynamics equations to the turbulent front is confirmed by suc-
cessful use of these equations both in the theory of the laminar
flame front [14] and in turbulence theory [19].

The chemical reaction taking place in the turbulent zone does not
affect the form of the equations of continuity and motion. Since the
turbulent combustion rate is far below the velocity of sound, it can
be assumed that the gas is incompressible and nonisothermal in the
combustion zone. We then have at any point of the front and at any
time

$$\varrho T = \varrho_1 T_1 = \text{const.} \tag{4.1}$$

The molecular weight is assumed constant, and ϱ and T are the
density and temperature of the mixture, respectively. In all of the
cases that follow, all physical parameters with the subscript "1" will
pertain to the fresh mixture and those subscripted "2"-to the burned
mixtures. For problems of turbulent combustion in a pipe, the constant
in condition (4.1) can be treated as a weakly varying function of the
coordinate along the pipe (due to the pressure drop).

We write the continuity equation in the form

$$\frac{\partial \varrho}{\partial t} + \frac{\partial \varrho u_i}{\partial x_i} = 0,$$ (4.2)

where u_i is the $i\underline{\text{th}}$ component of the instantaneous stream velocity at the particular point x_i and time t.

In study of turbulent combustion, the conservation equations of energy and m ss (fuel, oxidizer) are of greatest interest. In the most general form with constant pressure, they can be written [14]

$$c_p\varrho \frac{DT}{Dt} = c_p\varrho \left(\frac{\partial T}{\partial t} + u_i \frac{\partial T}{\partial x_i}\right) = z_{ik} \frac{\partial u_i}{\partial x_k} + \frac{\partial}{\partial x_i} \lambda \frac{\partial T}{\partial x_i} + \Phi(T; c);$$ (4.3)

$$\varrho \left(\frac{\partial c}{\partial t} + u_i \frac{\partial c}{\partial x_i}\right) = \frac{\partial}{\partial x_i} \varrho D_u \frac{\partial c}{\partial x_i} - W'(T; c),$$ (4.4)

where D_M is the molecular diffusion coefficient, λ is the coefficient of thermal conductivity, $\lambda/c_p\varrho = a$ is the thermal diffusivity, and σ_{ik} is the viscous-stress tensor [26].

The left side of Equation (4.3) represents the amount of heat acquired by a unit volume of gas per unit time at the point x_i (i = 1, 2, 3) at time t. We see from (4.3) that it is composed of the heat acquired by dissipation of kinetic energy with viscosity, the heat transferred into the volume in question by conduction, and the heat released per unit time due to the possible chemical reaction.

The physical significance of the terms in the equation of property (mass) conservation is analogous. The left side of Equation (4.4) — the rate of change of the concentration c of substance in a unit volume — equals the rate of influx of the substance by molecular diffusion minus the rate of disappearance of the substance in the chemical reaction. The effect of thermal diffusion is neglected in the terms for the diffusion heat and mass fluxes, i.e., it is assumed that the molecular heat flux is proportional only to the temperature

gradient, and the mass flux-only to the concentration gradient of the particular substance. Neglect of the heat released on decay of the turbulence [the first term on the right in (4.3)] is equally immaterial.

The concentration of the substance controlling the chemical reaction may be taken as the concentration c. This might be the concentration of oxygen, the concentration of fuel vapor, or the concentration of the intermediate reaction products (active centers), etc., depending on the physical conception of the heat-release mechanism that has been chosen. The quantity ρc is the mass of the particular substance in a unit volume. Obviously, there is a direct relation between the rate of disappearance of the concentration of the initial reaction products and the rate of heat release due to this reaction:

$$\Phi = H_u W,$$

where H_u is the heat effect of the reaction.

This relation can be applied by multiplying (4.4) by H_u and adding it to (4.3) to obtain the following relation for the enthalpy of the gas, provided that $\lambda / c_p \rho = D_u$:

$$\rho \frac{\partial H}{\partial t} + \rho u_i \frac{\partial H}{\partial x_i} = \frac{\partial}{\partial x_i} \frac{\lambda}{c_p} \frac{\partial H}{\partial x_i}, \quad (i = 1, 2, 3) \tag{4.5}$$

where $H = c_p T + H_u c$ is the enthalpy of a unit mass of the gas.

The equality of the diffusion coefficients D_M and the thermal diffusivity a is a known result of the classical theory of molecular diffusion. It is widely used as one of the hypotheses of the thermal theory of laminar combustion [96], [14], and [10]. It is satisfied with sufficient accuracy for fuel-air mixtures, although cases are possible in which departure from this equality proves significant, e.g., at rich-mixture ignition-range limits, when the distribution curves of u_n with respect to mixture composition are asymmetrical [14], etc.

By definition, the enthalpies are the same in the
fresh mixture and in the completely burned mixture, i.e.,

$$H_1(-\infty) = c_p T_1 + H_u c_0 = H_2(+\infty) = c_p T_2.$$

With these boundary and initial conditions, the solution of
Equation (4.5) is

$$H = c_p T + H_u c = c_p T_1 + q c_0 = c_p T_2 = \text{const.}^{*} \tag{4.6}$$

At any point of the zone, therefore, the two random functions T
and c are related by (5.16), the physical sense of which is that a
mobile equilibrium is established between the internal and chemical
energies at equal rates of molecular diffusion of heat and reacting
substance in a turbulent motion: their sum remains constant at any
point in the combustion zone at any point in time.

Formula (4.6), as the solution of (4.5), was first obtained by
Zel'dovich in an application to a laminar flame front; it is seen
from the arguments given above that it has a broader range of appli-
cation, remaining valid, for example, in the turbulent combustion
zone regardless of the combustion mechanism.

With (4.6), the equation system (4.3) and (4.4) can be reduced
to a single equation provided that the function $\Phi(T, c)$ or $W(T, c)$ is
known. Let us consider the form of the functions in greater detail.
We select an arbitrary "fluid volume" of fresh mixture small enough
so that the temperature and concentration in it will be constant
throughout its volume at all subsequent points in time. In inviscid
fluid dynamics, a "fluid volume" is a volume whose boundaries enclose
the same particles of the fluid. It is assumed in this case that this
volume does not exchange particles with the surrounding medium as a

*The question as to the uniqueness of this solution for arbitrary
initial conditions remains open. All subsequent treatments of turbu-
lent combustion are based on the solution (4.6).

result of fluid dynamic motions; however, its composition and temperature may vary as a result of molecular exchange with the surroundings, i.e., this volume must be much smaller than the smallest vortices (the smallest scales of the fluid-dynamic motion), but large enough so that it can be regarded as a continuous medium. The existence of such a volume is possible, since at atmospheric pressure the distance between molecules is ~30Å which is many orders smaller than the smallest vortices, whose dimensions range from the tens of millimeters to hundredths of a millimeter in the extreme case.

Exchange between the volume and the surrounding medium will in fact take place only as a result of molecular transport, since any turbulent fluctuations will transport it as a single whole. Thus the relations of molecular exchange and kinetics are fully applicable to this volume.

In the thermal mechanism, the rate of heat release at an arbitrary point of the turbulent flame is determined at any point in time by the relation

$$\Phi(T; c) \sim V \bar{T} c^\nu \exp\left(-\frac{E}{RT}\right)$$

or, in virtue of Condition (4.6), by the expression

$$\Phi(T) \sim V \bar{T}(T_2 - T)^\nu \exp\left(-\frac{E}{RT}\right). \tag{4.7}$$

where ν, E, and R are the total order of the reaction, the activation energy, and the gas constant, respectively, and are assumed to be the same for both laminar and turbulent flames.

The turbulent combustion zone is an infinite set of elementary fluid volumes, each of which is at a certain stage in chemical reaction, with the stages uniquely defined by the temperature of the volume in accordance with (4.6) and (4.7). If, therefore, a certain temperature is recorded at an arbitrary time and arbitrary point in the zone, it can be stated quite definitely which volume is situated at the point under consideration and, consequently, at which rate heat release is

occurring in an arbitrarily small unit volume surrounding the particular point. Formally, Equation (4.7) is no different from the relation for the rate of heat release in a homogeneous heat-insulated mixture, but in this case the rate of heat release is a function of a random argument (the temperature).

From the standpoint of dimension-theory description of the process, the considerations above mean that a physico-chemical parameter of the fuel-air mixture with the dimensions of time (the characteristic combustion term) remains the same in turbulent combustion as in laminar combustion.

The energy equation can be written in the following form with the continuity equation and relation (4.7):

$$c_\rho \left(\frac{\partial \varrho T}{\partial t} + \frac{\partial \varrho T u_i}{\partial x_i} \right) = \frac{\partial}{\partial x_i} \lambda \frac{\partial T}{\partial x_i} + \Phi(T)$$

or (since $\varrho T = $ const)

$$\frac{\partial u_i}{\partial x_i} = \frac{\partial}{\partial x_i} \frac{a}{T_1} \frac{\partial T}{\partial x_i} + F(T), \qquad (4.8)$$

where $F(T) = \frac{\Phi(T)}{c_\rho \varrho_1 T_1}$;

$$i = 1, 2, 3.$$

Equation (4.8) is interesting in that it is nearly linear, excepting the term F(T), and does not contain products of different random functions, so that no additional unknowns (correlation moments) appear on averaging.

The equations of momentum conservation can be simplified in similar fashion, but they are not used in the treatments that follow and therefore are not cited here. The equation system given above can be solved only on the basis of certain physical conceptions. In the sections that follow, we shall set forth physical conceptions of the development of turbulent combustion for jet engine chambers and give definitions of the fundamental physical parameters that characterize this process.

§3. Development Stages and Rate of Turbulent Combustion

The multistage nature of turbulent combustion was first discussed in the papers of A. S. Sokolik [94] and Yu. B. Sviridov [95]. It is set forth here in the light of recent data on turbulence and turbulent combustion.

Let us consider the simplest case: the development, in time, of a one-dimensional combustion zone from an initial interface between a fresh mixture and combustion products. Strictly speaking, this case is a physical ideal, but all cases of combustion in open streams and, with certain additional improvements, cases of pipe combustion (see §5) can be reduced to it with relatively small errors. The most exact physical equivalent of the one-dimensional zone is the combustion zone at the boundary of two plane-parallel streams (of fresh mixture and combustion products) flowing at the same velocity u (Figure 4.19). In this case, the variation of the parameters of this zone in a given cross section can be regarded with an error on the order of $u_i'^2/u^2$ as the variation of the parameters depthwise in a one-dimensional zone, while the parameter variation from one cross section to another, over a distance x_0 along the stream, can be treated as the variation of the one-dimensional zone in time $t = x_0/u$. This makes it possible to use existing experimental material on turbulent combustion in high velocity streams.

In analyzing the experimental material, we take note first of all of two experimental facts: the stationary nature of the turbulent combustion rate (for homogeneous turbulence of the free stream) and the nonstationary width of the turbulent-combustion zone (Figures 4.2 and 4.3). In the open stream, this difference is visually striking on the first observation of the plane-parallel turbulent flame jet: the spreading angle of the jet, which is proportional to $u_T/\bar{u}$, undergoes practically no change down the length of the jet, while the width of the bright zone (along the normal to the main stream) increases along the jet.
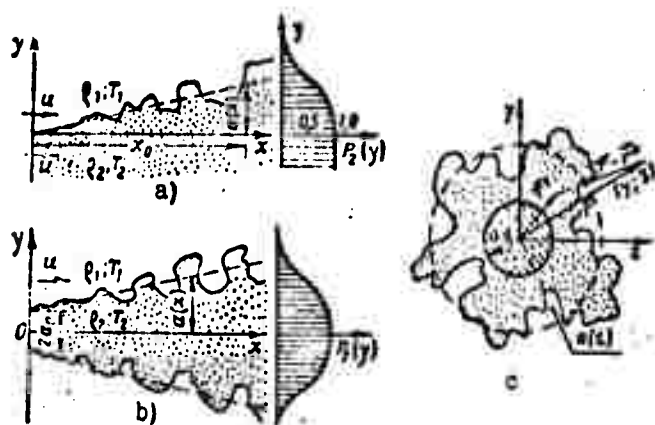
Figure 4.1. Illustrating determination of average temperatures in turbulent flame jet.

a — two-dimensional case; b — linear case; c — axisymmetric case.

Let us begin with the first-mentioned fact. For a one-dimensional zone, the equation of energy conservation (4.8) becomes, after averaging,

$$\frac{d\bar{u}}{dx} = D_{\scriptscriptstyle M} \frac{d^2\bar{T}}{dx^2 T_1} + \bar{F}(T). \tag{4.9}$$

Integrating it over x from $-\infty$ to $+\infty$, we obtain (with consideration of the mass-conservation equation $\rho_1 u_T = \rho_2 u_2$) a relation determining the rate of turbulent combustion:

$$u_1 = \frac{1}{(n-1)} \int\limits_{-\infty}^{\infty} \bar{F} dx = \frac{1}{(n-1)} \int\limits_{-\infty}^{\infty} \frac{\bar{\Phi}(T)}{c_p \rho_1 T_1} dx, \tag{4.10}$$

where $n = \frac{T_2}{T_1} = \frac{\rho_1}{\rho_2}$.

Relation (4.10) has a simple physical meaning: the rate of flame propagation equals the integral combustion rate of the mixture in the combustion zone. It can also be regarded as a certain modification of the mass conservation equation: the velocity with which volumes of fresh mixture move through a combustion zone that is non-moving in the mean equals the total rate of combustion of these volumes in the zone. Equation (4.10) is applicable to a combustion
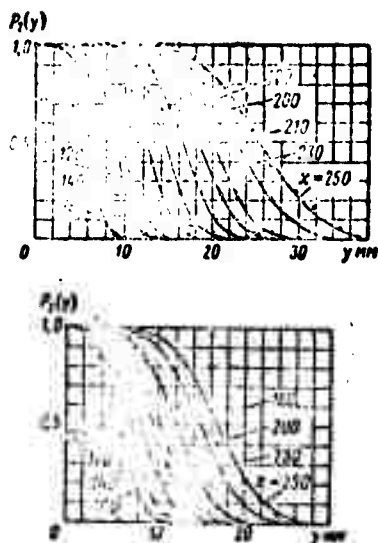
Figure 4.2. Distribution of probability of occurrence of combustion products over cross sections of open flame jet behind burner (α = 1.2; τ = 150° C; d_{pp} = 150 mm).
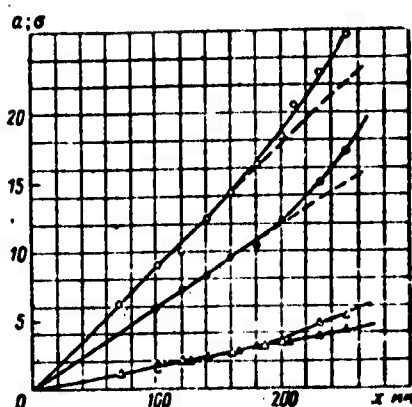
●, ○ — (according to A. I. Lushpa); ——— theory.

Figure 4.3. Distribution of average [radius] a(x) and dispersion $\sigma^2(x)$ of open flame jet behind point burner (according to A. I. Lushpa).

○ — $a(x)$; V = 23 m/sec; ● — $a(x)$; V = 43 m/sec; △ — $\sigma(x)$; V = 23 m/sec; ▲ — $\sigma(x)$; V = 43 m/sec; α = 1.2; τ = 150°C

model, including the laminar front. The fundamental differences in all existing combustion models consist only in the forms of the distribution function p(T, x), which enters into $\overline{\Phi}(T)$. For a laminar flame front, for example, the distribution function p(T) is such that a random function of temperature is simply equal to its own average value (the probability of the average temperature is unity). In this case, Relation (4.10) is reduced to the form first obtained by Zel'dovich:

$$u_\pi = \frac{1}{c_p \rho_1 (T_2 - T_1)} \int\limits_{-\infty}^{\infty} \Psi [T(x)] dx, \qquad (4.11)$$

from which we get

$$u_{\pi}/u_\pi = \int \overline{\Psi} dx \Big/ \int \Psi dx = \frac{\overline{s_{0r} a}}{s_{0s}} = \frac{s_{0r}}{s_{0s}}, \qquad (4.12)$$

where $\bar{\sigma}_{0c}$ is the linear characteristic of the chemical reaction zone in the turbulent front, σ_{0l} is the characteristic width scale of the chemical-reaction zone in the laminar front, $\bar{a}$ is the average number of reaction zones (fronts) intersecting the x axis, and σ_{0T} is the integral scale of the turbulent heat-release zone.

We note that for a laminar flame front, Equation (4.9) can be reduced to the familiar Zel'dovich-Frank-Kamenetskiy equation by the simple substitution

$$T = \bar{T}; \quad u = \bar{u} = u_\tau \frac{T}{T_1} \quad \text{and} \quad \Phi = \bar{\Phi}.$$

Let us now consider the physical significance invested in the function $p(T, x)$ in the case of turbulent combustion.

The formation of a one-dimensional combustion zone can be divided arbitrarily into three stages. The first few moments of initial stage of combustion-zone formation proceed in the same way as in a laminar stream, since, according to the Taylor equation, the eddy diffusivity equals zero.

Curvature (deformation) and broadening of the isothermal planes (combustion fronts) by the smallest vortices begins after a certain time. This occurs earlier, the smaller the internal turbulence scale η (the Kolmogorov scale), i.e., the larger the Re of the stream. For large Re, it intervenes practically immediately at the ignition source. The curvature (deformation) and broadening of the combustion front in the xOy plane are recorded formally as an increase in the average integral heat release in the direction of the x axis or, which is the same thing, in the scale $\bar{\sigma}_{0T}$. Here it is not possible in principle to distinguish whether the increase in the average integral of the heat-release rate is due to broadening of the combustion front by vortices smaller than and comparable to the instantaneous width of the front or as a result of curvature of the combustion "surface" at an angle

to the y axis by vortices larger than the front width. For large Re, therefore, it is impossible in principle to draw a clear boundary between the effects of "microbulk" and "surface" increases in combustion rate in the initial and subsequent (intermediate) stages. With time, larger and larger vortices come into action. Large vortices not only curve the "combustion surface" but also transport its elements bodily in either direction from its average position. For developed turbulence (Re $\geq 10^5$), the following rule is, on the average, observed: the larger the scale of the vortex, the larger will be its contribution to the turbulent transport of "surface" combustion, and the smaller its contribution to the deformation and broadening of this surface.

We note that the very concept of the "surface" is purely conventional: the Gouy-Mikhel'son principle is not satisfied on it, and it is not possible to define uniquely the exact boundaries of the surface or a combustion rate normal to this surface that is constant over its area.

The intermediate stage in development of the one-dimensional combustion zone is characterized by the uniqueness of the combustion surface: the x axis crosses the combustion front (more precisely, the layer of high heat-release probability) once on the average: a = 1. Strictly speaking, this stage lasts for a time on the order of l_L/u'. In high-velocity streams, this time is expressed in terms of distance from the ignition source: $x_0 = l_L\bar{u}/u'$. This distance is at least 50 — 100 mm for chambers with diameters d_c = 200 — 400 mm.

For the final stage, a more confused form of the combustion "surface" is, in principle, possible: the x axis may cross the surface more than once (three times, five times, etc.), although the surface will remain singly connected. The integral of the instantaneous heat release function with respect to x may be much larger on such cross sections than on single-valued cross sections. If we disregard the effect of "thinning" of the front on areas where large vortices stretch the combustion "surface" rapidly, the instantaneous contributions of these areas will be proportional to the instantaneous

combustion-surface area. If, on the other hand, we assume that $u_I \approx 0$ on the most severely stretched areas, we can neglect the correlation $\overline{a'\sigma'_{0C}}$. In this case, $u_T = \bar{a}\overline{\sigma_{0C}}/\sigma_{0L} = \bar{a}\bar{u}_{n} \cdot t/u_n$, where $u_{n \cdot t}$ is the average rate of microturbulent combustion along the ox axis for a single combustion front. The statistical average contribution of multiple intersections to the heat-release integral (when a = 3, 5, 7, etc.) will be more appreciable, the higher the probability of encountering such intersections.

The stages in the development of the one-dimensional combustion zone are clearly evident in the qualitative changes in the statistical distribution of the random variables T and Φ. This distribution can be plotted by examining an "oscillogram" of the particular variable change along the one-dimensional zone (along the y or z axis) [14].

In principle, the three stages in the development of the one-dimensional combustion zone embrace all possible cases of combustion. If the turbulence is such that all of its scales are comparable and smaller than the width of the laminar flame front, the process will not go beyond the initial stage of development: the front will pass through the vortex before the latter has time to cause a substantial deflection of the front surface from the average plane. If the Re of the stream is small (near critical), the turbulence microstructure is not developed, and the average turbulent scale is much larger than the width of the laminar front, combustion will proceed during the first stage by the "surface" mechanism in the treatment of K. I. Shchelkin [86]. The process will then remain in the second stage for a long time if u' $\ll u_n$ and develop rapidly to the third stage if u' $\gg u_n$ and the decay time of the individual vortex is comparable to or longer than the time of passage of the front through the vortex. Here the value of u_T should increase continuously with time from values on the order of u_n during the initial stage to values much larger than u_n.
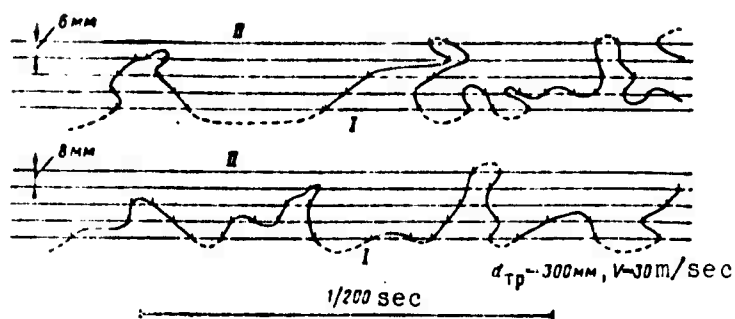
Figure 4.4. Instantaneous combustion surface.
I — burned-mixture zone; II — unburned-mixture zone (d_{pp} = 300 mm; V = 30 m/sec).

Experiment shows that for large Re (Re $\geq 10^5$), u_T becomes much larger than u_n even during the first stage, and thereafter remains constant at all flame-jet lengths that are of practical interest. This suggests that the main contribution to the heat-release integral comes, in the mean, from a single combustion layer. According to [88], the probability of finding triple intersections on the flame-jet lengths of practical interest does not exceed 0.1 — 0.2 ($\bar{a} \leq 1.2$ — 1.4) (Figure 4.4). The low probability of encountering a multivalued combustion surface can be explained by the finite lifetime of the vortices: as it turns, in the mean, through a quarter of a revolution, the vortex decays, transfering energy to smaller vortices and leaving the combustion surface single-valued in the mean.

Thus, analysis of experimental data indicate a dual nature for turbulent combustion. It proceeds by the "surface mechanism" to the extent that the main contribution to the combustion-zone width comes from large vortices $\left(P_s \simeq \frac{a_0 C}{a} \ll 1\right)$, and by the "microbulk mechanism" to the extent that small vortices make the main contribution to the turbulent combustion rate $u_T\left(\frac{a_0 C}{a_0 l} \gg 1\right)$.

The basic turbulence parameters determining the combustion rate u_T in the microbulk combustion model are the velocity scale v_0 of all vortices smaller than and comparable to the front width and the dissipation scale λ_0, defined as

$$\lambda_0 = \frac{v_0}{\overline{\left(\frac{\partial u}{\partial x}\right)^2}},$$

where

$$\overline{\left(\frac{\partial u}{\partial x}\right)^2}$$

is the mean square velocity gradient.

The local curvatures of the isotherms in a combustion microzone and the relative velocities of the micromoles are determined not by the velocity scale, but by the velocity gradient, and this is what is taken into account by introducing the second determining scale λ_0.

If Shchelkin's scheme is supplemented by taking account of local curvatures of the combustion surface due to microstructure vortices, it follows from geometrical or dimensional considerations that

$$\frac{u_T}{u_n} \sim \sqrt{1 + \frac{\sigma^2}{L_0^2} + \frac{v_0^2 \tau_\gamma^2}{\lambda_0^2}}. \tag{4.12a}$$

where $\tau_\gamma \sim \frac{\sigma_T}{u_T}$ is the characteristic combustion-time scale, σ_T is the characteristic width of the combustion front, $L_0 \sim l_E$ is the scale of the temperature inhomogeneity at the center of the combustion zone, l_E is the average dimension of the vortices (the integral Euler turbulence scale), and σ is the width scale of the combustion zone.

The behavior of the scale σ_T, determined from the width of the local instantaneous average-temperature profile, is quite complex, since it is determined by the sum of two scales: a scale of the "preheating-zone" type $\sigma_p \sim \frac{D_{\gamma} + v_0 l_0}{u_T}$ and the scale of the "combustion zone proper" $\sigma_{0c} \sim u_c$.

For the developed turbulence fine structure (for large u_T), in which case $\sigma_{\bullet c}$ becomes comparable with σ_p, the scale $\sigma_T \approx \sigma_p + \sigma_{\bullet c}$ will remain approximately constant as u_T increases.

In this case

$$u_T \sim \sqrt{\sigma_T \frac{v_0 u_0}{\lambda_0}}. \tag{4.12b}$$

In virtue of the relations

$$\lambda_0 \sim \frac{\sigma_0}{u'} \sqrt{\frac{\overline{\nu/\ell_E}}{\bar{a}}}; \quad u' \sim \bar{a}$$

known from local turbulence theory, we finally obtain

$$u_T \sim \frac{a^{0.75} \sigma_m^{0.5}}{\nu^{0.25} \ell_E^{0.25}}. \tag{4.12c}$$

In all intermediate cases, in which $\bar{a}$ is of substantial importance, it can, if necessary, be expressed in terms of the average number of revolutions of the vortex during the time in which it passes through the combustion zone and in terms of the average number of macrostructure vortices per unit of the average combustion-surface area. But then $\sigma_{\bullet c}$, which may be much smaller than σ_l in the case of a large and fast increase in combustion surface area and in the absence of microstructure vortices, still remains unknown. Also unknown is the correlation $\overline{a' \sigma'_{\bullet c}}$.

However, there is another, more convenient practical approach to determination of u_T when the macro- and microstructures are of equal importance or when the dominant influence on u_T remains with the macrostructure of the turbulence. In this case, there is no particular practical point in separating the parameters a and $\sigma_{\bullet c}$ (in some cases, it may prove to be practically impossible). It is

much more convenient to use the initial integral scale $\sigma_0 T$, defined
by relation (4.12), and $\sigma_0 l$ for the laminar front. The analogous
scales $\sigma_{M.T}$ and σ_M were introduced in Chapter I for the case of
diffusion without combustion, and the coefficient of accelerated
molecular diffusion $D_{M.T}$ was defined in accordance with the relation[*]

$$\frac{\sigma_M + \sigma_{M.T}}{Y_M} = \sqrt{1 + \frac{D_{MT}(t)}{D_M}}, \tag{4.13}$$

where $D_{M.T} + D_M$ is the effective molecular-diffusion coefficient in
the turbulent stream.

The effects of the large-scale turbulence on the scales $\sigma_0 T$ and
$(\sigma_M + \sigma_{M.T})$ will be largely similar, accurate to the combustion-time
factor τ_x. The factor τ_x is a minor one in the development of the
combustion surface by large scale turbulence (in the statistics of
the scales σ_{0c} and $\sigma_0 T$) (§4, Chapter IV). Thus, applying the well-
known arguments of dimension theory for the turbulent flame just as
for the laminar flame, we may write

$$\sigma_0 \sim \sqrt{[D_M + D_{M.T}(\tau_x)]\tau_x} \quad \text{and} \quad \sigma_x \sim \sqrt{D_M \tau_x} \tag{4.14}$$

or

$$\frac{\sigma_0}{\sigma_x} = \sqrt{1 + \frac{D_{M.T}}{D_M}},$$

where $\tau_x = c_1 T_1 c_p / \psi_{max}$ is a dimensionless combustion-time parameter that
is the same in turbulent and laminar streams.

Substituting (4.13) into (4.12), we obtain a relation similar in
form to the familiar Damköhler-Shchelkin-Zel'dovich relation [86],
[96],

---

[*]In Chapter I, the integral width scale of the grey-mixing layer
was introduced for brevity:

$$\sigma_c^2 = \sigma_M^2 + \sigma_{M.T}^2$$

$$\frac{u_\tau}{u_\mu} \approx \sqrt{1 + \frac{D_{M.T}(\tau_x)}{D_\mu}}.$$

(4.15)

However, this expression does not contain the total turbulent transport coefficient D_T, but instead the coefficient of accelerated molecular diffusion $D_{M.T}$ as a function of τ_x — Formula (4.15) links u_T to the single turbulence parameter $D_{M.T}$, which can be determined experimentally (see Chapter III). By its derivation, Relation (4.15) would be valid always: for large- and small-scale turbulence and for large and small Reynolds numbers. However, its physically most legitimate application is to the case in which there is only a large-scale increase in combustion rate or to the case of sluggish (non-frontal) combustion, when the dominant factor in determination of the scale $\sigma_\theta T$ will be the turbulent factor expressed in terms of the parameter $D_{M.T}$, and not the kinetic factor defined by τ_x, so that the influence of the factor τ_x on the form of the function $D_{M.T}$ can be neglected.

We note that in the general case, the parameter $D_{M.T}(\tau_x)$ is a function of the combustion time τ_x. This means that combustion may become stationary before the value of $D_{M.T}(t)$ becomes constant in the turbulent diffusion process. In other words, in the process of turbulent diffusion without combustion, $D_{M.T}(t)$ is determined with time by all vortices of the stream, while $D_{M.T}(\tau_x)$ and u_T are determined by the small-scale part of the turbulence, the part whose scale is comparable to the average width σ_T of the single combustion front.

An analysis of experimental data on u_T will be found in [14], which gives a summary of numerous experimental results on the rate of turbulent combustion and proposes the following approximate empirical formula as suitable for lean mixtures:

$$u_\tau \sim A u^{0.7} u_\mu^{0.3} \quad (A \approx 0.7 - 1).$$

§4. Parameters of the Turbulent Flame Jet

It follows from the discussion of the preceding section that it is always possible to distinguish two linear scales for a one-dimensional zone of homogeneous combustion: The average width of the entire turbulent combustion zone — the scale σ which determines the average peak-to-peak amplitude of the oscillations of the instantaneous combustion layers (fronts) — and the scale σ_0,[*] the resultant average width of the combustion front. The scale σ_0 can be understood as the integral scale over the depth of the one-dimensional zone, the scale occupied by the characteristic temperature range, in which practically all of the heat release is concentrated.

In the present treatment, what is implicit in the scale σ_0 — several laminar fronts or a single broadened (by the microstructure) turbulent front — is immaterial.

In virtue of the known experimental fact that the rate of turbulent combustion is stationary (for times larger than σ_0/u_T, given homogeneous turbulence), the scale σ_0 will also be stationary.

Let us now consider the scale σ in greater detail. It is now a well-known experimental fact that the width of the turbulent combustion zone is nonstationary.

Let us show that the zone width will, in principle, always be a nonstationary quantity, even the extreme case $u_T \gg u'$, provided, of course, that $l_E > \sigma_0$.

---

[*]We omit the second subscript "T" for brevity.

We define the zone scale σ quantitatively as the root-mean-square deviation of an element of the "surface" from its average position.[*] An equation analogous to the Taylor equation (see Chapter I) is easily derived for the dispersion σ^2:

$$\frac{1}{2} \frac{d\bar{\sigma}^2}{dt} = \int_0^t \overline{u(t)u(t')} \, dt, \qquad (4.16)$$

where u(t) is the velocity of an element of the combustion surface relative to its average position.

If necessary, the correlation function under the integral sign in (4.16) can be linked to the Euler and Lagrange correlation functions by various hypotheses [100], [97]. However, only the extreme case mentioned above is of interest for estimation of the least of the possible values of σ.

If the time $\sim l_E/u_T$ of passage of the combustion surface through the vortex is small enough, the turbulent velocity field will undergo practically no change during this time, so that Equation (4.16) can be written approximately:

$$\frac{1}{2} \frac{\overline{d\sigma^2}}{dt} = \overline{u^2}(0)t \quad \text{for} \quad t < l_E/u_T, \qquad (4.17)$$

and

$$\frac{1}{2} \frac{d\sigma^2}{dt} \approx \frac{\overline{u^2}(0)l_E}{u_T} \approx \frac{2D_T \sqrt{\overline{u^2(0)}}}{u_T} \quad \text{for} \quad t \geqslant l_E/u_T. \qquad (4.18)$$

After integration of (4.18), we obtain $\bar{\sigma}^2 \approx A \frac{D_T u'}{u_T} t$ (we set u' = $= \sqrt{\overline{u^2(0)}}$ and $l_E \approx 2l_L$ in accordance with Taylor and Townsend.

_____

[*]This definition is understandable for the particular case $u_T \gg u'$, when the combustion surface is definitely single-valued. In the general case of a multivalued surface, the scale σ can be given a more general definition: the scale σ is the root-mean-square deviation (in a given direction) of a volume element of the gas in the zone, including those volumes containing elements of the combustion "surface."

According to our estimate, the coefficient of l_L is even larger in technical pipes. The relationships obtained indicate the following:

1. No matter how large the ratio u_T/u', the zone width will always be nonstationary.

2. For values of $u_T \leq 2u'$, the turbulent combustion zone will expand in practically the same way as the turbulent mixing zone.

In high-velocity streams at ordinary turbulent-intensity levels ($\sim 5 - 20\%$), the value of u_T (if correctly measured) never exceeds $2u'$ (for hydrocarbon-air mixtures), so that the effect of the zone motion at the average velocity u_T with respect to the fresh mixture can be neglected, and we may assume that the expansion of the zone proceeds in the same way as in the turbulent diffusion of two neutral gases — a "cold" one and a "hot" one.

At the initial point in time, the turbulent velocity field is continuous and uniform throughout the entire space, while the fluctuation-velocity field induced by the motion of the combustion "surface" (self-turbulence) is obviously zero.*

Initially, therefore, the zone will diffuse with the diffusion coefficient D_T of the fresh mixture, which is assigned for time zero. For rapid burning, this value D_T will be quite adequate for calculation of the temperature fields (this is confirmed by experiment), since the jet will meet an oncoming jet or the wall of the pipe before the zone width has become large enough to influence D_T. In the case of flame-jet propagation in an unbounded space, the extent of the

---

*Even if it is assumed that the turbulent velocity field has a discontinuity on the initial interface, the value of D_T in (4.16) corresponds to the fresh-mixture turbulent velocity field because the deviations of the combustion surface elements from their average positions are registered through the turbulent displacements of the fresh mixture.
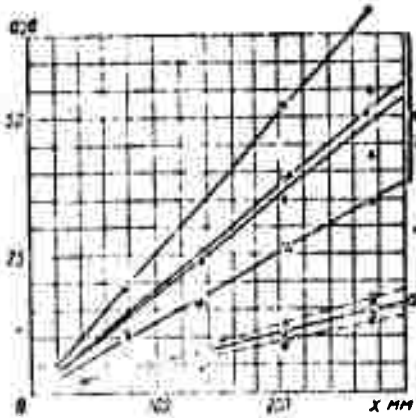
Figure 4.5. Distribution of average a(x) and dispersion σ of jet behind "point" burner.

According to Vlasov at V = 45 m/sec: Δ — α = 1.1; ▲ — α = 0.9.

According to A. I. Lushpa at V = 28 m/sec: • — α = 1.3; O — α = 1.1; ⊕ — α = 0.9.

combustion zone may become so large that it is necessary to take account of the variation of D_T over the depth of the zone: firstly because of the possible spatial inhomogeneity of the turbulence of the free stream of fresh mixture and, secondly, because of the possible secondary velocity fluctuations induced in the combustion zone by a strongly curved combustion surface (self-turbulence). In the general case, therefore, D_T must be regarded as a continuous function of the space coordinates, and the possible anisotropy of the turbulence must be taken into account by considering the matrix of values of D_{ij}.

But in the overwhelming majority of cases of combustion in high-velocity streams, the problem reduces within the existing chamber lengths (observation times) to one of turbulent transport in one direction (across the main stream), and experience and analysis of Relation (4.16) indicate that it is practically fully determined by the transverse component of the turbulent transport coefficient D_T of the free stream (with consideration of its inhomogeneity along and across the stream).

Let us consider examples that confirm these conclusions experimentally. Figures 4.3 and 4.5 show the average boundaries and the scale σ of the jet behind a "point" burner in an open stream, as calculated from the velocity-head fields (data of A. I. Lushpa [38] and K. P. Vlasov [14]). We see that the average boundaries vary with the velocity and composition of the mixture and that the scale σ does not depend on the velocity and composition of the mixture. According to Lushpa's data, which were obtained with a thermoanemometer, the

turbulent intensity of the cold stream in the region of the jet was $u'100/v = 1 - 2\%$. The values calculated from (4.17) fall into the same range. Lushpa's results indicate that σ is a purely fluid-dynamic parameter that does not depend on the combustion parameter u_T and is determined solely by the turbulence parameters of the free stream, even at values of $u_T \sim u_n$, much larger than $2u'$.

Vlasov's results were obtained in the stream behind a turbulence-generating grid with a turbulent intensity of ~5% [the same value is obtained by calculation from $\sigma(x)$]. Comparison of the function $\overline{Y}^2$ measured behind such a grid (the cold-stream dispersion) with the function σ^2 indicates that they are the same within the limits of measurement error. Vlasov processed data on the zone-width scale δ_T that he had obtained with an ion detector. The data are less accurate because of the measurement method, but they are interesting in that they cover a much wider range of velocities, mixture compositions, distances from the burner, and pipe diameters. In all cases, a stream with the natural pipe-turbulence level flowed onto the jet (see Chapter III):

$$\frac{u' \cdot 100}{\overline{u}} \approx 5\%; \quad \frac{D_\tau}{\overline{u} d_{\tau p}} \approx 0{,}001.$$

Using the approximate relation that prevails between the scales δ_T and σ [14],

$$\delta_\tau \approx 4{,}6\,\sigma,$$

we can plot all data in dimensionless coordinates on the same diagram, which is in practically full agreement with the dimensionless function $\overline{Y}^2$ for pipe turbulence (Figure 4.6), i.e., the scale σ is fully determined by the free stream turbulence at all jet lengths of practical interest.
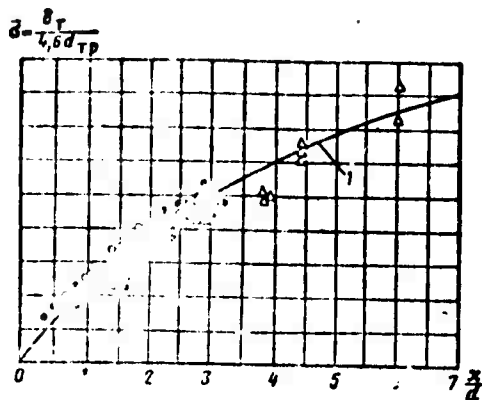
Figure 4.6. Width of combustion zone as a function of distance to ignition source (according to Vlasov):

$1 - \sqrt{\frac{u'}{a'}}$ -calculation;

$\circ -$ for d_{pp-} 150 мм; | $V - 35 - 50$ m/sec
$\bullet -$ for d_{pp-} 220 мм; | $\cdot - 0.5 - 1.5$;
$\triangle -$ for d_{pp-} 150 мм; $V - 35 - 75$ m/sec;
$\cdot - 0.6 - 1.3$

Let us briefly summarize the physical conceptions set forth above, with emphasis on the fundamental departures of these conceptions from the early ones of K. I. Shchelkin [86] and the later concepts of Karlovitz, Scurlock, Wohl, and others [97], [98], [99], [100].

Turbulent homogeneous combustion in jet engine combustion chambers is primarily a process of turbulent (mechanical) mixing of volumes of fresh mixture and combustion products, followed by combustion. The turbulent aspect of the process dominates over the kinetic aspect, and is the controlling factor in the development of combustion-zone width. K. I. Shchelkin [86], [89] originally assumed that the kinetic side of the process and the diffusion (turbulent) side were at equilibrium. This made the width σ of the turbulent combustion zone a stationary quantity determined by the equality between the time of turbulent motion of a mole and the existence (combustion) time of a fresh mole expelled into the burned mixture by the turbulent motion:

$$\frac{\sigma}{u'} \approx \frac{L_0}{a_n}. \tag{4.19}$$

The notions originally developed by K. I. Shchelkin are, as we noted in §3, applicable to a certain extent to the process unfolding in a combustion microzone.

To some extent, the notions set forth above are consistent with those of Scurlock, Wohl, Grover, Karlovitz, and others, but there are also fundamental differences. Scurlock and Wohl begin with a concrete, arbitrary scheme of a combustion surface that has a normal combustion rate u_n constant over its area, and offer, on the premises of this scheme, a complete list of all a priori conceivable effects determining the width and the average velocity of the turbulent combustion zone. As a result, the "accuracy" of their quantitative estimates for all effects is unjustified, and is seriously objectionable with respect to a number of questions (allowance for self-turbulence, mechanical addition of all transport effects, etc.). Their analysis produces a mass of transport effects, all of which are found to be equivalent, and this is not true. Experience has shown that a single effect is decisive: the turbulent diffusion, which is determined by the free-stream turbulence.

It appears that the basic physical error of these authors consists in the following. The velocity of the combustion "surface" element with respect to the fresh mixture is not assigned as u_n, but is obtained as a result of turbulent diffusion: it may be much smaller than u_n at some points and much larger than u_n at others. For developed turbulence microstructure, it makes no practical sense whatever to speak of any definite combustion surface element with a definite velocity value such as u_n. As a result, the mathematically quite precise reasoning of the authors, which was based on inoperative physical conceptions, led to results without practical justification.

With consideration of the nonstationary nature of the turbulent combustion zone, how can the combustion rate (Figure 4.7) be measured correctly? Obviously, this question does not arise for a stationary zone: in this case, beginning at the time at which the scales σ_0 and σ of the combustion zone become stationary, the velocities of all statistically averaged isotherms will be the same and equal to the rate of turbulent combustion.
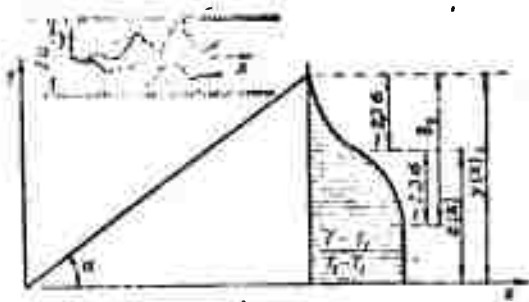
Figure 4.7. Illustrating
determination of velocity of
turbulent flame propagation
u_T and the width of the
combustion zone.

$$\bar{u}_r \left(u_t' + V \sin \alpha \right)$$

In the case of a nonstationary
zone, each isotherm has its own
velocity, and the question arises
as to the isotherm whose velocity
must be used as the turbulent
combustion rate? The rate of
turbulent (laminar) combustion
is the statistical-average volume
of fresh mixture burned per unit
time per unit area of the average
position of the combustion surface.[*]
This last reservation is immaterial
for a laminar front, since the
average and instantaneous positions
of the combustion front coincide.

In a turbulent combustion zone, the "combustion surface" has a statis-
tical-average (mean) position and a probability distribution of
instantaneous combustion-front positions (with dispersion σ^2) about
the mean. Here there exist two characteristic rates: the grow. ate
of the mean and the rate of increase of the zone-width scale σ. It
is the latter's rate of increase that corresponds directly, by defini-
tion, to the rate of turbulent combustion. In practice, to find the
mean position at time t, it is necessary to think of all of the mix-
ture that has been burned by this time as being collected at the
boundaries stated ty the initial conditions: if the initial boundary
was a plane, on one side of a plane parallel to the initial plane; if
the initial boundary was a sphere (point), on one side of a sphere
equidistant from the initial sphere, etc.

The rate of increase of the characteristic dimension (the normal
for a plane, the radius for a sphere, etc.) of the mean surface
determines at once the rate of decrease of the volume of fresh mixture
(in the coordinates of the fresh mixture at rest) referred to the

---

[*]In virtue of Relation (4.10), this definition is identical to
the following: the rate of turbulent combustion is the average
velocity (at infinity) of the fresh mixture flowing into a turbulent
combustion zone that is, in the mean, immobile.

entire mean combustion surface at time t, i.e., it is, by definition, the rate of turbulent combustion. A rather simple mathematical expression can be given for this practical operation if a Gaussian probability distribution is assumed for the turbulent displacements of the volumes in the turbulent combustion zone. This assumption is, first of all, confirmed by experiment. From this it follows directly that for a one-dimensional combustion zone, the turbulent combustion rate is determined by the velocity of motion of the isotherm at which the physical combustion efficiency equals 0.5. The one-dimensional combustion zone is the only case in which the mean surface is determined quite rigorously by the isotherm with 0.5 combustion efficiency. In other cases, the mean surface is determined rigorously by integration over the entire temperature profile with consideration of the variation of the average mixing-stream velocity in the submerged jet, etc. (see §5).

In a one-dimensional mixing zone, the "0.5 isotherm" moves at zero velocity. All other isotherms will move with different velocities relative to this isotherm, although there is no motion in the mean. The farther an isotherm has advanced into the fresh mixture from the "0.5 isotherm," the higher will be the rate at which it is displaced against the fresh mixture. An isotherm whose distance from the "0.5 istherm" equals the scale σ will move initially at a velocity u'; an isotherm removed by two scales σ will move at velocity 2u', and so forth ad infinitum, and with greater accuracy the closer the conformity of the outer branches of the true turbulent-velocity distribution curve to the Gaussian distribution.

Experimental research employs a method in which the combustion rate is measured at the "extreme" boundaries of the turbulent jet, and which reduces essentially to measurement of the velocity of some "extreme" isotherm. In measuring the turbulent combustion rate on "extreme" isotherms, experimenters often produce practically complete distortions of the essential physical picture of the process being studied.

For example, if we measure the true value of u_T according to A. I. Lushpa's data, we can easily satisfy ourselves that u_T is in fact close to u_p and independent of u' in the range of practical operating conditions (see Figure 4.3). If, on the other hand, the combustion rate is measured for the "extreme boundaries of the jet," thereby adding the large value $\sim 3u'$ to the constant, relatively small value of $u_T \approx u_n$, we arrive at the conclusion of direct proportionality between the combustion rate and the turbulence velocity u'. For distinction from the value of u_T, we shall call the velocity determined from the extreme isotherm the turbulent-flame propagation velocity and denote it by u'_T.

While admitting the possible coexistence of different concepts — the rate of turbulent-flame propagation u'_T and the rate of turbulent combustion u_T — in engineering research practice and engineering estimates of jet-engine, combustion chamber lengths, we must bear the following in mind: the propagation velocity u'_T formally incorporates a physico-chemical parameter — the turbulent combustion rate u_T — and a purely fluid-dynamic parameter — the rate of expansion of the turbulent combustion zone.

Here the magnitude and properties of the propagation velocity are determined basically by the magnitude and properties of the zone expansion rate, including the numerous methodological errors associated with the various methods of measuring it (thermocouple, air-pressure tube, ion detector, photography).

The turbulent combustion rate u_T is usually a small fraction of the turbulent propagation rate u'_T. The possibility cannot be excluded that it may be smaller than u_n under predetachment conditions (with respect to mixture composition or pressure). The turbulent velocity of the free stream is found to be more than adequate to account for the measured values of u_T with the aid of relation of the form (4.12)

without involking self-turbulization concepts. We recall that self-turbulence does not appreciably influence the rate of turbulent expansion of the zone, i.e., even from this standpoint, we should also expect independence for the average velocity of the zone motion.

§5. Equations of Continuity and Diffusion for the "Surface" Model of Turbulent Combustion

Since the combustion zone width σ increases in time, while the combustion front width σ_0 remains practically constant, the value of σ comes to be much larger than σ_0 beginning at a certain point in time ($>\sigma_0/u'$). In this case, the probability of appearance of intermediate values can be neglected with very little error in determining the distribution of the average parameters in the turbulent combustion zone, and the average parameters can be written in the following form under the hypotheses of the "black and white" mixing model (Chapter I):

$$\bar{T}=T_1 P_1' + T_2 P_2; \quad \bar{u} = \bar{u}_1 P_1 + \bar{u}_2 P_2$$

or, since $P_1 + P_2 = 1$:

$$\frac{\bar{T}-T_1}{T_2-T_1} = \frac{\bar{u}-\bar{u}_1}{\bar{u}_2-\bar{u}_1} = P_2 \qquad (4.20)$$

and

$$\bar{T}'^2 = (T_1-\bar{T})^2 P_1 + (T_2-\bar{T})^2 P_2 = (T_2-T_1)^2 P_1 P_2,$$

while

$$\overline{T'u'} = (T_2-T_1)(\bar{u}_2-\bar{u}_1) P_1 P_2,$$

where P_1 and P_2 are the probabilities of appearance of the volume of fresh (burned) mixture. Physically, P_2 is nothing other than the physical combustion efficiency at the particular point of the combustion chamber; T_1 is the temperature of the fresh mixture, and $T_2 = \eta_{chem} T_{max}$ is the temperature of the combustion products.

The combustion product temperature T_2 can be regarded as the product of the maximum adiabatic temperature of the burned mixture by the chemical combustion efficiency η_{chem}. As we know, the temperature behind the front does not immediately reach its limiting value, even in a laminar flame front, and for several reasons.

The chemical efficiency $\eta_{chem}(x)$ varies weakly along a turbulent flame jet. For real homogeneous flame jet lengths and stream velocities, its values vary from 0.85 at the beginning of the jet to 0.98 at the end of the jet under atmospheric pressure [14].

Thus, the problem of computing average temperatures in the zone of turbulent combustion reduces to determination of the probability of appearance of "cold" or "hot" volumes of mixture at a particular point in the zone.

The system of averaged fluid dynamics equations (see §2) for the surface model of turbulent combustion in a high velocity stream is written in the form

$$\frac{\partial \bar{\varrho}}{\partial t} + \frac{\partial \overline{\varrho u_i}}{\partial x_i} = 0; \tag{4.21}$$

$$\frac{\partial \bar{u}_i}{\partial x_i} = \bar{F}. \tag{4.22}$$

The influence of viscosity is manifested only in the flame front (in the shock), so that the velocity term has been discarded in (4.22). Let us expand the terms of Equations (4.21) and (4.22). Using Relation (4.20), and the Prandtl hypothesis, to determine the turbulent diffusion of mass flux, we obtain

$$\overline{\varrho u_i} = \bar{\varrho} \bar{u}_i - (\varrho_1 - \varrho_2)(\bar{u}_{2i} - \bar{u}_{1i}) P_1 P_2 - D_t \frac{\partial \bar{\varrho}}{\partial x_i}. \tag{4.23}$$

where $D_1 = \frac{1}{2}\frac{d\sigma^2}{dt}$ is the eddy diffusivity and $\bar{u}_{11}$ and $\bar{u}_{12}$ are the average velocity components after sample averaging only over the fresh mixture or only over the combustion products.

During mixing without combustion, these components have no discontinuity on the instantaneous interface between the two media, so that we may write

$$\overline{\varrho u_i} = \bar{u}_i \bar{\varrho} - D_1 \frac{\partial\bar{\varrho}}{\partial x_i}. \tag{4.24}$$

The physical significance of the parameter $D_1 = \frac{1}{2}\frac{d\sigma^2}{dt}$ was described in §4 for the case of a one-dimensional turbulent combustion zone. As we showed in §4, the dispersion σ^2 of turbulent mixing of the combustion front is determined by the dispersion of the turbulent displacements of cold volumes of the free stream.

The system of equations (4.21) and (4.22) is equivalent to the system

$$\frac{\partial P_1}{\partial t} + \bar{u}_{i1}\frac{\partial P_1}{\partial x_i} = D_1\frac{\partial^2 P_1}{\partial x_i^2} + \frac{dV_1}{S\,dt}P_s; \tag{4.25}$$

$$\frac{\partial P_2}{\partial t} + \bar{u}_{i2}\frac{\partial P_2}{\partial x_i} = D_1\frac{\partial^2 P_2}{\partial x_i^2} - \frac{\varrho_1 dV_1}{\varrho_2 S\,dt}P_s, \tag{4.26}$$

where $\frac{dV_1}{S\,dt} = -u_1$ is the rate of decrease of the volume V_1 of fresh mixture on a unit of the average combustion surface S (the rate of turbulent combustion) and p_S is the probability distribution density of the appearance of a combustion surface at the particular point.

The last terms in Equations (4.25) and (4.26) have been written only for a single ignition source (a single flame jet). The two equations constitute the mathematical formulation of the law of conservation of ensembles of "cold" and "hot" volumes with consideration

of the source (sink), turbulent diffusion, and the discontinuous nature
of the sample-averaged velocities, which represent a generalization
of the Fokker-Planck-Kolmogorov equation of the theory of stochastic
processes (see Chapter I).

We have introduced the term "sampled averaging" in which averaging
over time at an arbitrary space point is done selectively: only on
those time segments during which only fresh mixtures or only combustion
products are present at the particular point in space.   The ordinary
equations of fluid dynamics for an isothermal incompressible gas are
satisfied at these times.   In particular, the sample-averaged continu-
ity equations take the form

$$\frac{\partial \overline{u}_{1n}}{\partial x_l} = 0; \quad \frac{\partial \overline{u}_{2n}}{\partial x_l} = 0. \tag{4.27}$$

The equation of energy conservation (4.22) yields the same
relations after sampled averaging, since

$$\overline{F}_1 = \overline{F}_2 = 0.$$

Let us demonstrate the identity of the systems (4.21); (4.22) and
(4.25); (4.26).   Multiplying the first equation of (4.25); (4.26) by
ρ_1 and the second by ρ_2 and adding the two equations, we obtain the
continuity equation (4.21) with the aid of Relations (4.27).   If we
simply add Equations (4.25) and (4.26), we obtain the energy conserva-
tion equation (4.22) with the aid of Relations (4.20):

$$\frac{\partial \overline{u}_l}{\partial x_l} = (n-1)u_l P_3,$$

where

$$(n-1)u_l P_s = \overline{F}; \quad n = \frac{T_2}{T_1} = \frac{\rho_1}{\rho_2}.$$

Solution of the System (4.25) and (4.26) is found to be more convenient for most cases than solution of the system of averaged equations of mass and energy conservation, (4.21) and (4.22).

Let us consider a number of elementary problems whose solutions can be obtained by analytical integration of the original equation System (4.21), (4.22) or (4.25) and (4.26).

§6. Distribution of Average and Fluctuation Parameters in the Turbulent Flame Jet

1. One-Dimensional Turbulent Combustion Zone

The average interface between the fresh mixture and the combustion products is immobile and taken as the coordinate plane yOz.

The initial equation system for the one-dimensional combustion zone is written

$$\frac{\partial \bar{\rho}}{\partial t} + \frac{\overline{\partial \rho u}}{\partial x} = 0, \quad \frac{\partial \bar{u}}{\partial x} = u_1 \left(\frac{T_2}{T_1} - 1 \right) P_s(x). \tag{4.28}$$

The average density is determined for the relation

$$\frac{\bar{\rho} - \rho_2}{\rho_1 - \rho_2} = P_1 = \int_x^{\infty} P_s(x - x_0) dx_0 = \int_{x - x_0}^{\infty} P_s(\xi) d\xi, \tag{4.29}$$

where $P_s(x - x_0)$ is the probability density distribution of displacement of the combustion surface from point x_0 to point x during time t.

From (4.29), we have $P_s(x) = -\frac{\partial P_1}{\partial x}$ (the point x_0 is taken as the coordinate origin). Substituting this value into the second equation of (4.28) and integrating the latter over x from $-\infty$ to x, we obtain the average velocity distribution:

$$\bar{u} = u_1 P_1 + \frac{T_2}{T_1} u_1 P_2. \tag{4.30}$$

It is seen from Equations (4.30) and (4.20) that the average velocity, sample-averaged only over fresh mixtures, yields the value of u_T, while that averaged over the burned mixture gives $u_T T_2/T_1$. Here we find that $\overline{\rho u}$ equals

$$\overline{\rho u} = \rho_1 u_T - D_\tau \frac{\partial \overline{\rho}}{\partial x}.$$

(4.31)

The continuity equation assumes the form

$$\frac{\partial \overline{\rho}}{\partial t} = D_\tau \frac{\partial^2 \overline{\rho}}{\partial x^2} \quad \text{or} \quad \frac{\partial \rho_1}{\partial t} = D_\tau \frac{\partial^2 \rho_1}{\partial x^2}.$$

Its solution yields the density (temperature) distribution through the depth of the zone:

$$\frac{\overline{\rho} - \rho_2}{\rho_1 - \rho_2} = \frac{T_2 - \overline{T}}{T_2 - T_1} = \frac{1}{2}\left[1 - \Phi\left(\frac{x}{\epsilon}\right)\right].$$

2.   Velocity Fluctuations in a One-Dimensional Turbulent Combustion Zone

In the turbulent combustion zone, we can distinguish the root-mean-square turbulent velocity obtained by sampled averaging over a fresh mixture only $\sqrt{\overline{u_1'^2}}$ and the corresponding velocity $\sqrt{\overline{u_2'^2}}$ for the combustion products. In the general case, these values may be different owing to the stepwise change in the fluctuation velocities on deformation of the stream in the flame front (on the instantaneous combustion surface) or continuous variation over the depth of the zone (for very large diffusion times).

In addition to this velocity, there is also the incremental turbulent velocity fluctuation profile that results from the appearance of fresh and burned mixture by turns at a particular point (each having various sample-averaged average velocities). In fact, the overall mean square of the velocity fluctuations for the surface model of combustion can be written (provided that $\overline{u_1'^2}$, $\overline{u_2'^2}$ are constant through the depth of the zone) in the form

$$\bar{u}_i^{''} = \bar{u}_i^2 - (\bar{u})_i^2 = \bar{u}_{1i}^2 P_1 + \bar{u}_{2i}^2 P_2 - (\bar{u}_{1i} P_{2i} + \bar{u}_{2i} P_2)^2 =$$
$$= \bar{u}_{1i}^{''} P_1 + \bar{u}_{2i}^{''} P_2 + (\bar{u}_{2i} - \bar{u}_{1i})^2 P_1 P_2. \qquad (4.32)$$

or, for a one-dimensional zone, if $\bar{u}_1' = \bar{u}_2'$, in the form

$$\bar{u}^{''2} = \bar{u}_1^{''2} + u_1^2 (n-1)^2 P_1 P_2. \qquad (4.33)$$

Thus, even if the free-stream turbulent velocity field is homogeneous and isotropic, the fluctuation velocity field will be inhomogeneous and anisotropic over the depth of the zone. The same relation can be obtained from the equations of fluid dynamics. Multiplying the equation of energy conservation by the velocity component u_j and averaging, we obtain

$$\overline{u_j \frac{\partial u_i}{\partial x_i}} = \overline{F u_j}.$$

Here, assuming satisfaction of the conditions

$$\overline{u_2 \frac{\partial u_1}{\partial x_1}} = \overline{u_3 \frac{\partial u_1}{\partial x_1}} = 0; \quad \overline{F u_2} = \overline{F u_3} = 0,$$

we obtain for the one-dimensional zone

$$\frac{1}{2} \frac{\partial \overline{u^2}}{\partial x} = \overline{F u} \qquad (4.34)$$

(the unnecessary subscripts are omitted). Let us find the expanded form of the correlation moment $\overline{Fu}$. Since the random function F has zero values everywhere except on the interface, we have

$$\overline{Fu} = \overline{F}_s \cdot \bar{u}_s = u_1 (n-1) \left(\frac{\bar{u}_1 + \bar{u}_2}{2} \right) p_S(x) = \frac{u_1^2 (n^2 - 1)}{2} p_S(x),$$

where $\bar{u}_s = \frac{\bar{u}_1 + \bar{u}_2}{2} = \frac{u_1(n+1)}{2}$ is the average velocity at the point of discontinuity.

Substituting the expression obtained for the moment into (4.34) and integrating from $-\infty$ to x with the boundary condition and Relation (4.29) considered, we obtain

$$\bar{u}_2 - u_1^2 - \overline{u'^2}(-\infty) = u_1^2(n^2-1)P_2/P_1. \tag{4.35}$$

It is easily seen that Relations (4.32) and (4.35) are identical. Similar relationships can be studied for more complex cases.

Analysis of available experimental data for open turbulent flame jets on the basis of similar equations indicates that the fluctuation velocity distribution observed in this case is explained only by the effect: the variable sample-averaged average velocity of the stream in the combustion zone. Vortex deformation effects [39] are also observed due to the acceleration of the stream when there is a large longitudinal pressure gradient along the chamber.

3. Turbulent Flame Jet in an Open Stream

For a jet in an open stream, we may neglect diffusion along the stream and the variation of the longitudinal average velocity component (due to the absence of a static pressure drop along the stream).

Substituting the value of the average velocity along the jet $\bar{u}_1 = \bar{u}_2 = \bar{u} = $ const into the continuity equations (4.27), we obtain (with consideration of the boundary conditions $\bar{v}_1(0) = 0$ for a direct flame cone and $\bar{v}_2(0) = 0$ for an inverted plane-parallel flame cone) $\bar{v}_1 = 0$ or $\bar{v}_2 = 0$.

Equations (4.25) and (4.26) take the following form for the direct cone:

$$\bar{u}\frac{\partial P_1}{\partial x} = D_r\frac{\partial^2 P_1}{\partial y^2} - u_r p_S, \quad \frac{\partial \bar{v}}{\partial y} = u_r p_S(n-1) = u_r(n-1)\frac{\partial P_2}{\partial y}.$$

Substituting the value $p_S = -(\partial P_1/\partial y)$ into the first equation, we obtain

$$\bar{u}\,\frac{\partial P_1}{\partial x} - u_\tau \frac{\partial P_1}{\partial y} = D_\tau \frac{\partial^2 P_1}{\partial y^2}. \qquad (4.36)$$

Similarly for the inverted cone

$$\bar{u}\,\frac{\partial P_2}{\partial x} - n u_\tau \frac{\partial P_2}{\partial y} = D_\tau \frac{\partial^2 P_2}{\partial y^2},$$

$$\frac{\partial \bar{v}}{\partial y} = (n-1)u_\tau, \; p_S = -(n-1)u_\tau \frac{\partial P_2}{\partial y}. \qquad (4.37)$$

We note that the energy conservation equations have been written only for the upper half of the jet.

The general solution of Equations (4.36) and (4.37) takes the form

and

$$\left.\begin{aligned} P_1 &= \int_{y_1} p(y-y_0)\,dy_0 \\[2mm] P_2 &= \int_{y_2} p(y-y_0)\,dy_0 \end{aligned}\right\}. \qquad (4.38)$$

where $p(y - y_0)$ is the Gaussian probability distribution density for displacements of cold (hot) gas volumes and $y_1(x)$ is the average boundary of the jet, defined in the first case by the equation

$$y_1 = y_0 + \int_0^x \frac{u_\tau}{\bar{u}}\,dx,$$

and in the second by the equation

$$y_2 = y_0 + n \int_0^x \frac{u_\tau}{\bar{u}}\,dx.$$

Without their derivations, we cite the formulas for some of the most common cases of the turbulent jet in an open stream.

Turbulent jet behind a plane-parallel antechamber

$$P_2(x; y) = \frac{\bar{T} - T_1}{T_2 - T_1} = \frac{1}{2}\left[\Phi\left(\frac{y+a}{s}\right) - \Phi\left(\frac{y-a}{s}\right)\right],$$

(4.39)

where

$$a = \frac{T_2}{T_1}\int_0^x \frac{u_1(x)}{V}\,dx + a_0;$$

a_0 is the half-width of the antechamber (burner),

$$2a(x) = \int_{-\infty}^{\infty} P_2\,dy \quad \text{for} \quad a \geqslant 3s.$$

In particular, we obtain on the axis of the jet

$$P_2(x; a) = \Phi\left[\frac{a(x)}{s(x)}\right].$$

Turbulent jet behind an axisymmetric burner (inverted cone)

$$P_2(x; r) = \frac{\bar{T} - T_1}{T_2 - T_1} = \frac{1}{s^2}\int_0^a \exp\left(-\frac{r^2 + r_1^2}{2s^2}\right) I_0\left(i\frac{rr_1}{s^2}\right) r_1\,dr_1,$$

(4.40)

where I_0 is a zero-order Bessel function, $a = a_0 - \frac{T_2}{T_1}\int_0^x \frac{u_1}{u}\,dx$ is the average radius of the jet, and a_0 is the radius of the antechamber (burner):

$$a^2 = 2\int_0^{\infty} P_2 r\,dr.$$

In particular, on the jet axis

$$P_2(x; 0) = \left(1 - e^{-\frac{a^2}{2\sigma^2}} \right).$$ (4.40a)

Since $a - a_0 \sim x$ and $\sigma \sim \sqrt{x}$, the physical combustion efficiency on the jet axis decreases from unity at the burner exit cross section and then again tends to unity as $x \to \infty$.

Formulas (4.39) and (4.40) are valid for the case in which the temperature and velocity at which the hot gases leave the burner (antechamber) are near the corresponding values T_2 and $\bar{u}$ or when the initial dimensions of the burners are relatively small.

Turbulent flame jet behind a plane-parallel Bunsen burner

The boundary conditions are as follows: width of initial homogeneous-mixture stream $2a_0$, width of burners on margins of stream (at pipe exit cross section) $2b_0$, x axis coincident with stream axis:

$$P_2(x; y) = \frac{1}{2} \left\{ \Phi \left[\frac{y + (a_0 + b_2)}{\sigma} \right] - \Phi \left[\frac{y - (a_0 + b_2)}{\sigma} \right] + \right.$$
$$\left. + \Phi \left[\frac{y - (a_0 - b_1)}{\sigma} \right] - \Phi \left[\frac{y + (a_0 - b_1)}{\sigma} \right] \right\},$$ (4.41)

where

$$b_1 = b_0 + \int_0^x \frac{u_\tau}{\bar{u}} \, dx; \quad b_2 = b_0 + \left(\frac{T_2}{T_1} - 1 \right) \int_0^x \frac{u_\tau}{\bar{u}} \, dx;^*$$

$$2(b_1 + b_2) = \int_{-\infty}^{\infty} P_2 \, dy \quad \text{for} \quad b_1 \geqslant 3\sigma.$$

---

*Experience has shown that b_1 may increase somewhat more slowly at the end of the jet, with the result that b_2 will increase more rapidly, but in such a way that the increase of their sum remains at all times equal to

$$b_1 + b_2 = 2b_0 + \frac{T_2}{T_1} \int_0^x \frac{u_\tau}{\bar{u}} \, dx.$$

In this formula, the value of σ can be assumed variable over the entire volume of the jet with consideration of the spatial variations of eddy diffusivity and the variations of the average velocity. It can be assumed for most practical calculations that the entire jet is situated within the average velocity core, so that the longitudinal average velocity is constant and equal to the initial average velocity of the stream, but the turbulence parameters can by no means be assumed constant. Formula (4.41) admits of a number of simplifications in certain particular cases. For example, if the jets from the two burners are far enough apart, relation (4.41) will be written as follows in a coordinate system whose x axis coincides with the axis of one of the burners:

$$P_2(x; y) = \frac{1}{2}\left[\Phi\left(\frac{y+b_1}{\sigma}\right) + \Phi\left(\frac{b_2-y}{\sigma}\right)\right].$$

In one of the relatively simple but quite accurate methods of allowing for turbulence inhomogeneity, we may take in the first term the value of σ determined from the free stream turbulence parameters, and, in the second, the value σ ≈ 0.1 x determined from the average turbulence parameters in the zone of mixing of the submerged (hot) jet with the surrounding immobile space.

It follows from (4.41) that the variation of the physical combustion efficiency along the axis of the stream is determined by the relation (y = 0):

$$P_2(x; 0) = \Phi\left(\frac{a_0+b_2}{\sigma}\right) - \Phi\left(\frac{a_0-b_1}{\sigma}\right).$$

The combustion efficiency on the stream axis increases with distance from the burner exit until b_1 reaches the value a_0. The flame jets moving toward one another from the two burners meet, on the average, at this time, so that the combustion rate drops abruptly to zero (there is nothing to be burned). From this time on, the process will be basically one of diffusion, and the value of P_2 on the axis will begin to decrease as a result of diffusion of the jet into the

surrounding medium. Actually, there are a number of other physical factors operating in the final stage of combustion: the increase in chemical efficiency, joint appearances of combustion zones in the same volume, etc. If the original mixture contains an excess of fuel, a secondary effect, diffusion combustion (afterburning), will also be observed in the zone in which the combustion products mix with outside air.

Turbulent flame jet behind a Bunsen ring burner (without consideration of mixing with outside still air)

The relation for $P_1(x; r)$ inside the flame jet is similar to (4.40) for $P_2(x; r)$, but

$$a = a_0 - \int_0^x \frac{u_T}{u} \, dx$$

(a_0 is the radius of the igniting burner ring).

In particular, on the jet axis

$$P_1(x; 0) = e^{-\frac{a^2}{4s^2}}. \tag{4.42}$$

The relationships for determination of the combustion rate u_T from the experimental temperature profiles and the relations linking the values of u_T with the jet propagation velocity u_T' are given in [14].

§7. Turbulent Jet in a Pipe

Let us consider the case of a turbulent flame jet behind a linear ignition source placed in a plane-parallel pipe. A solution of this problem was given in the papers of Ya. B. Zel'dovich, Tsien, and Scurlock and later developed by A. V. Talantov, V. A. Khramtsov, and others [101], [102], [103], [104].

We note the fundamental difference between these solutions and that considered below. In the studies cited above, the real flame jet is replaced by a hypothetical surface of zero or finite thickness, in front of and behind which the authors use flowrate, momentum, and energy equations averaged over the cross section of the pipe. The resulting nonclosed equation system is closed by assigning the width of the combustion zone (or the combustion time), a combustion rate that satisfies Mikhel'son's law, and the law of average velocity (or average temperature) variation. The problem is to find the shape of the combustion "surface" (interface). Thus stated, the problem bears little resemblance to the real physical picture of combustion in a high-velocity turbulent stream. Even if such a surface existed at the initial point in time, it would be transformed at later times, by virtue of its inherent instability but chiefly under the action of the turbulent diffusion of the free stream, into a complex, confused combustion surface with a certain distribution of appearance probabilities at any point on the chamber cross section.

We place the coordinate origin in the source (see Figure 4.7), the x axis along the stream axis, the y axis perpendicular to it, and the z axis (along which all properties are assumed to homogeneous) along the linear source. We denote the pipe width by 2a, the average boundary of the upper half of the jet by $y_1(x)$, and the average boundary of the lower half of the jet by $y_2(x)$. In virtue of the axial symmetry, the absolute values of y_1 and y_2 are obviously equal. In the present problem, the following are assumed to be given: the average free stream velocity $u_1(0) = \bar{u}$, the coefficient of turbulent transport D_T of the free stream (constant over the pipe cross section), and the rate of turbulent combustion u_T. The value of u_T is uniquely defined by the microstructure of the free stream turbulence, irrespective of where combustion occurs (in the pipe or in the open stream) and regardless of whether the secondary turbulent velocity field induced by the flame is significant or not (see §6). It is more convenient to begin solution of the problem by solving the equations for the cold component of the stream, since the initial and boundary conditions are known for it. We shall neglect the variation of the

transverse average velocity component of the cold part of the stream, i.e., assume that $\bar{v}_1 = 0$ not only in the initial cross section and on the walls of the pipe, but also throughout the entire remainder of the cold part of the stream. At high stream turbulence velocities (velocities much higher than the average transverse velocity $\bar{v}_1$), this assumption is quite obvious. We note that the transverse component of average velocity in front of the flame front could also have been disregarded with no major error in the studies cited above, but there this component was to some extent supplanted by the transverse turbulence velocity, which was not taken into account.

Applying the condition $\bar{v}_1 = 0$, we obtain from the continuity equation (4.27), written with consideration of the density variation along the pipe,

$$\varrho_1(0)\,\bar{u}_1 = \varrho_1(x)\,\bar{u}(x). \tag{4.43}$$

We now neglect $\bar{v}_2$; this is a more serious simplification and yields sufficient accuracy only for large transverse turbulent velocities.

Then the equation for the cold volume appearance probability distribution density function can be written

$$\frac{\partial p_1}{\partial x} = \frac{D_T}{\bar{u}_1} \frac{\partial^2 p_1}{\partial y^2}. \tag{4.44}$$

The boundary condition at the wall is zero flow of cold volumes through the wall:

$$\left(\bar{v}_1 p_1 + D_T \frac{\partial p_1}{\partial y}\right)_{y=\pm a} = 0. \tag{4.45}$$

For the upper half of the flame, the solution of (4.44) with the boundary condition (4.45) takes the form

$$p_1(y,y) = \frac{1}{\sqrt{2\pi}\sigma}\left[e^{-\frac{1}{2}\frac{(y-y_0)^2}{\sigma^2}} + e^{-\frac{1}{2}\frac{(2a-y-y_0)^2}{\sigma^2}}\right] \tag{4.46}$$

and for the lower half of the jet

$$p_1(y_0, y) = \frac{1}{\sqrt{2\pi}\sigma} \left[e^{-\frac{1}{2}\frac{(y-y_0)^2}{\sigma^2}} + e^{-\frac{(2a+y+y_0)^2}{2\sigma^2}} \right]. \tag{4.47}$$

We note that, strictly speaking, the solutions are approximate: they take account only of the influence of the nearer wall, assuming that the effects of the opposite wall are practically negligible. The probabilities of finding fresh mixture and combustion products at an arbitrary point in the pipe are determined by the relation

and

$$\left. \begin{array}{l} P_1 = \int\limits_{-a}^{y_2} p_1 \, dy_0 + \int\limits_{y_1}^{a} p_1 \, dy_0 \\[2mm] P_2 = 1 - P_1 = \int\limits_{y_2}^{y_1} p_1 \, dy_0 \end{array} \right\}. \tag{4.48}$$

since $\int\limits_{-a}^{a} p_1 \, dy_0 = 1.$

Substituting the value of p_1 for the lower half of the flame into the first term of the function P_1, and the value of p_1 for the upper half of the flame into the second term, and recognizing that $y_2 = -y_1$, we obtain after various transformations

$$\left. \begin{array}{l} P_1 = \frac{1}{2} \Phi\left(\frac{y-y_1}{\sigma}\right) - \frac{1}{2} \Phi\left(\frac{y+y_1}{\sigma}\right) + \frac{1}{2} \Phi\left(\frac{2a-y-y_1}{\sigma}\right) + \\[2mm] \qquad + \frac{1}{2} \Phi\left(\frac{2a+y-y_1}{\sigma}\right), \\[3mm] P_2 = 1 - \frac{1}{2}\left[\Phi\left(\frac{y-y_1}{\sigma}\right) + \Phi\left(\frac{2a-y-y_1}{\sigma}\right) - \Phi\left(\frac{y+y_1}{\sigma}\right) + \\[2mm] \qquad + \Phi\left(\frac{2a+y-y_1}{\sigma}\right) \right]. \end{array} \right\}. \tag{4.49}$$

Plots of the function P_2 against x and y for the values

$$\frac{D_\tau}{2V_a} = 0.001 \quad \text{and} \quad \frac{u_\tau}{V_1} = 0.05$$
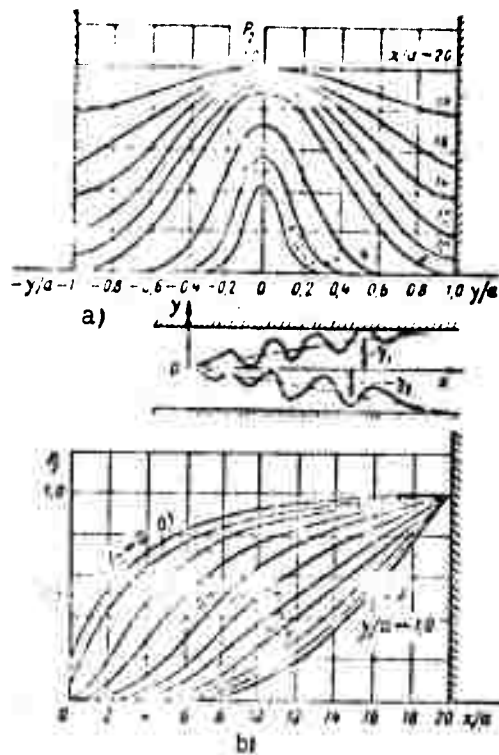
are given in Figure 4.8.

Figure 4.8. P_2 distribution of flame jet in plane-parallel pipe with $\frac{D_2}{2\bar{u}_1 a} = 0.001$; $u_\tau/\bar{u}_1 = 0.05$

The average boundary of the turbulent jet is determined by the relation

$$y_1(x) = \int_0^x \frac{u_\tau}{\bar{u}(x)} dx = \frac{1}{u_1} \int_0^x \frac{\varrho_1(x) u_\tau(x)}{\varrho_1(0)} dx. \quad (4.50)$$

According to (4.49), the value of y_1 is determined from the experimental average temperature profile by the equation

$$P_2(y_1) = 1 - \frac{1}{2}\left[\Phi\left(\frac{2a - 2y_1}{a}\right) - \Phi\left(\frac{2y_1}{a}\right) + \Phi\left(\frac{2a}{a}\right)\right].$$

A plot of this function for various values of

$$\frac{u_\tau}{u_1} \quad \text{and} \quad \frac{D_\tau}{u a} = 0.02$$

is given in Figure 4.9.

To determine $\bar{u}_2$ and $\bar{v}_2$, we use the energy conservation equation written in the form

$$-(\bar{u}_2 - \bar{n}_1)\frac{\partial p_1}{\partial x} - \bar{v}_2\frac{\partial p_1}{\partial y} - u_\tau(n-1)[p_1(y_1) + p_1(y_2)]. \quad (4.51)$$

Substituting the value of $\frac{\partial P_1}{\partial x}$ from (4.48) into this equation, we obtain after a number of transformations [14]

$$\left(\frac{\bar{u}_2}{u_1} - 1\right) = \frac{u_\tau(n-1)[p_1(y_1) + p_1(y_2)] - \bar{v}_2\frac{\partial p_1}{\partial y}}{u_\tau[p_1(y_1) + p_1(y_2)] - D_\tau\frac{\partial^2 p_1}{\partial y^2}}, \quad (4.52)$$
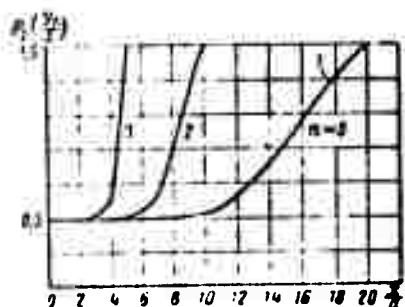
Figure 4.9. Illustrating experimental determination of average flame jet boundary $(D_T/u_1a = 0.002; \varrho_1/\varrho = 5)$:

$I - u_1/u_1 = 0.05, \ 2 - u_1/u_1 = 0.1, \ 3 - u_1/u_1 = 0.2$

where

$$n = \frac{\varrho_1(0)}{\varrho_2(0)} = \frac{\varrho_1(x)}{\varrho_2(x)};$$

$\bar{v}_2 = -\dfrac{\partial}{\partial x}\displaystyle\int_0^y \bar{u}_2\,dy$ according to the continuity equation (4.27).

Formula (4.52) can be expressed more simply on the jet axis (y = 0):

$$\frac{\bar{u}_2 - \bar{u}_1}{\bar{u}_1(n-1)} \tag{4.53}$$

$$\frac{2\left[1 + \exp\left(-\dfrac{2a(a-y_1)}{a^2}\right)\right]}{\left[1 + \exp\left(-\dfrac{2a(a-y_1)}{a^2}\right)\right] + \dfrac{2a}{y_1}\exp\left(-\dfrac{2a(a-y_1)}{a^2}\right)}.$$

In particular, as

$$y_1 \to 0 \quad \frac{\bar{u}_2 - \bar{u}_1}{\bar{u}_1(n-1)} \approx 0$$

and as

$$y_1 \to a \quad \frac{\bar{u}_2 - \bar{u}_1}{\bar{u}_1(n-1)} \to 1.$$

On the pipe wall (y = a), discarding the influence terms of the opposite half of the jet, we obtain

$$\frac{\bar{u}_2 - \bar{u}_1}{\bar{u}_1(n-1)} = \frac{2y_1}{a + y_1} \quad \text{as} \quad y_1 \to a \quad \frac{\bar{u}_2 - \bar{u}_1}{\bar{u}_1(n-1)} \to 1.$$

The profile of the velocity $\bar{u}_2$ can be calculated from Formula (4.52) by successive approximation. Putting $\bar{v}_2 = 0$ in (4.52), we find the $\bar{u}_2$ profile in the first approximation. Using the profile found for $\bar{u}_2$, we determine the first approximation of the profile $\bar{v}_2$ from the continuity equation and substitute it into (4.52), and so forth. For sufficiently large D_T, $\bar{v}_2$ practically vanishes, so that we may
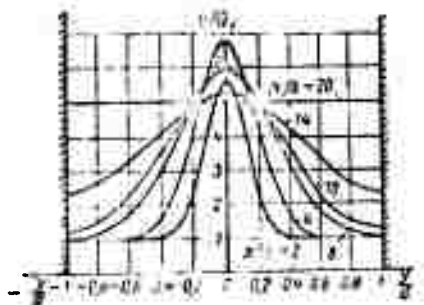
Figure 4.10. Distribution of average flame-jet velocities in pipe:

$D_{L,0}=0.0(8), u_T/u_1=0.05, n=5$

confine ourselves to the first order calculation of the profile. When D_T is small, it is necessary to consider $\bar{v}_2$. In the limit with $D_T \approx 0$, $\bar{v}_2$ may reach values $\sim u_T(n - 1)$ at certain points in the pipe. The value of $\bar{v}_2$ may be nonzero at the wall, since the probability of appearance of the flame front at the wall has a finite value.*

The profile of the average velocities $\bar{u}$ is determined from the formula

$$\bar{u} = \bar{u}_1 P_1 + \bar{u}_2 P_2 = \bar{u}_1 + (\bar{u}_2 - \bar{u}_1) P_2. \tag{4.54}$$

Plots of the $\bar{u}$ profile across the pipe for $u_T/V_1 = 0.05$ are given in Figure 4.10.

For practical calculations, it is sometimes more convenient to use equations averaged over the pipe cross section. The conservation equations of mass, energy, and momentum, averaged over the pipe cross section, will be written in the respective forms:

$$c_1\bar{u}_1 = \bar{u}_{cp}c_{cp}; \quad \bar{u}_{cp} - \bar{u}_1 = u_1(n - 1)\frac{x}{a}$$

and

$$c_1\bar{u}_1 u_1(n-1)\frac{x}{a} = p(x) - P_1,$$

where $p(x)$ is the static pressure in cross section x.

_____

*The "wall" in this problem is naturally to be understood as the outer boundary of the boundary layer, beyond which the effects of the pipe walls come into play.

The detailed derivation of these equations will be found in [14].

The momentum equation can be used to estimate the value of u_T from the static pressure drop along the pipe. We note that the sample-averaged momentum equations and the general equation were not used in solving the problem. These equations are satisfied with the elementary assumption that the static pressure is constant over y, $\tau = \overline{u'v'} = 0$, and $\overline{v'}^2 = \text{const.}$

However, if we use the more accurate assumptions ($\overline{v_2} \neq 0$, etc.), we can obtain a turbulent velocity distribution $\overline{v_2'}^2$ in the combustion products that satisfies the condition of zero pressure drop across the stream and is different from the distribution $\overline{v_1'}^2$. In addition to this velocity, there is also a profile of incremental turbulent velocity fluctuations, which is obtained by measuring the total velocity fluctuation in the combustion zone (see §6.2). All of this suggests the possibility of measuring the fluctuation velocity values in the zone and in the products of combustion of the flame jet in the pipe, which will differ substantially from the turbulent velocity of the free stream, although, as we saw from the solution, the basic parameters of the jet — the dispersion and the average y_1 — were determined by the free stream turbulence.

The solution given above is applicable to the combustion behind stabilizers and behind small antechambers if the temperature of the antechamber jet does not differ strongly from that of the combustion products. In this case, the coordinate origin is placed on the edge of the stabilizer (antechamber) and the distance a is the width of the gap between the stabilizer edge and the wall. The value of D_T assigned in the bottleneck in the stream in front of the stabilizer undergoes practically no change; only the average velocity increases from $\overline{u}_0$ to $\overline{u}_1$, so that the value $D_T/\overline{u}_1$ ($\overline{u}_1$ is the longitudinal average velocity in the bottleneck) should be substituted in the calculation for the assigned value of $D_T/\overline{u}_0$.
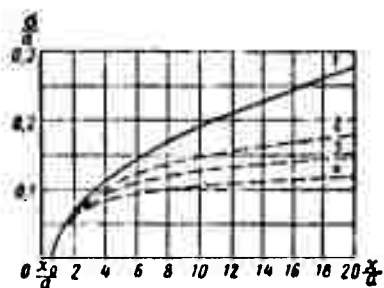
In a number of cases (e.g., combustion behind many ignition sources) with large variation of the longitudinal average velocities, it will evidentally be more correct in engineering calculations to use the average (over the pipe cross section) value of the dispersion, which is given by the formula

Figure 4.11. Dispersion of turbulent flame jet in pipe and in open stream.

1 — in open stream $\sigma_a = \sqrt{\dfrac{2D(\tau - \tau_0)}{\bar{u}_1 a^2}}$;

$\dfrac{D_\tau}{\bar{u}_1 a} = 0.02$; 2 — in pipe with $u_\tau \bar{u}_1 = 0.05$,

3 — in pipe with $u_\tau / u_1 = 0.1$;

4 — in pipe with $u_\tau / u_1 = 0.2$

$$\sigma^2 = 2 \int_{x_0}^{x} \frac{D_\tau \, dx}{\bar{u}_{cp}} = 2 \int_{0}^{x} \frac{D_\tau \, dx}{\bar{u}_1 \left[1 + \frac{u_\tau}{\bar{u}_1}(n-1)\frac{x}{a} \right]} = \frac{2 D_\tau x}{\bar{u}_{cp} - \bar{u}_1} \ln\left(\frac{\bar{u}_{cp}}{\bar{u}_1} \right),$$

(4.55)

$$\text{for } x \geqslant 2x_0 \left(\text{where } x_0 \approx \frac{D_\tau}{2\bar{u}_1} \right).$$

Plots of this function for various $u_\tau/\bar{u}_1$ are given in Figure 4.11. The value of u_τ is assigned for experimental data obtained by any of the methods given above for open stream measurements. The solution given in the present section may also serve as a basis for measurements of u_τ.

§8. Scales of Temperature Inhomogeneities in the Turbulent Combustion Zone

In a number of engineering problems, there is interest not only in the combustion rate and the width of the combustion zone, but also in the dimensions of the "cold" and "hot" volumes filling this zone.

It is convenient to study the relationships for these dimensions with reference to the example of the one-dimensional turbulent combustion zone. If necessary, they can be extended to the real flame jet in a high velocity stream by simple conversion.

We shall examine the statistics of the temperature inhomogeneity scales along one of the axes (for example, the y axis), along which the statistical properties of the randomly fluctuating combustion surface are homogeneous

Here it is natural to use the results obtained in the statistical geometry of random surfaces* [106]. For this purpose, we shall assume that the statistical distribution of the values of $\zeta(y)$ and its derivative $\partial\zeta/\partial y$ is a two-dimensional normal distribution:

$$P(\zeta, \zeta_1) = \frac{1}{2\pi \sqrt{\sigma^2 \sigma_1^2}} \exp\left[-\frac{\zeta^2}{2\sigma^2} - \frac{\zeta_1}{2\sigma_1^2}\right]. \tag{4.56}$$

where

$$\zeta_1 = \frac{\partial\zeta}{\partial y}; \quad \sigma_1^2 = \overline{\left(\frac{\partial\zeta}{\partial y}\right)^2};$$

ζ is the coordinate of the combustion surface.

As we know [106], the average number of crossings of the surface through the level $\zeta = x$ with the condition $\bar{\zeta} = 0$ per unit length is in this case

$$N_0 = \frac{1}{\pi} \frac{\sigma_1}{\sigma} \exp\left[-\frac{x^2}{2\sigma^2}\right]. \tag{4.57}$$

If L_1 is the average scale of the "cold" volume on the y axis and L_2 is the corresponding "hot" scale, we obviously have

$$L_1 + L_2 = \frac{2}{N_0} = \frac{2\pi\sigma}{\sigma_1} \exp\left(\frac{x^2}{2\sigma^2}\right). \tag{4.58}$$

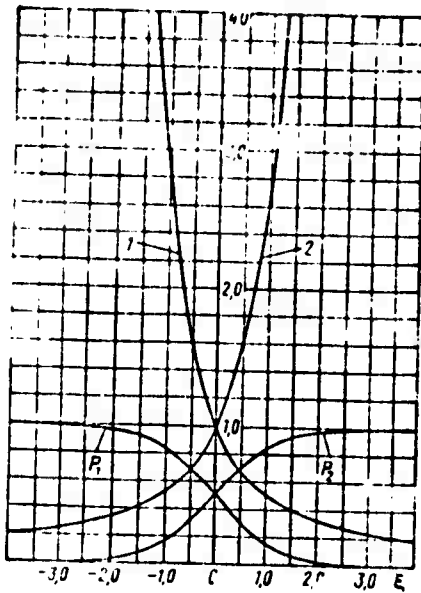*The analysis given below differs from that in [14], but leads to the same results.

Figure 4.12. Distribution of scales L_1 and L_2 through depth of combustion zone:

$$1 - L_1/L_0 = \left[1 - \Phi\left(\frac{x}{c}\right)\right] e^{\frac{x^2}{2c^2}};$$

$$2 - L_2/L_0 = \left[1 + \Phi\left(\frac{x}{c}\right)\right] e^{\frac{x^2}{2c^2}}$$

Figure 4.13. Scales L_1 and L_2 plotted against combustion efficiency for various stream velocities:

Experiment

L_1	L_2	•	▼
○	◑	1,6	38
□	■	1,6	70
△	▲	1,61	20

—— theory; distance from burner x_b = 500 mm.

Since

$$P_1 = \frac{L_1}{L_1 + L_2}, \quad P_2 = \frac{L_2}{L_1 + L_2},$$

where

$$P_1 = \frac{1}{2}\left[1 - \Phi\left(\frac{x}{c}\right)\right], \quad P_2 = \frac{1}{2}\left[1 + \Phi\left(\frac{x}{c}\right)\right],$$

we have

$$\left.\begin{array}{l} L_1 = (L_1 + L_2)P_1 = \frac{\pi z}{c_1}\exp\left(\frac{x^2}{2c^2}\right)\left[1 - \Phi\left(\frac{x}{c}\right)\right]; \\[2mm] L_2 = (L_1 + L_2)P_2 = \frac{\pi z}{c_1}\exp\left(\frac{x^2}{2c^2}\right)\left[1 + \Phi\left(\frac{x}{c}\right)\right]. \end{array}\right\} \qquad (4.59)$$
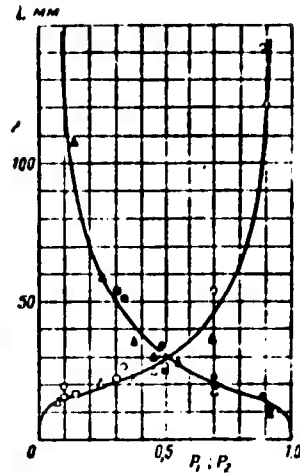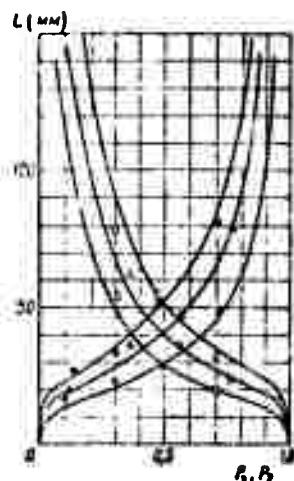
Figure 4.14. Scales L_1 and L_2 plotted against efficiency for various excess-air ratios:

Experiment

L_1	L_2	•	$\frac{\nabla}{}$m/sec	
				— theory; distance from burner x_b = 500 mm.
O	●	1,6	31	
△	▲	1,35	32	
□	■	1,13	3?	

Universal curves of $\frac{L_1(x)}{L(0)}$ and $\frac{L_2(x)}{L(0)}$ against x/σ are plotted in Figure 4.12. In Figure 4.13, the scales, constructed as functions of the observation probabilities, are compared with experiment [92].

We should note that the dependence of the parameter σ_1 on the physico-chemical properties of the mixture must be taken into account in plotting absolute values of the scales.

From physical and dimensional theory considerations, we have

$$\sigma_1 \sim \left(\frac{\sigma}{\lambda}\right)^r \left(\frac{u'}{u_T}\right)^q.$$

where r and q are certain exponents and λ is, as before, the dissipation scale. Since u_T decreases with increasing excess-air ratio α, the parameter σ_1 will increase, with a resulting decrease in the inhomogeneity scales, in full agreement with experimental data (Figure 4.14).

The results obtained enable us to find the scale distribution of the burned mixture for a flame jet in a high velocity stream. For the jet behind a plane-parallel antechamber, for example, the scale distribution for the fresh mixture above the jet (L_1^u) and below the jet (L_1^l) are obviously given by the formulas

$$L_1^u = \frac{\pi\sigma}{\sigma_1}\left[1 - \Phi\left(\frac{y - a_1}{\sigma}\right)\right] e^{\frac{(y - a_1)^2}{2\sigma^2}};$$

$$L_1^l = \frac{\pi\sigma}{\sigma_1}\left[1 + \Phi\left(\frac{y + a_1}{\sigma}\right)\right] e^{\frac{(y + a_1)^2}{2\sigma^2}}.$$

At the same time, by definition,

$$P_2 = \frac{L_2}{L_1^* + L_1^* + L_2}.$$

From this,

$$L_2 = \frac{P_2}{P_1}(L_1^* + L_1^*) = \frac{\pi \epsilon}{\epsilon_1} \frac{P_2}{P_1} \left\{ \left[1 - \Phi\left(\frac{y - a_\tau}{\epsilon}\right) \right] e^{\frac{(y - a_\tau)^2}{2\epsilon^2}} + \left[1 + \Phi\left(\frac{y + a_\tau}{\epsilon}\right) \right] e^{\frac{(y + a_\tau)^2}{2\epsilon^2}} \right\}.$$

where P_2 is described by the formula

$$P_2 = 1 - P_1 = \frac{1}{2}\left[\Phi\left(\frac{y + a}{\epsilon}\right) - \Phi\left(\frac{y - a}{\epsilon}\right) \right].$$

CHAPTER V

DIFFUSION COMBUSTION IN A TURBULENT STREAM

§1. The Single Open Diffusion Flame

1. Models of Diffusion Combustion

Combustion of unmixed gases is the case most frequently encountered in practice and has therefore long attracted the attention of investigators. However, it can be said that there is as yet neither a consensus as to the physical picture of the process nor a generally accepted and sufficiently reliable method of calculating the turbulent jet.

The work of Burke and Schumann [6], who studied laminar combustion for the case of coaxial streams of fuel and oxidizer flowing in a closed channel at the same velocity, and the work of Ya. B. Zel'dovich [96], [144] on the properties of the laminar diffusion flame strongly influenced later research in this field. The following assumptions are usually made in analyzing models of laminar diffusion combustion: (a) the combustion reaction is assumed to be infinitely rapid (instantaneous); (b) the diffusion coefficients and thermal diffusivities are assumed to be constant and equal. Thus, the flow field is divided into two zones: one inside the combustion surface (flame front) and the other outside of it. In each zone, combustible gas or oxygen diffuses in the direction toward the flame front, vanishing at the

front, while combustion products enter each zone from the flame front, where their concentration equals unity. The temperature on the flame front is equal to the adiabatic combustion temperature.

Neglect of the influence of heat release on the transport coefficients and the aerodynamics of the stream results in the fact that the location of the flame front found as a result of the solution coincides with the surface on which the fuel and oxidizer are in the stoichiometric ratio in cold mixing (mixing without reaction).

It is self-evident that a certain amount of caution is required in extending concepts that have justified themselves for the laminar flame to the case of the turbulent diffusion combustion.

For example, the assumption [1], [3] that a nonmoving flame front surface exists in the stream is highly arbitrary and justified only as a first approximation. Even if a thin instantaneous diffusion front were organized in the stream, it would be subject to random spatial fluctuations under the influence of the turbulence in the medium. This behavior of the flame front has been demonstrated by direct experiment in the combustion of a homogeneous mixture (see Chapter IV). It is also known that the highest average temperature is always found to be far below adiabatic in all turbulent diffusion flames.

It is understandable from physical considerations that allowance for the complex nature of mixing in a turbulent stream, which was treated in detail in Chapter I, is especially necessary in the study of diffusion combustion problems. It appears that Gaussorn, Widdel, and Hottel [108] were the first to take note of this fact on the basis of experiments during which the concentrations of the combustion products, fuel, and oxidizer were measured on the axis of a turbulent jet. These data permitted calculation of the molar concentrations of the combustible gas referred to its nonreacting constituents (the so-called reduced concentration). It was found that at that point on the jet axis at which the amount of air reaches

stoichiometry (on the average over time), its combustion is not yet complete (the combustible gas is present in a sample). A combustion efficiency of 99% is attained at rather large distances from the exit cross section at two or three times the stoichiometric amount of air.

This discrepancy indicates the need for introduction (we quote from [108]): "of an additional characteristic of the mixing process in addition to those based on the average concentration values. According to the physical picture of the turbulent flame, air eddies are extracted from the surrounding atmosphere and broken up into fragments of various sizes by viscous forces* in the jet. Combustion occurs when the flame completely envelopes the air eddies and unburned gas. Although the total area of the flame is several times the area attainable in the diffusion flame,** the final intimate mixing of the gas and oxygen can occur between eddies as a result of molecular diffusion . . . ."

The above picture of the process leads directly to the conclusion that instantaneous concentration fluctuations occur about a certain average value. Reference [108] suggests that the fluctuations are normally distributed. Since either oxygen or unburned gas should be absent in an instantaneous sample when the chemical reaction rates are high, the dispersion (the mean square of the fluctuations) in the postulated normal distribution characterizing the "mixing intimacy" of the gases can be determined from the average reduced concentrations of these gases. Thus, determination of this parameter involves gas analysis of the flame.

The direct conclusion drawn from [108] is that methods for calculation of the turbulent diffusion flame that essentially identify mixing on the average with molecular mixing will give low values

---

*Inertial forces are apparently what is meant.

**The reference is to the laminar diffusion flame.

for the burnup length as compared with that found in an experiment by chemical analysis. This difficulty can be overcome by generalizing the "two-stage" methods developed for calculation of nonisothermal jets in Chapters I and II to the case of mixing with reaction, regarding mixing as the decisive factor in accordance with the generally accepted view [1], [3], [108].

2. Method of Calculating Parameters of Diffusion Flame in an Open Stream

Let us first consider the method of calculation based on the microvolume diffusion combustion model using the single axisymmetric fuel jet as an example. The procedure of the calculation is as follows [153]:

1. The "cold" mixing of the jet of fuel with the oxidizer is determined from the laws of accelerated molecular diffusion, and quasilaminar fuel and oxidizer concentration profiles are found from the formulas of Chapter II, in which the grey mixing dispersion $\sigma_c^2(x)$ appears.

2. Following [108], we assume that a chemical reaction takes place at each point in space in accordance with the composition found for the mixture. The temperature found as a result corresponds to the adiabatic combustion temperature of a mixture of this composition.

3. We then account for the expansion of the gases on heating. If it is assumed that expansion takes place only in the transverse direction (open flame), a ring of area $2\pi r_0 dr_0$ will occupy an area

$$2\pi r_c dr_c = 2\pi \frac{\rho_c(r_0)}{\rho_{c,b}(r_0)} r_0 dr_0$$

after completion of heat release; here $\rho_m(r_0)$ is the density of the gas as a result of cold mixing and $\rho_{cb}(r_0)$ is the density of combustion products of the corresponding composition.

As a result of thermal expansion, therefore, a circle of radius r (and the values of the thermodynamic parameters corresponding to it) becomes a circle of radius r_c, determined by the relation

$$r_r = \sqrt{2 \int_0^{r'} \frac{\varrho_c}{\iota_{c,r}} r_0 \, dr_{0^*}} \qquad (5.1)$$

4. Constructing quasilaminar profiles with consideration of thermal expansion, we find the average profiles by superimposing the random convective transfer, which is described by a Gaussian probability density with dispersion $\sigma_r^2(x)$. For example, the average value of the temperature at a distance r from the axis of an axisymmetric flame is given by

$$\bar{T}(r) = \int T_{c,r}(r_r) p(\vec{r}, \vec{r}_r) d\vec{r}_r =$$

$$= \frac{1}{\sigma_r^2} e^{-\frac{r^2}{2\sigma_r^2}} \int_0^{\infty} e^{-\frac{r_r^2}{2\sigma_r^2}} I_0 \left(\frac{r \cdot r_r}{\sigma_r^2} \right) T_{c,r}(r_r) r_r \, dr_r. \qquad (5.2)$$

The step-by-step method of calculating turbulent diffusion combustion is based on the physical model of aged formation and decay of large vortices, which was examined in Chapter I. The large vortex that forms depends only on the velocity shear between the jet of combustible gas and the cocurrent oxidizer stream. The statistical ensemble of large vortices determines the convective transport velocity of gas volumes and the characteristic mixing scale σ. Since heat release in convective transport is negligible, it has practically no effect on the transport scale σ. Microturbulent mixing of the gaseous component takes place throughout the entire volume of the decay wakes, with simultaneous heat release and expansion of the combustion products, and the component concentrations are determined at each point of the wake by the convective transport of the large vortex even before combustion. Then the stage of large vortex formation is repeated. For a diffusion flame in a pipe (enclosed flame), expansion of the combustion products

results not in expansion of the average lateral boundaries of the flame, but in an increase in the longitudinal velocities, with a resulting change in the scale σ as a result of the changes in the diffusion coefficient and the average flow velocity. However, we shall consider diffusion combustion in chambers with large longitudinal pressure gradients in separate sections of this chapter.

In accordance with the above, the end of the flame corresponds (on the average) to stoichiometry on the axis of the jet with cold "grey" mixing, i.e., the flame length is found from the condition

$$\frac{\varrho_1}{L \cdot \varrho_2} = 1,$$ (5.3)

where ϱ_1 and ϱ_2 are the partial densities of the air and the combustible gas and L is the coefficient of stoichiometry for the combustible gas.

Since (see Chapter I, §1)

$$\frac{\varrho_1}{\varrho_2} = \frac{c_{01}}{c_{02}} \frac{P_1}{P_2} = n \frac{P_1}{P_2},$$

Relation (5.3) can be written

$$P_1 = \frac{L}{n + L} \quad \text{or} \quad P_2 = \frac{n}{n + L}.$$ (5.3')

Remembering that on the axis

$$P_1 = e^{-\frac{a_1^2}{x_c^2}}$$

we obtain from (5.3')

$$\frac{a_1^2}{2 a_c^2} = \ln\left(1 + \frac{n}{L}\right).$$

Or, since $\sigma_m = N\sigma$ (see Chapter III)

$$\frac{a_r^2(l_\phi)}{2 z^2(l_\phi)} = N^2 \ln\left(1 + \frac{n}{L}\right),$$ (5.4)

where l_f is the flame length determined from Relation (5.4).

Let us consider certain particular cases. When a flame forms in the cocurrent stream (cocurrency parameter $m = V_1/V_2$), we have at sufficiently large distances from the exit section

$$a_r^2 \to \frac{1}{m} a_0^2.$$

For m near unity, the dispersion is determined by the natural turbulence of the streams and can be represented in the form (see Chapter II, §3)

$$\sigma^2 = \frac{2 D_T}{\bar{u}} x.$$

Hence, the flame length is determined by the relation

$$\frac{l_\phi}{a_0} = \frac{1}{m} \frac{\bar{u} a_0}{2 D_T N^2 \ln\left(1 + \frac{n}{L}\right)}.$$ (5.5)

If the flame is formed in a large pipe, the ratio $D_T/\bar{u}$ is determined by pipe turbulence and does not depend on the velocity $\bar{u}$. Thus, the relative flame length in this case does not depend on the velocity of the flame and is proportional to the initial diameter. If, in addition, $n/L \ll 1$, we have

$$\frac{n}{L} \ll 1, \text{ then } \ln\left(1 + \frac{n}{c_0 L}\right) \simeq \frac{n}{L}$$

and then

$$\frac{l_\phi}{a_0} \approx \frac{\bar{u} a_0 L}{2 D_r N^2 nm} ,$$

i.e., the length of the flame is proportional to the coefficient of stoichiometry and inversely proportional to the ratio of the initial densities n and the cocurrency parameter m (without considering the influence of these parameters on the coefficient N).

At large distances from the nozzle exit in a submerged flame (see the formulas of Chapter II, §2)

$$\frac{a_r^2}{2 \sigma^2} \simeq \sqrt{n} \, \frac{a_0}{s} \simeq \sqrt{n} \, \frac{10 a_0}{x} .$$

Thus we have from (5.4)

$$l_\phi \simeq \frac{10 a_0 \sqrt{n}}{N^2 \ln\left(1 + \frac{a}{L}\right)} ,$$

or

$$\frac{l_\phi}{2 a_0} \simeq \frac{s}{N^2} \, \frac{L}{\sqrt{n}} . \tag{5.6}$$

It follows from (5.6) that the relative length of a submerged flame is independent of diameter and initial velocity, directly proportional to the stoichiometry coefficient, and inversely proportional to the square root of the initial density ratio.

All of the foregoing results were obtained without consideration of the Archimedean force, so that the calculated flame length may be on the high side for vertical outflow of the fuel jet.

Approximate allowance for the Archimedean force is possible with the aid of the following notation for the momentum equation:

$$\frac{d}{dx}\int_0^\infty \bar{\rho}\,\bar{u}^2 r\,dr = g\int_0^\infty (\rho_m - \bar{\rho}_r)\,r\,dr, \tag{5.7}$$

where $\bar{\rho}_c$ is the density in the flame as calculated from a formula of the type (5.2). Equation (5.7) is therefore written in the equivalent form

$$\frac{d}{dx}\int_0^\infty \bar{\rho}\,u^2 r\,dr = g\int_0^\infty\left[\int_0^\infty \rho_m p(r_1 r_0)\,r_0\,dr_0 - \int_0^\infty \rho_{c.r}(r_0)\,p(r_1 r_0)\,r_0\,dr_0\right]r\,dr =$$

$$= g\int_0^\infty r_0\,dr_0\left[\int_0^\infty \rho_m p(r_1 r_0)\,r\,dr - \int_0^\infty \rho_{c.r}(r_0)\,p(r_1 r_0)\,r\,dr\right] =$$

$$= g\int_0^\infty [\rho_m - \rho_{c.r}(r_0)]\,r_0\,dr_0.$$

Equation (5.7) gives a new relation between the diffusion parameters a_T and a_V for use instead of those obtained previously (see Chapter II, §2) and reduces to the earlier relations only at sufficiently large Froude numbers:

$$Fr = \frac{\bar{u}^2}{4 g a_0^2}.$$

Approximate analysis of the above equations indicates that considerable importance attaches to a number A of the form

$$A = \frac{\left(n - \dfrac{\rho_r}{\rho_{c.r}}\right)\dfrac{T_r}{T_{c.r}}\dfrac{n}{n+L}\,f\lambda^2 a_0^2 x}{3 Fr\, a_0^2},$$

where ρ_c and T_c are the density and combustion temperature of the stoichiometric mixture, $T_{g.m}$ is the mixture temperature obtained on mixing of stoichiometric quantities of combustible gas and oxidizer with their respective initial temperatures, and f is the number of moles of combustion products per mole of fuel.

If the condition $A \geq 10$ is satisfied at $x < l_f$, the flame length is expressed by the simple formula

$$\frac{l_\phi}{2a_,} = 0.4 \frac{(Pr)^{\frac{1}{5}}\left(\frac{T_2}{T_1} + \frac{\mu_2}{\mu_1} L_0\right)^{\frac{2}{5}}}{\left(\frac{T_r}{T_{c,r}}\right)^{\frac{1}{5}}\left(\frac{T_2}{T_1}\right)^{\frac{2}{5}} N^{1.2}}, \tag{5.8}$$

where μ_1 and μ_2 are the molecular weights of the oxidizer and the fuel.

The results set forth above pertained to an axisymmetric flame. Let us write the corresponding formulas for a plane-parallel turbulent flame and a mixing layer.

In the two-dimensional case, relation (5.1), which describes the influence of thermal expansion, is replaced by the obvious relation

$$y_r = \int_0^y \frac{\varrho_c}{\varrho_{c,r}} dy_r.$$

The average temperature profile is obtained by superimposing the random transport described by a Gaussian probability density with dispersion σ_r^2 on the quasilaminar profile constructed with consideration of thermal expansion:

$$\bar{T} = \frac{1}{\sigma_r \sqrt{2\pi}} \int_{-\infty}^{\infty} e^{-\frac{(y-y_r)^2}{2\sigma_r^2}} T_{c,r}(y_r) dy_r.$$

The length of the plane-parallel flame is determined from the condition

$$\Phi\left[\frac{\sigma_r(l_\phi)}{\sigma_c(l_\phi)}\right] = \frac{n}{1+n}.$$

Remembering that at sufficiently large distances from the flame exit section

$$a_t \to \frac{1}{m} a_{0},$$

we have for m near unity

$$\Phi\left(\frac{a_0^{1/2}}{mN\sqrt{\dfrac{2D_t}{\bar{u}}}\sqrt{\dfrac{l_\phi}{a_0}}}\right) = \frac{n}{L+n}.$$

From this,

$$\frac{l_\phi}{a_0} = \frac{a_j \bar{u}}{2m^2 N^2 D_t \left[\Phi^{-1}\left(\dfrac{n}{L+n}\right)\right]^2},$$

where Φ^{-1} is the inverse of the probability integral.

For example, when $\dfrac{n}{L+n} \ll 1$

$$\frac{l_\phi}{a_0} = \frac{1}{\pi} \frac{a_0 L^2}{m^2 n^4} \frac{\bar{u}}{D_t}.$$

For pipe turbulence, as we have noticed, $D_T/\bar{u}$ does not depend on velocity.

At large cocurrency parameters, therefore, the length of the plane-parallel flame is directly proportional to the square of the stoichiometry coefficient and inversely proportional to the product of the square of the cocurrency parameter by the fourth power of the initial-density ratio.

In a submerged plane-parallel flame at large distances downstream

$$\Phi\left(\frac{a_t}{z_t}\right) \simeq 1 - \frac{2}{\sqrt{2\pi}} \frac{a_t}{z_t} = 1 - \frac{2}{\sqrt{2\pi}} \frac{a_t}{N_t} \simeq \frac{n}{L} \quad \text{(for } L \gg n\text{)}.$$

Then

$$a_1^2 = \frac{a_0^\bullet}{2\gamma Pr} n\sqrt{\pi}(1+Pr).$$

From this, putting $\sigma \approx 0.1\,x$:

$$\frac{l_\phi}{2a_0} = \frac{5(1+Pr)}{n\sqrt{\pi Pr}}\,L.$$

Thus, as in the axisymmetric case, the relative length of the submerged plane-parallel flame does not depend on the dimensions of the burner or the initial velocity, and is directly proportional to the stoichiometry coefficient. At the same time, this length is inversely proportional to the initial-density ratio (and not to the square root of the ratio as in the case of the axisymmetric flame).

3. Comparison with Experiment

Before comparing the proposed calculation method with experimental data, it is necessary to answer the following natural question: Can the same values of the dispersion and degree of greyness that describe mixing in nonreacting jets be used for calculation of the flame? This question is most easily answered by direct experiments similar to those to be described below. The latter were run on a special experimental setup (Figure 5.1) composed of a cylindrical combustion chamber (diameter 49 mm) 1, fitted with two centrifugal nozzles 3 for delivery of fuel to form a heated (to 1100° K and higher) combustible mixture that ignites spontaneously at the exit from the chamber. The mixture is preheated with antechamber 2 and then by initiating the combustion downstream of the annular stabilizer 4, whose position on the length of the chamber has been adjusted to prevent vibrating combustion in the chamber. The cocurrent stream was formed in the 400 mm diameter pipe 5 with diffuser grid 6 to suppress disturbances. Air was fed into the combustion chamber from a system of compressed air cylinders. Ethyl alcohol was used as a fuel to control soot fouling and radiation of light in the diffusion
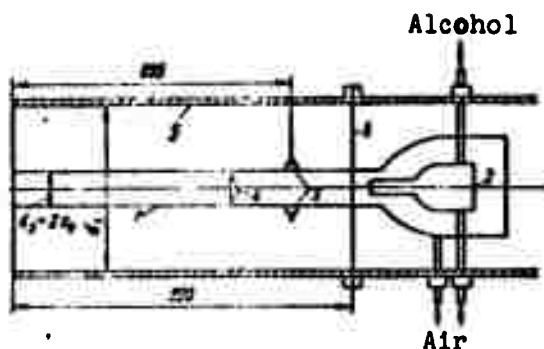
Alcohol

Air

Figure 5.1. Diagram of setup for study of dispersion in a diffusion flame.

1 — combustion chamber; 2 — antechamber; 3 — centrifugal nozzles; 4 — stabilizer; 5 — pipe; 6 — turbulence suppressor grid.

flame. Sodium atoms injected with an NaOH solution into antechamber 2 made the main contribution to the total luminous emission of the flame.

It is known that sodium atoms emit with an intensity that depends very strongly on temperature [through the factor $e - (h\nu/k_T)$]. It can therefore be assumed that if there is no emission in the volume of the jet at the flame exit section, the emittance distribution in a certain cross sec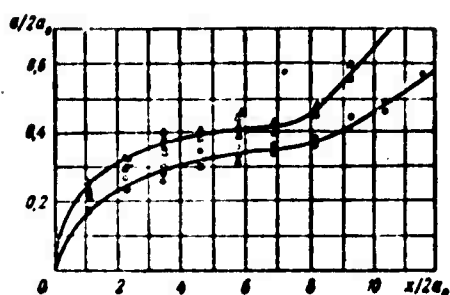tion is due to random fluctuations of a thin emitting surface, and specifically with fluctuations of the instantaneous diffusion flame front, where the maximum temperature is determined. Since the intensity distribution (found by densitometry of a photograph of the flame) in a cross section has a characteristic shape with two "humps" the width of a hump can be used to determine the dispersion of the flame front in the corresponding cross section. The initial concentration of the fuel in the jet was varied from $c_0 = 0.07$ to 0.13 kg/kg.

The notation of the maximum brightness surface varied quite substantially as a result.

Nevertheless, Figure 5.2 shows that the front dispersion calculated from flame emittance undergoes practically no change (at a constant cocurrency parameter m).

Data on the flame front dispersion are compared in Figure 5.3 with data on the jet dispersion determined under similar hydrodynamic conditions, also by the optical diffusion method (see Chapter III, §4).

Figure 5.2. Dispersion of front
of diffusion flame.

m = 0; Δ - c = 0.07 kg/kg;
▲ - c = 0.13 kg/kg; m = 0.28;
O - c = 0.07 kg/kg; ● - c =
0.13 kg/kg; experiments of
V. N. Sagalovich.

For comparison, Figure 5.3
also shows dispersion values
calculated from the temperature
profiles of a jet flowing out of
a strongly pinched nozzle, i.e.,
with low initial turbulence (experi-
ments of I. B. Palatnik [43]).

Inspection of this figure
shows that the dispersion is actu-
ally determined by the hydrodynamics
of the stream. The fact that the
dispersion is initially lower
according to Palatnik's experimental data is naturally explained by
the low initial turbulence level in his experiments. It is also
seen from Figure 5.3 that the dispersion straightens out on the main
segment of the jet, following a line with a given slope for a given
value of m. Thus, the experiment confirms that dispersion is inde-
pendent of heat release for the initial segment of a diffusion flame.

The above method permits investigations in a relatively narrow
range of conditions. In the preceding chapter, we demonstrated the
identity of the dispersions with and without combustion in a rather
broad range of initial conditions for a hotter homogeneous flame. We
may therefore expect this to hold even more strongly for the diffusion
jet flame, since the hydrodynamics of turbulence transport is more
important and the chemical reaction of the mixed gases less important
in burning fuel jets than in the homogeneous flame jet.

The possibility of using characteristics that describe "cold"
mixing of jets in these calculations can also be confirmed by simple
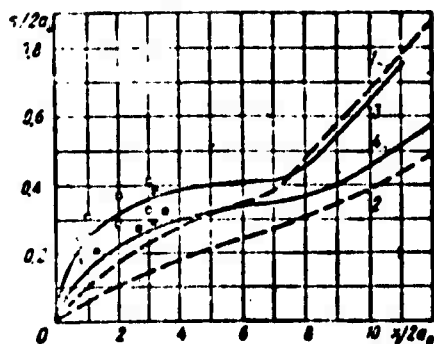comparison of the results of these calculations with observational
results.

Figure 5 3. Dispersions of diffusion flame and jet compared.

$\square$ - m = 0; $\blacksquare$ - $\dfrac{Jet}{m}$ = 0.3 (N. A. Zamyatina, tubular profile); 1 - m = 0; 2 - m = 0.3 (I. B. Palatnik, rectangular profile);

3 - m = 0; 4 - $\dfrac{Flame}{m}$ = 0.3.

Table 5.1a presents the results of calculations using Formula (5.6) with the experimental values of l_f obtained in [108].

In this study, the flame length was determined both visually and as the distance along the axis of the flame at which combustion efficiency reached 99%. The reference origin for the length was the end of the transitional segment to turbulence S.

In agreement with Chapter III, N = 0.5 — 0.6 for all cases. The calculation by Formula (5.8), which takes account of the Archimedean force, was compared with the data of S. N. Shorin and O. N. Yermolayev [112], who determined the flame length visually.

Table 5.1b shows that the agreement between the calculated and experimental values is quite satisfactory.

Formulas of the type (5.1) and (5.2) can be used to calculate the axial reduced concentration c_m'. Figure 5.4 compares theory with the experiments of Hottel, Gaussorn, and Waddell for three gases: propane, hydrogen, and city gas.

The agreement is again quite satisfactory.

Table 5.1a

<table>
<thead>
<tr><th>Composition</th><th>$n = \rho_{01}/\rho_{02}$</th><th>$\frac{1}{c_1}-1$</th><th>d_2 мм</th><th>Re</th><th>$\frac{V_2^2}{gd}$</th><th>l_f/d</th><th>S/d</th><th>N</th></tr>
</thead>
<tbody>
<tr><td>Hydrogen + propane</td><td>0,997</td><td>16,2</td><td>3,18</td><td>15300</td><td>36000</td><td>216</td><td>4</td><td>0,62</td></tr>
<tr><td>Carbon dioxide + city gas</td><td>0,99,</td><td>3,1</td><td>3,18</td><td>8800</td><td>36000</td><td>65 74</td><td>23</td><td>0,5</td></tr>
<tr><td>Acetylene</td><td>1,036</td><td>11,9</td><td>3,18</td><td>32400,</td><td>30700</td><td>177*</td><td>11</td><td>0,56</td></tr>
<tr><td>Carbon monoxide</td><td>1,034</td><td>2,38</td><td>6,36</td><td>5090</td><td>2415</td><td>41*</td><td>34,6</td><td>0,59</td></tr>
<tr><td>Propane</td><td>0,67</td><td>23,3</td><td>3,18</td><td>29000</td><td>54000</td><td>263</td><td>—</td><td>0,6</td></tr>
<tr><td>City gas</td><td>1,39</td><td>4,8</td><td>3,18</td><td>17500</td><td>201000</td><td>130*</td><td>5,6</td><td>0,48</td></tr>
<tr><td>Hydrogen</td><td>14,45</td><td>2,38</td><td>4,62</td><td>3580</td><td>158000</td><td>124</td><td>2,1</td><td>0,7</td></tr>
</tbody>
</table>

*Apparent length of flame.

TABLE 5.1b

<table>
<thead>
<tr><th>Composition</th><th>d_2 мм</th><th>V_2 m/sec</th><th>T_3 °K</th><th>$F_r \cdot 10^{-3}$</th><th>l/d (experiment)</th><th>calculation</th></tr>
</thead>
<tbody>
<tr><td rowspan="3">City gas</td><td>3</td><td>47,4</td><td>925</td><td>76,7</td><td>123,4</td><td>100</td></tr>
<tr><td>3</td><td>47,4</td><td>925</td><td>52</td><td>176</td><td>135</td></tr>
<tr><td>8</td><td>167</td><td>838</td><td>3</td><td>108,5</td><td>87</td></tr>
<tr><td rowspan="5">Propane</td><td>6</td><td>4,74</td><td>290</td><td>0,37</td><td>77—80</td><td>76</td></tr>
<tr><td>6</td><td>18,4</td><td>290</td><td>5,79</td><td>229</td><td>180</td></tr>
<tr><td>4,15</td><td>28,4</td><td>722</td><td>19,1</td><td>171,1</td><td>140</td></tr>
<tr><td>4,15</td><td>51,5</td><td>666</td><td>64,8</td><td>197</td><td>171</td></tr>
<tr><td>4,15</td><td>37,7</td><td>294</td><td>34,9</td><td>299</td><td>236</td></tr>
<tr><td rowspan="5">Hydrogen</td><td>5</td><td>102,6</td><td>554</td><td>214</td><td>116</td><td>121</td></tr>
<tr><td>5</td><td>156</td><td>705</td><td>492</td><td>106</td><td>120</td></tr>
<tr><td>3</td><td>12,4</td><td>293</td><td>5,2</td><td>90</td><td>73</td></tr>
<tr><td>3</td><td>24,7</td><td>297</td><td>30,7</td><td>123</td><td>108</td></tr>
<tr><td>3</td><td>145</td><td>297</td><td>715</td><td>191</td><td>195</td></tr>
</tbody>
</table>

As a last example, let us consider the experiments of Sh. A. Yershin and L. P. Yarin [109]. These authors studied the cone formed on outflow of a propane butane mixture ($c_0 = 0.085$ kg/kg) from a nozzle 20 mm in diameter at a velocity of 61 m/sec into a cocurrent stream. The initial temperature of the fuel-gas jet was 1300° K.
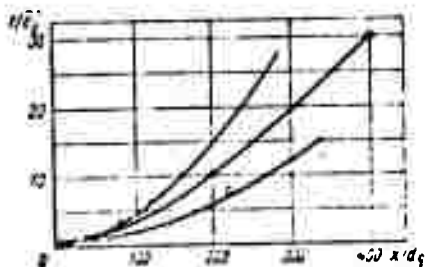
Figure 5.4. Reduced concentration on axis of diffusion flame. ×; ○; Δ — experiment; — — calculation.

The jet dispersion found above as a result of reduction of Palatnik's data from a study of mixing of a weakly preheated jet on a similar setup (see Figure 5.3) was used in the calculations.

The temperature rise in an elementary volume as a result of combustion was found from the formulas:

$$\Delta T = \frac{H_g c_0}{c_p} g \quad \text{for} \quad g \leqslant \frac{1}{Lc_0 + 1}; \qquad (5.9a)$$

$$\Delta T = \frac{H_q}{Lc_p} (1-g) \quad \text{for} \quad g \geqslant \frac{1}{Lc_0 + 1}, \qquad (5.9b)$$

where g denotes the concentration by weight of the jet substance in this volume for "grey" mixing, $g = \frac{P_{2c}}{nP_{1c} + P_{2c}}$, and it was further assumed that $H_u = 11,000$ kcal/kg and L = 15.6 kg/kg.

The variation of heat capacity (c_p) and molecular weight during combustion was neglected. The procedure of the calculation was indicated above. Since the flame was short in Yershin and Yarin's experiments, the degree of greyness N was taken equal to 0.6 (see Chapter III, §4, subsection 4).

Figures 5.5 and 5.6 illustrate the transformation of the temperature profile at the stages in the calculations for the submerged flame: the quasilaminar profile without consideration of thermal expansion (5.5b), the profile with consideration of thermal expansion (5.5a), and the average profile (Figure 5.6). In Figure 5.6, the calculated radial average temperature profiles are compared with experimental data from various cross sections of the flame.
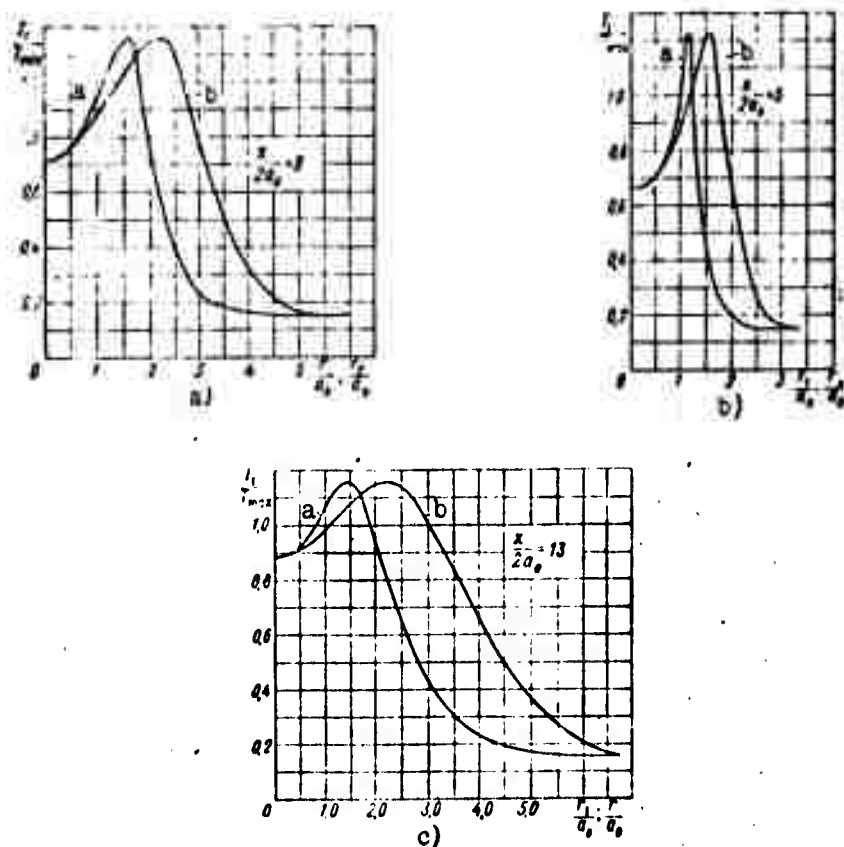
Figure 5.5. Transformation of temperature profiles in turbulent
diffusion flame ("grey" mixing).

a — with consideration of thermal expansion; b — without consider-
ation of thermal expansion (m = 0; n = 4.3; c_0 = 0.085 kg/kg; T_0 =
1300° K).

Figure 5.7 compares the calculation and experimental axial
temperatures; N = 0.5 was taken to find the parameters of the cocurrent
flame with cocurrency parameter m = 0.275 (see Chapter III, §4, sub-
section 4).
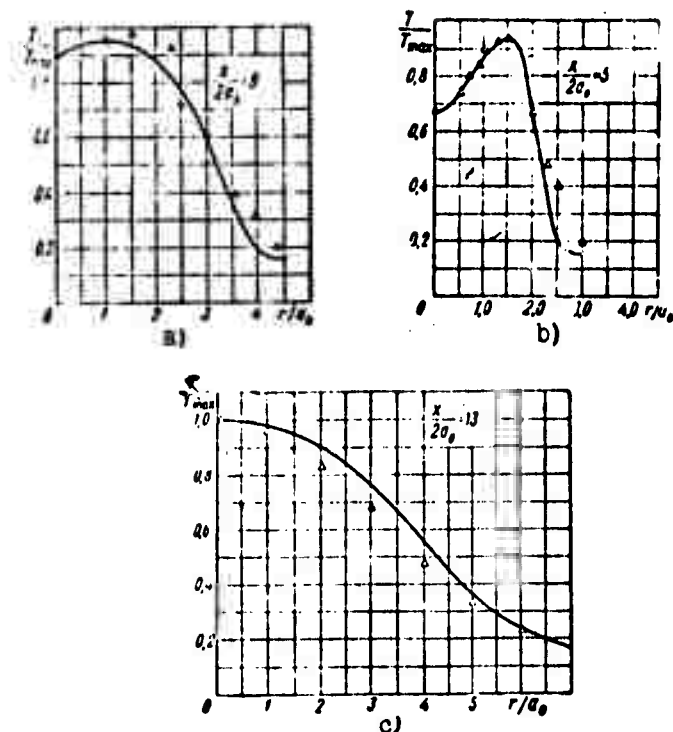
Figure 5.6. Temperature profiles in diffusion flame.
—— — calculation; Δ — experiments of Sh. A. Yershin and A. P. Yarin (m = 0; n = 4.3; c_0 = 0.085 kg/kg; T_0 = 1300° K).

§2.   Chamber Length in Diffusion Combustion

The concepts developed for the open diffusion flame can be used to obtain approximate analytical solutions for estimation of combustion chamber length for simple modes of delivery of the fuel gas, as well as computer solutions for more complex cases. Let us first examine a number of simple relationships for certain typical methods of delivering gaseous fuels: through slots along the walls of plane-parallel and round chambers, delivery of several jets spaced along the chamber and uniformly distributed around the cross section, etc.
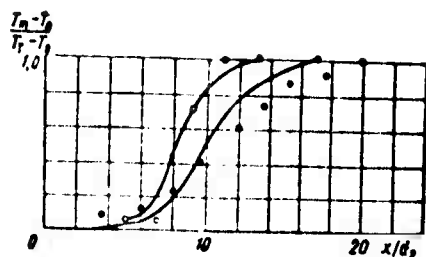
Figure 5.7. Temperature variation on axis of diffusion flame.

O — m = 0 and ● — m = 0.275, experiments of Sh. A. Yershin and L. P. Yarin; —— — calculation.

The chamber length on which the fuel is completely burned has the order of magnitude

$$L_{\kappa} \cong u(\tau_r + \tau_{c\kappa}), \qquad (5.10)$$

where u is the average longitudinal particle velocity of the reacting gases during mixing, τ_c is the sum of the ignition delay and the chemical reaction (combustion) time of the two gases, and τ_{mx} is the molecular mixing time of the turbulent fuel and oxidizer streams.

For the ignition delay and chemical reaction (combustion) times, we have both experimental overall kinetic relationships and the theoretical kinetic equations for many fuels. For example, the following analytical relation is proposed for gaseous hydrogen in [49]:

$$\tau_r = e^{\frac{10^4}{1,12T}} \frac{1}{p^{1,7}} + \frac{8 \cdot 10^{-3}}{p} e^{\frac{9400}{T}}, \qquad (5.11)$$

where τ_c is the time in μsec, p is the static pressure in kgs/cm², and T is the thermodynamic temperature of the mixed volume before combustion in °K.

An assumption is also made concerning the fraction of combustion products from the burned part of the fuel in the mixed volume. For hydrogen at $T_2 \approx 1000°$ K, u ≈ 2000 m/sec, and p = 3 kgs/cm², we obtain τ_c = 40 μsec and L_c = uτ_c = 0.08 m. With the same conditions and T ≈ 1500° K, we have L_c < 0.01 m. The characteristic diffusion mixing length L_{mx} = uτ_{mx} is an order of magnitude larger.

In most cases of practical interest, therefore, the parameters of the stream in the channel are such that the reaction time is much smaller than the mixing time. In these cases, the chemical kinetic effects can be disregarded, as in open flames.

A more accurate determination of chamber length can be made either from a surface combustion model or from the microbulk combustion model. The surface combustion model assumes that combustion of the fuel occurs in a thin flame front in accordance with the known laws of laminar diffusion combustion.

However, the flow of reacting components to the surface of the front is assumed in this case to be proportional not to the molecular diffusion coefficient, but to the coefficient of gradient microturbulent diffusion. The flame front (more precisely, its mean value) is placed where the fuel and oxidizer are in the stoichiometric proportions in cold microturbulent mixing without combustion.

The surface combustion model can be used to obtain rather simple analytical relations for estimation of the diffusion flame length when $\alpha < 1$ and $\alpha > 1$ (α is the excess oxidizer ratio). It is not possible to determine channel length from the position of the front when $\alpha = 1$, since the flame front is not closed in this case, either at the channel wall or at the axis of the stream. In this case, channel length is determined from the position of that cross section in which the integral combustion efficiency, which will be discussed below, reaches a value ≈ 0.95 (see §3, subsection 1).

The bulk combustion model assumes the presence of a reaction and heat release not only in the range of stoichiometric fuel and oxidizer proportions, but also in rich or lean regions; in other words, it is assumed that the reaction occurs at all points on the channel cross section in accordance with the local concentration values of the components at these points that insure predominance of microturbulent diffusion over combustion. The two computing methods yield results that agree as to the average position of the "flame front" for $\alpha > 1$,

$\alpha < 1$ and practically identical results for the integral combustion efficiency for all excess air ratios α.

The length of a diffusion flame in a turbulent stream is determined by the cross section of the flame in which the mass fraction of the deficient component (fuel for $\alpha > 1$ and air for $\alpha < 1$) is equal to the stoichiometric proportion determined for molecular (microturbulent) mixing. As in the open flame, this condition satisfies relation (5.3').

Relation (5.3) is valid both for the single fuel jet and for delivery of several jets. Chamber length can be estimated from the two extreme values of the diffusion flame length: for the jets that mix most rapidly and most slowly.

The form of the function P_{2c} and, consequently, the length of the combustion chamber depend on the mode of delivery of the jets of fuel into the channel, on the number of jets, etc. We shall write a number of relationships that determine the length of the chamber for a number of typical elementary fuel delivery methods.

In the case of delivery of plane-parallel jets through slots in the upper and lower walls, the function P_{2c} takes the form

$$P_2 = \frac{1}{2}\left[\Phi\left(\frac{\frac{H_x}{2}+a_\tau+y}{a_c}\right) + \Phi\left(\frac{a_\tau-y-\frac{H_x}{2}}{a_c}\right) + \Phi\left(\frac{y+a_\tau-\frac{H_x}{2}}{a_c}\right) + \Phi\left(\frac{a_\tau+\frac{H_x}{2}-y}{a_c}\right)\right], \quad (5.12)$$

where $a_\tau = \int_0^{\frac{H_C}{2}} P_2\,dy$ is the displacement thickness of the air stream due to the fuel jet (the average width of the wall jet) and H_c is the height of the plane-parallel channel (chamber).

The oy axis of our coordinate system is perpendicular to the channel wall, the ox axis coincides with the channel axis, and the xoz plane is the plane of symmetry of the channel. Relation (5.12) was obtained by simple addition of the two solutions of the gradient diffusion equation without combustion for the wall jet (see Chapter II, §3) with impermeable wall boundary conditions.

Relation (5.12) satisfies Condition (5.3') at $y = y_c$, where y_c is the ordinate of the average flame front position.

For $\alpha > 1$, the end of the chamber is determined as the cross section in which the flame front closes at the channel wall, i.e., by the value of the function P_2 at

$$y = y_r = \pm \frac{H_x}{2}.$$

For sufficiently large x and $a_T \ll \sigma_c$ and $a_T \ll H_c$, the function P_{2c} approaches the simpler form

$$P_x(y_r) \approx \frac{a_r}{\sqrt{2\pi}\sigma_c}. \tag{5.13}$$

The same formula can be used for delivery of a jet from the wall of a round chamber of radius R_c with $a_T \ll R_c$. When the fuel is delivered in the form of thin axisymmetric jets uniformly distributed over the channel initial cross section and spaced far enough apart (to preclude interaction between the jets), the length of the chamber is determined by attainment of the stoichiometric proportion on the axis of each filament:

$$P_x = \frac{a_r^2}{2\sigma_c^2}, \tag{5.14}$$

where a_T is the present average radius of the filament (without combustion).

The average jet radius a_T and the displacement thickness are determined for the wall jet by the relations given in Chapter I, which have the following simple forms at the end of the flame, when the velocities have been equalized:

for a plane-parallel jet

$$a_\tau = a_0 \frac{1}{m},$$
(5.15a)

where a_0 is the initial height of the jet;

for an axisymmetric jet

$$a_\tau = a_0 \frac{1}{\sqrt{m}},$$
(5.15b)

where a_0 is the initial radius of the jet. Here $m = V_1/V_2$ is the ratio of the initial velocity of the stream of air and the jet of fuel. In the case of a large pressure gradient along the chamber, it is necessary to consider the changes in the cocurrent stream velocity and the density of jet volumes. In this case we have for the plane-parallel jet

$$a_\tau = a_0 V_2 \varrho_2(0)/\varrho_2(x) V_1(x).$$

The value of a_0 is determined for given values of m, α, and L_0 from the flow rate equation for plane-parallel wall jets:

$$\frac{\varrho_1 V_1 (H_\kappa - 2a_0)}{2\alpha L_0} = a_0 V_2 \varrho_2$$

or

$$a_0 = \frac{mnH_\kappa}{\alpha L_0 \left(1 + \frac{mn}{\alpha L_0}\right)2}$$
(5.16a)

and for axisymmetric jets uniformly distributed over the channel cross section by

$$a_0 = \sqrt{\frac{r_c n S_k}{\pi N_c a L_0 \left(1 + \frac{mn}{aL_0}\right)}}, \qquad (5.16b)$$

where N_c is the number of jets on the chamber area S_c, $\alpha = G_a/L_0 G_T$ is the average excess air ratio, and G_a and G_T are the per second flow rates of the air and fuel.

Substituting the appropriate expressions for P_{2c} and a_0 and the empirical functions $\sigma_c \approx k_c(x - x_0)\gamma$ (see Chapter III) into Relation (5.3), we obtain formulas for estimation of the combustion chamber length:

$$L_{ns} = x_0 + \left[\frac{H_k(n + L_0)}{\sqrt{2\pi}aL_0\left(1 + \frac{mn}{aL_0}\right)k_c}\right]^{\frac{1}{\gamma}}; \qquad (5.17a)$$

$$L_{0c} = x_0 + \left[\frac{1}{k_c}\sqrt{\frac{S_k(n + L_0)}{2\pi N_c aL_0\left(1 + \frac{mn}{aL_0}\right)}}\right]^{\frac{1}{\gamma}}. \qquad (5.17b)$$

It is seen from (5.17a) and (5.17b) that a monotonic increase in k_c is required in both cases for preservation of chamber length.

Relations (5.17a) and (5.17b) are valid for subsonic streams and for supersonic streams at design fuel jet outflow. However, the values of k_c will be different in each case (see Chapter III).

If the velocity increases insignificantly along the main mixing segment (for example, for a diverging subsonic chamber), the value of k_c in (5.17) is constant along the jet and determined by experimental data for free jets. In the case of deformation of the stream, regardless of its cause, (convergence of the flow in the nozzle or heat release), the function $\sigma_c(x)$ can be converted using theoretical and experimental data (see Chapter III, §§5 and 3).
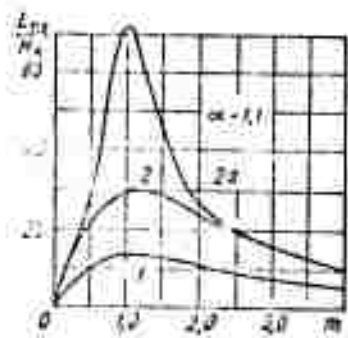
Figure 5.8. Relative length of plane-parallel chamber for various cocurrency parameters.

1 — supersonic jet in subsonic stream 2; 2a — supersonic jet in supersonic stream (2 — k_T according to Ferry); 2a — k_T according to A. R. Anderson [143]).

The simplest conversion assumes that the eddy diffusivity is constant. At large pressure gradients, there may be additional shear between the velocities of the cold and hot filaments and, as a result, a certain increase in the diffusivity along the deformation segment (see Chapter III, §5, subsection 4). As in the case of the turbulent spray of homogeneous mixture (see Chapter III, § 1), the dispersion increase due to lateral expansion of the combustion products was not observed in the experimental data. From the standpoint of the vortex model (see Chapter I), this can be explained by the fact that the combustion and subsequent expansion of the combustion products occur basically in the decay wakes, while both the scale of the total dispersion σ and that of the microturbulent dispersion σ_c, which is derived from the former, are determined by the new large vortices that form, the dimensions of which are determined basically only by the transverse shear of the two streams (the cocurrency parameter m).

Figure 5.8 presents a plot of the length of a constant pressure chamber, L_{pl}, into which fuel is delivered through plane-parallel slots at various rates (m = var). The length is given in multiples of channel height for $\gamma \simeq 1$: curve 1 corresponds to a supersonic jet in a subsonic stream, and curves 2 and 2a to subsonic and supersonic jets in a supersonic stream.

We see from Figure 5.8 that small values of L_{pl} can be obtained with $\alpha > 1$ only if the fuel is delivered at a velocity either much lower or much higher than the velocity of the air (m ≫ 1 or m < 0.5). We also see from Figure 5.8 that when the jet velocity is increased

without limit (the initial dimension of the jet is reduced), the channel length determined from the mixing length L_{mx} tends to zero (in much the same way as occurs during mixing in a Longwell reactor [10]). When the fuel jet delivery pressure is increased indefinitely, there is, in principle, no limit to the possible shortening of the combustion chamber. The condition $m \ll 1$ is more interesting than $m \gg 1$ because of the possibility of obtaining larger exhaust momenta at smaller displacement thicknesses.

Let us consider the length of the chamber in which fuel delivery is distributed over the wall at a length L_d. Distributed delivery is necessary to improve heat protection and reduce friction. The fuel concentration at the wall (weight fraction), g_2, is written in this case in the form

$$g_2(x, 0) = \int_0^{L_a} \frac{a_0'}{n_0 \mid \sqrt{2\pi}\sigma} \, dx_0; \text{ for } x > L_a,$$ (5.18)

where $n_0 = \frac{\rho_1}{\rho_{20}}$, ρ_{20} is the density of the injected gas, ρ_1 is the density of the cocurrent stream, a'_0 is the fuel delivery distribution density and $\sigma_c^2 = k_c^2 (x - x_0)^2$ is the dispersion of fuel particles coming from a point x_0 on the wall at point x.

The coefficient k_c varies with the cocurrency parameter m as described in Chapter III, §3, in accordance with the same universal laws as for free jets.

With uniform delivery of the fuel over the length L_d, we have from the flow rate equation

$$a_0' = \frac{a_0}{L_n} = \frac{\rho_1 H_1 V_1}{2a L_n \rho_2 V_2 L_0},$$ (5.19)

where a_0, ρ_2, and V_2 are the displacement thickness, density, and longitudinal velocity of fuel volumes at the end of the delivery length.

Substituting the value of g_2 into (5.3'), which determines the length of the flame, we obtain

$$L_p = \frac{L_d e^{L_d \gamma_1}}{e^{L_d \gamma_1} - 1}.$$
(5.20)

where L_d is the distributed fuel delivery length, $\gamma_1 = 1/L_{p1}$, and L_{p1} is the length of the plane-parallel chamber when all fuel is delivered in the initial cross section x = 0.

It is evident from (5.20) that as $L_d \to 0$ and $L_p \to 1/\gamma_1 = L_{p1}$, i.e., as the delivery length tends to zero (at a constant total fuel flow rate), the chamber length tends to the length L_{p1} of a chamber with plane-parallel delivery. We also see that the length of a channel with distributed fuel delivery is always larger than for plane-parallel delivery and, in particular, that the channel length with distributed delivery is 60% larger when $L_d = L_{p1}$.

We see from this that distributed fuel delivery is used to better advantage for film cooling of the channel walls and to reduce frictional losses (see §5). From the standpoint of high caloric combustion, this type of delivery is inferior to the cases considered previously. In coordinated solution of heat exchange, combustion, and friction problems, the optimum variant is distributed delivery of a fuel curtain along the chamber walls with simultaneous delivery of jets at the center of the chamber. The value of P_{2c} in condition (5.3'), which determines the length of the chamber, is then assigned as the sum of the encounter probabilities from all of the particular fuel delivery solutions.

Let us consider the case of excess delivery of plane-parallel fuel jets from the wall ($\alpha < 1$). Here the chamber length is estimated from the oxidizer concentration. The total probability of fuel from the upper and lower jets (curtains) reaching the center of the channel with microturbulent mixing, P_{2c}, is assigned, as before,

by Formula (5.12). Substitution of the value on the channel axis, $P_2(0)$, into Condition (5.3') yields the relation

$$\Phi\left(\frac{\frac{H_\text{u}}{2} - a_\tau}{a_c}\right) \approx \frac{L}{n + L}, \tag{5.21}$$

since when

$$\left(\frac{H_\text{u}}{2} + a_{na}\right)\Big/ a_c \geqslant 3$$

we have $\Phi(3) \approx 1$ or when

$$\left(\frac{H_\text{u}}{2} - a_{na}\right) \ll a_c$$

for very rich mixtures, we obtain

$$\frac{H_\text{u}}{2} - a_\tau \approx \frac{L a_c \sqrt{2\pi}}{n + L_0}$$

or

$$L_\text{u} = x_0 + \left[\frac{amH_\text{u}}{aL + mnk_c\sqrt{2\pi 2}}\right]^{1/\eta}. \tag{5.21'}$$

It is clear from (5.21') that when $\alpha \ll 1$, fuel delivery through plane-parallel jets from the wall leads, by itself, to small chamber lengths, and that the chamber will be shorter the larger m and the smaller α. Thus, the main problem for the chambers of the GPVRD hypersonic ramjets under design in the USA (see the paper by Ferry et al. [49]) for $m \gg 1$, $\alpha < 1$ with supersonic stream velocities in the chamber will be blockage of the channel by the large displacement thicknesses a_T rather than combustion efficiency.

For a combustion chamber with an arbitrary complex arrangement of the fuel delivery sources, in which case the addition of the concentration fields from many sources is possible at any given point in the chamber, it is simpler to estimate the length of the chamber not as the length of the diffusion flame from, for example, the most

weakly mixed filament, but as the average combustion efficiency η
over the cross section of the chamber. The average combustion
efficiency η at an average excess air ratio $\alpha \geq 1$ at the end of the
chamber is determined as the ratio of the per second flow rate of
burned fuel in the particular cross section of the chamber to the
total fuel flow rate. At an average $\alpha < 1$ at the end of the chamber,
efficiency is determined by the relative fraction of reacted oxidizer.
In other words, combustion efficiency is calculated on the basis of
the deficient component: from the burned fuel when $\alpha > 1$ and from
the used oxidizer when $\alpha < 1$. We note that α decreases along the
chamber in cases of distributed fuel delivery, so that whether $\alpha > 1$
or $\alpha < 1$ is determined at the end of the chamber.

Analytically, this definition of combustion efficiency is
written in the form of the following approximate relation (see §3):

$$
\tau = \frac{c_2 \int\limits_{\substack{P_1 < \frac{n}{n+L}}}^{\nu_T} u P_{2c}\, dy + \frac{c_1}{L} \int\limits_{\substack{P_1 > \frac{n}{n+L}}} (1 - P_{2c}) u\, dy}{\varepsilon \int\limits_0^{\frac{H_x}{2}} c_2 P_{2c} u\, dy}. \tag{5.22a}
$$

The first integral is taken over values of y at which the local
excess air ratio α are larger than unity $\left(P_1 < \frac{n}{n+L}\right)$, and the second
over the values of y at which the local α are smaller than unity
$\left(P_1 \geq \frac{n}{n+L}\right)$.

At the end of the chamber, where the velocity of the fuel
volumes is practically equal to the stream velocity, Formula (5.22a)
can be simplified to

$$
\eta = \frac{c_2 \int\limits_{\substack{P_1 < \frac{n}{n+L}}} P_{2c}\, dy + \frac{c_1}{L} \int\limits_{\substack{P_1 > \frac{n}{n+L}}} (1 - P_{2c})\, dy}{c_2 \int\limits_{-\frac{H_x}{2}}^{\frac{H_x}{2}} P_2\, dy}, \tag{5.22b}
$$

where $\dot{\xi} = 1$ when $\alpha \geq 1$ and $\xi = \alpha$ when $\alpha < 1$, P_{2c} is the total probability that fuel volumes will reach an arbitrary point of the chamber, as constructed from the "grey" mixing dispersions of all fuel delivery sources, ρ_1 and ρ_2 are the densities of the reacting gases, and u is the average velocity profile in the chamber.

In a first approximation with $\rho_1 \sim \rho_2$, this variation along the chamber is determined by the one-dimensional formulas from the efficiency value obtained from (5.22b), and the variation along y — by the relative variation of the elementary velocity profiles without combustion.

We note that, in conclusion, the efficiency value is calculated for mixing without consideration of the chemical kinetics, i.e., it is an efficiency that takes account of the physical incompleteness of fuel combustion. The chemical combustion efficiency, which is determined by kinetics and, in particular, by the kinetics of the heavy fractions of complex hydrocarbon fuels, can be taken into account in calculating the mass average temperature profile of the combustion products. The true temperature at chamber length x is determined as the product of the adiabatic temperature corresponding to the local value of α by a function of the chemical combustion efficiency that is monotonic over x: $\eta x(x)$. Theoretical estimations of this function can be made from the ignition delay and combustion times known for each fuel.

The chemical potentials are quite high (≥ 0.98) for subsonic chambers more than a meter long with $\alpha \geq 1$ and pressures around atmospheric; in these cases, therefore, it can be left out of account in view of the error level inherent in the relations given above. In all other cases, e.g., in the case of very low pressures, $p < 0.3$ atm and in the case of very high stream velocities and low initial mixture temperatures, the average chemical combustion efficiency over the chamber cross section at the end of the chamber can be calculated from a known chemical kinetic time of the type (5.11) and

the average stream velocity. The mass average temperature of the
original mixture in this relation is determined as the statistical
average temperature from the temperatures of the fuel T_2, the
oxidizer T_1, and the combustion products T_3:

$$\bar{T} = \frac{\varrho_1 T_1 \bar{P}_1 + \varrho_2 T_2 \bar{P}_2 + \varrho_3 T_3 \bar{P}_3}{\varrho_1 \bar{P}_1 + \varrho_2 \bar{P}_2 + \varrho_3 \bar{P}_3},$$

where

$$\bar{P}_1 = \frac{l(\alpha - \eta)}{1 + \alpha L}; \quad \bar{P}_2 = \frac{(1 - \eta)}{1 + \alpha L}; \quad \bar{P}_3 = \frac{\eta(1 + L)}{1 + \alpha L}$$

are the probabilities of appearance of oxidizer, fuel, and combustion
product particles, respectively, averaged over the chamber cross
section (for $\alpha > 1$).

The values of the functions $P_1(x); P_2(x); P_3(x)$ are also the total
relative cross sectional areas of a plane-parallel chamber that are
occupied by air, fuel, and combustion product volumes or, in other
words, the relative displacement thicknesses:

$$\bar{P}_1 = \frac{G_1 - L\eta G_2}{G_1 + G_2} = \frac{H_\kappa - 2a_2 - 2a_3}{H_\kappa}; \quad \bar{P}_2 = \frac{2a_2}{H_\kappa}; \quad \bar{P}_3 = \frac{2a_3}{H_\kappa},$$

where η is the physical combustion efficiency defined by (5.22), L is
the coefficient of stoichiometry, $2a_2$ is the displacement thickness
of the cocurrent stream by unburned fuel volumes, and $2a_3$ is the
displacement thickness of the cocurrent stream by combustion products.

Using the methods set forth previously, the relative temperature
profiles over the chamber cross section can be determined from the
displacement thicknesses obtained in this way and the known disper-
sions of the volumes along the chamber.

§3. Afterburning of a Coaxial Fuel Jet in the Cocurrent Stream of a Cylindrical Channel[*]

A typical practical example of this type of chamber is that of the rocket ramjet engine [115]. In the RRJ, the products of incomplete combustion in the main engine or generator are delivered in the form of one or more jets into an afterburner, where combustion is completed.

1. Method of Calculating Combustion Efficiency

Figure 5.9 presents a diagram of mixing of a coaxial jet in a channel. The fuel jet may be either subsonic or supersonic. In the latter case, when the generator pressure is high enough, the jet flowing out of it may be underexpanded, giving rise to a system of shocks in which the pressures of the jet and the surrounding stream are equalized. On the figure, x_1 indicates the distance to the isobaric cross section.

As in the case of free jets, $a_T(x)$ describes the behavior of the statistical average jet radius along the stream and has the same connotation as in that case.

The numerals 1, 2, and 3 identify the average volume concentration profile of the jet substance (which is identical to the probability of observation of jet substance introduced in §1, subsection 2 of Chapter I), the concentration profile determined by molecular mixing, and the average velocity profile, respectively.

The profile describing the overall molecular mixing in turbulent transport of gas volumes is obtained in the same way as in the case of the free jet, by the operation of determining the most

[*]Ye. A. Meshcheryakov assisted in the calculations of §3 and §5.
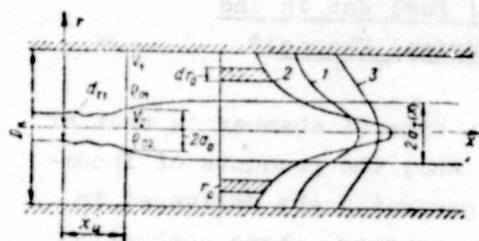
Figure 5.9. Mixing diagram of coaxial streams in channel.

1 — profile of average jet volume concentration P_2 (a_T, σ, and r); 2 — concentration profile determining molecular mixing, P_2 (a_T, σ_{MT}, r); 3 — average velocity profile

$$u(r) = [u_1(p) - u_2(p)] \, p \, (a_V, \sigma_V, r) + u_2(p)$$

probable molecular composition at a particular point of the chamber cross section. This operation consists essentially in redistribution of particles with different molecular compositions over the cross section at each point in time. To obtain profile 2, volumes of a certain molecular composition that are scattered over the cross section as a result of the turbulent nature of the flow must be located in the neighborhood of the jet axis in such a way that the relative concentration of jet substance will decrease with increasing distance from the axis.

The profile regrouping that results from this operation will obviously be less diffuse than the real average concentration profile, and the difference between them can be used to characterize the lag of the effective molecular mixing with turbulent exchange. We note that the definition of the "most probable molecular composition at a given point" is, strictly speaking, valid only for a Gaussian distribution of this composition over the chamber cross section in the neighborhood of the point under consideration. At points near the wall, we can obviously speak with less license of the mathematical expectation of a molecular composition at a given point. The concentration profiles for channel flow are approximated by the solution of the diffusion equation with the initial condition $P_2 = 1$ for $0 \leq r \leq a_T$ and $P_2 = 0$ for $a_T \leq r \leq R$ and the boundary condition

$$\frac{\partial P_2}{\partial r}\bigg|_{r=R} = 0 \quad \text{(boundary impermeable):}$$

$$\frac{\rho_1}{\rho_{02}} = P_2(r, a_r, \sigma) = \frac{a_r^2}{R^2} + \sum_{n=2}^{\infty} \frac{\frac{a_r}{R} I_1\left(\mu_n \frac{a_r}{R}\right)}{\frac{\mu_n}{2} I_0^2(\mu_n)} I_0\left(\mu_n \frac{r}{R}\right) e^{-\mu_n^2 \frac{\sigma^2}{2R^2}}, \qquad (5.23)$$

where the μ_p are the roots of the equation

$$I_1(\mu_n) = 0; \qquad (5.23^*)$$

$I_0(x)$ and $I_1(x)$ are Bessel functions of the zeroth and first orders, ρ_1 is the partial density of jet substance in the mixture, ρ_{02} is the initial density of the jet substance, and R is the chamber radius.

For profile 2, the parameter σ^2 will be denoted by σ_{MT}^2. The ratio $N = \frac{\sigma_{MT}}{\sigma}$ which indicates the relation between profiles 1 and 2, characterizes the fraction of molecular mixing in the total transport as in the case of the free jet.

The function $P_2(a_r, \sigma, r)$ can be used to describe the continuous development of the jet substance concentration profile from rectangular at the delivery nozzle exit ($\sigma^2 = 0$) to uniform (as $\sigma^2 \rightarrow \infty$) with a limiting probability $P_2(\infty) = \frac{a^2}{R^2}$ attained on complete equalization of the concentration.

The velocity profile is approximated by a similar expression with the parameters a_V and σ_V:

$$\frac{u - u_1}{u_2 - u_1} = P_{2V}(a_V, \sigma_V, r), \qquad (5.24)$$

where u_1 and u_2 are the cocurrent stream and jet velocities in the cross section under consideration. Here the boundary condition $\left.\frac{\partial P_{2V}}{\partial r}\right|_{r=R} = 0$ is essentially the assumption that there is no friction at the wall. As in the case of the free jet, the turbulent Prandtl number equals $Pr = \frac{\sigma_V^2}{\sigma^2}$.

We take note of a singularity of the parameter σ^2 when it is used to describe mixing in a channel. In contrast to the case of the free jet, for which σ^2 has the sense of the mean square of the deviation (dispersion) of the particles from their average trajectories, this is not so for chamber flows in which jet substance reaches the wall. In fact, in this case

$$\sigma^2(x) = 2 \int_0^x \left(\frac{D}{u}\right)_{sp} dx,$$

where D is a certain new function that takes the effects of the chamber walls into account. However, since profile equalization has already taken place in practice at σ smaller than the pipe radius, the dispersion can, as before, be determined from the same relation as that for the free jet.

In the channel, as contrasted to the free jet, the density ρ_{02} of the jet and the cocurrent stream and jet velocities will no longer be constant because of the pressure change. For relatively low stream velocities, it can be assumed that the variation of ρ_{01} and ρ_{02} along the channel will be adiabatic and that u_1 and u_2 vary in accordance with the energy equation for an adiabatic process.

Let us write the conservation laws for flow in a cylindrical channel.

The equations of conservation of cocurrent stream and jet materials will be

$$2\pi \int_0^R \rho_1 u r \, dr = 2\pi \rho_{01} \int_0^R [1 - P_2][(u_2 - u_1) P_2 v + u_1] r \, dr = G_1;$$ (5.25)

$$2\pi \int_0^R \rho_2 u r \, dr = 2\pi \rho_{02} \int_0^R P_2 [(u_2 - u_1) P_2 v + u_1] r \, dr = G_2,$$

where G_1 and G_2 are the flow rates of the cocurrent stream and the jet.

The momentum equation is

$$2\pi \int_0^R \varrho u^2 r\,dr + p\pi R^2 = 2\pi \int_0^R [(\varrho_{02} - \varrho_{01})P_{2V} + \varrho_{01}][(u_2 - u_1)P_{2V} + u_1]^2 r\,dr +$$
$$+ p\pi R^2 = G_1 u_{01} + G_2 u_{02} + p_0 \pi R^2, \qquad (5.26)$$

where p_0, u_{01}, and u_{02} denote the parameters in the initial chamber
cross section (or in the isobaric cross section in the case of non-
design outflow).

The unknown parameters on the left sides are

$$p(x), \ a_1(x), \ a_{1'}(x), \ \sigma(x), \ \sigma_{1'}(x), \ u_1(x), \ u_2(x), \ \varrho_{01}(x), \ \varrho_{02}(x).$$

Here the velocities and densities of the $i\underline{^{th}}$ gas are related to the
pressure by

$$\frac{\varrho_{0i}(p)}{\varrho_{0i}(p_0)} = \left(\frac{p}{p_0}\right)^{1/k} \qquad (i = 1, 2);$$
$$\frac{u_i^2(p)}{2} = \frac{u_i^2(p_0)}{2} + \frac{k}{k-1}\frac{p_0}{\varrho_{0i}(p_0)}\left[1 - \left(\frac{p}{p_0}\right)^{\frac{k-1}{k}}\right]. \qquad (5.27)$$

Assigning the Prandtl number, we have a system of seven equations
with eight unknowns. If the function $\sigma^2(x)$ is known, the number of
equations is sufficient for calculation of all parameters defining
the averaged profiles. If, moreover, the behavior of $\sigma_{u_1}^2(x)$ is
known, it is possible to plot the molecular mixing profile $P_2(a_\tau, \sigma_{u\tau}, r)$
(Figure 5.9, curve 2).

We note that Relations (5.27), which are valid accurate to the
terms for dissipation outside of the mixing zone, are violated in
the mixing zone itself because of the entropy increase in "black and
white" mixing that results from inelastic collisions of volumes.
This effect is stronger, the greater the difference between the stream
velocity, but at low velocities (in any event at $M \leq 1$), when the
relative fraction of kinetic energy in the overall energy flux balance
is small, it can be neglected at any ratio between the velocities.

Efficiency is determined from the profiles obtained on calculating the "cold" mixing of the jets.

When it is remembered that particles with a certain molecular composition α_0 have different velocities, which are determined by their positions, and if we denote by $P_2(r, r_0, \sigma_c)$ the probability density of occurrence at points with radius r [r_0 is the radius on the quasilaminar profile 2 (Figure 5.9) that corresponds to this concentration], the expression for combustion efficiency can be written*

$$\eta = \frac{\int_0^R \int_0^R \eta_* P_2(r_0, a_T, \sigma_{MT}) P_2(r, r_0, \sigma_T)[(u_2 - u_1) P_{2V}(r, a_V, \sigma_V) + u_1] r \, dr \, dr_0}{\int_0^R \int_0^R P_2(r_0, a_T, \sigma_{MT}) P_2(r, r_0, \sigma_T)[(u_2 - u_1) P_{2V}(r, a_V, \sigma_V) + u_1] r \, dr \, dr_0}, \qquad (5.28')$$

where

$$p_2(r, r_0, \sigma_T) \, dr_0 = \left[\frac{r r_0}{R^2} + \sum_{n=2}^{\infty} \frac{\frac{r_0}{R^t} I_0 \left(\mu_n \frac{r_0}{R} \right)}{\left(\frac{\mu_n}{2} \right) I_0^2 (\mu_n)} I_0 \left(\mu_n \frac{r}{R} \right) e^{-\frac{\mu_n^2 \sigma_T^2}{2 R^2}} \right] dr_0,$$

$$\eta_* = 1 \quad \text{for } \alpha > 1 \quad \text{and} \quad \eta = [(1 - \alpha) \eta_x + \alpha] \qquad \text{for } \alpha < 1$$

is the solution of the diffusion equation for an infinitesimally thin ring of radius r_0, η_x is the chemical efficiency in the generator (the fraction of fuel utilized in combustion in the generator), $\alpha = \frac{\varrho_1}{\varrho_2 L} = \frac{n}{L} \frac{p_1(\sigma_{MT})}{p_2(\sigma_{MT})}$ is the local excess oxidizer ratio in molecular mixing, and L is the coefficient of stoichiometry during burning of the jets.

The variation of $\eta \alpha$ can also be assigned differently:

---

*In the simplified efficiency expression (5.22), the same velocity $u(r_0)$ was assumed for all volumes with a certain concentration α_0.

$$\eta_a = 1 \quad \text{for} \quad p_2(r_0, a_{\tau}, \sigma_{M\tau}) < \frac{n}{n+L};$$

$$\eta_a = [(1-\alpha)\eta_z + \alpha] \quad \text{for} \quad p_2(r_0, \dot{a}_{\tau}, \sigma_{M\tau}) > \frac{n}{L+n}.$$

After integration over r, Relation (5.28') is written

$$\eta = \frac{\int_0^R \eta_a(r_0\sigma_{M\tau}) \, p_2(r_0, a_{\tau}, \sigma_{M\tau})[(u_2 - u_1) p_2 v + u_1 r_0] dr_0}{\int_0^R p_2(r_0, a_{\tau}, \sigma_{M\tau})[(u_2 - u_1) p_2 v + u_1 r_0] dr_0}.$$

Since

$$\int_0^R p_2(r, r_0, \sigma_{\tau}) r \, dr = r_0; \quad \text{and} \quad p_{2v}(r_0, a_v, \sigma_v, \sigma_{\tau}) =$$

$$= \int_0^R p_2(r, r_0, \sigma_{\tau}) p_2(r, a_v, \sigma_v) r \, dr = \left(\frac{a_v}{R}\right)^2 r_0 +$$

$$+ \frac{a_v}{R} r_0 \sum_{n=2}^{\infty} \frac{I_1\left(\mu_n \frac{a_v}{R}\right) I_0\left(\mu_n \frac{r_0}{R}\right)}{\left(\frac{\mu_n^2}{2}\right) I_0^2(\mu_n)} e^{-\mu_n^2 \frac{(\sigma_{\tau}^2 + \sigma_v^2)}{2R^2}}.$$

For a given σ^2 and Prandtl number, all parameters that appear in the definition of efficiency are determined from the system of equations (5.25), (5.26), and (5.27).

The numerical examples given below for the case of a sonic fuel jet and a subsonic cocurrent stream were carried through on the assumption of constant pressure along the chamber (approximately the situation that prevailed in the corresponding experiments). This approximation, which was found to be adequate for quantitative agreement between calculation and experiment, greatly simplified the computational aspect of the examples. In this case, the equation system assumes the form

$$m k_1 + (1-m) k_3 = \frac{a_0^2}{2},$$

$$m^2 (1-n) k_1 + 2nm(1-m) k_2 + 2m(1-m)(1-n) k_3 +$$

$$+ n(1-m)^2 k_4 + (1-n)(1-m)^2 k_5 = \frac{a_0^2}{2}(1-nm^2),$$

(5.28)

where

$$k_1 = \int_0^R p_2(a, \, \sigma, \, r) r dr = \frac{a_\tau^2}{2}; \quad k_2 = \int_0^{VR} p_2(a_V, \, \sigma_V, \, r) r dr = \frac{a_V^2}{2};$$

$$k_3 = \int_0^R p_2(a_1, \, \sigma, \, r) p_2(a_V, \, \sigma_V, \, r) r dr; \quad k_4 = \int_0^R p_2^2(a_V, \, \sigma_V, \, r) r dr;$$

$$k_5 = \int_0^R p_2(a_1, \, \sigma, \, r) p_2^2(a_V, \, \sigma_V, \, r) r dr.$$

Here a_0; $m = \frac{u_{01}}{u_{02}}$, $n = \frac{\varrho_{01}}{\varrho_{02}}$ are the parameters in the isobaric cross section.

2.   Comparison of Calculated Results with Experimental Data

Combustion efficiencies were calculated for the conditions of A. A. Klyachko's model experiments. A central fuel jet was formed in these experiments by burning a model solid fuel in a generator. The generator, which had interchangeable converging nozzles, was mounted on special pylons inside the air duct. The efficiencies were determined at known flow rates from the measured momentum of the jet flowing out of a converging nozzle at the end of the after-burner.

Because of the nondesign outflow of the fuel jet, mixing was calculated starting from the isobaric cross section, in which the velocity coefficient was assumed equal to unity for the converging nozzle in accordance with B. A. Zhestkov's experiments [1]. The length of the nondesign segment (x_0 on Figure 5.9) was disregarded.

Figure 5.10 shows an example of efficiency calculation and the experimental data, plotted against the length of a cylindrical chamber at a cocurrent air temperature of ~340° K and $\alpha_{av} = 2$.
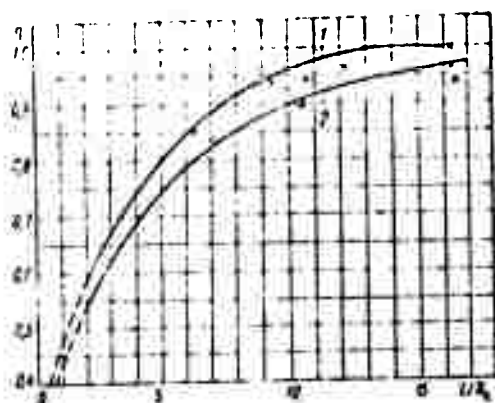
Figure 5.10. Combustion efficiency as a function of relative chamber length.

$\times$, Δ — experiment; ――― — calculation ($\kappa \approx 2$, $D_C = 100$ мм)

The calculations were performed for the two model fuels used in the experiments:

$$L = 2,8; \quad n = \frac{\varrho_{0n}}{\varrho_{0r}} = 1,2$$

(curve 1); L = 5.14; n = 2.7 (curve 2); air temperature ≈350° K; Pr = 0.5 and N = σ_{MT}/σ = 0.35.

By way of example, Figure 5.11 shows calculated and experimental plots of combustion efficiency against average excess air ratio. We see from the diagram that the efficiency decreases at $\alpha > 3$, something that is not explained by the laws of the mixing processes. L. A. Klyachko explains this decrease in combustion efficiency as due to a lowering of the chamber temperature levels with increasing excess air ratio, after which the afterburning of solid particles begins to be the factor limiting heat release (in special experiments using an attachment that broke the fuel jets up into several smaller jets, an increase in combustion efficiency was observed at low α because of the improved mixing, while the efficiency even decreased at large α).

Figures 5.12 and 5.13 present examples of calculations and experimental data illustrating the influence of cocurrent air temperature and generator nozzle diameter on combustion efficiency. The results indicate that the calculation method correctly describes the variation of combustion efficiency with geometry and the parameters of the streams.
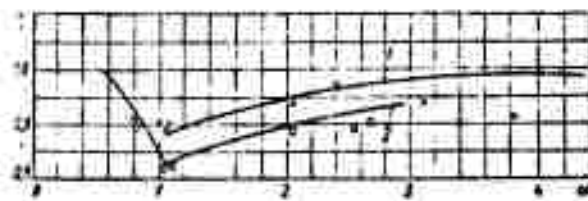
Figure 5.11. Combustion efficiency as a function of excess air ratio (L/D$_c$ = 10.5; D$_c$ = 100 mm; d$_{gg}$ = 10 mm).

§4.   Jet Trajectories in a Closed Entraining Stream

Gas may be delivered into the combustion chamber of an actual rocket ramjet engine in the form of several jets that are directed at an angle to the direction of the airstream. This gives rise to the problem of calculating the trajectories of a group of jets in a closed entraining stream. Past investigations have been devoted for the most part to the behavior of a single jet flowing out into an open stream at a large angle.

Under the present heading, we set forth an approximate method for calculation of jets in channels that are directed at an angle to the main stream.

Certain elementary physical arguments and experimental data are used in this method.[*]

The aerodynamic force acting on the single jet can be treated as no different in nature from the force acting on a solid body placed in the stream. It can therefore also be described by an aerodynamic drag coefficient c_x, representing the dimensionless proportionality factor between the force acting on a unit midsection area and the velocity head $\frac{\rho_1 u_1^2}{2}$ of the free stream. Using this

---

[*]F. K. Yevzerova participated actively in development of the procedure.
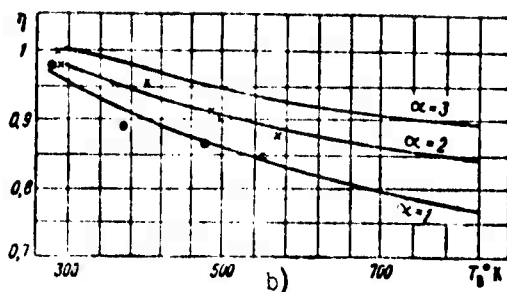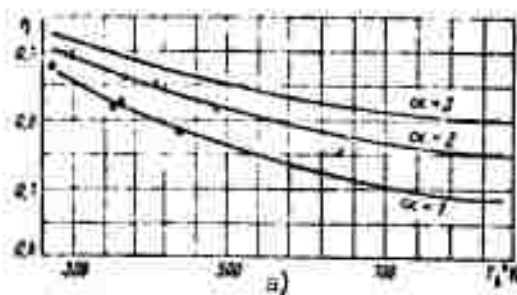
Figure 5.12. Influence of co-current air temperature on combustion efficiency.

$\bullet$, $\times$ — (α = 1.2, L/D_c = 10.5; D_c = 100 mm; d_{gg} = 10); a — L_0 = 5.14; b — L_0 = 2.8.

argument, a method for calculation of the jet axis (for application to a jet of dropping liquid in a stream of gas) was proposed in [116].

Aerodynamic forces of another kind must be considered in studying the behavior of a plane-parallel jet issuing at an acute angle to a certain surface. Suction between the jet and the surface creates a partial vacuum, and the resulting pressure gradient (Δp) deflects the jet, perhaps even back to the surface [in the so-called Coanda effect (see §4 of Chapter II and [117])]. The gradient Δp depends on the velocity head $\frac{\rho_a w_a^2}{2}$ of the jet and on the initial inclination angle α_0 [117].

In the case of outflow of several round jets spaced sufficiently close together, the formation of a film that is practically imperme-able to the entraining stream is possible at a certain distance; because of the above effect, this stream will be deflected consid-erably more rapidly, and its trajectory may even deviate downward from the maximum position reached.

It is also necessary to remember that the aerodynamic drag coefficients in closed channels (in chamber flows) depend strongly on the degree to which the channel cross section is encumbered.
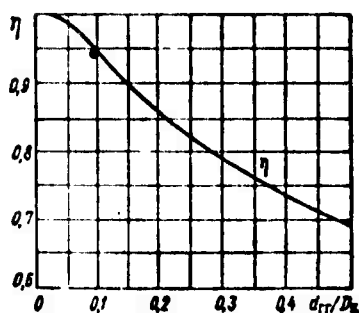
Figure 5.13. Combustion efficiency as a function of generator nozzle diameter.
● — experiment; —— — calculation.

It is shown in the literature [118] that the drag coefficient of a blunt body can be written

$$c_x = \frac{[1 + \sqrt{\eta(1-f)} - f]^2}{1-f} \cdot \frac{1}{f^2} ,$$

where $f = F_{fr}/F_c$ is the ratio of the cross sectional area not filled by the body (the free area) to the total chamber cross sectional area, η is the so-called inlet softening coefficient which depends, among other things, on the convergence after the flow past the obstacle. If such convergence does not occur, we have $\eta = 0$ and the expression for c_x assumes the form

$$c_x = \frac{1-f}{f^2} . \tag{5.29}$$

which we shall use below.

Let us now consider the particular case of a chamber in which jets are delivered at the same angle to the airstream from nozzles positioned at equal distances from the chamber axis (Figure 5.14).

The equation of the jet axes can be written by equating the aerodynamic to the centrifugal force:

$$-\frac{G_2 u_2}{R} = c_{x0} \frac{\rho_1 u_1^2}{2} L(x)\sin^2\alpha + L(x)\Delta p. \tag{5.30}$$

Here G_2 is the generator gas flowrate, u_2 is the initial velocity of the jet, R is the present radius of curvature of the trajectory, α is the present angle between the main stream velocity vector and the axis, $L(x)$ is the characteristic midships section width of the jet, Δp is the characteristic expansion, which is, generally speaking, a function of the velocity heads $\frac{\rho_2 u_2^2}{2}$ and $\frac{\rho_1 u_1^2}{2}$, the angle α, the

Figure 5.14. Calculated results for jet axes.

$\bullet$, 1 — single jet $(\alpha_0 - 18^\circ)$;
$\times$, 2 — group of 20 jets $(\alpha_0 - 18^\circ)$;
$\blacktriangle$, 3 — group of 20 jets $(\alpha_0 - 12^\circ)$;
$\blacksquare$, 4 — group of 20 jets $(\alpha_0 - 6^\circ)$

initial distances between jets, etc.:

$$2\frac{\Delta p}{\varrho_1 u_1^2} = c_{x1}\left(\frac{\varrho_1 u_1^2}{2}, \ \frac{\varrho_2 u_2^2}{2}, \ a, \ldots\right).$$

In choosing numerical values for the coefficients c_{x0} and c_{x1}, it is necessary to consider the aforementioned dependence of the drag coefficients on chamber encumbrance.

If $y = y_0(x)$ is the equation of the jet axis, we know that

$$\frac{1}{R} = \frac{y_0''}{(1 + y_0'^2)^{3/2}}, \quad \sin \alpha = \frac{y_0'}{\sqrt{1 + y_0'^2}}.$$

Since the initial angle α_0 is small, $y_0' \ll 1$, and we may write instead of (5.30)

$$y_0'' = -(c_{x1} + c_{x0}y_0') \frac{\varrho_1 u_1^2}{2} \frac{L(x)}{G_2 u_2}. \tag{5.31}$$

Since $G_2 = k\pi w_0^2 \varrho_2 u_2$, where k is the number of jets, we denote

$$a = c_{x0} \frac{nm^2}{2\pi k}\bar{L}, \quad b = c_{x1}\frac{nm^2}{2\pi k}\bar{L},$$

to obtain instead of (5.31)

$$\bar{y}_0'' = -(\bar{a}y'' + b)$$
$$\left(\bar{L} = \frac{L}{a_0}; \ \bar{y}_0 = \frac{y_0}{a_0}; \ \bar{x} = \frac{x}{a_0}\right). \tag{5.32}$$

In the particular case b = 0, we obtain on substituting a certain average value for the function a(x) (for simplicity in integration)

$$\bar{u}_0(\bar{x}) = \frac{1}{a} \ln(a\bar{x} \, \text{tg} \, \alpha_0 + 1).$$ (5.33)

This solution yields the equation for the axis of a single jet. When it is not necessary to consider cross section encumbrance, reduction of experimental data (for example, Shandorov's experiments [1]) yields

$$c_{x0} \simeq 3.8 - 5.3.$$

We shall henceforth assume $c_{x0} \simeq 4.4$.

To calculate the midships width L(x), the dimensions of the "shading" region created by the jets must be characterized in some fashion. For this purpose, we introduce the notion of the radius a_c of a jet with apparent mass. The value of $a_c(x)$ characterizes the dimensions of the region in which the accelerating effect of the jet is significant. We shall assume that within a region of radius $a_c(x)$, the volumes of generator gas and of the jet move at a certain average velocity $\bar{u}_c$, which we define for a round jet by the relation

$$\bar{u}_c = \bar{u}_1 \frac{a_0^2}{a_1^2}.$$

Then $a_c(x)$ is determined from the momentum conservation equation:

$$\varrho_{02} a_1^2 \bar{u}_c^2 + \varrho_{01}(a_c^2 - a_1^2)\bar{u}_c^2 = \varrho_{02} a_0^2 \bar{u}_1^2.$$

From this we have

$$\bar{a}_c(x) = \bar{a}_1 \sqrt{\left(1 - \frac{1}{n}\right) + \frac{\bar{a}_1^2}{n}}.$$ (5.33*)

It is henceforth assumed (for a single jet) that

$$\bar{L}(x) = 2\bar{a}_c(x).$$

Another particular case, $a = 0$, can be used to find an equation for the trajectory of a continuous sheet after merging of a uniform series of round jets from (5.32):

$$\bar{y}_0(\bar{x}) - \bar{y}_0(\bar{x}_{c,s}) = (\bar{x} - \bar{x}_{c,s}) \operatorname{tg} a_{c,s} - \frac{b(\bar{x} - \bar{x}_{c,s})^2}{2} . \qquad (5.34)$$

Here $\bar{x}_{mg}$ denotes the coordinate of the point of sheet formation and α_{mg} the inclination angle of the jet at the merging point. If the function $\bar{y}_0(\bar{x})$ increases monotonically for a single jet, we have in our case a maximum at the point

$$\bar{x}_{max} = \bar{x}_{c,s} + \frac{\operatorname{tg} a_{c,s}}{b} \qquad (5.35)$$

$$\left(\operatorname{tg} a_{c,s} = \frac{\operatorname{tg} a_0}{a \operatorname{tg} a_0 \bar{x}_{c,s} + 1} \right),$$

equal to

$$\bar{y}_{0\ max} = \bar{y}_0(\bar{x}_{c,s}) + \frac{\operatorname{tg}^2 a_{c,s}}{2b} . \qquad (5.36)$$

When $\bar{x} > \bar{x}_{max}$, the trajectory according to (5.34) is deflected downward and again assumes the value $\bar{y}_0(\bar{x}_{mg})$ at

$$\bar{x} = \bar{x}_{c,s} + \frac{2 \operatorname{tg} a_{c,s}}{b} . \qquad (5.37)$$

In the light of the above, the calculation for a group of jets spraying from nozzles arranged around a circle of radius R_c at intervals $l_o = \frac{2\pi R_c}{k}$ will be carried out in two stages, and since the manner in which the coefficients c_{x0} and c_{x1} vary along the length has not been studied in detail, we shall assume only one of the coefficients to be nonzero in each of the steps.

In the first step, up to the time of formation of the continuous sheet, the trajectory of the jets is described by Equation (5.33), but c_{x0} is calculated with consideration of the encumbrance of the stream. The merging point corresponds to the $x = x_{mg}$ at which the present distance between jets (l) becomes equal to the shading diameter $2a_c(x)$. Hence the merging condition

$$a_c(x_{c.a}) = \frac{l}{2} \simeq \frac{l_0}{2}$$

or, in virtue of (5.33*)

$$a_\tau \sqrt{\left(1 - \frac{1}{n}\right) + \frac{a_\tau^2}{a_0^2} \frac{1}{n}} = \frac{l_0}{2}. \tag{5.38}$$

Since the function $a_T(x)$ can be found with the formulas of Chapter II when the parameters of the jet and cocurrent stream are known, condition (5.38) enables us to determine x_{mg}. Here we do not take account of the possible shape distortion of the transverse cross section of the jet, since the inclination angles are assumed to be small.

The total area of the zone under consideration is

$$F = \pi [R_c + y_0(x_{c.a})]^2 - \pi R_c^2.$$

The unshaded area is equal to the sum of the areas of the k triangles:

$$F_{c.b} = k \frac{l_0 - 2a_0}{2} y_0(x_{.a}).$$

If $y_0(x_{mg})$ were known, we could calculate c_{x0} by substituting $f = F_{fr}/F$ into (5.29). We may substitute $x_{mg} \tan \alpha_0$ for $y_0(x_{mg})$ with practically acceptable accuracy, i.e., assume that

$$c_{x0} = \frac{1 - f_0}{f_0^2}.$$ (5.39)

where

$$f_0 = \frac{\frac{k}{2}(l_0 - 2a_0)\, \mathrm{tg}\, \alpha_0 x_{ca}}{\pi[(R_c + x_{ca}\, \mathrm{tg}\, \alpha_0)^2 - R_c^2]}.$$

Knowing c_{x0} from (5.32), it is easy to plot the axis of the jet as far as the merging point x_{mg}.

We note that the question as to the encumbered area at which the jets cease to influence one another and can be regarded as single jets has not yet been adequately studied. It is natural to assume that the value of f at which c_{x0} = 4.4 is critical in this case ($f_{cr} \approx 0.38$). For larger f, a value of 4.4 should be taken for c_{x0}.

The second step is calculation of the continuous sheet [the corresponding equation is (5.34)]. The total area of the zone under consideration — the area of the chamber — is

$$F = \pi (R^2 - R_c^2).$$

The free area is

$$F_{ca} = \pi[R^2 - (R_c + u_{0\,max} + a_i)^2] \simeq$$
$$\simeq \pi\left[R^2 - \left(R_c + y_0(x_{ca}) + \frac{tg^2 a_{cs}}{2b}\, a_0 + \frac{l_0}{2}\right)^2\right].$$

(The area in the gaps between jets is small, and we disregard it.)

Since $b = c x_1 \frac{nm^2}{2\pi k} L$, we use Formula (5.29) to obtain an equation for c_{x1}. When it is recognized that

$$\pi\left[R^2 - \left(R_c + y_0(x_{ca}) + \frac{\lg^2 \alpha_{c1}}{2b} + \frac{l_0}{2}\right)^2\right] \simeq$$
$$\simeq 2\pi R\left(R - R_c - y_0(x_{ca}) - \frac{l_0}{2} - \frac{\lg^2 \alpha_{c1}}{2b}\right),$$
$$L \simeq 2\pi\left(\overline{R}_c + \overline{y}_0(x_{ca}) + \frac{\overline{l}_0}{2}\right),$$

is a sufficiently accurate approximation, we obtain the following solution for this second degree equation:

$$c_{x1} = \frac{FB - 2BD - F^2}{2B^2} + \sqrt{\left(\frac{FB - 2BD - F^2}{2B^2}\right)^2 - \frac{D^2 - FD}{B^2}}, \qquad (5.40)$$

where

$$B = 2\pi R\left(R - R_c - y_0(x_{ca}) - \frac{l_0}{2}\right),$$
$$D = \frac{\pi R \lg^2 \alpha_{c1}}{nm^2\left(R_c + y_0(x_{ca}) + \frac{l_0}{2}\right)} ka_0^2.$$

The values of $y_0(x_{mg})$ and $\tan \alpha_{mg}$ are already known from the first step of the calculation.

The trajectory of the sheet is easily calculated from (5.35) with c_{x1} known. After the maximum has been reached at the point

$$\overline{x}_{max} = \overline{x}_{ca} + \frac{\lg \alpha_{c1}}{b}$$

the jets are deflected downwards. Pending a more detailed study, it is natural to assume that the axis of the sheet will again reach the value $\overline{y}_0(\overline{x}_{mg})$ and then proceed parallel to the chamber wall.

Figure 5.14 presents an example of calculation of the jet axes for the experimental data of Ya. I. Chesnokov's, which were obtained for $M_2 = 2.15$; $M_1 = 0.28$; $T_{02} = 670°$K and $T_0 = 260°$K, a critical generator nozzle radius $d_{cr} = 4$ mm, a chamber height of 73 mm for a single jet with
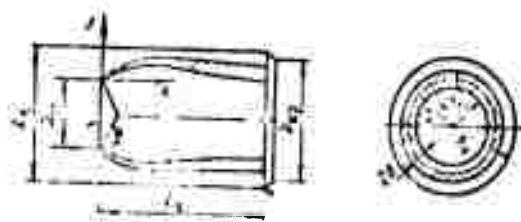
Figure 5.15. Diagram of model combustion chamber with fan type delivery of jets.

design outflow, and for a chamber radius R = 155 mm for a group of twenty jets and a radius R_c = 82 mm of the central body in the generator around whose circumference the jet nozzles were uniformly spaced.

§5. Peculiarities of Combustion in Afterburners with Annular Delivery of Several Generator Jets

The diagrams given in §3 indicate that good combustion efficiency requires a rather large relative chamber length. Multijet delivery of the fuel gas must therefore be provided in real engines to reduce the absolute length of the chamber. If the fuel jets are delivered along the air stream and the delivery nozzles are spaced uniformly over the inlet cross section of the afterburner, the variation of combustion efficiency as a function of the stream parameters and chamber geometry will have the same features as in the case of a single jet flow scheme. In addition, a multi-nozzle system with uniformly spaced nozzles can be represented in approximation as a set of n independent single jet engines with combustion chamber diameters $D_{eq} = D/\sqrt{n}$, where n is the number of fuel jets delivered. It can be assumed in this case that for a given equivalent chamber length L/D_{eq} and given relative flow sections of the gas and air passage, the single nozzle and multi-nozzle engines will have closely similar combustion efficiencies that can be determined from the diagram (see Figure 5.10).

These results have been observed by many investigators when the reciprocal effects between jets are insignificant. However, if these effects are strong, the behavior of the combustion efficiency as a function of flow parameters may differ qualitatively from the case of the single nozzle engine.

In the present section, we shall consider theoretical and experimental features of the combustion efficiency variation for fan pattern (annular) delivery of identical jets from the outside radius R_g of the generator base (Figure 5.15). In this scheme, after-burning occurs in the volume of the chamber that is not occupied by the body of the generator (downstream of the generator base).

The theoretical and experimental data indicate that a number of qualitative features different from those of the schemes considered earlier are observed when the jets are delivered in this way. These features of the combustion process can be explained if the reciprocal effects of the jets on their trajectory are taken into account. The error inherent in a calculation of jet trajectories when the jets are delivered at variable angles to the local airstream vector behind the generator base makes it possible to adopt a number of assumptions that complement those considered earlier.

We may conclude from the physical picture of the combined flow of several jets in a channel that a sheet will be formed if there are enough of these jets and if they are spaced close enough together. This will make it unnecessary to consider separate jets at the end of the channel. (An estimate from the formulas of §4 indicates that 7 — 8 jets are sufficient to justify the hypothesis that the jets merge into a sheet under the conditions of the present experiments.)

The central radius r_0 of the sheet (Figure 5.15) is determined by the ratio between the air flow rates on either side of the sheet. To simplify the analysis, we shall assume that the velocities at the exit from the chamber have been equalized, in contrast to the calculation in §3.

With the initial condition

$$\begin{cases} c=1 & r_0-\delta < r < r_0+\delta; \\ c=0 & 0 < r < r_0-\delta, \ r_0-\delta < r < R_a \end{cases}$$

the concentration profile of molecular (grey) mixing of the sheet substance is described by the solution of the diffusion equation in the form

$$c(r, r_0, s_{br}) = P_{2c}(r, r_0, s_{br}) = \frac{4 r_0^2}{R_s^2} +$$

$$+ \sum_{n=1}^{\infty} \frac{(r_0 + \lambda) I_1 \left(\mu_n \frac{r_0 + \lambda}{R_s} \right) - (r_0 - \lambda) I_1 \left(\mu_n \frac{r_0 - \lambda}{R_s} \right)}{\frac{\mu_n}{2} I_0^2(\mu_n)} \times$$

$$\times I_0 \left(\mu_n \frac{r}{R} \right) e^{-\mu_n \frac{s_{br}^2}{2 R_s^2}}.$$

$$(5.41)$$

where δ is the half width of the sheet.

The sheet half width δ can be found from the equation of jet substance conservation

$$\delta = \frac{G_p}{4 \pi r_0 C_p s} = \frac{R_s^2}{4 r_0} \frac{s}{n + \alpha L}.$$

Here $n = \rho_a / \rho_c$; $\alpha L = G_a / G_c$; α is the average excess air ratio; L is the stoichiometric coefficient. The value of r_0 can vary in the range

$$r_{0\,min} \leqslant r_0 \leqslant r_{0\,max},$$

$$r_{0\,max} = \frac{R_b}{2} + \sqrt{\frac{R_s^2}{4} - r_0 \delta}; \quad r_{0\,min} = \sqrt{r_0 \delta}.$$

In the case of equal velocities, the expression for combustion efficiency assumes the form

$$\eta = \frac{\int_0^{R_s} \eta_b(r, s_{br}) P_{2c}(r, r_0, s_{br}) r \, dr}{\int_0^{R_s} P_{2c}(r, r_0, s_{br}) r \, dr} = \frac{1}{4 \pi r_0^2} \int_0^{R_s} \eta_b P_2 \, r \, dr.$$

$$(5.42)$$
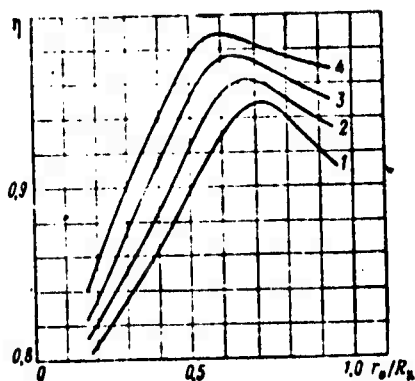
Figure 5.16. Combustion efficiency as a function of sheet center position.

$1 - {}_iL_e - 11.70;$ $2 - {}_iL_e - 14.15;$ $3 - {}_iL_e - 19.70$
$4 - {}_iL_e - 23.21$

Figure 5.16 shows an example of the calculation using Formula (5.42) and illustrates the influence of the position of the sheet on combustion efficiency. The curves indicate that a maximum occurs at a certain value $(r_0)_{max}$ that depends on the flow rate and on $\sigma_{мг}^2$. Combustion efficiency drops off to the right and left of these points because of the deterioration of mixing as the sheet is pulled together into a rope at the axis or as it approaches the chamber walls.

To determine r_0, it is necessary to find the fraction of the air flow rate that enters the sheet.

If the method given in §4 is used to calculate the jet trajectories, the amount of air entering the sheet through the free areas between jets, which are assumed to be triangular, is

$$O_{al} = Q_a u_a (\pi R_{rr} - k a_0) y_0 (x_{ca}).$$

The position r_0 of the sheet is determined from the flow rate equation using the relation

$$r_0 = R_к \sqrt{\frac{G_{a1}}{G_a + n G_r}} = R_к \sqrt{\frac{a L_0}{a L_0 + n} \frac{(\pi R_{rr} - k a_{0a}) J_0 (x_{ca})_1}{\pi R_{rr}^2} + k}$$

Calculations were made for A. S. Popov's model experiments. The chamber length L_c, the number and size of the generator nozzle orifices, and the delivery angle of the generator jets were varied in these experiments.
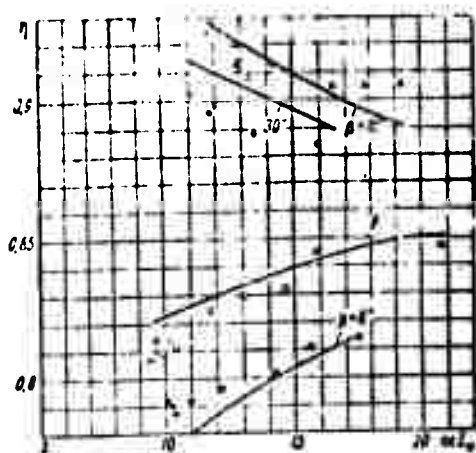
Figure 5.17. Influence of jet delivery angle on combustion efficiency.

■ — $\beta = 0°$; $T_a = 283°$ K; □ — $\beta = 8°$; $k = 1.2$; $d_{gg} = 4.5$ mm; △ — $\beta = 15°$; $D_c = 175$ mm; $I_c = 520$ mm; ○ — $\beta = 30°$; — — calculation.

The afterburner had a constant inside diameter $D_c = 175$ mm, and the flow rate of the air entering the chamber was varied by varying the attachment diameter D_a. The model engine was mounted to a pendulum type device so that its reaction force could be measured. The fuel jet flow rate varied during the experiment as the generator charge was burned, and this made it possible to obtain a curve of combustion efficiency against excess air ratio in a single experiment.

In the calculations, the radius a_c was assumed equal to $a_c = 2.6a_T$, at which, according to the experiments with $\beta_0 = 30°$, the sheet is situated near the chamber wall.

Certain typical results appear in the Figures 5.17 — 5.19, where η is the ratio of the experimental critical specific momentum to the ideal value corresponding to complete afterburning of the fuel (momentum efficiency).

The figures (5.17 — 5.19) also give the calculated results for this chamber. It follows from Figure 5.17 that the calculation gives a correct description of the behavior of η against α at various jet delivery angles: at small delivery angles ($\beta = 0°$; $8°$), η increases with increasing excess air ratio. At large delivery angles ($\beta = 15°$, $30°$), η decreases with increasing excess air ratio.

Figure 5.18. Combustion efficiency as a function of number of gas generator nozzles.

β_0 — 15°; L_c = 520 mm; Δ — k = 12; d_{gg} = 4.5 mm; $\bullet$ — k = 8; d_{gg} = 5.5 mm; —— calculation.
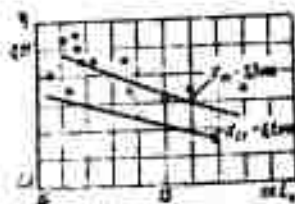
Figure 5.19. Influence of gas generator nozzle diameter on combustion efficiency.

$\bullet$ — d_{gg} = 5.5 mm; k = 12; β_0 — 15°; $\bigcirc$ — d_{gg} = 6.6 mm; — — calculation.

Simple physical considerations explain this property of the curves: at small jet delivery angles, the sheet lies along the axis, and the behavior of the curves is similar in nature to that in the case of the single nozzle engine with coaxial fuel jet (see §3). At large delivery angles, there is a decrease in the velocity head of the generator jet and its diameter as the flow rate of the generator gas declines. This causes the jets to turn and approach one another more rapidly, with the result that it is difficult for air to penetrate into the central zone. In the limiting case of small generator gas flow rates, afterburning efficiency should tend to the same value regardless of jet delivery angle, since the trajectories of the jets are practically the same as in the case $\beta = 0$.

Figure 5.18 shows a somewhat unexpected result according to which combustion efficiency decreases when the number of jets is increased from 8 to 12 in both experiment and calculation. This is also explained by the deterioration of mixing conditions with increasing number of jets. With the change from 8 to 12 jets, the amount of air entering the spaces between jets decreases, and this leads to a smaller r_0.

The calculated curves in Figure 5.19 indicate that the theory also explains the manner in which orifice size influences the behavior of the $\eta(\alpha)$ curves.

The value of $N = \sigma_{MT}/\sigma$ used for the calculations was put equal to 0.40 and was found from the condition of agreement between calculation and experiment for the particular case $\beta = 0$. This value lies in the range of experimental N measured in free jets, but differs from the $N = 0.35$ selected for the single jet engine scheme (§3). In addition to other errors of the calculation, this difference may have resulted from the additional assumption of constant velocities at the end of the chamber that was introduced into the calculation for the multi jet system. This corresponds to a sheet thickness 2δ larger than that in the real flow, so that a larger N is required to reach the same combustion efficiency. A calculation that takes account of the variability of the velocity over the cross section and length of the chamber, as well as the influence exerted on the trajectory of the jet by the dead zone formed behind the generator base might be expected to explain the experimental data with use of the same N as for the single nozzle engine.

APPENDIX I

CERTAIN INTEGRALS ENCOUNTERED IN THE THEORY OF THE JET

I. Mixing Layer

The law of mass flux conservation (1.94) can be rewritten in
the form

$$\int_{-\infty}^{\infty} y\, d(\alpha P_2) = 0. \tag{I.1}$$

Since

$$\alpha = (V_2 - V_1) P_{2v} + V_1, \tag{I.2}$$

we have

$$\int_{-\infty}^{\infty} y\, d(\alpha P_2) = (V_2 - V_1) \int_{-\infty}^{\infty} y\, d(P_{2v} P_2) + V_1 \int_{-\infty}^{\infty} y\, dP_2.$$

But

$$\int_{-\infty}^{\infty} y\, dP_2 = -a_r. \tag{I.3}$$

Further,

$$\int_{-\infty}^{\infty} y\, d(P_{2v} P_2) = \int_{-\infty}^{\infty} y P_2 \frac{\partial P_{2v}}{\partial y}\, dy + \int_{-\infty}^{\infty} y P_{2v} \frac{\partial P_2}{\partial y}\, dy.$$

We shall denote the first of the integrals on the right by S_1, and the second by S_2.

It is easily verified that, for example,

$$S_1 = -\left(a_V S_0 + \sigma_V^2 \frac{\partial S_0}{\partial a_V}\right),$$

where

$$S_0 = \int \frac{1}{\sqrt{2\pi}} e^{-\frac{(y-a_V)^2}{3\sigma_V^2}} P_3\, dy.$$

Obviously,

$$S_0 = \frac{1}{2}\left[1 - \Phi\left(\frac{a_V - a_1}{\sqrt{\sigma_V^2 + \sigma^2}}\right)\right].$$

Therefore

$$-S_1 = \frac{a_V}{2}\left[1 - \Phi\left(\frac{a_V - a_1}{\sqrt{\sigma_V^2 + \sigma^2}}\right)\right] - \frac{\sigma_V^2}{\sqrt{\sigma_V^2 + \sigma^2}}\frac{1}{\sqrt{2\pi}} e^{-\frac{(a_V - a_1)^2}{\sqrt{\sigma_V^2 + \sigma^2}}}.$$

Substituting the resulting expression for S_1, which is similar to the expression for S_2, and (I.3) into (I.1), we arrive at relation (2.40) of the main text. In the case $n \neq 1$ an integral of the form

$$\int_{-\infty}^{\infty} y\, dP_{2V}^2 P_3.$$

appears in the integral momentum flux conservation law. This integral reduces to those calculated previously if P_{2V}^2 is approximated by a function P_{3+} such that

$$P_{2V}^2 \simeq P_{3+} = \frac{1}{2}\left[1 - \Phi\left(\frac{y - a_+}{\sigma_+}\right)\right],$$

where the parameters a_+ and σ_+ are found from the conditions

$$\int_{-\infty}^{\infty} y\,dP_{2V}^2 = \int_{-\infty}^{\infty} y\,dP_{2+}; \quad \sigma_+ = -\frac{1}{\sqrt{2\pi}\left(\dfrac{\partial P_{2V}^2}{\partial y}\right)_{y+\sigma_+}}.$$

That is to say,

$$a_+ = a_V - \frac{\sigma_V}{\sqrt{\pi}}, \quad \sigma_+ = \frac{e^{\frac{1}{2\pi}}}{1+\Phi\left(\dfrac{1}{\sqrt{\pi}}\right)}\,\sigma_V.$$

II.   Plane-Parallel Jet

As in the case of the mixing layer, the problem of presenting the mass conservation law in analytical form reduces to evaluation of the integral S_1 and S_2, where, of course, P_2 and P_{2V} now have the form

$$\left. \begin{aligned}
P_2\left(\frac{y}{\sigma}, \frac{a_\tau}{\sigma}\right) &= \frac{1}{2}\left[\Phi\left(\frac{y+a_\tau}{\sigma}\right) - \Phi\left(\frac{y-a_\tau}{\sigma}\right)\right]; \\
P_{2V} &= \frac{1}{2}\left[\Phi\left(\frac{y+a_V}{\sigma_V}\right) - \Phi\left(\frac{y-a_V}{\sigma_V}\right)\right].
\end{aligned} \right\} \tag{II.1}$$

For example, the integral S_1 is therefore written

$$S_1 = \int_{-\infty}^{\infty} y\,\frac{1}{\sigma_V\sqrt{2\pi}}\left[e^{-\frac{(y+a_V)^2}{2\sigma_V^2}} - e^{\frac{-(y-a_V)^2}{2\sigma_V^2}}\right]P_2\,dy.$$

The obvious identity

$$S_0 = \int_{-\infty}^{\infty} \frac{1}{\sigma_V\sqrt{2\pi}}\,e^{-\frac{(y-x)^2}{2\sigma_V^2}} P_2\left(\frac{x}{\sigma}, \frac{a_\tau}{\sigma}\right)dx =$$

$$= P_2\left(\frac{y}{\sqrt{\sigma^2+\sigma_V^2}}, \frac{a_\tau}{\sqrt{\sigma^2+\sigma_V^2}}\right).$$

will then be found helpful.

Using this identity, we arrive at the following expression for the integrals S_1 and S_2:

$$S_1 = -\sigma_V^2 \frac{\partial}{\partial a_V} \left[\Phi\left(\frac{a_T - a_V}{\sqrt{\sigma^2 + \sigma_V^2}}\right) + \Phi\left(\frac{a_T + a_V}{\sqrt{\sigma^2 + \sigma_V^2}}\right) \right] -$$
$$- a_V \left[\Phi\left(\frac{a_T + a_V}{\sqrt{\sigma^2 + \sigma_V^2}}\right) + \Phi\left(\frac{a_T - a_V}{\sqrt{\sigma^2 + \sigma_V^2}}\right) \right];$$

$$S_2 = -\sigma^2 \frac{\partial}{\partial a_1} \left[\Phi\left(\frac{a_V - a_T}{\sqrt{\sigma^2 + \sigma_V^2}}\right) + \Phi\left(\frac{a_T + a_V}{\sqrt{\sigma^2 + \sigma_V^2}}\right) \right] -$$
$$- a_1 \left[\Phi\left(\frac{a_T + a_V}{\sqrt{\sigma^2 + \sigma_V^2}}\right) + \Phi\left(\frac{a_V - a_T}{\sqrt{\sigma^2 + \sigma_V^2}}\right) \right].$$

With the above, it is no longer difficult to obtain the final
Relation (2.43) or an expression for the momentum conservation law
for equal densities of the streams being mixed (n = 1), by substi-
tuting a_V for a_T and σ_V and σ in S_1.

III. Axisymmetric Jet

In this case

$$S_1 = \int_0^\infty \frac{r^2}{2} P_2 \frac{\partial P_{2V}}{\partial r} \, dr, \quad S_2 = \int_0^\infty \frac{r^2}{2} P_{2V} \frac{\partial P_2}{\partial r} \, dr,$$

where

$$P_2\left(\frac{a}{\sigma}, \frac{r}{\sigma}\right) = \Pi\left(\frac{a}{\sigma}, \frac{r}{\sigma}\right) = \frac{1}{\sigma^2} \int_0^a e^{-\frac{r^2 + r_0^2}{2\sigma^2}} I_0\left(\frac{rr_0}{\sigma^2}\right) r_0 \, dr_0$$

To calculate the derivative $\frac{\partial \Pi}{\partial r}$, it is convenient to use an
expression for Π in the equivalent form

$$\Pi\left(\frac{a}{\sigma}, \frac{r}{\sigma}\right) = 1 - e^{-\frac{a^2 + r^2}{2\sigma^2}} I_0\left(\frac{ra}{\sigma^2}\right) - \frac{1}{\sigma^2} \int_0^r \zeta I_0\left(\frac{\zeta a}{\sigma^2}\right) e^{-\frac{a^2 + \zeta^2}{2\sigma^2}} d\zeta. \qquad (III.1)$$

The proof of equality (III.1) or the equivalent relation

$$\varphi = \frac{1}{a^2} \int_0^r \zeta I_0\left(\frac{\zeta a}{a^2}\right) e^{-\frac{a^2+\zeta^2}{2a^2}} d\zeta =$$

$$= f = \frac{1}{a^2} \int_0^\infty \zeta e^{-\frac{r^2+\zeta^2}{2a^2}} I_0\left(\frac{r\zeta}{a^2}\right) d\zeta - e^{-\frac{a^2+r^2}{2a^2}} I_0\left(\frac{ra}{a^2}\right)$$

(III.1')

follows at once from the fact that

$$\frac{\partial^2 \varphi}{\partial r \partial a} = \frac{\partial^2 f}{\partial a \partial r} = \frac{r}{a^2} e^{-\frac{a^2+r^2}{2a^2}} \left[\frac{r}{a^2} I_1\left(\frac{ra}{a^2}\right) - \frac{a}{a^2} I_0\left(\frac{ra}{a^2}\right)\right].$$

From this

$$\frac{\partial^2(\varphi - f)}{\partial a \, \partial r} = 0.$$

Thus, with the boundary conditions

$$\varphi = f,$$

which proves (III.1') and, accordingly, (III.1). It follows from (III.1) that

$$\frac{\partial \Pi}{\partial r} = -\frac{a}{a^2} e^{-\frac{a^2+r^2}{2a^2}} I_1\left(\frac{ra}{a^2}\right).$$

(III.2)

Using (III.2) and the expression for the integral S_0

$$S_0 = \frac{1}{a^2} \int_0^\infty r e^{-\frac{a_r^2+r^2}{2a^2}} I_0\left(\frac{a_1 r}{a^2}\right) P_{2} \, dr = \prod\left(\frac{a_v}{\sqrt{a^2+a_v^2}} \cdot \frac{a_r}{\sqrt{a^2+a_v^2}}\right).$$

we can obtain expressions for the integrals S_1 and S_2 in the form

$$S_1 = -\frac{1}{2} a_1 a_v^2 e^{-\frac{a_v^2}{2a_v^2}} \frac{\partial}{\partial a_v} e^{\frac{a_v^2}{2a_v^2}} \prod\left(\frac{a_r}{\sqrt{a^2+a_v^2}} \cdot \frac{a_v}{\sqrt{a^2+a_v^2}}\right);$$

$$S_2 = -\frac{1}{2} a_1 a^2 e^{-\frac{a_r^2}{2a^2}} \frac{\partial}{\partial a_r} e^{\frac{a_r^2}{2a^2}} \prod\left(\frac{a_v}{\sqrt{a^2+a_v^2}} \cdot \frac{a_r}{\sqrt{a^2+a_v^2}}\right).$$

It is now easy to arrive at the final relation (2.47) or, by substituting a_V for a_T and σ_V for σ in S_1, at the momentum flux conservation law for $n = 1$ [Relation (2.48)].

APPENDIX 2

INFLUENCE OF STREAM DEFORMATION ON TURBULENCE CHARACTERISTICS

Let us consider the following problem: a homogeneous and isotropic turbulized medium is subjected to an axisymmetric uniform deformation such that the density of the medium and all characteristic linear dimensions and averaged turbulence characteristics are constant in space but variable in time. Required: to find the time variation of the turbulence characteristics.

We shall assume that the coordinate axes coincide with the principal axes of the deformation. Then the deformations ε_1 along these axes are $\varepsilon_i = \frac{\partial x_i}{\partial a_i}$ for $i = 1 - 3$ and $\frac{\partial x_i}{\partial a_j} = 0$ for $i \neq j$, where x_1 are the coordinates of the particle of gas at an arbitrary time t and the a_1 are the coordinates of the same fluid particle at t = 0.

The continuity equation can be written in Lagrangian variables in the form

$$\varepsilon_1 \cdot \varepsilon_2 \cdot \varepsilon_3 = \lambda^3,$$

where

$$\lambda^3 = \frac{\varrho_0}{\varrho} ;$$

ρ and ρ_0 are the densities at the arbitrary time t and at t = 0. Thus we may write for the axisymmetric deformation

$$\iota_1 = c \quad \text{and} \quad \iota_2 = \iota_3 = \frac{\lambda^{3/2}}{c^{1/2}} .$$ (2.0)

if x_1 coincides with the axis of symmetry.

Let us first consider the extreme case of very rapid deformation.

1. Rapid Deformation

In this case, inertia and viscosity forces have no substantial influence on the turbulent motion and the problem becomes linear. The variation of the rms fluctuations was examined in this formulation for a compressible fluid by Batchelor [19], and for the case of an incompressible medium by V. A. Frost [39], both of whom used the same method. Referring the reader to these sources for the derivation, we present only the final formulas for the compressible case:

(a) For

$$\bar{c} = \frac{c}{\lambda} > 1:$$

$$\mu = \frac{\overline{u_1^2}}{\overline{u_{10}^2}} = \frac{3}{4\bar{c}^2\lambda^2} \left\{ \frac{1+a^2}{2a^3} \ln\left(\frac{1+a}{1-a}\right) - \frac{1}{a^2} \right\} ,$$ (2.1)

$$v = \frac{\overline{u_2^2}}{\overline{u_{20}^2}} = \frac{\overline{u_3^2}}{\overline{u_{30}^2}} = \frac{3\bar{c}}{4\lambda^2} + \frac{3}{4\bar{c}^2\lambda^2} \left\{ \frac{1}{2a^2} - \frac{1-a^2}{4a^3} \ln\left(\frac{1+a}{1-a}\right) \right\} .$$ (2.2)

Here $a^2 = 1 - \frac{1}{\bar{c}^3}$.

(b) For $\lambda = \frac{c}{\lambda} < 1$

$$\mu = \frac{\overline{u_1^2}}{\overline{u_{10}^2}} = \frac{3}{4c^2\lambda^2}\left\{\frac{1}{\beta^2} + \frac{\beta^2-1}{\beta^3}\text{arctg}\,\beta\right\};$$ (2.3)

$$v = \frac{\overline{u_2^2}}{\overline{u_{20}^2}} = \frac{\overline{u_3^2}}{\overline{u_{30}^2}} = \frac{3c}{4\lambda^2} + \frac{3}{4c^2\lambda^2}\left\{-\frac{1}{2\beta^2} + \frac{1+\beta^2}{2\beta^3}\text{arctg}\,\beta\right\}.$$ (2.4)

Here $\beta^2 = \frac{1}{c^3} - 1$; $\overline{u_1^2}$, $\overline{u_2^2}$, $\overline{u_3^2}$, $\overline{u_0^2}$ are the mean square velocity fluctuations in the x_1, x_2, and x_3 directions of the deformed medium and the initial turbulence.

We note that these formulas differ slightly from the final results given in [39]. This is because the multiplier ρ/ρ_0 was overlooked in the initial momentum equation (1) of [39], so that an error appeared in the final formulas.

Let us now consider the variation of the turbulence scale for rapid deformation.*

The turbulence scale along the x_1 axis (the "longitudinal" scale) can be determined, for example, as

$$l_1 = \frac{1}{u_1^2}\int_{-\infty}^{\infty}\overline{u_1 u_1}(r_1)\,dr_1,$$ (2.5)

where u_1 and u_2 are the fluctuation velocities at points M and M, which are situated on a straight line parallel to the x_1 axis and separated by a distance r_1.

Similarly, the scale along the x_2 axis (which equals the scale along the x_3 axis, the "transverse" scale) can be defined as

---

*This result and those that follow in the Appendix were obtained by V. M. Iyevlev.

$$l_s = \frac{1}{u_2^2} \int_{-\infty}^{+\infty} \overline{u_2 u_2}(r_2)\, dr_2. \tag{2.6}$$

Here the points M and $\underset{\sim}{M}$ must be situated along the x_2 axis. If the Fourier transform of $\overline{u_1 u_1}(r_1)$ is denoted by $\Phi_{11}(\vec{x})$, $\vec{x}$ and $\vec{x}$ is the wave vector, we have

$$\overline{u_1 u_1}(r_1) = \int \Phi_{11}(\vec{x})\, e^{i x_1 r_1}\, d\vec{x}, \tag{2.7}$$

where the integration is extended over the entire wave space and

$$l_1 = \frac{1}{u_1^2} \int_{r_1 = -\infty}^{\infty} \int_{\vec{x}} \Phi_{11}(\vec{x})\, e^{i x_1 r_1}\, d\vec{x}\, dr_1. \tag{2.8}$$

Using the subscript "0" for the variables at t = 0, we obtain

$$\frac{l_1}{l_{10}} = \bar{l} = \frac{1}{\mu} \frac{\displaystyle\int_{r_1 = -\infty}^{+\infty} \int_{\vec{x}} \Phi_{11}(\vec{x})\, e^{i x_1 r_1}\, d\vec{x}\, dr_1}{\displaystyle\int_{r_1 = -\infty}^{\infty} \int_{\vec{x}} \Phi_{110}(\vec{x})\, e^{i x_1 r_1}\, d\vec{x}\, dr_1}. \tag{2.9}$$

If the turbulence at t = 0 is regarded as isotropic and characterized by the spectral function E(x), we have

$$\Phi_{110}(\vec{x}) = \frac{E(x)}{4 \pi x^2} \left(1 - \frac{x_1^2}{x^2} \right). \tag{2.10}$$

i.e., for axisymmetric deformation

$$\Phi_{11}(\vec{x}) = \frac{E(x')}{4 \pi \lambda^3 x'^2} \left\{ -c^3 \frac{x'^2 - x_1''^2}{x^2} + \frac{x^2 - x_1^2}{x^4} \left[c^3 (x'^2 - x_1''^2) + \frac{\lambda^3}{c} (x'^2 + x_1''^2) \right] \right\}. \tag{2.11}$$

where $\vec{x}'$ is a vector with the components $c x_1$; $\frac{\lambda^{3/2}}{c^{1/2}} x_2$; $\frac{\lambda^{3/2}}{c^{1/2}} x_3$; x_1, x_2, and x_3 are the components of the vector $\vec{x}$ [19], [39].

After substitution of (2.10) and (2.11) into (2.9) and evaluation of the integrals, we obtain

$$\bar{l}_1 = \frac{1}{\mu \lambda \bar{e}} \qquad (2.12)$$

and from similar calculations

$$\bar{l}_2 = \frac{\sqrt{\bar{e}}}{\lambda \nu}, \qquad (2.13)$$

where μ and ν are determined from expressions (2.1) — (2.4).

It follows from Formulas (2.12) and (2.13) that the variation of the turbulence scales during fast deformation is independent of the form of the initial turbulence spectral function $E(x)$.

Regarding the coefficients of proportionality between the Lagrangian scales and the Euler scales introduced above as constant under the deformation, we can write

$$\left.\begin{aligned}
\frac{D_1}{D_{10}} &= \frac{l_{1e}}{l_{0e}} \frac{\sqrt{\overline{u_1^2}}}{\sqrt{\overline{u_0^2}}} = \frac{1}{\lambda \bar{e} \sqrt{\bar{\mu}}}; \\
\frac{D_2}{D_{20}} &= \frac{D_3}{D_{30}} = \frac{l_{2e}}{l_{0e}} \frac{\sqrt{\overline{u_2^2}}}{\sqrt{\overline{u_0^2}}} = \frac{l_{3e}}{l_{0e}} \frac{\sqrt{\overline{u_3^2}}}{\sqrt{\overline{u_0^2}}} = \frac{\sqrt{\bar{e}}}{\lambda \sqrt{\bar{\nu}}},
\end{aligned}\right\} \qquad (2.14)$$

where D_1, D_2, D_3, and D_0 are the eddy diffusivities in the x_1, x_2, and x_3 directions of the deformed medium and the initial turbulence, and l_{1e}, l_{2e}, l_{3e}, and l_{0e} are the corresponding Euler turbulence scales.

We note that, in its application of the deformation of a one-dimensional and stationary (in the mean) turbulent stream flowing in a round channel with variable cross sections, this problem describes the variation of the turbulent parameters along the channel, with the initial parameters $u_0'^2$, l_0, D_0 pertaining in this case to the entrance segment of the channel (e.g., of the nozzle), in which the turbulence is assumed to be isotropic. In this case, the deformation in the longitudinal direction equals

$$u_1 = c = \frac{u_1}{u_{10}},$$

where u_1 and u_{10} are the velocities in the present and initial channel cross sections.

Estimates indicate that rapid deformation hypotheses do not hold for channels with realistic geometry. We shall therefore consider the case of slow deformation, in which inertia forces and viscous dissipation are strong factors (the rapid deformation hypotheses are evidently valid for passage of the stream through a compression shock).

II. Slow Deformation

According to experiments, inertia forces render the turbulence isotropic, so that in the extreme case of very strong inertia force effects and sufficiently slow deformation, it is natural to regard the turbulence as isotropic (despite an anisotropic deformation).

Let us derive an equation that describes the time variation of the isotropic turbulence spectral function for such deformation.

The momentum and continuity equations for any point in time can be written

$$\frac{\partial V_i}{\partial t} + V_k \frac{\partial V_i}{\partial x_k} = -\frac{1}{\rho} \frac{\partial p}{\partial x_i} + \nu \frac{\partial^2 V_i}{\partial x_k \partial x_k} , \quad i = 1, 2, 3. \tag{2.15}$$

$$\frac{\partial V_k}{\partial x_k} = -\frac{1}{\rho} \frac{d\rho}{dt} , \tag{2.16}$$

ν is the kinematic viscosity and summation is assumed over repeated indices.

Substituting the average and pulsation components $\bar{V}_t + V'_1$ and $\bar{p} + p'$ for the velocity components and the pressure V_1 and p, we obtain

$$\frac{\partial \bar{V}_k}{\partial x_k} = -\frac{1}{\varrho}\frac{d\varrho}{dt};\tag{2.17}$$

$$\frac{\partial V'_k}{\partial x_k} = 0;\tag{2.18}$$

$$\frac{\partial V'_i}{\partial t}+V'_k\frac{\partial \bar{V}_i}{\partial x_k}+\bar{V}_k\frac{\partial V'_i}{\partial x_k}+\frac{\partial V'_k V'_i}{\partial x_k}=\frac{1}{\varrho}\frac{\partial p'}{\partial x_i}+\nu\frac{\partial^2 V'_i}{\partial x_k \partial x_k}.\tag{2.19}$$

Equations (2.17) and (2.19) have been written for a certain point M of the stream. Similar equations can be written for any other point M, the parameters at which will be identified by underscoring with a wavy line. Multiplying (2.19) by $\underset{\sim}{V}_j$, multiplying the equation for $\underset{\sim}{V}_j'$, which is analogous to (2.19), by V_1' (V_1 and V_j at the same time t), adding these equations, and averaging, we obtain

$$\frac{\partial \overline{V'_i V'_j}}{\partial t}+\bar{V}_k\frac{\partial \overline{V'_i V'_j}}{\partial x_k}+\underset{\sim}{\bar{V}}_k\frac{\partial \overline{V'_i V'_j}}{\partial \underset{\sim}{x}_k}+\overline{V'_k V'_j}\frac{\partial \bar{V}_i}{\partial x_k}+\overline{V'_k V'_j}\frac{\partial \bar{V}_j}{\partial x_k}+$$
$$+\frac{\partial \overline{V'_k{}' V'_j}}{\partial x_k}+\frac{\partial \overline{V'_k V'_i V'_j}}{\partial \underset{\sim}{x}_k}=-\frac{1}{\varrho}\frac{\partial \overline{p' V'_j}}{\partial x_i}+\nu\frac{\partial^2 \overline{V'_i V'_j}}{\partial x_k \partial x_k}+\tag{2.20}$$
$$+\nu\frac{\partial^2 \overline{V'_i V'_j}}{\partial x_k \partial x_k}-\frac{1}{\varrho}\frac{\partial \overline{p' V'_j}}{\partial x_i}.$$

Here the average velocity values $(\bar{V}_1, \bar{V}_j)$ are determined by the deformation of the stream:

$$\frac{\partial \bar{V}_i}{\partial x_k}=\frac{\partial \bar{V}_i}{\partial x_k}=\left(\frac{3}{2c}\frac{dc}{dt}-\frac{3}{2\lambda}\frac{d\lambda}{dt}\right)\gamma_i \gamma_k+\left(\frac{3}{2\lambda}\frac{d\lambda}{dt}-\frac{1}{2c}\frac{dc}{dt}\right)\delta_{ik}.\tag{2.21}$$

$$\underset{\sim}{V}_k - V_k = r_k \left(\frac{3}{2\lambda} \frac{d\lambda}{dt} - \frac{1}{2c} \frac{dc}{dt} \right) + r_1 \left(\frac{3}{2c} \frac{dc}{dt} - \frac{3}{2\lambda} \frac{d\lambda}{dt} \right) \gamma_k. \qquad (2.22)$$

Here γ_1 is the 1th component of the unit vector $\vec{\gamma}$, which is directed along the symmetry axis of the deformation, i.e., along x_1; r_k is the component of the radius vector $\vec{r}$, which joins the points M and $\underset{\sim}{M}$ (so that $r_k = \underset{\sim}{x}_k - x_k$).

Since the turbulence is homogeneous, we obtain for any averaged turbulence characteristic

$$\frac{\partial}{\partial \underset{\sim}{x}_k} = \frac{\partial}{\partial r_k} \; ; \; \frac{\partial}{\partial x_k} = - \frac{\partial}{\partial r_k} \; ; \; \frac{\partial^2}{\partial x_k \partial x_m} = \frac{\partial^2}{\partial \underset{\sim}{x}_k \partial \underset{\sim}{x}_m} = \frac{\partial^2}{\partial r_k \partial r_m} \; . \qquad (2.23)$$

Substituting (2.21) –– (2.23) into (2.20), applying the Fourier transformation to the resulting equation, and integrating over a sphere of radius x in wave space (remembering that the turbulence remains isotropic during the deformation, i.e., $\Phi_{11} = \frac{1}{6} \frac{E(x)}{2\pi x^2}$), we find:

$$\frac{\partial E}{\partial t} = - \frac{2}{\lambda} \frac{d\lambda}{dt} E + \frac{1}{\lambda} \frac{d\lambda}{dt} \frac{\partial}{\partial x} (xE) - 2\nu x^2 E + 2B. \qquad (2.24)$$

Here B equals the integral of

$$A_{11} = ix_k (S_{1k,1} - S_{1,k1}),$$

over the sphere of radius x in wave space; $S_{1k,1}, S_{1,k1}$ are the Fourier transforms of

$$\overline{V'_i V'_k \underset{\sim}{V'_l}} \text{ and } \overline{V'_i \underset{\sim}{V'_k} V'_l}.$$

A property of Equation (2.24) is that the quantity c does not appear in it, i.e., slow deformation (deformation such that there is time for establishment of isotropy) of a stream of incompressible fluid ($\lambda = 1$) has no influence at all on the turbulence characteristics.

Integrating (2.24) over x in the range from 0 to ∞ and remembering that the integral of B vanishes [19], we obtain

$$\frac{d\overline{u'^2}}{dt} = -\frac{2}{\lambda}\frac{d\lambda}{dt}\,\overline{u'^2} - \frac{4\nu}{3}\int_0^\infty x^2 E(x)\,dx.$$ (2.25)

At large Reynolds numbers, the term containing the viscosity can be represented in the form

$$\frac{\alpha\overline{u'^2}^{3/2}}{l}$$

on the basis of dimensional considerations; here α = const (on the order of unity), l is the scale of the vortices carrying most of the energy [19], and Equation (2.25) assumes the form

$$\frac{d\overline{u'^2}}{dt} = -\frac{2}{\lambda}\frac{d\lambda}{dt}\,\overline{u'^2} - \frac{\alpha\overline{u'^2}^{3/2}}{l}.$$ (2.26)

We shall define the scale l as $\dfrac{k}{\overline{u'^2}}\displaystyle\int_0^\infty \frac{E(x)}{x}\,dx$, where k = const.

Dividing (2.24) by x and integrating over x,

$$\frac{d}{dt}(l\overline{u'^2}) = -\frac{1}{\lambda}\frac{d\lambda}{dt}\,l\overline{u'^2} - \frac{2\nu}{k}\int_0^\infty xE(x)\,dx + \frac{2}{k}\int_0^\infty \frac{B}{x}\,dx.$$ (2.27)

The term with ν can be disregarded at large Re [it is easily verified that the ratio of this term to the last term in (2.27) is of the order of 1/Re]. At large Re, the last term in (2.27) may depend only cn l and $\overline{u'^2}$ (for slow deformation, when the turbulence structure is determined basically by inertia forces); dimensional considerations yield $\beta\overline{u'^2}^{3/2}$, where β = const. With the above, Equation (2.27) assumes the following form after transformation with (2.26):

$$-\frac{dl}{dt} = \frac{l}{\lambda}\frac{d\lambda}{dt} + (\alpha+\beta)\,\mathbf{u}.$$ (2.28)

In the particular case in which deformation is absent, we obtain from (2.26) and (2.27)

$$\frac{d\left(l \frac{1}{\lambda}\,\overline{u'^2}\right)}{dt}=\left(\frac{a}{2}+\beta\right)\overline{u'^2}.$$

It is known from experiment that $l\overline{u'^2}^{1/2}$ is conserved (at large Re) as the turbulence decays, so that

$$\beta=-\frac{a}{2} \qquad\qquad (2.29)$$

and Equation (2.28) assumes the form

$$\frac{dl}{dt}=\frac{l}{\lambda}\frac{d\lambda}{dt}+\frac{a\overline{u'^2}^{1/2}}{2}.$$

We obtain from the system of equations (2.26) and (2.30)

$$l\overline{u'^2}^{1/2}=\text{const, т. е. }\frac{D}{D_0}=\frac{l\overline{u'^2}^{1/2}}{l_0\overline{u_0'^2}^{1/2}}=\text{const;} \qquad\qquad (2.31)$$

$$\mu=\frac{\overline{u'^2}}{\overline{u_0'^2}}=\lambda^{-3}\left(1+\frac{a\overline{u_0'}^{1/2}}{l_0}\int_0^t\frac{dt}{\lambda^2}\right)^{-1}. \qquad\qquad (2.32)$$

In the particular case of $\lambda=1$, we obtain from (2.32)

$$\frac{\overline{u_0'^2}}{\overline{u'^2}}=1+\frac{a\overline{u_0'}^{1/2}t}{l_0}, \qquad\qquad (2.33)$$

which agrees with the usual empirical formula for the decay of turbulence behind a grid. On comparing (2.33) with the experimental data of [19], we find

$$a\approx 1,1.$$

REFERENCES

1. Абрамович Г. Н. Теория турбулентных струй. М., Физматгиз, 1960.
2. Бай Ши-и. Теория струй. М., Физматгиз, 1960.
3. Вулис Л. А., Кашкаров В. П. Теория струй вязкой жидкости. М., Физматгиз, 1965.
4. Spalding D. B. A unified theory of friction, heat and mass transfer in the turbulent boundary layer and wall jet. ARC, No. 829, 1965.
5. Бродский А. И. Физическая химия. Т. I и II, М., Госхимиздат, 1948.
6. Хитрин Л. Н. Физика горения и взрыва. М., Изд. МГУ, 1957.
7. Кондратьев В. Н. Кинетика химических газовых реакций. М., Изд. АН СССР, 1958.
8. Иноземцев Н. В. Основы термодинамики и кинетики химических реакций. М., Машгиз, 1960.
9. Соколик А. С. Самовоспламенение, пламя и детонация в газах. М., Изд. АН СССР, 1960.
10. Щетинков Е. С. Физика горения газов. М., «Наука» 1965.
11. Щелкин К. И., Трошин Я. К. Газодинамика горения. М., Изд. АН СССР, 1963.
12. Льюис Б., Эльбе Г. Горение, пламя и взрывы в газах. М., ИЛ, 1948.
13. Иост В. Взрывы и горение в газах. М., ИЛ, 1952.
14. Раушенбах Б. В., Белый С. А., Беспалов И. В., Бородачев В. Я., Волынский М. С., Прудников А. Г. Физические основы рабочего процесса в камерах сгорания воздушно-реактивных двигателей. М., «Машиностроение», 1964.
15. Бондарюк М. М., Ильяшенко С. М. Прямоточные воздушно-реактивные двигатели. М., Оборонгиз, 1958.
16. Зуев В. С., Скубачевский Л. С. Камеры сгорания воздушно-реактивных двигателей. М., Оборонгиз, 1958.
17. Горбунов Г. М. и др. Сб. «Стабилизация пламени и развитие процесса сгорания в турбулентном потоке». М., Оборонгиз, 1961.
18. Ильяшенко С. М., Талантов А. В. Теория и расчет прямоточных камер сгорания. М., «Машиностроение», 1964.
19. Бэтчелор Дж. Теория однородной турбулентности. М., ИЛ, 1955.

20. Таунсенд А. А. Структура турбулентного потока с поперечным сдвигом. М., ИЛ, 1959.

21. Хинце И. О. Турбулентность. М., Физматгиз, 1963.

22. Монин А. С., Яглом А. М. Статистическая гидромеханика. М., «Наука», ч. I, 1965, ч. II, 1967.

23. Freumuth P. On transition in a separate laminar layer. «J. of Fluid Mech.». Vol. 25, p. 4. 1966.

24. Rotta I. C. Statistische Theorie nichthomogener Turbulenz. I, Zs. Phys., 1951, Nr 5. S. 547—572; 2. Zs Phys., 1951, Nr. I. S. 51—77.

25. Reichardt H. Gesetzmässigkeiten der freien Turbulenz. VDI-Forshungheft, 1942. S. 414.

26. Ландау Л. Д., Лифшиц Е. М. Механика сплошных сред. М., ГИТТЛ, 1954.

27. Michalke A. On the inviscid instability of the hyperbolictangent velocity profile. «J. Fluid Mech.», 1964, vol. 19, p. 4, pp. 543—556.

28. Martin Lessen, Sung—Hwan—Ko. Viscous instability of an incompressible fluid half — jet flow. «The Prysics of Fluids», 1966, Vol. 9, No 6.

29. Townsend A. A. The structure of the turbulent boundary layer. «Proc. Cambr. Phil. Soc.», vol. 47, No 2, pp. 375—395.

30. Шлихтинг Г. Возникновение турбулентности. М., ИЛ, 1962.

31. Corrsin S., Kistler A. Freestream boundaries of turbulent flows. NACA Rep., 1955, No. 1244.

32. Townsend A. A. The diffusion behind a line source in homogenous turbulence. «Proc. Roy. Soc.», 1954, vol. 24, No. 1150.

33. Чепмен С., Каулинг Т. Математическая теория неоднородных газов. М., ИЛ, 1960.

34. Прудников А. Г., Сагалович В. Н. Статистическое описание турбулентной струи. ДАН СССР, 1962, т. 144, № 6.

35. Замятина Н. А., Прудников А. Г. Сагалович В. Н. О диффузионных параметрах турбулентной струи. Известия ВУЗов. «Авиационная техника», 1966, № 2.

36. Frenkiel F. N. Turbulent diffusion: Mean concentration distribution in a flow field of homogenous turbulence. «Adv. Appl. Mech.», 1953, vol. 3, pp. 67—107.

37. Batchelor G. K. Diffusion in a field of Homogenous turbulence. I. «Austr. J. Sci. Res», 1949, ser. A, vol. 2, No. 4.

38. Лушпа А. И. Исследование структуры зоны горения однородных бензино-воздушных смесей в турбулентном потоке. — В сб. «Высокофорсированные огневые процессы». М.—Л., «Энергия», 1967.

39. Фрост В. А. Однородная быстрая деформация турбулентности в газе. ДАН СССР, 1960, т. 133, № 4.

40. Forstall W., Gayford E. Momentum and mass transfer in a submerged water jet. «J. Appl. Mech.», 1955, vol. 22, No. 2.

41. Кочин Н. Е., Кибель И. А., Розе Н. В. Теоретическая гидромеханика. М., ГИТТЛ, ч. II, 1948.

42. Masters I. Some application in physics of the P-function. «J. Chem. Phys.», 1955, vol. 23, No. 10.

43. Палатник И. Б. Исследование аэродинамики сложных неизотермических турбулентных струйных течений. Диссертация, Алма-Ата, 1961.

44. Albertson M., Day Y., Jensen R. Rouse H. Diffusion of submerged jets. «Proc Amer. Soc Civ. Eng». 1948, vol. 74, No. 10, pp. 1571—1596.

45. Gortler H. Berechnung von Aufgaben der freien Turbulenze auf Grund eines neuen Naherungsansatzes. ZAMM, 1942, Bd. 22, Nr. 5.

46. Weinstein A., Osterle I., Forstall W. Momentum diffusion from a slot jet into a moving secondary. «J Appl. Mech.», 1956, vol. 23, No. 9.

47. Corrsin, Uberoi. Further experiments on the flow and heat transfer in a heated turbulent air jet. NACA Rep, 1950, No. 998.

48. Alpinieri L. I. Turbulent mixing of coaxial jets. «AIAA», 1964, vol. 2, No. 9.

49. Ferry A. Review of problem in application of supersonic combustion. «Journal of the Royal Aeronautical Society», 1964, vol. 68, No. 645.

50. Sunavala P., Hulse C., Thring M. Combustion and flame, 1957, vol. 1, No. 2. Перевод: ВРТ, 1958, 2(44).

51. Abramovich G. N. and oth. An investigation into turbulent submerged jets over a wide temperature range. «J. Heat Mass Transfer», 1966, vol. 9, No. 10.

52. Ершин Ш. А., Сакипов З. Б. Исследование начального участка турбулентной струи сжимаемого газа. ЖТФ, 1959, т. XXIX, вып. I.

53. Вулис Л. А., Терехина Н. Н. Распространение турбулентной струи газа в среде иной плотности. ЖТФ, 1956, т. XXVI, вып. 6.

54. Batchelor G. K. Diffusion in free turbulent shear flows. «J. Fluid Mech», 1957, vol. 3, No. 1.

55. Козаченко П. С. III Всесоюзное совещание по теории горения. М., Изд. АН СССР, 1960, т. I, стр. 126.

56. Мандельштам С. А. Введение в спектральный анализ. М., Гостехиздат, 1964.

57 Навознов О. У., Павельев А. А. О смешении спутных газовых струй. М. Изв. АН СССР, «Энергетика и транспорт», 1958, № 2, стр. 52—57.

58 Прудников А. Г. Измерение оптико-диффузионным методом турбулентности воздушных потоков и пламен. Сб. «Горение в турбулентном потоке». М. Изд. АН СССР, 1959, стр. 88.

59 Замятина Н. А., Прудников А. Г. О скорости молекулярного смешения на начальном участке турбулентной струи. М., Изв. АН СССР, «Энергетика и транспорт», 1965, № 3.

6 Прудников А. Г., Замятина Н. А. О скорости молекулярного смешения на начальном участке турбулентной струи. Известия ВУЗов. «Авиационная техника», 1966, № 3.

61 Prudnikov A. G. Flame turbulence. Seventh symposium (international) on combustion. Baltimore, 1959.

62 Оптические измерения в газовой динамике и при горении. Под редакцией Р. У. Ладенбурга. М., ИЛ, 1957.

63 Кинг В. Р., Эллис X. X. Применение шлирен-метода для количественного исследования смешивающихся газов в струях. М., ИЛ, «Вопросы горения», 1963, № 2.

64 Баженова Т. В., Леонтьева З. С. Способ измерения поля плотности трехмерного объекта при помощи метода Теплера. М., Изд. АН СССР, «Газодинамика и физика горения», 1959.

65 Белоцерковский О. М. Определение поля плотности оптическими методами. Журнал прикладной механики и технической физики, 1964, № 3.

66 Баженова Т. В., Леонтьева З. С. Экспериментальное исследование поля плотности трехмерной сверхзвуковой струи. «Газодинамика и физика горения». М., Изд. АН СССР, 1959.

67 Замятина Н. А., Навознов О. И., Павельев А. А. Экспериментальное определение поля температур осесимметричных спутных струй методом Теплера. Сиб. отд. АН СССР, «Физика горения и взрыва», 1967, № 3.

68 Старк С. Б. Перемешивание газовых потоков в факеле. ЖТФ, 1953, т. 23, вып. 10.

69 Cleeves V., Boelter L. M. K. Isothermal and non-isothermal air jet investigations. «Chem. Eng. Progr.», 1947, vol. 43, N. 3, p. 123.

70 Щербина Ю. А. Расчет профилей температур в следе за плохообтекаемым телом при горении. Сборник по механике и прикладной математике. Труды МФТИ, № 3. М., Оборонгиз, 1958.

71 Вулис Л. А., Карелин В. Г., Устименко Б. П. Распространение турбулентной газовой струи в спутном потоке. М., Изв. АН СССР, «Механика жидкости и газа», 1966, № 3.

72 Forstall W., Shapiro A. H. Momentum and mass transfer in coaxial gas jets «J. Appl. Mech.», 1950, vol. 17, N. 14.

73 Щербина Ю. А. О влиянии начальной турбулентности на границу и дальнобойность затопленной струи. Труды МФТИ, № 7. М., Оборонгиз, 1961.

74 Вулис Л. А., Михасенко Ю. И., Хитриков В. Л. Об эффективном управлении распространением свободной турбулентной струи. М., Изв. АН СССР, «Механика жидкости и газа», 1966, № 6.

75 Broer, Reldijk. Measurements on supersonic free jets. «Appl. Sci. Res.», 1960, ser. A, vol. 9, N 6, pp. 465—477.

76 Johannesen N. H. Further results on the mixing of free axially-symmetrical jets of mach number 1, 4. ARCRaM, 1962, No. 3292.

77 Pitkin E. T., Glassman I. Experimental mixing profiles of a mach 2.6 free jet I. AS/S, 1958, vol. 25, No. 12, pp. 791—793.

78 Черкез А. Я. Об одномерной теории нерасчетной сверхзвуковой струи газа. М., Изв. АН СССР, ОТН. «Механика и машиностроение», 1962, № 5.

79 Love E. Experimental and theoretical studies of axisymmetrical free jets. NASA, TR, R-6, 1959.

80 Adamson T. S., Nicholls I. A. On the structure of jets from highly underexpanded nozzles into still air. «J. Aerospace Sciences», 1959, vol 1, No 26.

81 Дмитриев В. И. Исследование сверхзвуковых газовых струй высокой температуры, истекающих из осесимметричных и плоских сопел. Диссертация, Москва, 1964.

82 Абрамович Г. Н., Яковлевский О. В., Смирнова И. П., Секундов А. Н., Крашенинников С. Б. Исследование начального участка турбулентных струй различных газов в спутном потоке воздуха. М., Изв. АН СССР, «Механика жидкости и газа» 1966, № 6.

83 Roger Wills, Irvin Glassman. The mixing of unbounded coaxial compressible streams «Jet Propulsion», 1957, vil. 27, No. 6.

84 John G. Wilder, K. Hindersinn. Spreading of supersonic jets in supersonic streams «Jet Prop. Eng. Rev.», 1953, vil 12, No 10, pp 54—68.

85 Damköhler G. Der Einfluss der Turbulenz auf die Flammenge Schwindigkeit in Gasgemischen. Jahrbuch. D. L. F. S., 1939, S. 113.

86 Щелкин К. И. О сгорании в турбулентном потоке. ЖТФ, 1943, т. XIII, вып. 9—10, стр. 520.

87 Климов А. М. Ламинарное пламя в турбулентном потоке. ПМТФ, 1963, № 3.

88. Кокушкин Н. В. III Всесоюзное совещание по теории горения. М., Изд. АН СССР, 1960, т. 1, стр. 109.

89. Щелкин К. И. К вопросу о турбулентном горении и фазах сгорания в двигателе. М., Изв. АН СССР, ОТН, 1953, вып. 3, стр. 463—471.

90. Summerfield M. A. and oth. The physical structure of turbulent flames. «Jet Propulsion», 1954, vol 24, 1955, vol. 25.

91. Щетинков Е. С. Сб. «Горение в турбулентном потоке». М., Изд. АН СССР, 1959, стр 5.

92. Кокушкин Н. В. Исследование сгорания гомогенной смеси в турбулентном потоке посредством записи пульсаций температур. М., Изв. АН СССР, ОТН, 1958, № 8.

93. Прудников А. Г. Об определении средних параметров турбулентного факела взамен. М., Изв. АН СССР, ОТН, «Энергетика», 1960, № 1.

94. Соколик А. С., Воинов А. Н., Свиридов Ю. Б. Влияние химического и турбулентного факторов на процесс сгорания в условиях двигателя. М., Изв. АН СССР, ОТН, 1949, № 12.

95. Свиридов Ю. Б. О природе турбулентного горения. М., Изв. АН СССР, ОТН, 1953, № 11.

96. Зельдович Я. Б., Франк-Каменецкий Д. А. Турбулентное и гетерогенное горение. Изд. Московского механического института, 1947.

97. Scurlock A. C., Grover I Propagation of turbulent flames, Fourth symposium on combustion, Baltimore, 1953.

98. Wohl K. Burning velocity of unconfined turbulent flames. «Ind. Eng. Chem.», 1955, vol. 47, No. 4.

99. Wohl K., Shorel, Von Resenberg H., Weil C. W. The burning velocity of turbulent flames. Fourth simposium (international) on combustion, Baltimore, 1953.

100. Karlovitz B., and oth. Fourth simposium (international) on combustion, Baltimore, 1953.

101. Зельдович Я. Б. ЖТФ, т. XIV, 1944, вып. 3.

102. Tsien H. «J. Applied Mechanics», 1951, vol. 18. No. 2.

103. Scurlock A. Meteor Intern Rep. M. 1. T. 1948, No 19.

104. Талантов А. В. Известия ВУЗов. «Авиационная техника», 1958, № 2.

105. Povinelli L. A., Fuhs A. E. The spectral theory of turbulent-flame propagation Eigth Symposium (international) on combustion, Baltimore, 1962.

106. Лонге-Хиггинс М. С. Статистическая геометрия случайных поверхностей. Сб. «Гидродинамическая неустойчивость». М., «Мир», 1962, стр. 124.

107. Гиневский А. С. Теория турбулентных струй и следов. Интегральный метод расчета. М., «Машиностроение», 1969.

108. Гауссори, Уиддел, Хоттел. Смешение и горение в турбулентных газовых струях. Сб. «Вопросы горения». М., ИЛ, 1953.

109. Ершин Ш. А., Ярин Л. П. Исследование аэродинамики диффузионных факелов. Изв. АН Каз. ССР, сер. энергетическая, 1962, вып. 1(21).

110. Кузнецов В. Л., Игнатенко Ю. В., Фотометрический анализ и расчет плоского гомогенного турбулентного факела «Физика горения и взрыва», 1967, № 1, т. 3.

111. Соколик А. С., Карпов В. П., Семенов Е. С. О турбулентном горении газов. «Физика горения и взрыва», 1967, № 1, т. 3.

112. Шорин С. Н., Ермолаев О. Н. Характеристика горения и радиации турбулентного газового факела. «Теплоэнергетика», 1959, № 2.

113. Розеншток Ю. Л. Влияние пульсаций скорости на точность измерения температуры неизотермического турбулентного потока. Журнал прикладной математики и технической физики. 1964. № 2.

114. Власов К. П., Кокушкин Н. В. Об ошибках при измерении температуры при горении с помощью термопар. М., Изв. АН СССР, ОТН, 1957, № 8.

115. Орлов Б. В., Мазинг Г. Ю., Рейдель А. Л., Степанов М. И., Товсеев Ю. И. Основы проектирования ракетно-прямоточных двигателей. М., «Машиностроение», 1967.

116. Волынский М. С. О форме струи жидкости в газовом потоке. М., Оборонгиз, 1958.

117. Bourgue C., Newman B. G. Reattachment of a two dimensional incompressible jet to an adjacent flat plate. «The Aeronautical Quarterly», 1960, vil. XI, pp. 3, 201—233.

118. Идельчик И. Е. Справочник по гидравлическим сопротивлениям. М., Госэнергоиздат, 1960.

119. Osmon W. G. Hypersonic propulsion. «Space Aeronautics», 1964, vol. 41, N 3.

120. Barrere M., Moutet A. La propulsion par fusees hybrides. 14 Congr. internat. astronaut. 1963, Paris (Rapp. № 122 pp. 1 - 72.

121. Алемасов В. Е. Теория ракетных двигателей. М., Оборонгиз, 1962.

122. Баррер М. и др. Ракетные двигатели. М., Оборонгиз, 1962.

123. Абрамович Г. Н. Прикладная газовая динамика. М., Гостехтеориздат, 1953.

124. Pai S. I., Smith S. T. A theory of the cylindrical supersonic propulsive nozzle. «J. Roy. Astronaut. Soc.», 1958, vol. 62, No. 10.

125. Harold I. Hage, Ronald A. Segars. Choked flow a generalization of the concept and some experimental data. AIAA Journal, 1965, vol. 3, № 12.

126. Крокко Л. Одномерное рассмотрение газовой динамики установившихся течений. (В книге «Основы газовой динамики», ИЛ, 1963).

127. Эльсгольц Л. Э. Вариационное исчисление. М., Физматгиз, 1958.

128. Гиневский А. С., Назарова Л. И., Шубин Ю. М. Исследование микроструктуры турбулентной струи в спутном потоке. МЖГ, 1966, № 4.

129. Crocco L., Lees L. A mixing theory for the interaction between dissipative flows and nearly isentropic streams. IAS, 1952, vol. 10, No. 10. (Перевод: БРТ, 1953, № 2).

130. Хорнер С., Чепмен Д., Перкинс Э., Унк Р. К вопросу о донном вакууме. БРТ, 1964, вып. 3.

131. Korst H. H. A theory for base pressures in transonic and supersonic flow. «J. Appl. Mech.», 1956, vol. 23, No. 4 (Перевод: «Механика», 1957, № 5).

132. Nash I. F. An analysis of two-dimensional turbulent base flow, including the effect of the approaching boundary layer. ARC RM, 1963, No. 3344.

133. Тагиров Р. К. Влияние пограничного слоя на донное давление. М., Изд. АН СССР, МЖГ, 1966, № 2.

134. Антонов А. И., Бондарев Е. Н. Приближенный метод расчета турбулентного пограничного слоя при положительном градиенте давления. М., Изд. АН СССР, МЖГ, 1968, № 1.

135. Тарнопольский М. Д., Голиков Е. С. К вопросу определения донного давления за уступом при срывном течении. ИФЖ, 1966, № 6, т. X.

136. Chow W. L. On the base pressure resulting from the interaction of a supersonic external stream with a sonic or subsonic jet. IASS, 1959, vol. 26, N. 3 (Перевод: Механика, 1959, № 6).

137. Тагиров Р. К. Определение донного давления и донной температуры при внезапном расширении звукового или сверхзвукового потока. М., Изд. АН СССР, ОТН, «Механика и машиностроение», 1961, № 5.

138. Бондарев Е. Н. Приближенная оценка влияния турбулентного пограничного слоя и отношения удельных теплоемкостей на донное давление за плоским уступом. М., Изд. АН СССР, «Механика и машиностроение», 1964, № 3.

139. Page R. H., Korst H. H. Non-isoenergetic compressible jet mixing with consideration of its influence on the base pressure problem. Proc. Fourth Midwestern Conference Fluid Mech., Purdue Univ., Sept., 1955.

140. Нейланд В. Я. О расчете характеристик срывной зоны и донного давления при обтекании тел сверхзвуковым потоком газа. Инж. журнал, 1965, т. V, вып. 1.

141. Аубакирова В. Р., Трофименко А. Т. Изучение движения неизотермической струи вдоль твердой поверхности. Изв. АН Каз. ССР, Сер. энергетическая, 1962, № 2(22).

142. Pabst O. E. Die Ausbreitung heißer Gasstrahlen in bewegter Luft. «Luftfahrtechnik», 1960, Bd. 6, No. 9—10.

143. Artur R. Anderson, Frank R. Johns. Supersonic jets exhausting into quiescent air. Jet Propulsion, 1955, vol. 25, No. 1, pp. 13—15.

144. Зельдович Я. Б. К теории горения непеременшанных газов. ЖТФ, 1949, т. XIX, вып. 10.

145. Паттерсон Г. Молекулярное течение газов. М., Физматгиз., 1960.

146. Гиршфельдер Дж., Кертисс Ч. и Берд Р. Молекулярная теория газов и жидкостей. М., ИЛ, 1961.

147. Laurence C. L. Intensity, scale and spectra of turbulence in mixing region of free subsonic jet. Report NACA, 1956, No. 1292.

148. Kovaznay L. S. Turbulence in supersonic flow. «J. Aeronaut. Sci.», 1953, vol. 20, No. 10, pp. 657—674.

149. Атмосферная диффузия и загрязнение воздуха. Сборник материалов Оксфордского симпозиума под редакцией Ф. Н. Френкиля и П. А. Шеппарда. М., ИЛ, 1962.

150. Мальцев А. И. Экспериментальное исследование ускоренной молекулярной диффузии при турбулентном смешении спутных сверхзвуковых потоков в цилиндрическом канале. МЖГ, 1970, № 6.

151. Ламли Дж., Пановский Г. А. Структура атмосферной турбулентности. М., «Мир», 1966.

152. Прудников А. Г., Сагалович В. Н., Юкина Э. П. В сб. «Турбулентные течения». М., «Наука», 1970, стр. 154.

153. Прудников А. Г., Сагалович В. Н. В сб. «Кинетика и аэродинамика процессов горения газов». М., «Наука», 1969.

154. Зимонт В. Л. Экспериментальное исследование турбулентной диффузии в каналах переменного сечения. МЖГ, 1968, № 3.

155. Зимонт В. Л. В сб. «Турбулентные течения». М., «Наука», 1970.

TABLE OF CONTENTS

SYMBOL LIST

п	v	vapor
с	m	mixture
т	T	fuel
с	n	nozzle
и	v	vaporization
р	s	spray
м	M	Mach
зв	sd	sound
ж	l	liquid
см	mx	mixture
т	T	thermal
т	T	turbulent, turbulence
т	T	fuel
в	w	wave
в	a	air
мт	MT	microturbulent
о	0	stagnation
г	g	gas
г	c	combustion
д	d	dynamic
ст	st	static
ср	av	average
р	e	equilibrium
н	r	reference
и	i	integration
и	ev	evaporation
нас	s	saturation
кип	b	boiling
др	at	atomization
дин	dyn	dynamic
н	r	resting
н	s	saturation
р	a	atomizer

Ф	c	cone
КР	cr	critical
ПР	lim	limiting
МАХА	M	Mach
П.С	n.s	normal shock
Д	a	atomization
ОТБ	ch	choice
П	p	meaning unknown
Н.Г	l.b	lower boundary
В.Г	u.b.	upper boundary
К	d	drop
ЗАМК	cl	closed
НЕЗАМК	noncl	nonclosed
Э	e	experimental
А	at	atmospheric
М	m	median
Ж.Н	l	liquid leg
КАМ	c	chamber
К	c	chamber
П	f	flight
Н	H	meaning unknown
Р	d	decay, discontinuity
В	v	vortex
Л	l	laminar
ОВ	v.f	vortex formation
М	m	instantaneous
Ф	p	phase
Р.В	v.d	vortex decay
О	t	total
МВ	mv	molecular, vortex
МР	md	molecular, decay
С	c	grey
М	M	molecular
РАСЧ	calc	calculated
ИСT	true	true
С	p	property

Р	tk	tank
С	c	greyness
ЗФ	ef	effective
С	c	center
Ф	f	front
ТР	fr	friction
Н	n	normal
ТР	pp	pipe
Д	b	base
Н	e	external
Р	p	pressure
СВ	em	emission
ОН	Oo	off-design
Н	o	off-design
СК	sh	shock
Я	c	core
Н	I	initial
Т	s	stagnation
Ц	c	cylinder
Щ	s	meaning unknown
С	e	emission
С	c	channel
С	c	exit
Г	b	burner
П	p	preheat
ХИМ	chem	chemical
В	u	upper
Н	l	lower
Н.Т	n.t	microturbulent combusion
СГ	cb	combustion products
Ф	f	flame
С	c	jet

ОС	as	axisymmetric
ПЛ	pl	plane-parallel
П	d	delivery
И	i	isobaric
ГГ	gg	gas-generator
Г	g	generator
СВ	fr	free
СЛ	mg	merging
ЭКВ	eq	equivalent
П	a	attachment
Э	e	Euler
С.Г	g.m	mixture temperature